The 17th Symposium · Since 1994
Korea Japan Joint Symposium
On Building Materials & Construction

Sustainable
Korea × Japan
2026CNCC

The 17th

KOREA-JAPAN JOINT SYMPOSIUM ON BUILDING MATERIALS & CONSTRUCTION

Building a Sustainable Future-Carbon Neutrality
In Cement & Concrete

PROCEEDINGS

2026. 09. 03~05

Kongju National University

Cheonan, Korea

Symposium Homepage

Paper Download

Organizing Committee

Organizing Chairman

Kim Jinman, Kongju National University
Hama Yukio, Muroran Institute of Technology / Hokkaido Univ.

Vice Chairman

Kim Gyuyong, Chungnam National University
Kitagaki Ryoma, Hokkaido University

Advisers

Han Cheongoo, Cheongju University
Song Hayoung, Hanbat National University
Oh Sangkeun, Seoul National University of Science and Tech.
Tanaka Kyouji, Institute of Science Tokyo
ABE Michihiko, Kogakuin University
Ohkubo Takaaki, Hiroshima University

Organizing Committee

Cho Sunghyun, Hanil Cement
Choi Hyeonggil, Kyungpook National University
Choi Sejin, Wonkwang University
Choi Sunmi, CSM
Han Dongyeop, Gyeongsang National University
Han Mincheol, Cheongju University
Kang Sukpyo, Woosuk University
Kim Byoungil, Seoul National University of Science and Tech.
Kim Euichul, Korea Cement Association
Kim Haseog, Dodam E&C
Kim Sungjin, Hanbat National University
Kwon Youngjin, Hoseo University
Lee Donghoon, Hanbat National University
Lee Guncheol, Korea National University of Transportation
Lee Jaeyoung, Dongeui University
Lee Sangsoo, Hanbat National University
Lee Taegyu, Semyung University
Nam Jeongsoo, Chungnam National University
Park Heonil, Korea Conformity Laboratories
Park Sungyu, Mokwon University
Ra Jeongmin, Korea Aggregates Research Institute
Shin Sangchul, Kongju National University
Song Hun, Korea Institute of Ceramic Engineering and Tech.
Dosho Yasuhiro, Meijo University
Hamasaki Hitoshi, Shibaura Institute of Technology
Ishihara Saori, Chiba Institute of Technology
Ito Korekiyo, Tokai University
Kanematsu Manabu, Tokyo University of Science
Kim Jihoon, Muroran Institute of Technology
Kim Junho, Tokyo University of Science
Koga Junko, Institute of Science Tokyo
Koyama Tomoyuki, Kyushu University
Li Yutong, Tokyo University of Science
LI Zhuguo, Yamaguchi University
Sakihara Kohei, University of the Ryukyus
Sato Sachie, Tokyo City University
Seo Wonwoo, Kyushu Sangyo University
Taniguchi Madoka, Muroran Institute of Technology
Yuasa Noboru, Nihon University

Greeting

Welcome to Kongju National University

It is our great honor and pleasure to welcome all participants to the 17th Korea-Japan Joint Symposium on Building Materials and Construction, held at Kongju National University in Cheonan, Korea.

The Korea-Japan Joint Symposium originated in 1994 from laboratory-level academic exchanges between Chungnam National University and Hokkaido University in Japan. Over the past three decades, it has grown into a leading platform for academic exchange in the field of building materials and construction, bringing together universities, research institutes, and industries from both countries to promote technological cooperation and industrial development.

This year's symposium also carries special meaning as we remember the late Professor Moohan Kim, who first envisioned and founded this symposium in 1994 and devoted himself tirelessly to its growth over the past three decades. Professor Kim passed away earlier this year, and it is with deep gratitude and a profound sense of loss that we dedicate this 17th symposium to his memory. His vision of academic exchange and cooperation between Korea and Japan continues to live on through this gathering, and we remain committed to carrying forward the legacy he built.

In recent years, growing attention to decarbonization strategies and the realization of a circular economy particularly in the cement and concrete industries has highlighted the importance of closer collaboration between academia and industry. Reflecting this trend, the 17th symposium has been designed as a forum for in-depth discussions on technological solutions and future strategies involving both sectors.

Hosting this year's symposium at Kongju National University, an institution committed to academic excellence and international cooperation, adds special significance to the event. We hope that the setting of Cheonan and the university's supportive academic environment will foster productive discussions and meaningful exchanges.

We sincerely thank all organizing committee members, partner institutions, and contributors for their dedication and support. We wish all participants a rewarding symposium and a pleasant stay in Cheonan.

Prof. Jinman Kim
Organizing Committee Chair
Kongju National University

Program

Date	Time	Event			
9/3 (THU)	18:30~20:30	Welcome Reception			
9/4 (FRI)	09:00~09:30	Registration			
	09:30~09:50	Opening Ceremony			
		• Opening Address: Prof. Kim Jinman (Kongju National University) • Welcome Address: Dean of College of Engineering, Lee Dongju (Kongju National University) • Congratulatory Address: Vice Chairman, Lee Changki (Korea Cement Association) • History Report: Prof. Nam Jeongsoo (Chungnam National University)			
	09:50~10:00	Memorial Ceremony for the Late Prof. Kim Moohan			
		• Tribute Video in Memory of the Late Prof. Kim Moohan • Memorial Address: Prof. Kim Gyuyong (Chungnam National University) Prof. Kitagaki Ryoma (Hokkaido University)			
	10:00~12:00	Keynote Speeches			
		Speaker: Oh Sangkeun (Seoul National University of Science and Technology)	Speaker: Hama Yukio (Muroran Institute of Technology)	Speaker: Kwon Youngjin (Hoseo University)	Speaker: Dosho Yasuhiro (Meijo University)
		Topic: Advances in Waterproofing Technologies for Ensuring the Long-Term Durability of Concrete Structures	Topic: Memories of Prof. Kim Moo-Han and Concrete in Cold Regions	Topic: Fire Prevention Policy Research Activities Considering Major Fire Cases in Korea	Topic: Evaluation and Application of Optimal Building Materials and Construction Methods for Reducing Environmental Impact
	12:00~13:00	Lunch Break			
	13:00~15:00	Parallel Session I			
		Professional Session 1	Student Session 1 (Sustainable Materials I)	Student Session 2 (Material Properties I)	Student Session 3 (Binder & Hydration)
	15:00~15:20	Poster Session & Coffee Break			
	15:20~17:20	Parallel Session II			
		Professional Session 2	Student Session 4 (Sustainable Materials II)	Student Session 5 (Material Properties II)	Student Session 6 (Structure & Safety)
	17:20~17:30	Closing Ceremony			
		▪ Closing Address: Prof. Kim Jinman (Kongju National University) Prof. Hama Yukio (Muroran Institute of Technology) ▪ Group Photo			
	17:30~18:00	Transfer to Banquet Venue			
	18:00~20:30	Awards Ceremony & Banquet			
9/5 (SAT)	09:00~10:00	Memorial Visit to the Late Professor Moohan Kim's Gravesite			
	10:00~15:00	Baekje Cultural Tour in Buyeo			

Contents

Keynote Speeches

1. Advances in Waterproofing Technologies for Ensuring the Long-Term Durability of Concrete Structures (Presentation only)

Oh Sangkeun

2. Memories of Prof. Kim Moo-Han and Concrete in Cold Regions (Presentation only)

Hama Yukio

3. Fire Prevention Policy Research Activities Considering Major Fire Cases in Korea (Presentation only)

Kwon Youngjin

4. Evaluation and Application of Optimal Building Materials and Construction Methods for Reducing Environmental Impact 2

Dosho Yasuhiro

Professional Session 1

1. South Korea's Strategic Plan for Achieving Carbon Neutrality By 2050 (Presentation only)

Kim Euichoel

2. Fundamental Study of Comprehensive Deterioration Detection Model based on Multimodal contextual understanding AI 11

Kitagaki Ryoma, Oh Dayoung

3. Reliability-Based Design and Provisional Standardization of Low-Clinker Ternary Blended Cements Using a 1% Lower-Tail Strength Criterion 17

Kim Jinman, Shin Sangchul, Kim Geonwoo, Kang Namgyu

4. Investigation of Measures to Improve the Carbonation Resistance of Geopolymers 24

LI Zhuguo

5. Effect of Repeated Air Pressure on Chloride Transport in Reinforced Concrete of an OWC Wave Energy Structure 30

Kim Gyuyong, Ko Minjeong, Pebrian Candra Dwi, Eu Hamin, Nam Jeongsoo

Professional Session 2

1. Low-Carbon Cement and Concrete (Presentation only)

Jean-Michel Rey

2. A Basic Study on Automated Cross-Building Tile Debonding Detection Using Impact Sounds 36

Li Yutong, Imamoto Keiichi, Kiyohara Chizuru, Ohkubo Takaaki, Sugiyama Kazuya, Umeda Koichi, Sugiyama Tatsuya

3. A Study on the Revision Direction of the Korean Ordinary Portland Cement Standard 42

Shin Sangchul, Kang Namgyu, Kim Geonwoo, Kim Jinman

4. Development and Application of a Load Reduction Method for Slabs During Upper-Floor Demolition 49

Matsumoto Takuya, Yuasa Noboru, Aoki Takayoshi, Fukumoto Katsuya

5. Current Status of Aggregate Supply and Quality Control in Korea 59

Ra Jeongmin, Lee Jeahyung

Student Session 1 (Sustainable Materials I)

1. Analysis of the Hydration Behavior of Air-Classified Recycled Concrete Fines Used as Supplementary Cementitious Materials 64

Kim Geonwoo, An Taeyun, Kang Namgyu, Shin Sangchul, Kim Jinman

2. Effects of Various Factors on the Performance of Recycled Aggregate Concrete 68

Okada Yuta, Dosho Yasuhiro, Nishikigi Kenji

3. Evaluation of dry Bottom Ash as a Supplementary Cementitious Material Based on Its Pozzolanic Reactivity and Hydration Behavior 74

Kang Namgyu, Kim Geonwoo, An Taeyun, Shin Sangchul, Kim Jinman

4. Recycling of Concrete Waste Contaminated with Low-level Radioactive Materials 80

Yamasaki Riko, Dosho Yasuhiro, Murakami Kazuo

5. Properties of Artificial Stone Mixed with Sewage Sludge 86

Jeong Yeongseok, Kim Jihun, Chae Kyoungjun, Jeung Kwanyong, Cho Byoungjoon, Lee Sangsoo

6. Long-Term Strength Development Characteristics of Concrete Using Coal Gasification Slag Fine Aggregate at the Age of Five Years 90

Tsuji Takumi, Sato Sachie, Matsuura Tadataka, Koyama Akio

7. Analysis of Physical and Chemical Characteristics of Domestic Paper Sludge Ash and Evaluation of the potential for utilizing construction materials 96

Kim Sigon, Kim Wonchang, Im Hajun, Lee Taegyu

8. Carbon-Sequestering Green Cement Using Blast Furnace Slag and Fly Ash as Raw Materials 98

Ota Niman, Nishimura Jion, LI Zhuguo

Student Session 2 (Material Properties I)

1. Concrete Mix Design Using Machine Learning and Multi-Objective Optimization Methods Based on Experimental Data from Previous Studies 104

Tamura Shota, Sato Sachie, Yamada Yoshitomo

2. Electrical Properties of Cement-Based Materials Reinforced with Steel Fiber 110

Kim Yongjoon, Nam Jeongsoo, Lee Yaechan, Choi Byungcheol, Nguyen Thinh Phat, Pebrian Candra Dwi, Kim Gyuyong

3. Shrinkage Evaluation of Recycled Aggregate Concrete Considering Moisture-Induced Deformation of Recycled Aggregates 114

Hozoji Yuta, Sato Sachie, Honoka Kato, Tanano Hiroyuki

4. Evaluation of Mechanical and Self-Healing Performance of Alkali-Activated Composites with Self-Healing Capsules 120

Park Jeongyeon, Shin Minji, An Eunbee, Park Doyoung, Lee Jaein, Choi Sejin

5. Optimization of Mix Proportions of Recycled Aggregate Concrete-Class M Considering Environmental Assessment 124

Onoyama Kohta, Dosho Yasuhiro, Taguchi Takashi, Shimizu Keisuke

6. Bond Strength Characteristics of GFRP and CFRP in Highly Alkaline Environments 130

Kim Jusung, Lee Duhyuk, Park Sungyu

7. Relations between Surface Asperities and Various Performances in Epoxy Resin Floors 132

Minegishi Yuma, Fukuda Shintaro

8. Analysis of Radiation Shielding Properties of Concrete Incorporating Heavyweight Aggregates 138

Ko Minjeong, Nam Jeongsoo, Lee Yaechan, Lee Jeongtaek, Kim Yongjoon, Nguyen Thinh Phat, Kim Gyuyong

Student Session 3 (Binder & Hydration)

1. Influence of external mixing on the hydration process and compressive strength in fly-ash blended concrete: An Investigation Using Limestone Powder 144

Nguyen Thinh Phat, Kim Gyuyong, Eu Hamin, Lee Jeongtaek, Kim Yongjoon, Pebrian Candra, Nam Jeongsoo

2. Non-Destructive Evaluation of Hydration Progress in Cement Paste Based on Dielectric Relaxation Processes 150

Saito Shintaro, Sato Sachie, Sudo Seiichi

3. Properties of Carbonation Curing Cement Paste with $Ba(OH)_2$ and $Mg(OH)_2$ 156

Kim Jihun, Chae Kyoungjun, Jeong Yeongseok, Kim Dokyun, Lee Sangsoo

4. Effects of Anhydrite and Steam Curing Conditions on the Strength Development of Mortar Using Blast-Furnace Slag Cement Type C 160

Goda Rikuto, Kim Jihoon, Hama Yukio, Hirata Yasunobu

5. Effect of SiO_2/Al_2O_3 Molar Ratio and $Ca(OH)_2$ Content on the Compressive Strength of Waste Glass-Based Geopolymers 166

Park Kyueun, Kang Sukpyo

6. Densification Mechanism of the Microstructure in Hardened Alkali-activated Materials 170

Inden Ichito, Dosho Yasuhiro, Taguchi Shouta, Dao Thi Phuong

7. Sustainable Alkali-Activated Composites: Assessing Mechanical Properties and Fire Resistance Performance 176

Lee Jaein, Kim Insong, Kim Jinho, Shin Minji, Park Jeongyeon, Choi Sejin

8. Effect of Ground Granulated Blast-Furnace Slag Addition on Concrete Spalling 180

Toyoshima Akihiro, Kim Junho, Nishio Yuhei, Kanematsu Manabu

Student Session 4 (Sustainable Materials II)

1. Development of Carbon-Sequestering Green Cement Using Iron and Steel Slags 184

Nishimura Jion, Ota Niman, LI Zhuguo

2. Evaluation of Fundamental Properties and Reactivity of Lithium Slag Powder for Application as a New Cement Additives 190

An Taeyun, Kim Geonwoo, Kang Namgyu, Shin Sangchul, Kim Jinman

3. Concrete Waste Recycling in Vietnam 194

Tran Thi Phuc, Dosho Yasuhiro, Dinh Van Linh, Nguyen Anh Duc

4. Case study on engineering properties of mortar with waste plastic pyrolysis by-product 200

Youn Hyeyoung, Kim Gyuyong, Choi Byungcheol, Ji Sungjun, Go Yeonwoo, Song Seunghoon, Nam Jeongsoo

5. Development of Environmentally Friendly Concrete Fabricated Using Alkali-activated Materials and Low-quality Recycled Aggregates 205

Iwano Wako, Dosho Yasuhiro, Taguchi Shota, Kondo Naoto

6. Industrially Relevant Early-Age Carbonation Curing of High-Calcium Fly Ash Blended Mortars: CO_2 Uptake, Strength Development, and Dimensional Stability 211

Mahmudullah Md, Kang Sukpyo, Park Kyueun, Lee Byoungky

7. Effect of adding blast furnace slag to alkali activated cement made from Hokkaido volcanic glass powder on the properties 219

Kojima Kaishi, Kim Jihoon, Taniguchi Madoka, Hama Yukio

8. Physical Properties of Cement Paste Mixed with Waste Starfish 225

Chae Kyoungjun, Kim Jihun, Jung Yeongseok, Yoo Jaegyun, Lee Sangsoo

Student Session 5 (Material Properties II)

1. Correlation Analysis of Ultrasonic Pulse Velocity and Strength Characteristics of Eco-friendly Concrete Incorporating Non-sintered Hwangto 229

Im Hajun, Kim Taehyeong, Choi Jieun, Lee Taegyu

2. Fundamental Research on Evaluating Wet Conditions of Concrete Surfaces Using ACM-Type Corrosion Sensor 233

Sakon Shuya, Kanematsu Manabu, Kim Junho

3. Effects of Data Aggregation and Test Age on UPV Strength Assessment of Early-Age Frozen Concrete 237

Li Lei, Choi Hyeonggil

4. Corrosion Behavior of Hot-Dip Galvanized Reinforcing Bars Embedded in Concrete Containing Ground Granulated Blast-Furnace Slag 244

Jeong Juntaek, Choe Hongbok, Kanematsu Manabu

5. Assessment of Residual Mechanical Characteristic Factors of Concrete Exposed to High-Temperature History Using Weighted Analysis Techniques 250

Jang Younga, Kim Sigon, Kim Wonchang, Lee Taegyu

6. Time-Dependent Changes and Improvement Process in Wear Resistance of Surface Reinforcing Materials for Concrete Floors 252

Hamada Sohta, Fukuda Shintaro, Koga Junko

7. Review of the Possibility of Detecting Internal Fire Conditions Using External Heat Flux at Entrances in Building Compartment Fires 256

Nam Youngjin, Jang Younga, Kim Sigon, Lee Taegyu

8. Physical and Chemical Properties of Concrete in a 40-Year-Old Underground Retention Basin 258

Iura Yota, Hamasaki Hitoshi, Fukuda Sugio

Student Session 6 (Structures & Safety)

1. Experimental Research on the Influence of Steel Corrosion on Bond Performance with Concrete Using Neutron Diffraction Method 264

Hayashi Sotaro, Zhou Jiayuan, Kobayashi Kensuke, Kim Junho, Kanematsu Manabu

2. Analysis of Vibration Behavior of an Oscillating Water Column Under Marine Environmental Conditions 268

Pebrian Candra Dwi, Kim Gyuyong, Eu Hamin, Lee Jeongtaek, Ko Minjeong, Van Minh Triet, Nam Jeongsoo

3. A method to evaluate the habitability of walking-induced vibration on reinforced concrete residential buildings in China 272

Pan Ruiqi, Fukuda Shintaro

4. Complex Network Analysis of the Building Fire Ecosystem and Evaluation of Risk Control Utility by Policy Intervention 276

Kim Wonchang, Im Hajun, Kim Taehyung, Lee Taegyu

5. Verification of a Structural Framework for Layered Lamellar Grid Shells Utilizing Bamboo Craftsmanship —Experiments Using a Three-Layer Composite Grid Model— 278

Tsutsumi Asuka, Ejiri Norihiro

6. Assessment of Fire Damage Spread Factors and Risks According to Spatial Characteristics of Industrial Buildings in Cities 283

Choi Jieun, Nam Youngjin, Jang Younga, Lee Taegyu

7. Load Characteristics of Rubbing during Walking that Causes Floor Wear 289

Morita Ayuka, Fukuda Shintaro

8. A Structural Comparative Study on Japan's Jusen Crisis and Korea's Non-Bank Financial Institution Real Estate PF Distress 294

Hwang Suhyeon, Jeong Kyeongtae, Park Jaehyun, Yang Seungjin, Lee Donghoon

Poster Session

1. Waste Concrete-Derived Lysinibacillus fusiformis A15 as an Alkaline-Stable and Highly Sporulating Candidate for MICP in Cementitious Materials 301

Song Hayeon, Choi Sejin, Kim Jungmi

2. Development of a Quality Measurement An Algorithm for Building Finish 305

Jang Yoonho, Jeong Hojeong, Seo Seungha, Ji Sumin, Kim Seongjin

3. Physical and Thermal Properties of Cement Paste with Waste Plastics 311

Ryoo Changwoo, Chae Kyoungjun, Kim Jihun, Jung Yeongseok, Jung Hyunsoo, Lee Sangsoo

4. Synergistic flame retardancy enabled by boehmite/poly(acrylic acid)/ graphene oxide hybrid multilayered nanocomposites 315

Lee Inyoung, Cho Chungyeon

5. Effect of Core Diameter and Coarse Aggregate Content on the Material Properties of Small Diameter Concrete Cores 319

Lee Jeongtaek, Kim Gyuyong, Eu Hamin, Lee Yaechan, Ko Minjeong, Van Minh Triet, Nam Jeongsoo

6. Role of Kenaf Fibers in Improving the Spalling Resistance of Polymer-Modified Cement Mortar 323

Ji Sungjun, Kim Gyuyong, Choi Byungcheol, Youn Hyeyoung, Go Yeonwoo, Song Seunghoon, Nam Jeongsoo

7. Macrocell Corrosion Inhibition Effects of Repair Mortars with Application of Various Countermeasures for Chloride Attack 331

Kumamoto Soshi, Yamada Rikuo, Minami Maki, Takai Osamu, Hama Yukio

8. Relationship between Intra-filament Void Structure and Freeze-Thaw Resistance of 3D printed Concrete with Different Printing Parameters 337

Makino Takaya, Yamada Kaiya, Nakase Kota, Hashimoto Katsufumi, Hama Yukio

9. Study on affect of fly ash and slag on bond strength of geopolymer concrete 343

Nguyen Thien Thanh, Tran Cao Thanh Ngoc, Le Anh Tuan

10. Mechanical Strengths of High-Strength Concrete with Fly Ash Aggregate under Various Moisture States 347

Bui Phuong Trinh, Doan Dinh Khoi, Le Anh Tuan

11. From Site Planning to Material Production: A Decentralized Carbon-Neutral Framework for Post Disaster Housing Reconstruction 355

Allis Nurdini, Lily Tambunan, Dewi Larasati

01

KEYNOTE SPEECH

The 17th Korea-Japan Joint Symposium
on Building Materials & Construction

Building a Sustainable Future-
Carbon Neutrality in Cement & Concrete

環境負荷を低減する最適な建築材料・施工方法の評価と適用に関する一連の研究

Evaluation and Application of Optimal Building Materials and Construction Methods for Reducing Environmental Impact

道正泰弘*1
Yasuhiro Dosho

ABSTRACT

This research demonstrates that the careful evaluation and selection of building materials and construction methods can reduce environmental impacts while promoting sustainability. Key strategies for this purpose include resource conservation, recycling and demolition, and building longevity extension. The findings highlight approaches that enhance resource recyclability, lower carbon emissions, and improve environmental safety. In particular, the research comprises two main categories: I. Research on Recycling and Demolition, which addresses resource conservation and circular economy and II. Research on Building Longevity, which addresses the extension of service life of buildings. Category I comprises three research items: (1) recycled aggregate concrete, (2) the use of supplementary cementitious materials derived from industrial byproducts, and (3) demolition. Meanwhile, Category II comprises two research areas: (1) evaluation of building materials based on life cycle assessment and (2) evaluation methods for steel corrosion.

The results indicate substantial potential in reducing CO_2 emissions, increasing material reutilization, and improving building longevity. These outcomes are expected to be applicable worldwide, particularly in Asia, where rapid development is projected. Overall, the research provides evidence supporting the global transition toward sustainable environmental load in the construction sector.

1. Introduction

In December 1997, the President of the Architectural Institute of Japan (AIJ) [1] issued a statement that reducing the lifetime carbon dioxide (CO_2) emissions associated with newly constructed buildings by 30% requires the service life of buildings to be tripled. In June 2000, five architecture-related associations issued the "Charter on the Global Environment and Architecture," [2] which identified five key principles for realizing a sustainable, circular society: long service life, harmony with nature, energy conservation, resource conservation and recycling, and legacy.

This paper presents a compilation of my research on the evaluation of building materials and construction methods aimed at reducing the environmental impacts of buildings throughout their life cycles.

The research is divided into two main categories: I. Research on Recycling and Demolition, which addresses resource conservation and circular economy, and II. Research on Building Longevity, which addresses the extension of service life of buildings. Category I comprises three research items: (1) recycled aggregate concrete, (2) the use of supplementary cementitious materials derived from industrial byproducts, and (3) demolition. Meanwhile, Category II comprises two research areas: (1) evaluation of building materials based on life cycle assessment (LCA) and (2) evaluation methods for steel corrosion.

Figure 1 illustrates the background, objectives, and overall framework of this research. Table 1 lists the

*1 日本　名城大学　理工学部　環境創造工学科　教授　博士(工学)
Prof. Dept. of Environmental Technology, Meijo University, Japan, Dr. Eng.

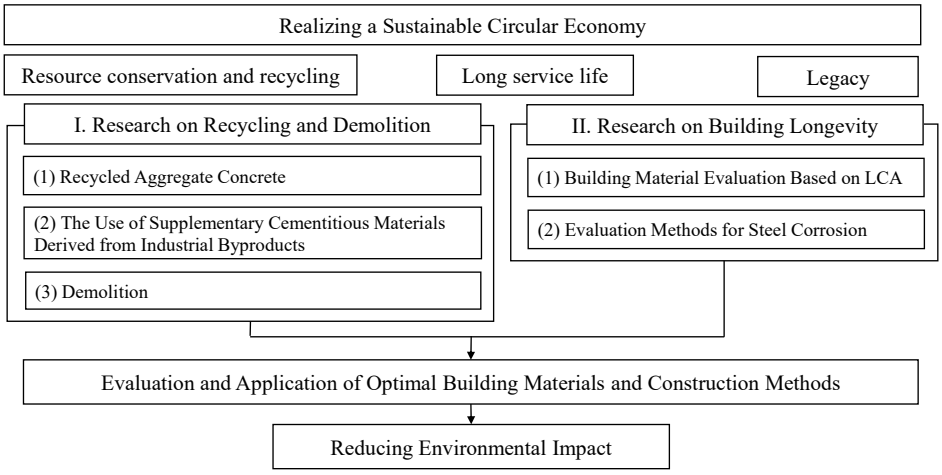

Figure 1 Background, objectives, and overall framework of this research

Table 1 Standard and guidelines related to the findings of this research*

Standard and guidelines	Year of publication/revision	Relevant chapters and appendices
Recommendation for Mix Design, Production, and Construction Practice of Concrete with Recycled Concrete Aggregate [3]	2014	Chapter 11: Recycled aggregate concrete-Class L used in reinforced concrete members Appendix 5: Application examples of recycled aggregate concrete using the aggregate replacement method
JIS A 5022:2018 (Recycled aggregate concrete-Class M)	2018	
Recommendation for Practice of Concrete with Fly Ash [4]	2024	Chapter 2: Required performance of structures and members Chapter 3: Selection and use of fly ash types Chapter 4: Environmental performance of fly ash concrete Chapter 5: Types and quality of fly ash concrete Chapter 7: Mix proportion Chapter 11: Concrete in which fly ash replaces part of the fine aggregate Appendix 5: Technical data on fly ash concrete
Recommendation for Demolition Work (Reinforced Concrete and Steel Structures) [5]	2024	Chapter 2: Performance and requirements for demolition work Appendix 6: Evolution of recycled aggregate concrete

* For papers published after the release of these recommendations and subsequent revisions to JIS, the relevant contents were reviewed and incorporated into the recommendations.

standard and guidelines related to the findings of this research to which I contributed through drafting or revision, including recommendations for recycled aggregate concrete [3], fly ash (FA) [4], and demolition work [5].

2. Research on Recycling and Demolition

2.1 Recycled Aggregate Concrete

The *Recommendation for Mix Design, Production, and Construction Practice of Concrete with Recycled Concrete Aggregate (RCA Recommendation)* [3] published in 2014 outlines a method for mixing recycled aggregate class L (Figure 2) [6] with original aggregate in building construction activities. In 2018, the JIS A 5022 standard was revised to specify recycled aggregate concrete-Class M in which recycled coarse aggregate class L and recycled fine

Figure 2 Appearance of recycled coarse aggregate class L [6]

aggregate class L are mixed with normal aggregate conforming to Annex A of JIS A 5308. Table 2 lists the types of recycled aggregate concrete and aggregate

Table 2 Types of recycled aggregate concrete and aggregate combinations specified in JASS 5 (2022) [7] (excerpt)

Type of recycled aggregate concrete	Coarse aggregate	Fine aggregate
Recycled aggregate concrete: Class M Type 1	All or a part of the coarse aggregate is recycled coarse aggregate class M A portion (volume mixing ratio of 50% or less) of the coarse aggregate is recycled coarse aggregate class L	Normal fine aggregate
Recycled aggregate concrete: Class M Type 2	All or a part of the coarse aggregate is recycled coarse aggregate class M	All or a part of the fine aggregate is recycled fine aggregate class M
		A portion (volume mixing ratio of 30% or less) of the fine aggregate is recycled fine aggregate class L
	A portion (volume mixing ratio of 50% or less) of the coarse aggregate is recycled coarse aggregate class L	All or a part of the fine aggregate is recycled fine aggregate class M
		A portion (volume mixing ratio of 30% or less) of the fine aggregate is recycled fine aggregate class L
	Normal coarse aggregate	All or a part of the fine aggregate is recycled fine aggregate class M
		A portion (volume mixing ratio of 30% or less) of the fine aggregate is recycled fine aggregate class L

* The gray hatched areas (■) correspond to the content addressed in this research.

combinations specified in JASS 5 (2022) [7]. The gray-hatched areas (■) indicate the combinations addressed herein.

My research aimed to replace normal aggregate with low-quality recycled aggregate class L, which contains trace elements such as hexavalent chromium and a high proportion of adhered mortar and paste and to produce concrete that satisfies performance criteria. The use of recycled aggregate instead of normal aggregate reduces environmental impacts and material costs; however, it requires mix proportioning and quality control as well as the use of admixtures such as FA and ground granulated blast-furnace slag (GGBFS) to improve concrete performance [8, 9]. Figure 3 shows the relative quality value method, which was included in the *RCA Recommendation* [3] after verifying its long-term effectiveness. The relative quality value method was used to evaluate the mix proportions of actual ready-mix concrete products [10]. Based on this evaluation, a systematic production process from mix proportion to quality control was developed and the compressive strength reduction ratio was introduced as a new design parameter in mix proportions [6].

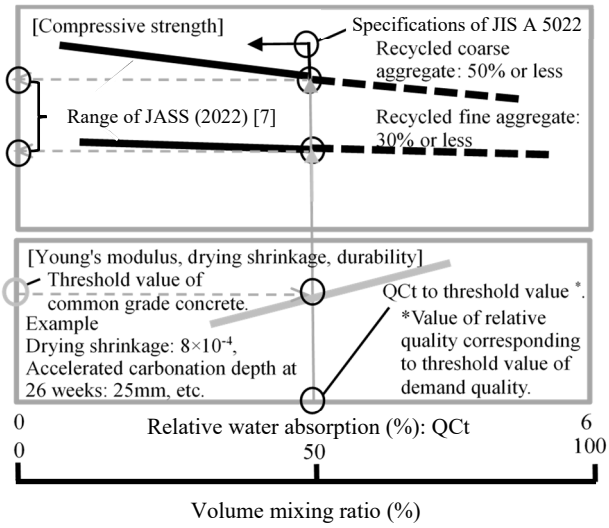

Figure 3 Example of the relationship between relative water absorption and the main properties of recycled aggregate concrete [6]

2.2 The Use of Supplementary Cementitious Materials Derived from Industrial Byproducts

The annual production of coal ash is 11.1 million metric tons. Of this amount, 61.21% is effectively utilized as a raw material for cement and only 1.6% is used in blended cement or as an admixture [11]. Against this background, the AIJ published the *Recommendation for Practice of Concrete with Fly Ash (FA Recommendation)* [4] in 2024. It clarifies that although FA is thought to accelerate carbonation, its use has a minimal impact on rebar corrosion. Rebar corrosion progresses rapidly only when carbonation reach es the rebar and sufficient moisture is present to support this corrosion. By controlling carbonation and moisture availability, such corrosion can be suppressed [12]. The environmental impact of FA-mixed concrete depends on the balance between performance improvements and resource recyclability [13]. As shown in Figure 4, a mix proportioning method was developed that accounts for environmental performance based on the strength contribution ratio (k-value) [14].

Major revisions in the *FA Recommendation* [4]

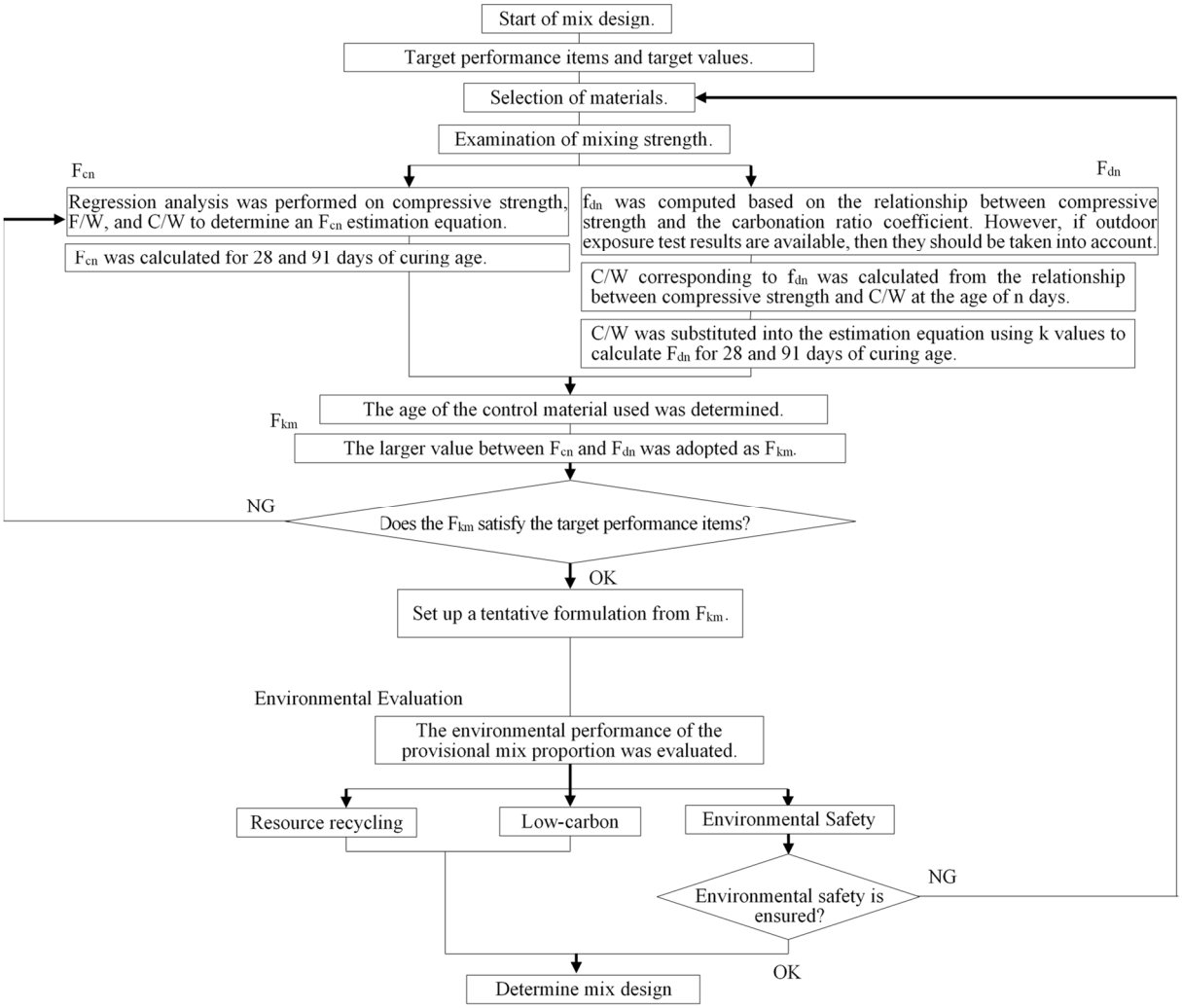

Figure 4 Flow of mix design based on k-values [14]

include those pertaining to the environmental performance of FA concrete and determination of the water–binder ratio based on k-values. As a part of the international demonstration and dissemination of these research findings, FA was used as an admixture in structural concrete in Vietnam [15].

As shown in Figure 5, I demonstrated the potential of cement matrixes incorporating FA and GGBFS in immobilizing radioactive cesium (Cs) dispersed as a result of the Fukushima Daiichi Nuclear Power Plant accident [16] and elucidated the mechanism by which FA suppressed Cs elution during immobilization [17].

2.3 Demolition

Demolition differs from other types of construction projects because it does not produce a tangible end product such as a building or other structures. However, the absence of a tangible end product does not mean that demolition work is free from societal and client requirements. Rather, safety and environmental performance criteria to be achieved must be established via consensus among clients, contractors, and other stakeholders while ensuring compliance with laws and regulations.

The *Recommendation for Demolition Work (Reinforced Concrete and Steel Structures)* [5] introduced a new section titled "Chapter 2: Performance and Requirements for Demolition Work," which establishes three indicators for evaluating demolition work: economic efficiency (cost), safety (risk level), and environmental performance (CO_2 emissions). As shown in Figure 6, these indicators can be compiled into a comprehensive performance index by representing them as vector components in a three-dimensional coordinate system. Simulations of different demolition methods and actual demolition

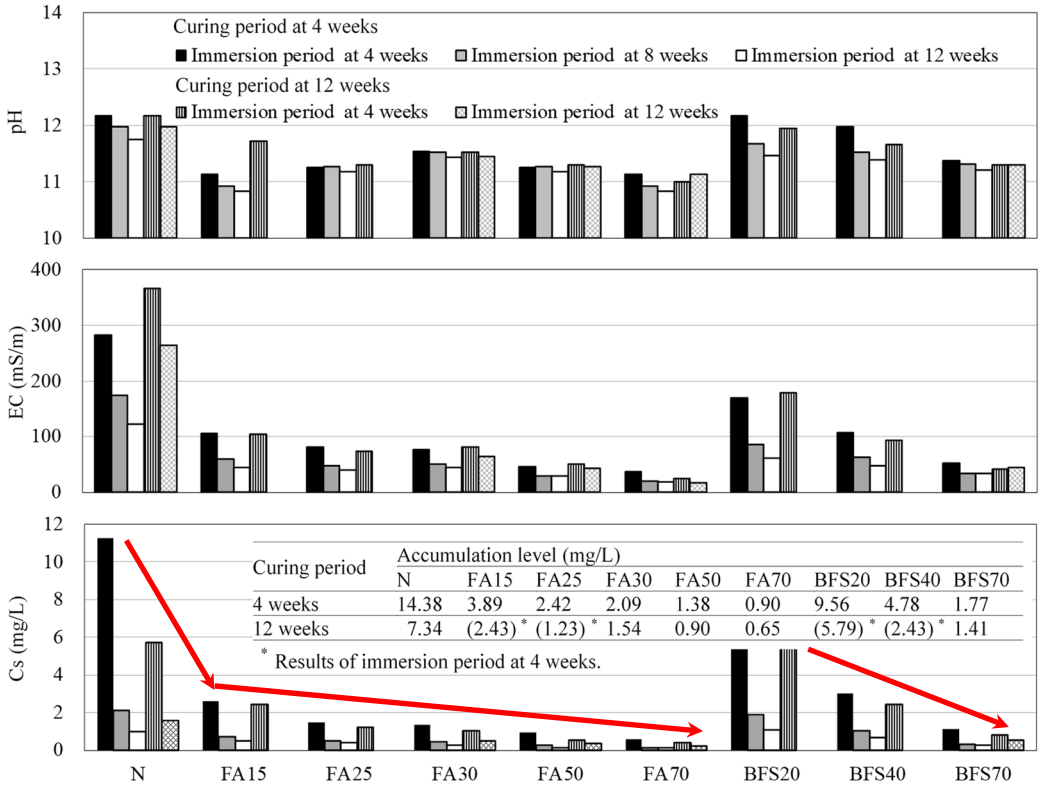

**N: Ordinary Portland cement; FA15–FA70: 15%–70% replacement of N with FA Type II; and BFS20–70: 20%–70% replacement of N with GGBFS4000.

Figure 5 Results of analysis of the immersion liquid of paste specimens [16]**

projects have demonstrated that these indicators can quantitatively and comprehensively evaluate the demolition performance [18].

3. Research on Building Longevity

3.1 Building Material Evaluation of Building Materials Based on LCA

New assessment tools and databases have been developed to evaluate the environmental impacts associated with building materials and building longevity. In Japan, the *Inventory Database for Environmental Analysis* is cited as an example for all industries [19]. In 2024, the AIJ published a guideline [20] that utilizes the 2015 Input–Output Tables for Japan provided by the Ministry of Internal Affairs and Communications and released an LCA tool [21].

In a previous study, I proposed a method for determining maintenance priorities based on the performance evaluation results of building components and parts [22]. In particular, the secondary structural members of large-scale industrial buildings were considered as the research object. I also

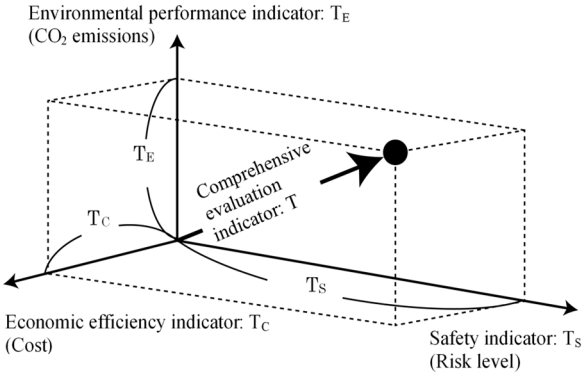

Figure 6 Indicators for evaluating demolition work [18]

demonstrated that an effective approach for extending the service life of buildings is to select maintenance methods according to the remaining service life of buildings estimated from LCA.

As shown in Figure 7, I used the relationship between resource recycling categories and integration of damage assessments of protected entities for environmental impacts in external materials for residential homes to demonstrate that the environmental impacts of all materials can be reduced by ensuring building longevity [23].

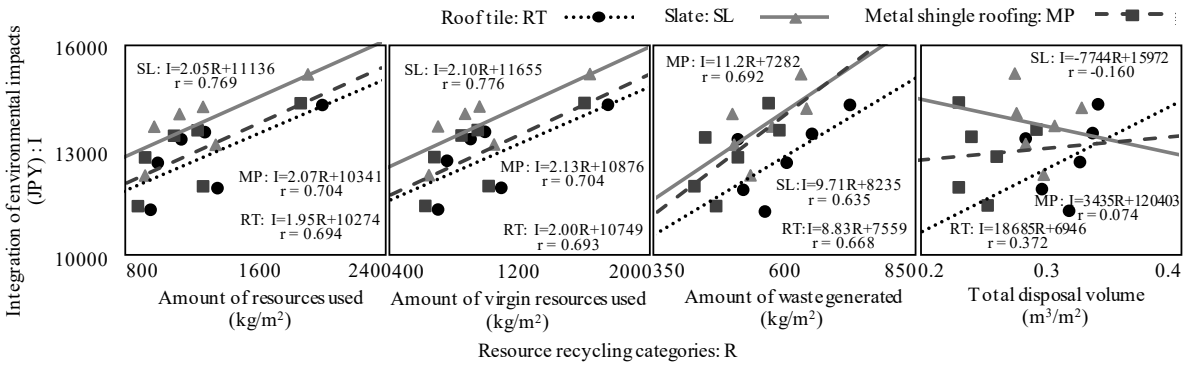

Figure 7 Relationship between resource recycling categories and integrated environmental impacts of roofing materials [23]

3.2 Evaluation Methods for Steel Corrosion

To date, limited data are publicly available on the corrosion of high-strength steel chimneys that have been in service for several decades. Corrosion can considerably affect the structural safety of reinforced concrete and high-strength steel structures. I evaluated the corrosion of rebar in reinforced concrete structures and the material properties of a 200-m-class ultrahigh-strength steel chimney at a thermal power plant that had been in operation for approximately 30 years.

I also investigated whether the extent of rebar corrosion could be evaluated simply from the occurrence of cracks in reinforced concrete structures and developed a method for predicting the amount of corrosion when the rebar diameter and concrete cover thickness are known [24].

I measured strength, fatigue characteristics, and residual stresses and conducted macrostructural and microstructural observations of corrosion-damaged members of the ultrahigh-strength steel chimney. Results revealed that the corroded regions did not adversely affect the material properties of the surrounding noncorroded regions. Therefore, the structural strength can be evaluated by treating the corroded areas as cross-sectional defects [25].

4. Conclusions

My research on recycling and demolition results in the following contributions:

- I establish mix proportioning and quality control methods for concrete incorporating low-quality recycled aggregate class L that can be applied to actual buildings and other structures.
- I establish a method for quantifying the environmental impacts of using recycled aggregates in combination with FA and GGBFS in concrete structures.
- I develop a mix proportioning method that considers the environmental performance of FA to promote its use in concrete structures.
- I demonstrate the importance of evaluating demolition work based on defined performance criteria and outline methods for conducting such evaluations.

My research on building longevity results in the following contributions:

- I demonstrate the usefulness of LCA for evaluating the quality of building materials and selecting appropriate maintenance methods.
- I address corrosion in reinforced concrete structures and ultrahigh-strength steel chimneys and propose specific methods for evaluating corrosion and its effect on the performance of such structures.

These contributions also lead to the following developments:

- Global recycling of concrete resources: As a part of the expansion of circular economy practices in Asia, I demonstrate that recycled aggregates can be used in structural concrete in Vietnam in accordance with the performance requirements of relevant standards [26]. In addition, I conduct a fundamental study on the use of FA as an admixture to promote its widespread adoption [15].
- Applications to other fields: I investigate the application of FA to pavement concrete [27] and shotcrete [28], contributing to the potential development of a broader resource recycling system.
- Suppression of the leaching of hazardous

substances: I demonstrate the potential of using cementitious materials incorporating FA and GGBFS to immobilize radioactive Cs and suppress its leaching following a nuclear power plant accident.

- Establishment of evaluation methods: I develop the first practical method for evaluating the performance of demolition work.
- Promotion of building longevity: I demonstrate the importance of LCA in evaluating building materials and construction methods to increase the longevity of large-scale industrial buildings and residential homes.
- Knowledge transfer: Through direct research guidance, I transfer the technologies developed in this research to the next generation of researchers and other stakeholders.

I hope that the contributions of this research will help reduce CO_2 emissions, promote resource recycling, and extend the service life of buildings. I also hope that these findings will be applied not only in Japan but also globally, particularly in Asia, and will contribute to the achievement of sustainable development on a global scale.

Acknowledgments

Since the beginning of my research career in 1993, more than three decades ago, I have received kind and thorough guidance from my mentor, the late Professor Masafumi Kikuchi of Meiji University. In my research on building longevity, I similarly received kind and thorough guidance from the late Professor Kazuhisa Shirayama, Professor Emeritus at the University of Tsukuba. I express my deepest gratitude to both professors for their support of my research and extend my condolences to their loved ones.

In compiling this research, I received thoughtful guidance from Professor Emeritus Shinji Kawabe of Nagoya Institute of Technology and valuable advice from Professor Zhuguo Li of Yamaguchi University. Professor Akio Koyama of Meiji University provided me with tremendous support throughout the course of this research.

I am deeply grateful to my co-researchers and to the graduates and former students of the Dosho Laboratory at Meijo University for their cooperation. I express my sincere gratitude to Meijo University and Tokyo Electric Power Company Holdings, Inc. for providing my research group with opportunities to conduct research and with a supportive research environment.

I would like to express my deepest gratitude to the late Professor Kim Moo Han, Professor Emeritus at Chungnam National University, for providing me with the opportunity for academic exchange and presentation. I also extend my condolences to his family.

References

[1] President's Statement from the Architectural Institute of Japan (AIJ); the Architecture Sector's Response to Global Warming, 1997. https://www.aij.or.jp/jpn/archives/971202.htm

[2] Charter on Architecture and the Environment; 2000. http://news-sv.aij.or.jp/kensho/kensh.pdf

[3] The Architectural Institute of Japan (AIJ); Recommendation for mix design, production and construction practice of concrete with recycled concrete aggregate, 2014.

[4] The Architectural Institute of Japan (AIJ); Recommendation for practice of concrete with fly ash, 2024.

[5] The Architectural Institute of Japan; Recommendation for demolition work (Reinforced Concrete and Steel Structures), 2024.

[6] Dosho Y., Contributions of Concrete Recycling Technology toward Sustainable Development, Standards and Technologies Related to Recycled Aggregate Concrete in Japan, Journal of materials and engineering structures, 7(4) (2020) 525-549. https://revue.ummto.dz/index.php/JMES/article/view/2615

[7] The Architectural Institute of Japan (AIJ); Japanese Architectural Standard Specification JASS 5 Reinforced concrete work 2022, 2022

[8] Dosho Y., Sustainable Concrete Waste Recycling System: Improving the Performance of Concrete Using Low-Quality Recycled Aggregate, Transportation Research Procedia, 85, (2025) 308-319. DOI https://doi.org/10.1016/j.trpro.2025.03.166

[9] Dosho Y., Effect of mineral admixtures on the

performance of low-quality recycled aggregate concrete, Crystals, 11(6) (2021), 596.
DOI https://doi.org/10.3390/cryst11060596

[10] Dosho Y., Dissemination of technic for concrete using low-quality recycled aggregate to achieve a sustainable environment: examination on design method and validity of recycled aggregate concrete, Journal of materials and engineering structures, 9(4) (2022) 395-402.
https://revue.ummto.dz/index.php/JMES/article/view/3299

[11] Japan Carbon Frontier Organization (JCOAL); Report on the nationwide survey of coal ash (FY 2023 Results), 2025.
https://www.jcoal.or.jp/ashdb/ashstatistics/

[12] Nishikigi K., Dosho Y. and Matsumoto K., Effect of fly ash on the rebar corrosion of concrete, AIJ Journal of Technology and Design, 27(65), (2021) 7-12.
DOI https://doi.org/10.3130/aijt.27.7

[13] Nishikigi K. and Dosho Y., Study on Evaluation of resource recyclability of concrete using fly ash, Proceeding of the Japan Concrete Institute, 45(1) (2023) 124-129.

[14] Nishikigi K., Dosho Y., Dao T. P. and Kondo N., Mix proportion of fly ash concrete based on the strength contribution ratio, Japan Architectural Review, 9(1) (2026) 1-29.
DOI https://doi.org/10.1002/2475-8876.70095

[15] Dao T. P., Dosho Y., Nishikigi K. and Nguyen A. D., Expanding the use of fly ash as an admixture in concrete in Vietnam, Journal of materials and engineering structures, 7(4), (2020) 695-702.
https://revue.ummto.dz/index.php/JMES/article/view/2630

[16] Dosho Y., Murakami K., Tao Y. and Yamamoto T., Control of cesium leaching from contaminated concrete wreckage by admixtures, Advances in Construction Materials, Proceedings of the Conmat'20 Sixth International Conference on Construction Materials - Performance, Innovations, and Structural Implications (2020) CD-ROM.

[17] Murakami K., Dosho Y. and Yamamoto T., Suppression mechanisms for cesium leaching from a fly ash–mixed cement matrix, Japan Architectural Review, 9(1) (2026) 1-18.
DOI https://doi.org/10.1002/2475-8876.70072

[18] Murakami K. and Dosho Y., Review on performance evaluation of building demolition, AIJ Journal of Technology and Design, 31(77), (2025) 109-114.
DOI https://doi.org/10.3130/aijt.31.109

[19] Kobayashi K., Shimokawa K., Matsuzaki R., Suzuki Y. and Isobe T., Development of a background database for building LCA-Analysis based on field survey and development of a unit-conversion database, Journal of Structural and Construction Engineering (Transactions of AIJ), 86(782) (2021) 388-398.
DOI https://doi.org/10.3130/aije.86.388

[20] The Architectural Institute of Japan (AIJ) LCA guidelines for buildings—An assessment tool for addressing global warming, resource consumption, and waste management—Revised edition, 2024.

[21] The Architectural Institute of Japan (AIJ), LCA Tool for buildings; General building edition, ver.6.06, 2024.

[22] Dosho Y., Maintenance priority judgment based on performance evaluation of a nonstructural member, AIJ Journal of Technology and Design, 24(57), (2018) 517-522.
DOI https://doi.org/10.3130/aijt.24.517

[23] Nishio N. and Dosho Y., Performance evaluation oh materials used in housing exteriors based on the life cycle assessment, Journal of Structural and Construction Engineering (Transactions of AIJ), 89(824) (2024) 1104-1115.
DOI https://doi.org/10.3130/aijs.89.1104

[24] Dosho Y. and Kojima M., Study on the estimation for degree of reinforcing bar corrosion by crack width due to reinforcing bar corrosion, Proceeding of the Japan Concrete Institute, 36(1) 2014 1180-1185.

[25] Dosho Y., Kumagai T. and Ura D., Research on changes in material characteristics of existing steel super-tall-chimney due to corrosion, AIJ Journal of Technology and Design, 13(26) (2007) 567-572.
DOI https://doi.org/10.3130/aijt.13.567

[26] Nguyen A. D. and Dosho Y., Performance evaluation and mix proportion design of concrete using low-quality recycled aggregate: Application for structural concrete in Vietnam, Japan Architectural Review, 7(1) (2026) 1-19.
DOI https://doi.org/10.1002/2475-8876.12417

[27] Kamishita R., Dosho Y., Yokota S. and Hasegawa G., The application of pavement materials used only recycled materials, Journal of Japan Society of Civil Engineers, Ser. E1 (Pavement Engineering), 78(2), (2023) I_1-I_9.
DOI https://doi.org/10.2208/jscejpe.78.2_I_1

[28] Dosho Y., Application of recycled aggregate in sprayed mortar and shotcrete, Journal of materials and engineering structures, 11(4) (2024) 471-483
https://revue.ummto.dz/index.php/JMES/article/view/3735

02

PROFESSIONAL SESSION

The 17th Korea-Japan Joint Symposium
on Building Materials & Construction

Building a Sustainable Future-
Carbon Neutrality in Cement & Concrete

Fundamental Study of Comprehensive Deterioration Detection Model based on Multimodal contextual understanding AI

北垣 亮馬※1、呉 多英※1
Ryoma KITAGAKI, Dayoung OH

ABSTRACT

While automated building deterioration detection has advanced, challenges remain regarding generalizability to complex backgrounds. This study proposes a Comprehensive Deterioration Detection Model (CDDM) that integrates a Multimodal Large Language Model (LLM) for contextual image understanding with a specialized segmentation model for quantitative extraction. Comparative experiments reveal that CDDM successfully isolates and quantifies exterior wall cracks amidst complex background noise, significantly outperforming conventional standalone segmentation models.

1. Introduction

Automatic detection of cracks and damage in photographs of buildings has advanced rapidly over the past decade, reaching a high level of accuracy and the ability to handle a wide variety of structural deterioration. However, it remains regarding generalizability to complex backgrounds, diverse materials, and environmental conditions, as well as the ability to perform fully automated quantitative assessments. First, for the detection of typical facade cracks without background noise, a combination of patch classification and pixel-level segmentation using a two-stage CNN + U-Net has been reported to achieve very high performance, with an F1 score of 94–96%[1] For patch classification on masonry walls, an F1 score of approximately 95% and a pixel-level F1 score of approximately 80% have been reported[2].

In another study, transfer learning achieved both accuracy and an F1 score of 100%[3]. Furthermore, for exposed concrete and similar surfaces, detection using models such as AlexNet has demonstrated an average accuracy of around 97%[4]. Furthermore, in comparisons of multiple deep learning models, cases have been reported where models such as InceptionV3 achieve accuracy close to 99–100%[5),6)]

Furthermore, high-precision crack detection has been achieved for photographs taken in environments containing complex background noise (such as windows, pipes, and vegetation)[7]. It has been reported that YOLOv5/YOLOv8-based models and models with attention mechanisms can rapidly detect small, low-contrast cracks and multiple types of "building deterioration (cracks, tile detachment, peeling, etc.)" amidst the cluttered backgrounds of urban environments[8].

Thus, much of the research on crack detection has shifted to machine learning and deep learning, and a wide range of methods—from classification to pixel-level quantification—have been systematized[9] .

Key challenges identified include a lack of high-quality data and the cost of labeling, generalization to complex backgrounds, different materials, and varying lighting conditions, the design of lightweight models capable of real-time operation, and defect extraction that accounts for architectural context (such as doors and windows). In response to these challenges, efforts to develop large-scale public datasets—such as a diverse dataset of over 10,000 facade defect images collected by UAVs—are also progressing[10]

AI technology capable of detecting and extracting exterior cracks and various surface defects from

photographs of buildings and their surrounding environments has reached a stage where it can operate with high accuracy and speed at the research level; however, for fully automated, general-purpose systems at the practical level, challenges remain to be resolved, such as securing more diverse data, improving generalization performance, and ensuring lightweight and real-time operation. While AI systems capable of detecting various concrete cracks do exist worldwide, these were developed by training models on a large volume of photographs taken by drones or similar devices, with the imaging area pre-defined to the "concrete surface." Consequently, these systems have not yet achieved the ability to extract cracks in specific building materials from photographs that include complex material compositions and background elements.

To build an AI capable of detecting and extracting exterior cracks and various surface defects from photographs that include both the building and its surrounding environment at a practical level, it is necessary to train the system on an extremely diverse range of background noise. However, since the actual designs of buildings and background noise are often unpredictable, there is a need for practical models that do not rely solely on training.

Therefore, based on this concept, this study constructed a Comprehensive Deterioration Detection Model based on Multimodal Contextual Understanding AI. We then conducted a comparative accuracy experiment using very common photographs with complex compositions that include areas of building deterioration, comparing the performance of this model against that of segmentation models traditionally used for deterioration extraction.

2. Methods and approaches

2.1 Difference between Multimodal LLM& Specialized Model(Based on Segmentation Model) on Deterioration Detection

Figure 1 shows a detection model using a multimodal LLM, illustrated using cracks in building exterior materials as an example. First, in a multimodal LLM, when an image is input, the image is divided into small patches (sets of pixels), which are then converted into high-dimensional vectors (tokens). At this stage, the system is not specifically searching for areas of deterioration such as "cracks" or "spalling," but rather comprehensively extracting visual features such as edges, textures, and color variations within the image. Next—and this is where it differs most from conventional image recognition AI—the extracted visual tokens are converted into vectors (arrays of numerical values) containing information on color, shape, and edges. These

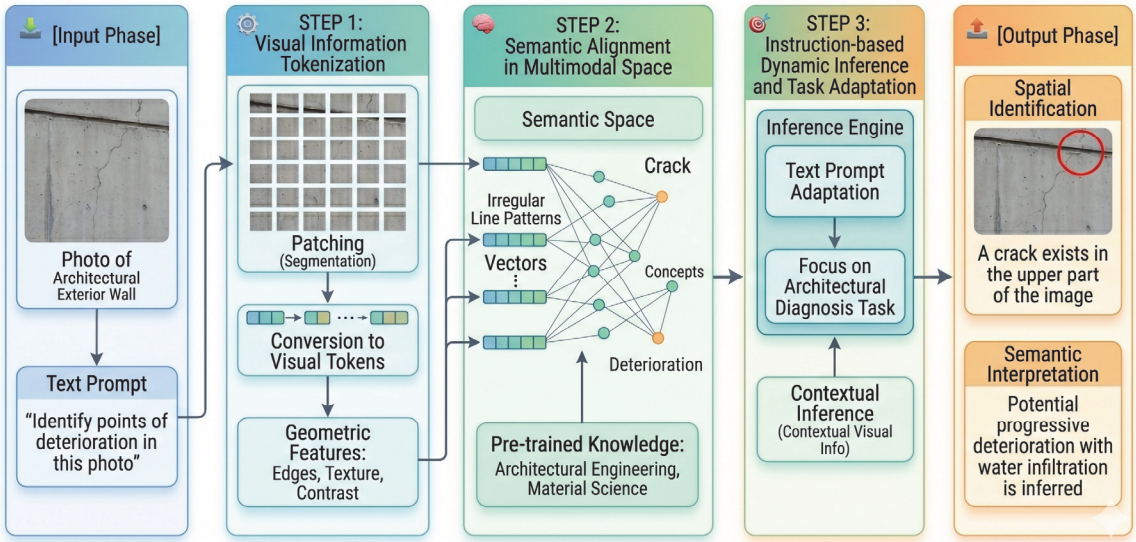

Figure 1 Process of Deterioration Detection by Multimodal LLM

are treated as entities analogous to the words used in LLMs and mapped onto the same vast "semantic space" as the "text" utilized as concepts. Through extensive pre-training, the model incorporates specialized knowledge in fields such as building materials science, cement chemistry, and structural mechanics. As a result, visual tokens within an image—such as "irregular white stains" or "diagonal cracks"—are linked in this space to specialized "concepts (textual knowledge)" such as "efflorescence" and "shear cracks." They are also linked to very common concepts contained within visual tokens, such as grass, trees, sky, clouds, pedestrians, and cars.

As a result, the result is established in which each visual token recognizes not only areas of deterioration but also general objects other than buildings that humans perceive.

Here, when given the prompt "Identify the cracks in the building in this photo," the LLM can output visual tokens corresponding to cracks in the building. Because concepts and visual tokens are linked, it does not detect cracks on the surface of trees or cracks in the ground. Nor does it detect shadows that appear to be cracks. This is because the LLM has already learned patterns of visual tokens that can be linked to various concepts understood by humans. However, in the case of multimodal LLMs, while they recognize cracks through this contextual understanding, their visual vectors are ultimately "meanings" connected to concepts, just like "Text". Therefore, they cannot calculate metrics such as the percentage of the surface area covered by cracks. As a result, they end up identifying a rectangular region containing the crack and providing a detailed description of the crack.

On the other hand, segmentation models (specialized models such as YOLO, SAM 2, DeepLab v3+, etc.), which have traditionally been used for detecting cracks in buildings, excel at precisely identifying (segmenting or object detecting) "where" and "how many pixels" of cracks exist based on geometric features at the pixel level. In this case, the AI is trained to recognize the diverse patterns of changes in the shape and color of cracks against a specific background; it attempts to detect cracks based on their shape and color characteristics without understanding

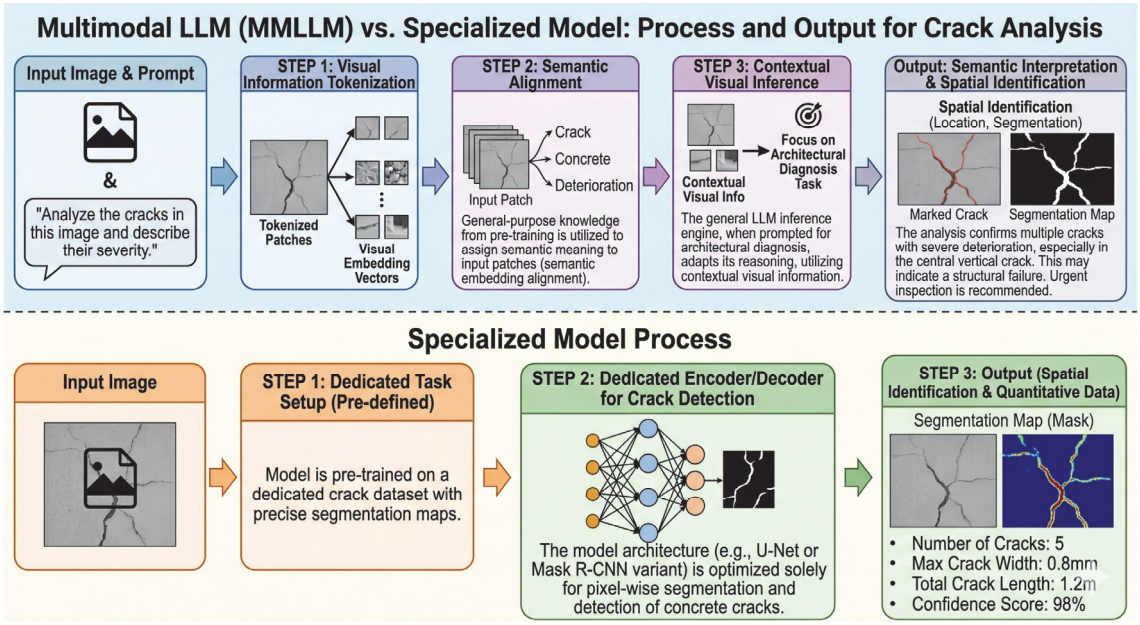

Figure 2 Comparison between Multimodal LLM and Specialized Segmentation model

whether the photograph depicts a tiled wall or a concrete wall. In this scenario, if the photograph shows only a single object, the corresponding area of deterioration can be extracted. However, it becomes difficult for the segmentation model alone to extract cracks in a building from a photo that also includes the ground, other buildings, or the background.

For example, it would detect both cracks in the ground caused by dry soil and cracks on the exterior wall. On the other hand, if the model can infer that a specific area of the image corresponds to a single concept, it can reliably identify the deteriorated area.

2.2 Composition of Comprehensive Deterioration Detection Model based on Multimodal contextual understanding AI

Having understood the differences in deterioration detection between the multimodal LLM and the specialized model (based on a segmentation model) described above, this study proposed a method for using them in combination.

Gemini-3-pro-image-preview was used as the API for the multimodal LLM. We constructed a tool that correctly understands the building's environment and complex structural composition regarding the components and deterioration within an image. While identifying specified areas of deterioration and recognizing the spatial context, the tool outputs "instruction data" that is easily interpretable by the segmentation model.

This data is then fed into the segmentation model, SAM (Segment Anything Model), which subsequently outputs the areas of deterioration in YOLO (You Only Look Once) format. This approach enables the concepts of deterioration detected by the Multimodal LLM to be connected to the segmentation model and quantified. In this paper, we refer to this model as the **Comprehensive Deterioration Detection Model (CDDM)**.

2.3 Experiments

(1) Photos

We prepared photos showing "only the exterior walls" of buildings with cracks, as well as photos that included the building's exterior walls along with other background elements (such as the ground or road) and exterior wall sections of different colors.

(2) We compared the accuracy of crack detection across three methods: cracks detected using only a Multimodal LLM, cracks recognized using only a Specialized Model, and cracks detected using CDDM, which combines both methods. For the Specialized Model, we used Meta's SAM2 with CVAT as the interface. For the Multimodal LLM, we used Gemini-3 Pro. CDDM was implemented using a custom program.

3. Results

(1) The results of crack detection in photographs showing only exterior walls are shown in the figure. In contrast, when using SAM2 for automatic detection, cracks can generally be detected. However, fine and discontinuous cracks cannot be detected. Additionally, the system incorrectly identifies part of the black circular stain in the lower left corner as a crack. On the other hand, in the case of the Multimodal LLM, while the main areas of the cracks are detected along with detailed descriptions of their shapes, the crack areas are not quantitatively recognized.

On the other hand, at the case of CDDM, cracks have been detected more precisely than the results by SAM2.

(2) Crack Detection in Photos Containing Background Noise

The results of crack detection in exterior wall photos containing background noise are shown in the figure below. First, SAM2 failed to detect the cracks and instead filled the entire image with red, treating it as a crack-affected area. Next, the detection method using a Multimodal LLM identified two rectangular

Figure 3-1 Original image

Figure 3-2 Crack detection by SAM2

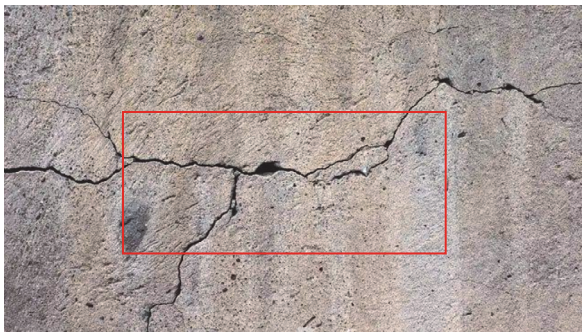

Cracks Using LLM
Central Main Crack:
A thick crack runs horizontally across the center of the image from left to right. This can be considered the "main branch" of this damage.
Lower Central Branch:
A branching line can be seen extending vertically from near the center straight down, meandering slightly as it goes.
Left Branch:
Just before reaching the center from the far left, a thin crack extends diagonally upward (toward the 10 o'clock position on a clock face) and splits into two branches. In summary, this crack is not a shallow surface hairline crack (a crack as fine as a strand of hair), but is presumed to be a relatively serious "structural crack" caused by some form of heavy load (such as drying shrinkage, differential settlement, or external forces like an earthquake) applied to the structural body. In particular, the area around the hole in the center where the concrete is beginning to peel away is in a state where, if left unattended, it is likely to cause further collapse of the surrounding concrete.

Figure 3-3 Results by Multimodal LLM

Figure 3-4 Crack detection by CDDM

regions on the cracked exterior wall as the outline of the cracks and generated a description of the cracks. In contrast, CDDM successfully and accurately recognized the cracked areas on the exterior wall despite the presence of background elements such as the ground and road, as well as exterior walls of different colors.

4. Conclusion

This study constructed a model that accurately detects cracks in exterior walls using CDDM—an approach distinct from conventional models—for images of building deterioration containing complex noise, and reported the results. By having the Multimodal LLM understand the context of the image itself and connecting that understanding to the segmentation model, this method demonstrated the potential to overcome background noise and quantitatively evaluate the specified areas of deterioration.

Reference

1) Chen, K., Reichard, G., Xu, X., & Akanmu, A. (2021). Automated crack segmentation in close-range building façade inspection images using deep learning techniques. *Journal of building engineering, 43*, 102913.
2) Dais, D., Bal, İ., Smyrou, E., & Sarhosis, V. (2021). Automatic crack classification and segmentation on masonry surfaces using convolutional neural networks and transfer learning. *Automation in Construction*.

Figure 4-1 Original image

Figure 4-2 Crack Detection by SAM2(Detection failed)

LLM Explanation of Cracks
Tortoise-shell (network-like) microcracks:
Fine, branching cracks resembling a mesh (map cracks/tortoise-shell cracks) have developed over a wide area, extending from the center to the lower part of the wall and across the column on the right side. This is a typical pattern caused not so much by structural tensile stress (strong force in one direction) as by the entire surface repeatedly contracting and expanding uniformly.
Vertical and diagonal cracks extending upward: At the top of the wall (the white-painted section), relatively single cracks extend vertically or diagonally upward from the dense cluster at the bottom, resembling branches growing from a tree.

Figure 4-3 Results by Multimodal LLM

Figure 4-4 Crack detection by CDDM

3) Deng, J., Singh, A., Zhou, Y., Lu, Y., & Lee, V. C. (2022). Review on computer vision-based crack detection and quantification methodologies for civil structures. Construction and Building Materials
4) Kim, B., & Cho, S. (2018). Automated Vision-Based Detection of Cracks on Concrete Surfaces Using a Deep Learning Technique. Sensors (Basel, Switzerland), 18
5) Krishnan, S., Karuppan, M., Khadidos, A., Khadidos, A. O., Selvarajan, S., Tandon, S., & Balusamy, B. (2025). Comparative analysis of deep learning models for crack detection in buildings. Scientific Reports, 15
6) Wang, P., Xiao, J., Qiang, X., Xiao, R., Liu, Y., Sun, C., Hu, J., & Liu, S. (2024). An automatic building façade deterioration detection system using infrared-visible image fusion and deep learning. Journal of Building Engineering.
7) Fan, Y., Mai, J., Xue, F., Lau, S., Jiang, S., Tao, Y., Zhang, X., & Tsang, W. (2025). UAV and Deep Learning for Automated Detection and Visualization of Façade Defects in Existing Residential Buildings. Sensors (Basel, Switzerland), 25
8) Chen, Y., & Li, D. (2025). Disease detection on exterior surfaces of buildings using deep learning in China. *Scientific Reports, 15*.
9) Yang, G., Jimmy, K., Zhang, J., Zhao, B., Zhao, Z., Chen, X., & Chen, B. M. (2022). Datasets and processing methods for boosting visual inspection of civil infrastructure: A comprehensive review and algorithm comparison for crack classification, segmentation, and detection. Construction and Building Materials
10) Zha, Q., Yao, Y., Zheng, Y., W., & Zhang, W. (2025). A dataset of building surface defects collected by UAVs for machine learning-based detection. Scientific Data, 12

強度分布の下側 1%を基準とした三成分系混合セメントの信頼性設計および標準化に関する研究

Reliability-Based Design and Provisional Standardization of Low-Clinker Ternary Blended Cements Using a 1% Lower-Tail Strength Criterion

金振晩※1、申相澈※2、金建佑※3、姜南圭※4
Jin-Man Kim, Sang-Chul Shin, Geon-Woo Kim, Nam-Gyu Kang

ABSTRACT

This study evaluated the compressive strength and performance limits of ternary blended cements containing GGBFS, FA, and LS at total replacement levels of 10–60%. Compressive strength was measured at 3, 7, and 28 days. Strength decreased with increasing SCMs content, with GGBFS-containing systems showing better strength retention than the FA–LS system. Regression and ANCOVA at 28 days revealed composition-dependent strength reduction, with the FA–LS system showing a significantly steeper decrease than the GGBFS-containing systems. Probabilistic analysis further identified reliability transition zones of approximately 40–50% SCMs for GGBFS–LS and 30–40% for FA–LS at a specified strength of 42.5 MPa. Increasing cement fineness and clinker C_3S content improved compressive strength and strength margins at 28 days. These results support a reliability-based approach to defining composition-dependent SCMs ranges for the provisional standardization of ternary blended cements.

1. Introduction

The cement industry is increasingly required to reduce clinker consumption as part of efforts to mitigate CO_2 emissions associated with cement production. Increasing the use of supplementary cementitious materials (SCMs) is one of the most practical approaches for reducing the clinker factor while maintaining compatibility with conventional cement manufacturing and concrete production systems. In particular, the combined use of multiple SCMs can provide greater flexibility in mixture design and material utilization than binary blended cement systems, thereby contributing to the broader use of available SCM resources.

However, increasing the replacement level of SCMs generally results in a reduction in compressive strength, and the extent of this reduction can vary depending on the types and proportions of SCMs used. Therefore, the applicable replacement level of SCMs cannot be determined solely on the basis of their total content. For ternary blended cements containing combinations of ground granulated blast-furnace slag (GGBFS), fly ash (FA), and limestone powder (LS), the different characteristics and reactivities of these constituents may result in different strength development, particularly at high replacement levels. Accordingly, it is necessary to evaluate the effects of both the total content and combination of SCMs when determining the practical performance range of low-clinker ternary blended cements.

In addition to mean strength, strength variability should be considered when defining the practical

※1 大韓民国 国立公州大学校 建築工学科 教授 博士(工学)
※2 大韓民国 国立公州大学校 建築工学科 研究教授 博士(工学)
※3 大韓民国 国立公州大学校 建築工学科 博士課程
※4 大韓民国 国立公州大学校 建築工学科 修士課程

performance limit of blended cement. Even when the mean compressive strength exceeds a specified strength level, individual results may fall below the requirement when the variability is large. Therefore, a probabilistic evaluation incorporating both the mean and standard deviation can provide additional information on the margin against strength nonconformance. Such an approach may provide a more rational basis for identifying the practical performance boundary of ternary blended cements with increasing contents of SCMs.

Furthermore, extending the applicable range of SCMs at high replacement levels requires measures to compensate for the strength reduction associated with clinker dilution. Increasing cement fineness and using clinker with a higher C_3S content were therefore examined in this study as potential approaches for improving strength performance at high contents of SCMs.

Accordingly, this study evaluates the compressive strength characteristics of ternary blended cements containing GGBFS, FA, and LS over a wide range of SCMs contents. The composition-dependent changes in strength are statistically analyzed, and the strength performance is further interpreted from a probabilistic perspective to evaluate the transition in reliability with increasing content of SCMs. In addition, the effects of increased fineness and higher C_3S content are examined to determine whether these approaches can improve the strength margin and extend the applicable range of ternary blended cements with high contents of SCMs.

2. Materials and Methods

2.1 Materials

A research cement (RC), consisting of Portland cement clinker and gypsum, was used as the base cement. Three types of SCMs, namely GGBFS, FA, and LS, were used to partially replace RC. The GGBFS was equivalent to Grade 3 specified in KS F 2563 [1], and the FA satisfied the requirements for Grade 2 fly ash specified in KS L 5405 [2]. The LS was produced by grinding limestone to a Blaine fineness of approximately 4,500-5,000 cm^2/g. Distilled water and standard sand conforming to KS L ISO 679 [3] were used for mortar preparation.

The physical properties of the cementitious materials are summarized in Table 1. The Blaine finenesses of RC, GGBFS, and FA were approximately 3,560, 4,220, and 3,660 cm^2/g, respectively. For the performance-enhancement experiments, an additional high-fineness RC was prepared by further grinding the original RC in a laboratory ball mill to a Blaine fineness of approximately 4,500 cm^2/g. In a separate clinker-composition experiment, three RCs produced using clinkers with C_3S contents of 64.2, 64.8, and 67.2% were used, while their fineness was maintained at approximately 3,500 cm^2/g.

2.2 Experimental program and mixture design

Three ternary blended cement systems were investigated: RC–GGBFS–FA, RC–GGBFS–LS, and RC–FA–LS. The total replacement level of SCMs ranged from 10 to 60% by mass of the binder. Within each system, the relative proportions of the two SCMs were systematically varied, resulting in 23 compositions per system and a total of 69 blended cement mixtures.

At a total SCMs content of 10%, the two SCMs were used at 5% each. As the total content of SCMs increased, the relative proportions of the two constituents were varied at intervals of 5 or 10%. For example, at a total SCMs content of 40%, four

Table 1 Physical properties of cementitious materials

Material	Description	Density(g/cm^3)	Fineness(cm^2/g)	PSD (Mean, ㎛)	LOI (%)
RC	Clinker + Gypsum	3.15	3,560	16.734	1.10
GGBFS	Grade 3, KS F 2563	2.90	4,220	15.333	0.20
FA	Grade 2, KS L 5405	2.20	3,660	14.240	2.20
LS	Ground limestone	2.80	4,500-5,000	26.128	37.15

combinations of 35/5, 30/10, 25/15, and 20/20% were investigated, whereas six combinations ranging from 55/5 to 30/30% were investigated at a total SCMs content of 60%. The overall experimental matrix is summarized in Table 2.

To evaluate approaches for compensating for the strength reduction at high replacement levels, representative mixtures containing equal proportions of the two SCMs were selected at total SCMs contents of 10, 20, 30, 40, 50, and 60%. Two performance-enhancement approaches were investigated: (1) increasing the Blaine fineness of RC from approximately 3,500 to 4,500 cm^2/g and (2) varying the C_3S content of the clinker from 64.2 to 67.2%. The same GGBFS, FA, and LS were used in these experiments to isolate the effects of cement fineness and clinker composition.

2.3 Mortar preparation and compressive strength test

Mortar specimens were prepared in accordance with KS L ISO 679 [3]. The mortar proportion was 1:3:0.5 by mass for binder, standard sand, and water, respectively. Prismatic specimens with dimensions of 40 × 40 × 160 mm were prepared using a standard mortar mixer. After casting, the specimens were maintained under controlled temperature and humidity conditions for approximately 20-24 h, demolded, and subsequently cured in water at approximately 20°C until testing.

Compressive strength was measured at 3, 7, and 28 days in accordance with KS L ISO 679 [3]. The prism specimens were divided into two halves, and compressive load was applied at a loading rate of approximately 2,400 ± 200 N/s until failure. The measured strength values were used to evaluate the effects of the total content and combination of SCMs as well as the performance-enhancement approaches.

2.4 Statistical analysis

The relationship between the total content of SCMs and compressive strength was evaluated separately for the three ternary systems at each testing age. Linear regression was used to quantify the strength reduction with increasing content of SCMs, and 95% confidence intervals were calculated for the fitted regression lines. Analysis of covariance (ANCOVA) was subsequently performed to determine whether the slopes of the regression lines differed significantly among the ternary systems. A significance level of $p \leq 0.05$ was used to identify statistically significant differences in the strength reduction trends.

To evaluate strength performance from a probabilistic perspective, the reliability index, β was calculated using Eq. (1).

$$\beta = \frac{\mu - S_{DS}}{\sigma} \quad (1)$$

Here, μ and σ are the mean and standard deviation of compressive strength, respectively, and S_{DS} represents the specified strength level. Assuming a normal distribution, the corresponding lower-tail probability, P_f was calculated using Eq. (2).

$$P_f = \Phi(-\beta) \quad (2)$$

Here, Φ denotes the cumulative distribution function of the standard normal distribution. Specified strength levels of 42.5, 37.5, and 32.5 MPa were considered.

Table 2 Composition matrix of ternary blended cements

Total SCMs (%)	RC (%)	Proportion of two SCMs (%)	No. of mixtures per system
10	90	5/5	1
15	85	10/5, 5/10	2
20	80	15/5, 10/10	2
30	70	25/5, 20/10, 15/15	3
40	60	35/5, 30/10, 25/15, 20/20	4
50	50	45/5, 40/10, 35/15, 30/20, 25/25	5
60	40	55/5, 50/10, 45/15, 40/20, 35/25, 30/30	6
Total		23 × 3 systems = 69 mixes	

A reliability index of β=2.33, corresponding approximately to a 1% lower-tail probability under the normality assumption, was adopted as the screening criterion. The criterion can be expressed as Eq. (3).

$$\mu - 2.33\sigma \geq S_{DS} \quad (3)$$

Mixtures satisfying Eq. (3) were classified as being within the reliable region for the specified strength level. The range of SCMs contents over which the strength performance shifted from the reliable region to a region with an increased probability of strength nonconformance was defined as the reliability transition zone (RTZ).

3. Results and Discussion

3.1 Effect of SCMs Content and Combination on Compressive Strength

Fig. 1 shows the compressive strength of the ternary blended cements according to the content and combination of SCMs at 3, 7, and 28 days. Regardless of the combination of SCMs, compressive strength generally decreased with increasing total content of SCMs at all testing ages. This trend became more pronounced at higher replacement levels, indicating that the reduction in clinker content had a dominant influence on strength development.

Clear differences were observed among the three ternary systems. The GGBFS–LS system generally exhibited the highest compressive strength, followed by the GGBFS–FA system, whereas the FA–LS system showed comparatively lower strength. The difference among the systems became more evident as the total content of SCMs increased, particularly at 28 days. These results indicate that the strength performance of ternary blended cement is governed not only by the total content of SCMs but also by their combination and relative proportions.

For the GGBFS–FA and GGBFS–LS systems, compressive strength decreased relatively gradually with increasing content of SCMs. In contrast, a greater reduction was observed in the FA–LS system at high replacement levels. When compared with the specified compressive strength of 42.5 MPa at 28 days, the GGBFS–FA and GGBFS–LS systems maintained the required strength up to a total SCMs content of

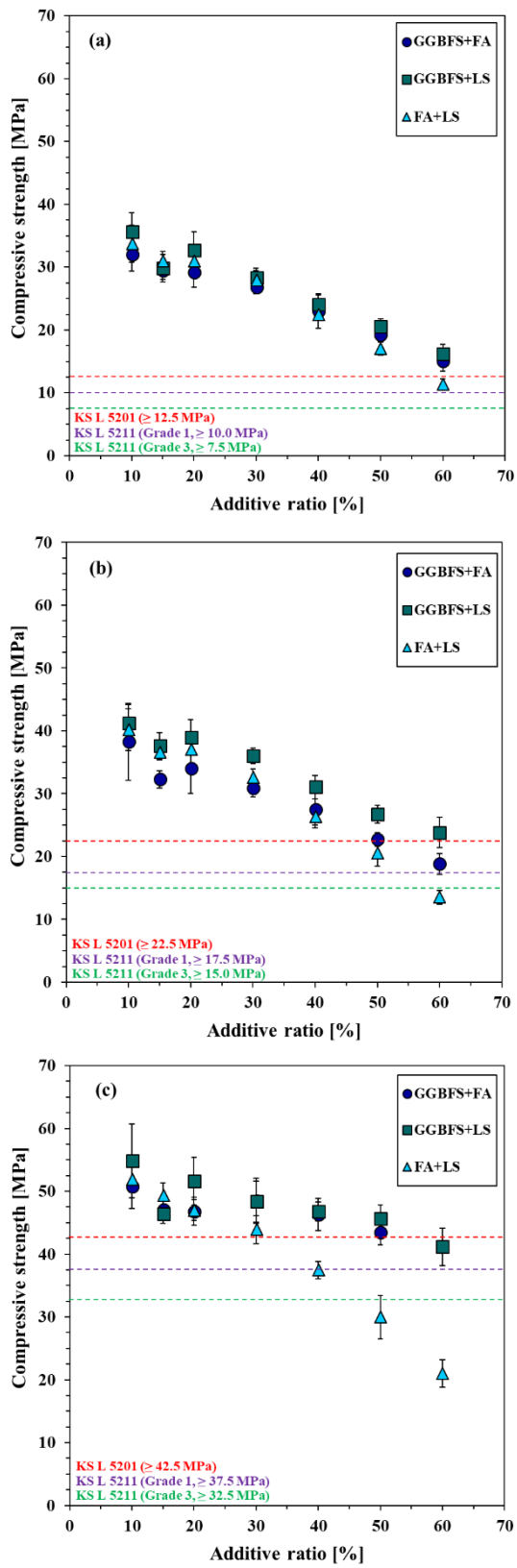

Fig. 1 Compressive strength of ternary blended cements with different contents and combinations of SCMs: (a) 3 days, (b) 7 days, and (c) 28 days.

approximately 40%, whereas the FA–LS system satisfied the requirement up to approximately 30%.

Overall, the results shown in Fig. 1 demonstrate a composition-dependent response to increasing SCMs content, suggesting that a single maximum SCMs content may not adequately represent the performance limit of ternary blended cements.

3.2 Statistical Comparison of Strength Reduction Trends

To quantitatively compare the strength reduction trends among the ternary systems, linear regression analysis was performed between the total content of SCMs and compressive strength, and the differences in regression slopes were evaluated using ANCOVA. Fig. 2 compares the regression results for the three pairs of SCMs combinations using the compressive strength results at 28 days.

As shown in Fig. 2(a), the GGBFS–FA and GGBFS–LS systems showed relatively similar strength reduction trends, and no statistically significant difference was observed between the slopes of the two regression lines (p>0.05). In contrast, the FA–LS system showed a distinctly steeper reduction in strength. Significant differences in regression slopes were observed between GGBFS–FA and FA–LS (Fig. 2(b)) and between GGBFS–LS and FA–LS (Fig. 2(c)) (p≤0.05).

These results statistically confirm the composition-dependent strength behavior observed in Section 3.1. The GGBFS-containing systems showed a comparatively moderate reduction in compressive strength with increasing content of SCMs, whereas the FA–LS system was more sensitive to increasing replacement levels. However, the regression analysis primarily describes the mean strength trend and does not directly account for the variability of individual strength results.

3.3 Probabilistic Evaluation and Reliability Transition Zone

The compressive strength results at 28 days were further evaluated from a probabilistic perspective by considering both the mean strength and its standard deviation. Assuming a normal distribution of

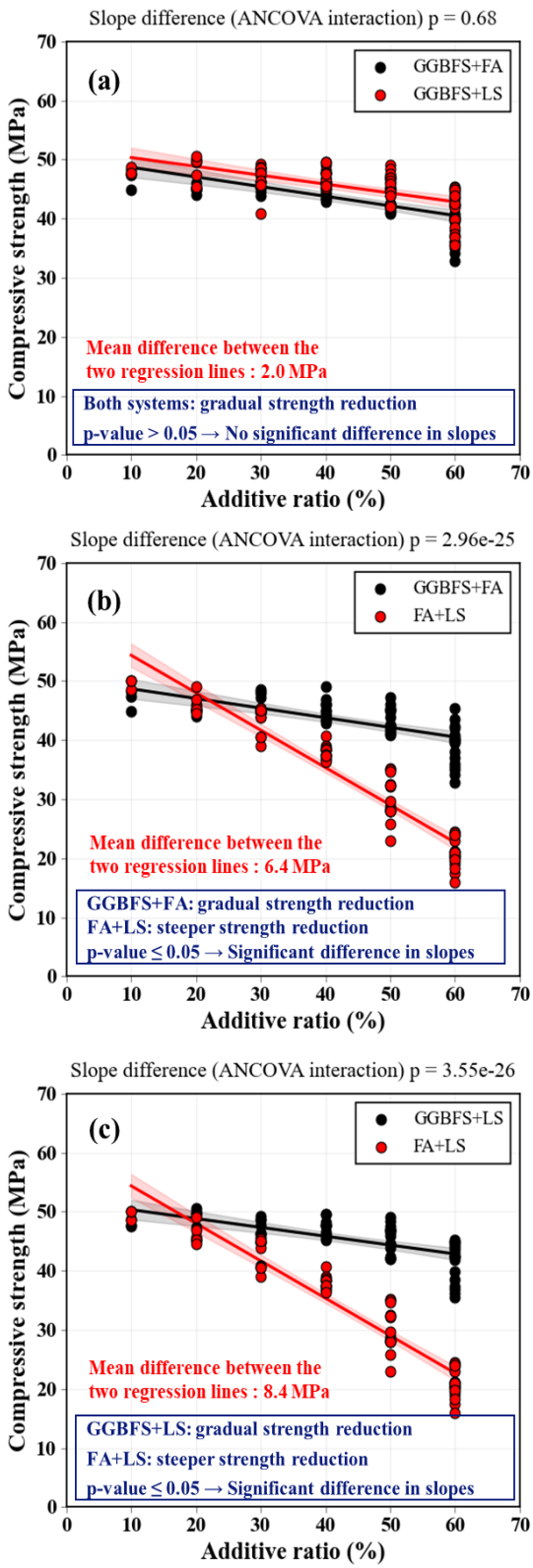

Fig. 2 Comparison of the relationship between total content of SCMs and compressive strength at 28 days: (a) GGBFS–FA and GGBFS–LS, (b) GGBFS–FA and FA–LS, and (c) GGBFS–LS and FA–LS.

compressive strength, the probability of falling below the specified strength level was estimated using the reliability index described in Section 2.4. A reliability index of 2.33, corresponding approximately to a 1% lower-tail probability, was used as the screening criterion.

Fig. 3 summarizes the RTZs of the GGBFS–LS and FA–LS systems for different specified strength levels at 28 days. At a specified strength of 42.5 MPa, the GGBFS–LS system maintained a sufficient strength margin up to 40% SCMs, whereas a sharp reduction in reliability occurred between 40 and 50%. Therefore, the 40–50% range was identified as the RTZ for this system. In contrast, the FA–LS system exhibited an earlier transition, with the RTZ occurring between 30 and 40% SCMs.

The position of the RTZ changed with the specified strength level, as shown in Fig. 3. At a specified strength of 37.5 MPa, the GGBFS–LS system remained within the reliable region up to 60% SCMs, whereas the FA–LS system showed a marked reduction in reliability between 30 and 40%. At 32.5 MPa, the GGBFS–LS system again remained reliable up to 60%, while the transition for the FA–LS system occurred at approximately 40–50% SCMs.

These results indicate that the practical replacement limit of SCMs cannot be defined by total SCMs content alone. Instead, the performance boundary varies according to both the combination of SCMs and the specified strength level.

3.4 Effect of Increased Fineness and C_3S Content on Strength Performance

To compensate for the strength reduction at high contents of SCMs, increased cement fineness and higher clinker C_3S content were investigated as performance-enhancement approaches.

Fig. 4 shows the effect of increasing the cement fineness from approximately 3,500 to 4,500 cm^2/g on compressive strength at 28 days. Increasing cement fineness improved compressive strength over a wide range of SCMs contents. The average strength improvements at 28 days were approximately 12.4, 8.9, and 6.6% for the GGBFS–FA, GGBFS–LS, and FA–LS systems, respectively.

Fig. 5 shows the effect of clinker C_3S contents of 64.2, 64.8, and 67.2% on compressive strength at 28 days. Compared with the reference C_3S content of 64.8%, increasing the C_3S content to 67.2% improved strength, particularly at high contents of SCMs. For the GGBFS–LS system, the compressive strengths reached 44.9 and 40.2 MPa at SCMs contents of 50 and 60%, respectively. For the FA–LS system, the strength at 40% SCMs increased to 43.6 MPa.

From the reliability perspective discussed in Section 3.3, the improvements shown in Figs. 4 and 5 increased the strength margin relative to the specified strength and shifted mixtures near the RTZ toward a

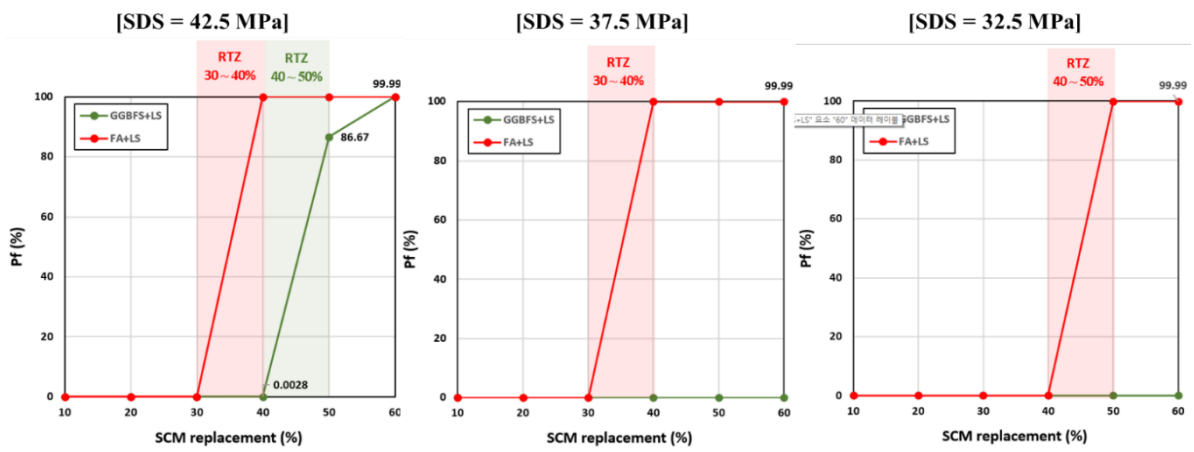

Fig. 3 Reliability transition zones of the GGBFS–LS and FA–LS systems at different specified strength levels at 28 days.

more reliable performance region. However, the effectiveness of these approaches remained dependent on the combination and content of SCMs.

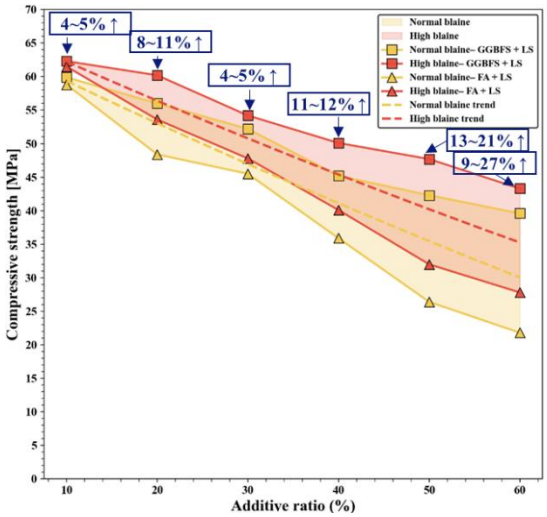

Fig. 4 Effect of increased cement fineness on the compressive strength of ternary blended cements at 28 days.

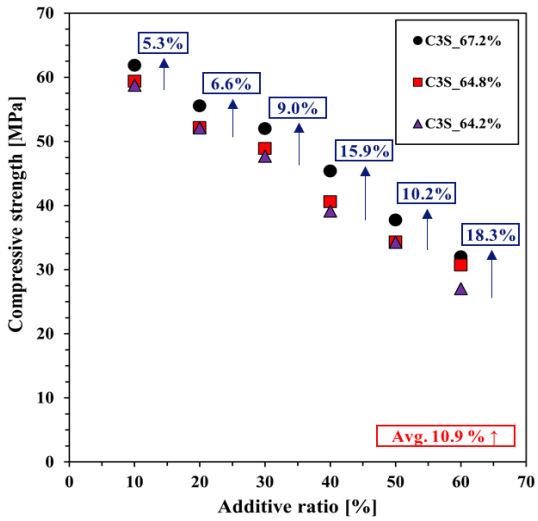

Fig. 5 Effect of increased clinker C_3S content on the compressive strength of ternary blended cements at 28 days.

4. Conclusions

This study evaluated the compressive strength characteristics of ternary blended cements containing GGBFS, FA, and LS. The main conclusions are as follows.

1) Compressive strength decreased with increasing content of SCMs, and the magnitude of the reduction depended on the combination of SCMs. The GGBFS-containing systems generally maintained higher strength than the FA–LS system.
2) At 28 days, regression, ANCOVA, and probabilistic analyses confirmed that the performance limit of ternary blended cements depended on both the combination and content of SCMs. For a specified strength of 42.5 MPa, the RTZ was identified at approximately 40–50% SCMs for GGBFS–LS and 30–40% for FA–LS. These results provide a basis for establishing provisional SCMs ranges according to the constituent combination and specified strength level.
3) Increasing cement fineness and clinker C_3S content improved compressive strength at 28 days and increased the strength margin relative to the specified strength, indicating their potential to extend the applicable range of SCMs.

Acknowledgment

This work was supported by the Technology Innovation Program (RS-2023-00266009, Development of admixture and blended cement using unused inorganic resource) funded by the Ministry of Trade, Industry and Resources (MOTIR, Korea) and the Technology Innovation Program RS-2026-25544240, Development of commercial-scale production and field demonstration technology for increased SCMs utilization in cement) funded by the Ministry of Trade, Industry and Resources (MOTIR, Korea)

Reference

[1] Korean Agency for Technology and Standards, KS F 2563:2020, Ground Granulated Blast-Furnace Slag for Use in Concrete, KATS, Republic of Korea, 2020.
[2] Korean Agency for Technology and Standards, KS L 5405:2023, Fly Ash, KATS, Republic of Korea, 2023.
[3] Korean Agency for Technology and Standards, KS L ISO 679:2022, Cement—Test Methods—Determination of Strength, KATS, Republic of Korea, 2022.

ジオポリマーの中性化抵抗性向上技術に関する研究

Investigation of Measures to Improve the Carbonation Resistance of Geopolymers

李柱国※1
Zhuguo Li

ABSTRACT

本研究は、低炭素型結合材として期待されるジオポリマー（GP）の中性化抵抗性向上を目的とし、アルミン酸ナトリウム（AN）を表面含浸材として用いた改質効果を検討したものである。高炉スラグ微粉末（BFS）、フライアッシュ（FA）、クリンカアッシュ（CA）を用いた GP モルタルを対象に、BFS 混合率、アルカリ刺激剤組成、含浸材濃度、塗布回数、養生条件の影響を調べた。その結果、AN 表面塗布は加温養生モルタルで中性化速度係数を約 70%低減し、常温養生材でも 30%以上の改善が確認された。特に FA/BFS 併用系で効果が顕著であり、加温養生では濃度が 40%である AN の 1 回塗布、常温養生では 2 回塗布が最適であった。さらに、CA を含む GP モルタルに対しても AN 処理は中性化開始の遅延と進行抑制に有効であることが示された。

1. Introduction

Concrete is one of the most extensively used construction materials worldwide, and the demand for Portland cement (PC), its primary binder, remains exceptionally high. However, the production of PC involves the calcination of limestone and the combustion of fossil fuels, processes that collectively generate substantial CO_2 emissions. Consequently, PC exhibits a high CO_2 emission intensity, making the cement industry responsible for approximately 7–8% of global anthropogenic CO_2 emissions[1]. Reducing the environmental burden associated with cement production has therefore become a critical challenge for achieving carbon neutrality in the construction sector.

To meet this challenge, the development and implementation of low-carbon binders have gained significant attention. Geopolymer (GP), synthesized primarily from industrial by-products such as fly ash (FA) and blast-furnace slag (BFS), represent one of low-carbon cements. Their production can reduce CO_2 emissions by up to 80% compared with PC, and numerous studies have explored their synthesis, performances, and potential applications[2]. GP hardens through polycondensation reactions accompanied by dehydration, during which micro-channels may form within the matrix. This feature facilitates CO_2 ingress and lead to a reduction in alkalinity after hardening. As a result, GP materials generally exhibit lower carbonation resistance than PC-based systems [3], Moreover, the alkalinity of hardened GP is strongly influenced by residual alkaline activators, which are water-soluble. Repeated wetting and drying cycles can leach these activators from the matrix, resulting in neutralization [4]. Lower carbonation and neutralization resistances pose a major obstacle to their application in reinforced concrete structures.

Due to the intrinsic characteristics of GP dehydration hardening and the absence of effective plasticizer or dispersant for GP systems, optimizing mix proportions alone is insufficient to significantly enhance carbonation resistance. In response to this challenge, the present study investigates the use of surface-applied impregnating materials as a method to improve the carbonation resistance of GP hardened bodies produced from BFS, FA, and clinker ash (CA). The effects of BFS content, alkaline activator composition, impregnating material concentration, and the number of application were examined. By establishing an effective method for enhancing carbonation resistance, this research provides a practical pathway for improving the durability of reinforced GP concrete.

※1 日本国 山口大学大学院 創成科学研究科工学系学域 建築系分野 教授 博士(工学)

2. Experamental Program

2.1 Raw materials

The fly ash of JIS grade II, and BFS of JIS 4000 class were used as active fillers (AF) of GP mortar. Three kinds of alkali activator solution (AS), named AS01, AS11 and AS31, were used, which were sodium hydroxide solution (NH) with 10 moles or a mixture of water glass aqueous solution (WG) and the NH according to the volume ratio of WG: NH = 1:1 or 3:1. The WG was prepared by diluting JIS No.1 grade sodium silicate (Na_2SiO_3) with distilled water by a volume ratio of 1:1.

Sea sand, washed in advance with tap water, was used as fine aggregate of the GP mortars. CA was utilized as the replacement of partial fine aggregate for GP mortars. The CaO content in CA is comparatively less, similar to that of FA. The components of CA are mainly crystalline, which results in low activity in the alkaline solution.

The sodium aluminate solution with a concentration of 40 wt.% was diluted with water, and used as surface-applied impregnating material. The physical properties of BFS, FA, CA, AN, NH, and sea sand are shown in **Tables 1,** and their chemical compositions are shown in **Table 2**, which were measured by X-ray fluorescence (XRF) analysis. The features of AS are shown in **Tables 3**.

2.2 Preparation and evaluation of specimens

The mix proportions of GP mortars used in this study are shown in **Table 4**. Based on the preliminary investigation, we found that series No.1 had adequate fluidity for specimen production, thus, it was used as the control mixture. Then, the other GP mortars were designed by adjusting the BFS blending ratio, WG/NH ratio by volume, and liquid-fillers ratio (AS/AF) by mass, as shown in **Table 4**, on the basis of series No.1. In this experiment, the ratio of fine aggregates (S) to AF was 2.0 throughout by mass. the AS/AF ratio was 0.5.

Also, for clarifying appropriate AN application condition, the effects of the AN solution concentration, AN surface application frequency

Table 1 Physical properties of raw materials used

Raw materials	Feature
FA	Specific gravity: 2.30, Blaine fineness: 4392 cm^2/g
BFS	Specific gravity: 2.88, Blaine fineness: 4180 cm^2/g
CA	Oven-dry density: 1.80 g/cm^3, water absorption: 31.4%, F.M. 2.03
Sea sand	Oven-dry density: 2.51, surface-dry density: 2.56, specific water absorption: 1.81%, solid content: 66.7%, F.M. 2.87
AN	Compositions: Na_2O 19%, Al_2O_3 20%, Molar ratio (Na_2O/Al_2O_3): 1.56, Specific gravity: 1.49 (40 wt.% concentration)
NH	Specific gravity: 1.33, molar concentration: 10 mole/L

Table 2 Chemical compositions of raw materials (XRF analysis)

Raw materials	Chemical compositions (%)								
	SiO_2	Al_2O_3	CaO	Fe_2O_3	MgO	Na_2O	K_2O	TiO_2	Others
FA	59.10	23.91	3.48	7.37	1.06	1.07	1.68	1.27	1.06
BFS	34.67	14.46	43.13	0.34	5.50	0.25	0.25	0.55	0.85
CA	57.00	27.00	4.43	6.60	0.67	0.58	1.09	1.63	1.00

Table 3 Alkali activator solution's components and density

Alkali activator solution	WG : NH, by volume	Specific gravity	Mole ratio of SiO_2/Na_2O	Molarity of Na_2O (mole/L)
AS01	0:1	1.330	0	5.000
AS11	1:1	1.359	0.696	2.438
AS31	3:1	1.374	1.255	3.108

Table 4 Mix proportions of heat/ambient-cured GP mortars

No.	Parameters	AS/AF	BFS/AF	S/AF
1	Control mix	0.5	3:7(0.3)	2.0
2	BFS blending ratio		0:1 (0)	
3			1:1 (0.5)	
4			1:0 (1)	
5	WG/NH ratio		3:7 (0.3)	
6				

[Note] 25 wt.% AN solution was applied twice at 3 days old, and the specimens were sealed as cured till 28 days after the treatment.

Table 5 Conditions of AN surface application for heat-cured GP

No.	Mortar Age, frequency of AN application	AN concentration by mass (%)	State during curing
1	No-AN application		Sealed
7	3 days, twice	10	
8		20	
9		30	
10		40	

[Note] Mix proportions of GP mortar of series 7-10 were the same as those of series No.1 shown in **Table 4**.

within 3 days, the age of mortar specimen when the AN surface application, whether the mortar specimens were sealed after the AN surface application during curing, and curing temperatures were investigated. Part of series are listed in **Table 5**. The GP specimens had the same mix proportion with series No.1.

2.3 Accelerated carbonation test

After 28 days of curing, four surfaces (two ends, top and bottom surfaces) of mortar specimens were sealed with an airtight sealing tape to ensure that CO_2 diffuses into the specimens only through the two side surfaces. Then, the specimens were placed into a carbonation test chamber with 5% of CO_2 concentration, 20℃, and R.H. 60%. At an interval of two weeks, the mortar specimen was cut at about 10 mm interval to measure carbonation depth. It should be noted that during the cutting, to ensure that the alkali matters were not washed away, spraying water was not used as a dust countermeasure.

The depth of the colorless region from the surface of the prism specimen was measured at 3 min. strictly after spraying the 1% phenolphthalein solution. The average value of six depths, three values on one side and 10 mm interval respectively, was recorded as carbonation depth. After the measurement of carbonation depth, the cut sections were sealed with airtight tape, and the remained GP mortar samples were returned to the CO_2 chamber to continue the carbonation test. The accelerated carbonation test lasted 18 weeks.

3. Results and Discussion

3.1 Effects of mix proportions on the effectiveness of AN surface application

The effects of AN treatment on the carbonation resistance of GP mortars were discussed on the basis of regression analysis of carbonation depth - carbonation time relationship. As described later, due to the AN surface treatment, the carbonation depth of part of the specimens could be detected only after a period, **Eq.(1)** was used for the regression analysis.

$$C_d = a \cdot \sqrt{CO_2\%/5.0} \cdot \sqrt{t-b} \qquad \textbf{(1)}$$

where C_d is carbonation depth (mm), t is carbonation period (week), CO_2% represents CO_2 concentration (%), a is proportional coefficient (mm/√week), and b is elapsed time until the depth of carbonation can be detected, i.e., onset time of neutralization (week, ≧0).

In **Eq. (1)**, the proportional coefficient a implies the rate of increase of the carbonation depth with elapsed time and therefore is called carbonation rate coefficient. The smaller the a, the higher the carbonation resistance of GP mortar. And the larger the b, the later the onset of neutralization, and therefore the higher the initial carbonation resistance.

(1) Effect of FA/BFS ratio

The figures were omitted here due to the space limited, which show the test results of the relationship between the carbonation depth and the elapsed time for the GP mortars with different

FA/BFS blending ratios by mass and under heat or ambient curing. Heat-cured FA/BFS blends showed smaller carbonation depths due to enhanced reactions and denser micro-structures after the AN application, whereas BFS-only mortars carbonated more because heat-curing increased shrinkage and porosity. FA-only mortars carbonated rapidly, though AN surface treatment delayed full carbonation from two weeks to one month.

For ambient curing, BFS-based mortars exhibited no detectable carbonation within 18 weeks, and AN treatment had little effect. FA-based mortars carbonated quickly but were moderately improved by the AN treatment. Carbonation resistance was evaluated using the parameters *a* (rate) and *b* (delay), both improved by AN treatment. Mortars with lower BFS content benefited most because higher porosity allowed deeper AN penetration, resulting in greater reduction of carbonation rate.

(2) Effects of WG/NH ratio

Fig.1 shows the relationship between the carbonation depth and the elapsed time for the 30% BFS/70% FA blend-based GP mortars produced by different AS solutions and cured at 80°C or 20°C. The AN surface treatment greatly improved carbonation resistance of GP mortars under all curing conditions, with the strongest effect in 80 °C-cured specimens, where both the carbonation rate *a* decreased and delay parameter *b* increased. The 80 °C-cured GP with a WG/NH ratio of 1:1 showed no carbonation for 18 weeks.

The SiO_2/Na_2O molar ratio strongly influenced carbonation behavior: higher ratios promote N-A-S-H gel formation, but excessive SiO_2 increases porosity, explaining why mortars with WG/NH = 3:1 carbonated more than those with 1:1. Residual Na^+ also contributed to the lower carbonation depth of the 1:1 mixture. Thus, an appropriate SiO_2/Na_2O ratio is essential for high carbonation resistance.

After AN treatment, mortars with higher porosity (WG/NH = 3:1) showed the greatest reduction in carbonation rate due to better AN penetration. That is to say, AN treatment was most effective for the mortars with initially high carbonation rates.

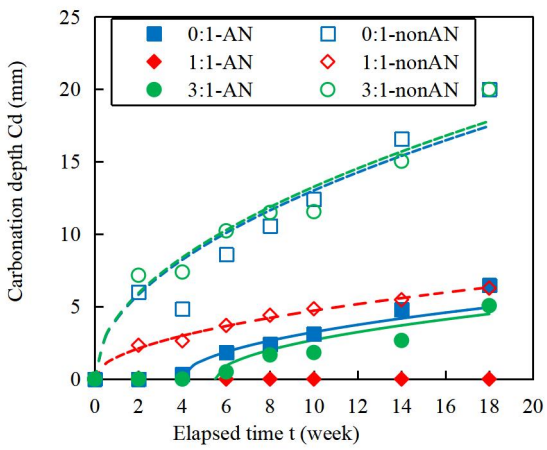

WG /NH	SiO_2 /Na_2O	AN treatment	Non-AN treatment	Decrease of *a* (%)
0:1	0.00	$C_d = 1.32\sqrt{t-4}$ $R^2 = 0.918$	$C_d = 4.11\sqrt{t}$ $R^2 = 0.978$	67.86
1:1	0.69	b>18	$C_d = 1.49\sqrt{t}$ $R^2 = 0.998$	-
3:1	1.25	$C_d = 1.27\sqrt{t-5.5}$ $R^2 = 0.876$	$C_d = 4.19\sqrt{t}$ $R^2 = 0.990$	69.68

(a) Heat-cured GP mortars

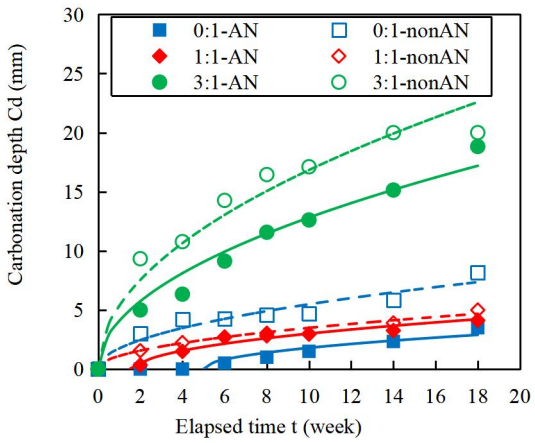

SiO_2/ Na_2O	AN treatment	Non-AN treatment	Decrease of a (%)
0.00	$C_d = 0.80\sqrt{t-4}$ $R^2 = 0.909$	$C_d = 1.73\sqrt{t}$ $R^2 = 0.985$	53.74
0.69	$C_d = 1.04\sqrt{t-1.8}$ $R^2 = 0.882$	$C_d = 1.10\sqrt{t}$ $R^2 = 0.958$	4.96
1.25	$C_d = 4.05\sqrt{t}$ $R^2 = 0.993$	$C_d = 5.32\sqrt{t}$ $R^2 = 0.992$	23.87

(b) Ambient-cured GP mortars

Fig.1 Carbonation depth of GP mortars with different WG/NH ratios (Series No. 1, 5, 6)

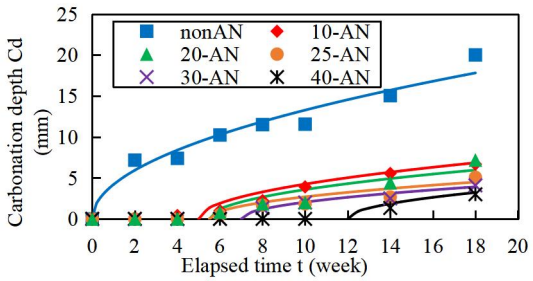

Conc. of AN	Regressive equation and R^2	Decrease of a (%)	Increase of b (week)
Non-AN	$C_d = 4.19\sqrt{t}$ $R^2 = 0.990$	-	-
10%	$C_d = 1.40\sqrt{t\text{-}5}$ $R^2 = 0.892$	54.75	3.5
20%	$C_d = 1.88\sqrt{t\text{-}5.5}$ $R^2 = 0.907$	59.81	5.5
25%	$C_d = 1.27\sqrt{t\text{-}5.5}$ $R^2 = 0.876$	69.73	5.5
30%	$C_d = 1.17\sqrt{t\text{-}7}$ $R^2 = 0.966$	71.91	7
40%	$C_d = 1.31\sqrt{t\text{-}12}$ $R^2 = 0.961$	68.68	12

(a) Heat-cured GP mortars

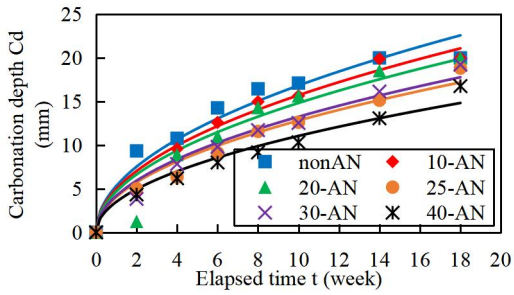

Conc. of AN	Regressive equation and R^2	Decrease of a (%)	Increase of b (week)
Non-AN	$C_d = 5.32\sqrt{t}$ $R^2 = 0.992$	-	-
10%	$C_d = 4.97\sqrt{t}$ $R^2 = 0.994$	6.62	0
20%	$C_d = 4.68\sqrt{t}$ $R^2 = 0.976$	11.91	0
25%	$C_d = 4.05\sqrt{t}$ $R^2 = 0.993$	23.88	0
30%	$C_d = 4.19\sqrt{t}$ $R^2 = 0.992$	21.27	0
40%	$C_d = 3.49\sqrt{t}$ $R^2 = 0.992$	33.32	0

(b) Ambient-cured GP mortars

Fig. 2 Carbonation depth of GP mortars with different concentrations of AN application (Series No. 1, 7～10)

3.2 Effects of treatment conditions on the effectiveness of AN surface treatment

(1) Concentration of AN solution

Fig.2 demonstrates the experimental results of the 70% FA/30% BFS blend-based GP mortars, which were applied on surfaces by different AN solutions with 10-40 wt.% concentrations. The experimental results showed that AN surface treatment improved carbonation resistance, with 40% AN being the most effective. For 80 °C-cured specimens, AN concentrations above 25% produced similar reductions in the carbonation rate ***a***, while higher concentrations increased the delay parameter ***b*** by densifying the surface layer. Lower concentrations penetrated deeper and reduced ***a***, but their effect was limited by insufficient active ingredients.

Ambient-cured mortars showed smaller improvements, yet 40% AN still reduced the carbonation rate by over 30%. Because early-age ambient-cured GP has a loose micro-structure, even concentrated AN could penetrate effectively.

Overall, 40% AN is recommended for both curing methods, significantly lowering carbonation rates and enabling GP concretes to reach carbonation resistance comparable to PC concretes when combined with optimized mixture design.

(2) Number of AN application cycles

The experimental results are not illustrated by figures due to length limited. For 80 °C-cured GP mortars, increasing AN application cycles did not change the carbonation rate coefficient ***a***, but two cycles increased the delay parameter ***b***, indicating a denser surface layer. Heat-cured specimens develop drying shrinkage cracks that allow AN to penetrate easily, so one treatment effectively reduces ***a***, while the second treatment mainly enhances surface densification and delays carbonation onset.

For ambient-cured mortars, two AN treatments reduced ***a***, but no delay in carbonation was observed (***b*** = 0). High moisture content and limited cracking hindered AN penetration, making multiple treatments necessary. Even with two treatments, the carbonation rate coefficient ***a*** did not change significantly. Overall, treatment effectiveness depends on moisture, cracking, and AN penetration behavior.

3.3 Effectiveness of AN application on GP mortar with CA as fine aggregate

Fig.3 illustrates the carbonation depths of GP mortars containing different amounts of CA while using the same alkali-activator solution. Increasing CA content rose the carbonation rates due to CA's high porosity, and all untreated specimens carbonated within one week. The AN surface treatment delayed carbonation onset, with delays of 11.5, 11, 5.5, and 3 weeks for 0%, 20%, 40%, and 100% CA, respectively. Even 100% CA mortars, fully carbonated in one week without the AN treatment, remained uncarbonated for three weeks after the treatment. Although AN effectiveness decreased with higher CA content, the carbonation rate coefficient still dropped by 57% at 40% of CA content.

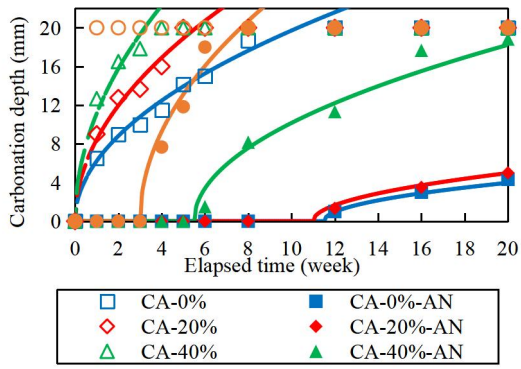

CA ratio	*a*		Decrease of *a* (%)	*b* (week)
	Non-AN treatment	AN treatment		
Non CA	6.23	1.36	78.14	11.5
20%	8.45	2.00	76.30	6
40%	11.14	4.78	57.04	5.5
100%	-	9.26	-	3

Fig.3 Carbonation depths of GP mortars with different replacing ratios of CA

4. Summary

This study demonstrated that AN surface application significantly improved the carbonation resistance of GP mortars. Heat-cured specimens showed about a 70% reduction in carbonation rate and, in some cases, no detectable carbonation for 18 weeks, while ambient-cured specimens improved by over 30%. FA/BFS-based geopolymers benefited most, especially under heat - curing, whereas BFS-only or FA-only GP systems showed smaller gains in the improvement of carbonation resistance.

For heat-cured GP, one application of 40% AN was sufficient, while ambient-cured GP required two applications at early age and sealed curing to achieve optimal performance. The higher effectiveness of AN treatment in heat-cured GP is attributed to the dry shrinkage-induced cracks.

The AN treatment also enhanced carbonation resistance in CA-containing GP materials by delaying carbonation onset and reducing the carbonation rate through surface densification and changes in the SiO_2/Al_2O_3 ratio. A higher NH proportion in the alkali activator further decreased the carbonation rate. Despite CA increasing porosity and reducing durability, AN treatment significantly improved CA-blended GP materials, achieving even better carbonation resistance than untreated GP without CA.

Acknowledgements

The author would like to express his sincere gratitude to Dr. Xuezhong Li, graduated from the Doctoral Program at the Graduate School of Sciences and Technology for Innovation, Yamaguchi University, for his valuable assistance throughout this study. The author also wish to thank Mr. Ota Niman, a graduate student of the same graduate school, for his support in editing this manuscript. This research was supported by the Japan Society for the Promotion of Science (JSPS) under the Grant-in-Aid for Challenging Research (Pioneering).

References

[1] Scrivener, K. L., John, V. M., and Gartner, E. (2018). Eco-efficient cements: Potential economically viable solutions for a low-CO_2 cement-based materials industry, *Cement and Concrete Research*, 114, 2–26.

[2] Davidovits, J. (2015). Geopolymer Chemistry and Applications, Geopolymer Institute.

[3] Li Z., and Li S.(2018). Carbonation resistance of fly ash and blast furnace slag based geopolymer concrete, *Construction and Building Materials*, 163, 668-680.

[4] Li Z., and Li S.(2020). Effects of wetting and drying on alkalinity and strength of fly ash/slag-activated materials. *Construction and Building Materials*, 254, 119069, 2020.

Effect of Repeated Air Pressure on Chloride Transport in Reinforced Concrete of an OWC Wave Energy Structure

Gyu-Yong Kim※1, Min-Jeong Ko※2, Pebrian Candra Dwi※2, Ha-Min Eu※3, Jeong-Soo Nam※1

ABSTRACT

Oscillating water column (OWC) structures are exposed to marine environments and repeated air pressure generated by water-level oscillations. This study evaluated pressure-induced chloride ingress through laboratory hydrostatic-pressure tests and long-term monitoring of the Jeju Yongsoo OWC structure. OPC and PSC concretes were exposed to 1 and 6 atm, and their chloride penetration, water-soluble chloride content, and pore structure were analyzed. Chloride ingress and capillary pore volume increased with pressure, whereas PSC maintained a lower chloride content than OPC. The bypass room subjected to repeated air pressure exhibited the highest chloride content, with accumulation mainly concentrated within 0~10 mm from the surface. The apparent clogging. Based on these findings, a chloride ingress model incorporating the depth- and time- dependent effects of pressure was proposed.

1. Introduction

The global transition toward carbon neutrality has accelerated the development of renewable energy technologies. Among these, wave energy has received increasing attention owing to its high energy density and potential for utilizing offshore space. Oscillating water column (OWC) systems generate electricity by driving an air turbine with reciprocating airflow induced by changes in the internal water level. As OWC structures are installed in coastal or offshore environments, their reinforced concrete components are continuously exposed to seawater immersion, wetting and drying cycles, seawater splash, and airborne sea salts.

Chloride ingress is a primary cause of deterioration in marine reinforced concrete structures. Chloride ions penetrate the concrete cover through diffusion, capillary absorption, convection, and permeation and accumulate around the reinforcing steel [1]. When the

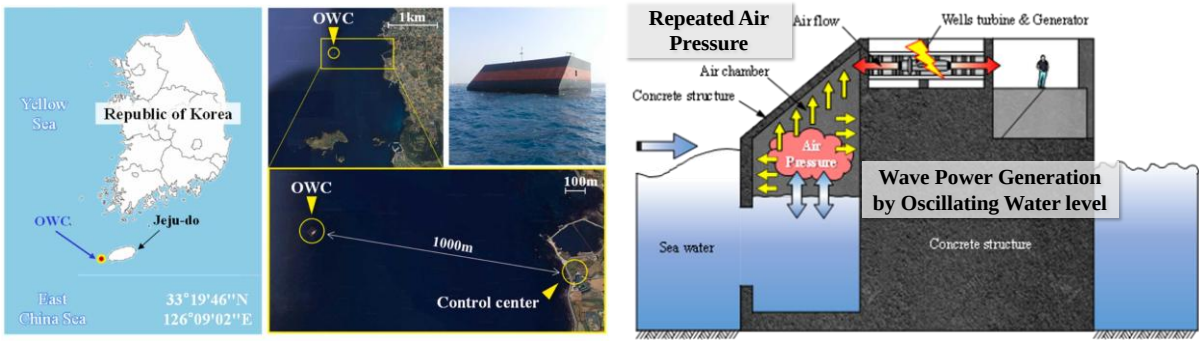

(a) **(b)**

Figure 1. Overview and exposure environments of the Jeju Yongsoo OWC wave power structure: (a) Location or external view, (b) operating principle

※1 Prof., Dept. of Architectural Engineering, Chungnam National University, Korea
※2 Master's Course, Dept. of Architectural Engineering, Chungnam National University, Korea
※3 Ph.D., Dept. of Architectural Engineering, Chungnam National University, Korea

chloride concentration exceeds a critical threshold, the passive film may be destroyed, initiating corrosion. The expansion of corrosion products can induce cracking and spalling, while the resulting cracks provide additional pathways for chloride transport. Therefore, evaluating chloride ingress is essential for predicting the service life of marine concrete structures and establishing maintenance strategies.

Chloride ingress in marine concrete is generally assessed according to submerged, tidal, splash, and marine atmospheric exposure zones. However, the air chamber of an OWC structure is additionally subjected to repeated air pressure generated by internal water-level oscillations. Previous studies have reported that hydrostatic pressure promotes water penetration into concrete, suggesting that pressure may accelerate chloride ingress [2]. Nevertheless, constant hydrostatic pressure applied in laboratory tests differs from the repeated air pressure acting on actual OWC structures in terms of loading characteristics and exposure duration. Therefore, the relationship between laboratory observations and the long-term chloride ingress behavior of actual OWC structures requires further investigation.

In this study, pressure-induced chloride transport was evaluated by combining laboratory hydrostatic-pressure tests with long-term field monitoring of the Jeju Yongsoo OWC wave power structure [3]. Ordinary Portland cement concrete and Portland slag cement concrete were exposed to different pressure conditions, and their chloride penetration depth, water-soluble chloride content, and pore structure were analyzed [4]. Field samples collected from the bypass room, tidal zone, and splash zone were also used to compare chloride profiles and apparent diffusion coefficients. Based on these results, chloride transport under repeated air pressure was investigated, and the need to incorporate the depth- and time-dependent effects of pressure into conventional chloride ingress models was examined.

2. Experimental Program

2.1 Laboratory Pressure Exposure

To evaluate the effect of hydrostatic pressure on chloride ingress in concrete, ordinary Portland cement concrete (OPC) and Portland slag cement concrete (PSC) with a water-to-binder ratio (W/B) of 0.38 were prepared, as presented in Table 1. After curing, all surfaces of the specimens, except for the designated exposure surface, were sealed to ensure unidirectional chloride ingress.

Table 1 Mix proportions of OPC and PSC concrete

Spec.	Fck [MPa]	W/B (%)	S/a (%)	Unit Weight [kg/m³]				
				W	OPC	PBC	S	G
OPC	35	0.28	44.6	164	429	-	752	967
PSC					-	429	748	962

The pressure exposure test was conducted using a custom-designed pressurized chloride exposure apparatus, as shown in Figure 2.

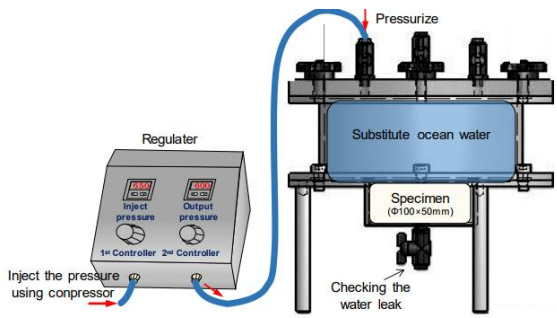

Figure 2. Pressurized chloride exposure apparatus

The applied pressures were 1 and 6 atm, and the exposure periods were 3, 7, 28, and 56 days. The 1 atm condition was used as the atmospheric-pressure reference, while the 6 atm condition was applied to simulate a marine environment subjected to hydrostatic pressure.

After each exposure period, the chloride penetration depth and water-soluble chloride content at different depths were measured. Mercury intrusion porosimetry (MIP) and scanning electron microscopy (SEM) were also conducted to analyze the pore-size distribution, cumulative pore volume, and

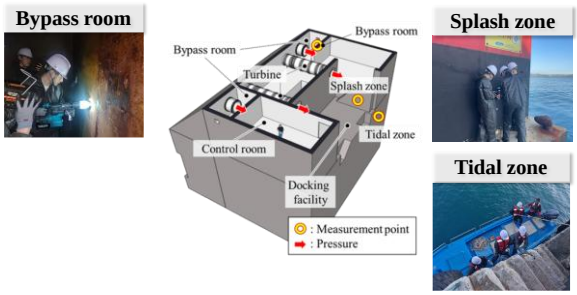

Figure 3. Field sampling locations and exposure zones of the Jeju Yongsoo OWC structure

microcracking induced by pressure exposure. Based on these results, the effects of binder type, pressure condition, and exposure period on chloride ingress and microstructural changes were evaluated.

2.2 Field Investigation of the OWC Structure

To evaluate the effect of repeated air pressure on chloride ingress in marine concrete, a field investigation was conducted at the Jeju Yongsoo OWC wave power structure. As shown in Figure 3, concrete samples were collected at specified depth intervals from the bypass room, tidal zone, and splash zone. These zones were subjected to repeated air pressure, wet–dry cycles, and seawater spray and airborne salts, respectively.

The water-soluble chloride content was measured at each depth, and the chloride profiles were compared among the exposure zones. The surface chloride content and apparent diffusion coefficient were calculated using the error-function solution to Fick's second law.

To evaluate long-term chloride ingress, the chloride profiles and apparent diffusion coefficients obtained in 2017 and 2023 were compared. The results were used to examine changes in chloride accumulation and diffusion with exposure time and the differences between the bypass room and conventional marine exposure zones.

3. Results and Discussion

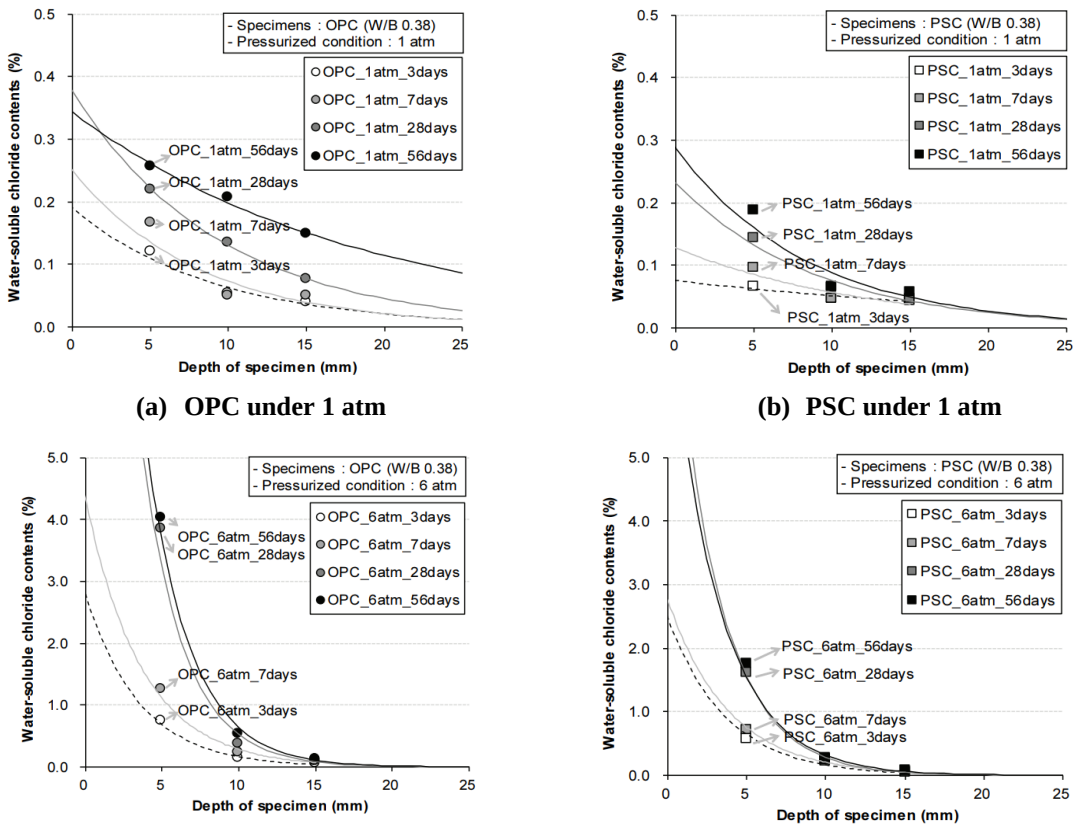

(a) OPC under 1 atm **(b) PSC under 1 atm**

(c) OPC under 6 atm **(d) PSC under 6 atm**

Figure 4. Depth profiles of water-soluble chloride content at different exposure periods

3.1 Effect of hydrostatic pressure on chloride penetration

The chloride penetration depth increased with exposure period for both OPC and PSC. OPC exhibited a greater penetration depth at 6 atm than at 1 atm, indicating that hydrostatic pressure promoted the transport of chloride-bearing moisture through the pore network. In contrast, PSC showed a lower penetration depth owing to pore refinement and chloride binding by blast-furnace slag.

As shown in Figure 4, the water-soluble chloride content increased with exposure period and was generally higher at 6 atm. The pressure effect was most pronounced within 0~5 mm from the surface and decreased with depth. OPC showed a marked increase at 6 atm, whereas PSC maintained relatively low chloride contents. These results indicate that hydrostatic pressure primarily promotes chloride ingress and accumulation near the concrete surface, depending on the binder type.

3.2 Pressure-induced pore structure change

Figure 5 shows the cumulative pore volume of OPC and PSC concretes under different pressure conditions. The MIP results showed that the volume of capillary pores ranging from approximately 5 to 100 nm increased in both mixtures under 6 atm

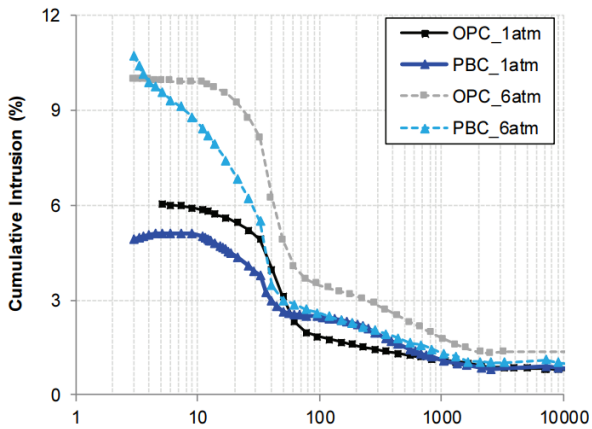

Figure 5. Cumulative pore volume of OPC and PSC concrete

compared with 1 atm, with a pronounced increase near 50 nm. The cumulative pore volume below 100 nm also increased under 6 atm. These results indicate that hydrostatic pressure affected the pore structure through deformation and microcracking of the concrete matrix.

The increase in capillary pores and microcracks may have enhanced pore connectivity and facilitated chloride transport. This is considered to have contributed to the increased chloride penetration depth and water-soluble chloride content under the high-pressure condition. Meanwhile, PSC exhibited a lower chloride content than OPC despite the pressure-induced increase in pore volume, which may be attributed to pore refinement and chloride binding associated with the hydration of blast-furnace slag.

3.3 Long-Term Chloride Ingress Behavior of the OWC Structure

Figure 6 shows the depth profiles of water-soluble chloride content measured in the bypass room, tidal zone, and splash zone of the OWC structure. Among the exposure zones, the bypass room subjected to repeated air pressure exhibited the highest chloride content, followed by the tidal and splash zones. A

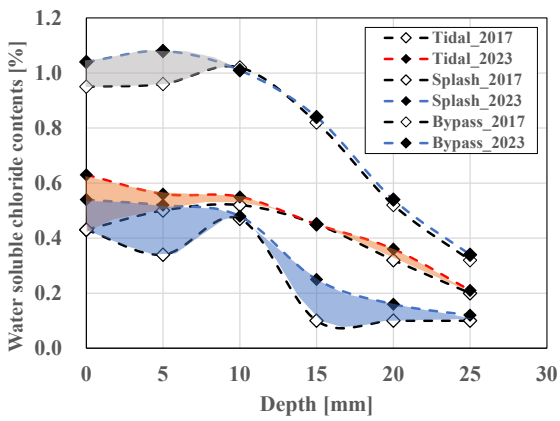

Figure 6. Depth profiles of water-soluble chloride content measured in 2017 and 2023

comparison of the measurements obtained in 2017 and 2023 showed that the chloride content in the bypass room increased mainly within the surface

region of 0~10 mm, whereas relatively little change was observed beyond 15 mm. This indicates that the

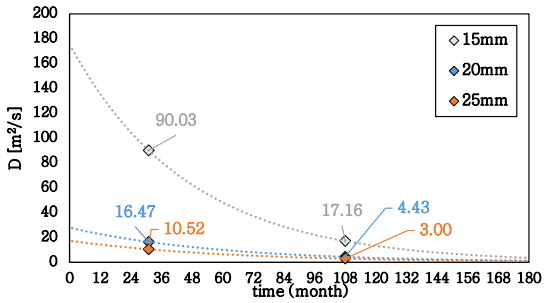

(a) Bypass room

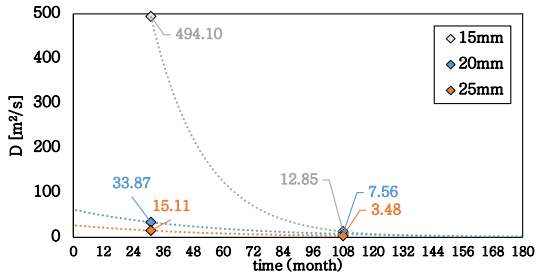

(b) Tidal zone

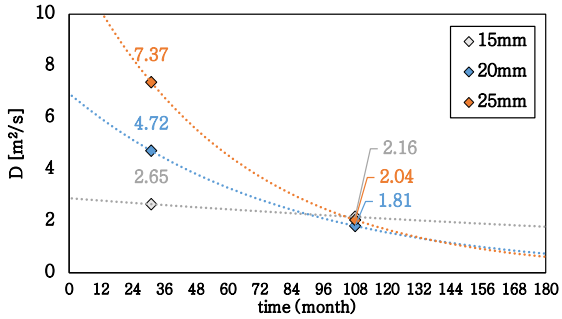

(c) Splash zone

Figure 6. Depth profiles of water-soluble chloride content measured in 2017 and 2023

effects of repeated air pressure and long-term chloride accumulation were concentrated near the concrete surface.

As shown in Figure 7, the apparent diffusion coefficient derived from the chloride concentration profiles decreased with increasing exposure duration and gradually converged. This suggests that repeated air pressure may promote chloride ingress during the early exposure period, whereas long-term chloride accumulation and changes in the pore structure near the surface may limit further chloride transport into

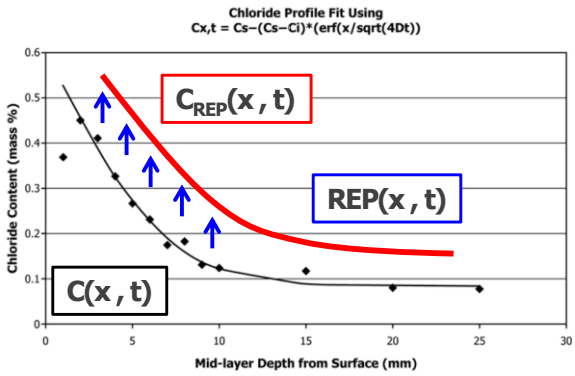

Figure 8. Conceptual chloride ingress prediction model repeated air pressure

the concrete.

3.4 Microstructural Analysis of the Pore-Clogging Mechanism

Figure 8 presents a chloride ingress prediction model considering repeated air pressure. The initial chloride profile was calculated using Fick's second law, and a depth- and time-dependent increment function, (REP(x,t)), was introduced to account for pressure-induced chloride ingress. The influence of repeated air pressure was assumed to decrease with increasing depth and exposure duration.

As shown in Figure 9, the diffusion coefficient in the OWC structure varied with depth owing to surface scaling, repeated air pressure, and long-term chloride accumulation. The concrete was therefore divided into a pressure-dominated surface region and

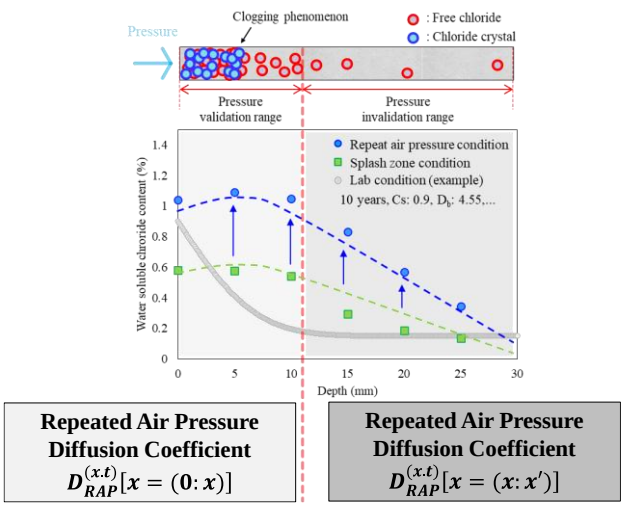

Figure 9. Conceptual chloride ingress prediction model repeated air pressure

an inner region with reduced pressure effects. The ratio of field to laboratory diffusion coefficient. decreased with depth and was lower in 2023 than in 2017, indicating that the pressure effect diminished over time. These depth- and time-dependent characteristics were incorporated into the proposed prediction model.

4. Conclusion

This study evaluated pressure-induced chloride ingress through laboratory hydrostatic-pressure tests and long-term monitoring of an OWC structure. The main conclusions are as follows.

1) Chloride penetration depth and water-soluble chloride content increased with pressure. The increase in capillary pores and microcracks under 6 atm indicated that pressure promoted chloride transport, while PSC maintained a lower chloride content than OPC.
2) The bypass room subjected to repeated air pressure exhibited the highest chloride content among the exposure zones. Chloride accumulation was mainly concentrated within 0~10 mm from the surface, with relatively little change beyond 15 mm.
3) The apparent diffusion coefficient decreased with exposure duration. The localized accumulation of Cl and Mg near the surface and pores suggested the possible occurrence of pore clogging by salts and reaction products.
4) The effect of repeated air pressure decreased with depth and exposure duration. Accordingly, a prediction model incorporating a depth- and time-dependent pressure function and transition depth was proposed.

Reference

[1] J. Sun, Z. Jin, H. Chang, W. Zhang, A review of chloride transport in concrete exposed to the marine atmosphere zone environment: Experiments and numerical models, J. Build. Eng. 84 (2024) 108591. https://doi.org/10.1016/J.JOBE.2024.108591.

[2] J. Xu, F. Li, J. Zhao, L. Huang, Model of time-dependent and stress-dependent chloride penetration of concrete under sustained axial pressure in the marine environment, Constr. Build. Mater. 170 (2018) 207–216. https://doi.org/10.1016/J.CONBUILDMAT.2018.03.077.

[3] J. Park, G. Kim, H. Eu, Y. Lee, S. Han, Y. Choi, S. Sasui, C. Lim, K. Kim, J. Nam, Monitoring long-term chloride penetration into wave power marine concrete structures under repeated air pressure, Constr. Build. Mater. 428 (2024) 136276.

[4] G.-T. Kim, C.-H.L. Gyu-Yong Kim, Jeong-Soo, Nam, Bo-Kyeong Lee, Effects of hydrostatic pressure on chloride ion penetration into concrete, Mag. Concr. Res. 68 (2019) 877–886.

打撃音を用いた建築物間タイル浮き自動検出の基礎的研究

A Basic Study on Automated Cross-Building Tile Debonding Detection Using Impact Sounds

李雨彤※1、今本啓一※1、清原千鶴※1、大久保孝昭※2、杉山和也※3、梅田幸一※3、杉山達哉※3
Yutong Li, Kei-ichi Imamoto, Chizuru Kiyohara, Takaaki Ohkubo, Kazuya Sugiyama, Koichi Umeda, Tatsuya Sugiyama

ABSTRACT

本研究では，実建築物 2 棟から取得した外壁タイルの打音データを用いて，建築物間でのタイル浮き判定手法の共通利用可能性を明らかにすることを目的として，タイル浮き検出モデルの汎化性能と少数サンプルによる対象建築物へのドメイン適応について検討した。建物 1 および建物 2 では，それぞれ 200 枚および 26 枚のタイルを対象とし，ロジスティック回帰（LR），サポートベクターマシン（SVM），ランダムフォレスト（RF），Extreme Gradient Boosting（XGBoost），および一次元畳み込みニューラルネットワーク（1D-CNN）の 5 種類を比較した。各建物内ではいずれのモデルも良好な分類性能を示したが，建物 1 で学習したモデルを建物 2 へ直接適用すると，Balanced Accuracy は 0.050～0.625 まで低下した。また，一部の音響特徴量では，健全部と浮き部の大小関係が建物間で逆転することを確認した。さらに，建物 2 から 0～10 枚のラベル付きタイルを用いてモデル更新および判定閾値を調整した結果，RF は 8 枚の適応データで平均 Balanced Accuracy 0.996 を達成した。以上より，建築物間のデータシフトは検出性能に大きく影響する一方，対象建物から少数のラベル付きデータを追加することで，高い検出性能が得られることを示した。

1. Introduction

Exterior wall tiles can debond because of material aging, environmental exposure, and construction variation. Debonded tiles may fall and create a safety risk. Conventional impact inspection depends on human listening. Its efficiency and consistency are affected by inspector experience and site conditions. Previous studies have used impact-sound signals to diagnose tile debonding [1] and employed spectral and time–frequency analyses to estimate debonding characteristics [2]. More recently, random forest has been applied to automated hammering inspection under UAV aerodynamic noise [3]. Support vector machines combined with acoustic features have also been applied to evaluate tile–wall bonding integrity [4]. In our previous work, a multi-feature framework incorporating time-domain, envelope, and frequency-domain acoustic indicators was proposed using field data collected from actual buildings [5], and the discriminative capability of both impact sounds and sweep sounds was verified [6].

However, previous studies have mainly focused on specimens or data from a single building, and the cross-building generalizability of the developed models remains unclear.

This study investigates the cross-building applicability of tile debonding detection models, the effects of building differences on the relationship between acoustic features and tile condition, and the effectiveness of using a small labeled sample from the target building to compensate for these differences. To achieve this, we first compared logistic regression (LR), support vector machine (SVM), random forest

※1 Faculty of Engineering, Department of Architecture, Tokyo University of Science, Japan.
※2 Department of Lifestyle Design, Yasuda Women's University, Japan.
※3 SUGITEC Co., Ltd., Japan.

(RF), extreme gradient boosting (XGBoost), and a one-dimensional convolutional neural network (1D-CNN) within buildings and under direct cross-building transfer. We then examined 13 acoustic features using Hedges' g, single-feature area under the receiver operating characteristic curve (ROC-AUC), and effect-direction consistency. Finally, we evaluated the effects of target-domain sample size, model updating, and classification-threshold adjustment under a common set of frozen splits.

2. Data and Methods

2.1 Buildings and Waveform Data

The same impact device, microphone, and operators were used in both buildings. Table 1 summarizes the site photographs, completion years, tile specifications, and dataset composition. Each tile was struck three times in principle. For four tiles in Building 2, only two valid impacts were retained. Label 0 indicates a sound tile, and label 1 indicates a detached tile. Waveforms were recorded at 96 kHz in 32-bit floating-point format. Abrupt changes were detected using a standard-deviation threshold of 5. The start point was set by tracing back 0.02 s, and each sample contained 0.1 s of data, or 9,600 points.

Table 1 Overview of the buildings, tiles, and datasets

Item	Building 1	Building 2
Site photograph		
Building and tile	Completed in 1987 Porcelain tile Scratched; unglazed	Completed in 2006 Porcelain tile Matte-glazed; lightly textured
Size and condition	100 × 60 × 17 mm Sound/detached: 100/100	145 × 45 × 10 mm Sound/detached: 10/16
Valid impacts	600	74

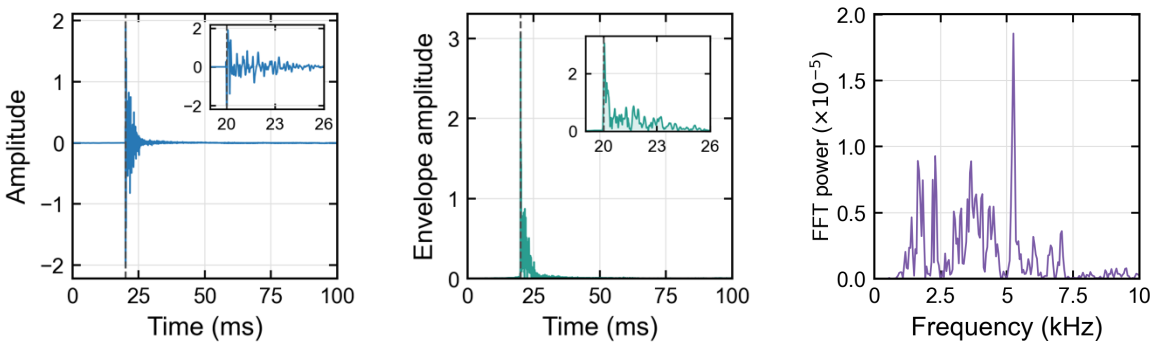

(a) Time-domain waveform (b) Hilbert envelope (c) FFT spectrum

Figure 1 Time-domain, envelope, and frequency-domain representations of one impact on a detached tile in Building 2

2.2 Acoustic Features and Classification Models

Based on previous multi-indicator impact-sound studies [5,6], 13 features were extracted from the time domain, Hilbert envelope, and fast Fourier transform (FFT) spectrum: Maximum Absolute Value, Root Mean Square (RMS), Envelope Area, Early Energy Ratio 1 ms, Temporal Centroid, Decay Time 10%, Peak Frequency, Peak Power, High Frequency Ratio >3000 Hz, Spectral Centroid, Spectral Skewness, Spectral Kurtosis, and Spectral Entropy. Figure 1 shows a time-domain waveform, Hilbert envelope, and FFT spectrum for one impact on a detached tile in Building 2. LR, SVM, RF, and XGBoost used the 13 features. Feature calculations followed Ref. [6]. The 1D-CNN directly used the raw waveform with 9,600 points.

LR used L2 regularization with C = 1. SVM used a radial basis function (RBF) kernel with C = 1 and gamma = scale. RF used 500 trees. XGBoost used a learning rate of 0.05 and a maximum depth of 3. The number of boosting rounds was determined by internal training on the source building. The 1D-CNN contained three convolutional blocks with 16, 32, and 64 channels. Their kernel sizes were 15, 9, and 5. Global average pooling, dropout of 0.3, and a binary classification layer followed the convolutional blocks. All final settings were fixed before cross-building testing. No results from Building 2 were used for retrospective tuning.

2.3 Evaluation Procedure and Target-Domain Adaptation

First, within-building cross-validation was used to evaluate tile-condition classification. All data were split at the tile level. Thus, repeated impacts from the same tile could not appear in both the training and test sets. Building 1 used five-fold cross-validation repeated five times. Building 2 used five-fold cross-validation repeated 20 times because of its smaller sample size. Each impact was entered into the model separately. Predictions from the same tile were averaged before evaluation.

Second, cross-building generalization was tested. All data from Building 1 were used to fit each model and its preprocessor. The fitted model then directly predicted Building 2. No Building 2 data were used for training, parameter selection, or threshold setting at this stage. The main evaluation metrics were balanced accuracy and ROC-AUC. All models used common, predefined tile-level splits and random seeds to ensure reproducible comparisons.

To explain changes in cross-building performance, Hedges' g, single-feature ROC-AUC, and bootstrap 95% confidence intervals were calculated at the tile level for all 13 features. Feature stability was evaluated using the smaller absolute effect size and the smaller direction-independent ROC-AUC across the two buildings. Features were classified as directionally consistent, reversed, or uncertain based on the effect directions and confidence intervals. Building 2 labels were used only to explain the observed cross-building failure. These labels were not used to build the direct-transfer models.

Finally, we examined whether a small labeled sample from the target building could improve the models. Twenty stratified splits were predefined and frozen. For each split, 0, 2, 4, 6, 8, or 10 tiles from Building 2 formed the adaptation set. The remaining tiles formed an independent test set. The feature-based models were refitted using the combined Building 1 data and adaptation set. Each building contributed 50% of the total training weight. For the 1D-CNN, only the final convolutional block and classification head were updated. The adaptation and test sets were strictly separated. Performance was evaluated using both the fixed classification threshold and a Youden threshold determined only from the adaptation set.

3. Results and Discussion

3.1 Within-Building Performance and Direct Cross-Building Generalization

Figure 2(a) shows that all five models achieved high balanced accuracy within both buildings. This result indicates that impact sounds contain information that can distinguish sound and detached tiles. Building 2 had a much smaller sample size, but its repeated cross-validation results remained close to those of Building 1.

In contrast, Figure 2(b) shows a clear performance

decrease after direct transfer from Building 1 to Building 2. Balanced accuracy and ROC-AUC were mostly below the random level for LR, SVM, RF, and XGBoost. The 1D-CNN performed better than the feature-based models, but its performance remained far below the within-building result. Therefore, near-saturated performance within a building does not demonstrate cross-building applicability.

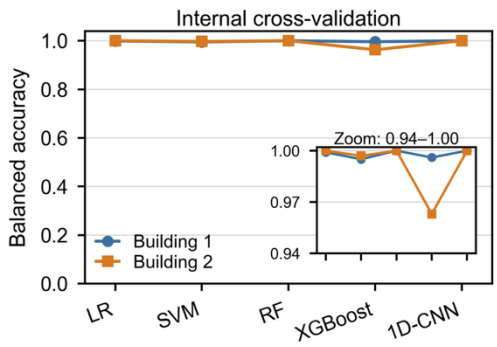

(a) Internal cross-validation

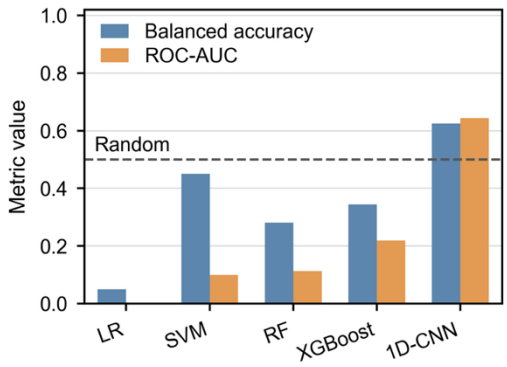

(b) Building 1 → Building 2

Figure 2 Within-building validation and direct cross-building generalization

3.2 Cross-Building Feature Stability and Failure Analysis

Figure 3 shows the cross-building stability, discriminative ability, and effect-direction consistency of the 13 acoustic features. The horizontal axis is the smaller absolute Hedges' g value across the two buildings. A feature farther to the right retains a stronger class effect in the less favorable building. The vertical axis is the smaller direction-independent ROC-AUC across the buildings. A feature farther upward retains stronger single-feature ranking ability. The dashed lines indicate the reference values adopted in this study (|Hedges' g| = 0.5 and ROC-AUC = 0.70) for exploratory feature screening.

These thresholds divide the plot into four regions according to whether each feature meets the effect-size and ranking-ability criteria. The green upper-right region satisfies both exploratory strength criteria. The other three gray regions fail at least one criterion. Point color indicates effect-direction consistency. Green indicates consistent effect directions between the two buildings. Orange indicates opposite effect directions between buildings. Gray indicates that the effect direction is uncertain in at least one building.

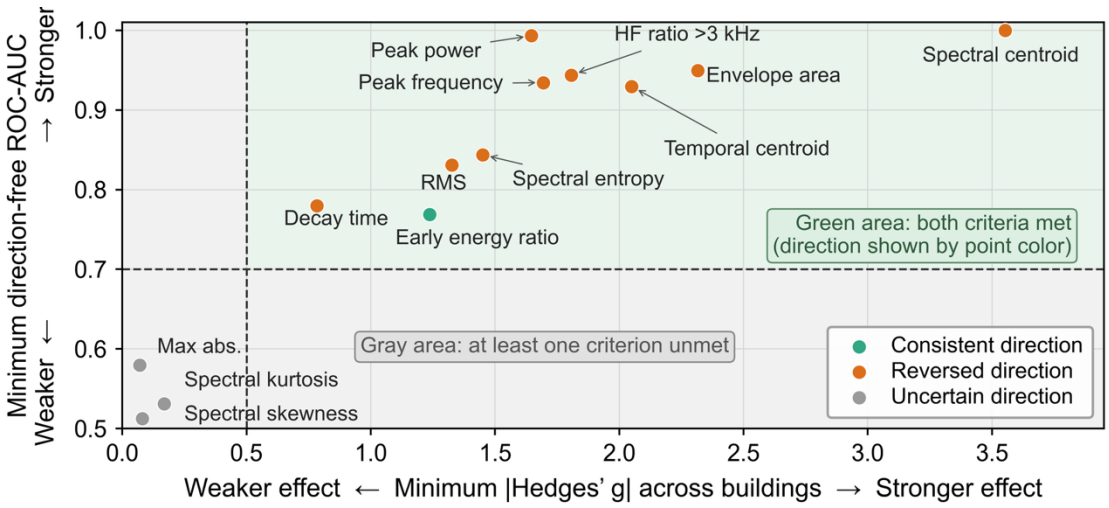

Figure 3 Stability of the 13 acoustic features across the two buildings

Most strong features in the upper-right region are orange. These include Spectral Centroid, Envelope Area, Peak Frequency, Peak Power, and High Frequency Ratio >3000 Hz. Thus, they distinguish the two classes within each building, but the class relationship is reversed. Only Early Energy Ratio 1 ms showed both strong discrimination and a robust, consistent direction. This finding explains the low ROC-AUC and reversed ranking observed during direct transfer of the feature-based models. It also shows that the cross-building problem is not limited to an incorrect fixed threshold. The relationship between features and class also changes.

3.3 Few-Shot Target-Domain Adaptation

Figure 4 shows how the balanced accuracy of each model changed as the number of labeled Building 2 tiles increased. Figures 4(a) and 4(b) present the results obtained using a fixed threshold and an adaptation-set Youden threshold, respectively. In Figure 4(a), the balanced accuracy of RF, XGBoost, and SVM increased rapidly and began to level off at approximately six to eight adaptation tiles. LR also improved, but its performance remained relatively low. The improvement of the 1D-CNN was limited and less stable than that of the stronger feature-based models. Figure 4(b) shows that selecting the classification threshold from the adaptation set further improved some results, although it did not change the overall model ranking. This indicates that threshold adjustment alone may not be sufficient when direct transfer produces an unsuitable class-ranking

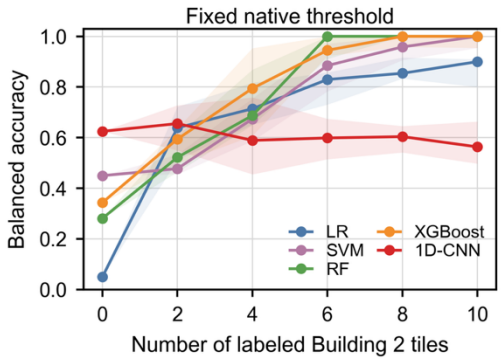

(a) Fixed native threshold

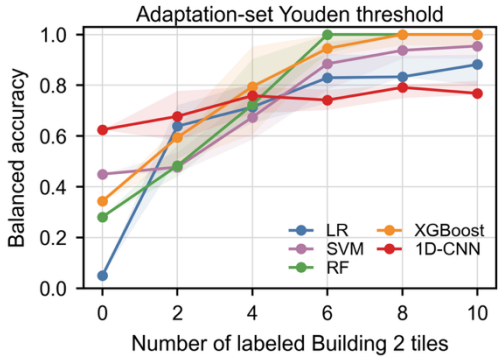

(b) Adaptation-set Youden threshold

Figure 4 Balanced accuracy at different target-domain sample sizes. Curves show the median of 20 frozen splits, and shaded areas show the interquartile range

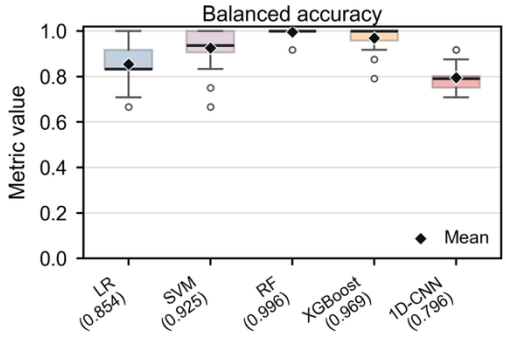

(a) Balanced accuracy

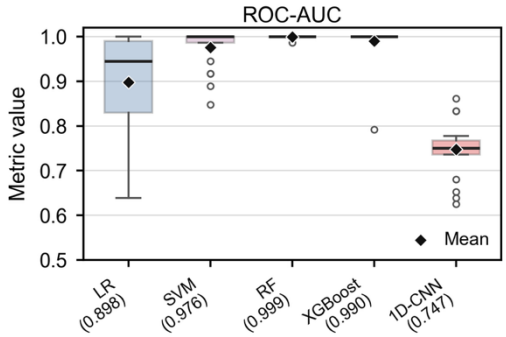

(b) ROC-AUC

Figure 5 Performance distributions of the five models with eight Building 2 adaptation tiles. Diamonds indicate the mean across 20 frozen splits

relationship.

Eight adaptation tiles were selected as a representative setting because the best-performing learning curves had nearly reached a plateau, while 18 tiles remained available for independent testing. Figure 5 compares the performance distributions of the models across the 20 frozen splits under the adaptation-set Youden threshold. In Figure 5(a), RF achieved the highest and most stable balanced accuracy, with a mean value of 0.996. XGBoost and SVM also performed well, whereas LR and the 1D-CNN showed lower performance and greater variation. In Figure 5(b), the ROC-AUC distributions show that RF, XGBoost, and SVM recovered strong ranking ability after few-shot adaptation, with mean values of 0.999, 0.990, and 0.976, respectively. Thus, adding a small target-domain sample restored an effective ranking relationship.

For the present dataset, six to eight labeled target-building tiles provided a favorable balance between model performance and labeling effort. This result supports collecting a small calibration set before applying an existing model to a new building. The calibration set should include both sound and detached tiles and must remain strictly separate from the final test data. Under the current few-shot conditions, the feature-based models generally adapted more efficiently than the one-dimensional convolutional neural network (1D-CNN) using raw waveforms. One possible reason is that the 13 features already summarize amplitude, decay, and spectral information. In contrast, the 1D-CNN must readjust a higher-dimensional waveform representation using only a limited number of target samples, which may restrict its adaptation.

4. Conclusions

Within-building cross-validation showed that impact sounds can distinguish sound and detached tiles. However, this relationship did not remain stable across buildings. Several strongly discriminative features reversed their effect direction. Differences in tile type, dimensions, and surface condition may change both the data distribution and the relationship between features and class. Therefore, high performance within one building is not sufficient evidence of practical generalizability.

After a small labeled sample from the target building was introduced, the feature-based models quickly reestablished an effective classification relationship. When the ranking direction changed, threshold adjustment alone could not replace model updating. In practice, a small labeled sample should be collected from each new building for calibration. Future studies will further explore the applicability of the proposed approach to a wider range of building types and field conditions.

Acknowledgements

This work was supported by the Obayashi Foundation. The authors also thank Masato Sato and Genta Hara, graduate students at the Imamoto Laboratory, Tokyo University of Science, for their valuable assistance.

Reference

[1] T. Soeta, T. Mikami, Basic study into a diagnostic system for exterior tile debonding, J. Struct. Constr. Eng. 81 (729) (2016) 1779–1787.

[2] Y. Kitamura, J. Takayama, Estimation of spalling properties of wall surface based on time frequency analysis of hammering sound, Meas. Sens. 18 (2021) 100182.

[3] D. Tanaka, Y. Ito, S. Kawabe, Effect of aerodynamic noise from a wall-contact type UAV on the tile detachment diagnosis using random forest-based machine learning, J. Struct. Constr. Eng. 91 (839) (2026) 63–74.

[4] F. Tong, X.M. Xu, B.L. Luk, et al., Evaluation of tile-wall bonding integrity based on impact acoustics and support vector machine, Sens. Actuators A Phys. 144 (1) (2008) 97–104.

[5] Y. Li, K. Imamoto, C. Kiyohara, et al., Multi-Indicator Evaluation of Tile–Wall Integrity Based on Hammering Tests toward Automated Inspection, J. Asian Concr. Fed. 12 (2) (2026) 39–53.

[6] Y. Li, K. Imamoto, C. Kiyohara, et al., Towards automated acoustic inspection for exterior tile debonding using in-situ impact and sweep sounds, Proceedings of fib Congress 2026, Lisbon, Portugal.

韓国における普通ポルトランドセメント規格の改正方向に関する研究

A Study on the Revision Direction of the Korean Ordinary Portland Cement Standard

申相澈※1、姜南圭※2、金建佑※3、金振晩※4
Sang-Chul Shin, Nam-Gyu Kang, Geon-Woo Kim, Jin-Man Kim

ABSTRACT

This study investigated the feasibility of increasing the mineral addition content permitted in Korean ordinary Portland cement (OPC) from 10% to 15%. Limestone powder (LP) was combined with ground granulated blast-furnace slag (GGBFS) or fly ash (FA), and the effects of cement fineness and C_3S content on hydration and strength development were evaluated. Increasing the mineral addition content caused little change in mortar flow and only moderately delayed setting, while all mixtures satisfied the relevant KS requirements. LP–GGBFS mixtures exhibited higher heat evolution and compressive strength than LP–FA mixtures. Increasing the Blaine fineness to 4,500 cm^2/g was particularly effective in improving early strength, whereas increasing the C_3S content from 61.3% to 64.2% helped maintain 28-day strength. These results demonstrate that OPC containing 15% mineral additions can achieve the required performance through appropriate material selection and optimization of cement fineness and C_3S content.

1. Introduction

Clinker production is responsible for the majority of CO_2 emissions associated with cement because of limestone decarbonation and kiln fuel consumption. Increasing the use of mineral additions is therefore one of the most immediately applicable measures for reducing the clinker factor. In Europe and the United States, blended cements occupy a substantial share of the market, whereas the Korean cement market, similar to that of Japan, remains dominated by OPC. Korean OPC represented more than 80% of total cement shipments in 2024. Consequently, reducing the clinker content within OPC is particularly important for achieving near- and medium-term carbon-reduction targets without requiring an abrupt change in market structure.

KS L 5201 currently permits LP together with one of GGBFS, FA, or pozzolan, with a total mineral-addition content of 10%. A proposed 2030 direction is to increase the permitted content to 15% while retaining performance comparable to current OPC. This would reduce the clinker-plus-gypsum fraction from 90% to 85%. However, dilution may decrease heat release and hydration-product formation, delay setting, and reduce compressive strength. The effects depend on both the type and proportion of the additions and cannot be judged from total replacement alone. Therefore, both hydration behavior and mechanical performance should be carefully evaluated.

This study investigated the performance of OPC containing 15% mineral additions and examined manufacturing adjustments capable of compensating for the associated strength loss. LP-GGBFS and LP-FA systems were compared at three ratios. Cement fineness was increased from approximately 3,500 to 4,000 and 4,500 cm^2/g, and C_3S content was increased from 61.3% to 64.2%. Flow, setting, heat evolution, and strength were evaluated to provide an experimental basis for revision of KS L 5201.

※1 大韓民国 国立公州大学校 建築工学科 研究教授 博士(工学)
※2 大韓民国 国立公州大学校 建築工学科 修士課程
※3 大韓民国 国立公州大学校 建築工学科 博士課程
※4 大韓民国 国立公州大学校 建築工学科 教授 博士(工学)

2. Experimental Program

2.1 Materials and mixture proportions

The experimental matrix is summarized in Table 1. Two cements containing 10% mineral additions were used as controls: L5G5 contained 5% limestone powder (LP) and 5% ground granulated blast-furnace slag (GGBFS), whereas L5F5 contained 5% LP and 5% fly ash (FA). In both controls, clinker plus gypsum accounted for 90% of the cement. Six test cements containing 15% additions were then prepared with the clinker-plus-gypsum fraction reduced to 85%. For each reactive addition, the LP-to-GGBFS or LP-to-FA ratio was varied as 5:10, 7.5:7.5, and 10:5. This design made it possible to distinguish the effect of the total addition content from the effect of the addition type and binary proportion.

As also indicated in Table 1, the reference cement condition, NB35-NA61, had a Blaine fineness of approximately 3,500 cm²/g and a C_3S content of 61.3%. Two higher-fineness conditions, HB40 and HB45, were produced by additional laboratory ball milling to approximately 4,000 and 4,500 cm²/g, respectively. A high-alite condition, HA64, retained a fineness close to 3,500 cm²/g but increased C_3S to 64.2%. The comparison of NB35, HB40, HB45, and HA64 therefore separated the physical acceleration caused by finer grinding from the chemical/ mineralogical acceleration caused by a higher alite content. All mortar mixtures were prepared at a water-to-binder ratio of 0.50 and a binder-to-sand ratio of 1:3.

2.2 Physical and mineralogical characteristics

The physical characteristics of the four cement conditions and three mineral additions are presented in Table 2. Increasing the nominal Blaine fineness from NB35 to HB40 and HB45 systematically decreased the 45 μm residue from 6.95% to 4.46% and 3.24%, respectively. The median particle size, D[0.5], similarly decreased from 12.99 μm for NB35 to 11.15 μm for HB40 and 10.40 μm for HB45. These changes confirm that the additional milling altered the entire particle-size distribution rather than only removing a small coarse fraction. HA64 had a particle-size distribution close to that of NB35, allowing the influence of C_3S content to be evaluated with limited interference from fineness.

Among the mineral additions listed in Table 2, GGBFS had a median particle size of 13.51 μm, similar to that of NB35, whereas LP showed a wider coarse tail with D[0.9] = 56.43 μm. FA was markedly coarser, with a 45 μm residue of 38.84%, D[0.5] = 28.88 μm, and D[0.9] = 110.23 μm. This difference is important when interpreting flow, hydration, and strength because FA simultaneously reduces the amount of rapidly reacting clinker and introduces a larger fraction of slowly reacting coarse particles. The clinker mineralogy also differed: C_3S increased from 61.3% in NB35/HB40/HB45 to 64.2% in HA64, while C_2S decreased from 15.9% to 13.6%.

2.3 Test Methods

Mortar flow was determined in accordance with KS L 5105 to identify changes in fresh-state consistency caused by the type and content of the mineral

Table 1 Experimental plan

Addition (%)	Mixture	Clinker + Gypsum(%)	LP (%)	FA (%)	GGBFS (%)	Blaine fineness (cm^2/g)	C_3S content (%)
10	L5G5	90	5	–	5	3,500 (NB35)	61.3 (NA61)
15	L5G10	85	5	–	10	3,500 (NB35) 4,000 (HB40) 4,500 (HB45)	61.3 (NA61) 64.2 (HA64)
	L7.5G7.5	85	7.5	–	7.5		
	L10G5	85	10	–	5		
	L5F10	85	5	10	–		
	L7.5F7.5	85	7.5	7.5	–		
	L10F5	85	10	5	–		

Table 2. Physical properties of raw materials

Material	Blaine (cm²/g)	45 μm residue (%)	Mean (μm)	D[0.1] (μm)	D[0.5] (μm)	D[0.9] (μm)
NB35	≈3,500	6.95	17.59	2.28	12.99	40.13
HB40	≈4,000	4.46	15.49	2.05	11.15	35.67
HB45	≈4,500	3.24	14.35	1.75	10.40	32.94
HA64	≈3,500	6.20	17.58	2.45	13.47	39.20
GGBFS	≈4,000	7.98	18.11	1.92	13.51	41.67
LP	≈3,900	13.51	21.05	1.72	12.56	56.43
FA	≈3,000	38.84	45.03	5.07	28.88	110.23

additions. Initial and final setting times were measured using the Vicat method in accordance with KS L ISO 9597. Hydration kinetics were evaluated by isothermal conduction calorimetry following ASTM C1702, and the heat-flow curves were normalized by binder mass. Mortar compressive strength was determined at 1, 3, 7, and 28 days in accordance with KS L ISO 679. The strength results were evaluated both as absolute values and as relative values normalized to the corresponding 10% control or NB35 baseline, as appropriate.

The combined test program was selected to establish a causal sequence rather than relying on compressive strength alone. Flow and setting characterize practical handling and early stiffening; calorimetry identifies changes in the rate of early hydration; and strength measurements show whether those kinetic changes translate into engineering performance. This framework is particularly relevant to standard revision because an increase in permitted additions should be assessed against all principal quality requirements, not only the nominal replacement percentage.

3. Results and Discussion

3.1 Flowability

Figure 1 shows the mortar-flow results for the two controls and six baseline cements containing 15% mineral additions. L5G5 exhibited a flow of 180.0 mm, while L5F5 reached 202.5 mm. Increasing the total addition content from 10% to 15% did not cause a measurable loss of flow in either series. All three LP-GGBFS mixtures recorded 180.0 mm, and the LP-FA mixtures ranged from 200.0 to 202.5 mm. The results demonstrate that the proposed increase in mineral additions does not inherently impair mortar workability under the investigated water-to-binder ratio.

The approximately 20 mm difference between the GGBFS and FA series in Figure 1 is more strongly related to material characteristics than to total replacement. As shown in Table 2, FA had a much coarser particle-size distribution than GGBFS and the cements. Its lower specific surface exposed to water and its limited reaction during the short flow-test period likely reduced early water demand. By contrast, the finer GGBFS fraction and its greater early surface activity produced a flow comparable to L5G5. Importantly, changing the LP proportion from 5% to 10% produced little variation within each series, indicating that the identity of the accompanying reactive addition exerted a greater influence on flow than the LP/GGBFS or LP/FA ratio.

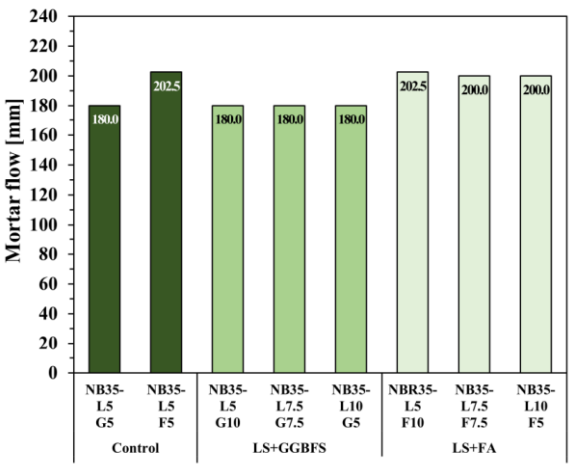

Figure 1 Mortar flow

3.2 Setting behavior

The initial and final setting times are presented in Figure 2. The initial setting times of L5G5 and L5F5 were 3.12 and 3.62 h, respectively, and their final setting times were 5.08 and 5.50 h. For the 15% LP-GGBFS mixtures, initial setting ranged from 3.22 to 3.40 h and final setting from 5.25 to 5.50 h. The LP-FA mixtures showed slightly longer times, with initial setting between 3.57 and 3.77 h and final setting between 5.58 and 5.85 h. The shift was moderate rather than excessive: every cement remained far above the KS minimum initial-setting requirement of 1 h and far below the maximum final-setting limit of 10 h.

Figure 2 also reveals a response consistent with the flow results. Replacing GGBFS with FA delayed both initial and final set because FA contributed less to early dissolution and reaction. Nevertheless, the interval between initial and final set remained relatively stable, suggesting that the main effect was a modest shift in the onset of stiffening rather than a fundamental change in the progression of setting. From the perspective of KS L 5201 revision, these results indicate that raising the mineral-addition limit to 15% is unlikely to create a practical setting-time problem, provided that the existing performance limits continue to apply.

3.3 Hydration kinetics

Figure 3 presents the normalized heat-flow curves up to 72 h. All cements followed the conventional sequence of an initial reaction, induction period, acceleration period, and deceleration period. Thus, increasing the addition content to 15% did not introduce an abnormal hydration pattern. The principal differences appeared in the magnitude and timing of the main silicate-hydration peak. The LP-GGBFS curves remained close to the L5G5 control and exhibited a higher main peak than the LP-FA curves. The lower peaks of the FA series are consistent with the lower early reactivity of FA and the reduced quantity of clinker available for rapid hydration.

The trends in Figure 3 clarify why the setting delay in Figure 2 was greater for the LP-FA series and why the early strength discussed below was lower. GGBFS can participate in early reactions under the alkaline conditions created by clinker hydration, whereas the pozzolanic contribution of FA develops more slowly. LP does not simply behave as an inert diluent: its fine fraction can provide nucleation sites and accelerate precipitation of clinker hydration products. Accordingly, the main peak tended to be better maintained as the LP fraction increased within the same 15% addition level.

Although cumulative heat is not separately plotted, the 72-h values support the heat-flow interpretation in Figure 3. The L5G5 and L5F5 controls released 289.0 and 281.9 J/g-binder, respectively. The LP-GGBFS mixtures ranged from 273.2 to 280.6 J/g-binder and averaged 276.5 J/g-binder, whereas the LP-FA mixtures ranged from 264.2 to 272.7 J/g-binder and averaged 268.8 J/g-binder. The reduction from the controls confirms the clinker-dilution effect, while the approximately 7.7 J/g-binder difference between the series confirms that GGBFS was more effective than FA in preserving early hydration.

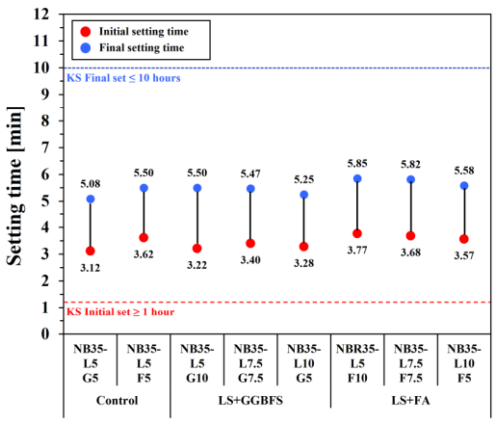

Figure 2 Setting time results

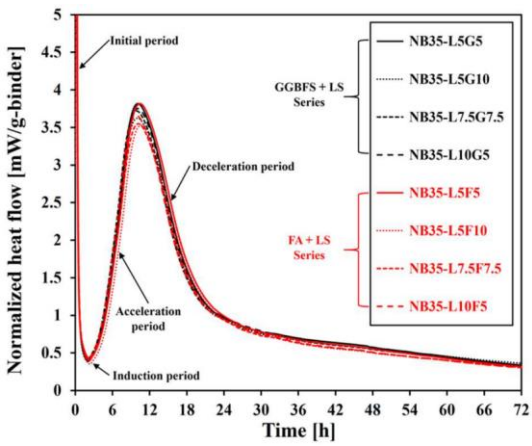

Figure 3 Heat flow results

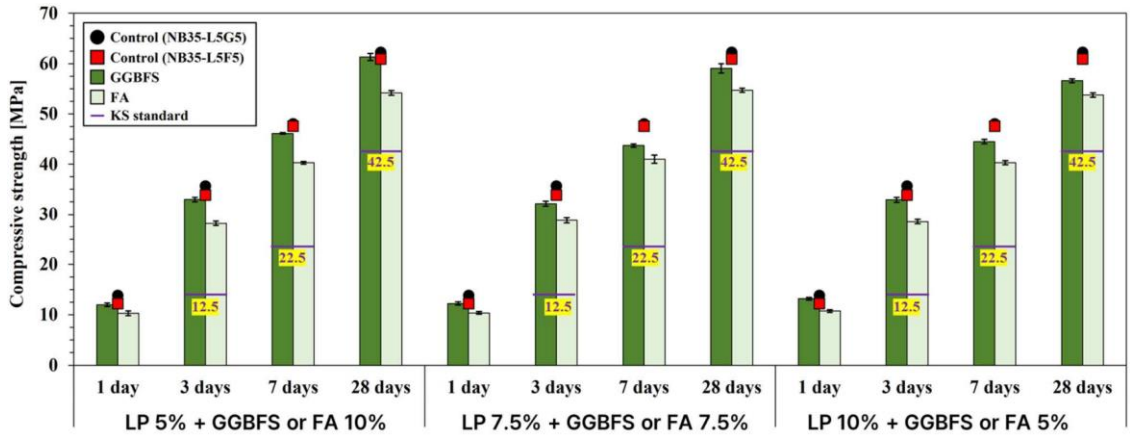

Figure 4 Compressive strength results

3.4 Compressive strength

The absolute compressive-strength results are shown in Figure 4. Increasing the mineral-addition content from 10% to 15% generally reduced strength at all ages because the mass fraction of clinker plus gypsum decreased from 90% to 85%. The reduction was most pronounced at early age, when secondary reactions had not developed sufficiently to compensate for clinker dilution. Nevertheless, every mixture exceeded the applicable KS strength criteria: 12.5 MPa at 3 days, 22.5 MPa at 7 days, and 42.5 MPa at 28 days. The compliance margin was substantial at 7 and 28 days, demonstrating that the 15% cements did not merely meet the limit marginally.

At identical LP contents, the GGBFS mixtures consistently outperformed the corresponding FA mixtures in Figure 4. This ranking agrees with the heat-flow curves in Figure 3 and demonstrates that the early reaction advantage of GGBFS translated directly into mechanical performance. Among the LP-GGBFS mixtures, L10G5 showed the smallest loss relative to L5G5 and retained approximately 95.2%, 92.4%, 92.6%, and 97.3% of the control strength at 1, 3, 7, and 28 days, respectively. The recovery toward the control at 28 days suggests that the combination of LP-induced nucleation and continued GGBFS reaction compensated for much of the initial dilution.

The LP-FA mixtures showed lower strength, but their 28-day values still remained clearly above the KS requirement. Their slower development is consistent with the coarse FA particle-size distribution reported in Table 2 and the lower heat evolution in Figure 3. These findings imply that a revised standard need not prescribe one fixed addition combination. Instead, it can permit several combinations while retaining performance-based strength requirements, allowing producers to balance material availability, carbon reduction, and strength development.

3.5 Performance improvement by fineness and C_3S content

Figure 5 compares the relative strength of the NB35, HB40, HB45, and HA64 conditions at four ages. At 1 day, the baseline NB35 mixtures retained only 84.3-95.2% of their respective 10% controls. Increasing fineness to HB40 raised relative strength to 106.6-133.0%, and HB45 produced 129.5-154.1%. Increasing C_3S content to 64.2% also improved 1-day performance, producing 112.2-142.2%. The fact that every HB40, HB45, and HA64 mixture exceeded 100% at 1 day demonstrates that manufacturing adjustments can fully compensate for the early dilution penalty, even for the less reactive LP-FA combinations.

The age-dependent results in Figure 5 distinguish the roles of fineness and clinker mineralogy. The benefit of HB45 was greatest at 1 day because smaller cement particles increased dissolution rate and the number of nucleation sites. At 3 days, HB45

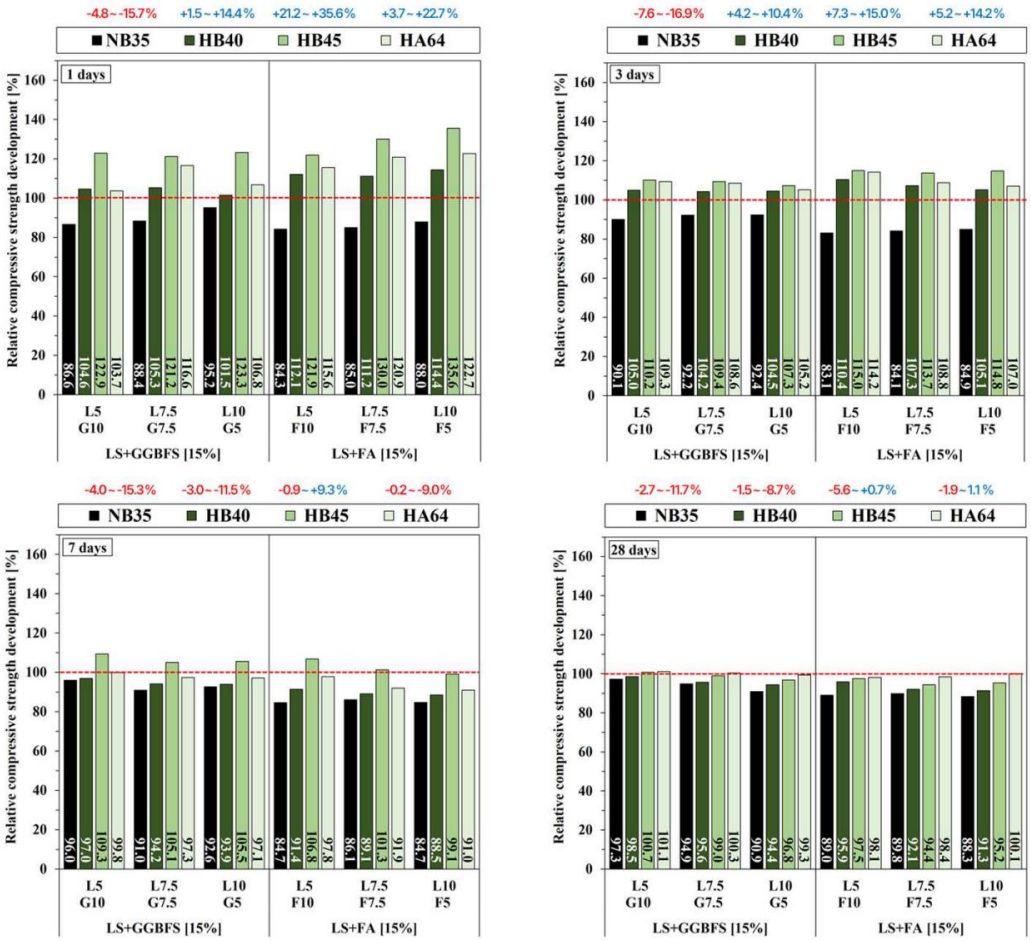

Figure 5 Effects of fineness and C3S content on strength

and HA64 remained approximately 3-4 MPa stronger than the corresponding NB35 mixtures, while at 7 days HB45 retained an average advantage of approximately 2.2 MPa. These trends confirm that finer grinding is primarily a kinetic intervention: it advances hydration and strength development rather than necessarily increasing the ultimate reaction capacity.

By 28 days, most fineness-modified mixtures converged toward the baseline, and some exhibited a slight reduction in relative strength. HA64 showed the most stable later-age response, limiting the average decrease to approximately 0.3 MPa and maintaining strength close to NB35. The higher C_3S content increased the amount of the principal strength-producing clinker phase without relying solely on accelerated consumption of the same clinker inventory. Therefore, HB45 is the more effective option when very early strength is the controlling requirement, whereas HA64 provides a more balanced solution when both early strength and 28-day retention are important.

4. Conclusions

1) Increasing the mineral-addition content from 10% to 15% caused no systematic reduction in mortar flow. LP-FA mortars were approximately 20 mm more fluid than LP-GGBFS mortars. Setting was moderately delayed, but all mixtures satisfied the KS limits.
2) The 72-h cumulative heat decreased with increasing addition content. The LP-GGBFS series averaged 276.5 J/g-binder, compared with 268.8 J/g-binder for the LP-FA series. Increasing the LP proportion increased cumulative heat within each series.
3) All 15% mixtures satisfied the KS compressive -strength requirements. LP-GGBFS mixtures developed higher and more stable strength than

LP-FA mixtures, and L10G5 retained 97.3% of the control strength at 28 days.

4) Increasing fineness to approximately 4,500 cm^2/g was the most effective route for accelerating early hydration and produced a maximum 1-day relative strength of approximately 154%. Increasing C_3S content to 64.2% was more effective in limiting the loss of 28-day strength.
5) The permitted mineral-addition content of Korean OPC can be increased to 15% without sacrificing required performance when the addition combination, fineness, and clinker mineralogy are appropriately controlled. The results provide a technical basis for revision of KS L 5201.

Acknowledgment

This work was supported by the National Research Foundation of Korea(NRF) grant funded by the Korea government(MSIT) (No. RS-2022-NR072408)

Reference

[1] KS L 5201, Portland Cement, Korean Agency for Technology and Standards, Republic of Korea.
[2] R. Snellings, Assessing, understanding and unlocking supplementary cementitious materials, RILEM Technical Letters 1 (2016) 50–55.
[3] R. Snellings, G. Mertens, J. Elsen, Supplementary cementitious materials, Reviews in Mineralogy and Geochemistry 74 (2012) 211–278.
[4] K.L. Scrivener, V.M. John, E.M. Gartner, Eco-efficient cements: Potential, economically viable solutions for a low-CO_2 cement-based materials industry, Cement and Concrete Research 114 (2018) 2–26.
[5] B. Lothenbach, K. Scrivener, R.D. Hooton, Supplementary cementitious materials, Cement and Concrete Research 41 (2011) 1244–1256.
[6] R. Snellings, X-ray powder diffraction applied to cement, in: K. Scrivener, R. Snellings, B. Lothenbach (Eds.), A Practical Guide to Microstructural Analysis of Cementitious Materials, CRC Press, 2016.

階上解体におけるスラブの負担軽減工法の開発と適用

Development and Application of a Load Reduction Method for Slabs During Upper-Floor Demolition

松本卓也※1，湯浅昇※2，青木孝義※3，福本克也※4
Takuya Matsumoto, Noboru Yuasa, Takayoshi Aoki, Katsuya Fukumoto

ABSTRACT

建築物の解体工法には，スラブに重機を積載させて解体する階上解体工法がある。この工法は重機がスラブに積載するため，スラブの荷重に影響を与える。したがって，スラブに作用する衝撃荷重に対する支保工の強度検討が必要不可欠である。この問題を解決するために，スラブの強度に頼ることのない解体工法の開発が望まれる。解決策として，「ブリッジ工法」という解体工法を開発した。本報告は，「ブリッジ工法」の概要および構成，補強計算結果に関する従来工法との比較，適用実績について報告する。

1. Introduction

The upper-floor demolition method is a deconstruction technique in which heavy machinery is lifted onto the roof or the uppermost floor of a building to perform demolition. In this method, slabs and beams are subjected to dynamic operational and machinery loads that are not considered in the original design; these structural members must be strengthened with temporary vertical supports beneath them.

However, standardized structural design methodology for such reinforcement has not yet been established [1]; thus, temporary support systems are frequently installed based on empirical judgement and practical experience. Consequently, even with temporary support in place, it may not be structurally sufficient, highlighting the risk of slab collapse during operations.

To solve this problem, a construction method has been developed which spans a “Bridge” between beams [2]. This made it possible to carry out demolition work with heavy machinery without relying on the slab’s strength or reinforcement. This paper presents an outline of the bridge method, a comparative study with the conventional method, and the results of its application.

2. Conventional method

Upper-floor demolition method is a demolition technique in which heavy machinery is used to demolish interior structural members (except exterior ones), exterior members and self-propelled transit of machinery to the lower floor, and this procedure is repeated sequentially for each floor. Generally, the upper-floor demolition method (hereinafter referred to as the conventional method), concrete rubble generated during demolition (hereinafter referred to as rubble), is spread over the slabs as shown in Photo 1, and heavy machinery operates on it.

3. Bridge method

3.1 Overview of the bridge method

In the developed bridge method [3], bridges are installed between structural beams to support machinery, which is operated on them. When moving machinery to a lower floor, a sloping bridge is

※1 三同建設 工事統括部 計画･技術グループ グループ長
※2 日本大学 生産工学部 建築工学科 教授･工博
※3 金城学院大学 デザイン工学部 建築デザイン学科 教授･工博
※4 三同建設 専務取締役

installed from the upper to the lower floor, allowing the heavy machinery to descend safely.

The primary feature of the bridge method is that the loads from the heavy machinery are supported by the structural beams through the bridges, thereby reducing the structural load acting on the slab. As shown in Photo 2, the bridges are gripped or lifted by heavy machinery and moved to the required locations, where demolition work is carried out on their tops. Aside from the usage of bridges, the demolition procedure is the same as the conventional method.

Furthermore, there is a method similar to the Bridge Method discussed in this paper [4]. Although both methods are similar in that heavy machinery demolishes girders installed between structural beams, the member configurations differ. In contrast to conventional systems that rely on standardized leased components, the bridge method features a custom design tailored to each building and is executed under our own company's responsibility.

3.2 Configuration of the bridge

As shown in Figure 1, the bridge consists of two main girders (H-beams) and several joists (square hollow sections) assembled in a ladder configuration.

The specifications of the girder members were assumed to vary with the building's beam span and the type of heavy machinery used. Therefore, the bridge length and span between supports shown in Figure 1 represent one example.

The joists are made of □-125×125×6 square steel tubes (section modulus 103 cm³, plastic section modulus 122 cm³). There are two types of joists: standard and suspended. The suspended type is designed to be moved by being grasped or suspended by heavy machinery. Suspended joists are installed at three locations: both ends and in the centre of the bridge.

The girder and joist members were connected by drilling bolt holes in the girder webs. L-shaped steel angles (L-100 × 100 × 10) with bolt holes at both ends were welded perpendicular to the square steel tubes, and the joist members were then fixed to the girder members using bolts.

The spacing between adjacent joist members was set at 500–600 mm centre-to-centre to account for the travelling performance of the heavy machinery. As the adjacent bridges were arranged in a staggered configuration, as shown in Figure 2 and Photo 3, the layout of the joist members required planning to account for the overlap length between adjacent girder members.

The Slope bridge was designed to be used in combination with the slope-support bridge. The Slope bridge is equipped with hook-type fasteners, and the slope-support bridge is equipped with pin-type fasteners, both of which are bolted to the ends of the girder members. As shown in Figure 3, Photos 4 & 5,

Photo 1 Conventional method

Photo 2 Bridge method

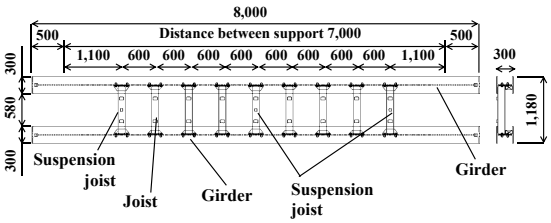

a. Plan

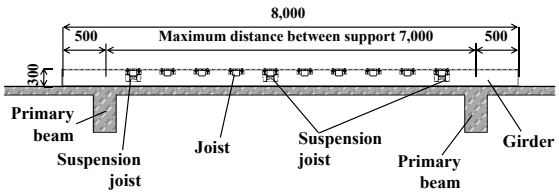

b. Cross section

Figure 1 Bridge composition (In the case of H-300×300×10×15)

the slope was formed by engaging the hooks with the pins. The lower-end-of-slope bridge was positioned onto a bridge previously installed on the lower floor. Slope bridge and slope-support bridge are fixed to each other at their ends to allow heavy machinery to descend. As shown in Figure 4, joists are installed up to the end of each girder member.

3.3 Criteria for adoption of the bridge method

The criteria for adopting the bridge method are shown below. The adoption of the bridge method is contingent on all the following criteria being met.

(1) Design documents must be available, and the beam locations must be verified from the drawings.

(2) The beams are in good condition and arranged regularly.

(3) The centre-to-centre distance of the supporting beams (span length between supports) must be 8m or less.

(4) A bearing length of at least 0.5m must be secured at both ends of the beams. Since the span is limited to 8m or less, the total bridge length must not exceed 9m.

(5) The building's floor plan must consist of at least three spans in the transverse direction and at least five spans in the longitudinal direction.

(6) When a slope bridge is used, installation must be possible at an inclination angle of 25° or less.

4. Bridge strength calculation

4.1 Prerequisites

The following are the assumptions adopted for the strength calculation of the bridge's girders and joists.

(1) The steel grade used for the girder and joist members was SS400 (design standard strength F=235N/mm^2).

(2) The allowable stress was taken as the yield strength (design standard strength) if the loads generated during demolition work act as short-term loads.

(3) The allowable bending stress was determined by comparing the smaller value between the allowable bending stress and the allowable

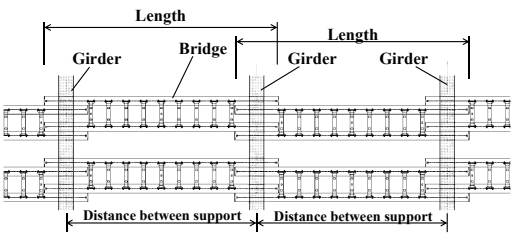

Figure 2 Bridge layout plan

Photo 3 Bridge place

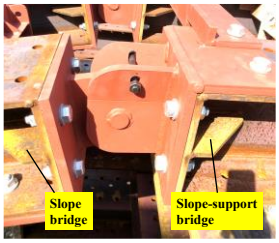

Photo 4 Slope bridge fixed

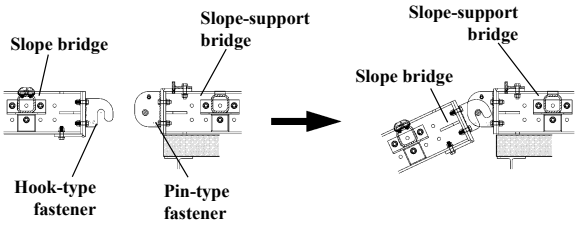

Figure 3 Slope bridge fixing detail

Photo 5 Slope bridge using

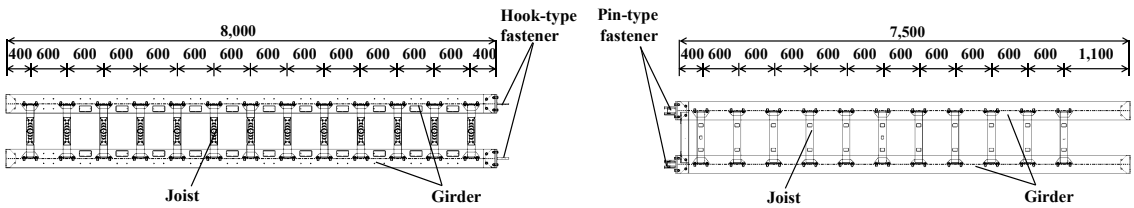

a. Slope bridge b. Slope-support bridge

Figure 4 Slope bridge and slope-support bridge configuration diagram

bending compressive stress, with the maximum value limited to 235 N/mm².

(4) The allowable shear stress was assumed to be 135 N/mm².

(5) Hydraulic machinery with 0.8m³ and 0.5m³ attachments (hereinafter referred to as the 0.8m³ machinery and the 0.5m³ machinery, respectively) and the specifications are listed in Table 1. Based on the Allowable Stress Design Standards for Steel Structures[5)], the machinery loads were determined by considering impact loads generated during operation, and a safety factor of 1.2 was applied to them.

Table 1 Heavy machinery specification

	Load (kN)	Crawler width (m)	Crawler center distance (m)	Ground contact length (m)
0.8m³ machinery	340.8	and0.6	2.39	3.66
0.5m³ machinery	201.6	0.5	1.99	3.05

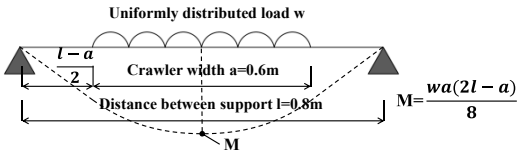

Figure 5 Concept of bending stress in joists

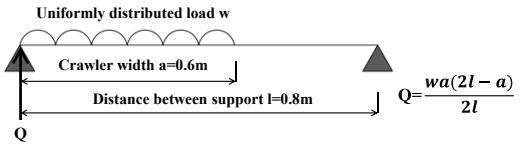

Figure 6 Concept of shear stress in joists

Table 2 Strength calculation of joists

	Stress (N/mm²)	Allowable stress (N/mm²)	Judgement
Bending	207	235	OK
Shear	57	135	OK

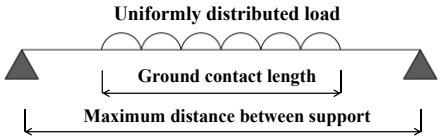

Figure 7 Concept of bending stress in girders

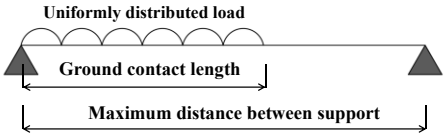

Figure 8 Concept of shear stress in girders

4.2 Joist strength calculation

The strength of the joist was evaluated by comparing the calculated bending stress and shear stress with the allowable values when the crawler of the 0.8³ machinery was positioned perpendicular to the joists. As shown in Figures 5 & 6, the joists were modeled as simply supported beams to obtain the maximum stress. The bending stress was evaluated assuming the machinery load acted at the centre of the joist. In contrast, the shear stress was evaluated under the condition that the machinery load acted at the joist edge. The distance between the joist support points was 0.8m, and the crawler width was 0.6m. The dynamic load was calculated by assuming that one joist supported half of the machinery load during operation. The load was then divided by the width of one crawler to obtain a uniformly distributed load, calculated as w = (340.8 × 0.5) / 0.6 = 284 kN/m.

The results are shown in Table 2. The calculated bending stress was 207 N/mm², which is below the allowable stress limit: 207 N/mm² < 235 N/mm². The calculated shear stress was 57 N/mm², which is below the allowable stress limit, 57 N/mm² < 135 N/mm². Since both calculated values were below the allowable limits, the structural safety of the joist members was verified.

4.3 Girders strength calculation

To determine the maximum stress values, the girders were analyzed as simply supported beams under a loading condition where the crawler is positioned parallel to the girder, as shown in Figures 7 & 8. For the bending stress analysis, the machinery was placed at the mid-span of the girder. For the shear stress analysis, it was placed at the girder end. The calculated bending and shear stresses were compared to the allowable values.

The calculation is considered for four loading conditions corresponding to the maximum span during demolition work (maximum beam spacing) and the maximum girder length during machine descent operations. These conditions included combinations of H-300×300×10×15 and H-350×350×12×19 girder sections with either 0.8 m³ or 0.5 m³ machinery.

During demolition work, the dynamic load was evaluated assuming that, when the machinery operated in a side-loading posture, one girder carried 80% of the machine load. This load was converted to an equivalent uniformly distributed load by dividing it by the contact area of one crawler track.

For the 0.8 m³ machinery:

w= (340.8×0.8) / (3.66×0.6) =124.15kN/m^2

For the 0.5 m³ machinery:

w= (201.6×0.8) / (3.05×0.5) = 105.76kN/m^2

The following four cases were evaluated:

- Pattern 1: 0.8m³ machinery, H-300×300×10×15 girder, 7m span
- Pattern 2: 0.5m³ machinery, H-300×300×10×15 girder, 8.5m span
- Pattern 3: 0.8m³ machinery, H-350×350×12×19 girder, 9.5m span
- Pattern 4: 0.5m³ machinery, H-350×350×12×19 girder, 12m span

Table 3 shows the girder strength calculation results, and Table 4 shows the maximum span for which the Bridge girders can be safely used.

The dynamic load occurs during the machinery's descent to the floor. Although a single girder carried 50% of the machinery load, a 60% load was assumed for safety. This load was divided by the contact area of one crawler track to obtain a uniformly distributed load.

For a 0.8m³ heavy machinery, w = (340.8 × 0.6) / (3.66 × 0.6) = 93.1kN/m², and for a 0.5m³ heavy machinery, w = (201.6 × 0.6) / (3.05 × 0.5) = 79.3kN/m².

The following four cases were evaluated:

- Pattern 1: 0.8m³ machinery, H-300×300×10×15 girder, girder length of 8.5 m
- Pattern 2: 0.5m³ machinery, H-300×300×10×15 girder, girder length of 10 m
- Pattern 3: 0.8m³ machinery, H-350×350×12×19 girder, girder length of 12 m
- Pattern 4: 0.5m³ machinery, H-350×350×12×19 girder, girder length of 14.5 m

Table 5 shows the girder strength calculation results for machine descent operations, and Table 6 shows the maximum allowable length of the girders.

For both demolition work and machine descent operations, the calculated stresses were below the allowable stress limits. Accordingly, the maximum spans and lengths for the bridge were verified to ensure safe operation.

5. Comparison of support for each method

5.1 Structural conditions

A comparative assessment of the required temporary support during demolition work between the conventional and bridge methods was conducted using a hypothetical structural model. The structural conditions of the model are summarized below.

(1) The structure was assumed to be a reinforced concrete (RC) structure.

Table 3 Girder strength calculation

		Stress (A) (N/mm^2)	Allowable stress (B) (N/mm^2)	Judgement (A/B<1)
Pattern 1 0.8 machinery, H300, 7m	Bending	233	235	OK
	Shear	66	135	OK
Pattern 2 0.5 machinery, H300, 8.5m	Bending	191	196	OK
	Shear	44	135	OK
Pattern 3 0.8 machinery, H350, 9.5m	Bending	207	229	OK
	Shear	53	135	OK
Pattern 4 0.5 machinery, H350, 12m	Bending	175	181	OK
	Shear	35	135	OK

Table 4 Maximum distance between support for girders

	H-300×300×10×15	H-350×350×12×19
0.8m^3 machinery	7m (Pattern 1)	9.5m (Pattern 3)
0.5m^3 machinery	8.5m (Pattern 2)	12m (Pattern 4)

Table 5 Girder strength calculation

		Stress (A) (N/mm^2)	Allowable stress (B) (N/mm^2)	Judgement (A/B<1)
Pattern 1 0.8 machinery, H300, 8.5m	Bending	177	196	OK
	Shear	41	135	OK
Pattern 2 0.5 machinery, H300, 10m	Bending	148	167	OK
	Shear	29	135	OK
Pattern 3 0.8 machinery, H350, 12m	Bending	165	181	OK
	Shear	33	135	OK
Pattern 4 0.5 machinery, H350, 14.5m	Bending	143	150	OK
	Shear	24	135	OK

Table 6 Maximum length girders when descent

	H-300×300×10×15	H-350×350×12×19
0.8m^3 machinery	8.5m (Pattern 1)	12m (Pattern 3)
0.5m^3 machinery	10m (Pattern 2)	14.5m (Pattern 4)

(2) As shown in Figure 9, the span was set at 6m × 6m. The slab dimensions were 3m in the transverse direction and 6m in the longitudinal direction. The beam length was 6m, and the floor height was 3.5m.

(3) The slab thickness was assumed to be 150 mm. As shown in Table 7, the slab reinforcement for both the top bar at the short-span edge and the bottom bar at the slab centre consisted of alternating φ9 and φ13 bars at 150 mm spacing.

(4) The secondary beam section was assumed to be 300mm × 600mm.

(5) The primary beams G1 and G2 were assumed to have cross-sectional dimensions of 400mm × 800mm.

(6) As shown in Table 8, the beam reinforcement was assumed as follows:
Secondary beams: 3-φ19 throughout the entire cross-section
Primary beams G1 and G2: φ4-25 throughout the entire cross-section.

(7) The concrete cover thickness was assumed to be 30 mm.

(8) All non-structural members were assumed to have been removed; however, a 30 mm thick layer of base mortar was assumed to remain on the structural surface.

(9) The unit weights of the materials were as follows:
- Reinforced concrete (RC): 24 kN/m³
- Mortar: 20 kN/m³
- Demolition debris (rubble): assumed to be 70% of the unit weight of RC; 24 kN/m³ × 0.7 = 16.8 kN/m³

(10) The design strength of the concrete was assumed to be 18 N/mm².

(11) The yield strength of the reinforcing bars was assumed to be SR235 for reinforcing bars of φ16 or smaller and SR295 for reinforcing bars larger than φ16 mm.

5.2 Prerequisites

The assumptions for the reinforcement calculation using the conventional method are summarized below.

(1) The allowable stresses of the structural materials were evaluated based on the assumption that the loads generated during demolition work act as short-term loading conditions.

(2) The allowable bending stress of reinforcing bars was taken as the yield strength point. Accordingly, the allowable stresses were assumed to be 235 N/mm² for SR235 and 295 N/mm² for SR295.

(3) The allowable shear stress of the concrete was taken as 0.9 N/mm² based on the design strength of the concrete.

(4) The structural dead load per unit area of the structural members was calculated as follows:
Slab own weight of slab thickness 150 mm = 0.15 × 24 = 3.6 kN/m^2
Mortar finishing load of mortar thickness 30 mm = 0.03 × 20 = 0.6 kN/m^2
Concrete rubble load of rubble thickness 500 mm = 0.5 × 16.8 = 8.4 kN/m^2.

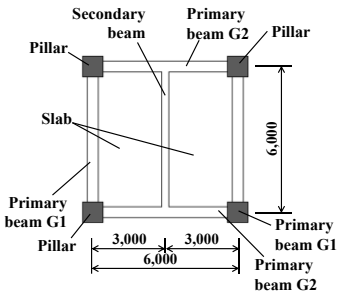

a. Plan

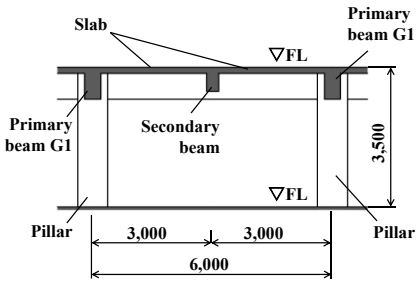

b. Cross section

Figure 9 Virtual model

Table 7 Slab reinforcement

	Short side end	Short side center
Upper reinforcement	φ9,13-@150	—
Lower reinforcement	φ9-@150	φ9,13-@150

Table 8 Beam reinforcement

	Secondary beam		Main beam	
	End	Center	End	Center
Upper reinforcement	3-φ19	3-φ19	4-φ25	4-φ25
Lower reinforcement	3-φ19	3-φ19	4-φ25	4-φ25

(5) The structural dead load per unit length of the structural members was calculated as follows: Secondary beam cross-section: 300mm × 600mm; 0.3 × 0.6 × 24 = 4.32 kN/m.
Primary beams cross-section: 400mm × 800mm; 0.4 × 0.8 × 24 = 7.68 kN/m.

(6) Worker load per unit area was assumed to be based on two workers, each having a load calculated as 0.75 kN/m^2, resulting in 0.75 × 2 = 1.5 kN/m^2.

(7) The dynamic load was determined based on the 0.8 m^3 machinery listed in Table 1.

(8) It was assumed that only one machine could be placed on a single slab or beam at the same time, and that simultaneous loading by two or more machines would not occur.

(9) Strong steel props were adopted as the temporary support system, such as shoring. As shown in Table 9, since the floor height is 3.5m, the CH-40 type prop with a maximum length of 4m was selected, and the allowable load capacity of each prop is 128kN.

5.3 Method of consideration

The calculation method for determining the required number of temporary supports and reinforced floors has not yet been specified in the Architectural Institute of Japan publication Guidelines and Commentary for Building Demolition Work (Draft) (Reinforced Concrete Structures and Steel Structures Editions). Therefore, the calculation was conducted using an original method independently developed by the organization to which the first author belongs. In this calculation method, it is assumed that the applied loads are uniformly distributed among the slabs and beams across multiple floors. The load generated during demolition work is divided by the allowable load capacity of the slab and beam per floor to determine the required number of reinforced levels. Based on the load carried by each level, the required number of temporary supports is then calculated.

Table 9 Shoring strength

Type	Max length (m)	Min length (m)	Allowable(kN)
CH24	2.4	1.82	147
CH32	3.2	1.85	147
CH40	4.0	2.65	128
CH50	5.0	3.65	98

5.4 Shoring support in the conventional method

Table 10 shows the shoring calculation results for the conventional method. The judgements shown in the table were obtained by comparing the calculated stress values with allowable stress values. The required number of slab or beam support layers was determined by dividing the calculated stress by the allowable stress for a single level. The required number of reinforcement layers was obtained by subtracting one from the calculated value. Among the values calculated for end bending, mid-span bending, and shear, the maximum value was adopted for the final assessment.

For the slab, three layers of slab and two layers of support were required. For the secondary beam, four layers of beam and three layers of support were required. For the primary beams G1 and G2, three layers of beam and two layers of support were required, respectively.

Table 10 Required layers of shoring props for conventional method

		End bending	Center bending	Shear
Slab	Stress (A)	30.3kNm	20.4kNm	113.8kN
	Allowable (B)	14.9kNm	14.9kNm	90.2kN
	Judgement (A/B<1)	NG	NG	NG
	Number of layers required (A/B)	3(2.1)	2(1.4)	2(1.3)
	Number of shoring layers required (A/B-1)	2	1	1
Secondary beam	Stress (A)	345.9kNm	373.0kNm	403.8kN
	Allowable (B)	121.1kNm	121.1kNm	130.3kN
	Judgement (A/B<1)	NG	NG	NG
	Number of layers required (A/B)	3(2.9)	4(3.1)	4(3.1)
	Number of shoring layers required (A/B-1)	2	3	3
Primary beam G1	Stress (A)	469.4kNm	434.7kNm	527.3kN
	Allowable (B)	379.4kNm	379.4kNm	235.8kN
	Judgement (A/B<1)	NG	NG	NG
	Number of layers required (A/B)	2(1.2)	2(1.1)	3(2.2)
	Number of shoring layers required (A/B-1)	1	1	2
Primary beam G2	Stress (A)	488.8kNm	454.2kNm	540.2kN
	Allowable (B)	379.4kNm	379.4kNm	235.8kN
	Judgement (A/B<1)	NG	NG	NG
	Number of layers required (A/B)	2(1.3)	2(1.2)	3(2.3)
	Number of shoring layers required (A/B-1)	1	1	2

The layout of support for the slab was examined by comparing the allowable load capacity of one support with the applied load carried by each support, as well as by comparing the shear stress due to the punching shear failure with the allowable shear stress. The load per single support was calculated and defined as the sum of the dead load and the dynamic load of the slab acting on its tributary area. Table 11 shows the results of the calculations. Based on a 1.5m x 2m slab tributary area per support, the design load is 123kN. Compared to the allowable load of a shoring prop, the ratio was 123kN/128kN < 1. For punching shear failure, the calculated shear stress was 0.81 N/mm², and the comparison with the allowable shear stress yield was 0.81 N/mm² / 0.9 N/mm² < 1. Since both values were less than 1.0, structural safety was verified. Consequently, the support diagram for a slab was determined to consist of two temporary supports, with the short span divided into two equal sections and the long span divided into three equal sections.

The required number of temporary supports for the beam was calculated by dividing the load to be carried by the allowable load capacity of a single support, then rounding up to the nearest whole number. The calculation results are shown in Table 12.

For the secondary beam, the required load to be supported was 403.8 kN - 130.3 kN = 273.5 kN. Therefore, the required number of supports was determined to be 273.5 kN / 128 kN = 2.14, which was rounded up to three supports.

For the primary beam G1, the required supported load was 527.3 kN – 235.8 kN = 291.5 kN, so the number of supports required was 291.5 kN / 128 kN = 2.28, which resulted in three supports.

For the primary beam G2, the required supported load was 540.2 kN – 235.8 kN = 304.4 kN, so the number of supports required was 304.4 kN / 128 kN = 2.38, which was also rounded up to three supports. By installing the required number of temporary supports beneath each beam, it was verified that the structural system was safe.

5.5 Shoring support in the bridge method

In the bridge method, the temporary support calculation focused only on the primary beams, since installing bridge members across the primary beams eliminates load transfer to the slabs and secondary beams. The conditions and methods of consideration were the same as those of the conventional method. Although the bridge members were installed directly on the primary beam, rubble generated during demolition work was expected to accumulate between the girder members and joists. Therefore, the load from accumulated debris was also considered in the structural calculation. In addition, the load of one bridge unit was assumed to be 18 kN, and one bridge unit was assigned to each crawler track of the heavy machinery. Accordingly, the load of two bridge units was added to the dynamic load acting on the main girders for the evaluation.

Table 13 shows the calculation results for Primary beams G1 and G2. For both beams, the stresses from end bending moments, mid-span bending moments, and shear exceeded the allowable values, indicating that structural reinforcement was required. As a result, both G1 and G2 required three beam support levels and two support reinforcement levels.

5.6 Comparison of shoring between the conventional method and the bridge method

Based on the results obtained, a comparison of the

Table 11 Slab shoring arrangement for conventional method

Size of slab supported by one shoring	Short side (m)	1.5
	Long side (m)	2
Load (A) (kN)		123
Allowable load of one shoring (B) (kN)		128
Judgement (A/B<1)		OK
Punching shear failure	Shear stress (C) (N/mm^2)	0.81
	Allowable shear stress (D) (N/mm^2)	0.9
Judgement (C/D<1)		OK

Table 12 Required number of beam shoring for conventional method

	Load (A) (kN)	Allowable load of one shoring (B) (kN)	Number (C=A/B)	Total allowable load of multiple shoring (D=B×C) (kN)	Judgement (A/D<1)
Secondary beam	273.5	128	3(2.1)	384	OK
Primary beam G1	291.5	128	3(2.3)	384	OK
Primary beam G2	304.5	128	3(2.4)	384	OK

temporary support diagram is shown in Figure 10. For each grid section, the conventional method required 19 supports, whereas the bridge method required only 12 supports. From the calculation,
100 - (12/19) × 100 = 36.84 %. It was indicated that the number of supports could be reduced by approximately 37% by applying the Bridge method. Furthermore, for primary beams G1 and G2, both the conventional method and the Bridge Method required two layers of structural reinforcement and three layers of support. These results indicate that the additional load on the bridge does not significantly affect the required number of reinforcement layers and support.

6. Application record of the bridge method

Table 14 shows the application records of the bridge method for demolition projects carried out between January 2016 and December 2025. A total of eight projects adopted the bridge method, seven of which involved large-scale buildings with a total floor area exceeding 10,000 m². By applying the bridge method, demolition works were performed safely and with minimal disruption owing to the strength and stiffness of the existing slabs.

In addition, an evaluation was conducted of the cost ratio and reduction rate for temporary support between the conventional and bridge methods.

In the cost comparison, both methods included the material cost of temporary support and the labour costs for installation and removal. For the bridge method, the material cost of the bridge members, fabrication and processing costs, and assembly and dismantling costs were also included. When bridge members were reused, material and fabrication costs were allocated based on the number of reuses.

For Projects A, C, E, G, and H, new bridge members were fabricated, whereas Projects B, D, and F reused previously fabricated bridge members. Among the eight projects, four demonstrated clear cost advantages. Cases where the cost ratio exceeded 1 were mainly associated with slabs having a thickness of 150 mm or greater, with reinforcement primarily consisting of φ13 bars, or with a slab aspect ratio (long span/short span) of 2 or greater. Under these conditions, the number of temporary supports required was relatively small, resulting in comparatively low support costs even for the conventional method. Therefore, to achieve greater economic benefits, it is considered necessary to reuse the bridge members at least three times. Minimizing damage to the bridge members during use remains an important issue for future improvement.

Table 13 Required layers of shoring props calculation for bridge method

		End bending	Center bending	Shear
Primary beam G1	Stress (A)	492.1kNm	467.2kNm	556.1kN
	Allowable (B)	379.4kNm	379.4kNm	235.8kN
	Judgement (A/B<1)	NG	NG	NG
	Number of layers required (A/B)	2(1.3)	2(1.2)	3(2.4)
	Number of reinforcement layers required (A/B-1)	1	1	2
Primary beam G2	Stress (A)	511.2kNm	486.7kNm	569.1kN
	Allowable (B)	379.4kNm	379.4kNm	235.8kN
	Judgement (A/B<1)	NG	NG	NG
	Number of layers required (A/B)	2(1.4)	2(1.3)	3(2.4)
	Number of reinforcement layers required (A/B-1)	1	1	2

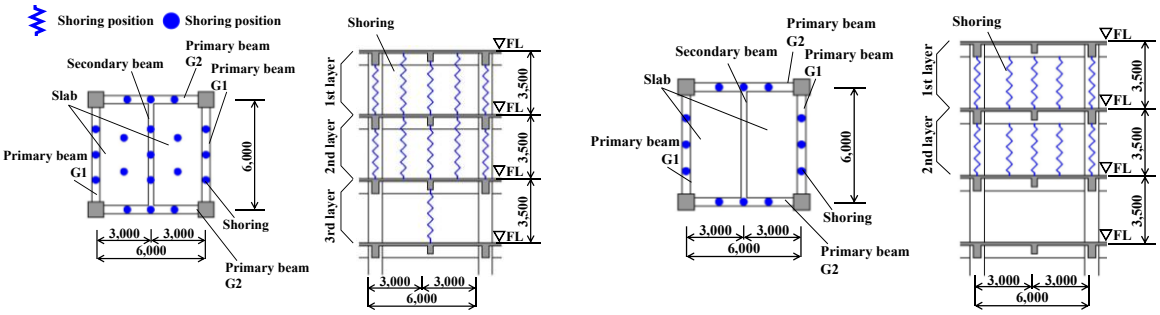

1.Plan 2. Cross section 3. plan 4. Cross section

a. Conventional method b. Bridge method

Figure 10 Shoring arrangement compareson

The reduction rate of temporary support was evaluated by taking the total number of supports used in the conventional method as 100%. All case studies achieved a reduction rate of more than 80%, demonstrating significant effectiveness.

In the C Company Housing Demolition Project, as shown in Figure 11, the structure had a short span of 6.3 m and a long span of 12 m. A sound reinforced concrete wall located beneath the main girder in the long-span direction was retained, and the bridge members were installed along the long-span beams. As a result, all temporary supports beneath the main girder were eliminated, achieving a 100% reduction rate in temporary supports and enabling demolition work without any supporting shoring. Although the total floor area was less than 10,000 m², substantial benefits were confirmed in both cost efficiency and construction safety.

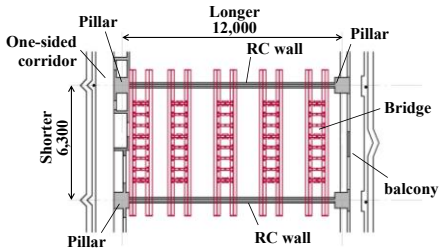

a. Plan

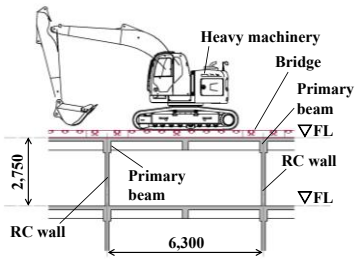

b. Cross section

Figure 11 Unsupported case bridge arrangement

7. Summary

The results presented in this report are as follows:

(1) The applicability of the bridge method to top-down demolition was verified for safe demolition operations.

(2) A comparison with the conventional method confirmed a reduction in the number of temporary supports required.

(3) Practical applications demonstrated that the bridge method enables safe demolition, along with measurable cost ratios and reduction effects.

References

1) Architectural Institute of Japan (2024): Guidelines for Building Demolition Work (Draft) and Commentary (Reinforced Concrete and Steel Structures), pp. 1-184.

2) Matsumoto, T. (2023, October). Safety in demolition work. Building Disaster Prevention, Vol. 549, pp.29–32.

3) SANDOH Construction Co., Ltd. (2017, October) Machinery support mechanism (Patent No. JP2017-193946)

4) Shinko Lease Co., Ltd. & Van-Quatre Co., Ltd. (2015, March): Demolition method using girder-type support system (Patent No. JP2015-48586)

5) Architectural Institute of Japan (2019, October): Allowable stress design standard for steel structures, pp.5

Table 14 Track record of using the bridge method

Project	Project name	Building use	Total floor area (Reinforced total floor area) (m^2)	Number of floors (Reinforced floors) (F)	Shoring reduction rate (%)	Cost ratio (Bridge/Conventional)
A	Commercial facility demolition work	Commercial facility	11,100(8,392)	8(5)	94	0.63
B	Commercial facility demolition work	Commercial facility	38,619(16,157)	8(5)	84	0.76
C	Company housing demolition work	Apartment complex	8,210(6,437)	8(7)	100	0.77
D	Office building demolition work	Office	15,520(7,589)	9(6)	96	0.44
E	Office building demolition work	Office	37,360(16,997)	15(13)	84	1.92
F	Office building demolition work	Office	26,230(12,218)	9(7)	92	1.03
G	Office building demolition work	Office	10,410(5,254)	7(5)	86	1.54
H	Multipurpose facility demolition work	Accommodation facilities, etc.	41,070(4,260)	30(4)	93	5.01

韓国の骨材供給および品質管理の現状

Current Status of Aggregate Supply and Quality Control in Korea

羅晶旻※1、李在馨※1
Jeong-Min Ra, Jea-Hyung Lee

ABSTRACT

This study investigated changes in the aggregate supply structure and the current status of aggregate quality control in Korea by analyzing aggregate production and supply data as well as quality inspection results. The results showed that the domestic aggregate supply structure has shifted toward quarry aggregates and processed crushed aggregates due to the declining supply of river and land aggregates, while regional imbalances in aggregate supply and demand have also emerged. Since 2022, the aggregate quality inspection system has been reorganized into a professional institution-based system, thereby improving the objectivity and reliability of quality inspections. According to the 2024 regular quality inspection results, 80 out of 702 producers failed to meet the required quality criteria, corresponding to a failure rate of 11.4%. The amount of material passing the 0.08 mm sieve was identified as the most frequent cause of nonconformity. In particular, relatively high failure rates were observed for processed crushed aggregates and aggregates for concrete, indicating the need for strengthened quality control in production and washing processes. Therefore, to ensure a stable aggregate supply and consistent quality, it is necessary to establish a supply system that reflects regional supply-demand conditions, improve aggregate production facilities, strengthen in-house quality control, and develop field-applicable quality assessment systems.

1. Introduction

Aggregates are essential construction materials used in concrete, asphalt concrete, roads, railways, and various types of infrastructure. Therefore, securing a stable aggregate supply and maintaining consistent quality are important for the construction industry. In recent years, however, the Korean aggregate industry has undergone structural changes due to the prolonged downturn in the construction industry, depletion of natural aggregate resources, stricter environmental regulations, and changes in aggregate sources. In particular, the declining supply of river and land aggregates has resulted in a shift toward quarry aggregates and processed crushed aggregates. Regional imbalances in aggregate supply and demand have also become increasingly evident.

Changes in aggregate sources also have significant implications for quality control. As the use of crushed and processed aggregates increases, variability in aggregate quality may increase depending on the characteristics of the source rock and production processes. Accordingly, the Korean aggregate quality inspection system has been strengthened to improve the objectivity and reliability of aggregate quality assessment.

This study analyzed domestic aggregate production and supply data and aggregate quality inspection results to identify recent changes in the aggregate supply structure, regional supply-demand characteristics, and major quality issues in Korea. Based on the results, future directions for securing a stable aggregate supply and improving aggregate quality control are discussed.

2. Current Status of Aggregate Supply in Korea

※1 大韓民国 韓国骨材産業研究院 品質管理センター 先任研究員

2.1 Changes in Aggregate Supply Structure

The aggregate supply structure in Korea has gradually shifted from natural aggregates obtained from rivers and land deposits toward aggregates produced from quarries and processing facilities. As the extraction of river and land aggregates has continuously declined, quarry aggregates and processed crushed aggregates currently account for a major portion of the domestic aggregate supply. In particular, the Seoul metropolitan area is highly dependent on processed crushed aggregates, and the use of crushed sand and recycled aggregates is also increasing as the availability of natural aggregates decreases.

In 2024, the total aggregate production in Korea was 116.124 million m³, consisting of 41.176 million m³ of fine aggregate and 74.948 million m³ of coarse aggregate. This represented a decrease of approximately 11% compared with 130.872 million m³ in 2023. Among the regions, Gyeonggi Province recorded the largest production volume at 34.787 million m³, followed by Chungcheongnam-do at 12.924 million m³, Gyeongsangnam-do at 10.662 million m³, and Gangwon State at 9.423 million m³.

Although the recent decline in aggregate production has not yet resulted in a significant nationwide shortage because of reduced construction demand, supply constraints may become more pronounced when the construction market recovers. Moreover, if the availability of natural aggregates continues to decrease, dependence on crushed and processed aggregates is expected to increase further.

2.2 Regional Imbalance in Aggregate Supply and Demand

Because transportation costs account for a substantial portion of the delivered cost of aggregates, the distance between production and consumption areas is an important factor affecting supply stability. Analysis of regional aggregate supply and demand

Table 1 Aggregate Production by Region in Korea in 2024

Region	No. of Producers	Aggregate Production in 2023	Aggregate Production in 2024 (1,000 m³)		
			Fine Aggregate	Coarse Aggregate	Total
Gwangju	0	-	-	-	-
Daegu	4	378	51	166	217
Daejeon	1	-	-	-	-
Busan	16	3,961	1,890	1,681	3,571
Seoul	0	-	-	-	-
Sejong	10	1,848	899	872	1,771
Ulsan	15	3,257	474	2,268	2,742
Incheon	26	6,185	4,434	4,678	9,111
Gangwon	77	9,715	3,652	5,771	9,423
Gyeonggi	132	39,887	13,608	21,179	34,787
Gyeongsangnam-do	86	12,989	3,385	7,276	10,662
Gyeongsangbuk-do	134	7,585	2,701	4,225	6,926
Jeollanam-do	80	8,190	1,051	6,475	7,526
Jeonbuk	48	5,483	563	3,955	4,518
Jeju	28	1,328	250	942	1,192
Chungcheongnam-do	67	17,287	2,935	9,989	12,924
Chungcheongbuk-do	80	8,971	2,740	5,472	8,212
EEZ	0	3,808	2,542	-	2,542
Total	**804**	**130,872**	**41,176**	**74,948**	**116,124**

showed that shortages have occurred in the Seoul metropolitan and Honam regions, whereas some areas in Gangwon and the Busan-Ulsan-Gyeongnam region have experienced excess supply.

In particular, a shortage of coarse aggregate has been observed in the Seoul metropolitan area, while the Honam region has experienced a shortage of fine aggregate. Such regional imbalances may increase transportation distances and logistics costs because aggregates must be supplied from other regions. Consequently, differences in aggregate prices among regions and instability in the aggregate supply chain may increase.

Therefore, future aggregate supply policies should consider not only the total national production capacity but also regional demand, available aggregate sources, transportation distances, and supply conditions.

3. Current Status of Aggregate Quality Control in Korea

3.1 Aggregate Quality Inspection System

Since 2022, the aggregate quality control system in Korea has been reorganized from a producer-centered self-inspection system into an inspection system led by professional quality control institutions. Under the previous system, aggregate producers conducted quality tests themselves or commissioned testing laboratories. Under the revised system, designated professional institutions directly collect aggregate samples at production sites and conduct testing and reporting. Procedures such as sample sealing, blind testing, and review by an impartiality committee have also been introduced to improve the objectivity and reliability of inspection results.

This institutional reform represents a transition from producer-led quality verification toward independent third-party inspection and provides an important framework for improving confidence in aggregate quality.

3.2 Quality Inspection Results and Major Issues

According to the 2024 regular aggregate quality inspection results, 622 of the 702 producers passed the inspection, while 80 producers failed to meet the

Table 2 Nonconforming Items in the 2024 Aggregate Quality Inspection

Type	Oven-dry Density	Fineness Modulus	Abrasion Resistance	Amount Finer than 0.08mm Sieve	Elongation	Absorption Rate	Soundness	Clay Lumps	Solid Content for Shape of Particle	Total
EA	6	9	4	50	2	8	3	31	1	114
%	5	8	4	44	2	7	3	27	1	100

Table 3 Nonconformities by Aggregate Type in the 2024 Aggregate Quality Inspection

Item	Screened/Crushed (Gravel)	Screened/ Crushed(Sand)	Forest (Gravel)	Forest (Sand)	Land (Gravel)	Land (Sand)	Marine Aggregate (Sand)	Total
EA	20	13	21	17	1	8	3	83
%	24	16	25	20	1	10	4	100

required quality criteria, resulting in a failure rate of 11.4%. The failure rate increased compared with 5.3% in 2023. In addition, the failure rate for special inspections reached approximately 31.3%, which was considerably higher than that of the regular inspections.

Analysis of the nonconforming items showed that the amount of material passing the 0.08 mm sieve was the most frequent cause of failure, accounting for more than half of the nonconforming items. Processed crushed aggregates showed a relatively high failure rate among aggregate types, and most of the quality issues were observed in aggregates intended for concrete.

These results indicate that, as the aggregate supply structure shifts toward crushed and processed aggregates, quality control of not only the source rock but also the crushing, screening, and washing processes becomes increasingly important. In particular, improved washing processes and production facilities are required to control excessive fines and maintain consistent grading. In addition, aggregate producers need to strengthen their in-house quality control systems.

4. Conclusions

This study analyzed the current status of aggregate supply and quality control in Korea based on aggregate production, regional supply-demand, and quality inspection data. The domestic aggregate supply structure has shifted toward quarry and processed crushed aggregates as the availability of natural aggregates has declined. Total aggregate production in 2024 decreased by approximately 11% compared with the previous year, and regional imbalances in aggregate supply and demand were observed, particularly in the Seoul metropolitan and Honam regions.

Regarding quality control, the introduction of a professional institution-based inspection system since 2022 has strengthened the objectivity and reliability of aggregate quality inspections. Nevertheless, the failure rate of the 2024 regular quality inspections was 11.4%, with the amount of material passing the 0.08 mm sieve being the most frequent nonconforming item. These results indicate the need for improved control of aggregate production, screening, and washing processes.

Therefore, ensuring a stable aggregate supply and consistent quality in Korea requires an integrated approach that considers regional supply-demand conditions and strengthened quality management. Improvements in production and washing facilities, enhanced in-house quality control, traceability throughout the distribution process, and the development of field-applicable rapid quality assessment methods will be important for improving the reliability and sustainability of the domestic aggregate industry.

Reference

[1] KS F 2527; Aggregates for concrete. Korea Standard Committee: Seoul, Republic of Korea, 2024.

03

STUDENT SESSION

The 17th Korea-Japan Joint Symposium
on Building Materials & Construction

Building a Sustainable Future-
Carbon Neutrality in Cement & Concrete

空気分級した廃コンクリート微粉末のセメント混和材としての水和挙動分析

Analysis of the Hydration Behavior of Air-Classified Recycled Concrete Fines Used as Supplementary Cementitious Materials

金建佑※1、 安泰尹※1、姜南圭※2、申相澈※3、金振晩※4
Geon-Woo Kim, Tae-Yun An, Nam-Gyu Kang, Sang-Chul Shin, Jin-Man Kim

ABSTRACT

Recycled concrete fines (RCF), an inevitable by-product of concrete recycling, have limited use as supplementary cementitious materials (SCMs) due to their low hydration reactivity and quality variability, particularly the significant reduction in early-age strength. This study aims to overcome these limitations by controlling the particle size and composition of RCF through dry air classification. RCF collected from a construction waste treatment facility (RCF_bulk) was separated into three fractions—RCF_A, RCF_B, and RCF_C—collected from the air-jet mill, cyclone separator, and dust collector, respectively. The physical and chemical properties of each fraction were characterized using PSA, XRF, XRD, and TGA, and their applicability as SCMs was evaluated through compressive strength, isothermal calorimetry, and pore structure (MIP) tests. The classification clearly separated the fractions by mean particle size (D50: RCF_A 57.2 μm > RCF_B 13.5 μm > RCF_C 4.1 μm), with finer fractions showing higher CaO and lower SiO_2 contents, indicating selective enrichment of cement paste components. Mortar containing 10% RCF_C achieved 99.2% of the strength of the control mix mortar at 3 days and 88.4% at 28 days, effectively mitigating early-age strength loss. Calorimetry results confirmed that fine particles act as nucleation sites, accelerating early hydration and densifying the matrix. These results suggest that air classification is an effective approach for improving the applicability of RCF as SCMs and establishing a high-value resource circulation system.

1. Introduction

With global urbanization and growing demand for infrastructure redevelopment, the generation of construction waste continues to increase, and its recycling has become a critical issue. To effectively reuse construction waste, it is essential to focus on the recycling of waste concrete, which accounts for the majority of the total generation (approximately 60% of all construction waste in Korea) [1]. In particular, establishing a circulation system that returns waste concrete-derived by-products to the cement and concrete manufacturing process is extremely important from a resource-circulation perspective.

However, recycled concrete fines (RCF), which are inevitably generated in this process, are extremely difficult to utilize as supplementary cementitious materials (SCMs) owing to their low hydration reactivity and quality variability. In particular, the significant reduction in early-age strength that occurs when RCF is used as SCMs undermines its reliability as a structural material. Owing to these technical limitations, the current use of RCF is limited to

※1 大韓民国 国立公州大学校 建築工学科 博士課程
※2 大韓民国 国立公州大学校 建築工学科 学士課程
※3 大韓民国 国立公州大学校 建築工学科 研究教授 博士(工学)
※4 大韓民国 国立公州大学校 建築工学科 教授 博士(工学)

low-value-added applications such as fillers, and most of it is disposed of in landfills.

This study aims to mitigate the reduction in early-age strength by controlling the particle size and composition of RCF through dry air classification, thereby providing fundamental data for establishing a high-value-added resource circulation system. In this paper, the physical and chemical properties of the classified samples were characterized, and their practical applicability as SCMs was evaluated through mortar tests.

2. Materials and Methods

2.1 Experimental Plan

The experimental program is summarized in Table 1. Fig. 1 shows the air classification system used in this study, which consists of an air jet mill, a cyclone separator, and a dust collector. The system induces particle-to-particle collisions using compressed air, thereby enabling simultaneous fine grinding and classification. As shown in Table 2, since the physical properties of the RCF constituents differ, the cement paste components (CaO-based) tend to be ground more finely than the aggregate components (SiO_2-based) under the same external force conditions [2-5].

2.2 Sample Preparation

The feed material used for air classification was recycled concrete fines derived from waste concrete generated at a construction waste intermediate treatment facility in Korea. The sample had a particle size of 150 μm or less, with CaO and SiO_2 contents of 19.67% and 48.56%, respectively, and was defined as RCF_bulk in this study. After the classification operation, the samples collected from the air jet mill, cyclone separator, and dust collector were designated as RCF_A, RCF_B, and RCF_C, respectively, according to their respective collection location.

2.3 Test Methods

In this study, the characteristics of the RCF samples separated by air classification and the

Fig. 1 Air classifier

Table 2 Representative mechanical properties of major RCF constituents

Minerals	Hardness	Elastic Modulus (GPa)
C-S-H	-	10–35
Calcite	3	34–77
Quartz	7	>100
Feldspar	6.5	45–85

Table 1 Experimental program

No.	Experiment	Replacement ratio (%)	W/B (%)	Binder: Sand	Test items
1	Physical and chemical properties of RCF fractions	-	-	-	- Particle size (PSA) - Composition analysis (XRF, XRD, TGA)
2	Hydration characteristics evaluation of RCF fractions	10, 20, 30	50	1:3	- Compressive strength (3, 28 days), - Isothermal calorimetry (~3 days), - Pore structure (3, 28 days)

applicability of each sample as SCMs were evaluated in stages. First, to examine the physical and chemical properties of the classified RCF samples, particle size distribution (PSA, Particle Size Analysis), chemical composition (XRF, X-ray Fluorescence), mineral composition (XRD, X-ray Diffraction), and thermal decomposition behavior (TGA, Thermogravimetric Analysis) were conducted. Next, to evaluate their applicability as SCMs, mortars were prepared by replacing Ordinary Portland Cement with each RCF fraction at replacement levels of 10, 20, and 30%. As shown in Table 1, the mortar mix proportions were set at a water-to-binder ratio of 50% and a binder-to-fine-aggregate ratio of 1:3, and the compressive strength was measured in accordance with KS L ISO 679. In addition, to analyze the hydration characteristics and matrix densification behavior, pastes with 30% RCF replacement were prepared, and isothermal calorimetry and pore structure (MIP, Mercury Intrusion Porosimetry) measurements were performed.

3. Results and Discussion

3.1 Physical and Chemical Properties of Classified RCF Samples

Fig. 2 shows the relationship of RCF_bulk and each classified sample between the mean particle size (D50) and the main chemical compositions (CaO, SiO_2). As a result of classification, based on the D50 values, the particle sizes were clearly separated in the order of RCF_A (57.2 μm) > RCF_B (13.5 μm) > RCF_C (4.1 μm). In particular, as the particle size decreased, the CaO content increased while the SiO_2 content decreased. These trends are attributed to differences in hardness and elastic modulus among the constituent phases. among the constituent minerals, suggesting that the cement paste components with relatively low hardness were selectively ground and concentrated in the fine fraction. This separation effect of air classification was also confirmed by the XRD and TGA.

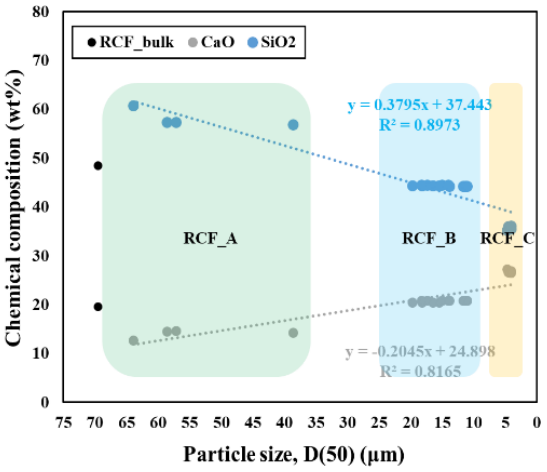

Fig. 2 Relationship between mean particle size (D50) and CaO and SiO_2 contents of bulk and air-classified RCF fractions

3.2 Hydration Characteristics of Classified RCF Samples

Fig. 3 shows the compressive strengths of the mortars at different RCF replacement levels. RCF_A, with a larger particle size, exhibited strength development comparable to that of RCF_bulk, whereas clear strength improvement was observed when the finer classified samples, RCF_B and RCF_C, were used. In particular, the specimen with 10% RCF_C replacement showed 99.2% of the strength of the Plain specimen at 3 days, effectively suppressing the reduction in early-age strength. This improvement is attributed to the nucleation effect of the fine particles, which promoted early hydration. At 28 days, the specimen with 10% RCF_C replacement showed a compressive strength of 88.4% relative to Plain. This value is higher than those of the

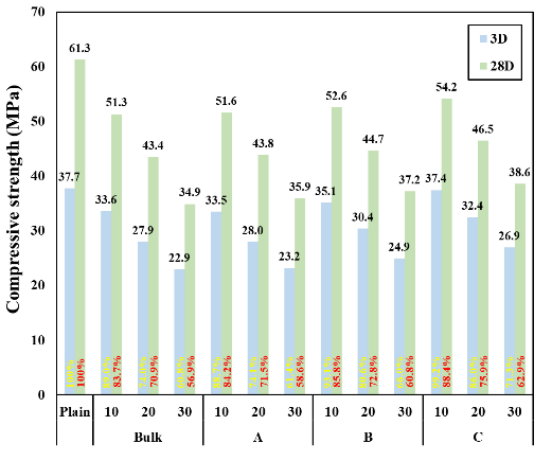

Fig. 3 Compressive strength of mortar specimens containing bulk and air-classified RCF fractions at 3 and 28 days

specimens using RCF_bulk and RCF_A, confirming that a relative strength improvement effect of classification was also obtained at 28 days.

This improvement in early-age strength is supported by the isothermal calorimetry results shown in Fig. 4. The paste containing RCF_C (C-30) exhibited the fastest heat evolution rate, and the cumulative heat release at 72 hours, normalized to that of the control paste, increased in the following order: A-30 (73.44%) < B-30 (81.78%) < C-30 (90.21%). These results indicate that the fine RCF particles selected by air classification effectively compensate for the reduction in early-age strength associated with reduced clinker content, suggesting their potential for use as SCMs.

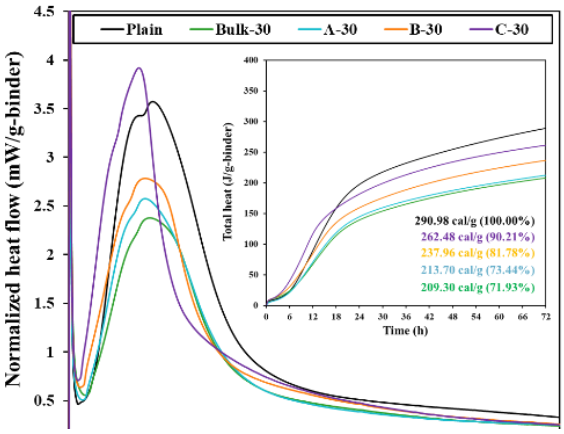

Fig. 4 Heat-flow curves and cumulative heat release of cement pastes containing bulk and air-classified RCF fractions

4. Conclusions

In this study, the physical and chemical properties and hydration characteristics of RCF separated by air classification were examined, and the following conclusions were obtained.

1) Air classification clearly separated RCF into fractions with distinct particle sizes. As the particle size decreased, the CaO content increased, whereas the SiO_2 content decreased.

2) Mortar containing 10% RCF_C exhibited relative compressive strengths of 99.2% at 3 days and 88.4% at 28 days compared with the control mortar.

3) The finely classified samples showed a pronounced nucleation effect in the early stage of hydration, promoted the densification of the matrix structure, and improved the early-age strength.

Overall, controlling the particle size and composition of RCF by air classification and selecting fine particles are considered to be effective approaches that contribute to strength development and improved applicability as SCMs through matrix densification and accelerated hydration.

Acknowledgment

This work was supported by the Technology Innovation Program (RS-2023-00266009, Development of admixture and blended cement using unused inorganic resource) funded by the Ministry of Trade, Industry and Resources (MOTIR, Korea) and the Korea Institute for Advancement of Technology (KIAT) grant funded by the Korea Government (MOTIR) (RS-2024-00410787, HRD Program for Industrial Innovation)

Reference

[1] Korea Environment Corporation, 2024. National Waste Generation and Treatment Status 2023. Ministry of Climate, Energy and Environment. (accessed 12.30.24)

[2] Guo, Y., Zhang, T., Huang, Y., Mai, J., Wang, A., Wei, J., Yu, Q., 2022. Clarifying the deformation restriction of unhydrated phase in cement paste to its autogenous shrinkage. Constr. Build. Mater. 331, 127297.

[3] Umemoto, S., Unuma, H., Cho, S., Goto, T., Sekino, T., 2025. Nano-silicate compounding for improved physical attributes of calcium carbonate ceramics. Ceram. Int. 51, 6174–6182.

[4] Cornu, P., Kane, M., Gennesseaux, M., Ropert, C., Do, M.T., Duc, M., 2025. Influence of aggregate minerals hardness and quartz content on long-term pavement friction and wear: An experimental analysis. Wear 206030.

[5] Zhang, Q., Liu, Z., Gui, C., Deng, Y., Luo, T., 2025. Quantifying Young's Modulus of Mudstone after Water Immersion: Insights from the Mechanical Properties of Micro-Mineral Compositions. Int. J. Civ. Eng. 23, 261–276.

再生骨材コンクリートの性能に及ぼす諸要因の影響

Effects of Various Factors on the Performance of Recycled Aggregate Concrete

岡田悠汰※1　道正泰弘※2　錦木健二※3
Yuta Okada※1,　Yasuhiro Dosho ※2,　Kenji Nishikigi ※3

ABSTRACT

本研究では，原コンクリート(OC)の水結合材比(W/B)，混和材利用，RL の炭酸化の諸要因がコンクリートの性能に及ぼす影響について検討を行った．その結果，RL に炭酸化処理を施すことで，骨材品質が改善された．RL の容積混合率および OC の W/B が増加すると，圧縮強度および凍結融解抵抗性は低下し，中性化速度係数は増加した．GGBFS と FA を併用した配合では，長期材齢における圧縮強度が向上し，混和材による性能改善効果が確認された．RL の炭酸化処理により圧縮強度も向上させ，RL の品質改善に有効であった．以上から，RLS の炭酸化と混和材の適切な使用により，再生骨材コンクリートの性能改善効果がみられた．

1. Introduction

The use of recycled aggregate class L (RL; JIS A 5023) is attracting growing attention as an effective means of resource utilization, contributing to waste reduction [1]. However, RL contains a large amount of adhered mortar originating from the original concrete (OC). This adhered mortar increases the water absorption of the aggregate, which deteriorates the quality of concrete containing RL by reducing its strength and durability. To address this issue, carbonation treatment of adhered mortar on RL is being investigated. Carbonation densifies the microstructure of the adhered mortar, is expected to improve the strength and durability of concrete containing RL. Moreover, because of the large amount of adhered mortar, RL also absorbs more carbon dioxide, as shown in Figure 1 [2]. Therefore, a greater improvement in concrete performance is expected with carbonation treatment.

The addition of admixture, such as ground granulated blast-furnace slag (GGBFS) and fly ash (FA), can improve the performance of concrete, particularly its durability. They enhance long-term strength development and mitigate the alkali–silica reaction (ASR) [3, 4]. This study aimed to promote the stable use and widespread application of RL. The effects of various factors, including the water-binder

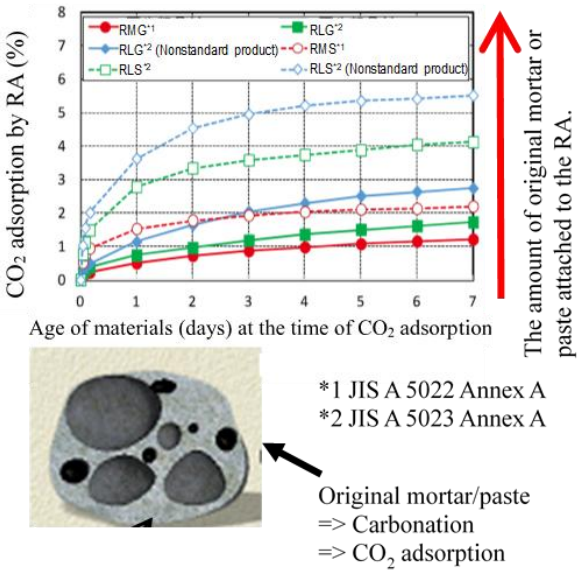

Figure 1 CO_2 adsorption (Modified from [2])

Table 1 Overview of OC

W/B (%)	Compressive strength at 13 weeks (N/mm²)	Carbonation depth after 26 weeks of accelerated carbonation test (mm)
	JIS A 1108	JIS A 1153
35	66.6	0.3
45	48.2	8.9
55	34.6	20.7
65	25.8	36.0

※1 日本　名城大学　理工学研究科環境創造工学専攻
※2 日本　名城大学　環境創造工学科　教授　博士（工学）
※3 日本　戸田建設(株)　博士(工学)

ratio (W/B) of the OC, the use of admixture, and the carbonation treatment of RL, on the performance of concrete were investigated.

2. Experiment programs

2.1 Materials

Table 1 shows an overview of the OC. Table 2 lists the materials used in this study. Ground-furnace slag aggregate (GGBFS), Class II FA (FAII), and limestone powder (LS) were used as admixture. The properties of the aggregates are presented in Table 3. Natural sand (NS), recycled fine aggregate class L (RLS), and carbonated recycled fine aggregate (RLS-C) were used as fine aggregates. Crushed stone (NG) and recycled coarse aggregate class L (RLG) were used as coarse aggregates. RLG and RLS were produced by crushing and grading OC with W/B of 35%, 45%, 55%, and 65%. The resulting recycled fine aggregates were designated RLS35, RLS45, RLS55, and RLS65, whereas the recycled coarse aggregates were designated RLG35, RLG45, RLG55, and RLG65, according to the W/B of the OC. The quality of the RLS and RLG satisfied the requirements specified in Annex A of JIS A 5023. In addition, RLS-C was prepared by spreading the RLS on a tray and exposing it to accelerated carbonation conditions (20°C, 60% RH, and 5% CO_2) for 14 days to carbonate the adhered mortar/paste. Carbonation was confirmed by visually observing the color change of phenolphthalein solution sprayed on the RLS. A comparison of RLS and RLS-C in Table 3 confirmed an increase in CO_2 content was confirmed for all aggregates. As a result of carbonation, the density in oven-dry condition increased for all aggregates except RLS35. In addition, the water absorption decreased for all RLS samples after carbonation, indicating an improvement in aggregate quality. This indicates that these aggregates experienced a greater degree of quality enhancement.

Table 2 Materials

	Symbol	Type	
Cement	OPC	Ordinary portland cement	
Admixture	GGBFS	Ground-furnace slag aggregate	
	FAII	Class II fly ash produced in Maizuru	
	LS	Crushed stone powder	
Fine aggregate	NS	River sand from the Ibi River	
	RLS35	Recycled fine aggregate class L	OC: W/B = 35%
	RLS45		OC: W/B = 45%
	RLS55		OC: W/B = 55%
	RLS65		OC: W/B = 65%
	RLS35C	Carbonated recycled fine aggregate class L	OC: W/B = 35%
	RLS45C		OC: W/B = 45%
	RLS55C		OC: W/B = 55%
	RLS65C		OC: W/B = 65%
Coarse aggregate	NG	Crushed hard sandstone from Shinshiro	
	RLG35	Recycled course aggregate class L	OC: W/B = 35%
	RLG45		OC: W/B = 45%
	RLG55		OC: W/B = 55%
	RLG65		OC: W/B = 65%
Air-entraining and water-reducing admixture	Ad	Modified lignosulfonate compound and polycarboxylate-based compound	

Regarding aggregate strength, the recycled aggregates produced from OC with a W/B of 65% exhibited a slightly higher 400kN crushing value, suggesting a reduction in aggregate strength. The ASR was classified as A for all aggregates, and the amount of impurities was 0%. These results indicate that the recycled aggregates used in this study were affected by the W/B of the OC and the carbonation treatment.

2.2 Test items and test methods

Table 6 summarizes the test items and methods. The improvement effects of carbonation treatment of RL were investigated using mortar specimens.

2.3 Mix proportions

Table 4 shows the concrete mix proportions. The unit water content was 172 kg/m³, and the W/B was 45%. GGBFS was used as an internal replacement for cement at replacement ratios of 40% and 70%, corresponding to blast-furnace slag cement Types B and C, respectively. FA and LS were used as external replacements for 10% of the NS. As chemical admixtures, a modified lignin sulfonate-based water-reducing and air-entraining admixture and a polycarboxylate-based water-reducing and air-entraining admixture were used to achieve the target slump and air content.

Table 5 shows the mortar mix proportions. The mortar mix proportions were prepared in accordance

Table 3 Properties of aggregates used

Item	Method	NS	RLS35	RLS45	RLS55	RLS65	RLS35C	RLS45C	RLS55C	RLS65C	NG	RLG35	RLG45	RLG55	RLG65
Density in oven-dry condition (g/cm^3)	JIS A 1109, JIS A 1110	2.57	2.03	1.95	1.97	1.95	2.01	2.05	2.10	2.05	2.64	2.28	2.27	2.30	2.27
Water absorption (%)		1.40	10.08	13.34	12.68	12.77	9.25	6.65	9.77	10.76	1.01	5.99	6.74	5.58	6.57
Fineness modulus (FM)	JIS A 1102	2.90	3.13	3.25	3.09	3.19	-	-	-	-	6.57	6.57	6.66	6.79	6.38
Content of materials finer than 75μm sieve (%)	JIS A 1103	1.7	4.1	5.1	3.2	9.0	-	-	-	-	1.1	0.8	0.5	0.6	1.2
Solid content (%)	JIS A 1104	66.2	56.5	58.7	57.0	57.1	-	-	-	-	62.1	59.0	59.3	60.0	57.7
Solid content for particle shape (%)	JIS A 5005	-	56.5	58.7	57.0	57.1	-	-	-	-	61.1	59.5	59.2	61.4	58.7
400kN crushing value (%)	BS 812-110	-	-	-	-	-	-	-	-	-	13.3	22.0	20.4	20.8	25.8
10% finens value (kN)	BS 812-111	-	-	-	-	-	-	-	-	-	371	152	142	148	177
Freeze–thaw resistance index	JIS A 5022	-	-	-	-	-	-	-	-	-	0.00	0.02	0.02	0.00	0.04
Alkali–silica reaction	JIS A 5021	-	-	-	-	-	-	-	-	-	A	A	A	A	A
Impurity content (mass%)	JIS A 5023	-	0	0	0	0	-	-	-	-	-	0	0	0	0
CO_2 content (%)	Thermo Analysis	-	8.56	8.03	8.80	6.61	10.52	12.04	11.38	10.16	-	-	-	-	-

Table 4 Concrete mix proportions

No.	OC W/B (%)	Volume mixing ratio (%)		Admixture replacement ratio (%)			W/B (%)	s/a (%)	Quantity of material per unit volume of concrete (kg/m^3)									Ad (B×%)
		S	G	GGBFS	FAII	LS			W	N	GGBFS	FAII	LS	NS	RLS	NG	RLG	
1	-	0	0	0	0	0	45	45.4	172	382	0	0	0	785	0	958	0	0.8
2	55	30	100	0	0	0		45.4		382	0	0	0	549	205	0	875	0.8
3	55	50	100	0	0	0		45.4		382	0	0	0	392	341	0	875	0.8
4	55	100	100	0	0	0		45.4		382	0	0	0	0	682	0	875	0.6
5	35	50	100	0	0	0		45.4		382	0	0	0	392	341	0	875	0.8
6	45	50	100	0	0	0		45.4		382	0	0	0	392	341	0	875	0.8
7	65	50	100	0	0	0		45.4		382	0	0	0	392	341	0	875	0.8
8	-	0	0	OPC×40	0	0		45.1		229	153	0	0	785	0	958	0	0.6
9	55	50	100	OPC×40	0	0		45.1		229	153	0	0	387	336	0	875	0.6
10	-	0	0	OPC×70	0	0		45.1		115	268	0	0	766	0	958	0	1.0
11	55	90	100	OPC×70	NS×10	0		45.1		115	268	68	0	0	599	0	875	1.0
12	55	90	100	OPC×70	0	NS×10		45.1		115	268	0	68	0	599	0	875	1.0

with Annex C of JIS A 5308. The target flow was set at 190 ± 5 mm.

3. Experiment results

3.1 Effects of OC and the Use of Admixture

3.1.1 Fresh properties

Table 7 shows the measured fresh concrete properties. By adjusting the dosage of the chemical admixtures, the target values for slump and air content were achieved. In addition, all mix proportions satisfied the chloride content limit of 0.30 kg/m³. The Quantity of material per unit volume of mortar decreased as the volumetric mixing ratios of RLS increased. This is because RL, GGBFS, and FA have lower densities than NG, NS, and OPC.

3.1.2 Hardened properties

(1) Compressive strength and static modulus of elasticity

Figures 2 show the results of the compressive strength tests. The compressive strength of concrete incorporating RL tended to decrease as the volumetric mixing ratios of RL increased. Matsuda et al. (2019) [6] reported that the adhered mortar/paste on recycled aggregates increases the void content in the interfacial transition zone, thereby affecting cement paste hydration and resulting in a weaker interface. In the current study, the decrease in compressive strength is also attributed to the formation of voids at the aggregate–paste interface in the RL.

Regarding the effect of the W/B of the OC, the compressive strength tended to decrease as the W/B of the OC increased at 91 days. According to Table 3, RLS and RLG showed an increasing trend in water absorption with increasing W/B. Therefore, it is considered that the increase in voids resulting from the larger amount of adhered mortar/paste contributed to the reduction in compressive strength.

For mix proportions incorporating both RL and admixture, a comparison between No.3 and No.9 showed that the compressive strength of the mix proportions containing GGBFS as an internal cement replacement was lower up to 28 days. However, at 91 days, the compressive strength of No.9 exceeded that of No.3. Similarly, a comparison between No.1 and

Table 5 Mortar mix proportions

No.	OC W/B (%)	Volumetric mixing ratio (%)	W/B (%)	Quantity of material per unit volume of mortar (kg/m³)					Fresh properties	
				W	N	Recycled fine aggregate Non-carbonated (RLS)	Recycled fine aggregate Carbonated (RLS-C)	Ad (C×%)	Flow (mm)	Density (kg/m³)
M-1	35	100	50	254	509	1310	-	2.0	185	1877
M-2	45					1292	-	0.0	192	2104
M-3	55					1298	-	0.8	194	2100
M-4	65					1296	-	0.0	190	2100
M-5	35					-	1286	1.0	191	1973
M-6	45					-	1321	0.0	194	2164
M-7	55					-	1351	0.3	190	2034
M-8	65					-	1327	0.0	190	2156

No.10 showed that the use of GGBFS reduced the compressive strength at 7 days, whereas the strengths were comparable at 28 days. At 91 days, the compressive strength of No.10 exceeded that of No.1. These results indicate that replacing cement with GGBFS reduces the early-age compressive strength but improves the long-term compressive strength.

The comparison between No.11 and No.4 showed that at 28 days, the compressive strength of the mix proportions containing both GGBFS and FA was comparable to that of the mix proportion containing no GGBFS or FA. At 91 days, however, the compressive strength of the mix proportion containing GGBFS and FA exceeded that of the mix proportion without admixture. Strength enhancement at early ages was limited because of the slow reaction rates of GGBFS and FA. At 91 days, the increase in long-term compressive strength is attributed to microstructural densification resulting from the pozzolanic reaction of FA and the latent hydraulic reaction of GGBFS. In contrast, the mix proportions containing LS exhibited a compressive strength comparable to that of No.4 indicating that LS had little influence on compressive strength.

Figure 3 shows the relationship between compressive strength and static modulus of elasticity. The modulus of elasticity was estimated according to the equation presented in the Standard Specifications for Concrete Structures: Design published by the Japan Society of Civil Engineers (JSCE) [6] and is shown in Figure 3. The mix proportions incorporating RL exhibited values lower than those calculated using the JSCE equation, whereas the mix proportions containing admixture showed values relatively close to the calculated values. Although the use of admixture improved concrete performance, the reduction in performance due to aggregate quality tended to be greater.

Table 6 Test items and test methods

Item	Test Item	Test method	Details
Concrete	Slump	JIS A 1101	18 ± 2.5cm
	Slump flow	JIS A 1150	-
	Air content	JIS A 1128	4.5% ± 1.5c
	Density	JIS A 1116	-
	Concrete temperature	JIS A 1156	-
	Chloride ion content	JIS A 5308	Normal concrete-
		JIS A 5023	Recycled aggregate concrete
	Compressive strength	JIS A 1108	7, 28, and 91 days
	Static modulus elasticity	JIS A 1149	
	Drying shrinkage	JIS A 1129-3	-
	Accelerated carbonation	JIS A 1153	-
	Freeze–thaw	JIS A 1148	Method A
Mortar	Flow	JIS R 5201	190 ± 5mm
	Density	JIS A 1116	-
	Compressive strength	JIS A 1108	-
	Drying shrinkage	JIS A 1129-3	-
	Accelerated carbonation	JIS A 1153	-

Table 7 Fresh properties of various concretes

No.	Slump (cm)	Flow (cm)	Air content (%)※	Concrete temperature (°C)	Density (kg/m³)	Chloride ion content (kg/m³) JIS A 5308	Chloride ion content (kg/m³) JIS A 5022
1	18.0	32.0	4.0	15	2603	0.04	-
2	18.0	36.0	4.7 (1.0)	18	2241	-	0.12
3	19.5	40.0	4.3 (1.0)	14	2366	-	0.12
4	19.5	36.0	4.6 (1.2)	14	2341	-	0.12
5	16.5	29.5	4.1 (1.0)	15	2143	-	0.12
6	16.5	34.5	4.0 (1.0)	17	2166	-	0.14
7	18.0	41.0	5.8 (1.0)	15	2006	-	0.16
8	20.5	45.5	4.0	17	2497	0.04	-
9	19.5	41.0	4.3 (1.0)	14	2591	-	0.05
10	19.0	37.0	3.7	15	2356	0.04	-
11	19.0	41.5	3.5 (1.2)	16	2100	-	0.09
12	16.5	34.5	4.5 (1.2)	17	2127	-	0.09

※ Values in parentheses indicate the aggregate correction factor.

(2) Accelerated carbonation

Figure 4 shows the relationship between compressive strength and the carbonation rate coefficient, including the regression line. The carbonation rate coefficient tended to decrease with increasing compressive strength; however, no clear correlation was observed.

The carbonation rate coefficient tended to increase as the W/B of the OC increased. This is because the porosity of the adhered mortar on the RLS decreased as the W/B of the OC decreased, thereby suppressing CO_2 penetration. According to Table 3, the water absorption decreased with decreasing W/B of OC. Therefore, it is considered that the porosity of the

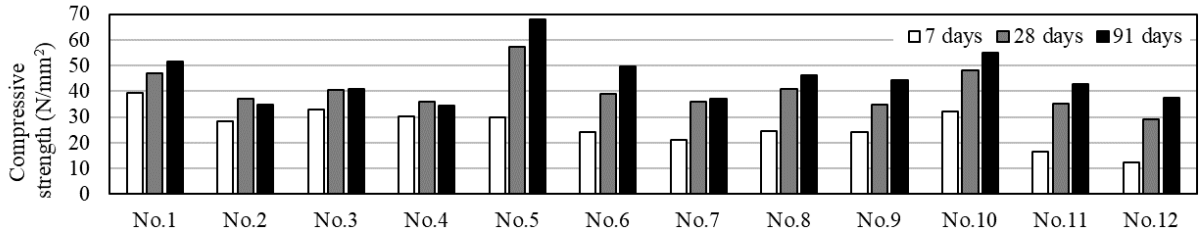

Figure 2 Compressive strength

adhered mortar on RLS also decreased, thereby suppressing CO_2 penetration. In contrast, for mix proportions with different RL volumetric mixing ratios, the carbonation rate coefficient increased as the RL volumetric mixing ratios increased. Accordingly, a negative correlation was observed between compressive strength and the carbonation rate coefficient.

(3) Freeze–Thaw

Figure 5 shows the results of the freeze–thaw resistance test. When the air content of the fresh concrete subjected to freeze–thaw action was within the target range of 4%–6%, the relative dynamic modulus of elasticity remained greater than 80% after 300 cycles. However, the relative dynamic modulus of elasticity tended to decrease as the volumetric mixing ratios of RL increased. In addition, the relative dynamic modulus of elasticity decreased as the W/B of the OC used to produce the RL increased. It has been reported that recycled aggregates with higher water absorption form a weaker mortar layer due to increased water content in the concrete during curing, resulting in lower freeze–thaw resistance [7]. Therefore, the use of RL is considered to increase the number of voids in the concrete, thereby reducing freeze–thaw resistance.

3.2 Improvement Effects of Carbonation of RL

3.2.1 Fresh properties

Table 5 shows the fresh properties of the mortar. By adjusting the dosage of the chemical admixtures, the target table flow of 190 ± 5 mm was achieved for all mix proportions. The unit mass tended to decrease as the W/B of the OC increased. In addition, the unit mass of RLS-C was generally higher than that of the corresponding uncarbonated RLS due to densification resulting from carbonation.

3.2.2 Hardened properties

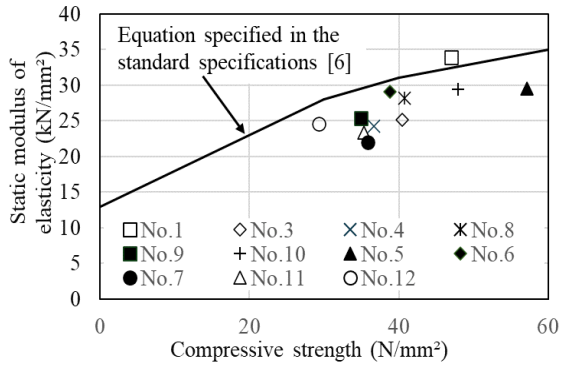

Figure 3 Relationship between compressive strength and static modulus of elasticity [6]

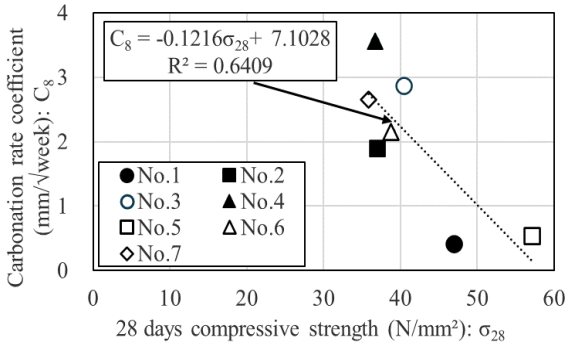

Figure 4 Relationship between compressive strength and carbonation rate coefficient

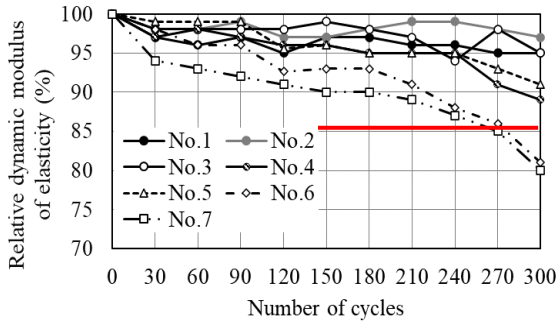

Figure 5 Results of the freeze–thaw test

(1) Compressive strength

Table 8 shows the experiment results of the mortar. For mix proportions incorporating RLS-C, the compressive strength tended to decrease as the W/B of the OC increased. In contrast, the compressive

strength of the mix proportions incorporating uncarbonated RLS was only slightly affected by the W/B of the OC. For all the RLS produced from OC with W/B of 35%–65%, carbonation increased the compressive strength, indicating the effectiveness of aggregate modification. According to Table 3, RLS-C exhibited higher CO_2 content and lower water absorption than RLS. This improvement is considered to result from the reaction of $Ca(OH)_2$ in the adhered mortar/paste of RL with CO_2, which forms calcium carbonate ($CaCO_3$). Consequently, the voids were filled, leading to the densification of the adhered mortar/paste.

(2) Length Change Ratio

The mix proportions containing RLS-C exhibited a lower length change ratio, indicating an improvement in shrinkage performance. This improvement is attributed to the carbonation of RLS, which densified the adhered mortar/paste and reduced the pore volume within the aggregate. Consequently, the moisture content of the aggregate decreased, leading to reduced moisture loss from the specimens.

4. Conclusions

The following conclusions can be drawn from the investigation of the effects of various factors on the performance of recycled aggregate concrete.

(1) Carbonation of RLS with different W/B of the OC increased the density in oven-dry condition and decreased the water absorption of all aggregates. In particular, RLS with a greater CO_2 uptake exhibited a improvement in water absorption.

(2) The compressive strength and modulus of elasticity of the concrete tended to decrease with increasing RL volumetric mixing ratios. For mix proportions incorporating RLS produced from OC with different W/B, the 91 days compressive strength decreased as the OC W/B increased. The combined use of GGBFS and FAII improved the long-term compressive strength, resulting in higher strength than that of mix proportions without GGBFS and FAII.

(3) For accelerated carbonation, the effect of the volumetric mixing ratios was investigated. The carbonation rate coefficient increased with increasing volumetric mixing ratios, and a relatively clear correlation was observed between the carbonation rate coefficient and the compressive strength.

Table 8 Experiment results of mortar

No.	Compressive strength (N/mm^2)		Length change ratio ($\times 10^{-6}$)	
	7 days	28 days	1 week	4 weeks
M-1	21.0	27.7	526	891
M-2	21.7	30.8	364	421
M-3	20.2	29.7	530	752
M-4	20.5	29.6	494	668
M-5	30.4	37.6	160	420
M-6	28.8	38.7	221	461
M-7	19.9	30.5	331	618
M-8	20.5	32.5	150	477

(4) The relative dynamic modulus of elasticity tended to decrease with increasing RL volumetric mixing ratios. In addition, the relative dynamic modulus of elasticity decreased as the W/B of the OC used to produce the RL increased.

(5) In the mix proportions incorporating RLS-C, the compressive strength tended to decrease with increasing W/B of OC. In addition, carbonation treatment of RLS increased the compressive strength, indicating an improvement in the quality of the recycled aggregate.

Based on these results, the carbonation of RLS and the appropriate use of admixture contributed to improving the performance of recycled aggregate concrete.

References

[1] Ministry of the Environment, Japan, Report on the FY2024 Survey and Study on the Recycling of Construction Waste, 2025.

[2] Matsuda N. et al. Proposal of Low Quality Recycled Aggregate Improved by Carbonation Technology and Infuluence on the Improved Recycled Aggregate on Concrete, Concrete Research and Technology, Vol.30, 65-76, 2019.

[3] Architectural Institute of Japan, Recommendations for Practice of Concrete with Fly Ash, 2024

[4] Architectural Institute of Japan, Recommendation for Design and Practice of Reinforced Concrete Building with Portland Blast-Furnace Slag Cement or Ground Granulated Blast-Furnace Slag, 2017

[5] Matsuda N. et al. Fundamental Study on the Interface between Aggregate and New Paste in Low-Quality Recycled Aggregate Concrete, Proceedings of the Japan Concrete Institute, Vol. 44, No. 1, 1018–1023, 2022.

[6] Japan Society of Civil Engineers, Standard Specifications for Concrete Structures, March, 2023.

[7] Sato Y. et al. Freeze–Thaw Resistance of Concrete Using Recycled Coarse Aggregate, Proceedings of the Japan Concrete Institute, Vol. 26, No. 1, 1503–1508, 2004.

乾式ボトムアッシュのポゾラン反応性および水和挙動に基づくセメント混和材としての適用性評価

Evaluation of dry Bottom Ash as a Supplementary Cementitious Material Based on Its Pozzolanic Reactivity and Hydration Behavior

姜南圭※1、金建佑※2、安泰尹※2、申相澈※3、金振晩※4
Nam-Gyu, Kang, Geon-Woo Kim, Tae-Yun An, Sang-Chul, Shin, Jin-Man Kim

ABSTRACT

To produce cement and concrete with lower CO_2 emissions, it is necessary to partially replace cement clinker with reactive supplementary cementitious material (SCM). In this study, the pozzolanic reactivity and mechanical performance of dry Bottom ash (dBA), an underutilized industrial by-product of coal-fired power plants, were evaluated in comparison with Fly ash (FA) using the Frattini test, the R^3 test, the strength activity index (SAI) test, and compressive strength testing. The results showed that both PF-dBA and PM-dBA exhibited pozzolanic reactivity, with PM-dBA showing higher reactivity than FA in the Frattini and R^3 tests. In the SAI and compressive strength tests, PM-dBA satisfied the KS L 5405 requirements and achieved performance comparable to or greater than that of FA, reaching an SAI of approximately 98% at 91 days, whereas PF-dBA failed to meet the requirements. These results indicate that PM-dBA is a strong candidate for use as a new SCM with the potential to replace conventional materials such as FA.

1. Introduction

The domestic cement industry is a major carbon-intensive sector, accounting for approximately 13% of total industrial carbon emissions. Most carbon dioxide emissions associated with cement production originate from the clinker calcination process, particularly from the calcination of limestone and the combustion of fuel, both of which generate substantial amounts of CO_2. Accordingly, the development of technologies to reduce carbon emissions from the cement industry has received increasing attention. In particular, reducing the clinker factor through the use of a supplementary cementitious material (SCM) and blended cements has been recognized as a key strategy for lowering CO_2 emissions [1].

Meanwhile, coal ash, a major industrial by-product of domestic coal-fired power plants, is generated at more than 8 million tons annually. Of this amount, dry Bottom ash (dBA)-which falls from the bottom of the boiler furnace onto a conveyor belt and is discharged as coarse, lump-like agglomerates after air cooling [2]-accounts for approximately 8–10% of the total coal ash generated. Owing to its porous structure and irregular particle shape resulting from the discharge process, dBA exhibits high water absorption and is currently disposed of in landfills or utilized mainly in low-value applications, such as embankment fill and aggregate for road construction [3,4].

However, dBA has an aluminosilicate-based structure and a chemical composition similar to that of Fly ash (FA), which is generated during the same coal combustion process. Therefore, when used as an SCM, dBA may contribute to improving the performance of

※1 大韓民国 国立公州大学校 建築工学科 修士課程
※2 大韓民国 国立公州大学校 建築工学科 博士課程
※3 大韓民国 国立公州大学校 建築工学科 研究教授 博士(工学)
※4 大韓民国 国立公州大学校 建築工学科 教授 博士(工学)

cement-based materials through pozzolanic reaction, as reported in several recent studies [5,6–13]. The use of dBA-conventionally limited to low-value applications-as an SCM is therefore expected to contribute simultaneously to reducing carbon emissions from the cement industry and promoting the high-value recycling of industrial by-products. Accordingly, this study investigates the pozzolanic reactivity and hydration behavior of finely ground dBA and evaluates its potential for use as an SCM.

2. Materials and methods

2.1 Materials

The dBA used in this study was obtained from the Shinboryeong Power Plant, Korea. Table 1 presents the physical and chemical properties of the dBA used in this study. Because the as-received dBA consisted of particles with a wide range of sizes, it was sieved to obtain the fraction finer than 150 ㎛, hereafter referred to as PF-dBA. However, owing to its relatively coarse particle-size distribution, PF-dBA did not satisfy the fineness requirement for Type II FA specified in KS L 5405 and thus could not be directly used as a SCM. Accordingly, PF-dBA was further ground to obtain PM-dBA, with a fineness comparable to that of Type II FA.

Table 1 Physical properties and chemical composition of inorganic recycled resources

Classification		Inorganic recycled resources		
		FA	PF-dBA	PM-dBA
Physical properties	Density (g/cm^3)	2.20	2.22	2.21
	Blaine (cm^2/g)	3660	Not measurable	3828
	Mean (㎛)	29.80	100.91	13.94
	D(0.1)	3.21	49.17	1.72
	D(0.5)	19.77	98.71	10.27
	D(0.9)	72.54	157.35	32.06
	45 ㎛ Residue rate (%)	25.91	91.76	2.22
Chemical composition (%)	CaO	10.83	5.23	5.44
	SiO_2	53.43	62.62	60.95
	Al_2O_3	20.16	21.10	20.34
	Fe_2O_3	6.94	7.02	9.42
	MgO	1.61	1.09	1.18
	Alkali (Na_2O+ K_2O)	1.34	0.98	0.96
	LOI	3.93	0.32	0.03
	Others	1.76	1.63	1.67
	SUM	100.0	100.0	100.0

2.2 Reactivity and mechanical property tests

To evaluate the feasibility of using dBA as a SCM, the following tests were conducted: (a) the Frattini test, (b) the R^3 test, (c) the strength activity index, (d) the compressive strength testing.

The Frattini test was conducted in accordance with EN 196-5 to evaluate the pozzolanic reactivity of the SCM. Ordinary Portland cement(OPC, 15 g) and SCM(5 g) were mixed with 100 mL of distilled water maintained at 40℃, and the mixture was stored in an oven at 40℃ for 8 days. The solution was then filtered, and 50 mL of the filtrate was titrated with 0.1 mol/L HCl using methyl orange as an indicator until the color changed from yellow to orange. The measured values were plotted against the OH^--Ca^{2+} saturation concentration curve at 40℃: data points located below the curve indicated pozzolanic reactivity, whereas those located above the curve indicated the absence of pozzolanic reactivity.

The R^3 test was performed in accordance with

Method B of ASTM C1897 to evaluate the chemical reactivity of the SCM based on their chemically bound water content. The test paste was prepared using SCM, calcium hydroxide, calcium carbonate, and a potassium solution containing 4.00 g of KOH and 20.0 g of K_2SO_4 per liter of distilled water. The SCM-to-calcium hydroxide and SCM-to-calcium carbonate mass ratios were set at 1:3 and 2:1, respectively, and the potassium solution-to-total solids mass ratio was set at 1.2. The prepared paste was placed in a sealed container and cured at 40 ± 2℃ for 7 days. After curing, the specimens were crushed to a particle size of less than 2 mm and dried at 40℃ for 24 ± 1 h. Approximately 5 g of the dried sample was then heated at 350 ± 10℃ for 2 h, and the chemically bound water content was calculated from the mass difference before and after heating.

The strength activity index (SAI) was determined in accordance with KS L 5405. For each mixture, OPC was replaced with the respective material at a rate of 25 wt.%. Mortar specimens were prepared in accordance with KS L ISO 679 using a binder-to-standard sand mass ratio of 1:3 and a water-to-binder ratio (W/B) of 0.50, and compressive strength was measured at curing ages of 28 and 91 days.

Compressive strength was measured in accordance with KS L ISO 679. Mortar specimens, prepared using a binder-to-standard sand mass ratio of 1:3 and a W/B of 0.50, were cast into 40 × 40 × 160 mm molds and cured in water at 20 ± 1℃. Compressive strength was measured at curing ages of 3, 7, 28, and 91 days using a universal testing machine (UTM) at a constant loading rate, and the average value obtained from at least three specimens at each curing age was reported.

3. Results and Discussion

3.1 Frattini test

The results of the Frattini test conducted at 8 days, along with the CaO fixation ratios calculated based on the theoretical CaO concentrations at the same age, are presented in Figure 1 and Table 2, respectively. OPC was located near the Ca^{2+} saturation curve and exhibited a CaO fixation ratio of -4.8%, indicating that no appreciable Ca^{2+} consumption occurred through a pozzolanic reaction.

In contrast, FA, PF-dBA, and PM-dBA were all located below the Ca^{2+} saturation curve, indicating that these materials consumed Ca^{2+} ions in the

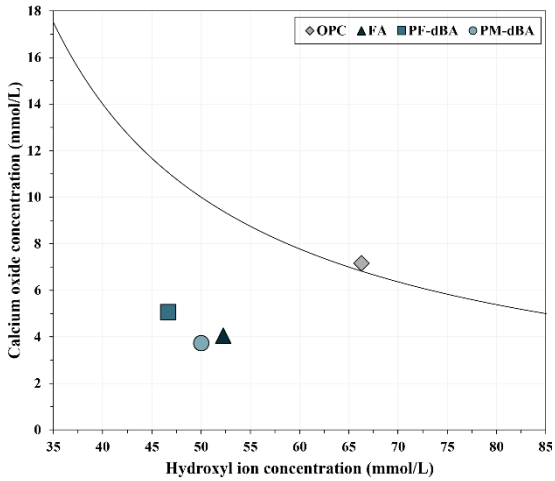

Figure 1 Result of the Frattini test

solution through pozzolanic reactions. For FA, the measured CaO concentration was 4.05 mmol/L at an OH^- concentration of 52.24 mmol/L, corresponding to a CaO fixation ratio of approximately 56.9% relative to the theoretical saturated CaO concentration of 9.40 mmol/L. PF-dBA exhibited a measured CaO concentration of 5.06 mmol/L at an OH^- concentration of 46.67 mmol/L, resulting in a CaO fixation ratio of approximately 54.2%, indicating that PF-dBA also possesses a considerable degree of pozzolanic reactivity. Notably, PM-dBA showed the lowest measured CaO concentration of 3.72 mmol/L at an OH^- concentration of approximately 50.03 mmol/L, corresponding to the highest CaO fixation ratio of approximately 62.8% relative to the theoretical saturated CaO concentration of 9.99 mmol/L.

Table 2 CaO fixation ratio with respect to OH^- ion

Sample	8 days		
	OH^- (mmol/L)	CaO (mmol/L)	CaO reduction (%)
OPC	66.28	7.16	-4.8
FA	52.24	4.05	56.9
PF-dBA	46.67	5.06	54.2

PM-dBA	50.03	3.72	62.8

Moreover, the CaO fixation ratio of PM-dBA was approximately 5.9 percentage points higher than that of FA, demonstrating its superior pozzolanic reactivity. This enhanced reactivity is attributed to particle refinement and the resulting increase in specific surface area achieved through additional grinding. Therefore, both PF-dBA and PM-dBA were confirmed to exhibit pozzolanic reactivity, and PM-dBA in particular showed a higher CaO fixation ratio than conventional FA, suggesting its high potential for use as an SCM.

3.2 R^3 test – bound water

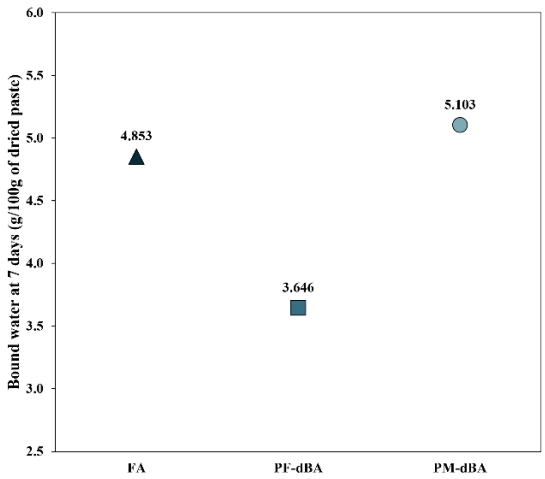

Figure 2 Bound water content of R^3 Paste (7 days)

Figure 2 presents the chemically bound water content of the R3 pastes after 7 days of curing. Chemically bound water content is used as an indirect indicator of the amount of hydration products formed through SCM reactions, with a higher bound water content generally indicating greater pozzolanic reactivity.

The chemically bound water content of FA was 4.853 g/100 g, while PF-dBA exhibited the lowest value of 3.646 g/100 g. PM-dBA, in contrast, showed the highest chemically bound water content, at 5.103 g/100 g. This result is attributed to the enhanced reactivity resulting from particle refinement and the increased specific surface area achieved through additional grinding, which promoted the formation of a greater amount of hydration products.

3.3 Strength Activity Index (SAI) Test

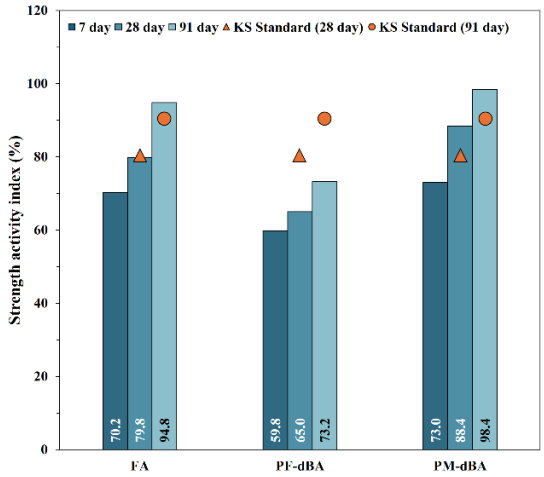

Figure 3 SAI of the SCM at 7, 28 and 91 days

Figure 3 presents the strength activity index (SAI) results. The SAI values of FA were 70.2%, 79.8%, and 94.8% at curing ages of 7, 28, and 91 days, respectively. At 91 days, FA satisfied the requirement for Type II fly ash specified in KS L 5405, namely an SAI of at least 90%. At 28 days, however, the SAI was 79.8%, which was close to but slightly below the specified requirement of 80%.

For PF-dBA, the SAI values were 59.8%, 65.0%, and 73.2% at curing ages of 7, 28, and 91 days, respectively. These values did not satisfy the KS L 5405 requirements at any curing age and were consistently lower than those of FA. This result is attributed to the relatively low amorphous content and coarse particle size of PF-dBA, which limited the effective surface area available for reaction.

In contrast, PM-dBA exhibited SAI values of 73.0%, 88.4%, and 98.4% at curing ages of 7, 28, and 91 days, respectively, thereby satisfying the KS L 5405 requirements of 80% at 28 days and 90% at 91 days. In particular, the SAI of PM-dBA at 91 days exceeded that of FA, indicating superior long-term strength development. This improvement is attributed to particle refinement and the resulting increase in specific surface area achieved through additional grinding, which enlarged the available reaction surface and promoted pozzolanic reactivity during cement hydration.

Moreover, despite having a lower amorphous content than FA, PM-dBA exhibited a higher SAI. This suggests that the physical filler effect and the accelerated reaction kinetics associated with particle refinement had a more dominant influence on strength development than the chemical reactivity attributable to amorphous content alone. Overall, PF-dBA did not satisfy the KS L 5405 requirements, whereas PM-dBA achieved the required quality criteria through additional grinding and exhibited reactivity comparable to or greater than that of FA.

3.4 Compressive strength

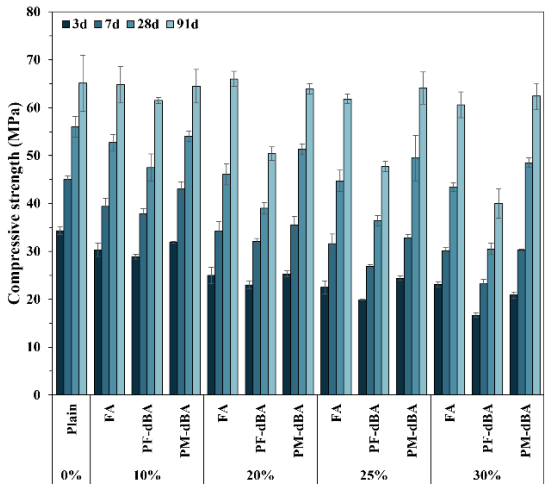

Figure 4 Compressive strength development

Figure 4 presents the compressive strength results of mortars incorporating PF-dBA and PM-dBA as SCM. The compressive strengths of the control mixture were 34.3, 45.0, 56.0, and 65.1 MPa at 3, 7, 28, and 91 days, respectively, showing a gradual increase with curing age. For the FA-containing mixtures, the 10% replacement mixture exhibited compressive strengths of 52.7 and 64.8 MPa at 28 and 91 days, respectively, which were comparable to those of the control mixture. At a replacement level of 20%, the 91-day compressive strength reached 66.0 MPa, slightly exceeding that of the control. However, as the replacement level increased to 25% and 30%, the 91-day compressive strength decreased to 61.8 and 60.6 MPa, respectively.

In contrast, the PF-dBA-containing mixtures exhibited lower compressive strength than the corresponding FA-containing mixtures at all replacement levels, and the reduction in strength became more pronounced as the replacement level increased. In particular, at a replacement level of 30%, the 28- and 91-day compressive strengths were 30.5 and 40.0 MPa, respectively, which were substantially lower than those of the FA mixture at the same replacement level, namely 43.4 and 60.6 MPa. This behavior is attributed to the porous structure and irregular particle morphology of PF-dBA, which increased the internal porosity of the mortar and weakened the interfacial bonding with the cement paste.

Meanwhile, the PM-dBA-containing mixtures exhibited higher compressive strength than the PF-dBA-containing mixtures at all curing ages under the same replacement conditions. In some cases, their strength was comparable to or even higher than that of the FA-containing mixtures. At a replacement level of 20%, the 28- and 91-day compressive strengths of the PM-dBA mixture were 51.3 and 63.9 MPa, respectively, substantially exceeding the corresponding values of 39.0 and 50.4 MPa for the PF-dBA mixture. These values were also comparable to those of the FA mixture, which exhibited compressive strengths of 46.1 and 66.0 MPa at 28 and 91 days, respectively. Furthermore, at a replacement level of 25%, the PM-dBA mixture exhibited compressive strengths of 49.5 and 64.1 MPa at 28 and 91 days, respectively, exceeding those of the FA mixture under the same conditions, which were 44.7 and 61.8 MPa. These results are attributed to the reduction in the average particle size of dBA from approximately 100 to 14 μm through additional grinding, which increased the specific surface area, enhanced the filler effect and particle-packing density, densified the microstructure, and improved the interfacial bonding with the cement paste.

Overall, PF-dBA exhibited limitations in terms of strength development compared with FA. In contrast, PM-dBA subjected to additional grinding showed compressive strength comparable to or, under certain replacement conditions, greater than that of FA, demonstrating its considerable potential for use as an

SCM.

4. Conclusions

In this study, the pozzolanic reactivity and mechanical performance of PF-dBA and PM-dBA were evaluated using the Frattini test, the R3 test, the SAI test, and compressive strength testing. The Frattini and R3 test results confirmed that both PF-dBA and PM-dBA exhibited pozzolanic reactivity, with PM-dBA showing a higher CaO fixation ratio and a greater chemically bound water content than FA. However, in the SAI and compressive strength tests, PF-dBA failed to satisfy the KS L 5405 requirements and consistently underperformed relative to FA, whereas PM-dBA met the specified requirements and achieved strength development comparable to or, in some cases, greater than that of FA. These improvements are attributed to the reduction in particle size and the resulting increase in specific surface area achieved through additional grinding. Therefore, PM-dBA, rather than PF-dBA, is considered a strong candidate for use as an SCM with the potential to replace conventional materials such as FA.

Acknowledgment

This work was supported by the Technology Innovation Program (RS-2023-00266009, Development of admixture and blended cement using unused inorganic resource) funded by the Ministry of Trade, Industry and Resources (MOTIR, Korea) and the Korea Institute for Advancement of Technology (KIAT) grant funded by the Korea Government (MOTIR) (RS-2024-00410787, HRD Program for Industrial Innovation)

Reference

[1] M.C.G. Juenger, R. Snellings, S.A. Bernal, Supplementary cementitious materials: New sources, characterization, and performance insights, Cem. Concr. Res. 122 (2019) 257–273.

[2] P.C. Hewlett, M. Liska (Eds.), Lea's Chemistry of Cement and Concrete, Butterworth-Heinemann.

[3] R. Permatasari, A. Sodri, H.A. Gustina, Utilization of Fly Ash Waste in the Cement Industry and its Environmental Impact: A Review, Jurnal Penelitian Pendidikan IPA 9 (2023) 569–579.

[4] V.-D. Nguyen, S.-H. Ngo, L.S. Ho, T.-P. Huynh, Sustainable Use of Coal Combustion Bottom Ash as A Fine Aggregate in Normal-Strength Concrete Production, J. Sci. Transp. Technol. 5, 177–197.

[5] P.D. Trifunovic, S.R. Marinkovic, R.D. Tokalic, S.D. Matijasevic, The effect of the content of unburned carbon in bottom ash on its applicability for road construction, Thermochim. Acta 498 (2010) 1–6.

[6] F. Özcan, M.E. Koç, Influence of ground pumice on compressive strength and air content of both non-air and air entrained concrete in fresh and hardened state, Constr. Build. Mater. 187 (2018) 382–393.

[7] C.B. Cheah, J.J. Liew, K.L.P. Kevin, R. Siddique, W. Tangchirapat, Influence of milling parameters on the properties of ground coal bottom ash and its blended cement, Constr. Build. Mater. 363 (2023) 129745.

[8] E.S.K. Tiu, S.N. Raman, D. Kong, M. Sofi, Towards decarbonization in the building industry: Understanding the hydration mechanism of cementitious binders with the incorporation of coal bottom ash, J. Build. Eng. 103 (2025) 112097.

[9] J.-B. Lee, S.-S. Kim, J.-Y. Lee, J.-S. Ryou, Study on the pozzolanic activity of finely ground bottom ash for cement replacement, Ceram. Process. Res. (2017).

[10] J.J. Liew, C.B. Cheah, K.L.P. Khaw, R. Siddique, W. Tangchirapat, Blended cement and mortar with various low-calcium ground coal bottom ash content: Engineering characteristics, embodied carbon and cost analysis, Constr. Build. Mater. 425 (2024) 135987.

[11] E.S.K. Tiu, S.N. Raman, D. Kong, M. Sofi, G. Geng, Correlating the reactivity and strength development of coal bottom ash and coal fly ash in cementitious system, Constr. Build. Mater. 466 (2025) 140318.

[12] X. Guan, L. Wang, L. Mo, Effects of ground coal bottom ash on the properties of cement-based materials under various curing temperatures, J. Build. Eng. 69 (2023) 106196.

[13] C.B. Cheah, J.J. Liew, K. Khaw Le Ping, R. Siddique, W. Tangchirapat, Properties of ternary blended cement containing ground granulated blast furnace slag and ground coal bottom ash, Constr. Build. Mater. 315 (2022) 125249.

低レベル放射性物質が付着したコンクリート塊の再資源化

Recycling of Concrete Waste Contaminated with Low-level Radioactive Materials

山﨑理瑚※1、道正泰弘※2、村上一夫※3

Riko Yamasaki, Yasuhiro Dosho, Kazuo Murakami

ABSTRACT

本研究では，低レベル放射性物質が付着した構造物の解体工事を対象に，性能評価手法を検討した．放射性汚染構造物では，一般解体工事の評価指標である経済性・安全性・環境性に加え，放射線防護や廃棄物管理など特有の要求性能が存在する．そのため，関係するステークホルダーの要求性能を整理し，評価体系を検討した．その結果，作業員の防護や物質の飛散防止対策は法令・行政指導への適合が前提条件であり，直接の評価対象ではなく経済性に反映すべき要素であることを示した．一方，低線量コンクリート塊の再利用は資源循環性の向上と保管施設の縮減に寄与し，建設・維持管理費を大幅に低減できることを明らかにした．

1. Introduction

In an earlier study [1], we proposed a performance-evaluation methodology for the demolition of general structures. However, the demolition of structures contaminated with low-level radioactive materials requires attention to specific issues such as radiation protection for the exposed workers and radioactive waste management. Therefore, the direct application of this methodology to general structures without modifications to the methodology is insufficient.

The Fukushima Daiichi Nuclear Power Station (1F) accident, which occurred in Japan on March 11, 2011, released a large quantity of radioactive materials into the surrounding environment, leading to the contamination of structures within the power plant. The primary radiation source was cesium; a vast amount of low-level radioactive waste currently remains on the site. To address these issues, there has been active investigation into new demolition methodologies that consider radiation protection. There is an urgent need for the safe treatment and disposal of low-level radioactive materials in order to prevent their diffusion.

Typically, the termination a standard nuclear power plants' operations is followed by a transition to decommissioning, with its demolition proceeding in accordance with the Reactor Regulation Act[*1]. However, owing to the unique nature of the 1F accident, the Special Measures Act was enacted [2]. In principle, the Ionizing Radiation Ordinance[*2] applies to operations involving the disposal of waste contaminated with the released radioactive substances. Nevertheless, a specialized review committee [3] was established, and the subsequent operations must comply with the committee's report [4].

Based on the performance evaluation of the demolition of general structures in our previous study, we investigate a performance-evaluation methodology for the demolition of structures contaminated with radioactive materials in this study.

Note 1) Act on the Regulation of Nuclear Source Material, Nuclear Fuel Material and Reactors

Note 2) Regulation on Prevention of Ionizing

※1 日本 名城大学大学院 理工学研究科環境創造工学専攻
※2 日本 名城大学 理工学部環境創造工学科 教授 博士(工学)
※3 日本 ㈱大崎総合研究所 博士(工学)

Radiation Hazards

2. Required Performance for Structural Demolition Work

In our previous study [1], we examined a performance-evaluation methodology for the demolition of general structures. Based on the previous framework, the system boundary for demolition was defined within the global human sphere to account for the comprehensive impact on the global environment. Specifically, the system was categorized into seven stakeholders: (1) the demolition site (contractor), (2) the project owner (client), (3) neighbors of the demolition site (local residents), (4) waste transportation (collection and transport companies), (5) intermediate waste treatment facilities (processing companies), (6) final waste-disposal facilities (disposal companies), and (7) administrative bodies (supervisory authorities). Although the flow among these stakeholders were illustrated via vectors, their specific relationships were defined as "guidance," "requirement," and "transportation." Based on the established framework, the differences in the demolition of structures contaminated with low-level radioactive materials can be summarized as follows:

The administrative body issues direct guidance to the project owner.

All radioactive waste must be disposed onsite, requiring intermediate treatment and final disposal facilities to be established within the plants' premises.

Safety precedes economic efficiency.

Reflecting on these differences, Figure 1 illustrates the stakeholder relationships in the demolition of structures contaminated with low-level radioactive materials. Based on the above stakeholder classification, the performances required for the demolition of such contaminated structures are summarized in Table 1.

3. Demolition Indices

In our previous study [1], we proposed the evaluation formulas for the demolition of general structures, considering three evaluation indices: cost efficiency, safety, and environmental impact. This section presents the index characteristics for the demolition of structures contaminated with radioactive materials. Regarding safety, many conditions are imposed on the client and the contractor. Accordingly, we initially consider safety, followed by environmental impact and cost efficiency.

(1) Safety

The following actions are mandatory for the operators:

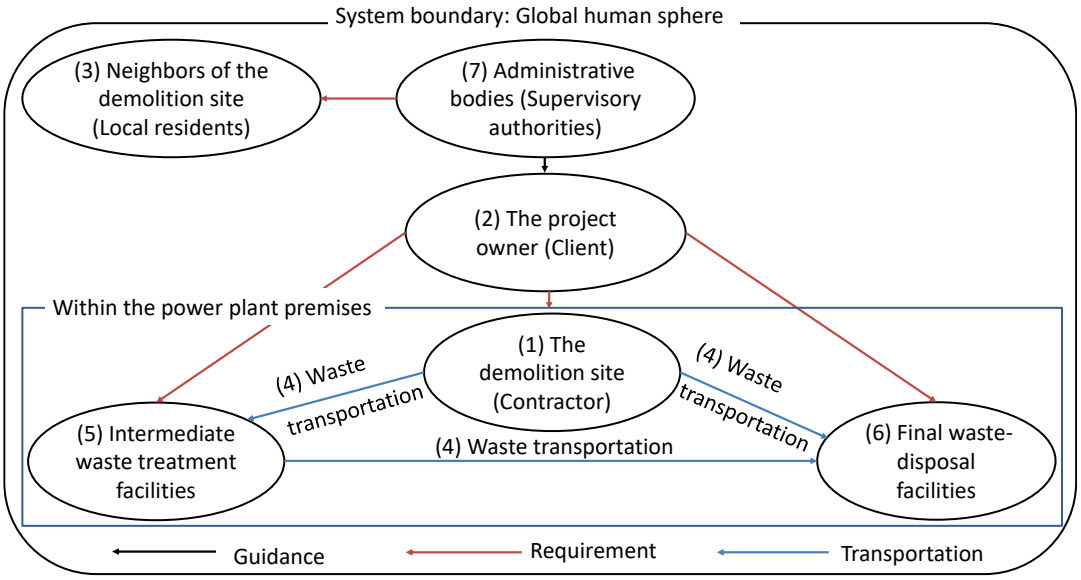

Figure 1 System Boundary and Stakeholders

1. Demarcation of Controlled Areas: Areas where the total effective dose received from external radiation and airborne radioactive materials may exceed 1.3 mSv per 3 months must be clearly designated. Assuming an annual duration of 2,000 labor hours, this threshold is practically determined based on whether the effective dose rate exceeds 2.5 mSv/h, which is standard for 1.3 mSv per 3 months.

2. Dose Measurement: External exposure is measured once every 3 months using radiation dosimeters in accordance with the Ionizing Radiation Ordinance. During the measurement, qualified personnel employ a whole-body counter when entering controlled areas because they might inhale, ingest, or otherwise absorb radioactive materials.

3. Provision and Use of Protective Equipment: Operators must provide effective respiratory protection to workers if airborne radioactive material concentrations exceed the regulatory limit (equivalent to 5 mSv annually). Table 2 presents the application range for each type of respiratory protective equipment. Furthermore, operators must provide and mandate the use of protective clothing, gloves, or footwear for tasks where surface contamination levels may exceed one-tenth of the threshold (4 Bq/cm^2). Table 2 outlines the application ranges for these protective garments.

4. Worker Education: Operators are required to provide specialized training to workers engaged in accident-derived waste disposal.

5. Health Management Measures: For workers continuously engaged in accident-derived waste disposal, operators must hire a physician to conduct initial and periodical (i.e., once every six months

Table 1 Performance requirements for the demolition of contaminated structures

Category	Performance requirements	Evaluation items	Symbol
The demolition site (contractor)	・Prevention of radioactive material dispersion through reinforcement of temporary containment structures	・Safety	C
	・Prevention of body surface contamination through the mandatory wearing of protective clothing	・Safety	C
	・Prevention of radioactive material inhalation through the mandatory mask wearing and proper ventilation	・Safety	C
The project owner (client)	・Compliance with laws and administrative guidance	・Safety	C
	・Development of appropriate construction plans	・Environment	E
Neighbors of the demolition site (local residents)	・Prevention of radioactive material dispersion	・Safety	C
	・Prevention of groundwater contamination	・Environment	E
Waste transportation (collection and transport companies)	・Prevention of radiation exposure to workers through the use of autonomous/remotely operated vehicles	・Safety	C
Intermediate waste treatment facilities (processing companies)	・Implementation of appropriate waste management practices through the use of steel container storage, sheet containment, and full rainwater-treatment systems	・Safety	C
final waste-disposal facilities (disposal companies)	・Ensuring safety during long-term storage through adequate radiation shielding and airtight performance	・Safety	C
administrative bodies (supervisory authorities)	・Validation of construction plans	・Safety	C
	・Verification of waste management safety	・Environment	E

Table 2 Respiratory protective equipment and Protective clothing, gloves, and footwear

Radioactivity concentration	Exceeding 2,000,000 Bq/kg	500,000 to 2,000,000 Bq/kg	500,000 Bq/kg or less
High-concentration dust work (Dust concentration > 10 mg/m^3)	Collection efficiency > 99.9% (Full-face mask) Double airtight full-body chemical protective suits over long-sleeved clothing, double rubber gloves over cotton gloves, and rubber boots	Collection efficiency > 95% (Half-face mask) Double airtight full-body chemical protective suits over long-sleeved clothing, rubber gloves over cotton gloves, and rubber boots	Collection efficiency ≤ 80% (Simple mask) Long-sleeved clothing, cotton gloves, and rubber boots
Work other than high-concentration dust work (Dust concentration ≤ 10 mg/m^3)	Collection efficiency ≤ 95% (Half-face mask) Double airtight full-body chemical protective suits over long-sleeved clothing, rubber gloves over cotton gloves, and rubber boots	Collection efficiency ≤ 80% (Simple mask) Long-sleeved clothing, rubber gloves over cotton gloves, and rubber boots	Collection efficiency ≤ 80% (Simple mask) Long-sleeved clothing, cotton gloves, and rubber boots

thereafter) medical examinations.

6. Establishment of a Safety and Health Management System: Operators must appoint a general safety and health manager, ensure that subcontractors designate their own health and safety officers, and convene a safety and health consultative committee.

7. Unified Management of Radiation Exposure: Operators must appoint a radiation supervisor to implement unified exposure management, encompassing subcontracted workers.

(2) Environmental Impact

The Ministry of Environment has provided guidelines on methodologies for waste contaminated with radioactive materials. All radioactive waste generated within the 1F premises is stored onsite. In accordance with storage management classifications, this waste is held in temporary storage areas and solid waste storage facilities.

As mentioned above, specific laws and standards have been established for 1F regarding safety and environmental impact. All these requirements will be added to the decommissioning cost. In particular, the following three factors notably affect cost efficiency:

1. Protection of workers from radiation
2. Measures for preventing radioactive material scattering
3. Radioactive waste treatment and disposal

Specifically, the disposal approach for accident-derived waste is fundamentally determined by a radioactivity concentration threshold of 8,000 Bq/kg. Waste exceeding this limit is managed by the national government as "Specified Waste" under strict safety protocols. Conversely, waste at or below the threshold is classified as standard waste and can be disposed of under conventional legal frameworks, which often involves wide-area disposal cooperation among local municipalities to accelerate regional cleanup [5]. Considering the highlighted factors, the breakdown of the demolition cost is presented in Figure 2.

Regarding resource circulation (recycling), relevant laws and regulations have not yet been fully established, and thus, they need to be addressed in future development; however, the Tokyo Electric Power Company is currently examining recycling options [6]. Furthermore, regarding the decontaminated soil outside the power plant premises, the first recycling action was implemented as a subgrade for the front yard lawn of the Prime Minister's official residence.

Additionally, Suzuki et al. investigated radioactive waste storage containers made of ultrahigh-density mortar containing radiocesium-contaminated ash and conducted performance-evaluation testing [7-11].

4. Cost Evaluation

For the demolition of general structures, pollution limits affecting local environments are set by laws, including the Noise Regulation Act and the Water Pollution Control Act. Noncompliant operations violate these laws and consequently cannot be executed. Accordingly, we treated these limits as work conditions rather than evaluation targets. Similarly, for structures contaminated with radioactive materials,

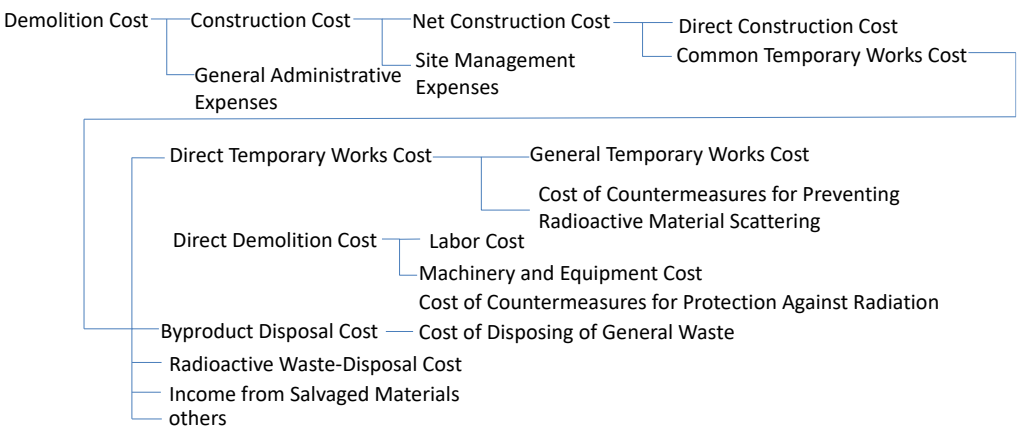

Figure 2 Composition of demolition costs

certain measures must comply with laws and administrative guidance. These include protecting workers from radiation and preventing the scattering of radioactive material. Consequently, these local environmental factors are considered work conditions, not evaluation targets. However, laws for radioactive waste recycling have not yet been established and should be enacted by the global environment. Nevertheless, some attempts on recycling should be made inside the affected site to ensure safety. In this section, we quantitatively evaluate the effects of specific cases from the cost-efficiency perspective.

Calculation parameters

The parameters values used for cost evaluation are presented below:

Volume of concrete debris contaminated with radioactive materials: 400,000 m^3

Volume of low-dose concrete debris with a dose rate of 0.01 mSv/h or less: 320,000 m^3

Construction cost of the low-dose concrete debris storage facility (including equipment cost): 300,000 yen/m^3

Operation cost: 1,500 yen/m^3 per year

Calculation Results

The cost savings of recycling 10% of the low-dose concrete debris are calculated as follows:

Storage facility construction cost saving: 320,000 m^3 × 0.1 × 300,000 yen/m^3 = 960 million yen

Operational cost saving: 1,500 yen/m^3 year ×

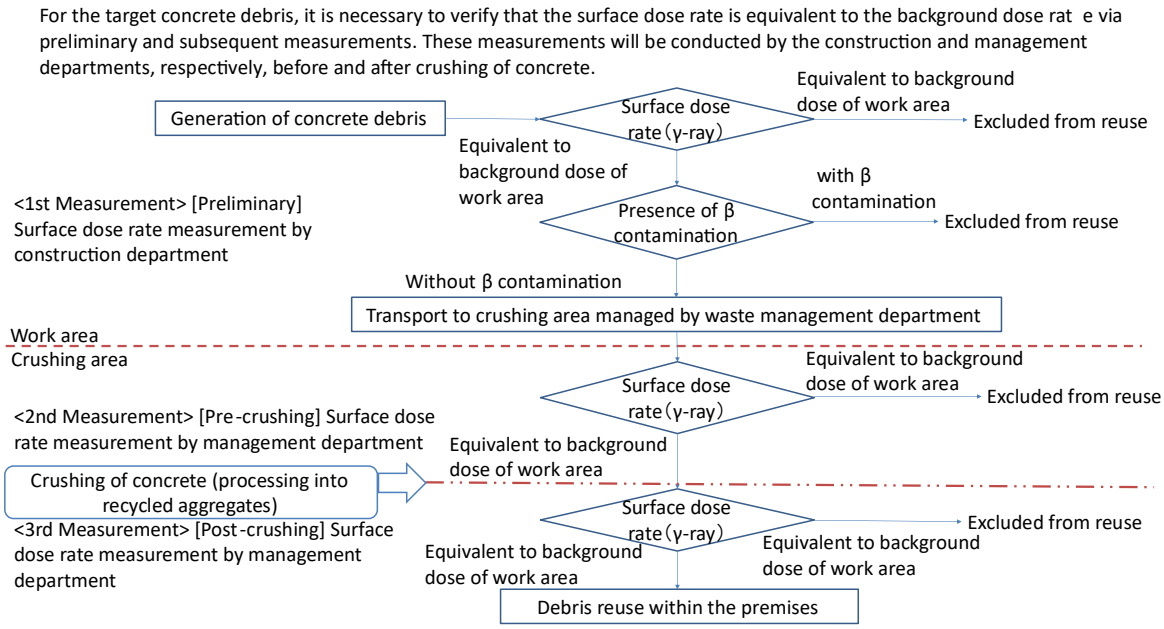

Figure 3 Verification flow for recycling [5]

Figure 4 Construction status of recycling inside the 1F premises: Roadbed material and Facing [12]

Table 4 Recycling track record within the 1F premises[12]

Location	Measured values during crushing		Measured values at reuse site	
	Surface dose rate of debris	Area ambient dose rate	Ambient dose rate before laying	Ambient dose rate after laying
Roadbed material	2 μSv/h	2 μSv/h	1 μSv/h	1μSv/h
Facing	2μSv/h	2μSv/h	21μSv/h	20μSv/h

270,000 m^3 = 405 million yen/year

These results indicate that reusing the low-dose concrete debris currently (or temporarily) stored onsite reduces the storage facility construction and streamlined operation costs by approximately 1 billion yen and by approximately 400 million yen/year.

Currently, 10 storage facilities have been constructed within the premises, with further expansion expected in the future. Therefore, initiating recycling operations as early as possible is highly desirable. Even under the current conditions, rules for recycling have been established, and very low-level concrete rubble has already been reused after confirming there is no adverse impact on the surrounding environment. Figure 4 and 5 and Table 4 present the rules and actual achievements toward this recycling effort.

5. Conclusions

The evaluation indices for the demolition of general structures presented in our previous study [1] can also be used in the demolition of structures contaminated with radioactive materials. However, for contaminated structures, measures for protecting workers from radiation and preventing the scattering of radioactive materials must strictly comply with laws and administrative guidance. Therefore, factors related to the local environment serve as prerequisites for executing the demolition work rather than as evaluation targets. Furthermore, the implementation cost for such measures is ultimately added to the cost-efficiency index. Therefore, developing construction methods that reduce radiation countermeasure costs can directly improve the overall performance evaluation.

Although enacting laws on radioactive waste recycling (resource circulation), which is the responsibility of the global environment, has not yet made desirable progress, evaluating the effects of reducing radioactive waste globally using recycling is as crucial as evaluating CO_2 emissions. In this study, we consider this to be a critical issue to be addressed in the future. We believe that doing so will significantly promote recycling activities.

References

[1] Murakami K., Dosho Y., REVIEW ON PERFORMANCE EVALUATION OF BUILDING DEMOLITION, AIJ Journal of Technology and Design, 31(77) (2025) 109-114. DOI 10.3130/aijt.31.109

[2] Act on Special Measures Concerning the Handling of Environment Pollution by Radioactive Materials Discharged by the Nuclear Power Station Accident Associated with the Tohoku District Off the Pacific Ocean Earthquake That Occurred on March 11, 2011

[3] Report by the Expert Meeting on Radiological Protection for Disposal Works of Decontamination-Removed Materials, Feb., 2013.

[4] Ministry of the Environment:Toward the Disposal of Waste Contaminated with Radioactive Materials, Dec., 2016.

[5] Tokyo Electric Power Company Holdings, Inc.: Fukushima Daiichi Nuclear Power Station Solid Waste Storage Management Plan: Fiscal 2021 Revision, Sep., 2021.

[6] "Recycling of Concrete Debris" Meeting of the Decommissioning, Contaminated Water and Treated Water Countermeasures Team/Secretariat Meeting, Tokyo Electric Power Company Holdings, Inc, April, 2018.

[7] Pareek S. et al., Experimental study on gamma radiation shielding performance evaluation of high-density mortar for various shielding situation Part1: Comparison of gamma radiation shielding performance in the different case of container shape and radioactive contamination levels, Summaries of Technical Papers of Annual Meeting, Architectural Institute of Japan, (2013) 653-654.

[8] Suzuki Y. et al., Evaluation of Gamma Radiation Shielding Performance by High-Density Mortar Containers Using Ashes Contaminated by Radioactive Cesium (Part2 Accelerated Carbonation Test and Gamma Radiation Shielding Performance Test for High-Density Mortar, Summaries of Technical Papers of Annual Meeting, Architectural Institute of Japan, (2013) 655-656.

[9] Araki Y. et al., A Fundamental Study on Change of Radioactive Rays Released from Mortar Mixed Ash Contaminated by Radioactive Cesium, Summaries of Technical Papers of Annual Meeting, Architectural Institute of Japan, (2013) 659-660.

[10] Mori H. et al., Demonstration Experiment on Durability of Concrete Containers Storing Incineration Fly Ash Contaminated with Radionuclides and Technical Requirements of such Containers, Concrete Journal, 56(4) (2018) 296–303.

[11] Suzuki Y. et al., Evaluation of Gamma Radiation Shielding Performance of Cylindrical Concrete Containers Using Soil Volume Source Contaminated by Radioactive Cesium, Journal of Japan Concrete Institute, 24(2) (2013) 43–52.

[12] Ministry of Economy, Trade and Industry (METI): Documents for the 124th Secretariat Meeting of the Team for Countermeasures for Decommissioning, Contaminated Water and Treated Water Management, March, 2024.

下水汚泥を混入した人造石の特性

Properties of Artificial Stone Mixed with Sewage Sludge

鄭渶錫※1、金智訓※1、蔡炅俊※1、鄭官龍※1、趙炳俊※1、李相洙※2

Yeong-Seok Jeong, Ji-Hun Kim, Kyoung-Jun Chae, Kwan-Yong Jeung, Byoung-Joon Cho, Sang-Soo Lee

ABSTRACT

This study evaluated the physical properties of artificial stone mixed with sewage sludge at ratios of 0%, 10%, 20%, and 30%. As the sewage sludge content increased, the unit weight and flexural strength decreased, whereas the air content increased. All specimens satisfied the aggregate exposure ratio requirement of KS F 4035; however, only the plain specimen met the flexural strength requirement of 5 MPa. These results indicate that the sewage sludge content should be controlled to maintain the required physical performance. Further studies are needed to determine the optimal content below 10% and improve flexural performance.

1. Introduction

Sewage sludge is a secondary waste generated during the treatment of pollutants contained in sewage and wastewater [1]. In Korea, sewage sludge generation has continuously increased due to the expansion of sewage treatment facilities and increasingly stringent water quality standards [2]. Sewage sludge contains large amounts of water and organic matter, resulting in high treatment and transportation costs. Improper management may also cause odors and soil and water pollution. Therefore, recycling methods are required to convert sewage sludge into a useful resource. Recently, extensive research has been conducted on utilizing industrial by-products and waste in cement-based construction materials to promote resource circulation and reduce environmental impacts. Sewage sludge may also be used as a constituent of construction materials when mixed at an appropriate ratio. However, its high moisture and organic matter contents may affect both fresh and hardened properties depending on the amount mixed; therefore, these effects must be investigated.

Artificial stone is an architectural finishing material manufactured by mixing aggregates, binders, and other materials, followed by curing and surface polishing. Its mix proportions and manufacturing conditions can be controlled to achieve consistent quality and various surface finishes. Furthermore, industrial by-products and waste can be mixed into artificial stone as constituent materials, demonstrating its potential as an environmentally friendly construction material [3]. Therefore, using sewage sludge as a raw material for artificial stone may reduce both the waste treatment burden and the consumption of natural materials while contributing to sewage sludge recycling.

This study analyzed the unit weight, air content, aggregate exposure ratio, and flexural strength of artificial stone mixed with different ratios of sewage sludge and evaluated its applicability as a building finishing material based on KS F 4035. The results provide fundamental data for sewage sludge recycling and the development of sustainable construction materials.

※1 大韓民国 国立 Hanbat 大学校 建設環境デザイン大学 建築工学科，修士課程
※2 大韓民国 国立 Hanbat 大学校 建設環境デザイン大学 建築工学科，教授 博士(工学)

Table 1 Experimental factors and levels

Experimental factor	Experimental level	Remarks
Binder conditions	OPC[1)]	1
Water/Cement (%)	50	1
coarse aggregate content (vol%[2)])	35	1
Admixture	Sewage sludge	1
Mixing ratio of admixture (wt%[3)])	0, 10, 20, 30	4
Curing condition	Water curing (Temperature: 20±2°C)	1
Experiment items	Unit weight, Air cotent, Aggregate exposure ratio, Flexural strength	4

1) OPC : Ordinary portland cement
2) vol% : Volume percent
3) wt% : Weight percent

2. Experimental overview

2.1 Experimental plan

In this study, ordinary portland cement was used as the binder, and the water-to-cement ratio (W/C) was set at 50%. Based on the results of preliminary experiments, the coarse aggregate content was set at 35%. The sewage sludge contents were set at 0, 10, 20, and 30%, and the specimens were cured in water at 20 ± 2 °C. The experimental program consisted of tests for unit weight, air content, aggregate exposure ratio, and flexural strength. The unit weight and air content tests were conducted in accordance with KS F 2409 (Standard Test Method for Unit Weight and Air Content of Fresh Concrete by the Gravimetric Method) and KS F 2421 (Standard Test Method for Air Content of Fresh Concrete by the Pressure Method), respectively [4,5]. The aggregate exposure ratio and flexural strength were evaluated in accordance with KS F 4035 (Precast Terrazzo). According to KS F 4035, the required aggregate exposure ratio and flexural strength are at least 50% and 5 MPa, respectively [6]. The experimental factors and levels are summarized in Table 1.

2.2 Properties of artificial stone

Artificial stone is a construction material manufactured by mixing binders, such as cement, with stone powder, aggregates, pigments, and other materials, followed by molding, curing, and surface polishing. It can reproduce the appearance and texture of natural stone and offers the advantage of achieving consistent quality as well as various colors and shapes by controlling the mix proportions and manufacturing conditions. In addition, artificial stone is easier to process and shape than natural stone and is therefore widely used as an interior and exterior finishing material for walls, columns, stairs, and floors. In particular, cement-based artificial stone has attracted attention as a construction material that can reduce the consumption of natural resources and promote waste recycling because industrial by-products and waste can be utilized as aggregates or supplementary materials during its production [3].

In this study, the surface cement paste layer of the artificial stone specimens was polished using a grinder to uniformly expose the internal aggregates, thereby reproducing the surface appearance of precast terrazzo and ensuring an adequate aggregate exposure ratio.

2.3 Properties of sewage sludge

Sewage sludge is a by-product generated during wastewater treatment and is mainly produced through primary and secondary sedimentation processes. It consists of organic matter, microorganisms, inorganic substances, and other constituents present in wastewater, and its composition and physicochemical properties vary depending on the characteristics of the wastewater, treatment process, season, and region [7]. Sewage sludge generally contains a large amount of water, resulting in high viscosity and low fluidity. After dewatering, its solids content increases, and it takes the form of a sludge cake [8].

In this study, dewatered sewage sludge cake obtained from a municipal wastewater treatment facility in City S was used. In its as-received condition, the sewage sludge had a density of

approximately 1.03 g/cm³ and a moisture content of approximately 80%.

3. Experimental results and discussion

3.1 Unit weight

Figure 1 presents the unit weight of artificial stone with different sewage sludge contents. The unit weight decreased from 2.341 g/cm³ for the Plain specimen to 2.134, 1.991, and 1.949 g/cm³ at sewage sludge contents of 10%, 20%, and 30%, respectively. The specimen containing 30% sewage sludge exhibited a 16.7% lower unit weight than the Plain specimen. This reduction was attributed to the relatively low density of sewage sludge (1.03 g/cm³) compared with cement and aggregates, which reduced the average density of the constituent materials. This trend is consistent with previous findings that concrete density decreased with increasing dry sewage sludge content [9].

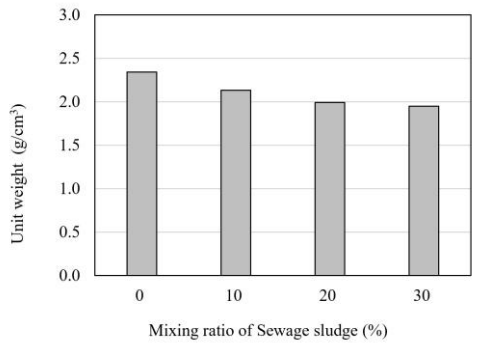

Figure 1 Unit weight

3.2 Air content

Figure 2 presents the air content test results of artificial stone with different sewage sludge contents. The air content of the Plain specimen without sewage sludge was 2.4%. As the sewage sludge content increased to 10%, 20%, and 30%, the air content increased to 2.9%, 3.2%, and 4.1%, respectively. In particular, the specimen containing 30% sewage sludge exhibited the highest air content, which was 1.7 percentage points higher than that of the Plain specimen.

These results are attributed to changes in the mixture composition and pore formation characteristics resulting from the increased sewage sludge content. An increase in porosity with the addition of dried sewage sludge to cement mortar has also been reported [10].

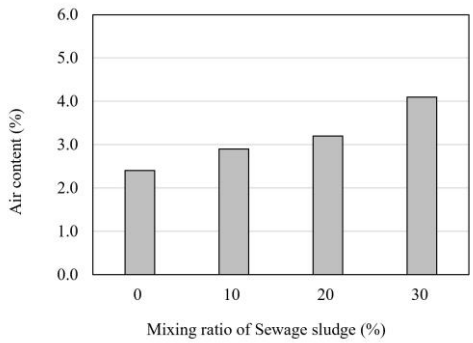

Figure 2 Air content

3.3 Aggregate exposure ratio

Figure 3 presents the aggregate exposure ratio of artificial stone with different sewage sludge contents. All specimens satisfied the minimum requirement of 50% specified in KS F 4035. This result was attributed to the identical coarse aggregate content in all mixtures and the uniform polishing of the specimen surfaces, which sufficiently exposed the internal aggregates.

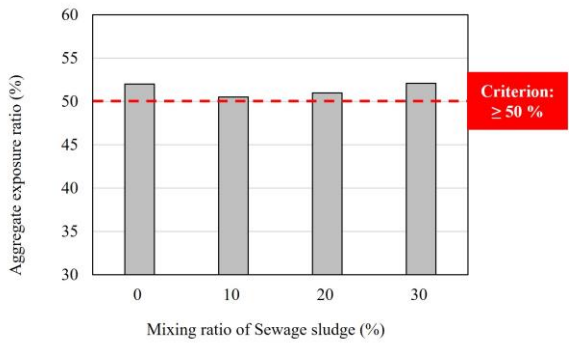

Figure 3 Aggregate exposure ratio

3.4 Flexural strength

Figure 4 presents the flexural strength of artificial stone with different sewage sludge contents. The flexural strength decreased by an average of approximately 1.0 MPa for every 10-percentage-point increase in sewage sludge content. Only the Plain specimen satisfied the minimum requirement of 5

MPa specified in KS F 4035, while the specimen containing 30% sewage sludge exhibited the lowest value, corresponding to approximately 62.7% of the requirement. This reduction was attributed to the reduced cement proportion and increased air content, which decreased the compactness of the specimens and weakened the bond between the aggregates and cement paste. Therefore, sewage sludge contents below 10% should be further investigated to determine an appropriate content.

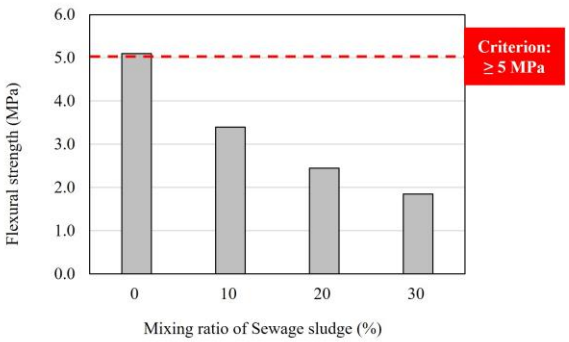

Figure 4 Flexural strength

4. Conclusions

This study evaluated the physical and physical properties of artificial stone with different sewage sludge contents and examined its applicability as an architectural finishing material. The main findings are as follows.

As the sewage sludge content increased, the unit weight decreased from 2.341 to 1.949 g/cm³, whereas the air content increased from 2.4% to 4.1%. The aggregate exposure ratio of all mixtures satisfied the minimum requirement of 50% specified in KS F 4035. The flexural strength decreased by approximately 1.0 MPa for every 10% increase in sewage sludge content, and only the Plain specimen satisfied the minimum requirement of 5 MPa.

Further studies should investigate sewage sludge contents below 10% to determine the optimal content and improve flexural performance by modifying the binder and mixing in fibers or supplementary materials.

Reference

[1] I.S. Choi, H.S. Jung, I.S. Han, Study on sludge reduction by sludge solubilization and change of operation conditions of sewage treatment process, J. Korean Soc. Environ. Eng. 31(12) (2009) 1113–1122.

[2] C.Y. Lee, W.J. Jung, J.T. Kim, A study on the development trends of wastewater sludge treatment technology, J. Korean Geo-Environ. Soc. 17(8) (2016) 5–15.

[3] Y.J. Yoo, S.S. Lee, H.Y. Song, Physical properties of artificial interior stone using waste resources, J. Korea Inst. Build. Constr. 14(3) (2014) 237–243.

[4] KS F 2409; Standard test method for unit weight and air content (gravimetric) of fresh concrete. Korea Standard Committee: Seoul, Republic of Korea, 2021. Available from: https://www.standard.go.kr/streamdocs/view/sd;streamdocsId=72622328641243366

[5] KS F 2421; Standard test method for air content of fresh concrete by pressure method. Korea Standard Committee: Seoul, Republic of Korea, 2021. Available from: https://www.standard.go.kr/streamdocs/view/sd;streamdocsId=72622328641383217

[6] KS F 4035; Precast terrazzo. Korea Standard Committee: Seoul, Republic of Korea, 2022. Available from: https://www.standard.go.kr/streamdocs/view/sd;streamdocsId=72059378688023329

[7] H. Chang, Y. Zhao, A. Xu, A. Damgaard, T.H. Christensen, Mini-review of sewage sludge parameters related to system modelling, Waste Manage. Res. 41(5) (2023) 970–976.

[8] U.S. Environmental Protection Agency, POTW Sludge Sampling and Analysis Guidance Document, Office of Water, Washington, DC, 1989. Available from: https://www.epa.gov/sites/default/files/2018-11/documents/potw-sludge-sampling-guidance-document.pdf?utm_source=chatgpt.com

[9] S. Valls, A. Yagüe, E. Vázquez, C. Mariscal, Physical and mechanical properties of concrete with added dry sludge from a sewage treatment plant, Cem. Concr. Res. 34(12) (2004) 2203–2208.

[10] A. Yagüe, S. Valls, E. Vázquez, Use of cement Portland mortar of stabilised dry sewage sludge in construction applications, WIT Trans. Ecol. Environ. 56 (2002) 527–536.

石炭ガス化スラグ細骨材を使用したコンクリートの材齢 5 年における長期強度発現特性

Long-Term Strength Development Characteristics of Concrete Using Coal Gasification Slag Fine Aggregate at the Age of Five Years

辻　拓実※1，佐藤幸恵※2，松浦忠孝※3，小山明男※4
Takumi Tsuji, Sachie Sato, Tadataka Matsuura, Akio Koyama

ABSTRACT

石炭ガス化スラグ（CGS）はコンクリート用細骨材として JIS に規定されているが，長期材齢における品質の検討例は少ない。本研究では，2020 年に作製した CGS 置換率 0，30，50，100%，目標スランプ 12 および 18cm の円柱供試体を用い，標準水中養生および現場封かん養生における材齢 5 年の圧縮強度，静弾性係数，ポアソン比を測定するとともに，インデント試験および電子顕微鏡を用いた界面観察を行い，強度発現性を評価した。材齢 5 年の圧縮強度は材齢 28 日および 91 日を大きく上回り，CGS 置換率が高いほど材齢 91 日以降の強度増進は大きくなった。静弾性係数はいずれの調合においても JASS 5 のヤング係数式を上回った。インデント試験より，CGS のヤング係数は天然骨材と同等でばらつきが小さいことが確認された。EDS ライン分析では，骨材-ペースト境界の Ca/Si 比が天然骨材では急激に低下するのに対し CGS では緩やかに低下しており，CGS 周囲にポゾラン反応相が生成していることを確認した。この反応相が界面の一体性を高め，長期強度発現に寄与したと考えられる。

1. Introduction

In recent years, integrated coal gasification combined cycle (IGCC) power generation has been increasingly introduced in Japan to improve generation efficiency and reduce CO_2 emissions. In an IGCC plant, the molten slag discharged from the gasifier is water-quenched, producing glassy coal gasification slag (CGS) as a by-product. Since CGS can be ground to adjust its particle size distribution and used as a fine aggregate for concrete, its application has been investigated; it was standardized as a JIS product in 2020, and in 2023 the Architectural Institute of Japan published the Recommendations for Mix Design, Production and Construction Practice of Concrete with Coal Gasification Slag Fine Aggregate [1].

The main constituents of CGS are SiO_2, Al_2O_3 and CaO, giving it a chemical composition close to that of fly ash [2]. It is therefore considered that a pozzolanic reaction occurs between CGS and the $Ca(OH)_2$ produced by cement hydration, densifying the microstructure [3]. A previous study [4] reported that the CGS replacement ratio has little influence on strength at 28 days, whereas at 91 days the compressive strength increases as the replacement ratio becomes higher. However, very few studies have examined the quality of such concrete at the long ages required in building construction. In this study, therefore, specimens produced in 2020 under conditions equivalent to those described above were used to evaluate the compressive strength, static modulus of elasticity, Poisson's ratio and microstructure at the age of five years, to clarify the long-term strength development characteristics of concrete using CGS fine aggregate.

※1 日本　東京都市大学　建築都市デザイン学部建築学科　学部 4 年
※2 日本　東京都市大学　建築都市デザイン学部建築学科　教授　博士（工学）
※3 日本　東京電力ホールディングス　経営技術戦略研究所　博士(工学)
※4 日本　明治大学　理工学部建築学科　教授　博士(工学)

2. Experimental outline

2.1 Materials and mix proportions

The experimental factors and levels are shown in Table 1, and the material properties are shown in Table 2. The water-cement ratio was kept constant for all levels. For the target slump of 12 cm, four CGS replacement ratios of 0, 30, 50, and 100% were adopted, and for 18 cm, three ratios of 0, 30, and 50% were adopted. The target air content was 4.5 ± 1.5 % in every case. The mix proportions are given in Table 3. The fine aggregate was a mixture of pit sand (S1) and crushed sand (S2) at a ratio of 4:6, in which CGS was substituted at the replacement ratios listed in Table 1. The coarse aggregate was a mixture of crushed stone (G1) and pit gravel (G2) at a ratio of 3:7.

2.2 Specimens

The concrete was produced on 30 and 31 October 2020 at a ready-mixed concrete plant in Namie Town, Futaba District, Fukushima Prefecture. It was placed and formed into specimens within the same town. The results reported here were obtained from specimens that had subsequently been cured continuously by the respective methods. The specimens were 100 x 200 mm cylinders, and two curing methods were used: standard water curing and on-site sealed curing. The sealed-cured specimens were sealed after demolding and stored outdoors away from direct sunlight; from 91 days onward, they were kept indoors at 20 ℃. The water-cured specimens were cured continuously in water at 20 ± 2 ℃ after demolding.

2.3 Test items

The compressive strength test was carried out in accordance with JIS A 1108. At the same time, the longitudinal strain was measured with a compressometer in accordance with JIS A 1149 to calculate the static modulus of elasticity, and the lateral strain was measured with strain gauges to calculate Poisson's ratio. The indentation test was performed with a maximum load of 20 mN, a loading rate of 4.9348 mN/s and a holding time at maximum load of 5 s, and the elastic modulus of the micro-regions of the aggregate and the paste was calculated from the slope of the unloading curve. In addition, backscattered electron (BSE) imaging and energy-

Table 1 Factors and levels used in the experiment

Factor	Level
W/C (%)	56.8
CGS replacement ratio (%)	0, 30, 50, 100
Target slump (cm)	12, 18
Testing age(days・years)	3, 7, 28, 91, 5years
Casting date	2020, Oct. 30 and 31
Curing	Standard water (w) Sealed on-site (s)

Table 2 Materials used

Materials	Symbol	Properties
Cement	C	Normal portland cement Density : 3.15g/cm^3
Fine aggregate	S1	Pit sand, oven-dry density: 2.54 g/cm^3 F.M.: 2.66
	S2	Crushed sand, oven-dry density: 2.64 g/cm^3, F.M.: 2.72
	S3	Coal gasification slag fine agg. Oven-dry density: 2.79 g/cm^3 F.M.: 2.72
Coarse aggregate	G1	Crushed stone, oven-dry density: 2.67 g/cm^3, Solid content: 59.9 %
	G2	Pit gravel, oven-dry density: 2.58 g/cm^3, Solid content: 65.1 %
	G	Solid content of blended agg.: 62.5 %
Admixture	AD1	High-range AE water-reducing agent: complex of modified lignin sulfonate and polycarboxylate compound
	AD2	AE agent: alkyl ether type anionic surfactant

Table 3 Mix proportions of concrete

Mix No.	W/C (%)	air (%)	Target slump (cm)	s/a (%)	CGS replacement ratio (%)	Unit weight (kg/m^3)								
						W	C	CGS	S1	S2	G1	G2	Ad(C×%)	AE(C×%)
18-0-00	56.8	4.5 ±1.5	18±2.5	46.8	0	175	308	0	343	495	295	663	0.9	0.055
18-A-30				46.8	30	175	308	268	239	347	295	663	0.9	0.065
18-A-50				47.2	50	171	302	453	175	253	295	663	0.9	0.095
12-A-00			12±2.5	44.7	0	161	284	0	338	490	316	710	0.9	0.050
12-A-30				44.7	30	161	284	265	236	344	316	710	0.8	0.065
12-A-50				45.0	50	159	280	444	171	248	316	710	0.8	0.070
12-A-100				45.0	100	159	280	889	0	0	316	710	0.8	0.090

dispersive X-ray spectroscopy (EDS) were carried out with a field-emission scanning electron microscope (FE-SEM) to examine the formation of hydration products, the presence of pozzolanic reaction products, and elemental distribution. The samples for the indentation test and SEM/EDS were cut from the cylinders, immersed in 2-propanol and vacuum-degassed to stop hydration, embedded in resin, and polished to a mirror finish.

3. Results and discussion

3.1 Compressive strength

The relationship between the CGS replacement ratio and the compressive strength is shown in Figs. 1 and 2. For every curing method and CGS replacement ratio, strength increased markedly from that at 28 and 91 days. It can also be seen that the higher the CGS replacement ratio, the greater the strength gain after 91 days. In the light of previous studies, this suggests that a pozzolanic reaction of CGS occurred and contributed to the strength gain. The ratio of the compressive strength at five years to that at 91 days is shown in Figs. 3 and 4. The ratio was larger for the sealed-cured specimens with a slump of 12 cm, reaching 1.3 to 1.5 for the levels containing CGS.

3.2 Static modulus of elasticity and Poisson's ratio

The relationship between the static modulus of elasticity and the compressive strength is shown in Fig. 5. The figure also shows the curve obtained from the Young's modulus equation (AIJ equation) given in the Japanese Architectural Standard Specification JASS 5 Reinforced Concrete Work of the Architectural Institute of Japan (hereafter JASS 5) [5]. At every replacement ratio, the static modulus tended to be higher than that given by the AIJ equation. Previous studies have also reported values approximately 1.1 to 1.2 times the AIJ equation [4], and the present results showed the same tendency.

$$E = 3.35 \times 10^4 \times k1 \times k2 \times (\gamma/2.4)^2 \times (Fc/60)^{1/3}$$

where, E: static modulus of elasticity of concrete (N/mm^2)

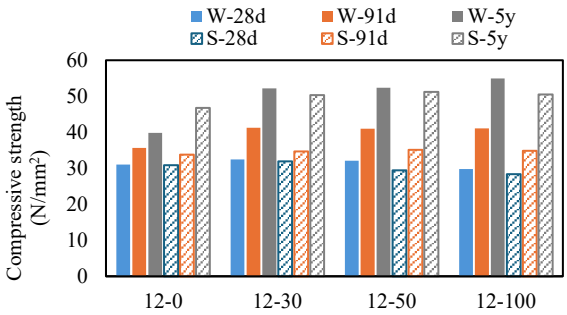

Fig.1 Relationship between CGS replacement ratio and compressive strength (Slump 12 cm)

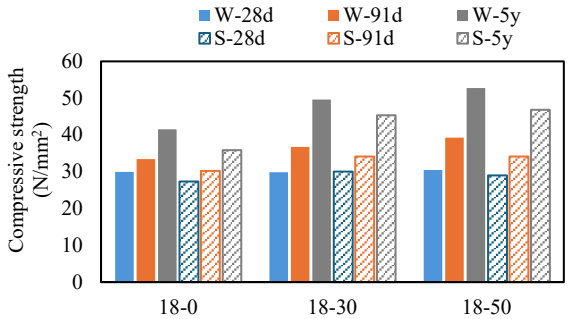

Fig.2 Relationship between CGS replacement ratio and compressive strength (Slump 18 cm)

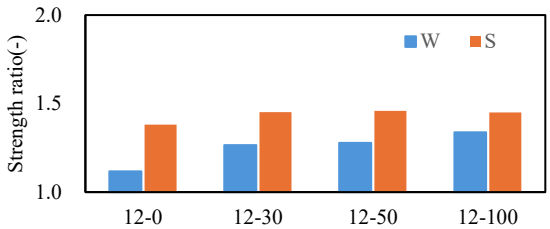

Fig. 3 Ratio of strength at 5 years to that at 91 days (slump 12 cm)

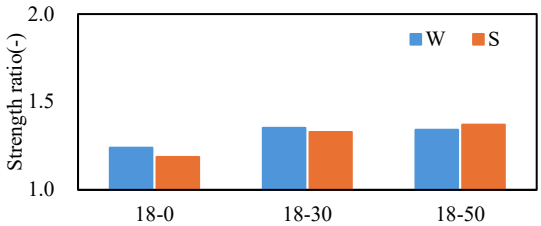

Fig. 4 Ratio of strength at 5 years to that at 91 days (slump 18 cm)

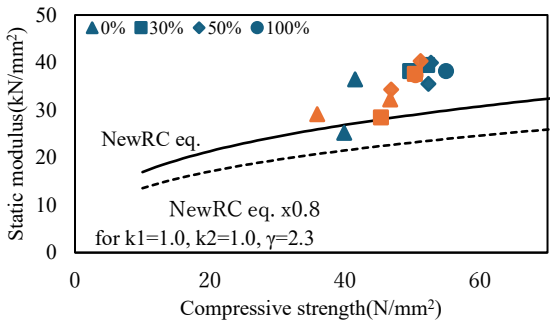

Fig. 5 Static modulus vs. compressive strength

γ: unit weight of concrete (kg/m^3),
Fc: compressive strength of concrete (N/mm^2),
k_1: correction factor determined by the type of coarse aggregate
k_2: correction factor determined by the type of admixture

The calculated Poisson's ratios are shown in Fig. 6. In every case, the value was larger for the water-cured specimens than for the sealed-cured specimens, whereas it showed no clear dependence on the CGS replacement ratio. The larger Poisson's ratio under water curing is considered to result from the long-term immersion in water: the pores inside the specimens were filled with water, which restrained the volume change under compressive loading, so that the lateral strain relative to the longitudinal strain became larger and Poisson's ratio increased.

3.3 Indentation test results

The Young's moduli of the fine aggregate phases (CGS and natural aggregate) obtained from the indentation test are shown in Fig. 7. Comparing the mean values, the Young's moduli of CGS and the natural aggregate were almost identical. The natural aggregate showed a large standard deviation and considerable scatter, partly because two types were used in combination, whereas CGS was confirmed to be generally uniform in quality. The relationship between the difference in Young's modulus and the compressive strength is shown in Fig. 8. Since the water-cement ratio was the same for all mixes in this study, the relationship with strength was not clear; a previous study has, however, shown that the compressive strength decreases as the difference in Young's modulus from the paste becomes larger [6]. One difference between CGS and natural aggregate is the smoothness of the surface. As shown in Fig. 9, CGS has a glassy, smooth surface, and its bond with the paste is therefore considered to affect strength development.

3.4 Observation by SEM and EDS

The backscattered electron images at the age of five years are shown in Fig. 10. Comparing a CGS

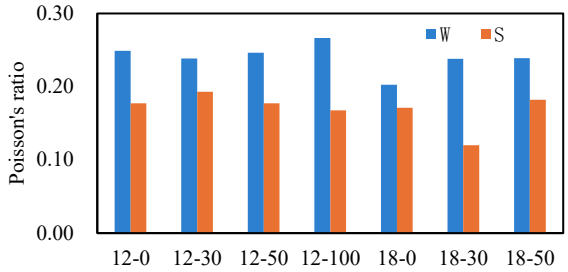

Fig. 6 Calculated Poisson's ratio

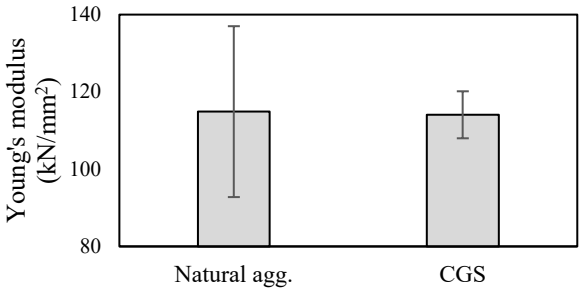

Fig. 7 Young's modulus of the fine aggregates

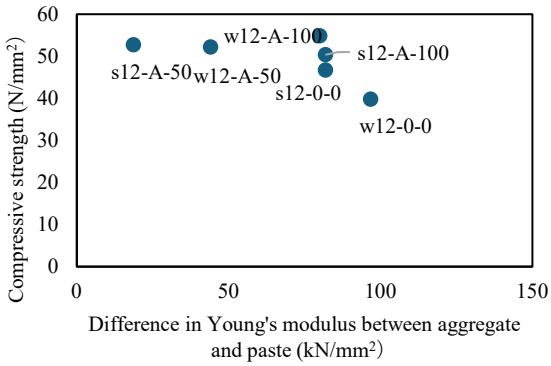

Fig. 8 Difference in Young's modulus between aggregate and paste vs. compressive strength

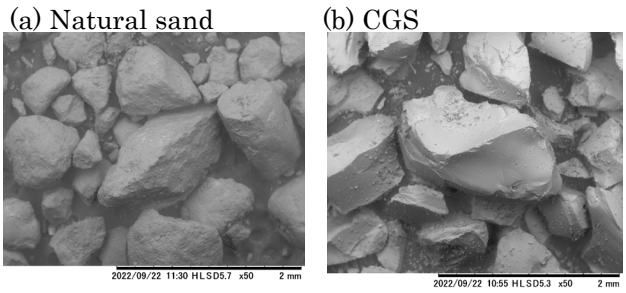

Fig. 9 Surface texture of the fine aggregates

replacement ratio of 0 % (natural aggregate only) with 100 %, hydration products appear to have formed at the aggregate interface in the 100 % CGS level. The results of the EDS line analysis are shown in Fig. 11. For the natural aggregate, Ca was not detected beyond the interface between the aggregate and the paste, and the aggregate region consisted mainly of Si. For CGS, on the other hand, Si increased gradually, and Ca

(a) W12-00 Natural aggregate

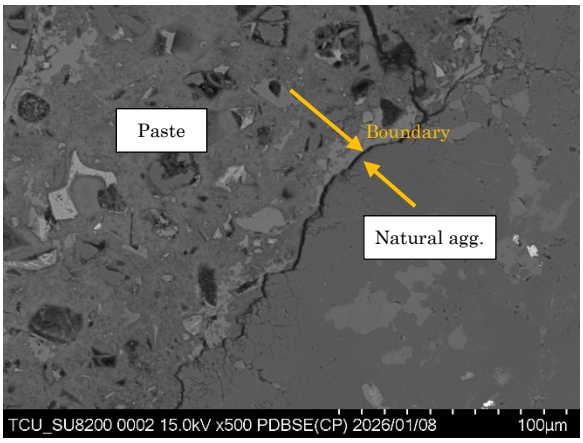

(b) W12-100 CGS

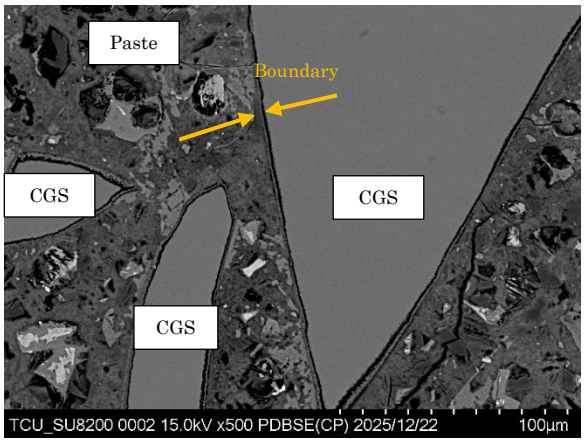

Fig. 10 BSE images around the aggregate interface

decreased gradually from the paste side towards the aggregate side near the boundary, suggesting the formation of a pozzolanic reaction phase. The Ca/Si ratio was then calculated from the line analysis results and compared, as shown in Fig. 12.

At a CGS replacement ratio of 0%, the Ca/Si ratio dropped sharply near the interface and became almost zero at 1 μm, whereas at 100% it decreased gradually toward the aggregate side and still showed a value of about 0.5 at 5 μm. This is considered to be because the amorphous SiO_2 in CGS reacted with the $Ca(OH)_2$ in the paste to form a pozzolanic reaction phase. The pozzolanic reaction phase formed around CGS thus improved the integrity between the aggregate and the paste and contributed to the long-term strength gain.

4. Conclusions

This study examined concrete using CGS fine aggregate at the age of five years, and the following findings were obtained.

(1) For every curing method and CGS replacement ratio, the compressive strength at five years greatly exceeded that at 28 and 91 days. The higher the CGS replacement ratio, the greater the strength gain after 91 days.

(2) The static modulus of elasticity exceeded the value given by the AIJ equation at every CGS replacement ratio, showing a tendency comparable to that reported in previous studies. Poisson's ratio was larger under

(a)W12-00 Natural aggregate

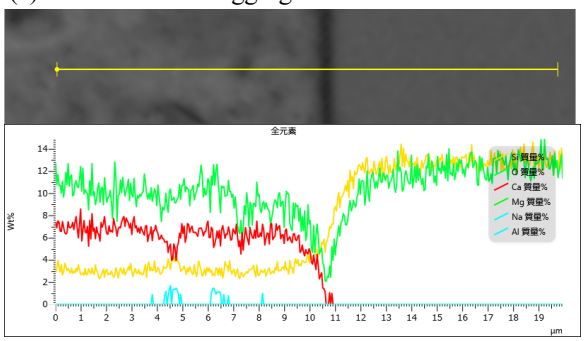

(b)W12-100 CGS

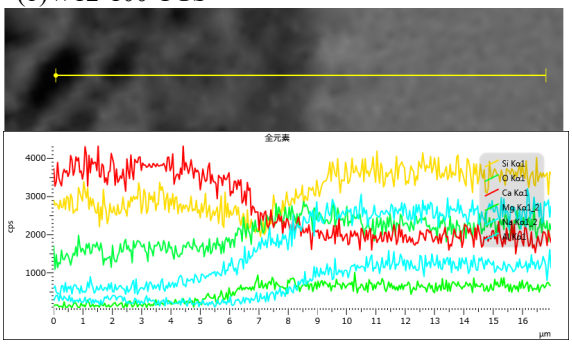

Fig. 11 EDS analysis of the interfacial transition zone

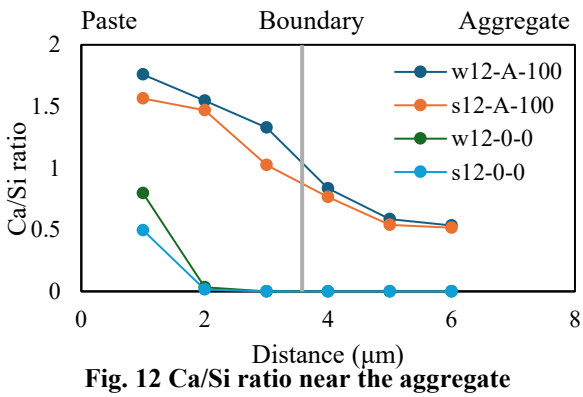

Fig. 12 Ca/Si ratio near the aggregate boundary

standard water curing than under on-site sealed curing, but showed no clear dependence on the CGS replacement ratio. This is considered to be because long-term immersion in water filled the pores and restrained volume change under compressive loading.

(3) The indentation test showed that the Young's moduli of CGS and the natural aggregate were almost identical on average, and that CGS was more uniform, with less scatter, than the natural aggregate. Within the scope of this study, the difference in Young's modulus between the aggregate and the paste showed no clear relationship with the compressive strength.

(4) Backscattered electron imaging and EDS line analysis confirmed a region considered to be a pozzolanic reaction phase around the CGS particles. The Ca/Si ratio at the aggregate-paste boundary dropped sharply near the interface for the natural aggregate, whereas it decreased gradually towards the aggregate side for CGS. The pozzolanic reaction phase formed around CGS is considered to have improved the integrity between the aggregate and the paste and contributed to the long-term strength gain.

Acknowledgement

The authors would like to express their gratitude to Ms. Mao Oba (Taisei Corporation, formerly an undergraduate student at Tokyo City University) for her cooperation in this study.

References

[1] Architectural Institute of Japan: Recommendations for Mix Design, Production and Construction Practice of Concrete with Coal Gasification Slag Fine Aggregate, 2023.10

[2] Matsuura, T., Kobayashi, Y., Onaka, A. and Nagataki, S.: Characteristics of Coal Gasification Slag Fine Aggregate and Its Influence on the Strength Properties of Concrete, Journal of the Society of Materials Science, Japan, Vol.71, No.10, pp.847-852, 2022.10 (in Japanese)

[3] Yamamoto, T.: A Study on the Strength Development Mechanism Accompanying the Pozzolanic Reaction of Fly Ash Concrete, CRIEPI Report N06018, 2007.6 (in Japanese)

[4] Matsuura, T., Sato, S. et al.: Basic Properties of Concrete Using Coal Gasification Slag Fine Aggregate, Parts 8-9, Summaries of Technical Papers of Annual Meeting, Architectural Institute of Japan (Tokai), pp.45-48, 2021.9 (in Japanese)

[5] Architectural Institute of Japan: Japanese Architectural Standard Specification JASS 5 Reinforced Concrete Work, 2022

[6] Otaka, S.: Basic Experiments on the Influence of Coal Gasification Slag Fine Aggregate on the Strength Development of Concrete, Graduation Thesis, Tokyo City University, 2023 (in Japanese)

韓国産製紙スラッジ灰の物理・化学的特性分析および建設材料への活用可能性評価

Analysis of Physical and Chemical Characteristics of Domestic Paper Sludge Ash and Evaluation of the potential for utilizing construction materials

金 時坤※1, 金 源昌※2, 林 廈峻※2, 李 泰圭※3

Si-Gon Kim, Won-Chang Kim, Ha-Jun Im, Tae-Gyu Lee

ABSTRACT

Paper sludge ash (PSA) is generated through the incineration of paper sludge, and its properties may vary depending on the raw materials and treatment conditions of the papermaking process. In this study, PSA generated from Jeonju Paper Co., Ltd. was examined by XRF, XRD, TG/DTA, and particle size analysis. Cement pastes containing 0, 10, 20, and 30% PSA were also prepared for basic comparison. XRF showed that CaO was the dominant component at 64.57%. XRD, TG/DTA, and particle size analyses were used to identify the mineralogical, thermal, and particle-size characteristics of the PSA; detailed raw data are not presented in this summary. The results provide basic information for understanding the material characteristics of domestic PSA.

1. Introduction

Paper sludge is generated during paper production and wastewater treatment and contains fibers and inorganic materials originating from the papermaking process. When paper sludge is treated by incineration, paper sludge ash (PSA) is produced. Previous studies have examined the recycling of PSA as an inorganic material and its application to cement-based materials.

The characteristics of PSA can differ depending on the raw materials, inorganic additives, sludge composition, and treatment conditions used at each paper mill. Therefore, before considering further applications, it is necessary to first understand the basic characteristics of the PSA itself. In this study, PSA generated from Jeonju Paper Co., Ltd. was examined using XRF, XRD, TG/DTA, and particle size analysis. In addition, cement pastes containing PSA were prepared as a basic experimental series.

2. Materials and Experimental Methods

2.1 Materials

The PSA used in this study was collected from the paper-sludge incineration process of Jeonju Paper Co., Ltd. Sludge generated during papermaking is dewatered and dried before incineration. Ordinary Portland cement (OPC) was used for the cement paste mixtures.

2.2 Experimental Methods

XRF, XRD, TG/DTA, and particle size analyses were conducted to examine the basic characteristics of the PSA. XRF was used to determine chemical composition, while XRD, TG/DTA, and particle size analysis were used to examine mineralogical, thermal, and particle-size characteristics, respectively. For the cement paste series, PSA replacement ratios were set at 0, 10, 20, and 30%, and the water-to-binder ratio (W/B) was fixed at 0.40.

※1 大韓民国　世明大学校　消防防災学科　修士課程
※2 大韓民国　世明大学校　消防防災学科　博士課程
※3 大韓民国　世明大学校　消防防災学科　教授　博士(工学)

Table 2. Chemical composition of OPC and PSA (wt.%)

Material	CaO	SiO_2	Al_2O_3	Fe_2O_3	MgO	SO_3	K_2O	Na_2O
Cement	**60.34**	**19.82**	**4.85**	**3.30**	**3.83**	**2.88**	**1.08**	**-**
PSA	**64.57**	**7.03**	**4.21**	**1.94**	**2.25**	**1.19**	**0.29**	**0.19**

Table 1. Mix proportions of cement paste

PSA replacement ratio (%)	OPC (%)	PSA (%)	W/B
0	100	0	0.40
10	90	10	0.40
20	80	20	0.40
30	70	30	0.40

3. Results and discussion

3.1 Chemical Characteristics of PSA

XRF analysis showed that CaO had the highest content at 64.57%. SiO_2 and Al_2O_3 were 7.03% and 4.21%, respectively, and smaller amounts of Fe_2O_3, MgO, SO_3, K_2O, and Na_2O were also identified. The PSA used in this study therefore showed a composition characterized by a high proportion of Ca-based components.

3.2 Basic Characteristics Identified by XRD, TG/DTA, and Particle Size Analysis

XRD analysis confirmed that the PSA contained Ca-bearing crystalline phases, with Lime and Calcite identified among the major phases. TG/DTA analysis showed a distinct mass-change region at high temperature, indicating that the PSA contains components that undergo thermal change in this range. Particle size analysis showed that the PSA consisted of particles distributed over a relatively broad size range rather than being concentrated at a single particle size. In this summary, these analyses are discussed only in terms of their main characteristics, and detailed patterns, curves, distributions, and numerical particle-size data are not presented. The cement-paste XRD comparison also showed differences in the major crystalline-phase peaks according to PSA replacement ratio and curing age. Because the present document is intended as a brief basic-characterization summary, detailed XRD patterns and peak-intensity data are reserved for subsequent research and are not disclosed here.

4. Conclusion

This study examined the basic characteristics of PSA generated from Jeonju Paper Co., Ltd. XRF confirmed that CaO was the dominant chemical component. XRD, TG/DTA, and particle size analyses further showed that the PSA has identifiable mineralogical, thermal, and particle-size characteristics, while cement-paste XRD indicated changes associated with PSA replacement ratio and curing age. The present results are limited to basic characterization and are intended to serve as preliminary information for subsequent studies on PSA.

高炉スラグ微粉末とフライアッシュを主原料とした炭素固定型グリーンセメント

Carbon-Sequestering Green Cement Using Blast Furnace Slag and Fly Ash as Raw Materials

二万桜太※1、西村慈温※1、李柱国※2
Ota Niman, Jion Nishimura, Zhuguo Li

ABSTRACT

本研究では，高炉スラグ微粉末(BFS)，フライアッシュ(FA)，再生微粒粉(WC)や再生微粉(WCp)および炭酸ソーダ粉末からなるグリーンセメント(GC)の製法の確立を目指して，GC の強度の影響要因について考察を行った。その結果として，WCp と WC のいずれにおいても最適な混合率は 20%であり，両者のいずれを用いた場合でも GC の圧縮強度は 材齢 28 日で 45 MPa を上回った。ただし，WCp と比較すると WC を用いた場合は強度のばらつきが大きい傾向が認められた。さらに，BFS と FA のブレーン値についてはそれぞれ 6000 cm²/g 程度で十分であることを確認した。

1. Introduction

In recent years, the researches on low-carbon cements have been rapidly advancing both domestically and internationally from the perspective of mitigating global warming. One example is geopolymer (GP), which utilizes ground granulated blast-furnace slag (BFS) or/and fly ash (FA) as reactive fillers activated by an alkaline solution. Although GP has a lower CO_2 emission intensity, its two-part formulation (separate solid and liquid components) poses inconveniences for transportation, storage and use, as well as higher cost, compared to Portland cement (PC). Furthermore, when a strongly alkaline NaOH aqueous solution is used, safety during handling GP becomes a major concern. In addition, sodium silicate increases the viscosity of GP concrete, creating challenges in production and construction processes such as mixing, pumping, and placing. Consequently, the practical application of geopolymers utilizing alkaline solution as activator remains limited at present.

Against this background, Li et al. have proposed a "Green Cement" (GC) technology that utilizes wastes as the primary raw materials, eliminates both the use of limestone and the calcination process of PC clinker, and is capable of sequestering CO_2 [1]. The GC technology integrates the technical principles of PC's mineral admixtures based on the latent hydraulicity of BFS and the pozzolanic reaction of FA, the GP hardening mechanism of polymerization, and the concrete technical principle utilizing calcium carbonate as binder. GC can be classified into two types: the iron & steel slags-$NaHCO_3$ system, and the BFS-FA-WC or WCp-Na_2CO_3 system.

Wasted concrete powder (WCp) is generated as a by-product during the crushing of wasted concrete to produce recycled aggregates, with a particle size ranging from 0 to 0.075mm. The fine particles (WC) of 0.6mm or less contained in recycled fine aggregate have a high content of hardened cement paste, resulting in low density and high water absorption. For this reason, it is difficult to manufacture recycled fine aggregate that satisfies JIS specifications, and the utilization of recycled fine aggregate remains limited now [2]. However, these recycled powders and fine particles (hereinafter abbreviated as recycled fine particle & powder) are rich in $Ca(OH)_2$. Therefore, they are

※1 日本国 山口大学 創成科学研究科 博士前期課程
※2 日本国 山口大学 創成科学研究科 教授 博士(工学)

expected to be utilized for the hardening of FA and BFS, as well as for carbon sequestration, through pozzolanic reaction, latent hydraulicity, and carbonation. Sasaki and Li investigated the optimal dosages of WC and sodium carbonate in the BFS-FA-WC–Na_2CO_3 system, as well as the carbon sequestration amount of GC mortar, thereby demonstrating its effectiveness [3]. This study prepared GC mortar to investigate the effects of the fineness of BFS and FA, and curing age on GC's strength, and to clarify optimal mixing ratio of WCp and WC, respectively, and the effect of the difference between WC and WCp on the strength of GC.

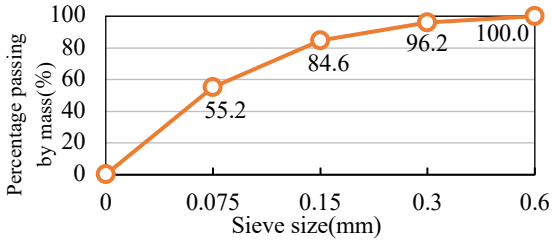

Fig.1 Particle size distribution of WC

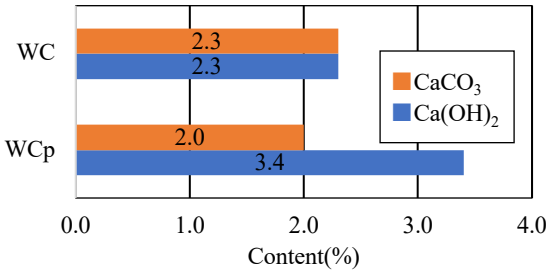

Fig.2 $CaCO_3$ and $Ca(OH)_2$ contents of the WC and the WCp samples

2. Materials Used

2.1 Reactive Fillers

JIS 4000, 6000, and 8000 grade ground granulated blast-furnace slag (hereinafter abbreviated as BFS4000, 6000, and 8000 in the text, and as B4, 6, and 8 in the figures and the tables), and JIS Class I and II fly ash (hereinafter abbreviated as FAI and II in the text, and as FI and II in the figures and the tables) were used. The chemical compositions and physical properties of BFS and FA are shown in **Table 1**.

2.2 Alkali activators

As one of the alkali activators (abbreviated as AA), recycled fine particles (WC) of wasted concrete or wasted concrete powder (WCp) was used as a 20% replacement for the reactive filler. Their chemical compositions and densities are shown in **Table 1** too, and their particle size distributions are shown in **Fig.1**.

Thermogravimetry–differential thermal analysis (TG-DTA) was conducted on the WC and the WCp. The thermal decomposition ranges of calcium hydroxide ($Ca(OH)_2$) and calcium carbonate ($CaCO_3$) were determined from the DTA curves, and the contents of $Ca(OH)_2$ and $CaCO_3$ were estimated from the TG curves. The results are shown in **Fig.2**. Compared to the WC, the contents of $Ca(OH)_2$ and $CaCO_3$ in the WCp were higher. This is because the WCp contained a higher amount of hardened cement paste. The $CaCO_3$ was formed due to the natural carbonation that occurred during the service life of the concrete, as well as during its crushing and storage. From the perspective of

Table 1 Chemical compositions and physical properties of raw materials used

Materials Name	Metal oxide contents (wt.%)										Density (g/cm^3)	SSA (cm^2/g) or grading
	SiO_2	CaO	Al_2O_3	Fe_2O_3	Na_2O	K_2O	MgO	TiO_2	SO_3	Others		
BFS4000(B4)	32.6	45.1	13.7	0.3	-	0.3	4.9	0.6	1.8	0.6	2.90	4080
BFS6000(B6)	31.7	46.6	13.6	0.4	0.2	0.4	4.8	0.7	1.4	0.2	2.91	6417
BFS8000(B8)	32.2	46.0	13.7			0.3	4.9	0.6		0.3	2.92	7954
FAI(FI)	58.0	2.4	27.2	5.8	0.5	1.8	1.0	1.5	0.6	1.1	2.39	7853
FAII(FII)	58.6	3.6	24.6	6.1	1.1	1.6	1.2	1.2	-			4390
WC	50.4	14.5	13.5	4.9	2.2	2.3	2.6	0.6	0.7	8.0	2.69	0-0.6mm
WCp	51.4	20.8	13.3	5.3	2.1	2.6	2.2	0.7	1.0	0.6	2.56	0-0.075mm

[Note] SSA represents specific surface area

promoting the hardening reaction of BFS and FA, the use of WCp is considered more favorable.

The second alkali activator was sodium carbonate powder (Na_2CO_3, abbreviated as N). Its density is 2.54 g/cm³. Synthetic sodium carbonate can be obtained by thermally decomposing the sodium bicarbonate, which can be produced by recycling CO_2 exhaust [4].

2.3 Fine aggregate

For the preparation of GC mortar, saturated surface-dry sea sand (abbreviated as MS in the tables and the figures) was used as fine aggregate. The physical properties of the sea sand were a oven-dry density of 2.56 g/cm³, a water absorption of 1.81%, a solid volume percentage of 65.0%, a chloride ion content of 0.002%, and a fineness modulus (F.M.) of 2.87. To evaluate the impurity content in the sea sand, the samples were heated at 550°C and 800°C for 1hour each. The mass loss after heating at 800°C, which corresponds to the loss on ignition (LOI) at 800°C, was 3.3%. Based on the mass difference between the two heating temperatures, the $CaCO_3$ content was estimated at 8.3%. If assuming that the primary component of seashells is $CaCO_3$, the seashell content is considered to be at least 8.3%.

3. Experimental Program

3.1 Preparation of specimens

In the GC system composed of BFS, FA, sodium carbonate (N), and WC or WCp, the specific surface area and particle size of each powder were varied. The mass ratio of water to the GC and the mass ratio of MS to GC were set as 0.50 or 0.55 and 2.0 or 3.0, respectively. We confirmed that the optimal addition ratio of sodium carbonate is 8-10%, and the optimal proportions of WC and WCp in the powder are 20%, as described later, these mixing ratios were adopted for the specimen preparation. The amount of each material required to prepare the necessary volume of GC mortar was weighed based on their respective proportions or addition ratios. Next, BFS, FA, WC or WCp, and N were dry-mixed in a mortar mixer at a low speed (139rpm) for 60 seconds. Then, water was added to the mixer and mixed at a low speed (139 rpm) for 60 seconds, after which the sea sand was added and mixed at a high speed (591 rpm) for 90 seconds. The resulting mortar was cast by self-gravity into a 3-cell steel prismatic mold with dimensions of 4cm×4cm×16cm. Due to the low fluidity when the MS-GC mass ratio was 3.0, the mortar was compacted using a table vibrator for 15 seconds after filling into the mold. After setting, the specimens were sealed with plastic wrap and cured in air at 20±3°C for 24 hours. Subsequently, the specimens were demolded, resealed with plastic wrap, and cured in a constant temperature and humidity chamber at 20 ± 2°C and 60 ± 5% R.H. until the ages of 28 and 91 days.

3.2 Strength tests

After curing, the prismatic specimens were subjected to the flexural test using a three-point loading method on a universal testing machine, and an average of the three specimens was taken as the flexural strength. The compressive strength was measured using the broken halves after the flexural test. The compressive strength was determined as an average of the six broken halves.

4. Results and Discussion

4.1 Effect of filler fineness on GC properties

(1) Ground granulated blast-furnace slag

Fig.3 shows the strengths of the GC mortars prepared with different specific surface areas of the fillers. **Fig.4** and **5** show the comparisons of the 28-day compressive strength, and the 91-day flexural and compressive strengths, respectively. As shown in **Fig.3**, the strength of the GC mortar reached its maximum when BFS8000 was used. This is considered to be because the increased specific surface area enhanced the reactivity of BFS with WCp and N, thereby increasing the reaction products of BFS at the curing age of 28 days.

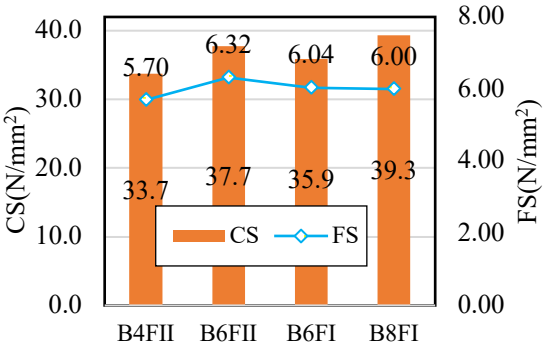

Fig.3 Effect of filler fineness on strength
(BFS:FA:WCp=5:3:2, Na_2CO_3:10%, W/GC: 0.55, MS/GC: 2.0)

However, the flexural strength exhibited almost no change at a fineness of BFS6000 or higher. Although the underlying reason remains unclear at present, it is speculated to be a result of the offsetting effects between the strength enhancement due to the increased reaction products and the occurrence of cracking induced by the increased drying shrinkage.

Comparing the compressive strengths of the B4FII and B6FII series shown in **Fig.4**, it can be confirmed that the compressive strengths at both 28 and 91 days increased with the increase in the specific surface area of BFS. However, a comparison between the results of B6FI and B8FI reveals that while the 28-day compressive strength increased with the higher fineness of BFS, the 91-day compressive strength exhibited almost no change. This is presumably because the reaction progression of BFS6000 was moderate in the early stage, whereas a sufficient amount of reaction products was generated in the long term. In addition, for BFS8000, the rapid initial reaction might have promoted the drying shrinkage, potentially affecting the strength development. As shown in **Fig.5**, increasing the specific surface area of BFS also improved the flexural strength, however, no clear difference in strength was observed between BFS6000 and BFS8000 at both 28 and 91 days. Therefore, BFS that satisfies the JIS 6000 specification is considered sufficient for the use in GC.

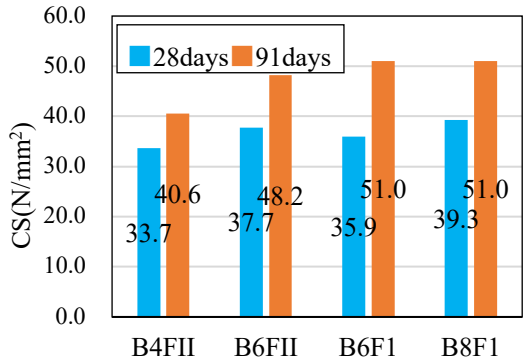

Fig.4 Changes in compressive strength of GC with filler fineness and curing Age

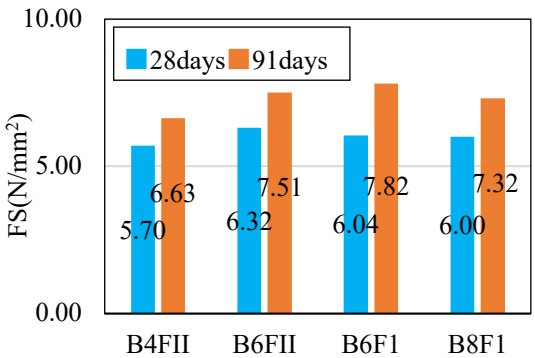

Fig.5 Changes in flexural strength of GC with filler fineness and curing Age

(2) Fly ash

Fig.3 shows the strengths of the GC mortars prepared with JIS Class I (FI) and JIS Class II (FII) fly ash. **Fig.4** and **5** show their compressive and flexural strengths at 28 and 91 days of curing, respectively. As shown in **Fig.3**, it was found that both the compressive and flexural strengths were not affected by the specific surface area of the FA. This is because although FA is vitreous (glassy), its pozzolanic reaction requires time even when the fineness is high. The reaction of FA is negligible at the curing age of 28 days [5, p.1264-1265], and therefore, it is considered to have no impact on the strength. However, as shown in **Fig.4**, a comparison of the results between the B6FI and B6FII series reveals that the compressive strength at 91 days increased with the higher specific surface area of FA. This is presumably because a larger specific surface area of FA enhanced the dissolution of its

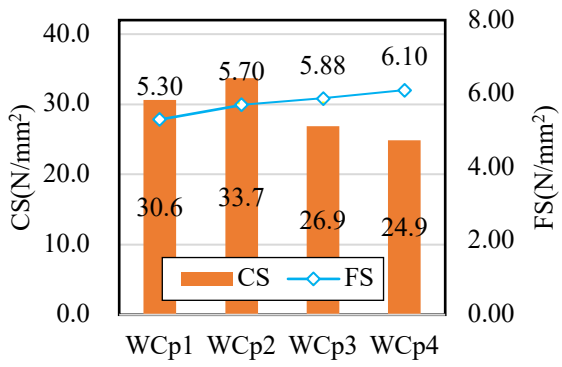

Fig.6 Effect of WCp mixing ratio on the strength of GC
(B4 : FII+WCp=5:5, Na_2CO_3:10%, W/GC:0.55, MS/GC:2.0)

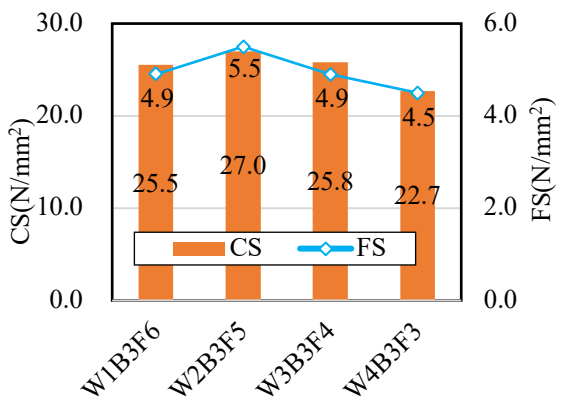

Fig.7 Effect of WC mixing ratio on the strength of GC [3]
(B4:FII+WC=3:7, Na_2CO_3:10%, W/GC:0.55, MS/GC:2.0)

major active components, SiO_2 and Al_2O_3, thereby increasing the reaction products in the long term.

4.2 Optimal mixing ratio of WCp and WC

Fig.6,7 shows the strength of the GC mortar with varying mixing ratios of WCp and WC in the powders. The maximum compressive strength was achieved when the ratio of WCp and WC in the powders was 20%, respectively. This may be due to that: when the ratio was less than 20%, the alkaline activation to the active filler was insufficient; conversely, when it exceeded 20%, the formation of $CaCO_3$, a reaction product, increased. On the other hand, the flexural strength showed a slight upward trend with increasing the ratio of WCp in

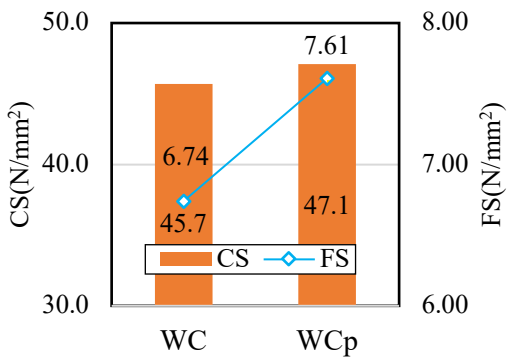

Fig. 8 Effect of the difference between WC and WCp on the strength of GC
(B8:FI:WCp=5:3:2, Na_2CO_3:10%, W/GC:0.50, S/GC:3.0)

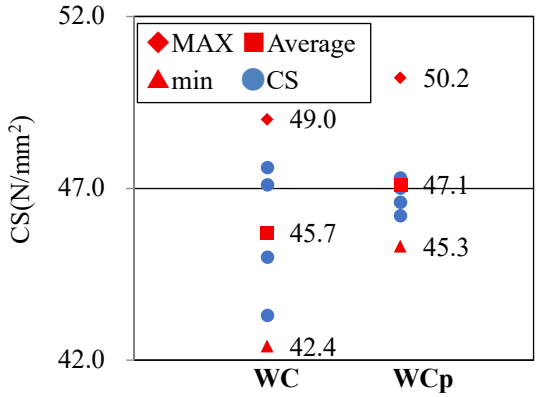

Fig. 9 Distribution of measured CS values for GC mortars using WC and WCp

the powders. This is presumably because the increase in the WCp ratio led to more formation of $CaCO_3$, which subsequently acted as a binder of the fine aggregate. However, in the case of WC, similar to the compressive strength, the flexural strength reached its maximum when the ratio in the powders was 20%. Further investigations are required to clarify the precise reaction mechanisms regarding the effect of the WCp and WC ratios in the powders on the flexural strength of GC.

4.3 Effect of WC and WCp on GC Strength

The flexural and compressive strengths of the GC mortars prepared with WC or WCp are plotted in **Fig.8**, and the compressive strengths of the six broken halves along with their average values are plotted in **Fig.9**. As shown in **Fig.8**, it was found that the use of WCp improved the compressive strength of the GC mortar, compared to the use of

WC. The reasons for this are considered to be that the specimens became denser when using the WCp, and that the higher $Ca(OH)_2$ content in WCp promoted the reaction of BFS and FA in the GC. Regarding the improvement in flexural strength, it is speculated that one factor might be the increase in the amount of $CaCO_3$, which is a reaction product of sodium carbonate and the $Ca(OH)_2$ abundantly contained in WCp compared to WC, however, this will be further investigated in the future.

As shown in **Fig.9**, the maximum compressive strength of the GC mortar prepared with the WC was close to that of the GC mortar prepared with WCp. However, the measured values of each broken half exhibited large scatter. This was caused by the fact that because the WC particles are coarse and contain more sand than WCp, the distribution of the hardened cement paste tends to be more non-uniform, and thus there are variations in the strength and reactivity of the WC particles themselves.

5. Conclusions

The findings obtained in this study are summarized below.

1) The strength of the GC with BFS/FA/WC or WCp-N system at the curing age of 28 days increased as the specific surface area of the BFS bec a me larger. Although the 28-day flexural strength and 91-day compressive strength were also improved, they remained unchanged after exceeding a certain specific surface area.
2) Increasing the specific surface area of the FA did not enhance the strength of the GC at the curing age of 28 days. However, at the curing age of 91 days, the strength increased with increasing the specific surface area of FA.
3) The optimal ratios of WCp and WC in the powder were found to be 20%, respectively.
4) The use of WCp increased the strength of the GC. On the other hand, the use of WC led to a larger scatter in measured values of strength.

Reference

[1] Z. Li, S. Fukatani：Study on a Hybrid Binder of Geopolymer and Calcium Carbonate (Part 1): CO_2 Absorption, Alkaline Properties, and Reaction Products, *Summaries of Technical Papers of Annual Meeting*, Architectural Institute of Japan (Hokkaido), pp.1235-1236, 2022. 9

[2] T. Matsumura, et al.: Production of high-quality recycled fine aggregate by wet separation method, *Proceedings of the Japan Concrete Institute*, Vol.25, No.1, pp.1475-1480, 2003

[3] A. Sasaki, Z. Li : Study on Carbon-Fixing One-Part Geopolymer Using Waste Concrete Powder and Sodium Carbonate as Alkali Activators, *Proceedings of the Japan Concrete Institute*, Vol.47, No.1, pp.708-713, 2025

[4] New Scientist, UK's largest carbon capture project will turn CO_2 into baking soda : https://www.newscientist.com/article/2325858-uks-largest-carbon-capture-project-will-turn-co2-into-baking-soda/ (Date of access: 2026.1.18)

[5] O. Niman, Z. Li : Development of Unfired & Carbon-Fixing Green Cement Using Ground Granulated Blast Furnace Slag and Fly Ash as Main Raw Materials, *Proceedings of the Japan Concrete Institute*, Vol.48, No.1, pp.1260-1265, 2026.7

既往研究実験データを用いた機械学習と多目的最適化手法による コンクリート調合設計

Concrete Mix Design Using Machine Learning and Multi-Objective Optimization Methods Based on Experimental Data from Previous Studies

田村祥大※1、佐藤幸恵※2、山田義智※3

Shota Tamura, Sachie Sato, Yoshitomo Yamada

ABSTRACT

本研究は、Random Forest による強度予測モデルと NSGA-III を組み合わせ、目標圧縮強度を満たしつつ CO2 排出量を最小化するコンクリート調合の多目的最適化を行う。Random Forest は、28 日圧縮強度のみを目的変数として 963 件の調合データで学習させ、30～140 N/mm²の 12 段階の目標強度に対して最適化を行った。化学混和剤は、強度よりも主に施工性に影響を与えるため、設計変数から除外した。最適化された調合は、130.1 N/mm²までは一貫して高炉スラグセメント B 種が選択され、約 120～150 kg-CO2/m³の CO2 排出量を達成した一方、最高強度のケースでは中庸熱ポルトランドセメントが必要となり、CO2 排出量は 456.5 kg-CO2/m³であった。学習データとの比較では、一部の目標強度でセメント量と混和材置換率が実測範囲から外れていたが、W/B は明示的な制約により範囲内に収まっていた。これらの結果は、本フレームワークが幅広い強度範囲にわたって体系的に低炭素な調合を導出できることを示す一方、ワーカビリティの組み込みは今後の課題であることを示している。

1. Introduction

Concrete is widely used in architecture and civil engineering, where engineers can freely design for target properties such as strength and durability, with current mix design practice based on empirical methods drawing on ACI guidelines. To reduce environmental impact, demand has been increasing for utilizing industrial by-products as supplementary cementitious materials or aggregates. However, their effects on concrete's mechanical properties, durability, and workability vary by material, and while increasing their usage ratio enhances CO2 reduction, it can also reduce strength and durability. As material diversification increases the complexity of mix design, the time and cost required to search for an optimal mix are expected to grow.

To address this challenge, mix design optimization using machine learning has attracted attention. Prior studies have mainly built forward prediction models using methods such as Random Forest (RF) to predict compressive strength [(1)]. However, what is essentially important in practical design is the inverse problem of determining mix conditions that ensure required performance[(2)]. This has led to growing interest in multi-objective optimization that simultaneously minimizes CO2 emissions and ensures target strength. In this study, using a database built from previous papers and experimental data, we aim to rationally design mixes that ensure required performance through machine learning-based prediction and optimization.

※1 日本　東京都市大学院　建築都市デザイン専攻　建築学領域　修士課程
※2 日本　東京都市大学　建築都市デザイン学部　建築学科　教授　博士（工学）
※3 日本　琉球大学　工学部　工学科建築学コース　教授　博士（工学）

2. Machine Learning-Based Strength Prediction Model

2.1 Data Collection Method

In this study, in order to build a machine learning-based prediction model for concrete compressive strength, papers published in the "Proceedings of the Japan Concrete Institute" (Japan Concrete Institute, hereafter JCI) were used as the data source. The target period was set to 2000–2021, and from the papers published over these 21 years, those that described concrete mix proportions in detail and reported values such as slump, air content, and 28-day compressive strength were extracted.

2.2 Data Preprocessing

Since the collected mix proportion database contained missing values, the following preprocessing was performed.

Rows in which the objective variable, 28-day compressive strength (fc28), was missing were excluded, and slump, which showed little relevance to the objective variable, was excluded from the explanatory variables.

For items that could be calculated from other variables—such as unit cement content (C), unit water content (W), binder content (B), water-to-binder ratio (W/B), replacement ratios of supplementary cementitious materials (BFS, FA, SF), fine aggregate ratio (s/a), and air content—missing values were supplemented by back-calculation from related variables (W/C, W/B, absolute volume, etc.).

Missing aggregate and admixture density/absorption values were supplemented using the median for the same product name, or the overall median where unavailable. Cement density, which is nearly fixed by JIS standards per type, was supplemented with the corresponding standard value, using the overall median only when the type was unknown.The densities of BFS, FA, and SF (2.90, 2.20, and 2.20 g/cm³, respectively) and the density of water (1.00 g/cm³) were treated as fixed values based on industrial standards.

CO2 emissions were calculated by multiplying the emission factor of each material by its usage amount and summing the results. The CO2 emission factors used in this study are shown in Table 1.

Table 1. CO2 Emission Factors of Binder Material

material	Emission (kg-CO2/kg)
Ordinary Portland Cement	0.7413
High-Early-Strength Portland Cement	0.7413
Moderate-Heat Portland Cement	0.7413
Low-Heat Portland Cement	0.7413
Blast-Furnace Slag Cement Type B	0.4233
Fly Ash Cement	0.6129
Ground Granulated Blast-Furnace Slag (BFS)	0.0241
Fly Ash (FA)	0.0179
Silica Fume (SF)	0.0179
Fine Aggregate (S)	0.0035
Coarse Aggregate (G)	0.0028

Table 2. Basic Statistics (Training Data)

	Minimum	Median	Maximum
Cement (kg/m³)	270	422	1348
Water(kg/m³)	150	165	185
W/B (%)	11.5	38	65
CO2 emissions (kg-CO2/m³)	114	303	1008
Supplementary cementitious material replacement ratio (%)	0	0	50

After preprocessing, 963 mixes remained. A portion of the basic statistics is shown in Table 2.

2.3 Strength Prediction Model

Compressive strength (fc28) was predicted using Random Forest, an ensemble method that aggregates multiple decision trees and is well suited to capturing nonlinear relationships between mix variables and strength.

2.4 Optimization

2.4.1 Design Variables

Table 3 shows the variables designed through optimization and their search ranges. Unit cement content, unit water content, the replacement ratios of blast-furnace slag, fly ash, and silica fume, fine aggregate ratio (s/a), fine aggregate density, and coarse aggregate density were all treated as variables that the optimization could freely explore within the ranges shown in Table 3. Note that silica fume was permitted for use only in the high-strength range of target

strength ≥100 N/mm², and was fixed at 0 for target strengths below this value.

Six cement types (ordinary, high-early-strength, moderate-heat, and low-heat Portland cement, fly ash cement, and blast-furnace slag cement type B) were set as candidates, and the optimization selected among them.

2.4.2 Given Conditions

Air content was not treated as a design variable, but was instead handled as a given condition with values specified in advance for each target strength band. These values were calculated for each target strength based on the results of a regression analysis of the relationship between strength and air content in the training data. The air content for each strength range, based on the training data, is shown in Figure 1. Although air content is used as a feature input to the Random Forest, it is fixed as a common value across all individuals within the search for a given target strength.

2.4.3 Objective Functions

(1) Minimization of deviation from the target strength

The target strength was set at 12 levels ranging from 30 N/mm² to 140 N/mm² in 10 N/mm² increments, and the absolute value of the difference between the strength predicted by the RF model from the mix and the target strength was minimized, with a symmetric penalty applied for both cases where the strength exceeds and falls below the target.

(2) CO2 emissions

No target value was set for CO2 emissions. Unlike target strength, this is a monotonic evaluation in which lower values are simply better. CO2 emissions are calculated from the mix using the CO2 emission factors described in Section 2.2.

2.4.4 Constraints

While the design variable ranges each constrain a single decision variable, the three conditions described in this section instead constrain calculation results combining multiple decision variables (total supplementary cementitious material replacement ratio, W/B, and coarse aggregate bulk volume), which cannot be controlled through a single variable alone.

Table 3. Design Variables and Search Ranges

Design variable	Unit	Search range
Cement	kg/m³	270～
Water	kg/m³	150～180
BFS	%	0～46
FA	%	0～30
SF	%	0 ～15
s/a	%	45～49
Fine aggregate	g/cm³	searched from the training data
Coarse aggregate	g/cm³	searched from the training data
Cement type	－	selected from six types

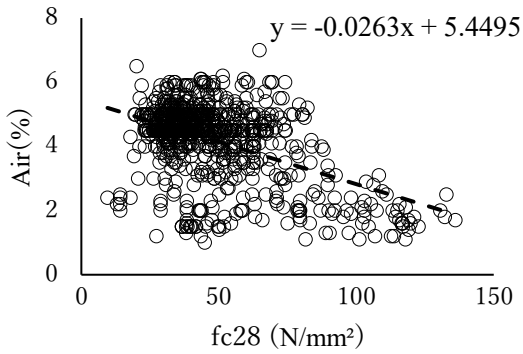

Figure 1. Air Content vs. Strength (Training Data)

Table 4. Optimization Constraints and Ranges

Constraint	Range
Min. supplementary cementitious material ratio	BFS+FA+SF replacement ≥ 10%
Bulk volume	0.53～0.60
W/B	1st–3rd quartile range of training data, by target strength band

Each of these constraints is shown in Table 4.

(1) Lower limit on supplementary cementitious materials

The constraint was set such that the sum of the replacement ratios of blast-furnace slag, fly ash, and silica fume does not fall below 10%. This was intended to avoid selecting mixes that use no supplementary cementitious materials at all, thereby ensuring, to a certain extent, the use of supplementary materials for reducing CO2 emissions.

(2) W/B range

For each target strength band, the constraint was set so that W/B falls within the range from the first quartile to the third quartile calculated from the measured values in the training data. Since W/B is a variable that has a dominant influence on strength (Section 3.3), setting this range avoided the exploration of unrealistic

W/B values that deviate substantially from the distribution of the training data.

(3) Bulk volume range

The bulk volume of coarse aggregate was constrained to 0.53–0.60. Since the actual yield ratio of aggregate could not be extracted for each mix, a fixed value of 60% was used. As bulk volume is calculated from the design variables, this constraint kept aggregate content within a practically reasonable range.

2.4.5 Algorithm and Parameters

For multi-objective optimization, NSGA-III, which is well suited to many-objective optimization, was used. The target strength was set at 12 levels ranging from 30 N/mm² to 140 N/mm² in 10 N/mm² increments, and optimization was carried out independently for each target strength. After optimization was completed for each target strength, individuals satisfying all of the constraints described in Section 2.4.4 were treated as feasible solutions, from which the Pareto front (the set of non-dominated solutions) was extracted via non-dominated sorting. Reference points were generated for two objectives using the Das–Dennis method, with the number of reference point divisions set to 99. The number of individuals was set to 200 and the number of generations to 200, and optimization was performed.

3. Results and Discussion

3.1 RF and Feature Importance

The prediction accuracy of the constructed Random Forest model is shown in Figure 2. The coefficient of determination for the training data was R^2=0.993, with an RMSE of 3.72 N/mm². For the test data, which was not used in training, the values were R^2=0.964 and RMSE=8.43 N/mm². In addition, the R^2 from 5-fold cross-validation was 0.945±0.010, a level roughly consistent with the test data results.

For both the test data and cross-validation, R^2 remained in the range of 0.94–0.96 with no substantial degradation from the training data, and the small cross-validation standard deviation (0.010) indicates stable, high generalization performance.Based on

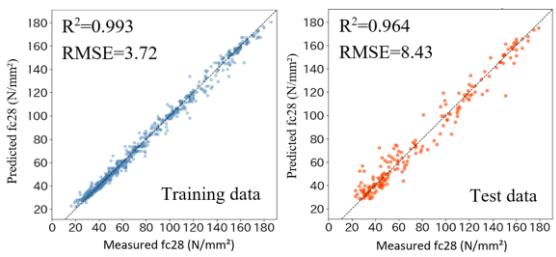

Figure 2. Predicted vs. Measured Compressive Strength (RF)

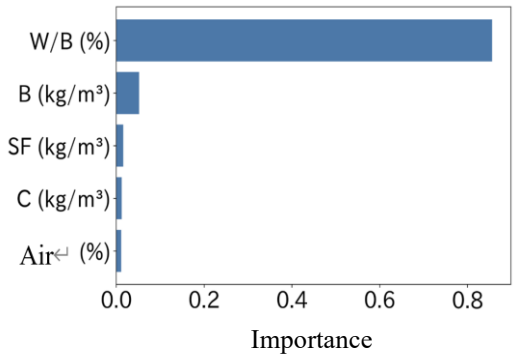

Figure 3. Feature Importance (Top 5)

Table 5. Optimization Results

Predicted strength (N/mm²)	CO2 emissions (kg-CO2/m³)	Cement type ※	W/B (%)	s/a (%)	Air (%)	Coarse aggregate bulk volume (m³/m³)	Unit content (kg/m³)							Supplementary cementitious material replacement ratio(%)	Fine aggregate SSD density (g/cm³)	Coarse aggregate SSD density (g/cm³)
							W	Binder (B)				S	G			
								C	BFS	FA	SF					
30.0	122.0	BB	51.5	47.8	4.7	0.59	168	273	30	23	0	798	844	16.4	2.48	2.4
40.0	120.4	BB	52.4	47.9	4.4	0.60	162	270	0	38	0	844	899	12.4	2.56	2.51
50.0	120.8	BB	44.9	48.2	4.1	0.60	150	270	0	64	0	825	877	19.1	2.48	2.45
60.0	121.6	BB	41.0	47.9	3.9	0.59	150	270	0	96	0	861	901	26.3	2.65	2.55
70.0	122.5	BB	35.0	48.2	3.6	0.57	150	270	45	114	0	779	844	37.0	2.46	2.48
80.0	123.8	BB	30.5	48.6	3.4	0.54	150	270	80	141	0	802	801	45.1	2.6	2.46
90.0	124.2	BB	29.2	45.1	3.1	0.58	150	270	111	133	0	699	847	47.5	2.46	2.45
100.0	124.4	BB	27.9	46.4	2.8	0.55	150	270	81	138	49	730	796	49.8	2.54	2.40
110.0	125.9	BB	24.5	45.3	2.6	0.54	150	270	163	88	91	663	782	55.9	2.46	2.40
120.0	126.5	BB	24.4	45.0	2.3	0.54	151	270	146	122	79	791	809	56.3	2.96	2.48
130.1	150.1	BB	21.4	45.0	2.0	0.53	150	324	269	2	105	695	840	53.7	2.67	2.64
138.9	456.5	M	19.6	45.0	1.8	0.53	150	605	73	82	4	685	840	20.8	2.63	2.64

※BB : Blast-Furnace Slag Cement Type B M : Moderate-Heat Portland Cement

these results, it was judged that a model capable of predicting 28-day compressive strength with sufficient accuracy for practical use had been constructed. The top five features by importance are shown in Figure 3, with W/B (0.855) dominating all others by a large margin.

3.2 Optimization Results

Optimization was performed for each target strength, and the solution closest to the objective function was taken as the representative solution, as shown in Table 5. In the range of predicted strengths from 30 to 120, blast-furnace slag cement type B (BB) was consistently selected as the cement type, and CO_2 emissions fell within a narrow range of 120.4–126.5 kg-CO_2/m³, with unit cement content C confined to a narrow range of 270–273 kg/m³. Within this range, W/B decreased monotonically from 51.5% to 24.4%, while the supplementary cementitious material replacement ratio increased monotonically from 16.4% to 56.3%.

During this range, s/a varied between 47.8% and 48.6%, and the bulk volume of coarse aggregate, ranging from 0.54 to 0.60, showed a tendency to decrease slightly as the target strength increased. Unit water content W was 168 kg/m³ at a predicted strength of 30, but from a predicted strength of 50 onward it remained pinned close to 150 kg/m³, the lower bound of the search range.

In contrast, the predicted strengths of 130.1 and 138.9 showed results that deviated from these trends. At a predicted strength of 130.1, CO_2 emissions increased sharply to 150.1 kg-CO_2/m³, and at 138.9 to 456.5 kg-CO_2/m³, with unit cement content C also increasing to 324 kg/m³ and 605 kg/m³, respectively. Furthermore, at a predicted strength of 138.9, the cement type shifted from blast-furnace slag cement type B to moderate-heat Portland cement. In both of these cases, bulk volume and s/a took values near the lower bound of the search range, at 0.53 m³/m³ and 45.0%, respectively.

3.3 Comparison with Training Data

The optimization results for each target strength were compared with box plots of the training dat a for the corresponding strength band (Figures 4–6). The items compared were unit content (C, W, B), W/B, and the replacement ratio of suppleme ntary cementitious materials (hereafter abbreviated as SCM, as also used in Figures 4–6). Most ite ms fell within the training data distribution, exce pt for unit cement content C at target strength 9 0 and the replacement ratio at target strengths 40 and 90. At a target strength of 90, the candidat e solution's C fell below the distribution of the t raining data. Since cement's CO_2 emission factor is substantially larger than that of other materials, minimizing CO_2 emissions tends to drive the so lution toward suppressing unit cement content, lik ely explaining the lower value than observed in t he training data.

The replacement ratio exceeding the training dist ribution at target strengths of 40 and 90 likely re flects SCM compensating for the reduced unit ce ment content.

3.4 Discussion

(1) Selection of cement type

Across predicted strengths of 30.0–130.1, blast-furnace slag cement type B (BB) was consistently selected. This is thought to be because, among the CO_2 emission factors by cement type (Section 2.2), the emission factor for blast-furnace slag cement type B is substantially lower than that of ordinary Portland cement and other types. Since CO_2 emissions are minimized as the objective function, preferentially selecting lower-emission cement types is a consistent outcome of the optimization design.

(2) Workability

The mixes obtained showed reasonable results in terms of both target strength and CO_2 emissions, but

none of the mixes included any chemical admixtures. Since fc28 was the sole objective variable, the effects of admixtures on workability were not captured by the model because fc28 was the sole prediction target had their workability effects left uncaptured by the model.

(3) Concerns regarding extrapolation at target strengths of 130 and 140

As shown in Table 5, the predicted strengths of 130.1 and 138.9 exhibited trends that differed from those at lower predicted strengths (a sharp increase in CO2 emissions, a sharp increase in unit cement content C, and a change in cement type). As described in Section 3.1, this is likely because the number of samples in the high-strength range (fc≥110 N/mm² or so) is relatively small in the training data, raising the possibility that the Random Forest's predictions in this range are being made in a sparse region of the training data, or in a region close to outside its range.

4. Conclusions

In this study, a framework was developed that combines a Random Forest prediction model for 28-day compressive strength with multi-objective optimization using NSGA-III to derive concrete mixes that minimize CO2 emissions while ensuring target strength. The framework developed in this study was shown to be capable of deriving mixes with reduced CO2 emissions for each target strength.

On the other hand, unit cement content and the supplementary cementitious material replacement ratio were also found to sometimes deviate from the training data distribution. This is because the optimization uses only strength and CO2 emissions as evaluation criteria, without directly evaluating concrete's workability.To derive mixes that are practically valid, it will be necessary to introduce constraints that reflect workability considerations. Future work should therefore focus on designing new features or model structures capable of quantitatively evaluating workability, so that the effects of chemical admixtures can be appropriately reflected.

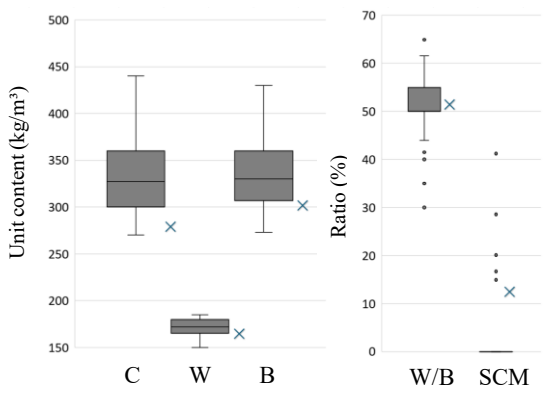

Figure 4. Box Plots of Features at 40 N/mm² Target

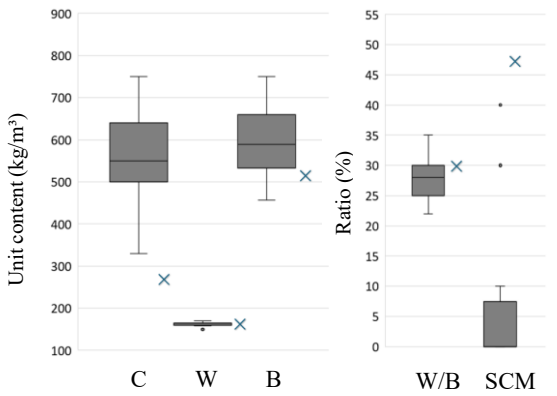

Figure 5. Box Plots of Features at 90 N/mm² Target

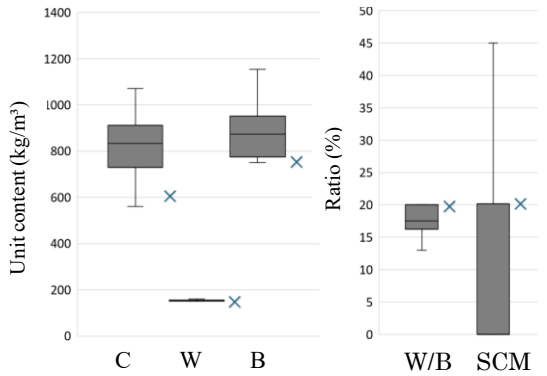

Figure 6. Box Plots of Features at 140 N/mm² Target

References

[1] Ryota Isobe：Prediction Model Construction of High-Strength

[2] Kanta Shimizu, Shuya Hirano, Yoshitomo Yamada, Kohei Sakihara：Mix Design for the Flowability of High-Flowability Concrete: A Multi-Objective Optimization Method Using a Machine Learning Model as a Surrogate Model, The 80th annual meeting of cement and concrete engineering

Electrical Properties of Cement-Based Materials Reinforced with Steel Fiber

Yong-Joon Kim※1, Jeong-Soo Nam※2, Yae-Chan Lee※3, Byung-Cheol Choi※4, Thinh Phat Nguyen※1, Candra Pebrian※1, Gyu-Yong Kim※2

ABSTRACT

This study evaluated the electrical properties of cement-based materials reinforced with different types of steel fibers. Three types of steel fibers, namely amorphous metallic fiber, hooked steel fiber, and smooth steel fiber, were used in this study. The electrical conductivity and electromagnetic pulse (EMP) shielding performance varied depending on the type and content of the steel fibers. Among the investigated fibers, amorphous metallic fiber exhibited the highest electrical conductivity and EMP shielding performance owing to its relatively large specific surface area. These results indicate that the specific surface area of steel fibers is an important factor influencing the electrical properties and EMP shielding performance of cement-based materials.

1. Introduction

The Electromagnetic Pulse (EMP) shielding effectiveness of cement-based material depends on the electrical conductivity of the cement-based material. To develop material with superior shielding effectiveness, it is necessary to increase the electrical conductivity of the cement-based material [1-3].

Although extensive research has been conducted on cement-based materials reinforced with steel fiber, studies on their electrical properties remain insufficient [4, 5]. Representative steel fibers - amorphous metallic fiber (AF), hooked steel fiber (HSF), and smooth steel fiber (SSF) - inherently possess electrical conductivity; therefore, cement-based materials reinforced with steel fiber are expected to demonstrate superior electrical conductivity. In particular, AF, owing to its high aspect ratio and specific surface area, is expected to contribute significantly to the enhancement of EMP shielding effectiveness [6, 7]. Accordingly, this study aims to compare the electrical conductivity and EMP shielding effectiveness of cement-based materials reinforced with AF, SSF, and HSF. Furthermore, the study seeks to evaluate the effect of the length and specific surface area of AF on shielding effectiveness.

2. Experimental plan

In this study, the mechanical properties of AF, SSF, and HSF were investigated. Table 1 summarizes the mechanical properties of each steel fiber, including fiber length, diameter, aspect ratio, density, tensile strength, and intrinsic electrical conductivity. AF was classified into two types based on its length, namely 30 mm and 15 mm.

The intrinsic electrical conductivity of each steel fiber was evaluated in this study. The results indicated that the electrical conductivity of AF was approximately 10 times lower than that of SSF and HSF, which is attributed to the internal voids within the AF that restrict electron mobility [8].

In this study, cement-based materials reinforced with steel fibers were prepared with a water-to-binder ratio of 0.4. Three types of steel fibers were incorporated into the cement-based materials, and AF was further classified into two lengths. Accordingly, the specimens reinforced with 30 mm AF, 15 mm AF, SSF, and HSF were designated as 30AFRCC, 15AFRCC, SSFRCC, and HSFRCC, respectively. To minimize the influence of moisture on the electrical conductivity and shielding effectiveness, the moisture

※1 Master's Course, Dept. of Architectural Engineering, Chungnam National University, Korea
※2 Prof., Dept. of Architectural Engineering, Chungnam National University, Korea
※3 Ph.D. Course, Dept. of Architectural Engineering, Chungnam National University, Korea
※4 Ph.D., Dept. of Architectural Engineering, Chungnam National University, Korea

Table 1 Mechanical Properties of the fibers used

Mechanical properties	Type of fiber			
	AF		SSF	HSF
Length (mm)	30.0	15.0	16.3	30.0
Diameter (mm)	0.25*	0.25*	0.20	0.25
Aspect ratio	120.0	60.0	81.5	120.0
Density (g/cm³)	7.20	7.20	7.85	7.85
Number of fibers (EA/kg)	100,000	200,000	250,000	22,000
Specific surface area (m²/kg)	11.6	9.6	2.6	1.0

* Equivalent Diameter

content of the cement-based materials was adjusted to 4% prior to testing.

To evaluate electrical conductivity, specimens measuring 400 × 100 × 100 mm were fabricated. Silver-plated copper plates were used as electrode materials to minimize corrosion, and four electrodes were arranged at 100 mm intervals based on the four-point probe method. EIS measurements were conducted from 1 MHz to 0.01 mHz while maintaining an alternating current amplitude of 1000 mV rms.

Figure 1 illustrates a schematic of shielding effectiveness based on the law of energy conservation. Shielding effectiveness evaluation was conducted in accordance with MIL-STD-188-125 [9]. Rectangular parallelepiped specimens with dimensions of 300 × 300 × 100 (Thickness) mm were fabricated for the shielding effectiveness evaluation.

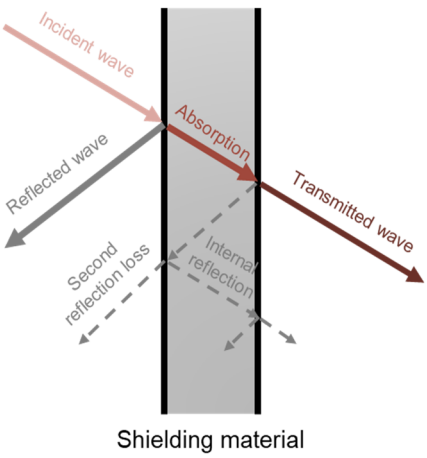

Figure 1 Concept of shielding effectiveness

3. Experimental results and discussion

Figure 2 shows the Nyquist plots of 30AFRCC with different steel fiber volume fractions. All specimens exhibited a typical dual-arc pattern. The first peak, which represents the AC resistance of the cement-based material, shifted to the left with increasing steel fiber volume fraction, indicating that the AC resistance of the cement-based material decreased.

Figure 3 presents the electrical conductivity of the cement-based materials as a function of the steel fiber volume fraction. In all specimens, the electrical conductivity increased with increasing steel fiber volume fraction. This tendency was consistently observed regardless of the type of steel fiber. Among the investigated specimens, 30AFRCC exhibited the highest electrical conductivity at all volume fractions,

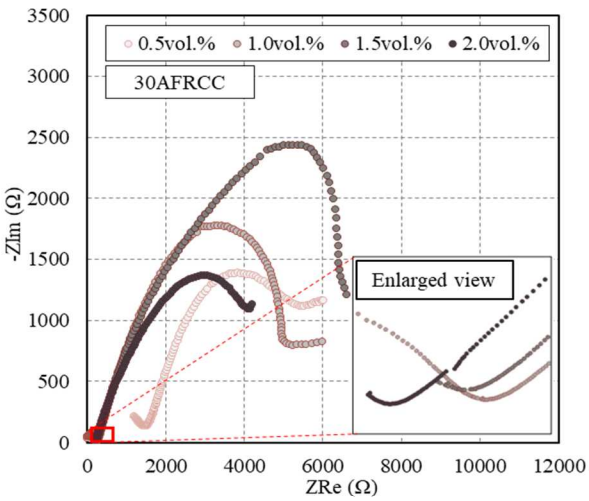

Figure 2 Nyquist plots of 30AFRCC

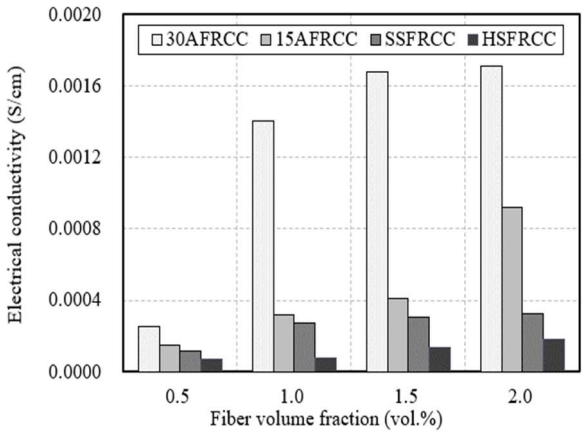

Figure 3 Electrical conductivity with fiber volume fraction

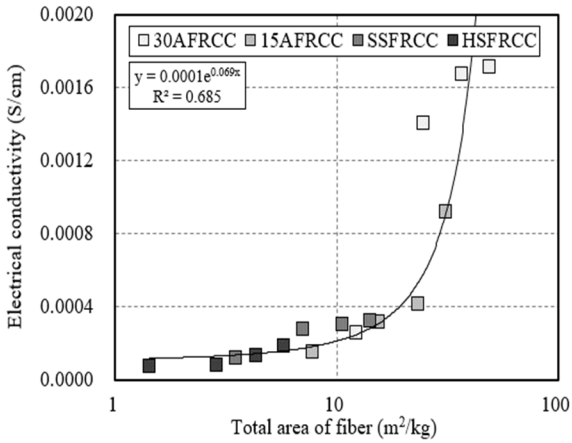

Figure 4 Electrical conductivity according to total area

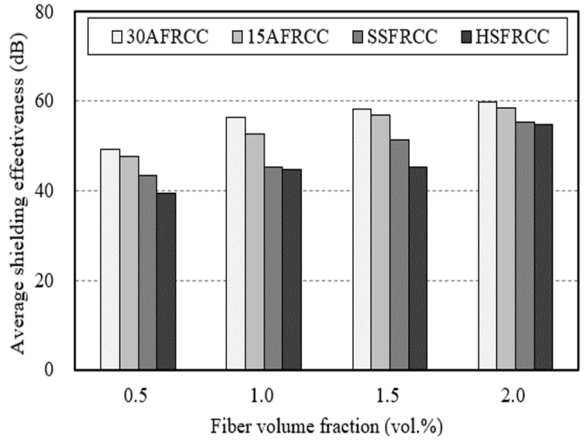

Figure 5 Average shielding effectiveness according to steel fiber volume fraction

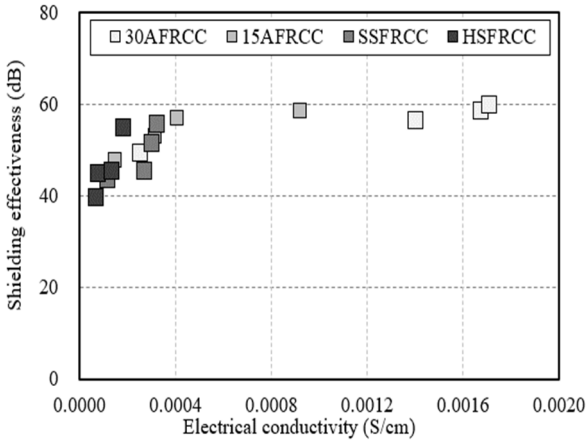

Figure 6 Electrical conductivity vs Shielding

whereas SSFRCC and HSFRCC showed relatively lower electrical conductivity. These results indicate that the volume fraction of steel fibers significantly influences the electrical conductivity of cement-based materials.

Figure 4 presents the electrical conductivity of the cement-based materials as a function of the specific surface area of the steel fibers. The electrical conductivity increased with increasing specific surface area of the steel fibers. Among the investigated specimens, 30AFRCC exhibited the highest electrical conductivity. These results indicate that the specific surface area of steel fibers significantly influences the electrical conductivity of cement-based materials. Furthermore, the specific surface area of the steel fibers was found to have a greater influence on the electrical conductivity than the intrinsic electrical conductivity of the steel fibers.

Figure 5 presents the average shielding effectiveness of cement-based materials reinforced with different types and volume fractions of steel fibers. In all specimens, the shielding effectiveness tended to increase with increasing steel fiber volume fraction. Among the investigated specimens, 30AFRCC exhibited the highest shielding effectiveness, followed by 15AFRCC, SSFRCC, and HSFRCC. These results indicate that both the type and volume fraction of steel fibers significantly influence the shielding effectiveness of cement-based materials.

Figure 6 shows the relationship between the electrical conductivity and shielding effectiveness of the cement-based materials. In general, the shielding effectiveness tended to increase with increasing electrical conductivity. Among the investigated specimens, 30AFRCC exhibited the highest electrical conductivity and shielding effectiveness, whereas

HSFRCC showed relatively lower values. These results indicate that the electrical conductivity of cement-based materials is closely related to their shielding effectiveness.

4. Conclusions

Based on the experimental results, the effects of the steel fiber type and volume fraction on the electrical properties and EMP shielding performance of cement-based materials were evaluated, and the relationship between electrical properties and shielding effectiveness was investigated. The main conclusions are summarized as follows.

(1) Analysis of the effects of steel fiber on the electrical conductivity and shielding effectiveness of cement-based materials revealed that the most critical factor is not the intrinsic electrical conductivity of the fiber, but rather its specific surface area. Consequently, AF, which possesses a larger specific surface area, was found to be more advantageous than SSF or HSF in forming conductive pathways and enhancing shielding effectiveness.

(2) Shielding effectiveness tended to increase with increasing electrical conductivity, suggesting that electrical conductivity is a significant factor governing the shielding effectiveness of the cement-based material. These results indicate that improving the electrical conductivity of cement-based materials is important for enhancing EMP shielding effectiveness.

Further studies are required to establish the optimum steel fiber characteristics and mixture design for improving the electrical properties and EMP shielding performance of cement-based materials.

Reference

[1] Y. Lee, S. Lee, G. Kim, H. Eu, M. Son, S. Han, J. Nam, Electrical conductivity and shielding effectiveness of fiber-reinforced cementitious composites according to steel fiber shape, Constr. Build. Mater. 495 (2025) 143497.

[2] A. Ohlan, K. Singh, A. Chandra, S.K. Dhawan, Microwave absorption properties of conducting polymer composite with barium ferrite nanoparticles in 12.4–18 GHz, Appl. Phys. Lett. 93 (2008) 053114.

[3] X. Zhang, W. Sun, Microwave absorbing properties of double-layer cementitious composites containing Mn–Zn ferrite, Cem. Concr. Compos. 32 (2010) 726–730.

[4] H.N. Yoon, D. Jang, H.K. Lee, I.W. Nam, Influence of carbon fiber additions on the electromagnetic wave shielding characteristics of CNT-cement composites, Constr. Build. Mater. 269 (2021) 121238.

[5] M. Jung, Y.S. Lee, S.G. Hong, J. Moon, Carbon nanotubes (CNTs) in ultra-high performance concrete (UHPC): Dispersion, mechanical properties, and electromagnetic interference (EMI) shielding effectiveness (SE), Cem. Concr. Res. 131 (2020) 106017.

[6] S. Lee, G. Kim, H. Kim, M. Son, Y. Lee, Y. Choi, J. Nam, Electromagnetic wave shielding properties of amorphous metallic fiber-reinforced high-strength concrete using waveguides, Materials 14 (22) (2021) 7052.

[7] A. Ohlan, K. Singh, A. Chandra, S.K. Dhawan, Microwave absorption properties of conducting polymer composite with barium ferrite nanoparticles in 12.4–18 GHz, Appl. Phys. Lett. 93 (2008) 053114.

[8] M.S. Kim, Structure and properties of amorphous materials, J. Corros. Sci. Soc. Korea 8 (1979) 24.

[9] MIL-STD-188-125-1; High-Altitude Electromagnetic Pulse (HEMP) Protection for Ground-Based C4I Facilities Performing Critical, Time-Urgent Missions—Part 1: Fixed Facilities. U.S. Department of Defense: Washington, DC, USA, 1998.

再生骨材の吸水・乾燥変形特性を考慮した再生骨材コンクリートの収縮評価

Shrinkage Evaluation of Recycled Aggregate Concrete Considering Moisture-Induced Deformation of Recycled Aggregates

寶藏寺雄大※1、佐藤幸恵※2、加藤穂佳※3、棚野博之※4
Yuta Hozoji, Sachie Sato, Honoka Kato, Hiroyuki Tanano

ABSTRACT

本研究では、再生粗骨材 L の吸水・乾燥に伴う変形を直接測定し、その結果に基づいて再生骨材コンクリートの乾燥収縮挙動を検討した。再生骨材にひずみゲージを貼り付け、吸水過程およびその後の乾燥過程における変形を測定するとともに、比較として、付着モルタルを除去した原骨材および天然骨材についても同様に試験した。その結果、再生粗骨材 L の収縮は同一ロット内でも大きくばらつき、付着モルタルの影響を強く受けることが確認された。得られた収縮の経時変化を指数関数で近似して時間定数を求め、有効湿気拡散係数を算定した。これらの物性値を用いて複合則により再生骨材コンクリートの乾燥収縮を予測した結果、AIJ 予測式よりも実測値と良好な一致を示した。さらに、付着モルタル量の実測値に基づいて殻厚を設定した 2 次元メソスケール RBSM 解析を行い、局所的な損傷が付着モルタル界面近傍に集中することを示した。

1. Introduction

In recent years, the use of recycled aggregates produced from demolished concrete has been promoted from the viewpoint of resource circulation. Recycled aggregates are classified by JIS into three grades: H, M, and L. Classes M and L contain larger amounts of attached mortar and generally cause greater drying shrinkage than natural aggregates, which limits their applications [1].

Drying shrinkage of recycled aggregate concrete has traditionally been evaluated macroscopically using concrete specimens, for example by length change tests. However, unlike concrete made with natural aggregates, the drying shrinkage behavior of recycled aggregate concrete is considered to be affected by the properties of both the attached mortar and the original aggregate. In addition, recycled aggregates exhibit large variations in quality, and the authors' previous study showed that the trends obtained from conventional aggregate quality tests do not always correspond to those observed in drying shrinkage tests [2]. Therefore, to clarify the influence of recycled aggregate quality on the drying shrinkage of recycled aggregate concrete, it is necessary to separately investigate the deformation characteristics of the attached mortar and the original aggregate within recycled coarse aggregates.

In this study, the deformation of recycled coarse aggregates during water absorption and drying was directly measured using strain gauges. Based on the measured results, effective moisture diffusivity was evaluated and used to predict the drying shrinkage of recycled aggregate concrete. Furthermore, a two-dimensional meso-scale rigid-body spring model (RBSM) consisting of original aggregate, attached (old) mortar, and new mortar was developed to analyze the distributions of internal stress and damage

※1 日本　東京都市大学　建築都市デザイン学部　建築学科　学部 4 年
※2 日本　東京都市大学　建築都市デザイン学部　建築学科　教授　博士（工学）
※3 日本　一般財団法人建材試験センター
※4 日本　国立研究開発法人建築研究所　工学博士

caused by differential shrinkage among the phases.

2. Direct measurement of moisture-induced deformation of recycled coarse aggregates

2.1 Materials

Since recycled aggregates are produced from demolished concrete, the quality of their original aggregates and parent concrete is unknown. Therefore, in this study, the drying shrinkage of recycled aggregates was measured directly using strain gauges in order to clarify the shrinkage behavior of the recycled aggregates, the attached mortar, and the original aggregates.

Recycled coarse aggregate of class L was used. The aggregates were sampled from four lots (L1–L4) produced in different months at the same plant. Natural aggregate (N) was also tested for comparison. Table 1 shows the saturated surface-dry density and water absorption of the aggregates used.

2.2 Measurement method

Following the studies of Ohta [3] and Yamada et al. [4], the shrinkage of the aggregates was measured during the water absorption and drying processes. Figure 1 shows an outline of the strain gauge attachment to the aggregate. After the strain gauges were waterproofed, the aggregates were immersed in water at 20 ± 2 °C until the strain change during absorption became negligible and the specimens could be regarded as being in a saturated state. The specimens were then removed from the water, and after wiping off the surface water to obtain a saturated surface-dry condition, drying was started in a room at 20 ± 2 °C and 50 ± 5% RH. The measurement was continued until the strain change during drying was considered to have converged. For the recycled aggregates, after this measurement, the attached mortar was removed, and strain gauges were attached to the original aggregates in the same manner for further measurement. Six specimens were tested for the recycled aggregates and ten for the natural aggregate.

Table1 Density and water absorption of the aggregates used

Type	Symbol	SSD Density (g/cm^3)	Water absorption (%)
Recycled aggregate L (Lot 1)	L1	2.43	6.44
Recycled aggregate L (Lot 2)	L2	2.41	6.49
Recycled aggregate L (Lot 3)	L3	2.41	6.80
Recycled aggregate L (Lot 4)	L4	2.42	6.04
Natural Aggregate	N	2.66	0.56

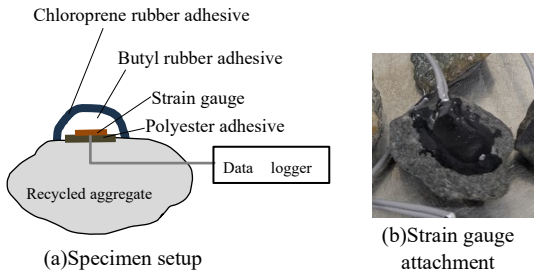

Fig. 1 Outline of the aggregate shrinkage test

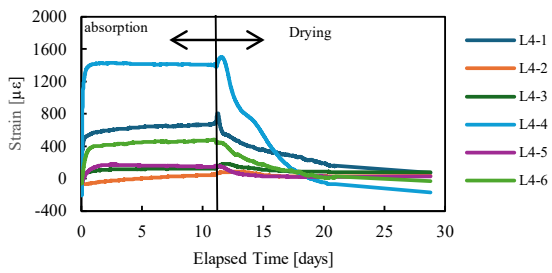

Fig. 2 Time history of shrinkage strain of recycled aggregate L (lot 4)

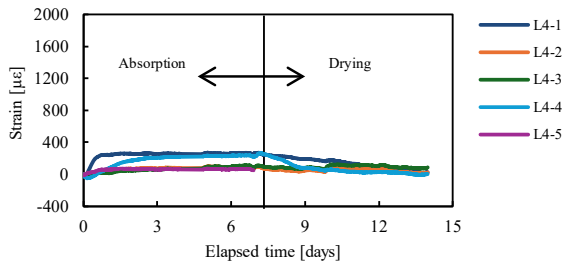

Fig. 3 Time history of shrinkage strain of the original aggregates of recycled aggregate L (lot 4)

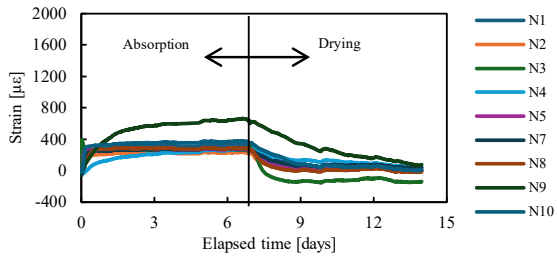

Fig. 4 Time history of shrinkage strain of natural aggregate

2.3 Results of the shrinkage test

Fig.2 shows the time history of the shrinkage strain of recycled aggregate L from lot 4 (L4-1 to L4-6) during the water absorption and drying processes. Similarly, Fig. 3 shows the time history obtained when the attached mortar was removed from L4, leaving only the original aggregates. As shown in Fig. 2 and 3, the shrinkage strain of the original aggregates alone was considerably smaller than that of the recycled aggregates. Fig.4 shows the time history of the strain of natural aggregate N during the water absorption and drying processes. Although some scatter was observed, the strain change was small, as in the case of the original aggregates. Since there was no marked difference in the strain change between the original aggregates and the natural aggregate, the shrinkage characteristics of the recycled aggregates are considered to be strongly influenced by the attached mortar.

3. Calculation of the effective moisture diffusivity of the aggregate

Based on the results of the shrinkage tests, the strain change during the drying process was approximated by Eq. (1). Assuming the aggregate particles to be spherical, the general solution of Fick's second law was obtained, and the effective moisture diffusivity was calculated using Eq. (2).

$$\varepsilon(t) = \varepsilon_{\infty}\left(1 - e^{\left(\frac{-t}{\tau}\right)}\right) \quad (1)$$

where t is the elapsed drying time [s], τ is the time constant [s], ε(t) is the drying shrinkage strain [$\times 10^{-6}$], and ε∞ is the final shrinkage [$\times 10^{-6}$]]

$$D_{eff} = \frac{R^2}{\pi^2 \tau} \quad (2)$$

where D_eff is the effective moisture diffusivity [m²/s], τ is the time constant [s], and R is the radius of the aggregate [m].

Figure 5 shows the calculated effective moisture diffusivity (hereafter referred to as the diffusivity) of the recycled aggregates, the original aggregates, and the natural aggregate. The diffusivity of the recycled aggregates was large, whereas those of the original aggregates and the natural aggregate were sufficiently

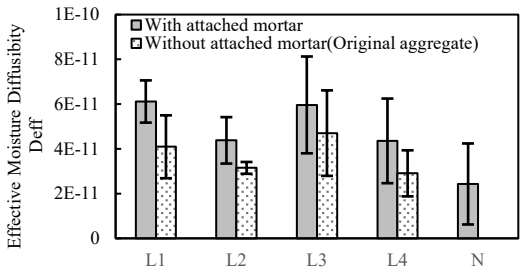

Fig. 5 Calculated effective moisture diffusivity of the aggregates

small even when the variation among individual particles was considered. This confirms that the diffusivity of the recycled aggregates is strongly influenced by the attached mortar.

4. Prediction of the drying shrinkage of recycled aggregate concrete

Using the effective moisture diffusivity of each aggregate shown in Fig. 5, the drying shrinkage of recycled aggregate concrete was predicted. The specimen dimensions considered were 100 × 100 × 400 mm. The diffusivity of the concrete as a whole was constructed by a composite model based on the volume fractions of the mortar (new mortar and fine aggregate) and the coarse aggregate. The volume fractions were taken from the mix proportion [5] of concrete using the same recycled coarse aggregate as in this study, and the diffusivity of the mortar was taken as $D_m = 5.8 \times 10^{-11}$ m²/s based on a previous study [6]. The drying shrinkage of the concrete as a whole was formulated from the relationship with the drying shrinkage strain, assuming that each phase (mortar and coarse aggregate) shrinks in proportion to the change in relative humidity (Eq. (3)). The time-dependent change in the average relative humidity Ht in the concrete was obtained from the general solution of Fick's second law for a plate of 100 × 100 mm, and the drying shrinkage strain of the concrete at an age of t days was expressed by Eq. (4).

$$\varepsilon(t) = K(h_0 - h) \quad (3)$$

$$\varepsilon_{conc}(t) = \varepsilon_{\infty}^{conc}(1 - H_t) \quad (4)$$

Where K is Shrinkage coefficient,$(h_0 - h)$is change in relative humidity (-), $\varepsilon_{conc}(t)$ is drying shrinkage

of the concrete at an age of t days [$\times 10^{-6}$], and H_t is the average relative humidity in the concrete at an age of t days[-].

Prediction results were compared with the measured values reported in the previous study by the authors [5] and with the drying shrinkage prediction equation given in AIJ Guidelines on Design and Construction Practice for Control of Shrinkage Induced Cracking in Reinforced Concrete Buildings (hereafter, the AIJ equation) [7].

$$\varepsilon_{sh}(t,t_0) = \varepsilon_{sh\infty}\left(\frac{(t-t_0)}{1.7\times\left(\frac{V}{S}\right)+(t-t_0)}\right)^{0.8} \quad (5)$$

$$\varepsilon_{sh\infty} = 1.50 \times K_1 \times t_0^{-0.08}\left\{1-\left(\frac{h}{100}\right)^3\right\} \times K_4 \quad (6)$$

Where $\varepsilon_{sh}(t,t_0)$ is drying shrinkage strain at an age of t days for a drying start age of t_0, $\varepsilon_{sh\infty}$ is final shrinkage strain [$\times 10^{-6}$], h is relative humidity [%] (40% ≤ h ≤ 100%), V is volume [mm^3], S is the surface area exposed to the environment [mm^2], V/S is volume-to-surface ratio (V/S ≤ 300mm), and K_1 and K_4 are coefficients.

Where,

$$K_1 = 1.16 \times \varepsilon_{sh26w}$$

ε_{sh26w} is drying shrinkage strain of the concrete at 26 weeks [$\times 10^{-6}$]

When 50mm< V/S ≤ 300mm

$$K_4 = 2.1 \times (V/S)^{-0.19}$$

When V/S ≤ 50mm

$$K_4 = 1.0$$

Fig. 6 shows the comparison. As shown in Fig. 6, the proposed equation showed better agreement with the measured values than the AIJ equation. This indicates that a prediction that considers the properties of the aggregates during the water absorption and drying processes is effective for recycled aggregate concrete.

5. Meso-scale damage analysis using RBSM

5.1 Analysis model

Based on the results obtained in the preceding chapters, a two-dimensional meso-scale analysis was carried out to examine the distributions of stress and damage generated in the aggregate and mortar phases within the concrete cross section by the difference in

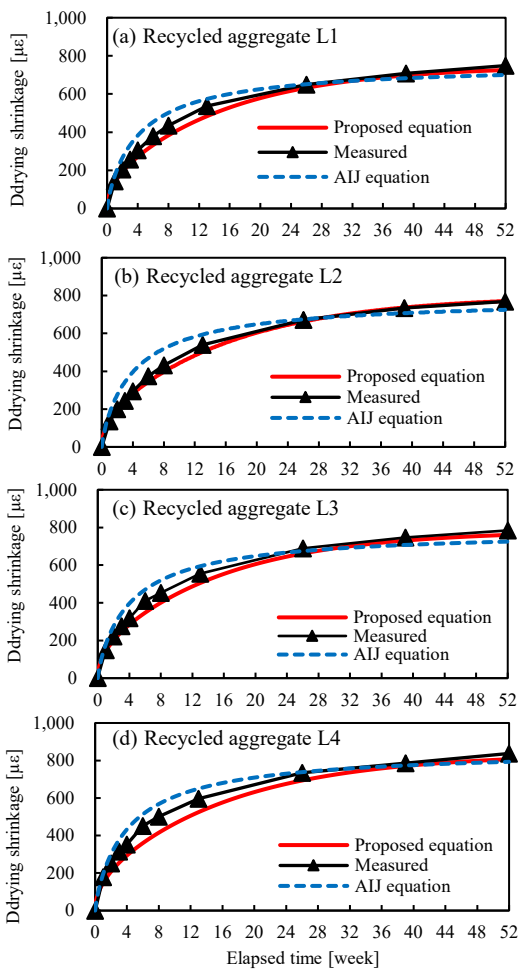

Fig. 6 Comparison of predicted and measured drying shrinkage of recycled aggregate concrete

shrinkage among the aggregate particles. The humidity distribution within the cross section was obtained by the finite volume method (FVM). The free shrinkage strain of each phase was given from the obtained humidity distribution using Eq. (3), and the internal stress and damage propagation were analyzed using the rigid body spring model (RBSM) [8].

The analysis cross section was modeled as an assembly of rigid cells generated by Voronoi tessellation, and adjacent cells were connected by normal and shear springs. Three material phases were considered: the original aggregate, the old mortar (attached mortar), and the new mortar. The recycled aggregate was represented as a structure in which an old mortar shell surrounds an original aggregate core. The maximum size of the coarse aggregate was 20 mm. Since the measured fineness modulus of the recycled coarse aggregate L used in the experiment ranged from

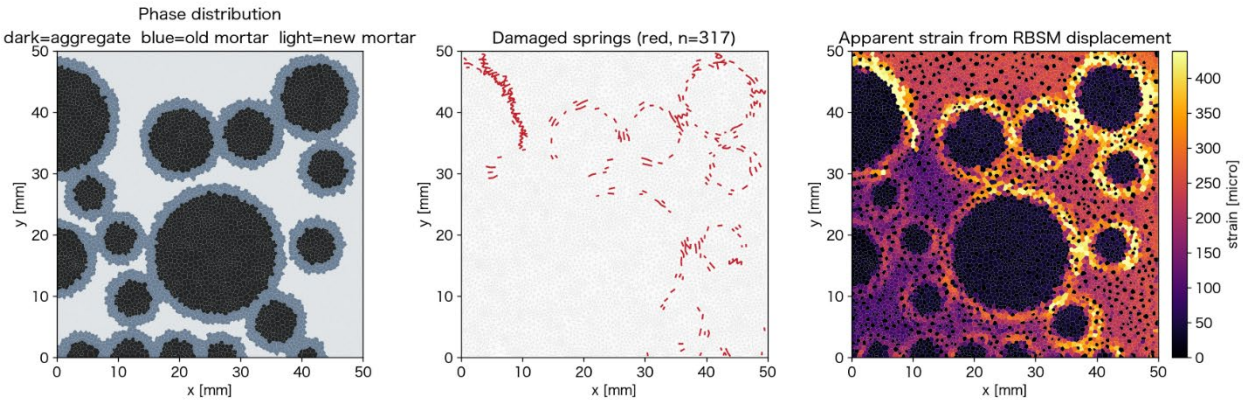

(a) Phase distribution (b)Distribution of damage springs (c)Apparent strain distribution

Fig.7 Fig. 7 RBSM analysis results for an attached mortar thickness of 1.65 mm: (a) phase distribution, (b) distribution of damaged springs, and (c) apparent strain distribution

6.47 to 6.60, a fineness modulus of 6.5 was adopted in the analysis, and the volume fraction of the coarse aggregate was set to approximately 35% based on the mix proportion used in the experiment. The analysis domain was 50 × 50 mm, corresponding to one quarter of a 100 × 100 mm cross section. On the symmetry planes, the moisture flux was set to zero, and the displacement normal to the plane was constrained, while the outer surfaces were treated as drying surfaces.

The free shrinkage strain of each phase was set to reflect the experimentally observed tendency that the shrinkage of the original aggregate is small whereas that of the attached mortar is large. The Young's modulus and tensile strength of each phase were taken from the macroscopic properties of the mortar and the aggregate reported in a previous study [9]. For the attached mortar, considering its history of drying, carbonation, and crushing, the values were assumed to be 0.7 times those of the new mortar. The thickness of the attached mortar of the recycled coarse aggregate was set to approximately 1.65 mm as the reference value, determined from the measured volume fraction of the attached mortar in the recycled aggregate reported in a previous study [10] using the same lot of recycled aggregate, assuming the aggregate particles to be spherical. Thicknesses of 0.5 mm and 2.5 mm were also examined for comparison. The cell size was set to 0.6 mm. In the calculation, a spring was ruptured when its tensile stress reached the interfacial strength, and the recalculation with stress redistribution was repeated at each step until no further rupture occurred.

Table2 Attached mortar thickness and damage concentration ratio

Attached mortar thickness (mm)	Damage concentration ratio (%)
0.50	76
1.65	96
2.50	99

5.2 Analysis results

Fig. 7 shows the phase distribution, the distribution of damaged springs, and the apparent strain distribution calculated from the RBSM displacements, for the case in which the attached mortar shell thickness was set to 1.65 mm based on the measured results. Approximately 96% of the damaged springs were concentrated at the interfaces adjacent to the old mortar, confirming the tendency for shrinkage-induced damage to occur preferentially around the recycled aggregate particles. Table 2 shows the damage concentration ratio at the attached mortar interfaces when the attached mortar thickness was varied to 0.5, 1.65, and 2.5 mm. As shown in Table 2, the damage concentration ratios were 76%, 96%, and 99%, respectively, indicating that damage tends to concentrate at the interfaces as the attached mortar thickness increases. Therefore, in recycled aggregates with a non-uniform attached mortar thickness, the damage propagation path may differ depending on local thickness variation.

6. Conclusions

In this study, the deformation of recycled coarse aggregate L during the water absorption and drying processes was measured directly using strain gauges, and the drying shrinkage behavior of recycled aggregate concrete was examined based on the deformation characteristics obtained. In addition, a two-dimensional meso-scale RBSM analysis reflecting the measured results was carried out to examine the tendency of local damage caused by the difference in shrinkage. The results obtained in this study are summarized as follows.

(1) The moisture-induced deformation of recycled coarse aggregate L varied widely even within the same lot and was strongly influenced by the attached mortar.

(2) The drying shrinkage of recycled aggregate concrete was predicted well by using the effective moisture diffusivity calculated from the deformation characteristics of the aggregates.

(3) In the RBSM analysis, damage was concentrated near the attached mortar interfaces, indicating that the thickness of the attached mortar may affect the location of damage initiation and its propagation path.

Reference

[1] Architectural Institute of Japan: Recommendation for mix design, production and construction practice of concrete with recycled concrete aggregate, 2014.10 (in Japanese)

[2] Hiroyuki Tanano, Matsuzawa Koichi, Sachie Sato: Examination for Utilizing concrete using Recycled Coarse Aggregate M in Building Structures Part3. Drying Shrinkage, Summaries of Technical Papers of Annual Meeting (Hokkaido), Architectural Institute of Japan, pp.499-500,2022.9 (in Japanese)

[3] Tatsumi Ota: An Evaluation on Various Characteristics of Gravels in Shizuoka Part 3 Drying Shrinkage of River Gravels Manufactured in Shizuoka, Summaries of Technical Papers of Annual Meeting (Kanto), Architectural Institute of Japan, pp.113-114,2024.8 (in Japanese)

[4] Hiroshi Yamada, Hiroshi Katahira, Hiroshi Watanabe: Study on the Evaluation for Drying Shrinkage Properties of Coarse Aggregate, Journal of Japan Society of Civil Engineers, Ser. E2 (Materials and Concrete Structures), Vol.68, No.1, pp.63-71, 2012 (in Japanese)

[5] Ryota Isobe, Hiroyuki Tanano, Sachie Sato: Examination for Utilizing concrete using Recycled Coarse Aggregate M in Building Structures Part5 Effect of Recycled Aggregate Quality Variation on Freshness and Drying Shrinkage Properties of Concrete, Summaries of Technical Papers of Annual Meeting (Kinki), Architectural Institute of Japan, pp.575-578, 2023.9 (in Japanese)

[6] Kenji SAKATA, Osamu KURAMOTO: A Study on the Water Diffusion and Shrinkage in Concrete by Drying, Proceedings of the Japan Society of Civil Engineers, Issue316, pp.145-152,1981 (in Japanese)

[7] Architectural Institute of Japan: Guidelines on Design and Construction Practice for Control of Shrinkage Induced Cracking in Reinforced Concrete Buildings, 2023.2 (in Japanese)

[8] Kawai, T.: New discrete models and their application to seismic response analysis of structures, Nuclear Engineering and Design, Vol.48, pp.207-229, 1978

[9] H. Sasano, I. Maruyama, Mechanism of drying-induced change in the physical properties of concrete: a mesoscale simulation study, Cement and Concrete Research, 143, 106401 (2021)

[10] Taihei Marui: A Study on the Freeze-Thaw Deterioration Behavior of Recycled Aggregate Concrete, Bachelor's Thesis, Tokyo City University, 2026.3 (in Japanese)

自己治癒カプセルを用いたアルカリ活性化複合体の力学的特性および自己治癒性能の評価

Evaluation of Mechanical and Self-Healing Performance of Alkali-Activated Composites with Self-Healing Capsules

朴正娟※1、申民知※2、安은비※3、朴堵營※3、李在寅※4、崔世珍※5

Jeong-Yeon Park, Min-Ji Shin, Eun-Bee An, Do-Young Park, Jae-In Lee, Se-Jin Choi

ABSTRACT

In this study, to reduce carbon dioxide emissions from cement production, alkali-activated composites were prepared using blast furnace slag powder and fly ash as binders. To compensate for the cracking susceptibility of the alkali-activated composites, self-healing capsules based on industrial by-products were manufactured and incorporated, and the performance of the composites was evaluated. As a result of the evaluation, the BFP05 sample showed a compressive strength approximately 8.7% higher than the control sample, and the sample incorporating 5% self-healing capsules showed relatively higher compressive strength compared to the sample incorporating 10%. When measuring the compressive strength recovery rate, the sample incorporating 10% self-healing capsules showed a superior recovery rate of approximately 112-118% compared to the control sample.

1. Introduction

Concrete is the most widely used material in the construction industry. However, it is known that the production of 1 ton of cement[1], the binder for concrete, generates approximately 1 tons of carbon dioxide, accounting for about 7% of global carbon dioxide emissions[2]. Recently, active research has been conducted on alkali-activated composites utilizing industrial by-products such as blast furnace slag and fly ash to reduce carbon dioxide emissions from cement production[3, 4]. These alkali-activated composites are known to be capable of reducing carbon dioxide emissions compared to cement composites[5]. However, since industrial by-products such as blast furnace slag and fly ash do not react directly with water, alkali activators must be used in combination to induce a reaction. Furthermore, as the type and incorporation ratio of the alkali activator can affect composite performance, such as durability and strength, it is necessary to select the appropriate type and ratio of the activator[6]. Alkali-activated composites have been reported to possess mechanical performance similar to or relatively higher than that of cement composites, as well as fire and acid resistance[7]. However, alkali-activated composites are known to be susceptible to cracking due to their low fracture energy and high shrinkage rates[8, 9]. If harmful agents penetrate through these cracks, it can accelerate the deterioration of the composite and reduce its strength and durability[10]. To address these issues, research on self-healing composites

※1 大韓民国 圓光大学校 建築工学科 修士課程
※2 大韓民国 圓光大学校 建築工学科 学席士課程
※3 大韓民国 圓光大学校 建築工学科 学部生
※4 大韓民国 圓光大学校 建築工学科 博士（工学）
※5 大韓民国 圓光大学校 建築工学科 教授博士（工学）

capable of self-healing cracks is actively underway. Self-healing technologies utilize methods such as microcapsules, microorganisms, and polymers[11-14]. In particular, microcapsule-based self-healing technology is known to repair cracks by releasing healing substances as the capsules rupture upon crack formation. In this study, we manufactured self-healing capsules using industrial byproducts such as blast furnace slag powder, fly ash, and ferronickel slag powder, incorporated them into an alkali-activated composite, and aimed to compare and analyze the mechanical performance and self-healing performance of the alkali-activated composite.

2. Materials and methods

2.1 Materials

In this study, blast furnace slag powder (Dae-han slag, Korea) with a specific gravity of 2.93 g/cm³ and a fineness of 4,210 cm²/g, and fly ash (Dangjin Thermal Power Plant, Korea) with a specific gravity of 2.21 g/cm³ and a fineness of 3,710 cm²/g were used as binders. Additionally, CaO, $Ca(HCOO)_2$, $Ca(NO_3)_2$, and NaOH were incorporated as binder substitutes to activate the reaction of the binders, and the characteristics of the alkali activators used in this study are shown in Table 1. For the fine aggregate, mountain sand from Namwon with a fineness modulus of 2.45 and a specific gravity of 2.60 g/cm³ was used. Self-healing capsules were fabricated by mixing blast furnace slag powder(BFS), fly ash(FA), and ferronickel slag powder(FSP), and the material composition ratios for each type of self-healing capsule are shown in Table 2. Polyvinyl alcohol (Amos, Korea) was used to improve cohesion during the capsule manufacturing process, and the capsules were coated with a polyurethane solution (KCC, Korea) to prevent capsule destruction before being used in the experiment. These self-healing capsules were prepared by mixing capsules of sizes 0.3–0.6 mm and 2.5–5.0 mm in a 5:5 ratio and were used to replace 0, 5, and 10% of the fine aggregate weight, respectively.

Table 1 Physical porperties of alkali-activator

Type	pH	Density (g/cm^3)	After ignited (%)
CaO	-	3.3	97.5
$Ca(HCOO)_2$	7.31	1.9	99.4
$Ca(NO_3)_2$	6.0	1.9	98.8
NaOH	-	2.13	99.1

Table 2 Self-healing capsule constituent materials and ratios

Type	BFS (%)	FA (%)	FSP (%)
FAFP	-	50	50
BFP	50	-	50
BFF	60	20	20

2.2 Experimental methods

Table 2 shows the mixing proportions used in this study, and the experiment was conducted with the water-to-binder ratio fixed at 40% and the fine aggregate ratio at 42%. Cube specimens measuring

Table 3 Mixing proportions

Mix	W/B (%)	S/a (%)	Binder (kg/m_3)	AMC (S*wt%)	BFS (B*%)	FA (B*%)	CaO (B*%)	$Ca(HCOO)_2$ (B*%)	$Ca(NO_3)_2$ (B*%)	NaOH (B*%)
Control	40	42	400	-	75	10	2.5	5	5	2.5
FAFP05				5						
FAFP10				10						
BFP05				5						
BFP10				10						
BFF05				5						
BFF10				10						

50x50x50 mm were fabricated to measure compressive strength and compressive strength recovery rate. The specimens were demolded 24 hours after fabrication and steam-cured at 40℃ with 100% relative humidity. Compressive strength, which evaluates mechanical performance, was measured according to the KS L 5105 standard. To measure the compressive strength recovery rate, a load equivalent to 70% of the 28-day compressive strength result was applied to the specimens to induce microcracks, followed by re-curing, and the compressive strength recovery rate was measured at ages 7, 28, and 56.

3. Results and Discussion

3.1 Compressive strength

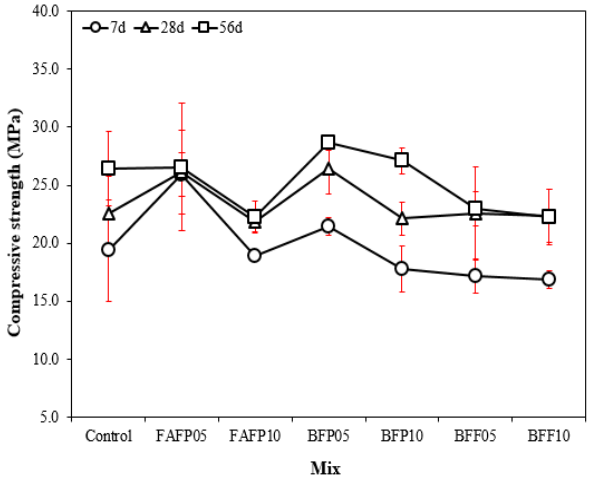

Figure 1 Compressive strength

Figure 1 shows the results of compressive strength measurements by age. The control sample at 7 days of age showed approximately 19.4 MPa. Among the samples incorporating 5% self-healing capsules, the FAFP05 sample exhibited the highest compressive strength at approximately 25.9 MPa. The samples incorporating 10% self-healing capsules showed a relatively lower compressive strength of approximately 16.9–18.9 MPa compared to the samples incorporating 5%. For the compressive strength at 28 days of age, the samples incorporating 5% self-healing capsules showed similar or relatively higher compressive strength compared to the control sample, and similar to the trend at 7 days of age, the samples incorporating 10% self-healing capsules showed relatively lower compressive strength compared to the samples incorporating 5%. At 56 days of age, the BFP05 sample exhibited the highest compressive strength among all samples at approximately 28.7 MPa, and in the case of samples incorporating 10% of self-healing capsules, the BFP10 sample also showed a high compressive strength of approximately 27.1 MPa. It is believed that the reason the compressive strength decreases as the incorporation rate of self-healing capsules increases is that the bonding force with the matrix is weakened due to the round shape of the capsules.

3.2 Compressive strength recovery rate

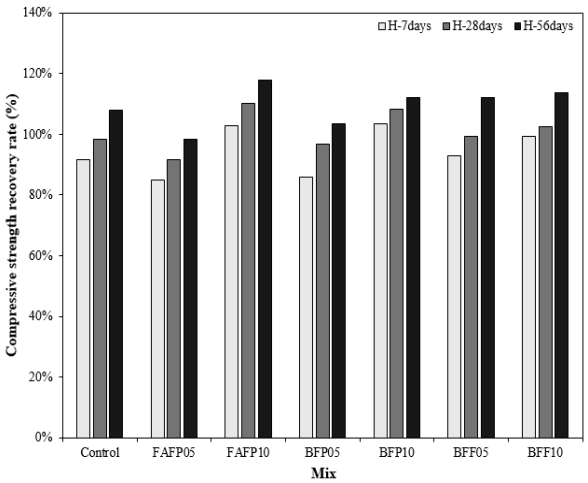

Figure 2 Compressive strength recovery ratio

Figure 2 shows the results of the compressive strength recovery rate by curing age. At a healing age of 7 days, the Control sample showed a compressive strength recovery rate of approximately 92%. In the case of samples incorporating self-healing capsules, the samples with 10% incorporation showed a relatively higher compressive strength recovery rate of approximately 99–103% compared to the samples with 5% incorporation. At a healing age of 28 days, the Control sample showed a compressive strength recovery rate of approximately 99%, while the samples with 5% self-healing capsules showed a compressive strength recovery rate of approximately 92–99%. Similar to the 7-day curing age, the samples with 10% self-healing capsules showed a relatively higher compressive strength recovery rate compared

to the samples with 5% self-healing capsules. At a healing age of 56 days, the control sample showed a compressive strength recovery rate of approximately 108%, while the sample containing 10% self-healing capsules showed a high compressive strength recovery rate of approximately 112–118%. The high compressive strength recovery rates observed in samples containing self-healing capsules, with the exception of some samples, are believed to be the result of the capsule constituent materials, which were damaged during load application, continuing to react over time.

4. Conclusions

In this study, self-healing capsules were fabricated and incorporated using industrial by-products to compensate for the crack brittleness of alkali-activated composites, and their performance was evaluated. Compressive strength measurements showed that the sample incorporating 5% of self-healing capsules exhibited excellent compressive strength, whereas the sample incorporating 10% showed relatively lower compressive strength. Compressive strength recovery rate measurements revealed that, with the exception of some samples, the healing effect due to capsule incorporation became distinct as the healing age increased, and the sample incorporating 10% showed the best compressive strength recovery rate.

Acknowledgements

This research was supported by the National Research Foundation of Korea (NRF) grant funded by the Korean government (MSIT) (RS-2024-00405537).

Reference

[1] I. Sanal, Discussion on the effectiveness of cement replacement for carbon dioxide (CO2) emission reduction in concrete, Greenh. Gases: Sci. Technol. 8 (2017) 366-378.

[2] M.B. Ali, R. Saidur, M.S. Hossain, A Review on Emission analysis in cement industries, Renew. Sustain. Energy Rev. 15 (2011) 2252-2261.

[3] S.J. Choi, J.I. Lee, C.Y. Kim, J.H. Mun, Effects of combined amorphous metallic fibers and carbon nanotubes on the performance of alkali-activated composite, Emergent Mater. 8 (2025) 5919-5934.

[4] J. Yin, Z. Qiu, J. Wang, Y. Liu, Y. Miao, Valorization of industrial by-products and waste shredded tire into sustainable alkali-activated material: resource efficiency activated material: resource efficiency, microstructure, and circular potential, Ceram. Int. 52 (2026) 14023-14036.

[5] I.P. Segura, N. Ranjbar, A.J. Damo, L.S. Jensen, M. Canut, P.A. Jensen, A review: Alkali-activated cement and concrete production technologies available in the industry, Heliyon. 9 (2023) e15718.

[6] M. Jegan, R. Annadurai, P.R.K. Rajkumar, A state of the art on effect of alkali activator, precursor, and fibers on properties of geopolymer composites, Case Stud. Constr. Mater. 18 (2023) e01891.

[7] R.K. Paswan, P. Kumar, V. Kumar, R.Y. Sembeta, Mechanical properties of alkali activated slag binder based concrete at elevated temperatures, Discov. Sustain. 6 (2025) 744.

[8] P. Zhang, Y. Zhu, W. yuan, J. Zheng, Z. Gao, A state-of-the-art review on fracture properties of geopolymer composites, Theor. Appl. Fract. Mech. 132 (2024) 104480.

[9] R. Cao, B. Li, N. You, Y. Zhang, Z. Zhang, Properties of alkali-activated ground granulated blast furnace slag blended with ferronickel slag, Constr. Build. Mater. 192 (2018) 123-132.

[10] J. Yang, Z. Sun, N.D. Belie, D. Snoeck, Self-healing ability of cracks in alkali-activated slag systems incorporating superabsorbent polymers, Dem. Concr. Res. 170 (2023) 107183.

[11] B. Liu, M. Wu, L. Jiang, H. Li, J. Li, D. Zuo, Q. Ding, The Application of Self-Healing Microcapsule Technology in the Field of Cement-Based Materials: A Review and Prospect, Polymers. 15 (2023) 2718.

[12] B. Aytekin, A. Mardani, S. Yazici, State-of-art review of bacteria-based self-healing concrete: Biomineralization process, crack healing, and mechanical properties, Constr. Build. Mater. 378 (2023) 131198.

[13] J. Ahmed, J.E. Jeong, J.C. Kim, S. Lone, I.W. Cheong, Self-healing polymers for surface scratch regeneration, RSC Adv. 13 (2023) 35050-35064.

[14] X.Wen, A.M. Pagcaliwagan, H. Hou, X. Yin, Advancements in Self-healing concrete: Material mechanism, durability assessment, and implications for infrastructure lifecycle management, Alex Eng J, 131 (2025).

環境性を考慮した再生骨材コンクリートＭの最適調合設計に関する研究

Optimization of Mix Proportions of Recycled Aggregate Concrete-Class M Considering Environmental Assessment

小野山皓太※1、道正泰弘※2、田口孝※3、清水啓介※4
Kohta Onoyama, Yasuhiro Dosho, Takashi Taguchi, Keisuke Shimizu

ABSTRACT

持続可能な社会の実現にむけて，高炉セメント B 種(BB)を用いた再生骨材コンクリート M(RACM)の大臣認定の取得を見据え，再生粗骨材 L(RLG)を用いた，RACM における調合設計の最適化を目的に検討を行った. その結果, 乾燥収縮や凍結融解の影響のない構造部材への使用検討が必要であることを示した．RACM の調合設計は相対品質値により，RLG の品質が JIS 規定値内で変動しても性能への影響は少なく, 調合設計時に容積混合率を若干調整することで，同じ水結合材比の普通コンクリートと同等の性能確保が可能であること，BB および RLG の使用で環境性に貢献できることを明らかにした.

1. Introduction

In recent years, the practical application of recycled aggregate concrete (RAC), which reuses concrete waste, has attracted considerable attention because of the need to achieve a sustainable society and reduce environmental impacts. Therefore, the authors reported that the required performance can be achieved in structural concrete using recycled aggregate Class L produced at the first aggregate plant in the Tokai region (Aichi Prefecture) by adjusting the volumetric mixing ratio and other factors [1].

The 2018 revision of JIS A 5022 (recycled aggregate concrete-Class M (RACM)) permits the use of recycled coarse aggregate class L (RLG) in RACM when blended with normal aggregate conforming to Annex A of JIS A 5308 at or below a specified volumetric mixing ratio [2]. However, to use RACM for the main structural parts of buildings, it is necessary to comply with the standards for designated building materials under Article 37, Paragraph 2, of the Building Standards Act [2]. Accordingly, the acquisition of approval from the Minister of Land, Infrastructure and Transport (MLIT) is required.

Further, in the JASS 5 (2022) [2] revision, environmental assessment was added as a required criterion. From the perspectives of global warming and environmental pollution, efforts aimed at achieving “carbon neutrality” and virtually zero emissions of greenhouse gases such as CO_2 by 2050 are strongly needed. Therefore, the use of Portland blast-furnace slag cement is being promoted because it produces lower CO_2 emissions than Portland cement [2]. In addition, Portland blast-furnace slag cement Type B (BB) is a low-carbon cement of high grade that is commonly used at virtually all ready-mixed concrete plant nationwide [2]. This study examined the optimization of the mix proportion for RACM using RLG manufactured at the first plant established in the Tokai region (Aichi Prefecture), aiming to obtain MLIT certification for RACM using BB.

2. Materials and methods

2.1 Materials

Tables 1 and 2 show the materials used and the

※1 日本　名城大学大学院理工学研究科環境創造工学専攻
※2 日本　名城大学理工学部環境創造工学科 教授 博士(工学)
※3 日本　矢作建設工業㈱エンジリアリングセンター 博士(工学)
※4 日本　矢作建設工業㈱建築事業本部技術工務部

Table 1 Materials used

	Item		Code
Binder	Portland blast-furnace slag cement Type B	Density: 3.04g/cm^3, Specific surface area: 3740cm^2/g	BB
Fine aggregates	Normal fine aggregates	Shinshiro crushed sand	CS
		Seto mountain sand	MS
		Blast-furnace slag aggregate	BFS
Coarse aggregate	Normal coarse aggregate	Shinshiro hard sandstone crushed stone 2005	NG
	Recycled coarse aggregate	RLG2005	RLG
Mixing water	Tap water	-	W
Chemical admixture	Air-entraining and water-reducing admixture		AE
	Air-entraining and high-range water-reducing admixture		SP
	Air-entraining admixture		Ad

Table 2 Quality of aggregates

Item	Test method		NG	RLG	CS	MS	BFS
Density in oven-dry condition (g/cm^3)	JIS A 1109,		2.64	2.29	2.65	2.40	2.71
Water absorption (%)	JIS A 1110		1.01	5.81	1.28	2.87	0.20
Fineness modulus (F.M.)	JIS A 1102		6.67	6.56	2.82	2.82	2.31
Content of materials finer than 75-μm sieve (%)	JIS A 1103		1.1	0.6	4.9	2.6	2.9
Solid content in aggregate (%)	JIS A 1104		61.1	60.4	65.5	65.5	60.8
Solid content of particle shape (%)	JIS A 5005		-	60.6	55.0	57.1	63.5
400kN crushing value (%)	BS 812-110		13.3	19.5	-	-	-
10%finens value (kN)	BS 812-111		371	-	-	-	-
Freeze–thaw resistance index	JIS A 5022 Annex D		-	0.01	-	-	-
Alkali–silica reaction	JIS A 5021 Annex D		A	A	-	-	-
Chloride content (%)	JIS A 1154		-	0.004	-	-	-
Amount of contained impurities (mass%)	JIS A 5023 Annex A	A	-	0.24	-	-	-
		B	-	0	-	-	-
		C	-	0.05	-	-	-
		D	-	0	-	-	-
		E	-	0	-	-	-
		F	-	0	-	-	-
		G	-	0	-	-	-
		Total	-	0.29	-	-	-

quality of aggregates, respectively. The binder used was BB. Normal fine aggregates were Shinshiro crushed sand (CS), Seto mountain sand (MS), and blast-furnace slag aggregate (BFS). Normal coarse aggregate was Shinshiro hard sandstone crushed stone (NG). For the RLG, RLG2005 was used, derived from returned concrete with a nominal strength of 24–30 as the original concrete. RLG was manufactured in the same way as in reference [1]. Note that RLS was not manufactured.

The overall quality of RLG was equivalent to the RLG specified in JIS A 5023 Annex A. Alkali–silica reactivity was harmless. Tap water was used as the mixing water (W). Concrete mixing was performed in accordance with JIS A 1138.

2.2 Mix proportion

Table 3 shows the mix proportions of the concrete. A total of nine types of specimens were prepared: normal concrete using normal aggregate (NC), RACM using RLG at a volumetric mixing ratio of 50%, and recycled aggregate concrete-Class L (RACL) using RLG at a volumetric mixing ratio of 100% for comparison. The volumetric mixing ratio of fine aggregates in each concrete was CS:MS:BFS = 50:25:25. The water–binder ratio (W/B) was established at three levels: 45%, 55%, and 65%. The target slumps were 23 ± 2.0, 15 ± 2.5, and 18 ± 2.5 cm, with the target air content being 4.5% ± 1.5%. For the target slump of 23 cm, an air-entraining and high-range water-reducing admixture (SP) was added at 0.73% of the cement mass. For the target slump levels of 15 and 18 cm, an air-entraining and water-reducing admixture (high-performance type) (AE) was added at 0.8%–1.5% of the cement mass. In addition, an air-entraining admixture (Ad) was added at 0.002%–0.005% of the cement mass to adjust the air content.

The mix proportions for NC and RACM were determined with reference to the mix proportions used by a ready-mixed concrete plant with a track record of supplying RACL.

2.3 Test methods

Table 4 shows the experimental and test methods. For fresh concrete, the slump, slump flow, air content, density, concrete temperature, and chloride ion content were measured. For the hardened concrete, various tests were performed, including compressive strength,

Table 3 Mix proportions of concrete

No.	W/B (%)	Target slump (cm)	Target air content (%)	s/a (%)	Volumetric mixing ratio (%) RLG	Unit weight (kg/m^3) W	Chemical admixture (B×%) AE	HAE	Ad
1				48.0	0	173	-	0.73	0.002
2	45	23 ± 2.0		47.8	50	170	-	0.73	0.004
3				48.5	100	170	-	0.73	0.006
4				48.0	0	180	1.3	-	0.002
5	55	18 ± 2.5	4.5 ± 1.5	47.8	50	180	0.8	-	0.004
6				47.8	100	180	1.5	-	0.005
7				48.4	0	174	1.5	-	-
8	65	15 ± 2.5		48.3	50	174	1.0	-	0.002
9				47.7	100	181	1.5	-	0.003

Table 4 The experimental and test methods

Item			Test method	Note
Fresh concrete	Slump		JIS A 1101	-
	Slump flow		JIS A 1150	-
	Air content		JIS A 1128	-
	Density		JIS A 1116	-
	Concrete temperature		JIS A 1156	-
	Chloride ion content	NC	JIS A 5308	Mohr method
		RACM, RACL	JIS A 5022	-
Hardened concrete	Compressive strength		JIS A 1108	Standard curing at 7, 28 and 91 days
	Static modulus of elasticity (Young's modulus)		JIS A 1149	
	Accelerated carbonation		JIS A 1153	-
	Drying shrinkage		JIS A 1129-3	-
	Durability factor		JIS A 1148	-

Table 5 Experimental results of fresh concrete

No.	Slump (cm)	Slump flow (cm)	Air content (%)*	Density (kg/m^3)	Concrete temperature (°C)	Chloride ion content (kg/m^3) JIS A 5308	JIS A 5022
1	25.0	58.5	5.3	2231	16	0.05	-
2	23.5	57.0	5.3 (1.0)	2183	16	-	0.07
3	23.5	52.5	4.8 (1.0)	2183	24	-	0.08
4	20.0	38.0	5.9	2293	16	0.05	-
5	20.0	36.5	5.5 (1.0)	2139	15	-	0.06
6	20.0	32.0	6.0 (1.0)	2124	22	-	0.03
7	15.0	27.0	5.4	2220	15	0.04	-
8	16.0	28.0	5.8 (1.0)	2141	15	-	0.05
9	17.5	28.5	4.4 (1.0)	2121	22	-	0.03

*Values in parentheses indicate the aggregate correction factor.

Young's modulus, drying shrinkage, accelerated carbonation, and freezing and thawing. Concrete specimens were prepared in accordance with JIS A 1138, and hardened concrete specimens were prepared in accordance with JIS A 1132.

The individual specimens used for each hardened concrete test complied with the relevant JIS standards.

3. Experiment results

3.1 Fresh concrete

Table 5 shows the experimental results of fresh concrete. The slump, slump flow, and air content reached the target values through adjustments to the chemical admixtures. The aggregate correction factor for RACM and RACL was 1.0%. Density of RACM and RACL tended to decrease as the volumetric mixing ratio increased. This is due to the influence of RLG. The concrete temperature ranged from 15°C to 24°C. In calculations according to JIS A 5022, the chloride ion content increases when recycled aggregate class L is used. Therefore, the chloride ion content of RACL tended to be higher than that of RACM. All mix proportion met the criterion value of 0.30 kg/m^3 or less specified in JIS A 5308 and JIS A 5022.

Table 6 compressive strength, Young's modulus, and carbonation velocity coefficient of concrete

No.	Compressive strength (N/mm^2) 7 days	28 days	91 days	Young's modulus (kN/mm^2) 7 days	28 days	91 days	carbonation velocity coefficient (mm√week) 8 weeks
1	24.3	39.5	48.8	21.3	28.1	33.9	-
2	27.6	39.0	46.3	21.6	25.8	32.4	-
3	22.6	-	-	22.3	-	-	-
4	20.2	32.8	45.4	21.4	22.6	30.1	4.41
5	17.5	30.6	37.9	18.3	21.7	30.1	-
6	16.5	27.2	-	17.8	19.9	-	-
7	15.8	25.9	36.6	19.9	21.2	21.2	5.52
8	16.1	25.4	34.5	18.1	21.0	27.7	6.00
9	15.2	25.3	-	18.2	20.5	-	-

3.2 Hardened concrete

Table 6 shows compressive strength, Young's

modulus, and carbonation velocity coefficient of concrete.

3.2.1 Compressive strength and Young's modulus

Compressive strength tended to decline as the W/B increased. RACM exhibited compressive strength approximately 90% of that of NC. The use of RLG at a 50% volumetric mixing ratio had little effect on compressive strength. In addition, using BB resulted in greater long-term strength.

Young's modulus exhibited a trend similar to that of compressive strength. Young's modulus tended to decline as the W/B increased. RACM exhibited Young's modulus approximately 95% of that of NC.

3.2.2 Carbonation velocity coefficient

The carbonation velocity coefficient tended to increase as the W/B increased. RACM exhibited a carbonation velocity coefficient comparable to that of NC.

3.2.3 Drying shrinkage

Figure 1 shows length change ratio of concrete. The length change ratio tended to increase with the age of the material. According to JASS 5 (2022) [2], concrete using recycled aggregate class L has a large amount of paste adhering to the aggregate, which is said to increase the length change ratio. In this study as well, RACM tended to show a greater length change ratio than NC, which was clearly observed after 8 weeks. This is considered to be caused by the effect of the water absorption of RLG. Accordingly, it is necessary to consider the application of RACM to structural members unaffected by drying shrinkage.

3.2.4 Freezing and thawing

Figure 2 shows the relationship between as-mixed air content and durability factor. According to JASS 5 (2022) [2], concrete with an air content of 4.0%–6.0% at the time of mixing is considered to possess superior resistance to freezing and thawing. For concrete subjected to severe freezing and thawing action with a target value on JASS 5, the durability factor at 300 cycles of the freezing and thawing test is required to be 60 or higher; however, under conditions where freezing and thawing action occurs within a relatively short period after placement, cements with slower hydration reaction are reported to be disadvantageous. In this study, the durability factors of NC and RACM

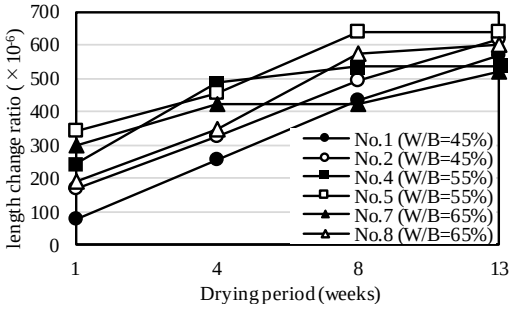

Figure 1 Length change ratio of concrete

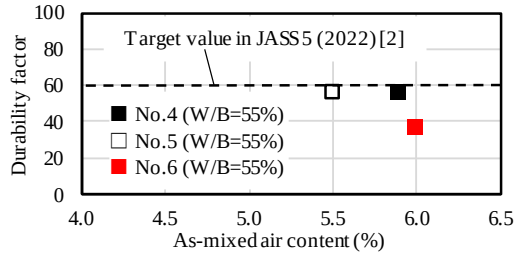

Figure 2 Relationship between as-mixed air content and durability factor

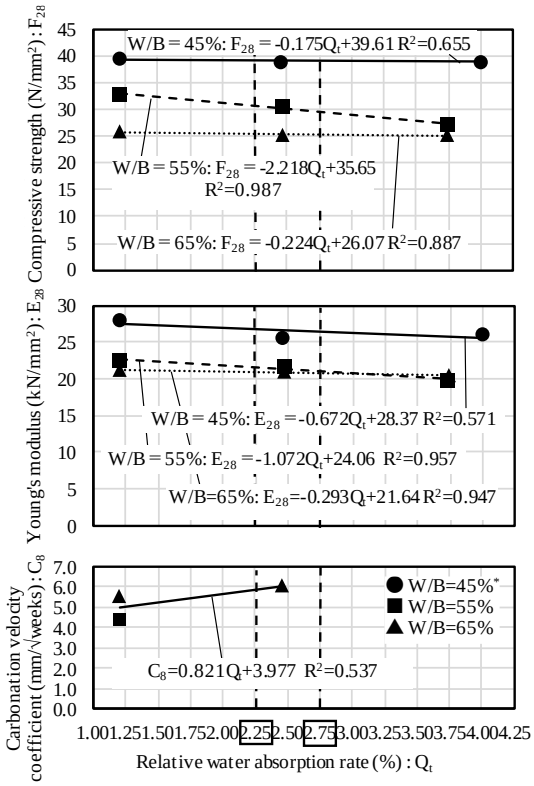

*For RACL with W/B = 45%, according to reference [1].

Figure 3 Relationship between relative water absorption rate and the main physical properties of concrete

were both 56, failing to satisfy the threshold of 60 or higher, which can be attributed partly to the use of BB. Notably, aggregates with low water absorption should be used to improve the resistance to freezing and thawing of concrete [2]. Consequently, the durability

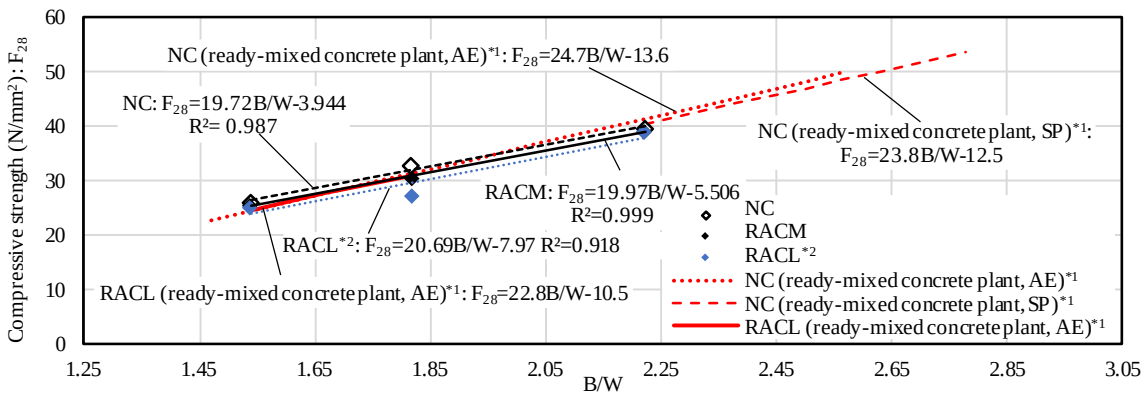

*1: This used at the ready-mixed concrete plant [1]. *2: For RACL with W/B = 45%, according to reference [1].

Figure 4 Relationship between B/W and compressive strength

factor of RACL was 36. These results suggest that the application of RACM should be limited to structural members not exposed to freezing and thawing.

3.2.5 Relative quality value method

Figure 3 shows the relationship between the relative water absorption rate of the aggregate and the main performance of concrete. The Q_t thresholds of 2.25% and 2.75% were derived from the lower limit (5.0%) and upper limit (7.0%) for the water absorption of RLG specified in JIS A 5023. A correlation was observed among compressive strength, Young's modulus, the carbonation velocity coefficient, and relative water absorption rate. In this study, the Q_t of RACM at a volumetric mixing ratio of 50% ranges from 2.45% to 2.47%, with only slight variation. Therefore, even if the water absorption of RLG varies in the JIS-specified range for RLG (5.0%–7.0%), the effect on compressive strength, Young's modulus, and the carbonation velocity coefficient is small.

Furthermore, equivalent performance can be achieved by slightly adjusting the volumetric mixing ratio during the mix proportion process.

Figure 4 shows Relationship between binder-water ratio (B/W) and compressive strength. This is a comparison between the strength calculation formula for RACM from this study with the strength calculation formula actually used at the ready-mixed concrete plant. Furthermore, the strength calculation formula used by ready-mixed concrete plant incorporates a 5% reduction in advance to account for actual manufacturing conditions. A strong correlation between compressive strength and B/W was observed for all concretes. According to Dosho et al., it has been

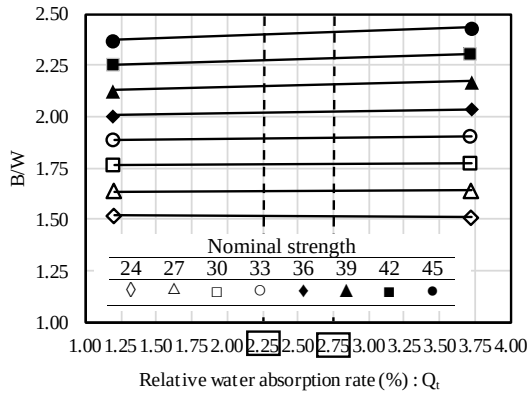

Figure 5 Relationship between relative water absorption rate and B/W

reported that, because of the effects of mixing time and mixing performance, the compressive strength observed in operational plant tests is approximately 10% lower than that observed in laboratory tests for the same mix proportion [3]. In this study as well, the laboratory test and actual plant test prediction equations exhibited similar trends and were nearly coincident.

Figure 5 shows the relationship between relative water absorption rate and B/W for NC and RACL by nominal strength. Notably, Figure 5 uses the strength calculation formula actually employed at the ready-mixed concrete plant.

Based on the relationship between the two, even if the water absorption of RLG varies within the JIS-specified range for RLG (5.0%–7.0%), RACM can be designed with a W/B equivalent to that of NC.

4. Environmental assessment

Regarding environmental performance, resource

Table 7 Environmental assessment

No.	Resource circulation*1	Low-carbon performance*2 (CO_2 reduction ratio)	Environmental safety	Note
1	▲	-	No problem	45%, BB+BFS+NC
1'	×	4%	No problem	45%, NC
2	○	4%	No problem	45%, BB+BFS+RACM
3	○	-83%	No problem	45%, BB+BFS+RACL
4	▲	14%	No problem	55%, BB+BFS+NC
4'	×	17%	No problem	55%, NC
5	○	19%	No problem	55%, BB+BFS+RACM
6	○	-43%	No problem	55%, BB+BFS+RACL
7	▲	29%	No problem	65%, BB+BFS+NC
7'	×	32%	No problem	65%, NC
8	○	32%	No problem	65%, BB+BFS+RACM
9	○	-23%	No problem	65%, BB+BFS+RACL

*1 ○: High ▲: Average ×: Low *2 CO_2 reduction ratio for No.1.

recyclability was evaluated in accordance with JASS 5 (2022) [2], and low-carbon performance was estimated. Environmental safety was assumed as the materials were intended for use in concrete. Table 7 shows the environmental evaluation results. Resource circulation improved significantly with the use of RLG and BFS. Low-carbon performance was evaluated using the CO_2 reduction ratio. Notably, No.1', 4', and 7' are comparative data cited from reference [1], and the aggregate conditions for No.1', 4', and 7' are identical to those for the corresponding No.1–9, respectively. However, they use conventional Portland cement (N) as the binder.

CO_2 emissions generally tended to decrease as the W/B increased. Furthermore, because there is no notable difference in CO_2 emissions among RACM, NC, and RACL at the same W/B, the impact of RLG is minimal.

5. Conclusions

This study investigated the optimization of mix proportion in RACM using RLG, with the aim of obtaining MLIT certification for RACM using BB.

(1) By adjusting chemical admixtures, the slump, slump flow, and air content met their respective target values. Furthermore, the chloride ion content satisfied the requirement of 0.30 kg/m^3 or less.

(2) The compressive strength of RACM was approximately 90% of that of NC, RACM exhibited Young's modulus approximately 95% of that of NC.

(3) RACM exhibited a carbonation velocity coefficient comparable to that of NC.

(4) RACM also tended to exhibit a greater length change ratio than NC.

(5) Durability factor of RACM did not meet the requirement of 60 or higher, despite the entrainment of air content.

(6) Even if fluctuations occur in the JIS-specified range for RLG owing to its water absorption, the effects on compressive strength, Young's modulus, and the carbonation velocity coefficient are minimal. Moreover, performance equivalent to NC can be ensured by slightly adjusting the volumetric mixing ratio during mix proportion.

(7) The strength estimation formula adjusted for a 5% reduction to account for ready-mixed concrete plant production conditions showed close agreement with the laboratory test estimation formula. In addition, the relationship between relative water absorption rate and B/W for each nominal strength indicates that RACM can be designed at the same W/B as NC.

(8) Regarding environmental performance, resource circulation was significantly improved by using RLG and BFS. Furthermore, CO_2 emissions of RACM were comparable to those of NC and RACL at the same W/B, confirming that the impact of RLG is minimal.

References

[1] Onoyama K. and Dosho Y., Performance of Concrete Using Recycled Aggregate Class-L Manufactured by an Actual Plant, Proceedings of the Japan Concrete Institute, 48(1) (2026) 1098-1103.

[2] Architectural Institute of Japan; Japanese Architectural Standard Specification JASS 5 Reinforced Concrete Work, 2022.

[3] Dosho Y., Ue T., Kaneko Y. and Otabe Y., Application of recycled coarse aggregate concrete based on aggregate replacing method to building structure, Proceedings of the Japan Concrete Institute, 28(1) (2006) 1493-1498.

Bond Strength Characteristics of GFRP and CFRP in Highly Alkaline Environments

金周成※1、李頭赫※2、朴善圭※3

Ju-sung, Kim, Du-Hyuk, Lee, Sun-Gyu, Park

ABSTRACT

Reinforced concrete (RC) structures suffer from durability degradation due to steel corrosion caused by environmental exposure. To overcome the limitations of conventional protection methods such as coating damage and increased dead loads Fiber Reinforced Polymer (FRP) bars, particularly Carbon FRP (CFRP) bars with high strength and excellent corrosion resistance, have emerged as promising alternatives. However, experimental studies on the bond behavior of Glass FRP (GFRP) and CFRP bars under highly alkaline environments remain limited. Since the bond between reinforcement and concrete is critical for stress transfer and overall structural performance, this study experimentally evaluates and compares the bond strength characteristics of GFRP and CFRP bars subjected to a highly alkaline environment.

1. Introduction

Reinforced concrete (RC) structures are the most widely used structural system in the construction industry because of their excellent structural performance, economic efficiency, and durability. The composite action between reinforcing steel and concrete is achieved through their strong bond, making RC structures highly reliable under external loading [1,]. When embedded in concrete, reinforcing steel is protected by a passive film formed in the highly alkaline pore solution. This stable iron oxide (FeO)-based layer suppresses electrochemical reactions and prevents the ingress of corrosive agents, thereby protecting the steel from corrosion [2]. However, long-term exposure to aggressive environments, particularly carbonation and chloride ion ingress, gradually reduces the alkalinity of concrete, resulting in passive film breakdown and the initiation of steel corrosion [3,4]. The expansion of corrosion products subsequently causes cracking and spalling of concrete, reduces the cross-sectional area of reinforcing steel, and ultimately impairs the structural durability of RC structures [5]. Conventional protection methods, such as epoxy-coated reinforcing bars and increased concrete cover, have been proposed to delay steel corrosion; however, they are limited by coating damage during transportation and construction, increased construction costs, and higher structural dead loads [6]. To overcome these limitations, fiber-reinforced polymer (FRP) bars have been extensively investigated as an alternative to conventional steel reinforcement [7,8]. Among them, carbon fiber-reinforced polymer (CFRP) bars possess approximately one-fifth the density of steel and exhibit higher tensile strength, a higher elastic modulus than glass fiber-reinforced polymer (GFRP) bars, and excellent corrosion and weather resistance, making them promising alternatives to steel reinforcement [9,10]. Nevertheless, despite the increasing interest in FRP bars, experimental studies on the bond behavior of GFRP and CFRP bars under highly alkaline environments remain limited.

The structural performance of reinforced concrete members depends primarily on the bond between reinforcement and concrete, which governs the

※1 大韓民国 牧園大学校 建築工学科 博士課程
※2 大韓民国 牧園大学校 建築工学科 学士・修士統合課程
※3 大韓民国 牧園大学校 建築学部 教授 博士(工学)

transfer of stresses under external loading[11]. Therefore, this study aims to evaluate and compare the bond strength characteristics of GFRP and CFRP bars under a highly alkaline environment through experimental investigation.

2. Experimental plan

The experimental plan of this study was designed to evaluate the bond performance of Glass Fiber-Reinforced Polymer (GFRP) and Carbon Fiber-Reinforced Polymer (CFRP) reinforcing bars after exposure to a highly alkaline environment. Concrete specimens were prepared with three distinct strength levels: high strength, normal strength, and low strength. To simulate the highly alkaline environment, a commercially available pH buffer solution with a pH of 13 was used. The GFRP and CFRP bars were immersed in the alkaline solution for 28 days and subsequently air-dried to remove any residual solution from their surfaces before being embedded in the bond test specimens. All specimens were cured at a temperature of 20°C, and the bond test specimens were fabricated in accordance with the requirements of CSA S806.

in the case of the pull-out test, the loading was continued until the free-end slip of the CFRP bar exceeded 20 mm. The maximum bond strength was determined based on the peak load recorded by the data logger connected to the load cell. For each test condition, three bond test specimens were tested, and the average value was adopted as the representative bond strength. The bond strength was calculated using Eq. (1).

$$u = \frac{P}{\pi d_b l_d}$$

u =Average bond strength
P= Load applied to the specimen
d_b =Diameter of the reinforcing bar
l_d=Embedded length of the reinforcing bar

Reference

[1] C.S. Kim, D.W. Seo, S.W. Shin, J.M. Ahn, B.S. Han, Effect of concrete strength on concrete beams reinforced with FRP bar, in: Celebrating the 60th Anniversary of the Founding of the Architectural Institute of Korea, Seoul, Republic of Korea, Architectural Institute of Korea, 2005, pp. 24–25.

[2] H.H. Kim, S.M. Jang, S.Y. Noh, Crack behavior of reinforced concrete tension member under steel corrosion, J. Archit. Inst. Korea Struct. Constr. 23(9) (2007) 99–106.

[3] D.W. Choi, S.S. Ha, C.H. Lee, Development length of GFRP rebars based on pull-out test, J. Korea Concr. Inst. 19(3) (2007) 323–331.

[4] H.Y. Moon, S.S. Kim, Effect of corrosion inhibitor for reinforcing steel in concrete containing chlorides, J. Korea Concr. Inst. 10(6) (1999) 325–333.

[5] J.M. Yang, H.O. Shin, K.H. Min, Y.S. Yoon, Flexural behavior of FRP bar reinforced HSC beams with different types of reinforcing bar and fiber, J. Korea Concr. Inst. 23(3) (2011) 273–280.

[6] R. Okelo, R.L. Yuan, Bond strength of fiber reinforced polymer rebars in normal strength concrete, J. Compos. Constr. 9(3) (2005) 203–213.

[7] A. Nanni, A. De Luca, H.J. Zadeh, Reinforced Concrete with FRP Bars: Mechanics and Design, CRC Press, Boca Raton, FL, USA, 2014, pp. 35–63.

[8] B. Benmokrane, P. Wang, T.M. Ton-That, H. Rahman, J.F. Robert, Durability of glass fiber reinforced polymer reinforcing bars in concrete environment, J. Compos. Constr. 6(3) (2002) 143–155.

[9] M. Baena, L. Torres, A. Turon, C. Barris, Experimental study of bond behaviour between concrete and FRP bars using a pull-out test, Compos. Part B Eng. 40(8) (2009) 784–797.

[10] B. Benmokrane, C. Nazair, M.A. Loranger, A. Manalo, A field durability study of vinylester-based GFRP rebars in concrete bridge barriers, J. Bridge Eng. 23(12) (2018) 04018094.

[11] S.J. Park, T.S. Kang, D.Y. Moon, A study on the flexural minimum reinforcement for prevention of brittle failure specified in KCI and EN codes, J. Korea Concr. Inst. 26(2) (2014) 211–218.

エポキシ樹脂系塗り床を対象とした微細な表面凹凸と諸性能の関係

Relations between Surface Asperities and Various Performances in Epoxy Resin Floors

峯岸佑守※1，福田眞太郎※2
Yuma Minegishi，Shintaro Fukuda

ABSTRACT

Epoxy resin floors are required to provide various performances, including slipperiness and susceptibility to graze, which are related to daily safety, as well as gloss, which is related to aesthetics. Slipperiness and susceptibility to graze, as well as slipperiness and gloss, are considered to be conflicting performances that are difficult to achieve simultaneously; however, all of these performances are considered to be influenced by surface asperities of the floor. Therefore, this study aimed to elucidate the mechanisms by which surface asperities influence each performance of epoxy resin floors. The results revealed the wavelength ranges of surface asperities that affect each performance and demonstrated that the influential wavelength ranges differ depending on the performance. These findings provide fundamental knowledge for the development of flooring materials that achieve a well-balanced combination of multiple performances.

1. Introduction

Floors are the building components that come into contact with people most frequently and, as such, are required to satisfy a wide range of performance requirements. Appropriate measurement methods for many of these performances are specified in the Architectural Institute of Japan Guidelines for Floor Performance Evaluation [1] and the Japanese Industrial Standards (JIS). Among these methods, those applicable regardless of floor material or construction method tend to be relatively complex; however, they are widely used by building designers and owners to compare and select among different types of flooring.

On the other hand, for manufacturers aiming to develop floors that achieve a well-balanced combination of multiple performances within a specific flooring material, methods that enable the simple assessment of multiple performances are preferable to those requiring complex procedures to evaluate individual performances. For example, in Japan, epoxy resin floors used in facilities such as factories and swimming pools are required to satisfy multiple performances, such as slipperiness and susceptibility to graze caused by contact with the floor, which are related to daily safety, as well as gloss, which is related to aesthetics. However, slipperiness and susceptibility to graze, as well as slipperiness and gloss, are generally considered to be conflicting performances, and achieving both simultaneously is considered difficult.

Here, all of these performances are considered to be influenced by surface asperities of the floor. Therefore, clarifying which characteristics of surface asperities affect each performance would provide a method for easily assessing performance and offer clues for achieving a balance among performances that are considered difficult to reconcile.

Accordingly, this study aimed to elucidate the

※1 東京科学大学 環境・社会理工学院 建築学系 修士課程
※2 東京科学大学 環境・社会理工学院 建築学系 准教授 博士（工学）

mechanisms by which surface asperities influence each performance of epoxy resin floors, and this paper reports the process and results of the investigation.

2. Overview of Test Specimens

The test specimens consisted of 29 types of epoxy resin floors with various surface asperities, each applied to 3-mm-thick flexible panels. Specifically, the test specimens comprised six smooth specimens (hereinafter referred to as "Smooth"), 19 anti-slip specimens with surface asperities formed by incorporating aggregates of different particle sizes (hereinafter referred to as "Anti-Slip"), two specimens with surface asperities created without aggregates (hereinafter referred to as "Textured"), and two smooth specimens coated with PP resin wax (hereinafter referred to as "Wax").

3. Measurement and Analysis of Surface Asperities

Surface asperities were measured using an Auto-Scan 3D sensor (KEYENCE LJ-S8000). For each test specimen, 10 profile curves, each 25.6 mm long and spaced 7.5 mm intervals, were acquired. Figure 1(1) shows examples of profile curves.

The profile curves were analyzed using the fast Fourier transform (FFT) to determine the asperity amplitudes corresponding to wavelengths λ ranging from 0.025 to 12.8 mm. The asperity amplitude spectrum for each test specimen was obtained by averaging the asperity amplitudes from the 10 profile curves. Figure 1(2) shows examples of asperity amplitude spectra. The asperity amplitude at wavelength λ [mm] is denoted by $f_{(\lambda)}$ [μm]. Since surface asperities in the relatively short wavelength range were expected to have a greater influence on the performance indices investigated in this study, the asperity amplitudes and wavelengths were converted to logarithmic scales to account for the Weber−Fechner law. Specifically, the asperity amplitudes were converted to $g_{(\lambda)}$ [dB] using Equation (1), and the wavelengths were converted to $h_{(\lambda)}$ [dB] using Equation (2) for the subsequent analyses.

$$g_{(\lambda)} = 10\log_{10}\{f_{(\lambda)}/10^{-3}\} \quad \cdots (1)$$

$$h_{(\lambda)} = 10\log_{10}\lambda \quad \cdots (2)$$

The reference values for the asperity amplitude and wavelength were set to 0.001 μm and 1.0 mm, respectively. Figure 1(3) shows examples of asperity amplitude spectra converted to $g_{(\lambda)}$ and $h_{(\lambda)}$.

4. Measurement of Various Performances

4.1 Slipperiness

Slipperiness was measured using ONO-YOSHIOKA・PULL SLIP METER (O-Y・PSM) developed by Ono et al. [2]-[5], to determine the

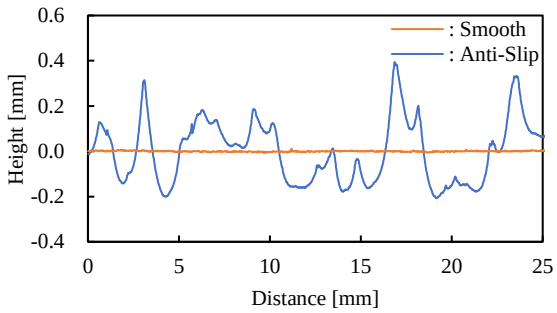

(1) Examples of profile curves

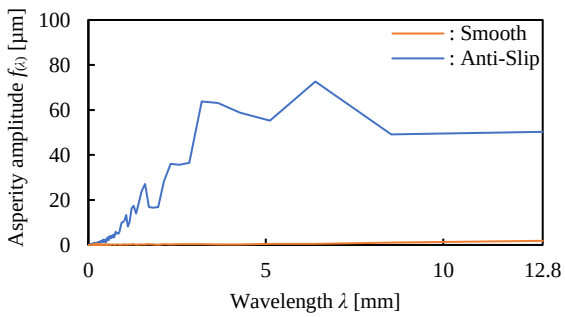

(2) Examples of asperity amplitude spectra

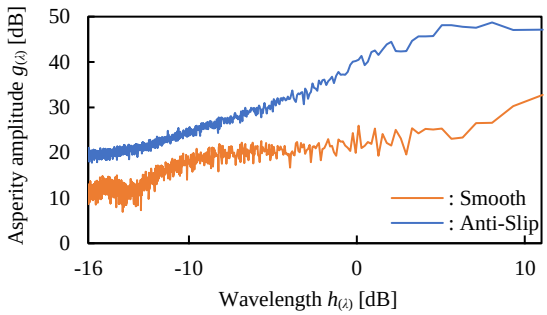

(3) Examples of asperity amplitude spectra Converted to $g_{(\lambda)}$ and $h_{(\lambda)}$

Fig.1 Examples measurement and analysis of surface asperities

Coefficient of Slip Resistance (*C.S.R*). Photo 1 shows an overview of the O-Y・PSM. This device reproduces the foot condition during the push-off phase of human gait, which is considered to influence slipping. Specifically, a slider subjected to a vertical load of 80 kgf by a counterweight is pulled diagonally upward at an angle of 18° to the horizontal at a specified loading rate of 80 kgf/s. *C.S.R* is calculated by dividing the maximum tensile load measured until slipping occurs by the vertical load.

The slider simulates the sole of a human foot. By applying materials specified in JIS A 1454 [6] or actual shoe sole materials, slipperiness can be measured under conditions simulating various types of footwear or barefoot walking. Furthermore, by sprinkling intervening substances standardized by Ono et al. [7] onto the surface of the test specimen, conditions in which substances such as dust, sand, or water are present between the sole and the floor surface can be replicated.

The slipperiness measurement conditions described in this study were established based on typical use conditions for epoxy resin floors. Assuming that footwear was worn, two types of slider materials were used: a rubber sheet simulating a hard-soled men's dress shoe (Shore A hardness: 72-80; thickness: 3-6 mm; hereinafter referred to as "Hard-Soled Shoes") and an athletic shoe sole (Shore A hardness: 30-35; hereinafter referred to as "Athletic Shoes"). The floor surface condition was set to either "cleaned and dry" (hereinafter referred to as "Cleaned") or "covered with water and dust" (hereinafter referred to as "Muddy Water"), resulting in a total of four test conditions.

In addition, assuming barefoot walking, two test conditions were established. Under the "Cleaned" condition, Coefficient of Slip Resistance with Bare Feet (*C.S.R・BF*) [8] was measured using a foam rubber slider (Shore A hardness: 18-20; thickness: 10 mm). Under the water-covered condition, the Coefficient of Slip Resistance of Bathroom floor (*C.S.R・B*) [9],[10] was measured using a textured rubber sheet (Shore A hardness: 75; thickness: 6.5 mm) as the slider.

Furthermore, it has been established that *C.S.R* corresponds well to subjective evaluations of slip resistance by human subjects; a higher *C.S.R* indicates that the floor is less slippery.

4.2 Susceptibility to Graze Caused by Contact with the Floor

The susceptibility to graze caused by contact with the floor was evaluated using a modified O-Y・PSM based on the measurement method proposed by Ono et al. [11]. A foam rubber sheet (Shore A hardness: 35; thickness: 3 mm) was attached to a slider subjected to a vertical load of 40 kgf. The tensile load was measured after applying baby powder at a density of 2 g/m² to the specimen surface. The susceptibility to graze was expressed as the maximum tensile load, *G* [kgf]; a higher value of *G* indicates greater susceptibility to graze.

4.3 Gloss

Gloss was measured in accordance with JIS Z 8741 [12] using a gloss meter (KONICA MINORUTA GM-268) at an incident angle of 60°.

Photo 1 O-Y・PSM

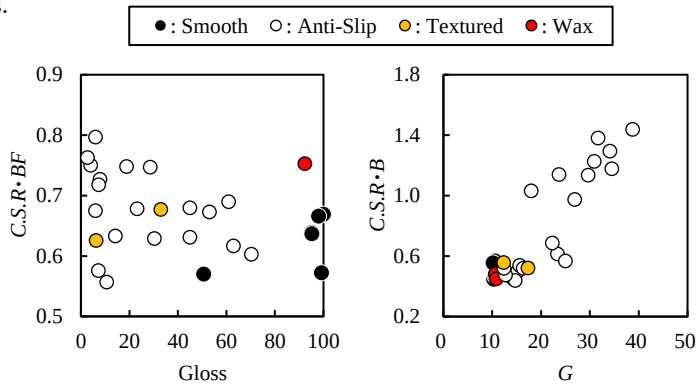

(1) *C.S.R・BF* and Gloss **(2) *C.S.R・B* and *G***

Fig.2 Examples of relationship between performances

4.4 Relationships between the Two Performances

Figure 2 shows examples of the relationships among the measured performances. As shown in Figure 2(1), some combinations showed no correlation between the two performances, whereas Figure 2(2) shows combinations in which a general correlation was observed, although the order of some plots was reversed. The relationships among other performances not shown in the figure were similar to these examples. In other words, no combination was identified in which the various performances measured in this study were perfectly consistent with each other. This suggests that different wavelength ranges of surface asperities influence each performance.

5. Investigation of the Relationship between Surface Asperities and Performance

The relationship between the asperity amplitude spectrum obtained in Section 3 and the performance measurements described in Section 4 was investigated. From the asperity amplitude spectrum, $R_{a\text{-}b}$, which represents the magnitude of asperities within the wavelength range of *a*-*b* mm, was calculated using Equation (3). The relationships between the measured performances and $R_{a\text{-}b}$ were then examined by varying a and b, each in increments of $10^{n/4}$ mm.

$$R_{a-b} = \int_a^b \frac{g_{(\lambda)}}{h_{(b)}-h_{(a)}} d\lambda \qquad \cdot\cdot\cdot (3)$$

As a result of the analysis, clear correlations between the measured performances and the corresponding $R_{a\text{-}b}$ values, regardless of the classification of test specimen, were identified for *C.S.R*(Hard-Soled Shoes, Muddy Water), *C.S.R*(Athletic Shoes, Muddy Water), *C.S.R*・*B*, and *G*. The results are shown in Figure 3(1)-(4).

For *C.S.R*(Hard-Soled Shoes, Muddy Water), shown in Figure 3(1), $R_{3.2\text{-}12.8}$ exhibited the highest correlation. In other words, surface asperities with wavelengths in the range of 3.2-

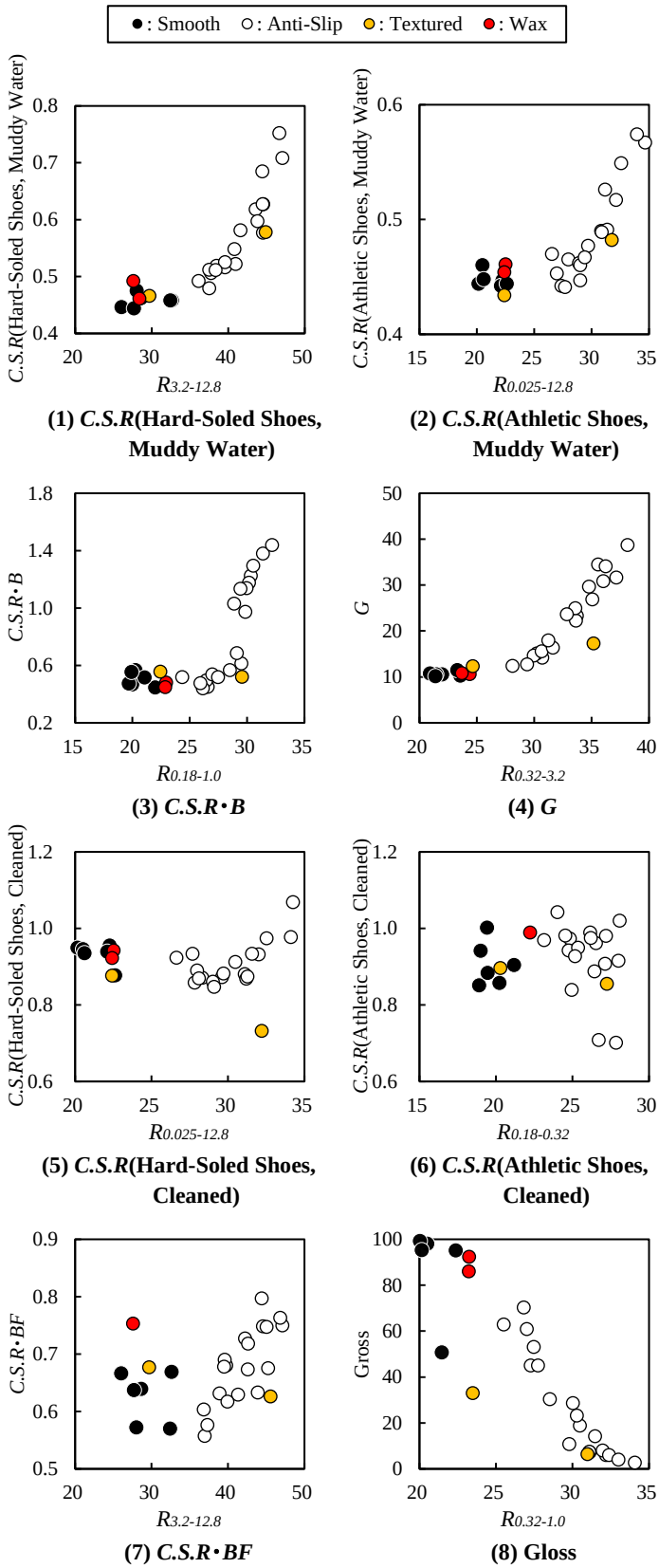

Fig.3 Relationship between performance and $R_{a\text{-}b}$

12.8 mm strongly influence slipperiness. This is presumed to be because the water and dust applied during the muddy water slip test penetrate into depressions with relatively large wavelengths, thereby reducing the influence of the intervening substances on slipperiness.

For *C.S.R*(Athletic Shoes, Muddy Water), shown in Figure 3(2), $R_{0.025\text{-}12.8}$ exhibited the highest correlation, indicating that surface asperities across the entire wavelength range analyzed in this study influence slipperiness. Although the mechanism is basically the same as that for *C.S.R*(Hard-Soled Shoes, Muddy Water), the athletic shoe sole is softer and has a more uneven surface than the slider used for Hard-Soled Shoes. Therefore, it is presumed that relatively short-wavelength surface asperities also influence slipperiness because the softer athletic shoe sole deforms and penetrates into the surface asperities.

For *C.S.R・B*, shown in Figure 3(3), $R_{0.18\text{-}1.0}$ exhibited the highest correlation, indicating that surface asperities with intermediate wavelengths in the range of 0.18-1.0 mm influence slipperiness.

For *G*, shown in Figure 3(4), $R_{0.32\text{-}3.2}$ exhibited the highest correlation, indicating that surface asperities with relatively longer wavelengths ranging from 0.32-3.2 mm influence the susceptibility to graze.

Furthermore, for *C.S.R*(Hard-Soled Shoes, Cleaned), *C.S.R*(Athletic Shoes, Cleaned), *C.S.R・BF*, and gloss, various analyses revealed that appropriate $R_{a\text{-}b}$ values exhibiting correlations with the respective performances could generally be identified, except for some plots indicated by ●, ●, and ●. The results are shown in Figure 3(5)-(8). Since wavelength ranges outside those analyzed in this study may also influence these performances, the analysis range will be expanded and further investigations will be conducted in the future.

6. Conclusions

We investigated the relationship between fine surface asperities and various performances of epoxy resin floors and identified the wavelength ranges of surface asperities that influence slipperiness and susceptibility to graze. These findings will contribute to the development of floor coatings that achieve a good balance among multiple performances that have previously been considered incompatible.

Although this study focused on epoxy resin floors, similar investigations will be conducted on other flooring materials in future studies.

Acknowledgement

The authors would like to thank the members of the Technical Committee of the Japan Coating Floor Industry Association for providing the test specimens.

Reference

[1] Architectural Institute of Japan: Guidelines for Floor Performance Evaluation, 2015.11

[2] Hidenori Ono et al.: Study on the Slipperiness of Building Floors and it's Evaluating Method, Methodology of Study and the Scaling of Human Sense on Slipperiness Part1, Journal of Structural and Construction Engineering (Transactions of the Architectural Institute of Japan), No.321, pp.1-8, 1982.11

[3] Hidenori Ono: Study on the Slipperiness of Building Floors and it's Evaluating Method, Accumulation of Data for the Design, Development and Conceptualization of a New Slipperiness Tester Part2, Journal of Structural and Construction Engineering (Transactions of the Architectural Institute of Japan), No.333, pp.1-7, 1983.11

[4] Hidenori Ono et al.: Study on the Slipperiness of Building Floors and it's Evaluating Method, Design and Development of a New Slipperiness Tester Part3, Journal of Structural and Construction Engineering (Transactions of the Architectural Institute of Japan), No.346, pp.1-8, 1984.12

[5] Hidenori Ono et al.: Study on the Slipperiness of Building Floors and it's Evaluating Method, Evaluation Method of the Slipperiness of Building Floors Part4, Journal of Structural and Construction Engineering (Transactions of the Architectural Institute of Japan), No.356, pp.1-8, 1985.10

[6] Japanese Industrial Standards Committee: JIS A 1454: Test Methods-Resilient Floorcoverings, 2016

[7] Hidenori Ono et al.: Standardization of Substances Adhered to Floor Surfaces for Evaluating Slip Resistance of Floors, Journal of Structural and

Construction Engineering (Transactions of AIJ), No.450, pp.7-14, 1993.8

[8] Hidenori Ono, Noboru Ochiai: Study on the Evaluation Method of Slipperiness of Floors with Bare Feet, Journal of Structural and Construction Engineering (Transactions of AIJ), No.537, pp.21-26, 2000.11

[9] Hidenori Ono et al.: Study on the Evaluation Method of Slipperiness of Bathroom Floors and Bathtub Bottoms from a Viewpoint of safety, Study on the Measuring Method of Slip Resistance and the Relation between the Easiness to Cross the Bathtub's Edge and its Sectional Proportion Part1, Journal of Structural and Construction Engineering (Transactions of the Architectural Institute of Japan), No.384, pp.26-33, 1988.2

[10] Hidenori Ono et al.: Study on the Evaluation Method of Slipperiness of Bathroom Floors and Bathtub Bottoms from a Viewpoint of safety, Presentation of the Evaluating Indexes and the Evaluating Method of Slipperiness of Bathroom Floors and Bathtub Bottoms Part2, Journal of Structural and Construction Engineering (Transactions of the Architectural Institute of Japan), No.387, pp.1-7, 1988.5

[11] Hidenori Ono et al.: A Study on a Method for Evaluating the Roughness of Floors from a Viewpoint of the Graze and Pain Caused by Contact with the Floor, Journal of Structural and Construction Engineering (Transactions of the Architectural Institute of Japan), No.392, pp.10-17, 1988.10

[12] Japanese Industrial Standards Committee: JIS Z 8741: Specular Glossiness-Methods of Measurement, 1997

Analysis of Radiation Shielding Properties of Concrete Incorporating Heavyweight Aggregates

Min-Jeong Ko※1, Jeong-Soo Nam※2, Yae-Chan Lee※3, Jeong-Taek Lee※3, Yong-Joon Kim※1, Thinh phat Nguyen※1, Gyu-Yong Kim※2

ABSTRACT

Recent advances in nuclear power generation, medical radiation, radioactive waste management, and nuclear fusion technologies have increased the demand for concrete with both structural performance and radiation shielding capability. This study developed radiation shielding concrete incorporating hematite and boron carbide (B_4C) and evaluated its mechanical and shielding properties. Hematite was selected as the heavyweight aggregate due to its high density. The concrete achieved a density of 3,687 kg/m³ and a 28-day compressive strength of 46.8 MPa, satisfying the target performance. Compared with conventional concrete, the gamma-ray penetration ratio decreased by approximately 30%, while the fast and thermal neutron penetration ratios decreased by approximately 17 ~ 23% and 51%, respectively. These results demonstrate that concrete incorporating hematite and boron carbide provides excellent mechanical performance and effective radiation shielding, indicating its applicability to radiation shielding structure.

1. Introduction

Recent advances in nuclear power generation, medical radiation, radioactive waste management, and nuclear fusion technologies have increased the demand for ensuring the safety and reliability of radiation shielding structures [1]. In particular, facilities such as nuclear power plants and radiation therapy centers require adequate shielding performance to protect workers and the surrounding environment from radiation exposure, while maintaining sufficient structural strength and durability. Radiation is emitted in the form of energetic particles or electromagnetic waves, and, as shown in Figure 1, its interaction with matter and penetration characteristics vary depending on the type of radiation [2]. Since each type of radiation exhibits different penetration capabilities and biological effects, appropriate shielding materials should be selected according to the characteristics of the radiation.

Conventional radiation shielding structures have generally achieved shielding performance by increasing the thickness of concrete walls. However, this approach results in several disadvantages, including increased self-weight, higher construction costs, and reduced space utilization. As an alternative, considerable attention has been given to radiation shielding concrete incorporating heavyweight aggregates, which enhance gamma-ray shielding performance by increasing the unit weight of concrete. In particular, heavyweight aggregates such as hematite, magnetite, and barite possess high density and high atomic numbers, making them effective in improving gamma-ray attenuation.

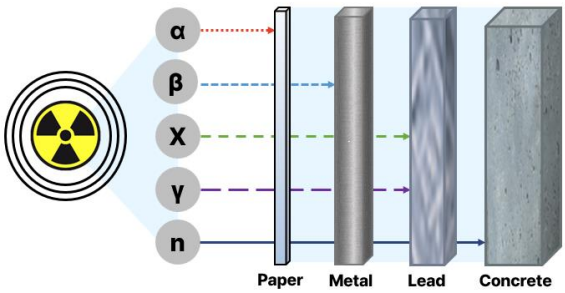

Figure 1 Concrete Density as a function of aggregate-to-binder ratio.

※1 Master's Course, Dept. of Architectural Engineering, Chungnam National University, Korea
※2 Prof., Dept. of Architectural Engineering, Chungnam National University, Korea
※3 Ph.D. Course, Dept. of Architectural Engineering, Chungnam National University, Korea

Gamma-ray shielding performance is governed by the Beer–Lambert law and is strongly influenced by the linear attenuation coefficient, which is proportional to the density of the shielding material. Consequently, the transmission of gamma rays decreases as the density of concrete increases [3]. In contrast, neutron shielding cannot be achieved simply by increasing material density. As shown in Figure 2 Fast neutrons must first be moderated to thermal neutrons before being absorbed; therefore, both neutron moderation and absorption mechanisms should be considered in shielding design [4, 5]. Boron (B), which possesses a high thermal neutron absorption cross-section, is widely used as a neutron-absorbing material. Among boron-based materials, boron carbide (B_4C) has attracted considerable attention owing to its excellent neutron absorption capability and chemical stability, making it a suitable additive for radiation shielding concrete.

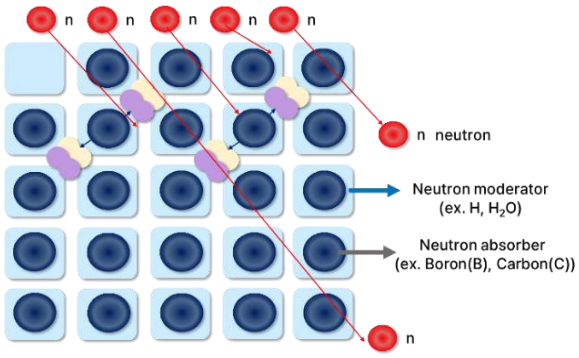

Figure 2 Neutron shielding mechanism.

Accordingly, this study compared the densities of various heavyweight aggregates to identify the most suitable aggregate for radiation shielding concrete. Based on the comparison, radiation shielding concrete incorporating hematite as the heavyweight aggregate and boron carbide (B_4C) as a neutron absorber was developed. The density, compressive strength, and shielding performance against gamma rays, fast neutrons, and thermal neutrons were evaluated to investigate its applicability as a radiation shielding material.

2. Experimental Program

2.1 Mix Design

In this study, the type of heavyweight aggregate and the aggregate-to-binder (A/B) ratio were selected as the main experimental variables. Five types of heavyweight aggregates applicable to radiation shielding concrete were considered: hematite, magnetite, oxidized slag, copper slag, and ferro-nickel slag. Since the density of aggregates is a key parameter affecting both the unit weight of concrete and its gamma-ray shielding performance, the aggregate densities were measured in accordance with KS F 2510 [6].

The measured densities of the aggregates showed that hematite exhibited the highest density of approximately 4.8 g/cm³, followed by magnetite at approximately 4.5 g/cm³. In contrast, oxidized slag, copper slag, and ferro-nickel slag exhibited relatively lower densities of approximately 3.5, 3.4, and 3.1 g/cm³, respectively. Furthermore, as shown in Figure 3, the density of concrete increased with increasing aggregate-to-binder ratio for all aggregate types. Among the investigated aggregates, hematite achieved the target concrete density even at relatively low aggregate-to-binder ratios. Therefore, hematite was selected as the heavyweight aggregate for the radiation shielding concrete used in this study. The target performance of the concrete was established considering its application as a radiation shielding material, with a target density of 3,600 kg/m³ or greater and a 28-day compressive strength of 43.5

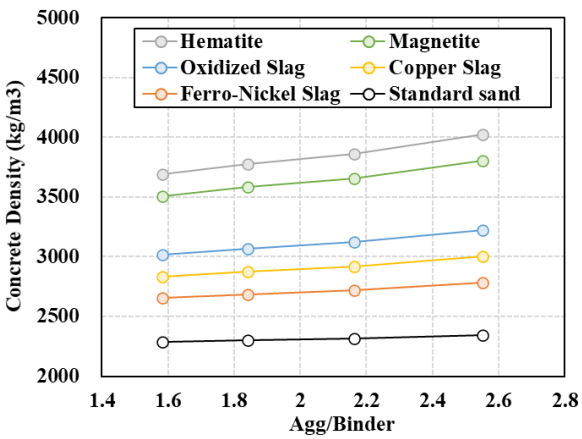

Figure 3 Concrete Density as a function of aggregate-to-binder ratio.

MPa or greater.

The water-to-binder ratio was fixed at 0.28, and the total binder content was 600 kg/m³. Ordinary Portland cement, ground granulated blast-furnace slag, and fly ash were used as binder materials. The aggregate-to-binder ratio and fine aggregate ratio were set to 1.63 and 45%, respectively. To enhance neutron shielding performance, 0.3 wt.% boron carbide (B_4C), based on the total weight of concrete, was incorporated into the mixture. Boron carbide was added to improve thermal neutron shielding while maintaining the gamma-ray shielding performance provided by the heavyweight aggregate. The final mix proportions are presented in Table 1.

Table 1 mix proportions of heavyweight concrete

W/B	A/B[1)]	S/a [%]	Unit Weight (kg/m³)					
			W	C	GGBS	FA	S	G
0.28	1.63	45	168	153	24	27	1314	1606

1) A/B: Aggregate to Binder ratio

2.2 Experimental Methods

The mechanical properties of the concrete were evaluated in terms of density and compressive strength. The concrete density was measured in accordance with KS F 2409 [7], Standard Test Method for Unit Weight of Fresh Concrete, using cylindrical specimens with dimensions of Ø 100 × 200 mm. The unit weight of the concrete was determined based on the measured mass and specimen volume.

Compressive strength tests were conducted in accordance with KS F 2405 [8], Standard Test Method for Compressive Strength of Concrete, using Ø 100 × 200 mm cylindrical specimens at curing ages of 3, 7, and 28 days. Three specimens were tested for each curing age, and the average value was adopted as the representative compressive strength.

The radiation shielding performance was evaluated against gamma rays, fast neutrons, and thermal neutrons. Gamma-ray shielding tests were performed

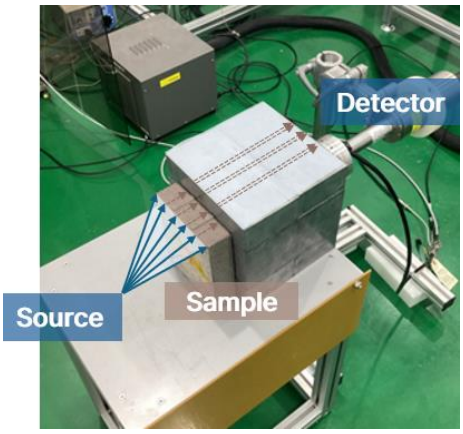

(a) Gamma-ray

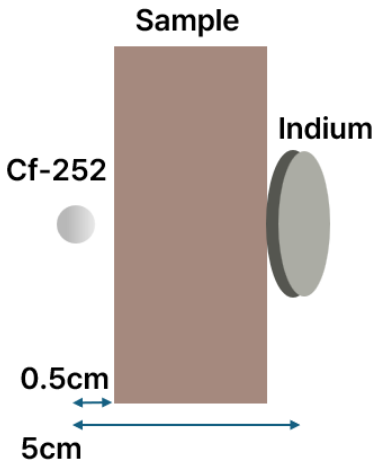

(b) Fast neutron

(c) Thermal neutron

Figure 4 Gamma-ray penetration of normal and heavyweight concrete.

using 200 × 200 × 50 mm specimens. Four gamma-ray sources, Co-60, Cs-137, Na-22, and Eu-152, covering an energy range of approximately 0.3 ~ 1.6 MeV, were employed. The gamma-ray penetration ratio was calculated as the ratio of the net peak count measured after transmission through the specimen to that measured without the specimen.

The fast neutron shielding performance was

evaluated for using a Cf-252 neutron source. Indium-115 neutron activation analysis (NAA) was employed to determine the transmitted neutron intensity. The fast neutron penetration ratio was calculated by comparing the net counts measured with and without the specimen.

Thermal neutron shielding performance was evaluated using a Cf-252 neutron source equipped with a high-density polyethylene (HDPE) moderator.

Thermal neutron penetration ratios were determined by comparing the measured neutron counts obtained with and without the specimens. All radiation shielding tests were conducted under identical experimental conditions, and a schematic illustration of the test setup is presented in Figure 4.

3. Results and Discussion

3.1 Mechanical Properties

The density of the radiation shielding concrete incorporating hematite was measured to be 3,687 kg/m³, satisfying the target density of 3,600 kg/m³ established in this study. This value is approximately 50% higher than that of conventional concrete (approximately 2,300 ~ 2,400 kg/m³), indicating that the high density of hematite (approximately 4.8 g/cm³) contributed significantly to increasing the unit weight of the concrete. These results demonstrate that hematite is an appropriate heavyweight aggregate for radiation shielding concrete.

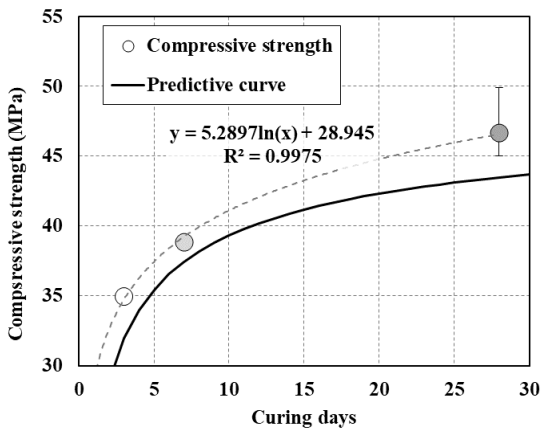

Figure 5 Compressive Strength Development with Curing Age.

Figure 5 presents the development of compressive strength with curing age. The compressive strengths at 3, 7, and 28 days were 35.0 MPa, 38.9 MPa, and 46.8 MPa, respectively, showing continuous strength development with increasing curing age. In particular, the 28-day compressive strength exceeded the target value of 43.5 MPa, indicating that the developed concrete satisfies the mechanical strength requirements for structural radiation shielding applications. This strength development is attributed to the continued hydration of cement, which increased the amount of hydration products and resulted in a denser interfacial transition zone (ITZ) between the cement paste and hematite aggregates, thereby improving load transfer within the concrete [9].

3.2 Radiation Shielding Performance

Figure 6 compares the gamma-ray penetration ratios of conventional concrete and the radiation shielding concrete incorporating hematite. The radiation shielding concrete exhibited lower penetration ratios than conventional concrete over the entire gamma-ray energy range, with an average reduction of approximately 30%. This improvement is attributed to the increased linear attenuation coefficient of the concrete resulting from the high density and iron (Fe) content of the hematite aggregate. These results demonstrate that replacing conventional aggregates with hematite effectively enhances the gamma-ray shielding performance of

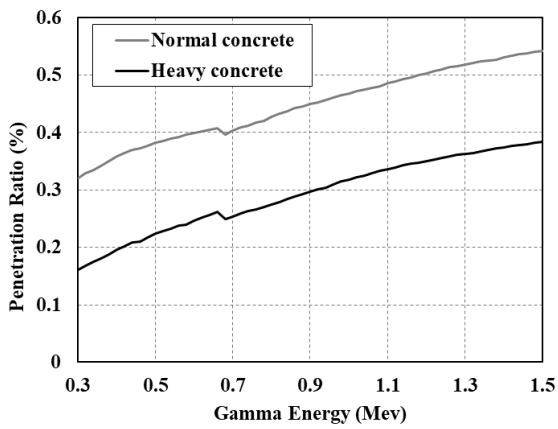

Figure 6 Gamma-ray penetration of normal and heavyweight concrete

concrete [10,11]. Furthermore, comparison with the MCNP simulation as shown in Figure 7, indicated that the difference between the experimental and simulated values was within 3% for most energy levels, confirming the reliability of the experimental results.

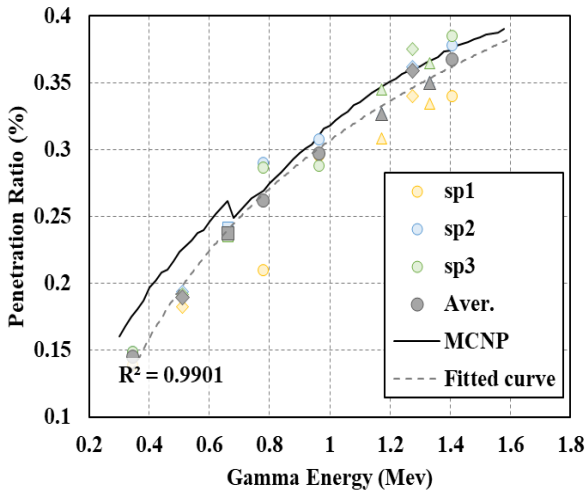

Figure 7 Comparison of experimental data and MCNP simulated gamma-ray penetration curves.

The results of the fast neutron shielding test are summarized in Table 2. The fast neutron penetration ratios of the radiation shielding concrete ranged from 47.7% to 54.1%, representing a reduction of approximately 17 ~ 23% compared with that of conventional concrete (71.1%). This improvement is attributed to the increased frequency of neutron–material interactions resulting from the higher concrete density, which promoted energy loss through elastic scattering. In addition, three specimens prepared using the same mixture proportions, exhibited similar penetration ratios, indicating good reproducibility of the experimental results [12].

The results of the thermal neutron shielding test are

Table 2 Net count and experimental penetration ratio of fast neutrons

	No Sp	Normal	Sp 1	Sp 2	Sp 3
Net count	7,562	5,377	3,610	3,893	4,094
Ratio (%)	100.0	71.1	47.7	51.5	54.1

Table 3 Net count and experimental penetration ratio of thermal neutrons

	No Sp	Normal	Sp 1	Sp 2	Sp 3
Net count	280,383	231,316	87,578	88,864	87,544
Ratio (%)	100.0	82.5	31.2	31.6	31.2

presented in Table 3. The thermal neutron penetration ratio of the radiation shielding concrete was approximately 31% for all specimens, representing a reduction of about 51% compared with that of conventional concrete (82.5%). Although heavyweight aggregates improve gamma-ray shielding performance by increasing the density of concrete, their ability to absorb thermal neutrons is limited. Therefore, 0.3 wt.% boron carbide (B_4C), based on the total weight of concrete, was incorporated to utilize the high thermal neutron absorption cross-section of boron (B) [13-15]. Consequently, the superior shielding performance of the developed concrete can be attributed to the combined effects of the increased density provided by hematite, which enhanced gamma-ray and fast neutron shielding, and the neutron absorption capability of boron carbide, which significantly improved thermal neutron shielding.

4. Conclusions

In this study, the mechanical properties and radiation shielding performance of concrete incorporating hematite and boron carbide (B_4C) were evaluated. Based on the experimental results, the following conclusions can be drawn:

1) The radiation shielding concrete incorporating hematite achieved an average density of 3,687 kg/m³, satisfying the target density of 3,600 kg/m³. These results confirm that hematite is an effective heavyweight aggregate for radiation shielding concrete.
2) The compressive strengths at curing ages of 3, 7, and 28 days were 35.0 MPa, 38.9 MPa, and 46.8 MPa, respectively, demonstrating

continuous strength development with increasing curing age. The 28-day

3) compressive strength exceeded the target value of 43.5 MPa, indicating that the developed concrete provides sufficient mechanical performance for structural radiation shielding applications.

4) In the gamma-ray shielding test, the developed concrete exhibited an average reduction in the penetration ratio of approximately 30% compared with conventional concrete. This improvement is attributed to the increased linear attenuation coefficient resulting from the high density and iron (Fe) content of the hematite aggregate.

5) In the fast neutron shielding test, the penetration ratio decreased by approximately 17 ~ 23% compared with conventional concrete, while the thermal neutron penetration ratio decreased by approximately 51%. In particular, the incorporation of boron carbide (B_4C) significantly enhanced the thermal neutron absorption performance of the concrete.

Reference

[1] Y. Maki, H. Ohnuma, Application of concrete to the treatment and disposal of radioactive waste in Japan, Nucl. Eng. Des. 138 (2) (1992) 179–188.

[2] K. Gunoglu, I. Akkurt, Radiation shielding properties of concrete containing magnetite, Prog. Nucl. Energy 137 (2021) 103776.

[3] H.O. Tekin, E. Kavaz, E.E. Altunsoy, O. Kilicoglu, O. Agar, T.T. Erguzel, M.I. Sayyed, An extensive investigation on gamma-ray and neutron attenuation parameters of cobalt oxide and nickel oxide substituted bioactive glasses, Ceram. Int. 45 (8) (2019) 9934‑9940.

[4] M.K.A. Roslan, M. Ismail, A.B.H. Kueh, M.R.M. Zin, High-density concrete: Exploring ferro boron effects in neutron and gamma radiation shielding, Constr. Build. Mater. 215 (2019) 718–725.

[5] N. Ahmad, M.I. Idris, A. Hussin, J. Abdul Karim, N.M. Azreen, R. Zainon, Enhancing shielding efficiency of ordinary and barite concrete in radiation shielding utilizations, Sci. Rep. 14 (2024) 10893.

[6] Korean Agency for Technology and Standards (KATS), KS F 2510: Standard Test Method for Density and Absorption of Aggregates, Korea, 2022.

[7] Korean Agency for Technology and Standards (KATS), KS F 2409: Standard Test Method for Unit Weight of Fresh Concrete, Korea, 2022.

[8] Korean Agency for Technology and Standards (KATS), KS F 2405: Standard Test Method for Compressive Strength of Concrete, Korea, 2022.

[9] T. Daungwilailuk, C. Yenchai, W. Rungjaroenkiti, P. Pheinsusom, C. Panwisawas, W. Pansuk, Use of barite concrete for radiation shielding against gamma-rays and neutrons, Constr. Build. Mater. 326 (2022) 126838.

[10] I.I. Bashter, Calculation of radiation attenuation coefficients for shielding concretes, Ann. Nucl. Energy 24 (17) (1997) 1389–1401.

[11] M. Gharieb, Y.A. Mosleh, M. Alwetaishi, E.E. Hussein, M.E. Sultan, Effect of using heavy aggregates on the high performance concrete used in nuclear facilities, Constr. Build. Mater. 310 (2021) 125224.

[12] O. Gencel, Physical and mechanical properties of concrete containing hematite as aggregates, Phys. Sci. 66 (2011) 184–191.

[13] T. Piotrowski, M. Mazgaj, A. Żak, J. Skubalski, Importance of atomic composition and moisture content of cement-based composites in neutron radiation shielding, Procedia Eng. 108 (2015) 616–623.

[14] B. Aygün, Neutron and gamma radiation shielding properties of high-temperature-resistant heavy concretes including chromite and wolframite, J. Radiat. Res. Appl. Sci. 12 (1) (2019) 428–434.

[15] M. Gharieb, Y.A. Mosleh, M. Alwetaishi, E.E. Hussein, M.E. Sultan, Effect of using heavy aggregates on the high performance concrete used in nuclear facilities, Constr. Build. Mater. 310 (2021) 125224.

Influence of external mixing on the hydration process and compressive strength in fly-ash blended concrete. An Investigation Using Limestone Powder

Thinh-Phat Nguyen※1, Gyu-Yong Kim※2, Ha-Min Eu※3, Jeong-Taek Lee※4,
Yong-Joon Kim※1, Candra Pebrian※1, Jeong-Soo Nam※2

ABSTRACT

This study investigated the effects of adding limestone powder to fly ash-based concrete through thermal and mechanical experiments, specifically measuring hydration heat evolution and compressive strength at early and later ages. Laboratory-scale experiments were conducted to determine the optimal dosage of limestone powder required to enhance the early-age compressive strength of the concrete. Additionally, fly ash was utilized to partially replace Portland cement to control the internal temperature of the concrete under high ambient temperatures. Furthermore, mock-up tests were executed in three countries—namely South Korea, Vietnam, and Japan—to investigate the influence of externally mixed materials and varying weather conditions (such as temperature and humidity) on the hydration process and compressive strength. The findings indicate that the external addition of limestone powder significantly increases early-age compressive strength while slightly reducing the peak heat of hydration. Consequently, the role of externally mixed limestone powder in altering hydration kinetics is discussed to propose a novel mechanistic understanding of the hydration reactions.

1. Introduction

The heat of hydration is a critical factor affecting to the long-term performance of hot weather concrete. Various studies have investigated the replacement of Portland cement with supplementary cementitious materials (SCMs), such as fly ash, to reduce and delay the peak hydration heat of concrete. However, the reduction in cement content significantly decreases the quantity of reactive clinker phases available for generating essential hydration products, such as portlandite, ettringite, and C-S-H. This result in the degradation of short-term compressive strength. To compensate for these drawbacks, the external mixing approach introduces the addition of other SCMs to the concrete mixture to improve mechanical capacities when replacement methods are insufficient.

In this study, fly ash-based concrete – a common form of partial cement replacement – is utilized to mitigating the peak temperature throughout hydration process. Additionally, limestone powder is introduced via the external mixing method to compensate the strength loss and enhance the early-age compressive strength of the concrete.

The initial experiment was carried out at lab-scale before mock-up tests was conducted in three hot weather countries – namely Korea, Vietnam and Japan. These mock-up tests were executed under various geographical location, ambient temperature and weather conditions (see Figure 1).

2. Materials and methods

2.1 Materials and mix-proportion

Fly ash (FA) is a by-product collected from electrostatic precipitator after combustion at a pulverized coal-firing boiler of a power plant [1]. FA

※1 Master's course, Department of Architectural Engineering, Chungnam National University, Korea
※2 Prof., Dept. of Architectural Engineering, Chungnam National University, Korea
※3 Ph.D., Department of Architectural Engineering, Chungnam National University, Korea
※4 Ph.D. Course, Dept. of Architectural Engineering, Chungnam National University, Korea

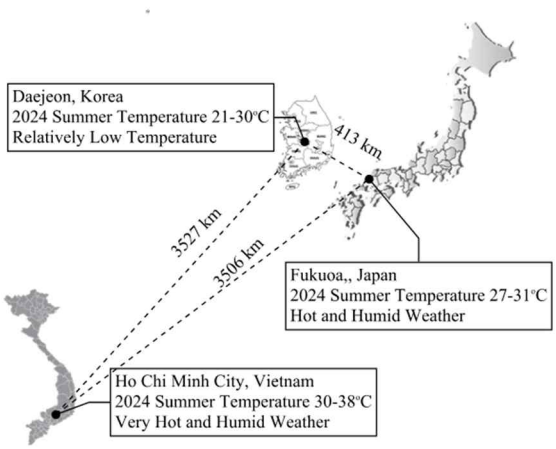

Figure 1. Location and Weather Conditions

is classified based on its calcium oxide proportion, CaO, with class F being characterized by its low-calcium content. Furthermore, fly ashes consist mainly of silicon dioxide (SiO_2), but can contain also significant quantities of aluminum oxide (Al_2O_3) [2] (see Table 1a). Fly ash is widely utilized to reduce an amount of Portland cement in concrete mixture. Through the pozzolanic reaction between silicon dioxide and portlandite (CH) – a primary hydration product – additional calcium silicate hydrate (C-S-H) gel is continuously generated, enhanced long-term concrete strength. However, the use of fly ash delays the setting time of concrete, which results in a degradation of early-age compressive strength.

Limestone powder (LSP) – a by-product of the limestone quarry, is crushed and ground from natural lime-stone [4]. It has a high calcium oxide content and finer than ordinary cement. Moreover, limestone powder increases the early-age compressive strength of concrete through three main mechanisms: the filler effect, the nucleation effect, and the chemical effect. However, if the proportion of limestone powder added to concrete mixture exceeds 15%, the excess material will not participate in ongoing hydration reaction [3].

In this research, low-calcium Class F fly ash is utilized as a 20% cement replacement to reduce internal heat generation. To investigate the optimal proportion for external limestone powder addition, limestone powder was added to the concrete mixtures at dosages of 5%, 10%, and 15% in the laboratory (see Table 2a). Based on the laboratory-scale results, a 10% addition of limestone powder was selected for the mock-up tests. However, to effectively compare the mechanical behavior of the limestone powder in the concrete mixture, a separate mix was prepared where limestone powder replaced the cement at the same 10% ratio, rather than being added externally (see Table 2b).

Table 1. Material prpoerties in laboratory-scale (a) and on mock-up test in three countries (b)

a) Material properties in laboratory-scale

Binder types	Density (g/cm^3)	Fineness (cm^2/g)	Component contents (%)			
			CaO	SiO_2	Al_2O_3	MgO
Cement	3.14	3388	66.5	16.5	4.5	2.5
Fly-ash	1.9~2.3	3290	3.10	36	25.03	1.24
Limestone powder	2.71	3956	44 $CaCO_3$ (80)	15	4.5	3.5

b) Features of binders from three countries

Region	Korea		Vietnam		Japan	
Binder types	Density (g/cm^3)	Fineness (cm^2/g)	Density (g/cm^3)	Fineness (cm^2/g)	Density (g/cm^3)	Fineness (cm^2/g)
Cement	3.14	3388	3.1	3280	3.15	3310
Fly-ash	1.9~2.3	3290	2.1	3100	2.29	4300
Limestone powder	2.71	3956	2.7	3000-4000	2.71	3500-4500

Table 2. Proportion of concrete mixture in laboratory-scale (a) and mock-up test (b)

a) Proportion of concrete mixture in laboratory

Specimens	f_{ck} (MPa)	W/B (%)	Slump (mm)	S/a $(vol\ \%)$	Unit Weight (kg/m^3) OPC	FA	LSP	S	G
NSC100					360	-	-		
NSC80FA20					288	-	-		
NSC80FA20LSP5	30	50	80±20	45	288	72	18	766.48	955.11
NSC80FA20LSP10					288	72	36		
NSC80FA20LSP15					288	72	54		

b) Proportion of concrete mixture on the mock-up test

Specimens	f_{ck} (MPa)	W/B (%)	Slump (mm)	S/a $(vol\ \%)$	Unit Weight (kg/m^3) OPC	FA	LSP	S	G
NSC100					360	-	-		
NSC80FA20	30	50	80±20	45	288	72	-	766.48	955.11
NSC80FA20LSP10					288	72	36		
NSC70FA20LSP10					252	72	36		

2.2 Compressive test method

A Universal Testing Machine (UTM) was utilized in this research to evaluate the mechanical performance of cylindrical concrete specimens (ϕ100× 200mm). The compressive strength of concrete specimens was measured after 1, 3, 7, 28 and 56 days of curing to closely analyze the effect of fly ash and limestone powder on the compressive strength properties of concrete.

2.3 Simplified Hydration Heat test method

Simple insulation heat of hydration test equipment was used to record the hydration heat over a 5 day-period. Temperature measurements were recorded at 10-minute intervals throughout this period.

The size of the test piece for the hydration heat test was 300mm×300mm×300mm. Three sensors were installed inside the mold: at the center, and at distance 75mm and 150mm from the center, respectively. (Figure 2)

3. Results and Discussion

3.1 Laboratory scale results

The compressive strength results indicate strength development of these specimens. The original concrete (L_NSC100) exhibited the highest strength at the early-stage, while the internal replacement concrete reduced mechanical strength. Furthermore, the addition of limestone powder on internal mixing

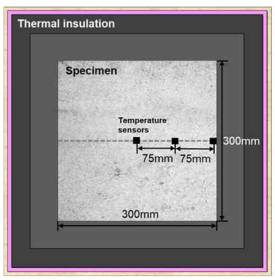

a) Simplified hydration heat test drawing

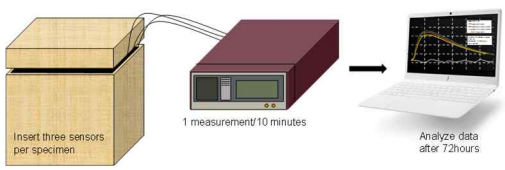

b) Hydration heat measurement procedure

Figure 2 Simple Insulation Heat of Hydration Test Equipment

specimens displayed an increase in compressive strength over the testing period. Through its filler, chemical and nucleation effects, the LSP enhances the early setting time of concrete and compensates the delayed setting time caused by fly ash replacement. The compressive strength continues to increase in the long-term due to the pozzolanic reaction between silicon dioxide and portlandite. Therefore, the long-term compressive strength for both internal mixing and external mixing is improved, reaching or exceeding that of the OPC control (See Figure. 3a).

Additionally, the hydration heat recorded by the simplified insulation hydration heat machine showed the highest peak heat in the ordinary concrete. The addition of limestone powder to the concrete mixture was initial predicted to increase the hydration heat due to these effects. However, an accelerating the setting time not only increased the early-strength of concrete but also reduced the hydration heat. It can be concluded that the external mixing method affects the hydration process and alters the mechanical properties.

Based on the laboratory results, the 10% limestone power dosage demonstrated the highest efficiency between compressive strength and hydration heat reduction. Therefore, a 10% limestone powder proportion was applied in the mock-up tests in the three countries namely Korea, Vietnam and Japan.

3.2 Mock-up test results

In the mock-up tests, the simplified insulation hydration heat testing set was scaled up for concrete blocks with dimensions of 1000×1000×1000 mm. Three sensors were installed inside the mold: at the center, and at distance 250 mm and 500 mm from the center, respectively. These mock-up tests were conducted under various environmental conditions in hot-weather countries. The variations in temperature humidity, and local material properties caused significant discrepancies in the mechanical and thermal results.

Compressive strength data from the specimens cured on the laboratory conditions in Korea and Japan displayed almost the same trends as the lab-scale test. In these cases, the mixture utilizing a 10% external addition of limestone powder (NSC80FA20LSP10) increased the compressive strength at both early and later ages. Moreover, the internally mixed specimen (NSC70FA20LSP10) demonstrated lower mechanical performance. Conversely, the externally mixed specimens in Vietnam exhibited the different trend. The externally mixed specimens indicated the lower strength compared to internally mixed specimens. Additionally, the specimens containing limestone powder (both internal and external mixing method) in the Vietnam tests demonstrated lower strength compared to the original control concrete and the fly ash replacement concrete. (See Figure 4a,4b,4c). Core specimens for compressive strength testing were extracted from the 1000mm × 1000mm × 1000mm hydration blocks, and the resulting data exhibited a different trend compared to the specimens cured in the laboratory. The different curing condition between laboratory and realistic field conditions (outside-lab) caused these various results. The core compressive str-

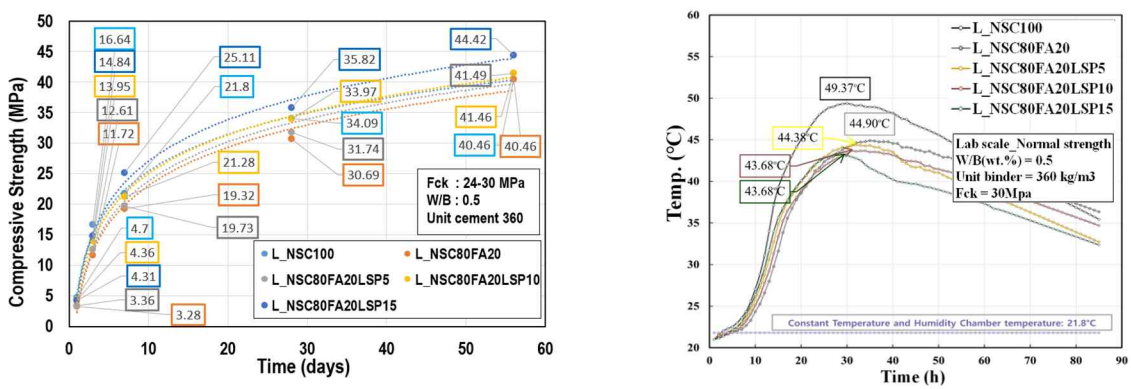

a) Normal concrete compressive strength b) Normal concrete hydration heat

Figure 3. Compressive strength and hydration heat (in laboratory scale)

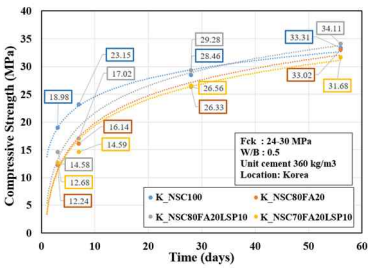

a) Compressive strength – Korea

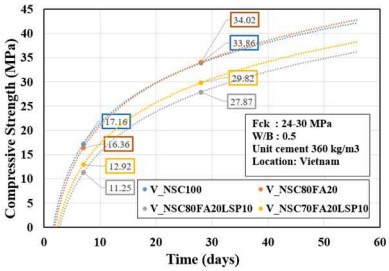

b) Compressive strength – Vietnam

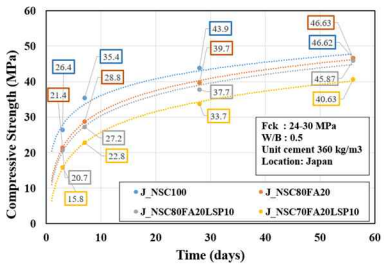

c) Compressive strength – Japan

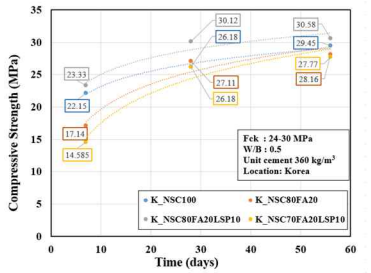

d) Coring compressive strength – Korea

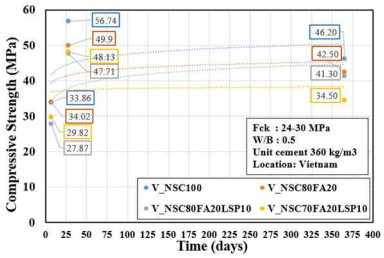

e) Coring compressive strength – Vietnam

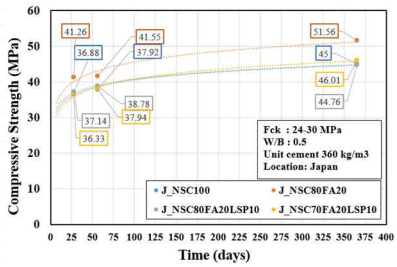

f) Coring compressive strength – Japan

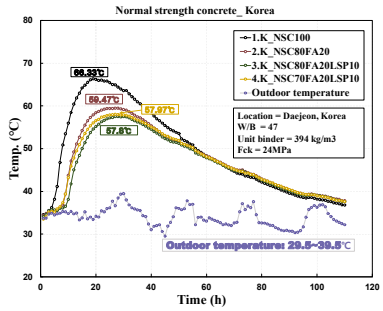

g) Hydration heat – Korea

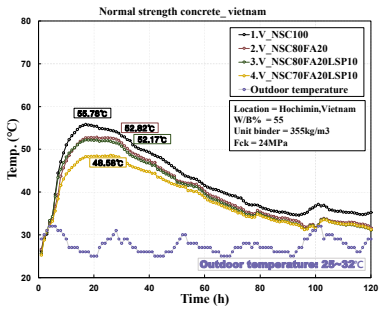

h) Hydration heat – Vietnam

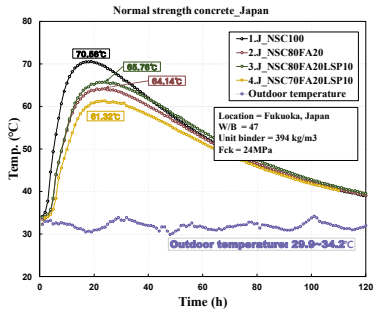

i) Hydration heat – Japan

Figure 4 Compressive strength and hydration heat (in mock-up test) in three countries

-ength values from Korea and Vietnam displayed the same trend, where the externally mixed concrete had higher strength than the internally mixed concrete. Furthermore, the concrete containing limestone powder addition demonstrated lower strength than conventional concrete and fly-ash replacement concrete. In contrast, the test specimens from Japan demonstrated the efficacy of limestone powder for both external and internal mixing; the compressive strength of these specimens exceeded that of the ordinary concrete, but was still lower than the binary replacement concrete. Specifically, core specimens from Vietnam and Japan were extracted and measured for compressive strength at a 1-year age. In Vietnam, the compressive strength of all specimens decreased after 1 year. Meanwhile, in Japan, the strength of the ternary internally mixed concrete increased, surpassing the externally mixed concrete after 1 year. (See Figure 4d,4e,4f).

The ordinary concrete displayed the highest peak hydration temperature across all the hot-weather countries. Additionally, the fly ash replacement concrete showed a reduction in the peak heat of hydration. The results from Korea exhibited the same trend as the lab-scale results, where the external addition of limestone powder reduced the peak heat, while the internally mixed limestone powder increased the heat of hydration. Moreover, the hydration heat results in Vietnam and Japan followed the same trend; the internally mixed concrete NSC70FA20LSP10 displayed the lowest hydration heat because the amount of cement removed was greater than in the

other specimens. In Vietnam, the hydration heat of the externally mixed limestone powder specimens did not increase, whereas in Japan, it increased slightly by $1.6°C$ (See Figure. 4h,4h,4i).

3.3 The role of external mixing

Based on the lab-scale and mock-up test results, it is evident that both external and internal mixing altered the hydration process and mechanical properties of the concrete mixtures. Some researchers have claimed that limestone powder mainly displays a nucleation effect, accelerating the hydration of tricalcium silicate (C_3S) during the hydration process [4]. In addition, the particle size of the limestone powder affects the setting time, accelerating it and shortening the induction period [5]. Although the mock-up test results varied due to the diverse environmental conditions in the three countries, the specimens containing limestone powder in Vietnam and Korea displayed a slight decrease in peak hydration heat. However, the compressive strength results between them showed a significant discrepancy; the Korea specimens increased in strength compared to the OPC specimens, while the Vietnamese specimens exhibited the lowest strength. This altered relationship between the compressive strength and the hydration heat profiles indicates a different mechanism of hydration product formation through the external mixing method. Furthermore, due to the pozzolanic reaction of the fly ash, the long-term compressive strength consistently enhances over time. Therefore, the external mixing method mitigates the drawbacks of fly ash replacement concrete while preserving the beneficial effects of the fly ash in the mixture.

4. Conclusions

In this study, lab-scale and mock-up test results from three countries demonstrated that externally mixed limestone powder significantly affects fly ash-based concrete. The external addition of limestone powder not only increases the early-age compressive strength of the concrete but also preserves the beneficial behavior of the fly ash within the mixture. However, the diverse conditions in the three countries including temperature, humidity, and local material properties caused variations in the experimental results. Ultimately, this research provides foundational findings for future investigations into the external mixing method.

Reference

[1] Lee, Hong Joo Kim, Etsuo Sakai, Masaki Daimon, Effect of particle size distribution of fly ash–cement system on the fluidity of cement pastes, Cement and Concrete Research, Volume 33, Issue 5, 2003, Pages 763-768, ISSN 0008-8846.

[2] Barbara Lothenbach, Karen Scrivener, R.D. Hooton, Supplementary cementitious materials, Cement and Concrete Research, Volume 41, Issue 12, 2011, Pages 1244-1256, ISSN 0008-8846.

[3] Serhat Demirhan, Kazim Turk, Kubra Ulugerger, Fresh and hardened properties of self consolidating Portland limestone cement mortars: Effect of high volume limestone powder replaced by cement, Construction and Building Materials, Volume 196, 2019, Pages 115-125, ISSN 0950-0618.

[4] Dehui Wang, Caijun Shi, Nima Farzadnia, Zhenguo Shi, Huangfei Jia, Zhihua Ou, A review on use of limestone powder in cement-based materials: Mechanism, hydration and microstructures, Construction and Building Materials, Volume 181, 2018, Pages 659-672, ISSN 0950-0618.

[5] Dehui Wang, Caijun Shi, Nima Farzadnia, Zhenguo Shi, Huangfei Jia, A review on effects of limestone powder on the properties of concrete, Construction and Building Materials, Volume 192, 2018, Pages 153-166, ISSN 0950-0618.

誘電測定で観測される緩和過程に基づいた コンクリートの水和進行の非破壊評価に関する研究

Non-Destructive Evaluation of Hydration Progress in Cement Paste Based on Dielectric Relaxation Processes

濟藤慎太郎※1,佐藤幸恵※2,須藤誠一※3,

Shintaro Saito※1, Sachie Sato※2 and Seiichi Sudo※3

ABSTRACT

セメント系材料の水和進行は，コンクリート構造物の品質，耐久性および強度発現に大きな影響を及ぼす．本研究では，セメントペースト供試体を対象として誘電測定を行い，材齢に伴う誘電緩和挙動の変化を調査した．測定には，インピーダンスアナライザ，時間領域反射法（TDR），およびテラヘルツ分光法を用い，広帯域の周波数範囲で測定を実施した．さらに，水和生成物に関連する結合水量を定量評価するために熱重量分析（TG）を行った．その結果，約 100 MHz および 20 GHz 付近に誘電緩和過程が確認された．20 GHz 付近で観測された緩和過程の緩和強度は材齢の進行に伴って減少し，自由水の減少を示唆した．一方，100 MHz 付近で観測された緩和過程では，緩和強度および緩和時間が材齢の進行に伴って増加し，水和生成物によって拘束された水の増加を示唆した．また，TG 分析により得られた結合水量と 100 MHz 付近の緩和過程の緩和強度との間には強い相関が認められた．これらの結果より，誘電測定はセメント系材料の水和進行を非破壊で評価する手法として有効であることが示された。

1. Introduction

The quality and durability of reinforced concrete structures are strongly influenced by curing conditions and environmental factors during construction. In cast-in-place concrete, proper wet curing promotes hydration and improves long-term durability, whereas insufficient curing reduces surface quality and strength development.

Conventional evaluation methods based on core sampling are destructive and cannot be applied without damaging the specimen. Therefore, a simple non-destructive technique for evaluating hydration progress is required. Our previous studies have shown that dielectric measurements are sensitive to changes in the water state of cementitious materials. However, the relationship between dielectric relaxation behavior and hydration products has not been fully clarified. Dielectric measurements are sensitive to changes in the state of water molecules during cement hydration(1). As hydration progresses, the mobility and bonding state of water molecules change, leading to changes in the dielectric response. Therefore, dielectric measurements have the potential to evaluate hydration progress non-destructively(2).

To clarify the issue, dielectric measurements were combined with TG and XRD analyses to investigate the

1* 日本 東京都市大学院 建築都市デザイン専攻 建築学領域 修士課程

2* 日本 東京都市大学 建築都市デザイン学部 建築学科 教授 博士（工学）

3* 日本 東京都市大学 理工学部 自然科学科 教授 博士（理学）

relationship between dielectric relaxation behavior and cement hydration. In this study the objective was to clarify the correspondence between dielectric relaxation processes and bound water content and to evaluate the applicability of dielectric measurements as a non-destructive technique for monitoring hydration progress[3].

2. Materials and methods

2.1 Materials and specimens

The experimental conditions and materials are summarized in Tables 1 and 2. Cement paste with a water-to-cement ratio of 0.50 was prepared using research-grade cement and deionized water. The specimens were sealed and cured at 100% relative humidity and tested at ages of 1, 3, 7, 28, and 91 days[4].Broadband dielectric measurements were conducted over a frequency range from 40 Hz to 2 THz. To cover this wide frequency range, three complementary measurement systems were employed: an impedance analyzer, time-domain reflectometry (TDR), and terahertz (THz) spectroscopy.Because each measurement system requires a different specimen configuration, two specimen geometries were prepared, as shown in Figure 1. Plate specimens (70 × 10 × 50 mm) were used for TDR and impedance analyzer measurements (Figure 1(a)), whereas disk specimens (Φ100 × 0.3 mm) were used for THz spectroscopy (Figure 1(b)). The paste was mixed until homogeneous and carefully placed into molds to minimize entrapped air, which may affect the dielectric response and mass-loss measurements. The specimen shapes were selected to ensure stable contact with each measurement system and to reduce the influence of specimen geometry. Before dielectric measurements, the specimens were removed from the sealed curing condition, and surface moisture was gently wiped off with paper towels. Dielectric measurements were performed immediately to minimize changes in the moisture state of the specimens. After dielectric measurements, the specimens for TG and XRD analyses were immersed in isopropanol to stop hydration before further sample preparation.

Table 1. Experimental Conditions

Parameter	Condition
Age(days)	1, 3, 7, 28, 91
Curing Condition	RH 100%
Specimen Dimensions(mm)	70×10×50, Φ100×0.3

Table 2. Materials Used

Material	Specification
Cement*	Research-grade cement (Density3.17g/cm^3)
Water	Deionized water

*The mineral composition of the research-grade cement was 55 wt.% C_3S, 19 wt.% C_2S, 10 wt.% C_3A, and 9 wt.%

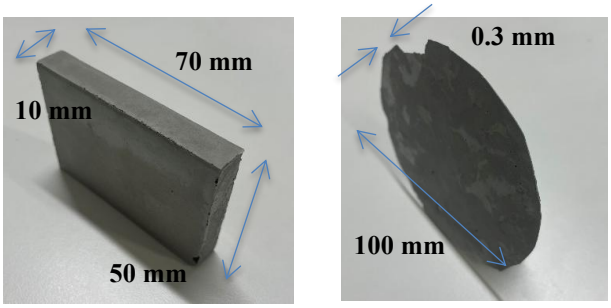

(a)Plate specimen **(b)Disk specimen**

Figure 1. Fabricated specimens

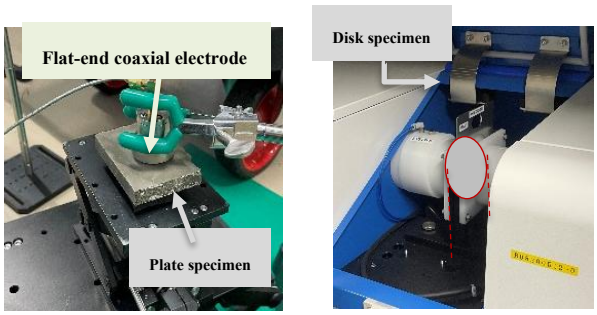

(a)Flat end coaxial electrode for impedance analyzer **(b)THz spectroscopy system**

Figure 2. Experimental setup for dielectric measurements

(a)TG **(b)XRD**

Figure 3. Experimental setup for TG and XRD analyses

2.2 Dielectric measurement

Dielectric measurements evaluate the dielectric constant ε′, representing polarization, and the dielectric loss ε″, representing energy dissipation caused by molecular motion and electrical conduction. These parameters are expressed as complex permittivity:

$$\varepsilon^* = \varepsilon' - j\varepsilon''$$

Dielectric measurements were performed using three complementary measurement systems to cover a wide frequency range. An impedance analyzer was used in the frequency range from 40 Hz to 110 MHz, time-domain reflectometry (TDR) was used from 10 MHz to 20 GHz, and a terahertz spectroscopy system was used from 30 GHz to 2 THz. The impedance analyzer and TDR measurements were conducted using the plate specimens, whereas the THz measurements were conducted using the disk specimens. The impedance analyzer was mainly used to observe the dielectric relaxation process around 100 MHz, while the TDR system was used to examine the relaxation process around 20 GHz. The THz spectroscopy

$$\varepsilon* = \varepsilon\infty + \Delta\varepsilon / (1+(j\omega\tau)^{1-\alpha})$$

system was used to investigate the dielectric response in the higher-frequency region. To estimate the relaxation parameters, the measured dielectric spectra were fitted using the Cole–Cole equation.

$\varepsilon\infty$ is the high-frequency permittivity, $\Delta\varepsilon$ is the relaxation strength, τ is the relaxation time, α is the distribution parameter ($0 \le \alpha \le 1$), and ω is the angular frequency. The relaxation strength ($\Delta\varepsilon$) and relaxation time (τ) shown in Figure 8 were obtained from the fitting results.

2.3 TG analysis

Thermogravimetric analysis (TG) was conducted to quantify the bound water content and evaluate the hydration progress of the cement paste. The TG apparatus used in this study is shown in Figure 3(a). The measurements were performed under an argon atmosphere from room temperature to 950°C at a heating rate of 10 K/min. The mass losses in the temperature ranges of 100–200°C, 450–500°C, and 650–700°C were attributed to the dehydration of AFm and C–S–H, the decomposition of calcium hydroxide (CH), and the decomposition of calcium carbonate ($CaCO_3$), respectively.

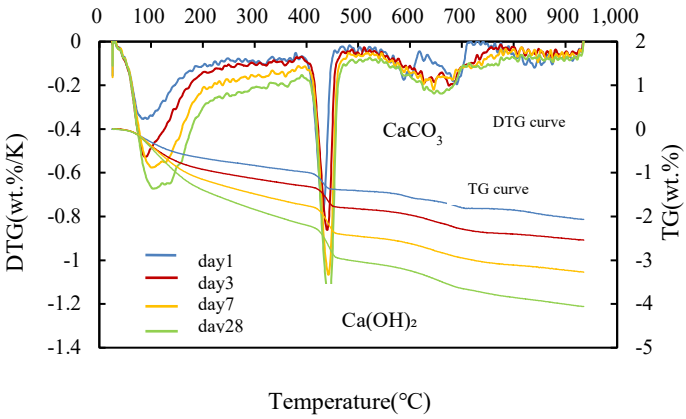

Figure 4. The TG and DTG curves at different curing ages

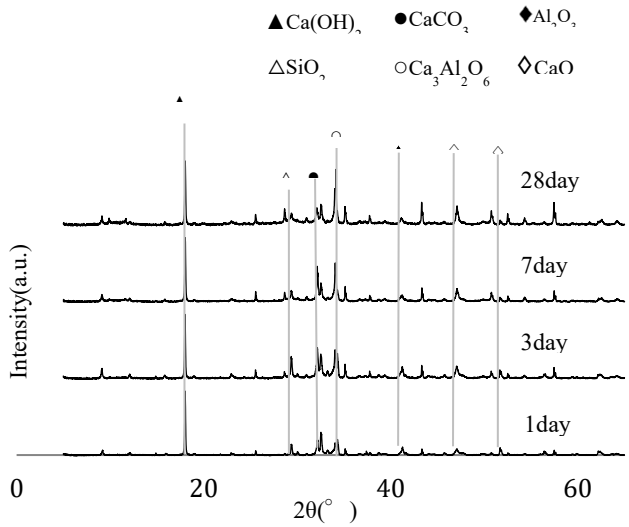

Figure 5. The XRD curves at different curing ages

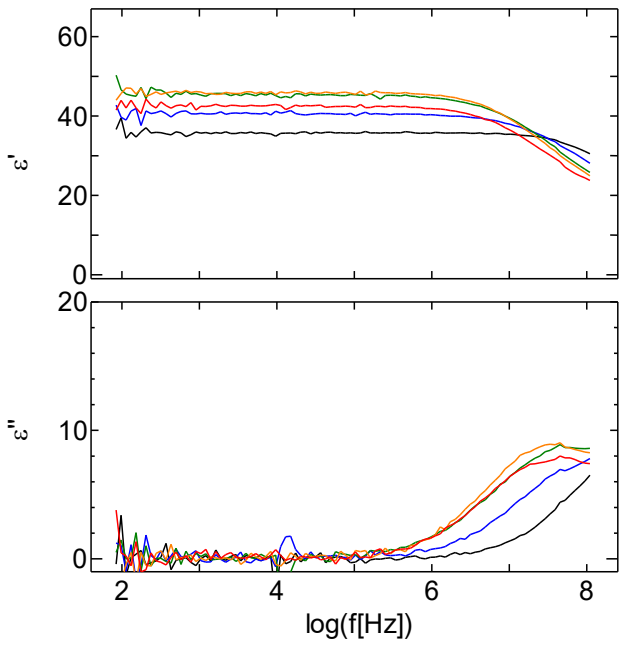

Figure 6. Frequency dependence of the dielectric constant (ε′) and dielectric loss (ε″) of cement paste in the frequency range measured using impedance analyzer.

The bound water content was calculated from the ignition loss between 105°C and 950°C. The derivative thermogravimetric (DTG) curves were calculated from the TG data. The TG and DTG results were used to evaluate the evolution of hydration products during curing and were subsequently compared with the dielectric relaxation characteristics obtained from dielectric measurements.

2.4 XRD analysis

X-ray diffraction (XRD) analysis was performed to identify hydration products and crystalline phases in the cement paste specimens. The XRD instrument used in this study is shown in Figure 3(b). Diffraction patterns were measured using a Rigaku SmartLab X-ray diffractometer with Cu-Kα radiation. The obtained diffraction data were analyzed to evaluate changes in the diffraction peaks of major hydration products, including calcium hydroxide (CH) and calcium carbonate ($CaCO_3$), as a function of curing age. These results were compared with the dielectric relaxation parameters to investigate the relationship between hydration progress and dielectric properties.

3. Results and Discussion

3.1 TG and DTG results

Figure 4 shows the TG and DTG curves of the cement paste at different curing ages. The mass loss observed in the temperature range of approximately 100–200°C, attributed to the dehydration of AFm and C-S-H, increased with curing age, indicating the progressive formation of hydration products. In addition, the DTG peak corresponding to the decomposition of calcium hydroxide ($Ca(OH)_2$) at approximately 450–500°C became more pronounced with curing age, suggesting the continued progress of cement hydration. A mass-loss peak attributed to the decomposition of calcium carbonate ($CaCO_3$) was observed at approximately 650–700°C, and its change with curing age was relatively small compared with those of AFm, C-S-H, and $Ca(OH)_2$. These TG and DTG results indicate that the hydration products continuously developed as curing progressed.

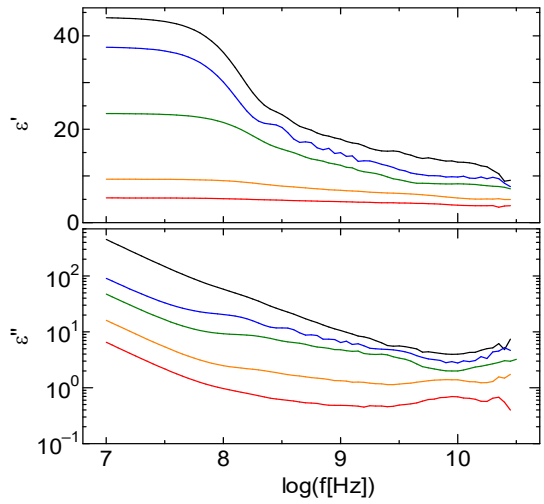

Figure 7. Frequency dependence of the dielectric constant (ε′) and dielectric loss (ε″) in the frequency range measured using TDR.

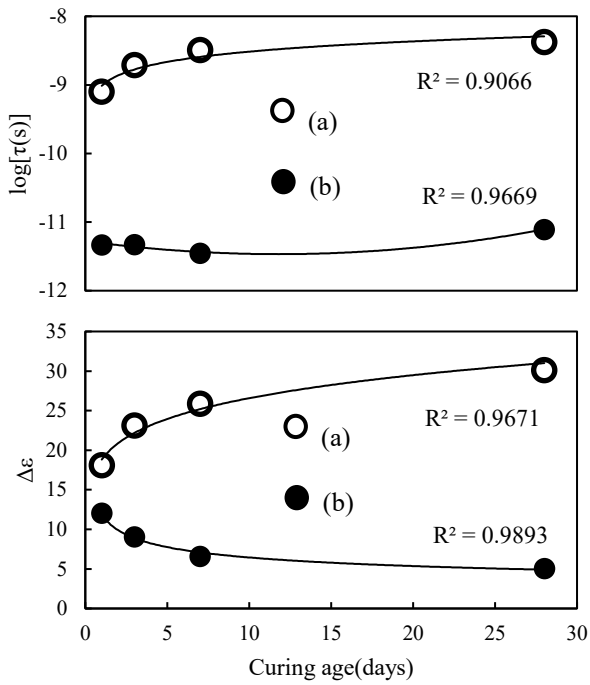

Figure 8. Changes in relaxation time(τ) and relaxation strength(⊿ε)with curing age.

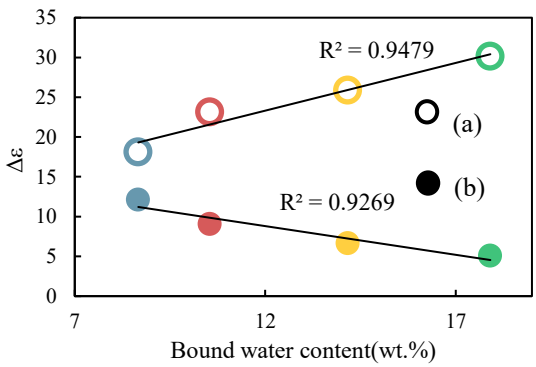

Figure 9. Relationship between bound water content and relaxation strength (Δε) for the relaxation processes observed around (a) 100 MHz and (b) 20 GHz.

3.2 XRD results

Figure 5 shows the XRD patterns of the cement paste at different curing ages. The relative intensity of the diffraction peaks corresponding to calcium hydroxide ($Ca(OH)_2$) generally increased with curing age, indicating the progress of cement hydration. In contrast, the relative intensity of the calcium carbonate ($CaCO_3$) peaks showed only slight changes throughout the curing period. Peaks attributed to SiO_2 and CaO were observed at all curing ages. Although the diffraction peak positions remained almost unchanged, variations in the relative peak intensities reflected changes in the crystalline phases during hydration.

3.3 Dielectric spectra

Figure 6 shows the frequency dependence of the dielectric constant (ε′) and dielectric loss (ε″) of cement paste measured in the impedance analyzer frequency range. The dielectric constant decreased with increasing frequency over the entire frequency range. A dielectric relaxation process was observed around 100 MHz in the dielectric loss spectrum. The relaxation strength of this process increased with curing age, indicating that a larger amount of water became constrained by hydration products as hydration progressed.

Figure 7 shows the dielectric spectra measured in the TDR frequency range. In this frequency range, another relaxation process was observed around 20 GHz. Unlike the relaxation process around 100 MHz, the relaxation strength around 20 GHz decreased with curing age, suggesting a reduction in free water consumed during cement hydration.

These dielectric responses are consistent with the TG and XRD results, which showed continuous formation of hydration products with curing age. The increase in the relaxation strength around 100 MHz corresponds to an increase in constrained (bound) water, whereas the decrease around 20 GHz reflects the reduction in free water. These results demonstrate that broadband dielectric spectroscopy can distinguish different water states during cement hydration and can therefore be used for non-destructive evaluation of hydration progress.

Figure 8. Changes in relaxation time (τ) and relaxation strength (Δε) with curing age. Open symbols represent the relaxation process around 100 MHz, whereas closed symbols represent the relaxation process around 20 GHz.

For the relaxation process around 100 MHz, both the relaxation strength (Δε) and relaxation time (τ) increased with curing age. The increase in Δε indicates that a larger amount of bound water participated in the relaxation process, whereas the increase in τ suggests that the molecular mobility of bound water became more restricted as hydration progressed.

In contrast, for the relaxation process around 20 GHz, the relaxation strength (Δε) decreased with curing age, whereas the relaxation time (τ) showed only a slight change.

These results suggest that the relaxation process around 100 MHz is closely related to the formation of hydration products and bound water, whereas the relaxation process around 20 GHz reflects the decrease in free water during hydration.

3.4 Relationship between bound water content and relaxation strength

Figure 9(a) shows the relationship between the bound water content and the relaxation strength around 100 MHz, whereas Figure 9(b) shows the corresponding relationship around 20 GHz. The relaxation strength around 100 MHz increased with increasing bound water content, exhibiting a strong positive correlation (R^2 = 0.9479). This result indicates that the relaxation process around 100 MHz is closely associated with water molecules constrained by hydration products. In contrast, the relaxation strength around 20 GHz decreased as the bound water content increased, showing a strong negative correlation (R^2 = 0.9269). This behavior suggests that the relaxation process around 20 GHz mainly reflects the reduction of free water consumed during cement hydration.

4. Conclusion

The hydration behavior of cement paste was investigated using broadband dielectric spectroscopy together with TG and XRD analyses. Two dielectric relaxation processes were identified around 100 MHz and 20 GHz. The relaxation strength around 100 MHz increased with curing age and showed a strong positive correlation with bound water content, whereas the relaxation strength around 20 GHz decreased with curing age and showed a strong negative correlation with bound water content.

These results indicate that the relaxation process around 100 MHz is associated with bound water formed during cement hydration, whereas the relaxation process around 20 GHz reflects the reduction of free water consumed during hydration. The combined dielectric, TG and XRD analyses provided insight into the physical origin of the two relaxation processes, demonstrating that broadband dielectric spectroscopy can distinguish changes in different water states during cement hydration. Therefore, broadband dielectric spectroscopy has strong potential as a non-destructive technique for evaluating the hydration progress of cementitious materials.

Reference

[1] Shinozaki, S., et al. *Evaluation of Water in Cement Paste by Broadband Dielectric Spectroscopy*. Journal of Structural and Construction Engineering (AIJ), Vol. 90, No. 832, 2025 (in Japanese).

[2] Uchida, N., et al. *Study on Non-Destructive Evaluation of Heat-Damaged Concrete Using Dielectric Measurements*. Summaries of Technical Papers of Annual Meeting, Architectural Institute of Japan, Kyushu, pp. 119–120, 2025 (in Japanese).

[3] Huang, L., and Swenson, H. *Distribution and Dynamics of Water in Blended Paste Unraveled by Thermoporometry and Dielectric Properties*. Cement and Concrete Research, Vol. 174, Article 107333, 2023.

[4] Scrivener, K. L., Snellings, R., and Lothenbach, B. *A Practical Guide to Microstructural Analysis of Cementitious Materials*. CRC Press, 2016.

水酸化バリウム及び水酸化マグネシウムを混入した炭酸化養生セメントペーストの特性評価

Properties of Carbonation Curing Cement Paste with $Ba(OH)_2$ and $Mg(OH)_2$

金智訓※1、蔡炅俊※1、鄭渶錫※1、金度均※2、李相洙※3
Ji-Hun Kim, Kyoung-Jun Chae, Yeong-Seok Jeong, Do-Kyun Kim, Sang-Soo Lee

ABSTRACT

This study investigated the effects of carbonation curing (CC) and the replacement of ordinary portland cement (OPC) with barium hydroxide ($Ba(OH)_2$) and magnesium hydroxide ($Mg(OH)_2$) on the physical properties, mechanical strength, and carbonation depth of OPC paste. $Ba(OH)_2$ and $Mg(OH)_2$ were substituted at 0, 5, 10 and 15 wt% of cement mass at a water-to-binder ratio of 37% and cured under 20±1% CO_2, 60±5% relative humidity and 20±2°C. The flexural strength of the $Mg(OH)_2$ paste increased continuously with the replacement ratio, while its compressive strength peaked at 10% and decreased slightly at 15%. In contrast, both the flexural and compressive strength of the $Ba(OH)_2$ paste decreased monotonically with increasing replacement ratio, attributed to a $BaCO_3$ surface layer that restricts internal CO_2 diffusion. At a fixed ratio of 5%, carbonation-cured OPC and $Mg(OH)_2$ pastes developed higher strength than the $Ba(OH)_2$ paste, whereas the carbonation depth showed the opposite tendency, with the $Ba(OH)_2$ paste exhibiting the smallest depth of penetration (6.25 mm at 28 days versus 12.40 mm for OPC). These results indicate that $Ba(OH)_2$ forms a $BaCO_3$-rich surface layer that suppresses carbonation-front progression and shows potential as a functional admixture for controlling carbonation depth, while $Mg(OH)_2$ allows more uniform internal carbonation while maintaining strength comparable to plain OPC.

1. Introduction

The construction industry is a major source of global greenhouse-gas emissions, and low-carbon binder and curing technologies are essential for achieving carbon neutrality [1,2]. Carbonation curing (CC), which injects CO_2 during the curing of cement-based materials, accelerates early strength development while fixing CO_2 as $CaCO_3$. However, the conversion of $Ca(OH)_2$ into $CaCO_3$ lowers the pore-solution pH, which can raise the risk of reinforcement corrosion; CC is therefore mainly applied to non-reinforced precast products such as blocks and panels [2].

Barium hydroxide ($Ba(OH)_2$), a strong base, forms low-solubility barium carbonate ($BaCO_3$) upon carbonation and has been reported to buffer the internal pH while filling pore space [3]. Magnesium hydroxide ($Mg(OH)_2$) similarly reacts with CO_2 to form $MgCO_3$ and has been studied as an admixture for carbonation curing [4]. Quantitative comparisons of how the replacement ratio of these two hydroxides governs strength development and carbonation-front progression remain limited.

This study evaluated OPC paste containing $Ba(OH)_2$ and $Mg(OH)_2$ at replacement ratios of 0-15 wt% under carbonation curing, and, at a fixed ratio, compared carbonation curing with water curing. Density, absorption, air content, unit weight, flexural and compressive strength, and carbonation depth were evaluated to clarify the strength-development and carbonation-resistance mechanisms of each admixture.

2. Experimental overview

2.1 Experimental plan

Ordinary portland cement (OPC) was used as the

※1 大韓民国 国立Hanbat大学校 建設環境デザイン大学 建築工学科, 修士課程
※2 大韓民国 国立Hanbat大学校 建設環境デザイン大学 建築工学科, 博士課程
※3 大韓民国 国立Hanbat大学校 建設環境デザイン大学 建築工学科, 教授 博士(工学)

binder, and the water-to-binder ratio was fixed at 37%. $Ba(OH)_2$ and $Mg(OH)_2$ were used as admixtures at 0, 5, 10 and 15 (wt%) of cement mass, with carbonation curing (20±2°C, 60±5% RH, 20±1% CO_2) applied to determine the optimum replacement ratio through flexural and compressive strength. Based on these results, a ratio of 5% was adopted as the reference dosage, and OPC, $Ba(OH)_2$ and $Mg(OH)_2$ pastes at 5% were additionally compared under water curing (WC, 20±2°C) to isolate the effect of curing condition. Density and absorption were measured per KS F 2459 and KS F 2609 [5,6]; air content and unit weight per KS L 2421 and KS F 2409 [7,8]; flexural and compressive strength per KS L ISO 679 [9]; and carbonation depth by the phenolphthalein method per KS F 2596 [10]. The experimental factors and levels and mix proportions are summarized in Table 1.

Table 1 Experimental factors and levels

Experimental factor	Experimental level	Remarks
Binder conditions	OPC[1)]	1
Water/Binder (%)	37	1
Admixture	$Ba(OH)_2$, $Mg(OH)_2$	2
Mixing ratio of admixture (wt%)	0, 5, 10, 15	4
Curing condition	CC[2)], WC[3)]	2
Experiment items	Flexural strength, Compressive strength, Carbonation depth	3

1) OPC : Ordinaty portland cement
2) CC : Carbonation curing
3) WC : Water curing

2.2 Materials

Barium hydroxide octahydrate ($Ba(OH)_2 \cdot 8H_2O$) and magnesium hydroxide ($Mg(OH)_2$) were used as received; both are white solids at room temperature. Their physical properties, together with those of OPC, are summarized in Table 2. $Mg(OH)_2$ has a higher density and melting point than $Ba(OH)_2 \cdot 8H_2O$, while both admixtures are less dense than cement.

Table 2 Physical properties of materials

Material	Density (g/cm^3)	Molecular weight (g/mol)	Melting point (°C)
OPC[1)]	3.15	-	-
$Ba(OH)_2 \cdot 8H_2O$	2.18	315.46	78
$Mg(OH)_2$	2.34	58.32	350

1) OPC : Ordinaty portland cement

3. Experimental results and discussion

3.1 Flexural strength by replacement ratio

Figure 1 shows that the flexural strength of the $Mg(OH)_2$ paste increased continuously with replacement ratio, reaching 7.70 MPa at 15% (about 132% of the 0% value, 3.32 MPa), as pore-filling $MgCO_3$ densified the microstructure [2]. Figure 2 shows that the flexural strength of the $Ba(OH)_2$ paste increased slightly up to 10% (4.20 MPa) but decreased at 15% (2.88 MPa), attributed to a $BaCO_3$ surface layer that restricts inward CO_2 diffusion and limits densification in the specimen interior [3].

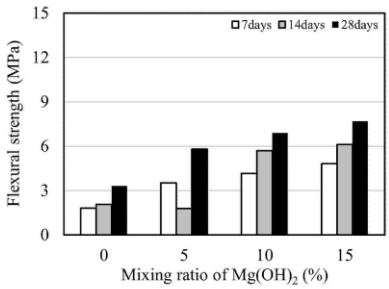

Figure 1 Flexural strength

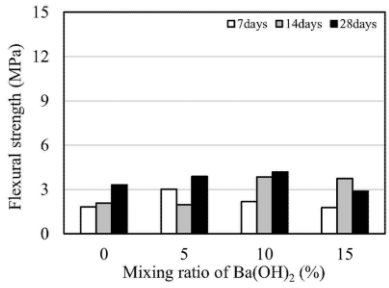

Figure 2 Flexural strength

3.2 Compressive strength by replacement ratio

Figure 3 shows that the compressive strength of the $Mg(OH)_2$ paste increased up to 10% (68.69 MPa) but decreased slightly at 15% (54.39 MPa), likely due to unreacted particles and residual pores formed at excessive dosage. Figure 4 shows that the compressive strength of the $Ba(OH)_2$ paste decreased monotonically from 80.23 MPa at 0% to 45.87 MPa at 15%, consistent with the restricted internal carbonation discussed above. Considering this trade-off, 5% was selected as the reference dosage for both admixtures in the subsequent curing-condition comparison.

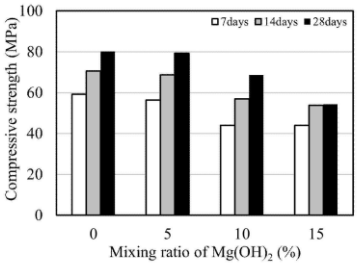

Figure 3 Compressive strength

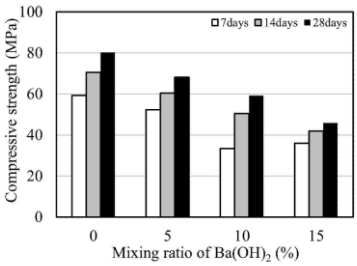

Figure 4 Compressive strength

3.3 Carbonation depth

At the fixed ratio of 5%, 28-day compressive strength under CC was highest for OPC (80.23 MPa), similar for $Mg(OH)_2$ (79.23 MPa), and lowest for $Ba(OH)_2$ (68.13 MPa); under water curing the same order was observed, with OPC at 73.80 MPa, $Mg(OH)_2$ at 71.97 MPa, and $Ba(OH)_2$ at 54.90 MPa. The $Ba(OH)_2$ paste showed the lowest strength under both conditions, indicating that it contributes little to either hydration- or carbonation-driven strength gain relative to OPC and $Mg(OH)_2$.

Figure 5 shows carbonation depth measured by the phenolphthalein method. Depth increased with age for OPC, from 5.82 mm (7 d) to 12.40 mm (28 d), reflecting continued conversion of $Ca(OH)_2$ to $CaCO_3$. The $Mg(OH)_2$ paste remained nearly constant (7.62-7.27 mm), while the $Ba(OH)_2$ paste showed the smallest depth at every age (2.53-6.25 mm), about half that of OPC at 28 days, because rapid early $BaCO_3$ formation concentrated near the surface acted as a diffusion barrier.

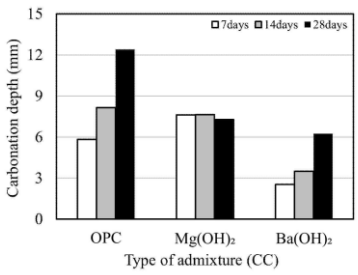

Figure 5 Carbonation depth

3.4 XRD analysis

Figure 5, Figure 6 and Figure 7 shows XRD patterns of the carbonation-cured pastes. Calcite was the dominant phase in the OPC paste, confirming typical carbonation. The $Mg(OH)_2$ paste showed $MgCO_3$-related peaks together with calcite, while the $Ba(OH)_2$ paste exhibited its highest peak near 2-theta~29 degrees, where the main $BaCO_3$ peak overlaps with the calcite peak, confirming that $Ba(OH)_2$ reacts directly with CO_2 rather than acting as an inert filler.

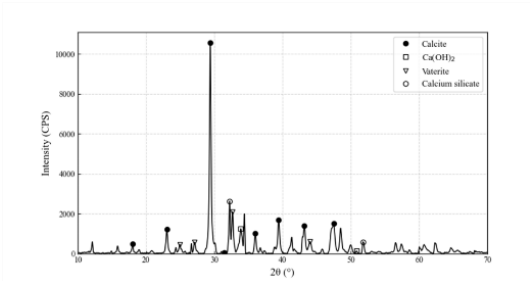

Figure 5 XRD patterns

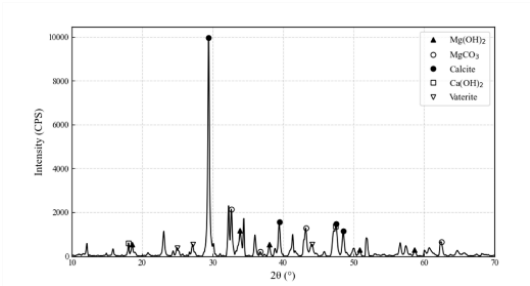

Figure 6 XRD patterns of MG

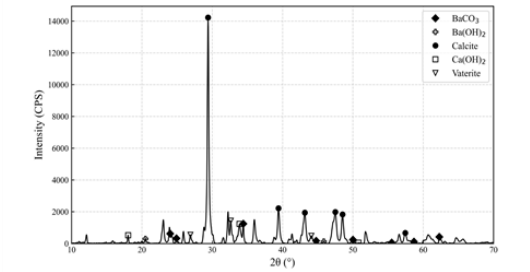

Figure 7 XRD patterns of BA

4. Conclusions

In this study, OPC paste containing $Ba(OH)_2$ and $Mg(OH)_2$ was evaluated under carbonation curing to determine the effect of admixture type and replacement ratio on strength development and carbonation depth. The following conclusions were drawn.

(1) Under carbonation curing, the $Mg(OH)_2$ paste

gained strength through pore-filling $MgCO_3$, whereas the $Ba(OH)_2$ paste showed lower strength than OPC at every age because an early $BaCO_3$ surface layer restricted internal CO_2 diffusion and densification.

(2) The $Ba(OH)_2$ paste exhibited the smallest carbonation depth at all ages, about half that of OPC at 28 days, indicating that the surface $BaCO_3$ layer acts as an effective barrier against CO_2 penetration.

(3) Based on these results, $Ba(OH)_2$ shows potential as a functional admixture for restricting carbonation depth despite its lower strength contribution, while $Mg(OH)_2$ maintains strength comparable to OPC; follow-up research will evaluate the long-term durability and reinforcement-corrosion behavior of $Ba(OH)_2$-admixed concrete.

(4) Calcite was the dominant phase in the OPC paste, confirming typical carbonation. The $Mg(OH)_2$ paste showed $MgCO_3$-related peaks together with calcite, while the $Ba(OH)_2$ paste exhibited its highest peak near 2-theta~29 degrees, where the main $BaCO_3$ peak overlaps with the calcite peak, confirming that $Ba(OH)_2$ reacts directly with CO_2 rather than acting as an inert filler.

Reference

[1] W. Ashraf, Carbonation of cement-based materials: challenges and opportunities, Constr. Build. Mater. 120 (2016) 558-570.

[2] D. Zhang, Z. Ghouleh, Y. Shao, Review on carbonation curing of cement-based materials, J. CO_2 Util. 21 (2017) 119-131.

[3] I. Karatasios, V. Kilikoglou, B. Colston, P. Theoulakis, D. Watt, Setting process of lime-based conservation mortars with barium hydroxide, Cem. Concr. Res. 37(6) (2007) 886-893.

[4] Z.X. Chen, H.S. Lee, Physicochemical properties of cement paste containing $Mg(OH)_2$ cured by CO_2 curing method, J. Korea Inst. Build. Constr. 18(3) (2018) 203-210.

[5] KS F 2459, Apparent density, water content, and water absorption of cellular concrete, Korea Standard Committee.T.

[6] KS F 2609, Method of test for water absorption of aggregate, Korea Standard Committee.S.C.

[7] KS L 2421, Air content of fresh concrete by the pressure method, Korea Standard Committee.Chen,

[8] KS F 2409, Unit weight and air content (gravimetric) of fresh concrete, Korea Standard Committee.

[9] KS L ISO 679, Cement-test methods-determination of strength, Korea Standard Committee, 2022.

[10] KS F 2596, Method of test for carbonation depth of concrete, Korea Standard Committee.

[11] X. Gao, Effect of carbonation curing regime on strength and microstructure of Portland cement paste, J. CO_2 Util. 34 (2019) 74-86.

[12] Bae, S.M. Cho, Review on the hardening characteristics of cementitious materials reacting with CO_2 by utilizing mineral carbonation, Mag. RCR 16(4) (2021) 30-36.

[13] N.I. Kim, Analysis on the carbonation characteristics of waste concrete and mortar application evaluation, Master's Thesis, Hanyang University, 2023.

Effects of Anhydrite and Steam Curing Conditions on the Strength Development of Mortar Using Blast-Furnace Slag Cement Type C

高炉セメントC種を用いたモルタルの強度発現特性に対する無水石膏と蒸気養生条件の影響

合田陸人※1、金志訓※2、濱幸雄※3、平田康修※4
Rikuto Goda, Jihoon Kim, Yukio Hama, Yasunobu Hirata

ABSTRACT

高炉セメント C 種を用いたモルタルを対象に，蒸気養生条件が強度発現および細孔構造に及ぼす影響を検討した。前置き時間，最高温度および保持時間を要因として設定し，無水石膏添加量を変化させた供試体について，圧縮強度，長さ変化および細孔径分布を評価した。その結果，無水石膏の添加および高温条件により初期の強度発現が促進されるが，長時間の高温養生は長期材齢における強度増進を抑制する傾向を示した。細孔構造の分析から，初期材齢に形成される細孔構造が長期性能に影響することが確認された。

1. Introduction

In recent years, the construction industry has faced a serious labor shortage due to fewer young workers and the departure of experienced workers, while efficient maintenance of aging social infrastructure has become necessary. In 2016, the Ministry of Land, Infrastructure, Transport and Tourism formulated the i-Construction policy and promoted precast concrete (hereinafter referred to as PCa) products as part of the standardization of concrete construction specifications[1, 2].

PCa products are structural members manufactured in factories and assembled at construction sites, offering shorter construction periods, labor savings, and stable quality. At PCa factories, products are often demolded at 18–24 h, and steam curing is widely used to ensure early-age strength. However, long-term strength and durability may decrease depending on the curing conditions[3, 4], making appropriate temperature control and post-curing important.

Meanwhile, cement production accounts for approximately 8% of global CO_2 emissions[5], and cement replacement with ground granulated blast-furnace slag (hereinafter referred to as BFS) has attracted attention. In Japan, blast-furnace slag cement Type B, with a BFS replacement ratio of approximately 40–45%, is mainly used, but blast-furnace slag cement Type C, with a higher replacement ratio, can further reduce CO_2 emissions. However, increasing the BFS replacement ratio reduces early-age strength[6], presenting a challenge for PCa products requiring early demolding. As a countermeasure, anhydrite addition has been reported to promote ettringite formation and improve early-age strength[7]. However, the influence of SO_3 content under steam-curing conditions remains insufficiently clarified. In addition, concrete subjected to high-temperature histories may undergo expansion deterioration due to delayed ettringite formation (hereinafter referred to as DEF), and such cases have been reported in steam-cured PCa products[8, 9].

In this study, mortar using blast-furnace slag cement Type C was examined to investigate the effects of pre-curing time, maximum temperature, and holding time on strength development and microstructure. In addition, pore structure and length change were analyzed, focusing on gypsum-induced ettringite formation, to propose steam-curing conditions that achieve both early-age strength and long-term performance.

Table 2 Mixture Proportions and Fresh Properties of Mortar

Mixture	W/B (%)	SO_3 (%)	Unit Content (kg/m^3)					AE Agent* (%)	Mini-Slump (cm)	Air (%)
			W	OPC	BFS	Gyp	S			
BC	50	0.61	294	176	411	0	1307	0.4	10.5	3.5
BC-S2	50	2.01	294	172	401	14	1307	0.4	10.5	3.5
BC-S4	50	3.99	294	166	387	34	1306	0.7	10.5	3.6

* AE agent dosage is expressed as a percentage of binder mass. The AE agent was used as a 100-fold diluted solution.

2. Experimental Program

2.1 Materials and Mixture Proportions

Ordinary Portland cement (hereinafter referred to as OPC), BFS without added gypsum, and anhydrite (hereinafter referred to as Gyp) were used as the binders (B). Blast-furnace slag cement Type C (hereinafter referred to as BC), in which 70% of OPC was replaced with BFS, was used as the reference, and three mixtures were prepared by adjusting the SO_3 content to 2% and 4% through the addition of Gyp. The water-to-binder ratio was set at 50%, and the amount of AE agent added was adjusted to achieve a target mini-slump of 9.5 ± 1.0 cm and a target air content of 4.5 ± 1.0%.

2.2 Specimen Preparation

Mixing was conducted in accordance with JIS R 5201. After the fresh property tests, the mortar was immediately cast into Φ50 × 100 mm plastic cylindrical molds, cured under each condition, and demolded at an age of 24 h. Specimens for evaluating later ages were prepared based on the compressive strength results at an age of 1 day.

2.3 Steam Curing Conditions

Table 3 shows the steam-curing conditions. Eight conditions were established using three factors at two levels: pre-curing times of 2 and 4 h, maximum temperatures of 40 and 55°C, and holding times of 4 and 6 h. The heating rate was controlled to reach the maximum temperature within 2 h. After the holding period, the specimens were naturally cooled in a room period, the specimens were naturally cooled in a room at 20°C and 60% RH. They were demolded at 24 h and air-cured under the same conditions until testing.

Table 1 Materials

Material	Symbol	Type and Physical Properties
Water	W	Tap water
Cement	OPC	Ordinary Portland cement Density: 3.16 g/cm^3; SO_3: 2.03%
Mineral admixture	BFS	Ground granulated blast-furnace slag (without gypsum addition) Density: 2.91 g/cm^3; Specific surface area: 3,950 cm^2/g
	Gyp	Anhydrite Density: 2.88 g/cm^3
Fine aggregate	S	River sand (Shiraoi, Hokkaido, Japan) Saturated surface-dry density: 2.62 g/cm^3; Water absorption: 2.31%
Chemical admixture	AE	Air-entraining (AE) agent

Table 3 Steam Curing Conditions

Curing Condition*1	Pre-curing Time (h)	Maximum Temperature (°C)	Holding Time (h)	Cumulative Temperature*2 (°C·h)
p2-m40-h4	2	40	4	260
p2-m40-h6			6	340
p2-m55-h4		55	4	335
p2-m55-h6			6	445
p4-m40-h4	4	40	4	300
p4-m40-h6			6	380
p4-m55-h4		55	4	375
p4-m55-h6			6	485

*1 Pre-curing time (h) – Maximum temperature (°C) – Holding time (h).

*2 Cumulative temperature from casting to the end of the holding period (reference temperature: 0°C).

2.4 Test Methods

(1) Compressive Strength Test

The compressive strength test was conducted using Φ50 × 100 mm cylindrical specimens at ages of 1, 7, 28, and 56 days in accordance with JIS A 1108. In this study, 12 MPa, which is generally considered sufficient to allow lifting, was set as the target demolding strength.

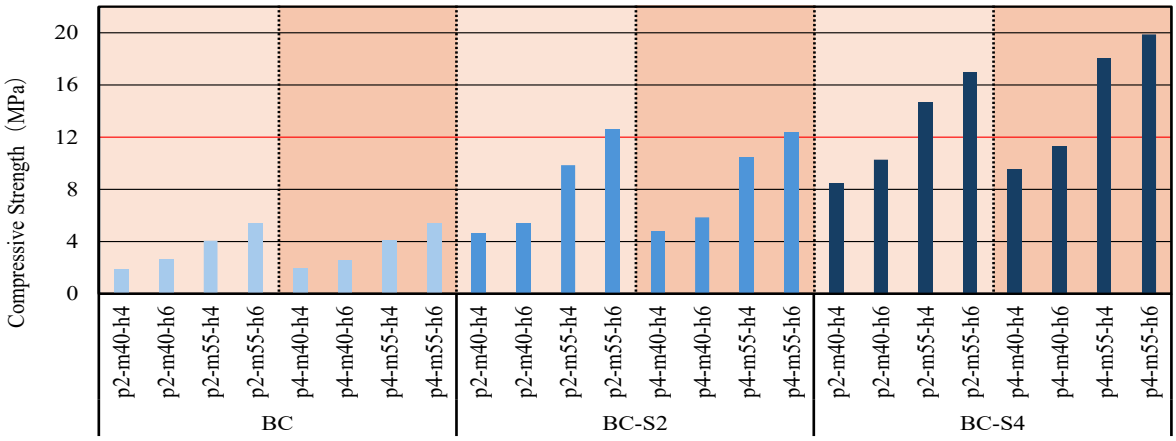

Fig. 2 Compressive Strength of Mortar at 1 Day under Mixture Proportions and Steam Curing Conditions

(2) Length Change and Mass Change

Length change and mass change were measured using 40 × 40 × 160 mm prismatic specimens in accordance with JIS A 1129-3. Measurements were conducted daily up to an age of 7 days and at one-week intervals after an age of 7 days.

(3) Pore Size Distribution

The pore size distribution was measured by mercury intrusion porosimetry (MIP). One Φ50 × 100 mm cylindrical paste specimen was prepared for each level. At the testing age, the specimen was cut into approximately 5 mm cubes, immersed in acetone for 24 h to stop hydration, and then dried for 24 h using a vacuum freeze-drying apparatus before measurement. The pore diameters measured ranged from 7 nm to 10 μm.

3. Results and Discussion

3.1 Compressive Strength

(1) Compressive Strength at the Age of 1 Day

Figure 2 shows the compressive strength at an age of 1 day according to the mortar mixture proportions and steam-curing conditions. The level without anhydrite addition (BC) did not satisfy the target demolding strength of 12 MPa under any condition. In contrast, for the levels with anhydrite addition, the compressive strength increased with increasing SO_3 content. This is considered to be because anhydrite promoted ettringite formation.

As shown in Photo 1, the conditions with longer pre-curing times showed fewer irregularities on the specimen surfaces after polishing. This is presumed to be because hydration reactions and microstructure formation progressed before steam curing. In addition, the compressive strength increased with increasing maximum temperature and holding time.

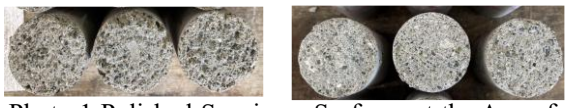

Photo 1 Polished Specimen Surfaces at the Age of 1 Day (Left: p2, Right: p4)

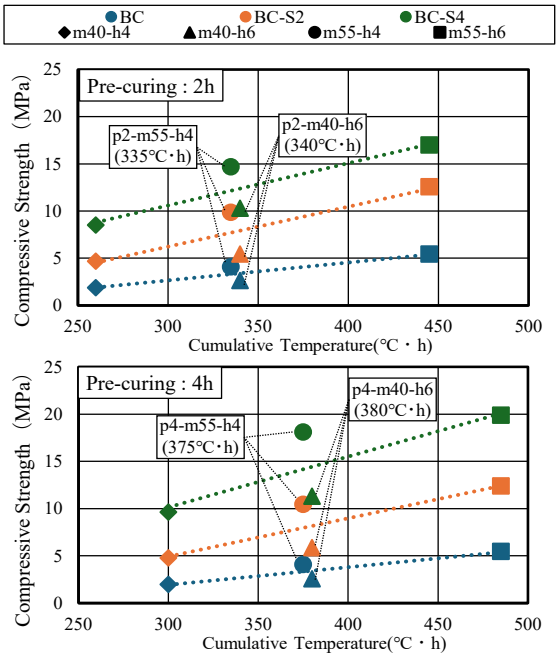

Fig. 3 Relationship between Cumulative Temperature up to the End of the Holding Period and 1-Day Compressive Strength (Top: p2, Bottom: p4)

Figure 3 shows the relationship between the cumulative temperature from immediately after casting to the end of the holding period at the maximum temperature and the compressive strength at

an age of 1 day. Regardless of the pre-curing time, the 55°C–4 h condition showed higher compressive strength than the 40°C–6 h condition, despite having a lower cumulative temperature. This suggests that the maximum temperature had a greater influence on strength development at an age of 1 day than the holding time or cumulative temperature.

For the levels shown in Table 4, including one level that did not satisfy the target demolding strength, compressive strength, length change, mass change, and pore size distribution were measured up to an age of 56 days.

(2) Compressive Strength Development

Figure 4 shows the compressive strength up to 56 days. Comparing SO_3 contents, No. 5 (BC-S4/p4-m55-h6) showed higher strength than No. 2 (BC-S2/p4-m55-h6) at all ages. Strength development was greater in No. 5 from 1 to 7 days and in No. 2 from 7 to 56 days. In No. 5, increased anhydrite promoted early ettringite formation[10] and early-age strength, whereas sulfate ion consumption may have slowed subsequent hydration relative to No. 2.

Comparing pre-curing times, No. 1 (BC-S2/p2-m55-h6) and No. 2 showed no clear difference at 1 and 7 days, but No. 2, with the longer pre-curing time, showed higher strength after 28 days. This may be because longer pre-curing stabilized the initial microstructure and promoted subsequent hydration.

Comparing maximum temperatures, No. 3 (BC-S4/p4-m40-h6) and No. 5 showed no marked difference in strength development from 1 to 7 days, but development under the 40°C condition was smaller after 7 days. This may be because curing at 55°C promoted cement and BFS reactions.

Comparing holding times, No. 5 showed higher strength than No. 4 (BC-S4/p4-m55-h4). Strength development was greater in No. 5 up to 28 days and in No. 4 from 28 to 56 days, suggesting that prolonged high-temperature holding may suppress later-age strength development.

3.2 Length Change and Mass Change

Figure 5 shows the length change rate, and Figure 6 shows the mass change rate. In the comparison of SO_3 content between No. 2 and No. 5, No. 5, with the larger amount of anhydrite, showed smaller length change and mass change rates. This is considered to be because the increase in anhydrite promoted ettringite formation and densification of the pore structure, thereby suppressing moisture loss.

In the comparison of pre-curing time between No. 1 and No. 2, no clear differences were observed in the

Table 4 Specimens for Long-Term Age Evaluation

No.	Mixture	Curing Condition	Comparison
1	BC-S2	p2-m55-h6	Pre-curing time
2	BC-S2	p4-m55-h6	
3	BC-S4	p4-m40-h6	Maximum temperature/ Holding time
4	BC-S4	p4-m55-h4	
5	BC-S4	p4-m55-h6	

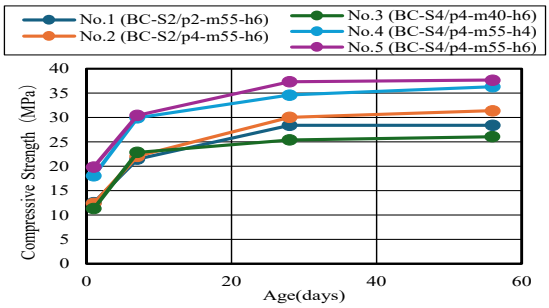

Fig. 4 Compressive Strength under Different Steam Curing Conditions

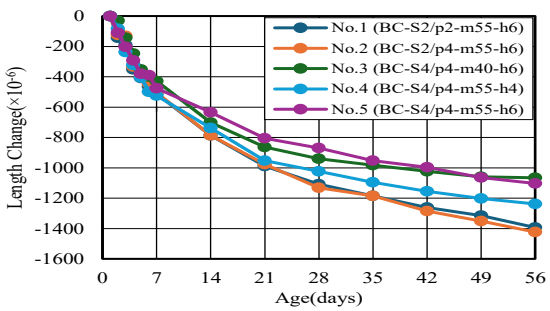

Fig. 5 Length Change

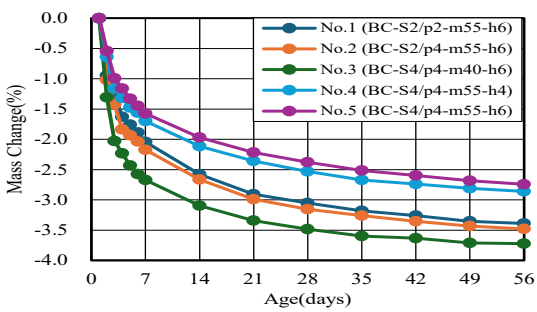

Fig. 6 Mass Change

length change or mass change rates.

In the comparison of maximum temperature between No. 3 and No. 5, No. 3 under the 40°C condition showed the smallest length change rate at an age of 56 days, whereas it showed the largest mass change rate. This is considered to be because the hydration reaction proceeded slowly and coarse pores remained, resulting in low capillary tension relative to moisture loss and suppression of length change.

In the comparison of holding time between No. 4 and No. 5, No. 5, with the longer holding time, showed smaller length change and mass change rates. This is considered to be because extending the holding time densified the pore structure at early ages.

In all levels except No. 3, the length change and mass change rates generally showed similar tendencies. Because greater mass loss was accompanied by greater length change, drying shrinkage rather than autogenous shrinkage was considered to be dominant in this study.

3.3 Pore Size Distribution

Figure 7 shows the pore size distributions and cumulative pore volumes at ages of 1, 28, and 56 days. At an age of 1 day, capillary pores at approximately 300–350 nm were observed in No. 2, with the lower SO_3 content, whereas the peak shifted toward the denser side in No. 5, with the larger amount of anhydrite. This is considered to be because anhydrite promoted the densification of the initial microstructure.

In the comparison of pre-curing time between No. 1 and No. 2, both showed peaks at approximately 300–350 nm, and no clear difference was observed. In the comparison of maximum temperature between No. 3 and No. 5, many capillary pores at approximately 300–400 nm were observed in No. 3 under the 40°C condition. In the comparison of holding time between No. 4 and No. 5, capillary pores at approximately 200–450 nm were observed in No. 4. Based on the above, the pore structure at an age of 1 day was particularly strongly affected by the maximum temperature, and in No. 3, the hydration reaction may not have progressed sufficiently, leaving coarse pores.

At ages of 28 and 56 days, the peaks shifted toward the denser side except in No. 3. In contrast, the peak at approximately 300–400 nm remained in No. 3. In

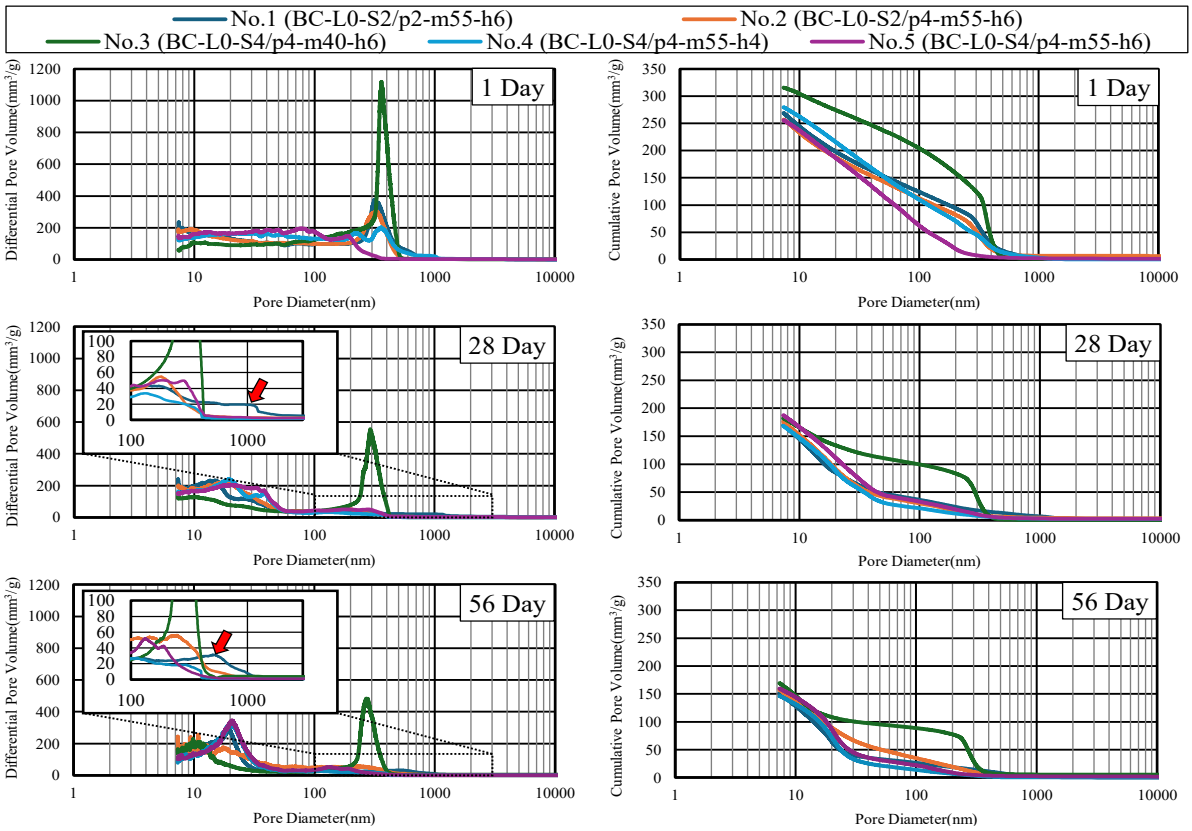

Fig. 7 Pore Size Distribution (Left) and Cumulative Pore Volume (Right) at Different Ages

addition, relatively coarse pores were observed in No. 1, whereas in No. 5, the peak shifted toward the denser side with age.

Because no large differences in cumulative pore volume were observed among the ages or levels, the steam-curing conditions are considered to affect the pore size distribution rather than the pore volume. Although the pore structure became denser with age, differences due to the steam-curing conditions may remain until an age of 56 days.

4. Conclusions

The findings obtained in this study are presented below.

1. The addition of anhydrite improved the compressive strength, and conditions satisfying the target strength were confirmed at an SO_3 content of 4%. In addition, length change was suppressed with increasing anhydrite content.
2. At a maximum temperature of 55°C, the early-age and long-term strengths were higher than those at 40°C. Extending the holding time from 4 to 6 h improved the early-age strength, but long-term strength development tended to be suppressed.
3. The difference in strength at early ages due to the pre-curing time was small, but after an age of 28 days, higher strength was observed with a pre-curing time of 4 h.
4. The steam-curing conditions greatly affected the pore structure at early ages. In particular, under the conditions of a pre-curing time of 2 h, a maximum temperature of 40°C, and a holding time of 6 h, capillary pores tended to remain until an age of 56 days.
5. Within the scope of this study, the condition with a pre-curing time of 4 h, a maximum temperature of 55°C, and a holding time of 4 h (No. 4) was effective in terms of strength development and curing efficiency. Durability evaluation remains a subject for future study.

References

[1]Hashimoto R: Study on the Expanded Use of Ground Granulated Blast-Furnace Slag as Fine Aggregate for Precast Concrete Products, Doctoral Dissertation, Kumamoto University, 2024. (in Japanese)

[2]Ministry of Land, Infrastructure, Transport and Tourism (MLIT): i-Construction: Productivity Revolution in Construction Sites. Available at: https://www.mlit.go.jp/common/001127288.pdf (accessed Jan. 13, 2026).

[3]Sumiyoshi H, Kuboyama K, Imahashi T, and Shiotani M: Effects of Steam Curing on the Microstructure and Properties of Concrete, Cement Technology Annual Report, Vol. 35, pp. 290–293, 1981. (in Japanese)

[4]Ohno Y: Study on Drying Behavior of Concrete Products during the Steam Curing Process, Master's Thesis, Tokyo Metropolitan University, 2019. (in Japanese)

[5]Chatham House: Making Concrete Change: Innovation in Low-carbon Cement and Concrete, The Royal Institute of International Affairs, London, 2018.

[6]Takatsu H, Miyauchi Y, Wachi M, Ikeo Y, Mitsui K, and Yonezawa T: Development of Structural Concrete Using Energy and CO_2 Minimum (ECM) Cement and Concrete, AIJ Journal of Technology and Design, Vol. 17, No. 37, pp. 891–896, 2011. (in Japanese)

[7]Wachi M, Kanai R, Tsuji D, Inoue K, Mitsui K, and Yonezawa T: Fundamental Properties of Concrete Using High-Volume Ground Granulated Blast-Furnace Slag Cement, Takenaka Technical Research Report, No. 67, pp. 1–6, 2011. (in Japanese)

[8]Yoshida N: Deterioration of Concrete Caused by Delayed Ettringite Formation (DEF), GBRC, Vol. 46, No. 1, pp. 31–40, 2021. (in Japanese)

[9]Kawabata Y and Matsushita H: Investigation of DEF Expansion in Concrete Subjected to High-Temperature Steam Curing, Journal of JSCE, Series E2 (Materials and Concrete Structures), Vol. 67, No. 4, pp. 549–563, 2011. (in Japanese)

[10]Yang Y, Zhang Q, Shu X, Wang X, and Ran Q: Influence of Sulfates on Formation of Ettringite during Early C_3A Hydration, Materials, Vol. 15, No. 19, 6934, 2022.

廃ガラス系ジオポリマーの圧縮強度に及ぼす SiO_2/Al_2O_3 モル比および $Ca(OH)_2$ 添加量の影響

Effect of SiO_2/Al_2O_3 Molar Ratio and $Ca(OH)_2$ Content on the Compressive Strength of Waste Glass-Based Geopolymers

朴奎垠※1、姜錫杓※2
Kyu-Eun Park, Suk-Pyo Kang

ABSTRACT

This study evaluated the effects of the SiO_2/Al_2O_3 molar ratio and $Ca(OH)_2$ content on the compressive strength of waste glass-based geopolymers. The SiO_2/Al_2O_3 molar ratio was varied from 3.03 to 15.03, while the Na_2O/SiO_2 molar ratio and W/B were fixed at 0.28 and 0.35, respectively. $Ca(OH)_2$ was also added at 0–9 wt% at a fixed SiO_2/Al_2O_3 molar ratio of 9.05. Compressive strength was measured at 3, 7, and 28 days. The highest 28-day compressive strength of 76.87 MPa was obtained at a SiO_2/Al_2O_3 molar ratio of 9.05, while further increases in the ratio reduced the strength. $Ca(OH)_2$ addition resulted in lower strength than the mixture without $Ca(OH)_2$, although partial recovery was observed with increasing $Ca(OH)_2$ content. Therefore, a SiO_2/Al_2O_3 molar ratio of approximately 9.05 was the most favorable for strength development within the investigated range.

1. Introduction

Ordinary Portland cement (OPC) accounts for approximately 5–8% of global CO_2 emissions, with about 0.85 tons of CO_2 emitted per ton of clinker produced [1,3]. Geopolymers have attracted attention as low-carbon alternatives because they form three-dimensional Si–O–Al networks through alkaline activation and can reduce CO_2 emissions by up to 70–80% compared with OPC [2–4]. In calcium-rich systems, N-A-S-H and C–(A)–S–H gels may contribute to strength development [5].

Although fly ash and ground granulated blast-furnace slag are widely used as geopolymer precursors, their future availability is expected to decline. Waste glass (WG) is a promising alternative due to its high SiO_2 content and amorphous structure. In alkaline media, WG releases reactive silicate species, while fine grinding can enhance its reactivity and suppress alkali–silica reaction expansion [6,7].

However, WG generally contains less than 3 wt.% Al_2O_3, which may limit aluminosilicate network formation. Therefore, controlling the Si/Al molar ratio through an additional Al source is important [8]. Excessively high Si/Al ratios may restrict gel formation, while calcium addition can affect strength development through C–(N)–A–S–H-type reaction products [5]. This study investigated the effects of the Si/Al ratio and $Ca(OH)_2$ addition on the compressive strength and physicochemical characteristics of WG-based geopolymers.

2. Experimental Plan and Methods

2.1 Experimental Plan

In this study, the mixtures were designed as shown in Table 1 to evaluate the effects of the SiO_2/Al_2O_3 molar ratio and $Ca(OH)_2$ content on the compressive strength and reaction product formation of waste glass-based geopolymer binders. All mixtures were

※１ 大韓民国　又石大学校　建設融合システム学科　博士課程
※2 大韓民国　又石大学校　建設融合システム学科　教授

proportioned to a total of 100 wt% and were divided into I-Series and II-Series according to the main experimental variables.

For the I-Series, the SiO_2/Al_2O_3 molar ratio was varied at 3.03, 6.08, 9.05, 12.03, and 15.03 without $Ca(OH)_2$ addition. As the molar ratio increased, the waste glass content was increased while the $Al(OH)_3$ content was decreased. To minimize the influence of activator composition, the amounts of water glass and NaOH were adjusted so that the Na_2O/SiO_2 molar ratio was maintained at 0.28 for all mixtures.

The II-Series was based on the SA9 mixture of the I-Series, with a SiO_2/Al_2O_3 molar ratio of 9.05, to evaluate the effects of $Ca(OH)_2$ addition on reaction characteristics and microstructural development. The $Ca(OH)_2$ content was set at 0, 3, 6, and 9 wt% of the total mixture mass, while the SiO_2/Al_2O_3 and Na_2O/SiO_2 molar ratios were maintained at 9.05 and 0.28, respectively.

The SiO_2/Al_2O_3 and Na_2O/SiO_2 molar ratios presented in Table 1 were calculated based on the amounts of raw materials and their oxide-equivalent molar quantities. The W/B ratio was fixed at 0.35 for all mixtures. In this study, the binder content was defined as the total mass of waste glass powder, $Al(OH)_3$, and $Ca(OH)_2$, while the total water content was defined as the sum of the added water and the water contained in the water glass. The amount of added water was adjusted for each mixture to maintain a constant W/B ratio despite changes in the raw material and water glass contents. Through this mixture design, the effects of the SiO_2/Al_2O_3 molar ratio and $Ca(OH)_2$ content were compared under constant W/B and Na_2O/SiO_2 ratios of 0.35 and 0.28, respectively.

Table 1 Experimental Plan

Series	Mix ID	binder				Water glass	NaOH	Water content	W/B	SiO2 /Al2O3
		WG	$Al(OH)_3$	$Ca(OH)_2$	sum					
Ⅰ-Series	SA3	40.57	24.92	0.00	65.49	7.53	4.06	22.92	0.35	3.03
	SA6	49.47	14.13	0.00	63.6	9.19	4.95	22.26		6.08
	SA9	53.28	9.51	0.00	62.79	9.90	5.33	21.98		9.05
	SA12	55.45	6.89	0.00	62.34	10.30	5.54	21.82		12.03
	SA15	56.85	5.20	0.00	62.05	10.56	5.68	21.71		15.03
Ⅱ-Series	SA9-C0	53.28	9.51	0.00	62.79	9.90	5.33	21.98		9.05
	SA9-C3	51.12	9.13	3.00	63.25	9.49	5.11	22.14		9.05
	SA9-C6	48.96	8.74	6.00	63.7	9.09	4.90	22.3		9.05
	SA9-C9	46.81	8.36	9.00	64.17	8.69	4.68	22.47		9.05

Table 2 Physical and Chemical Properties of Waste Glass Powder

Type	Density (g/cm^3)	Composition ratio(%)									
		SiO_2	Na_2O	CaO	Al_2O_3	MgO	K_2O	Fe_2O_3	SO_3	Others	LOl
WG	2.5	70.8	12.1	11.0	2.7	1.5	0.8	0.4	0.1	0.6	0.08

2.2 Materials

Soda-lime waste glass (WG) powder was used as the main precursor. The WG was washed, dried, ball-milled, and adjusted to a particle size below 75 μm. Its Blaine specific surface area and density were 3,200 cm^2/g and 2.50 g/cm^3, respectively. As shown in Table 2, WG mainly consisted of SiO_2 (70.8 wt%), Na_2O (12.1 wt%), CaO (11.0 wt%), and Al_2O_3 (2.7 wt%). The particle size distribution and XRD pattern are shown in Figs. 1 and 2, respectively. The Dv50 and Dv90 were approximately 30.9 and 75.2 μm, and the XRD pattern exhibited a broad amorphous hump at approximately 20–35° 2θ.

$Al(OH)_3$ and $Ca(OH)_2$ were used as aluminum and

calcium sources, respectively. For mixture design,

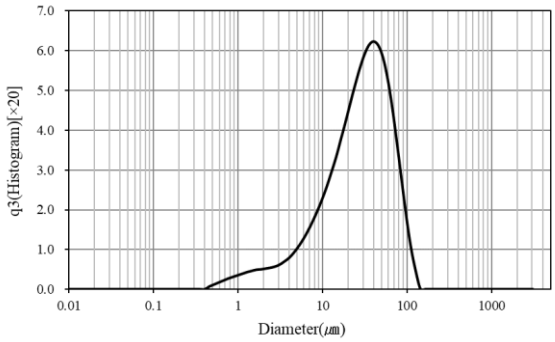

Figure 1 Particle size distribution

they were converted to Al_2O_3- and CaO-equivalent contents using conversion factors of 65.4 and 75.7 wt%. The alkaline activator consisted of NaOH and liquid sodium silicate containing 28.5 wt% SiO_2, 8.5 wt% Na_2O, and 63.0 wt% H_2O. These compositions were considered in the calculation of the molar ratios and total water content.

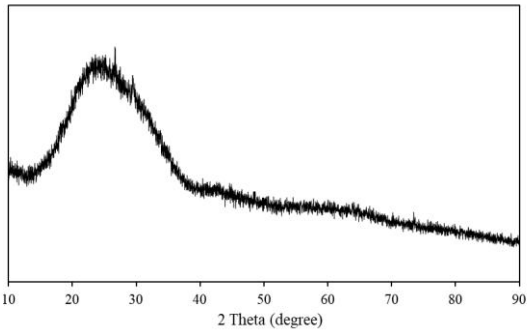

Figure 2 XRD pattern of waste glass

2.3 Experimental Methods

According to the mixture proportions presented in Table 1, waste glass, $Al(OH)_3$, and $Ca(OH)_2$ were weighed and dry-mixed for 2 min. The alkaline activator was prepared by dissolving NaOH in the mixing water, cooling the solution for approximately 30 min, and then adding liquid sodium silicate. The prepared activator was added to the dry-mixed powders, followed by mixing at low speed for 3 min and high speed for 2 min to produce the geopolymer paste. The specimens were sealed with plastic film and cured at 60℃ and 90% relative humidity for a total of 3 days, followed by curing at 20℃ and 95% relative humidity until 28 days.

Compressive strength was measured using 50 × 50 × 50 mm cubic specimens at 3, 7, and 28 days. Three specimens were tested for each mixture and age, and the average value was reported. For reaction product and microstructural analyses, samples were collected from the central portion of the specimens after the compressive strength test. The collected samples were immersed in absolute ethanol for 24 h to stop further reaction and then dried in a vacuum oven at 40℃.

XRD, FT-IR, and SEM analyses were performed on the 28-day samples. XRD analysis was conducted using a BRUKER AXS D6 PHASER over a 2θ range of 10°–70°. FT-IR analysis was performed in ATR mode over the range of 650–4,000 cm^{-1} with a resolution of 4 cm^{-1}.

3. Results and Discussion

3.1 Compressive Strength

Figs. 3 and 4 show the compressive strength at different ages according to the SiO_2/Al_2O_3 molar ratio and $Ca(OH)_2$ content, respectively. The compressive strength increased with curing age for all mixtures, and the 3-day strength corresponded to approximately 72–79% of the 28-day strength. This indicates that a substantial portion of the 28-day strength developed during the initial high-temperature curing period, while further strength development continued with age.

For the I-Series without $Ca(OH)_2$ addition, the compressive strength increased as the SiO_2/Al_2O_3 molar ratio increased from 3.03 to 9.05, but decreased when the ratio was further increased to

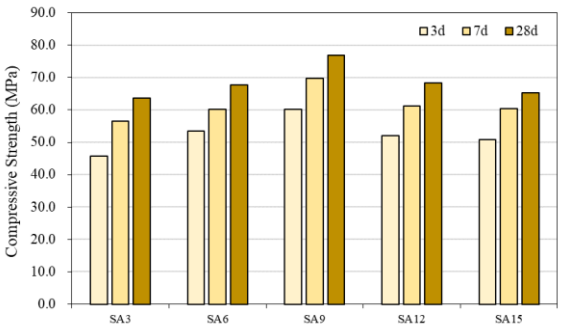

Figure 3 Effect of SiO_2/Al_2O_3 molar ratio on compressive strength

12.03 and 15.03. SA9 exhibited the highest compressive strength at 3, 7, and 28 days, reaching a

maximum value of 76.87 MPa at 28 days. In contrast, the strengths of SA12 and SA15 decreased, indicating that, within the range investigated in this study, a SiO_2/Al_2O_3 molar ratio of approximately 9.05 was the most favorable for strength development.

For the II-Series, in which the SiO_2/Al_2O_3 molar ratio was fixed at 9.05, $Ca(OH)_2$ addition reduced the compressive strength compared with the reference mixture SA9-C0. The largest reduction was observed in SA9-C3 with 3 wt% $Ca(OH)_2$. As the $Ca(OH)_2$ content increased from 3 to 9 wt%, the compressive strength gradually recovered. At 28 days, the compressive strengths of SA9-C3 and SA9-C9 were 59.84 and 66.09 MPa, respectively; however, SA9-C9 was still 14.0% lower than SA9-C0. Therefore, $Ca(OH)_2$ addition within the range of 3–9 wt% did not improve the compressive strength beyond that of the mixture without $Ca(OH)_2$.

The ratio of the 3-day strength to the 28-day strength ranged from 71.8 to 78.8% for the I-Series and from 75.1 to 78.4% for the II-Series. The relative strength development from 3 to 28 days was therefore similar between the two series, suggesting that the SiO_2/Al_2O_3 molar ratio and $Ca(OH)_2$ content had a greater influence on the overall compressive strength level than on the relative rate of strength development with age.

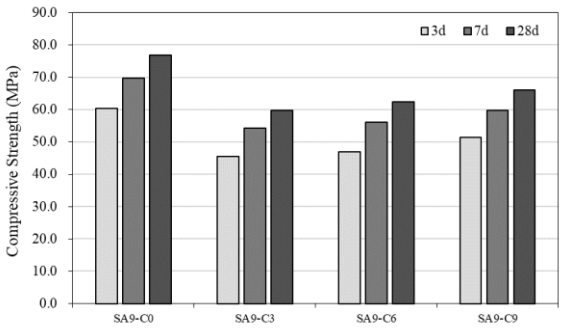

Figure 4 Effect of $Ca(OH)_2$ content on compressive strength

4. Conclusions

In this study, the effects of the SiO_2/Al_2O_3 molar ratio and $Ca(OH)_2$ content on the compressive strength of waste glass-based geopolymers were investigated. The highest 28-day compressive strength of 76.87 MPa was obtained at a SiO_2/Al_2O_3 molar ratio of 9.05. Further increases in the molar ratio reduced the strength. $Ca(OH)_2$ addition also decreased the compressive strength compared with the mixture without $Ca(OH)_2$, although the strength partially recovered as the $Ca(OH)_2$ content increased from 3 to 9 wt%. Therefore, a SiO_2/Al_2O_3 molar ratio of approximately 9.05 was the most favorable for strength development, while $Ca(OH)_2$ addition did not improve compressive strength within the investigated range.

Reference

[1] V. Shobeiri, B. Bennett, T. Xie, P. Visintin, A comprehensive assessment of the global warming potential of geopolymer concrete, J. Clean. Prod. 297 (2021) 126669.

[2] J.L. Provis, S.A. Bernal, Geopolymers and related alkali-activated materials, Annu. Rev. Mater. Res. 44 (2014) 299–327.

[3] S.G.K. Mohan Kumar, J. Kinuthia, J. Oti, B.O. Adeleke, Geopolymer chemistry and composition: A comprehensive review of synthesis, reaction mechanisms, and material properties—oriented with sustainable construction, Materials 18 (2025) 3823.

[4] A.S. Shamsol, N.M. Apandi, W.W.A. Zailani, K.N.K. Izwan, M. Zakaria, Graphene oxide as carbon-based materials: A review of geopolymer with addition of graphene oxide towards sustainable construction materials, Constr. Build. Mater. 404 (2023) 135336.

[5] B. Walkley, R. San Nicolas, M.-A. Sani, G.J. Rees, J. Hanna, Phase evolution of C-(N)-A-S-H/N-A-S-H gel blends investigated via alkali-activation of synthetic calcium aluminosilicate precursors, Cem. Concr. Res. 89 (2016) 120–135.

[6] A. Adesina, Durability and microstructural characteristics of alkali activated materials made with waste glass as precursor: A review, Clean. Mater. 5 (2022) 100121.

[7] Y. Gökşen, U. Durak, S. İlkentapar, İ.İ. Atabey, M. Kaya, Synergistic effect of waste glass powder and fly ash on some properties of mortar and notably suppressing alkali-silica reaction, Rev. Constr. 22 (2023) 52463.

[8] M.U. Christiansen, L.L. Sutter, Waste glass for use in geopolymers, in: ACI SP-294: Advances in Green Binder Systems, American Concrete Institute, Farmington Hills, MI, 2013.

AAM 硬化体組織の緻密化メカニズム

Densification Mechanism of the Microstructure in Hardened Alkali-activated Materials

位田一斗※1, 道正泰弘※2, 田口翔大※3, ダオテイフォン※4
Ichito Inden, Yasuhiro Dosho, Shouta Taguchi, Phuong Dao Thi

ABSTRACT

本研究は，活性フィラーに高炉スラグ微粉末(GGBFS)を用いたアルカリ活性材料(AAMs)の硬化体組織の緻密化が不十分になりやすいという課題を解決することを目的とした．GGBFS 中の石膏含有量の違いが初期強度やフロー値に及ぼす影響は軽微であった．アルカリ刺激剤の割合を高めることで強度は向上した．SEM 観察により，アルカリ刺激剤や石膏量によって初期の反応性や水和生成物の形態に差異が生じた．材齢経過とともに，いずれの配合でも C-S-H 系水和物が発達した．これが未水和粒子周辺や空隙を充填し，緻密な組織を形成された．EDS 分析から，GGBFS からの Si の持続的な溶出に伴って Ca/Si が低下し，Si に富むゲル相へ変化していくことが判明した．Si に富んだ C-S-H への移行が AAMs の長期的な組織緻密化および強度増進に寄与することが明らかとなった．

1. Introduction

In 2020, against the background of global warming, Japan declared the aim of achieving carbon neutrality by 2050 [1]. In addition, achieving decarbonization through a reduction in CO_2 emissions throughout the life cycle of materials as well as extending their lifespan has become important in the construction industry [2]. The production of cement, in particular, emits large amounts of CO_2; therefore, alkali-activated materials (AAMs) that utilize industrial byproducts such as ground granulated blast-furnace slag (GGBFS) are attracting attention as suitable alternatives [3]. AAMs are hardened materials produced by activating aluminosilicate precursors with alkali activators, with silica (SiO_2)-based reactive fillers often incorporated to modify reaction kinetics and material properties. Their use thus has the potential to suppress CO_2 emissions compared to the use of ordinary Portland cement (herein referred to as NC) [4]. However, the densification of the hardened body tends to be inferior to that produced by NC. In addition, the strength of AAMs tends to stagnate with age, and they are less durable than NC [5]. However, the development of the circular economy requires the effective utilization of recycled aggregates [6]. In particular, the utilization of low-quality recycled aggregates is highly economically efficient and environmentally desirable. Aggregates have high absorption due to the presence of adhered mortar and cement paste, so they can affect the formation of the structure that forms upon combination with AAMs [7]. Therefore, in the context of achieving decarbonization and resource circulation, it is important to clarify the densification mechanism of the hardened body structure that is produced using these low-quality materials from a microscopic viewpoint. In this study, the production of environmentally friendly concrete using low-quality recycled aggregate combined with AAMs and an alkali activator was investigated. The authors have previously investigated an environmentally friendly concrete material prepared by combining a GGBFS-based AAM (an AAM that incorporates GGBFS as a reactive filler) and low-quality recycled aggregate for its applicability as a pavement material; however, many details of the densification process and the morphological changes that occur in the hydrates

※1 日本　名城大学大学院理工学研究科環境創造工学専攻
※2 日本　名城大学理工学部環境創造工学科 教授 博士(工学)
※3 日本　名城大学大学院理工学研究科社会環境デザイン工学専攻
※4 日本　鹿島道路(株)技術研究所 修士(工学)

remain unclear [8, 9].

Furthermore, while concrete and mortar densify, it is known that their chemical compositions, especially the Ca/Si ratio, greatly affect the compressive strength and packing density of the C–S–H's microscopic structure, which is a factor affecting the development of material strength [9]. Specifically, it is thought that changes in the Ca/Si alter the hydrate's microscopic structure. This alteration is observable and directly affects strength characteristics [9]. It is also thought that, during the formation of AAMs, the ratio of Ca ions to Si ions supplied by alkali activators and GGBFS affects the densification of the hardened body, but how the details of this depend on the combination of different solidifying agents and alkali activators also remains unclear.

This study aimed to clarify the densification mechanism of the microstructure of hardened AAMs. This study evaluated the strength characteristics of an AAM system combining GGBFS with multiple alkali activators, characterized the hardened materials using scanning electron microscopy (SEM), and analyzed the Ca/Si ratio (Ca/Si) using energy dispersive X-ray spectroscopy (EDS).

2. Experiment

2.1 Materials

Table 1 shows details of the mortar test pieces used in this study. For the binder, two types of GGBFS materials were used: (i) GGBFSa with a normal gypsum content and (ii) GGBFSb with a higher gypsum content than GGBFSa. For the alkali activator (P), which promoted the latent hydraulicity of the GGBFS, slaked lime consisting mainly of $Ca(OH)_2$ (A1), non–Japanese Industrial Standards (JIS) slaked lime (A2), or dolomite series (B) were used. The Rietveld analysis results for each alkali activator were adopted from a previous study [8]. For comparison of the strength development, ordinary Portland cement (NC) and high-early-strength Portland cement (HC) were used. Standard sand (S) was used as the fine aggregate, and tap water (W) was used for mixing.

Table 1. Materials

Item	Material	Symbol	Remarks
Binder	Granulated blast-furnace slag A	GGBFSa	JIS A 6206
	Granulated blast-furnace slag B	GGBFSb	JIS A 6206
Alkali activators	Slaked lime	A1	Main ingredient: $Ca(OH)_2$
	Dolomite series	B	Main ingredient: $CaCO_3$
	Non-JIS slaked lime	A2	Main ingredient: $Ca(OH)_2$
	Ordinary Portland cement	NC	JIS R 5210
	High-early-strength Portland cement	HC	JIS R 5210
Aggregate	Standard sand	S	-
Mixing water Admixture	Tap water	W	-

Table 2 Mix proportion

No.	B		P/B (%)	Mass (g)			
	Binder	P		W	GGBFS	P	S
1	GGBFSa	A1	10	225	405	45	1350
2			13.9		387	63	
3			20		360	90	
4		B	10		405	45	
5			20		360	90	
6		A2	10		405	45	
7			20		360	90	
8		NC	10		405	45	
9			30		315	135	
10			50		225	225	
11		HC	10		405	45	
12			30		315	135	
13			45		247.5	203	
14			50		225	225	
15	GGBFSb	B	10		405	45	
16			20		360	90	
17		A2	10		405	45	
18			20		360	90	
19		NC	10		405	45	
20			30		315	135	
21			50		225	225	
22		HC	10		405	45	
23			30		315	135	
24			50		225	225	

Table 3 Test items and methods

Evaluation item	Test method		Age (days)
Fresh concrete	Slump flow	JIS R 5201	-
Strength properties	Flexural strength	JIS R 5201	7, 28, and 91
	Compressive strength	JIS R 5201	7, 28, and 91
Characterization	SEM	Observation and analysis using a JST-IT200	7, 28, and 91
	Ca/Si analysis via EDS		28

2.2 Mix proportion

Table 2 shows the mix proportion. Experiments were conducted using mortar specimens with varying replacement ratios of each alkali activator to the binder and a constant water–binder ratio of 50%.

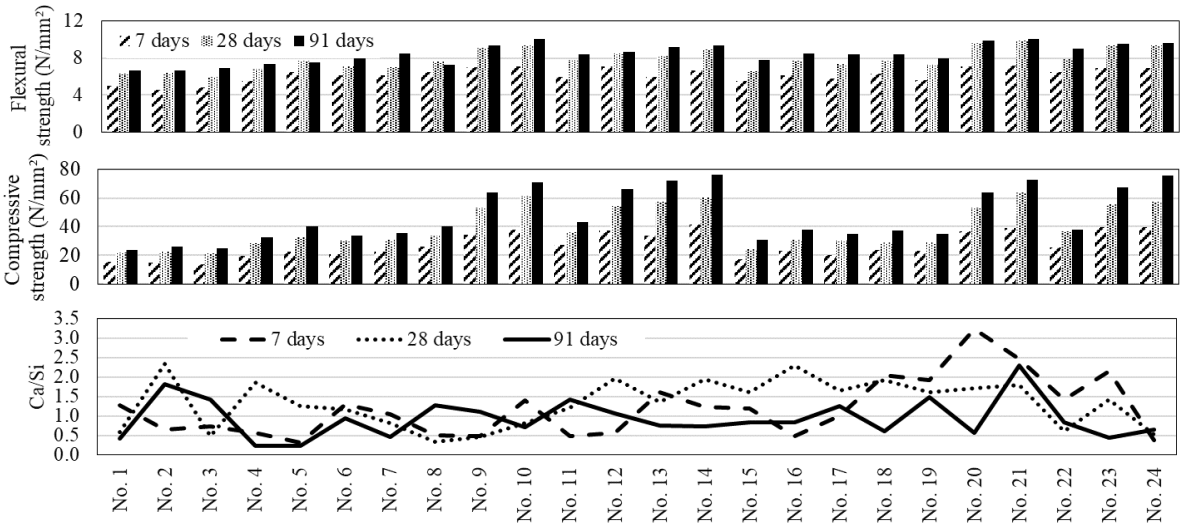

Figure 3 Flexural strength, Compressive strength and Ca/Si analysis via EDS

2.3 Test items and methods

Table 3 lists the test items and methods. For the freshly produced mortar, the flow value was measured. The flexural strength and compressive strength were also determined.

The mortar test pieces (40mm × 40mm × 160mm) were prepared according to JIS R 5201. Compressive strength was measured using the broken halves resulting from the flexural strength tests. The test pieces were demolded after 24h at 20ºC ± 2°C, and underwater curing was performed at 20ºC ± 1°C until ages of 7, 28, and 91 days were reached.

For SEM observations and Ca/Si analysis via EDS, 10mm × 10mm × 160mm samples were cut around the center of the specimens after strength testing. These were then immersed in acetone for 15min, vacuum-dried for at least 20h. Following this, Au was vapor-deposited onto the surface of the test pieces for 60s. The SEM observations were performed at a magnification of ×5000.

3. Experimental results

3.1 Fresh concrete

Although GGBFSb exhibited a higher gypsum content than GGBFSa, both samples showed similer flow values.

3.2 Strength properties

3.2.1 Flexural strength

As shown in Figure 3, the flexural strength of sample No. 1 was 6.3N/mm^2 at a material age of 28days. In the mix proportion incorporating B and A2, the flexural strength increased only slightly to 6.8–7.1 N/mm^2, whereas in the mix proportions incorporating NC and HC, it further increased to 8.5–9.4N/mm^2. Thus, comparing the alkali activators, there is a tendency for the strength to increase in the order A1 < B ≈ A2 < NC < HC. There is also a tendency for the flexural strength to increase as the proportion of the alkali activator in the sample increases.

3.2.2 Compressive strength

As shown in Figure 3, No. 1 showed a compressive strength of 21.8N/mm^2 at an age of 28 days. The mix proportions with B and A2 showed slightly higher strengths of 28.4N/mm^2 and 30.2N/mm^2, respectively, at the same P/B ratio compared to A1. Meanwhile, the mix proportions with NC and HC showed significantly higher compressive strengths. No. 14 showed a compressive strength of 60.3N/mm^2 at an age of 28 days, achieving a considerably higher strength compared to A1, A2, and B. This result suggests that HC increased the compressive strength. Furthermore, all mix proportions showed an increase in the compressive strength from an age of 7days to 91days. Additionally, a comparison based on the type of GGBFS revealed no distinct differences in flexural and compressive strengths as well as no improvement

in early-age flexural and strengths.

3.3 Investigation of the Ca/Si

Figure 3 shows the EDS Ca/Si analysis results. The C–S–H chemical composition changed clearly at 28 and 91days, with structural densification depending on the GGBFS type. Generally, C–S–H gels with a low Ca/Si ratio exhibit longer silicate chains. For GGBFSb, the initially high Ca/Si at 7days decreased with age. This likely occurred as the initial abundant Ca^{2+} from the activator and high gypsum content was consumed, while continuous silica elution from the GGBFS gradually formed Si-rich C–S–H gels. Conversely, GGBFSa showed no such Ca/Si decrease; its lower initial Ca concentration due to lower gypsum content facilitated the formation of Si-rich C–S–H gels from an early age.

3.4 Surface structure of the mortar specimens

3.4.1 Identification of hydrates

For all mix proportions, many residual particles and voids were observed at an age of 7days along with dispersed hydration products. The authors identified the hydrates by referring to SEM images in references [10, 11]. Additionally, the identification of each product in the SEM images was based primarily on morphological characteristics. In particular, for fine needle-like products and gel-like products observed at early ages, AFt, AFm, and C–S–H may be observed partially overlapping.

3.4.2 Evaluation of the C–S–H gel

The morphological differences between the different C–S–H gels that formed and the densification of the hardened structure were evaluated based on the SEM images. Four features were considered. First, the proportion of interparticle voids was considered along with whether a scattered or continuous phase was visible. The second feature considered was shape—whether it was fibrous, foil- or flake-like, massive or aggregate-like, or film-like. Third, the solidity of the structure was evaluated by examining the surface roughness, its density and smoothness, and the degree to which the surfaces of unhydrated particles were exposed. The fourth feature considered was

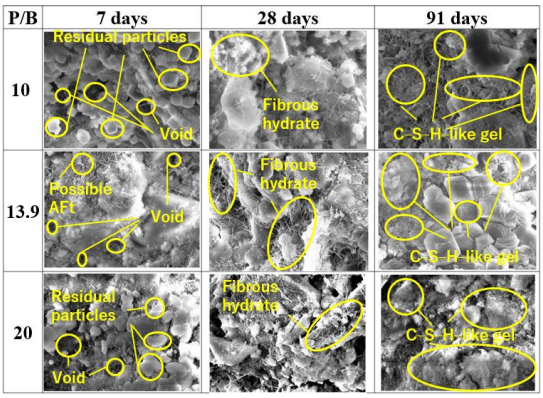

Figure 4 No. 1, No. 2, No. 3

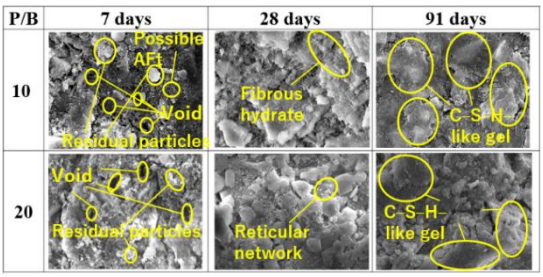

Figure 5 No. 4, No. 5

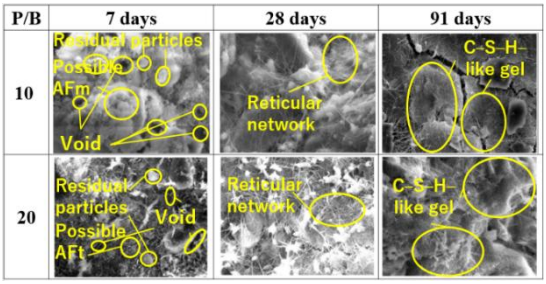

Figure 6 No. 6, No. 7

connectivity—that is, whether the individual products in the structure were isolated or networked. In Figures 4–12, it can be seen that the material with an age of 91 days exhibits a continuous C–S–H gel phase that surrounds the unhydrated particles and fills the interparticle voids; the overall coverage of the surface of the unhydrated particles by the gel phase has also increased. In contrast, in the case of the material with an age of 7days, the products are localized and dispersed, and the outlines of the unhydrated particles and the voids between them remain clear.

3.4.3 Influence of different alkali activators on the initial reactivity

The alkali activator used affected the reactivity. The dissolution and reaction of GGBFS did not proceed well at the initial stage, thus delaying the formation of hydration products even though some $Ca(OH)_2$ was present in the A2 activator. At a material

age of 7days, when using A1 (Figure 4) and A2 (Figure 6) as the activators—with $Ca(OH)_2$ as the main component—the initial reactivity was different. Despite A2 containing a larger amount of $Ca(OH)_2$ than A1 (as reported in a reference [8]), A1 produced a smaller amount of unhydrated particles than A2 and needle-like products were produced at an earlier stage (Figures 4, 6). This demonstrates that a higher $Ca(OH)_2$ content does not simply lead to a faster initial reaction—it also affects the number of unhydrated particles and the time at which the needle-like products appear.

3.4.4 Influence of gypsum content

The influence of the gypsum content of the GGBFS was also investigated. Originally, it was expected that the higher gypsum content of GGBFSb would promote the initial generation of ettringite. However, Figures 5, 6, 9, and 10 show that at an age of 7days, if there was insufficient initial alkali stimulation, differences in the gypsum content alone did not lead to significant differences in the hydration products. Furthermore, as the material aged, the initial needle-like ettringite decreased and transitioned to more stable monosulfate and C–S–H gels in the A2 mixtures (Figures 6, 10) and the cement-based mixtures with high replacement rates (Figures 7, 8, 11, 12).

3.4.5 Structure formation at greater material ages

During the microstructure formation from an age of 28days to a long-term age of 91days, the difference in the Ca^{2+} supply resulting from gypsum affected the morphology of the products and variation in the Ca/Si. It further likely manifested as a difference in the formation of fibrous or massive microstructures. For GGBFSb in particular, which had a large initial Ca^{2+} supply (see Figures 9–12), there was a tendency for massive, filling-type products to form. In contrast, in the case of GGBFSa (see Figures 4–8) fibrous or reticular products readily appeared from the initial stage onward. Consequently, although in both cases the material densified over the long term, there were differences in how the voids around unhydrated particles were filled, in the fibrous remnants, and in the continuity of the massive gels.

3.4.6 Relationship between the Ca/Si and structure densification

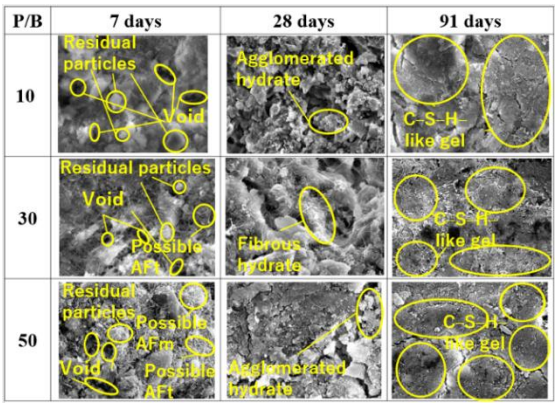

Figure 7 No. 8, No. 9, No. 10

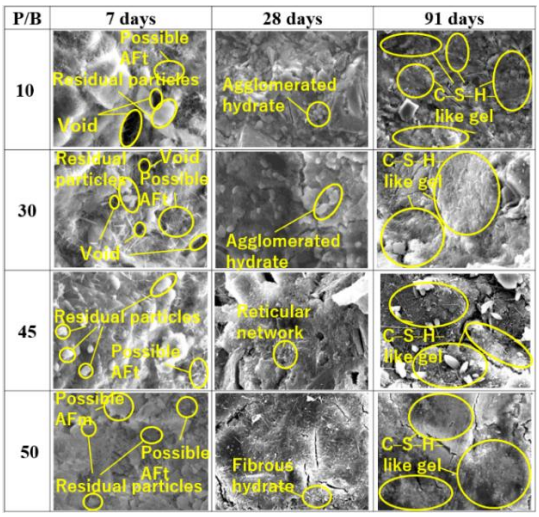

Figure 8 No. 11, No. 12, No. 13, No. 14

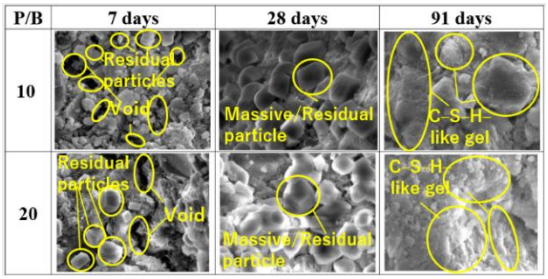

Figure 9 No. 15, No. 16

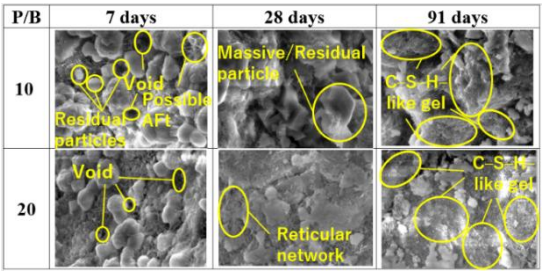

Figure 10 No. 17, No. 18

The decrease in the Ca/Si is thought to correspond to an increase in the degree of polymerization of the silicate chains in C–S–H [9, 12]. Although the length

of the silicate chains could not be directly observed using the SEM, the formation of continuous, dense gel phases that surrounded the unhydrated particles and filled the voids see the images of material with an age of 91days in Figures 9–12 was confirmed together with a decrease in the Ca/Si as the material aged (see Figure 5). Therefore, it is highly likely that the transition to Si-rich C–S–H affected the void filling and structure densification over the long term.

4. Conclusions

This study aimed to clarify the densification mechanism of the microstructure of hardened AAMs and investigated a GGBFS-based AAM system incorporating GGBFS and multiple alkali activators. The following results were obtained.

(1) The densification of the microstructure in the GGBFS-based AAM system was governed by early and long-term mechanisms, namely the differences in the initial reactivity caused by the alkali activator and changes in the chemical composition of C–S–H-based hydrates with aging.

(2) The difference in the gypsum content of GGBFS caused certain differences in the morphology of the products and the time-dependent change in the Ca/Si ratio, although it exerted only a minor effect on the flow value and early strength development.

(3) During long-term aging, the formation of Si-rich gel phases progressed as the Ca/Si decreased. These gel phases densely filled spaces around residual particles and voids, contributing to a higher degree of microstructure densification and strength enhancement.

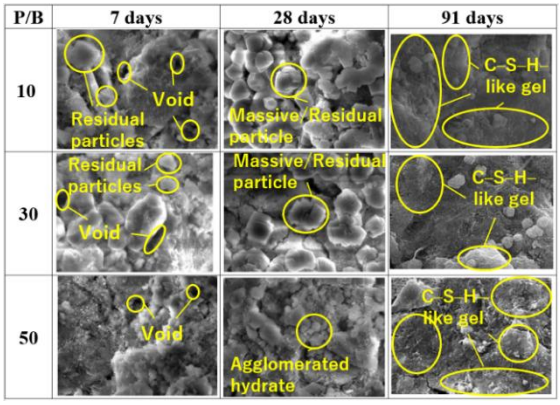

Figure 11 No. 19, No. 20, No. 21

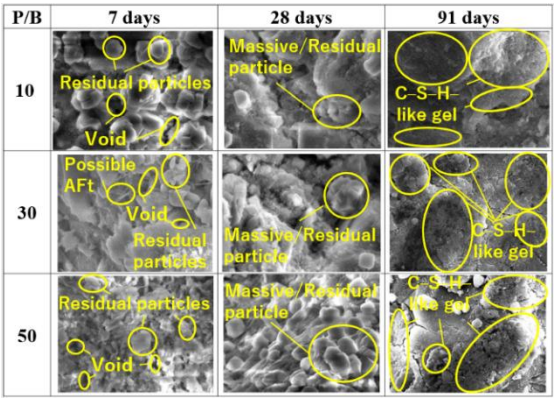

Figure 12 No. 22, No. 23, No. 24

References

[1] Ministry of the Environment; Plan for Global Warming Countermeasures (Cabinet Decision on February 18, 2025). https://www.env.go.jp/content/000291669.pdf

[2] Ministry of Land, Infrastructure, Transport and Tourism; Efforts to Accelerate Carbon Neutrality in the Building Construction Sector. https://www.mlit.go.jp/policy/shingikai/content/001493862.pdf

[3] Japan Science and Technology Agency (JST); A Projection of Cement Demand by Usage of Japan and an Assessment of CO_2 Emission from Building Materials, LCS Report, 2022. https://www.jst.go.jp/lcs/pdf/fy2022-pp-01.pdf

[4] JFE Steel Corporation; Development of Alkali-Activated Material Concrete that Achieves Both CO_2 Reduction and Effective Utilization of Resources. https://www.env.go.jp/earth/ondanka/min_action_award//files/winners_r07_08.pdf

[5] Kamishita R. et al., THE DURABILITY EVALUATION OF PAVEMENT MATERIALS USED ONLY RECYCLED MATERIALS, Japanese Journal of JSCE, Vol. 79, No. 21, 1-11, 2023. DOI https://doi.org/10.2208/jscejj.23-21007

[6] Ministry of Land, Infrastructure, Transport and Tourism; The 18th Subcommittee for Studying Construction Recycling Promotion Measures (Document 1: Summary of Main Discussions and Issues to Date). https://www.mlit.go.jp/policy/shingikai/content/05_shiryou1.pdf

[7] Tao Y. et al., Quality improvement of recycled concrete using low-quality recycled aggregate by admixtures, Proceedings of the Japan Concrete Institute, Vol. 42, No. 1, 1330-1335, 2020.

[8] Kondo N. et al., Study on Alkali Activator and Strength Propreties of Mortar Using AAM, Proceedings of the JSCE Annual Meeting 2026, V-866.

[9] W. Kunther, et al., Influence of the Ca/Si ratio on the compressive strength of cementitious calcium–silicate–hydrate binders, Journal of Materials Chemistry A, Vol. 5, No. 33, 17401-17412, April 24, 2017.

[10] Japan Cement Association; Common Sense of Cement, June 1996.

[11] Z. Zuo, et al., Effect of Curing Regime on the Mechanical Strength, Hydration, and Microstructure of Ecological Ultrahigh-Performance Concrete (EUHPC), Journals, Vol. 15, No. 5, February 23, 2022. DOI https://doi.org/10.3390/ma15051668

[12] T. Vehmas, et al., Effect of Additional Surfaces on Ordinary Portland Cement Early-Age Hydration, Materials Sciences and Applications, Vol. 8, No. 12, 859-872, 2017. DOI https://doi.org/10.4236/msa.2017.812063

持続可能なアルカリ活性複合材料：機械的特性および耐火性能の評価

Sustainable Alkali-Activated Composites: Assessing Mechanical Properties and Fire Resistance Performance

李在寅※1、金仁松※2、金晋鎬※2、申民知※3、朴正娟※4、崔世珍※5

Jae-In Lee, In-Song Kim, Jin-Ho Kim, Min-Ji Shin, Jeong-Yeon Park, Se-Jin Choi

ABSTRACT

To reduce cement consumption in the construction industry, alkali-activated composites utilizing ground granulated blast-furnace slag (GGBS), fly ash (FA), and ferronickel slag (FNS) powder as alternatives have attracted significant attention. This study investigated the mechanical and fire-resistant properties of GGBS-based cement-free composites incorporating FA and FNS as binders. The results revealed that the cement-free composites developed higher compressive strength under ambient curing than under water curing. Furthermore, the FNS-incorporated specimens demonstrated superior fire resistance, exhibiting an internal specimen temperature approximately 11% lower than that of the FA specimens.

1. Introduction

Recently, many studies are being conducted in various industrial fields to achieve carbon neutrality. In the construction sector, research on low-cement composites or cement-free composites that do not utilize cement is actively underway to achieve carbon neutrality [1]. Cement-free composites are composites that completely eliminate the use of cement and have the advantage of being able to reduce carbon dioxide emissions by up to 90% compared to currently used cement composites. In addition, while exhibiting low carbon dioxide emissions, they can maintain performance levels similar to general cement composites, and some studies have reported results showing even higher mechanical performance. In particular, numerous results have been reported showing that cement-free composites have superior fire resistance compared to general cement composites, which may be attributed to the fact that the reaction of blast furnace slag powder used as a binder does not form calcium hydroxide ($Ca(OH)_2$) [2]. Generally used Portland cement contains calcium hydroxide, and when exposed to high temperatures, $Ca(OH)_2$ undergoes dehydration and thermal decomposition in the range of approximately 400–500℃. Changes in the pressure and volume of water vapor generated during this process have a negative impact in high-temperature environments, such as causing cracks within the composite matrix and loosening the structure. For this reason, cement-free composites that do not generate calcium hydroxide exhibit relatively superior fire resistance compared to conventional cement composites. However, cement-free composites using only blast furnace slag as a single binder have limitations in terms of workability and durability, such as rapid setting characteristics and the occurrence of drying shrinkage cracks. To compensate for this, various methods are being explored to incorporate industrial by-products such as fly ash. Recently, research on construction materials utilizing ferronickel slag, which is generated as a by-product in the

※1 大韓民国 圓光大学校 建築工学科 博士(工学)
※2 大韓民国 圓光大学校 建築工学科 学士課程
※3 大韓民国 圓光大学校 建築工学科 学修士統合課程
※4 大韓民国 圓光大学校 建築工学科 修士課程
※5 大韓民国 圓光大学校 建築工学科 教授 博士(工学)

manufacturing processes of stainless steel and ferronickel, has been reported. According to research on cement composites using ferronickel slag, the incorporation of ferronickel slag has a positive effect on mitigating performance degradation, such as preventing a decrease in residual compressive strength of the composite exposed to high temperatures and maintaining the thermal stability of the internal structure. This is believed to be because magnesium compounds contained in ferronickel slag maintain a thermally stable phase in high-temperature environments. However, despite these potential advantages, systematic research on the fire resistance performance of cement-free composites incorporating ferronickel slag remains limited. In particular, research on the mechanical and fire resistance performance before and after high-temperature exposure when various industrial by-products are incorporated into blast furnace slag-based cement-free composites is very scarce. In this study, to maximize the fire resistance performance of slag-based cement-free composites, the performance with ferronickel slag powder was evaluated under high-temperature exposure.

2. Materials and methods

2.1 Materials

In this study, ground granulated blast-furnace slag (GGBS), fly ash (FA), and ferronickel slag (FNS) were used as binders to manufacture blast furnace slag-based cement-free composites. Unlike cement, these binder materials do not exhibit hydraulic properties, so alkali activators must be used to activate the reaction of the materials. Accordingly, in this study, experiments were conducted using powdered alkali activators CaO, $Ca(NO_3)_2$, and NaOH, and the incorporation amounts of the activators were referenced from previous studies [3]. Additionally, cement composites were manufactured simultaneously to compare the fire refractory performance of the cement-free composites and the cement composites; ordinary Portland cement (Sampyo Cement, Republic of Korea) was used as the cement. Information on the binders used is shown in Table 1, and the incorporation rates of the alkali activators are shown in Table 2.

2.2 Experimental methods

2.2.1 Mix Proportions and Specimen Preparation

The detailed mix proportions design used in this study is presented in Table 2. All specimens were classified and tested separately as paste and mortar. The water-to-binder (W/B) ratio was kept constant at 56.5% for the cement-based mixtures and 53% for the cement-free mixtures. For the cement-based composites, ordinary Portland cement (OPC), fly ash (FA), and ground granulated blast-furnace slag (GGBS) were applied as binders. On the other hand, the cement-free composites were categorized into two types, which are the GFA sample incorporating GGBS and FA, and the GFN sample utilizing GGBS

Table 1 Information on the binder used

Classification		Binders			
		OPC	GGBS	FA	FNS
Physical properties	Density(g/cm^3)	3.15	2.93	2.21	3.09
	Blaine(cm^2/g)	3,430	4,210	3,710	15,890
Chemical composition (%)	CaO	64.4	64.40	2.58	1.1
	SiO_2	17.43	17.43	64.88	48.8
	Al_2O_3	6.50	6.50	20.56	2.8
	Fe_2O_3	3.57	3.57	6.06	13.7
	MgO	2.55	2.55	0.80	30.6
	K_2O	1.17	1.17	1.45	-

Table 2 Mixing proportions of sample

Mix	W/B (%)	Water (kg/m^3)	Binder (kg/m^3)	OPC (B*%)	GGBS (B*%)	FA (B*%)	FNS (B*%)	CaO (B*%)	$Ca(NO_3)_2$ (B*%)	NaOH (B*%)
CGF-P	56.5	175	310	70	20	10	-	-	-	-
CGF-M										
GFA-P	53	180	340	-	75	10	-	5	5	5
GFA-M										
GFN-P					80	-	5			
GFN-M										

and ferronickel slag powder. In addition, to control the fluidity of the composites, a superplasticizer dosage was fixed at 0.1% for the paste mixtures and 0.3% for the mortar mixtures by weight of the binder.

2.2.2 Mechanical Performance Evaluation

First, compressive strength tests were conducted in accordance with KS L 5105, using the average of three identical specimens. The curing conditions were differentiated: unheated specimens underwent either water curing or ambient-temperature curing, while all specimens designated for high-temperature exposure were subjected exclusively to ambient-temperature curing to prevent thermal shock and excessive moisture loss. To evaluate residual strength after heating, specimens were heated to 800℃ in an electric furnace, maintained for 2 hours, and then naturally cooled at room temperature (23±2℃) for 24 hours before testing. Concurrently, a unit weight test was performed by comparing specimen weights before and after heating to trace physical and structural alterations.

2.2.3 Fire Resistance Performance Evaluation

The fire resistance was evaluated using two methods simultaneously to achieve multi-faceted verification. For Method 1 (Laboratory-Scale Fire Test), cylindrical specimens Ø100x50mm with a pre-installed central K-type thermocouple were prepared. After 28 days of ambient-temperature curing, the specimens were heated in a furnace to 800°C at 10℃/min and maintained for 2 hours while a data logger recorded the internal temperature.

For Method 2 (Unexposed Surface Temperature Test), experiments complied with the KS F 2257-7 standard. Specimens with a 40 mm thickness were prepared, and a 3 mm thick steel plate with a temperature sensor was attached to their back surface to simulate structural boundaries. Two replicate specimens per mix were tested. Among the cement-free composites, only the GFA sample was selected due to its superior compressive strength. The front surface was heated, and the unexposed surface temperature rise was monitored to analyze insulation efficiency

3. Results and Discussion

3.1 Compressive strength

The compressive strength measurements indicated that the cement-based composites exhibited superior strength development characteristics compared to the cement-free composites across all curing ages. The relatively lower early and long-term compressive strength development of the cement-free composites is attributed to the delay in the initial polymerization process; although high-temperature environments generally favor the activation of geopolymerization, the curing in this study was conducted under water and ambient conditions at 20℃. Particularly, in the comparison of the curing conditions for the cement-free composites, the ambient-cured specimens showed higher compressive strength than those cured in water. This outcome is likely because the alkali activator within the specimens leached and diluted into the surrounding water during the water curing process, which consequently hindered the polymerization reaction and led to a decrease in the matrix density.

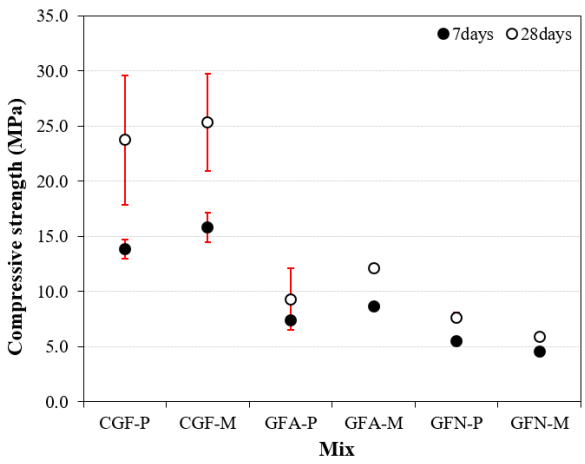

(a) Water curing

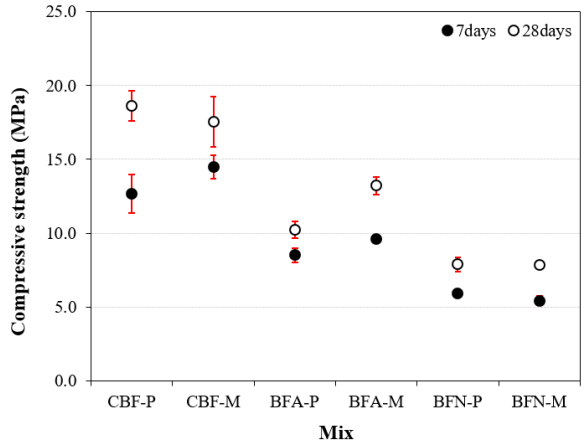

(b) Ambient curing

Figure 1 Compressive strength

3.2 Fire resistance performance

The results of the laboratory-scale fire resistance performance evaluation are presented in Figure 2. Note that the CGF-M sample was excluded from the analysis due to thermocouple damage that occurred during the measurement. The maximum temperatures of the cement-free mortar samples reached approximately 800℃, exhibiting a similar level of performance among them. In contrast, comparing the paste samples, the CGF sample exhibited the highest temperature, whereas the cement-free samples maintained temperatures below 600℃, demonstrating an excellent thermal insulation effect. Among the cement-free samples, the temperature of the specimen incorporating FNS rose significantly less than that using FA, confirming that the application of FNS effectively enhances fire resistance performance.

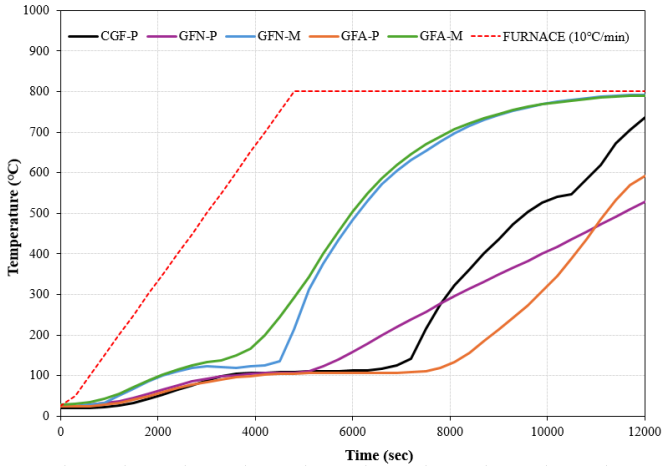

Figure 2 Fire resistnace performance

4. Conclusions

In this study, the fire resistance performance of GGBS-based cement-free composites incorporating FA and FNS was evaluated. The compressive strength was higher in the specimens incorporating FA than in those with FNS. However, the fire resistance test revealed that the addition of FNS significantly improved thermal performance. Consequently, FNS is considered an effective material for enhancing the fire resistance of blast furnace slag-based cement-free composites.

Acknowledgements

This research was supported by a grant from the National Research Foundation of Korea (NRF) funded by the Korea government (MIST) (RS-2024-00405537).

Reference

[1] J.I Lee, C.Y. Kim, J.H. Yoon, H.J. Lee, S.J. Choi, Characteristics of alkali-activated composites containing blast-furnace slag aggregate and ferronickel slag pwoder, Mag Concr Res, 2025.

[2] J.I. Lee, C.Y. Kim, J.H. Yoon, S.J. Choi, Compressive strength and chloride ion penetration resistanace of GGBFS-based alkali-activated composites containing ferronickel slag aggregates, Materials, 2024.

[3] J.I. Lee, C.Y. Kim, J.H. Yoon, H.J. Lee, S.J. Choi, Effect of curing method on the mechanical properteis and durability of blast furance slag-based Geopolymer composites containing ferronickel slag powder, J. KCI, 2024.

高炉スラグ微粉末の混和が爆裂に与える影響

Effect of Ground Granulated Blast-Furnace Slag Addition on Concrete Spalling

豊島明紘※1，金準鎬※2，西尾悠平※3，兼松学※4
Akihiro Toyohima, Junho Kim, Yuhei Nishio, Manabu Kanematsu

ABSTRACT

This study aimed to clarify the effects of ground granulated blast furnace slag (GGBFS), used as a mineral admixture, on concrete spalling and the factors influencing spalling. In addition, the study investigated how polypropylene (PP) fibers, which are known to suppress spalling, affect concrete containing GGBFS. Neutron radiography was employed to obtain relative moisture content images of concrete specimens during heating, and the influence of moisture distribution on spalling behavior was examined. The results showed that the incorporation of GGBFS tended to increase the frequency of spalling, whereas the addition of PP fibers effectively suppressed spalling even in concrete containing GGBFS. Furthermore, analysis of the relative moisture content images revealed differences in the drying rate, which were closely related to the occurrence of spalling.

1. はじめに

鉄筋コンクリート構造物が火災の高温環境下にある時, 表面が剥離する爆裂現象を生じることがある。爆裂現象は高強度のコンクリートにおいて発生しやすいとされており, 既往の研究では爆裂の主な発生要因として水蒸気圧説[1)], 熱応力説[2)]，それらの複合作用説[3)]などがある。また，PP(ポリプロピレン)繊維を混入させることで爆裂が抑制されることが知られている。

一方で, 近年では持続可能性の観点から環境配慮コンクリートの導入が進められており, 高炉スラグ微粉末(以下 GGBFS)を混和材として用いたコンクリートの使用が拡大している。岩村ら[4)]は中性子ラジオグラフィ装置を用いた加熱試験を行い, 混和材が水分状態や爆裂影響を与えることを明らかにした。しかしながら，相対含水率としての定量化による分析やGGBFSがPP繊維の爆裂抑制効果に与える影響の検討については未だ行われていない。

そこで本研究では，GGBFSの混和がコンクリートの爆裂およびPP繊維の爆裂抑制効果に与える影響について, 中性子ラジオグラフィ装置を用いて明らかにすることを目的とする。

2. 実験概要

2.1 試験体概要

実験は, GGBFSの使用の有無とPP繊維の有無を水準とした。各水準において圧力測定用試験体3 体と熱電対挿入用の孔を設けた温度測定用試験体1 体の計4 体で加熱試験を行った。

試験体概要を **Figure 1** に示す。

試験体寸法は100×70×30mm（幅×高さ×厚さ）とした。圧力測定用試験体は, 加熱面より5mm, 10mm の位置に圧力測定用のステンレスパイプ（φ3mm）と熱電対を埋め込んだ。

各水準のコンクリートの使用材料および基準調合を **Table 1**，**Table 2** に示す。

シリカフュームをバインダーに対して 10%置換し，BB，BB-pp の水準の試験体はGGBFSをセ

※1 東京理科大学 創域理工学研究科 建築専攻 修士課程
※2 東京理科大学 創域理工学部 建築学科 講師
※3 国立研究開発法人 建築研究所 防火研究グループ 主任研究員
※4 東京理科大学 創域理工学部 建築学科 教授

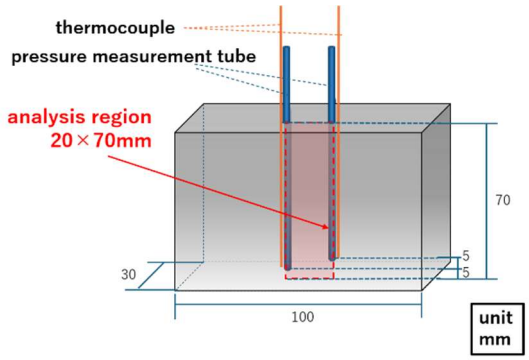

Figure 1　Schematic of the Specimen

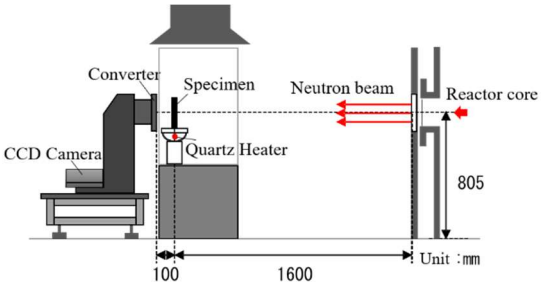

Figure 2　Schematic of the Neutron Radiography System

メント量に対して約 40%置換した。試験体は打設後 24 時間で脱型し，材齢 14 日まで水中養生しその後，試験日まで 20℃60%RH 環境で約 2 週間保管した。

Table 3 に試験体の基礎的性状を示す。

圧縮強度はφ10cm×20cm の試験体を 1 水準当たり 3 本ずつ作成し，水中養生後の材齢 14 日での強度を求めた。

2.2 実験方法

本研究では，2.1 で作製した試験体について，約 10 分間の加熱を行なった。加熱開始と同時に温度，圧力，中性子ラジオグラフィの測定を行い，爆裂時間(音による判別)を確認した。

(1)中性子ラジオグラフィの測定

中性子ラジオグラフィは，中性子が強く減衰される性質を利用することで，非破壊で水分を検出することができる。測定は，京都大学複合原子力科学研究所に設置されている研究用原子炉の B-4 ポートにて実施した。

使用した測定装置の概要を **Figure 2** に示す。

この装置では，炉心から入射した中性子線が試料に照射され，試料を透過した中性子が蛍光板に

Table 1　Materials

Name	Symbol	Remarks
Tap water	W	
Ordinary Portland Cement	C	Density 3.16g/cm³
Ground Granulated Blast-Furnace Slag	B	Saturated Surface-Dry Density 2.91g/cm³
Silica Fume	SF	Bulk Density 260～380kg/m³
Land Sand	S	Saturated Surface-Dry Density 2.63g/cm³
Crushed Stone	G	Saturated Surface-Dry Density 2.65g/cm³ Maximum Aggregate Size 10mm
High-Range Air-Entraining Water-Reducing Admixture	SP	Polycarboxylate-based
Polypropylene Fiber	PP	Fiber Length 12mm

Table 2　Mix Proportions

Specimen Type	[kg/m³]						SP (%)	PP (vol%)
	W	C	B	SF	S	G		
N	173	787	0	87	490	857	1.4	0
BB	173	433	295	87	490	857	1.4	0
N-pp	173	787	0	87	490	857	1.5	0.2
BB-pp	173	433	295	87	490	857	1.5	0.2

Table 3　Basic Properties of Concrete

Specimen Type	Air(%)	SF(mm)	Compressive Strength (N/mm²)	Density (g/cm³)
N	1.2	430×410	118	2.46
BB	1.0	640×590	123	2.46
N-pp	2	500×464	125	2.46
BB-pp	1.6	525×560	124	2.46

より可視光へと変換される。変換された可視光は，CCD カメラによって撮影・記録される [5]。試料中に水分を多く含む部分では，透過量が減少し，画像上では暗い領域（影）として捉えられる。撮像地点における L/D はおおよそ 20 程度，想定中性子束は 1MW 運転時で 1×107n/sec/cm² である。

(2) 加熱実験

加熱実験では，試験体の下部に耐熱ボードを設置し，試験体の形状に合わせた開口部を設けて加

Table 4　Average number of spalling events

Specimen Name	Spalling time	Remarks
N_atsu2	6:49	Heater failure
N_atsu_3	10:23	Heater failure
N_atsu_4	7:34	
N_temp	6:19，7:48	
BB_atsu1	6:30，8:28	Heater failure
BB_atsu_2	7:14，8:30	
BB_atsu_3	6:38，8:48，9:12	
BB_temp	7:13	
N-pp_atsu_1	8:31	Heater failure
N-pp_atsu_2		
N-pp_atsu_4	7:09	Heater failure
N-pp_temp		
BB-pp_atsu_1	8:06，10:49	
BB-pp_atsu_2		
BB-pp_atsu_3	7:00，7:40	
BB-pp_temp		

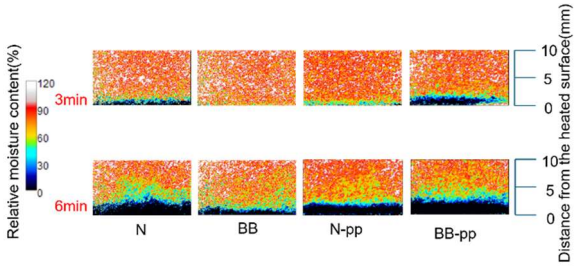

Figure 3　Relative Moisture Content Image

熱を行った。熱源には，コーツヒーター（100V，750W）を用い，加熱面の温度が ISO 834 の標準加熱曲線に準拠するように温度制御を行った。

3. 解析概要

本研究では，撮影された画像から，予め実施したキャリブレーション試験の結果を用いて試験体の厚さ方向に対する単位体積当たりの相対含水率を算出し分析に用いた。相対含水率の算出には(1)式を用いた。

$$\varphi = \frac{\Delta\rho'}{\Delta\rho'_s} = \frac{\Delta\rho}{\rho_s} \qquad (1)$$

ここで，φ:相対含水率，Δρ′:差分質量吸収係数，$\Delta\rho'_s$:飽水時と絶乾時の差分質量吸収係数，Δρ:試験体の水かさ密度(g/cm^3)，ρ_s:飽水時の水かさ密度(g/cm^3)である。

加熱時の透過画像をΔρ′画像に，初期状態の透過画像を$\Delta\rho'_s$画像に変換することで相対含水率画像を求めた。

4. 結果および考察

4.1 爆裂傾向

試験体の爆裂時刻を **Table 4** に示す。

N および BB の水準では 4 体すべてで爆裂が生じた一方で N-pp および BB-pp の水準では 4 体のうち 2 体のみで爆裂が生じた。このことから PP 繊維の爆裂抑制効果は GGBFS を混和したコンクリートに対しても有効であることが示された。

爆裂回数は N が 1~2 回，BB が 2~3 回であり，BB の方が多かった。N-pp と BB-pp の爆裂が生じた試験体の爆裂回数は N-pp で 1 回，BB-pp で 2 回であり，PP 繊維を混入させた場合も GGBFS の混和により爆裂回数が増加する傾向が見られた。

4.2 乾燥速度と爆裂の関係性

Figure 3 に各水準の試験体における加熱から 3 分および 6 分経過時点での相対含水率画像を示す。上段が 3 分経過時を，下段が 6 分経過時での相対含水率を示している。

相対含水率が 0%以下になっている範囲は 6 分経過時には，N が加熱面から 3mm 程度まで，BB が 1mm 程度までであった。乾燥が起こっている範囲の違いから BB は N よりも乾燥速度が遅い傾向が確認できた。Damdelen らの研究 [6] において GGBFS の混和により熱伝導率が低下することが確認されており，熱伝導率の違いが乾燥速度に影響を与えたことが示唆される。

一方で BB-pp は BB よりも乾燥速度が速いという結果であった。これは PP 繊維が熱の通り道となったことでコンクリートの熱伝導率の影響が緩和されたことが要因として推察される。

既往の研究 [7]より乾燥速度の違いが爆裂に影響を与えることが示唆されており，N と BB の水準における温度上昇の違いと乾燥速度の違いが確認できたことから熱伝導率の違いによる乾燥速度の低下によって BB の爆裂回数が増加したことが示唆される。

4.3 温度と水蒸気圧の経時変化

Figure 4 に圧力測定用試験体における温度および圧力の経時変化を示す。赤い線は爆裂時刻を

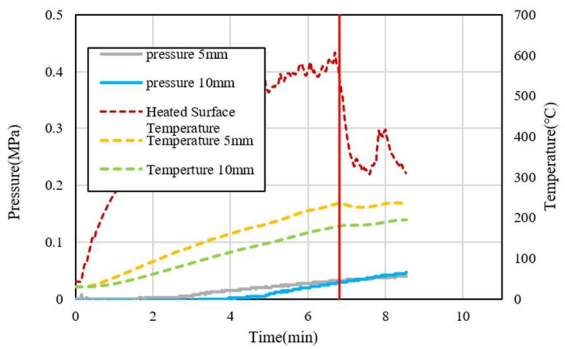

(a)N_atsu_2

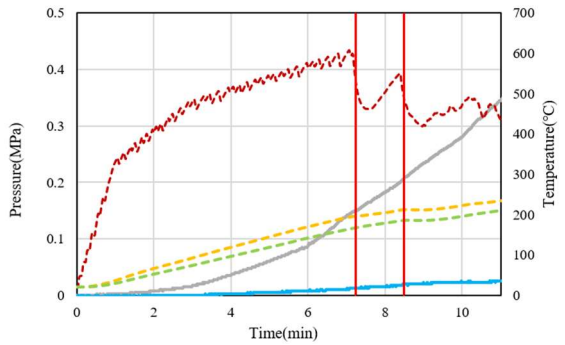

(b)BB_atsu_2

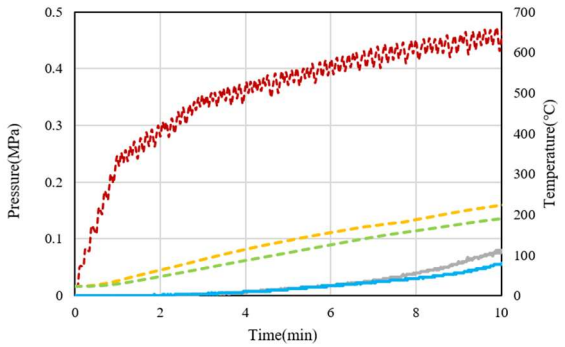

(c)BB-pp_atsu_2

Figure 4　Time Histories of Pressure and Temperature

示し, N_atsu_2 はヒーターが途中で故障したためその時点までのデータとなっている。

N_atsu_2 では 5mm の圧力の上昇の後に 10mm の圧力が上昇しているが BB_atsu_2 では 5mm の圧力のみが上昇している。これは GGBFS の混和により内部が緻密化したことで圧力の逃げ場が無くなり局所的な範囲で圧力が上昇した結果と考えられる。

BB-pp では 10mm の圧力も 5mm に伴い上昇していることから PP 繊維の溶融により水蒸気の逃げ道ができたと考えられる。

5. まとめ

本研究によって得られた知見を以下に示す。

1) 混和材として GGBFS を使用すると普通ポルトランドセメントと比較して爆裂回数が増える傾向が確認できた。これは乾燥速度の違いや圧力の局所的な上昇が関係していると考えられる。
2) PP 繊維の爆裂抑制効果は GGBFS を使用したコンクリートに対しても効果が見られ，PP 繊維の混入により圧力の局所的な上昇が抑制される傾向が確認できた。

謝辞

本研究は京都大学複合原子力科学研究所の令和 7 年度共同利用研究 R7P1-5 「鉄筋コンクリートに熱応力により生じるひび割れと付着性能とを統合的観察」 で実施した。中性子ラジオグラフィの測定にあたり，京都大学の斎藤泰司様，伊藤大介様，大平直也様にご助力を頂いた。ここに記して謝意を示す。

参考文献

1) Saito H. “Explosive spalling of prestressed concrete in fire” Japanese Building Research Institute， Occasional Report 22， Ministry of Construction， 1965.
2) Harmathy T. Z. “Effect of moisture on the fire endurance of building materials” Moisture in Materials in Relation to Fire Tests， ASTM Special Technical Publication No.385， pp 74-95， 1965.
3) 森田武ら：高強度コンクリート梁の加熱実験―爆裂防止対策の検討と爆裂に関する一考察，日本火災学会研究発表会梗概集，1998
4) 岩村和眞：混和材料の異なる高強度コンクリートの爆裂現象に関する研究，アップグレードシンポジウム論文集，2025
5) 兼松学，土屋直子，野口貴文：熱中性子ラジオグラフィによるコンクリート中の吸水過程の解明，日本建築学会構造系論文集，2013
6) Omer Damdelen, Costas Georgopoulos and Mukesh Limbachiya.“Measuring thermal mass of sustainable concrete mixes”, Journal of Architectural Engineering， Vol.8, No. 2, pp. 213-22， 2014.
7) 吉岡樹哉：コンクリートの水分状態が爆裂現象に与える影響，東京理科大学修士論文， 2023

鉄鋼スラグを主原料とした炭素固定型グリーンセメントの開発

Development of Carbon-Sequestering Green Cement Using Iron and Steel Slags

西村慈温※1、二万桜太※1、李柱国※2
Jion Nishimura, Ota Niman, Zhuguo Li

ABSTRACT

本研究では，高炉スラグ微粉末（BFS），遊離石灰を含有する製鋼スラグ粉末（SS）および CO_2 のリサイクルにより製造可能な重曹粉末（Sb）を用いた炭素固定型グリーンセメント（GC）の製法を検討した。SS および Sb の最適な混合率を明らかにするとともに，原料粉体の粉末度，養生材齢が GC の強度に及ぼす影響を検討した。その結果，SS と Sb の最適な混合率はそれぞれ 20–30%および 10–12%であり，BFS と SS の適切なブレーン値は 6000 cm^2/g および 4000 cm^2/g であった。GC モルタルの圧縮強度は養生材齢の増加に伴い向上し，28 日材齢と 91 日材齢ではそれぞれ 40.0 MPa、50.0 MPa を超えた。

1. Introduction

Portland cement (PC) production in Japan amounted to 32.08 million tonnes in fiscal year 2024 [1,2]. During the manufacturing process of PC, a large amount of CO_2 is emitted as a result of calcination at 1,450 °C and the thermal decomposition of limestone. Therefore, the development and application of low-carbon cement technologies that do not require sintering or limestone as a primary raw material are strongly required.

Meanwhile, 16.49 million tonnes of granulated blast-furnace slag and 8.59 million tonnes of steelmaking slag were generated in fiscal year 2024, amounting to a total of 25.08 million tonnes [3]. At present, ground granulated blast-furnace slag (BFS) is widely used in blended cement and concrete, whereas steelmaking slag containing free lime is used mainly as road-base material. If cement can be produced using iron and steel slags as major raw materials, it would contribute not only to reducing CO_2 emissions but also to promoting the effective utilization of by-products and wastes in both the cement and steel industries.

In recent years, geopolymer (GP) technology has been extensively investigated as a low-carbon alternative binder. In GP systems, reactive fillers such as BFS and fly ash (FA) undergo polycondensation reactions in alkaline solutions, such as sodium silicate and sodium hydroxide solutions, resulting in the formation of a hardened matrix. BFS/FA-based GPs contribute to the recycling of industrial by-products and waste materials, and the CO_2 emission intensity of concrete using the BFS/FA-based GP as a binder can be reduced to 30–60% of that of PC concrete, depending on the concrete mixtures [4]. However, GP systems that use alkaline solutions are generally costly. In addition, conventional GP systems require solid precursors and liquid alkaline activators to be stored and handled separately, making their storage, transportation, mixing, and placement more complicated than those of PC. Furthermore, the use of highly alkaline solutions raises occupational safety concerns during production, handling, and application.

Against this background, the authors proposed a production method for a new type of low-carbon cement that can be handled in the same manner as PC while reducing both cost and environmental burden [5]. This method combines three concepts: the GP hardening mechanism of polycondensation reactions, admixture technology for PC concrete utilizing the latent hydraulicity of BFS, and carbon-sequestering concrete technology using calcium carbonate as a

※1 日本国 山口大学大学院 創成科学研究科 修士課程
※2 日本国 山口大学大学院 創成科学研究科 教授 博士(工学)

binder. The proposed cement consists mainly of BFS, steelmaking slag powder (SS), and sodium bicarbonate powder (Sb). The weakly bonded amorphous structure of BFS is disrupted by alkaline SS, with a pH of 12.0–13.0 in its aqueous extract, thereby inducing polycondensation reactions similar to those observed in GP systems. In addition, calcium carbonate precipitation occurs simultaneously, in which Ca^{2+} leached from BFS and free lime contained in SS react with Sb (pH of the aqueous solution: 8.0–9.0) to form calcium carbonate. Sodium bicarbonate can be produced by utilizing CO_2 from exhaust gas [6,7]. Because the cement produced by this method generates both C-A-S-H gel and $CaCO_3$ after mixing with water, it cannot be strictly classified as a conventional GP. In this study, this cement is referred to as non-sintered, carbon-sequestering green cement, abbreviated as GC.

This study aimed to clarify the factors affecting the performance of GC and to optimize the GC production method. To achieve these objectives, the optimum mixing ratios of SS and Sb were investigated respectively. In addition, the effects of powder fineness and curing age on the strength of GC were evaluated.

2. Materials Used

2.1 Blast furnace slag

The three types of ground granulated blast-furnace slag (BFS) used in this study contained no added gypsum and met the requirements for grades 4000, 6000, and 8000 specified in JIS A 6206. BFS4000 had a density of 2.90 g/cm^3 and a Blaine fineness of 4,080 cm^2/g; BFS6000 had a density of 2.91 g/cm^3 and a Blaine fineness of 6,395 cm^2/g; and BFS8000 had a density of 2.92 g/cm^3 and a Blaine fineness of 7,900 cm^2/g. The chemical compositions of the three types of BFS, as determined by X-ray fluorescence (XRF) analysis, are presented in Table 1.

2.2 Steelmaking slag

The chemical composition of converter steelmaking slag (SS) used in this study was determined by XRF analysis, and the results are presented in Table 1. The density of the SS was 3.34 g/cm^3. The pH of the filtrate obtained after immersing the SS in deionized water for 24 h at an SS-to-water mass ratio of 1:10 was 12.9. Hard coarse particles that were difficult to grind were removed, and the remaining material was ground in a mill to obtain a Blaine fineness of approximately 3,800–4,200 cm^2/g. This material is hereafter referred to as SS4000. In some experiments, SS from which the hard coarse particles had not been removed and SS ground to a Blaine fineness of approximately 4,800–5,200 cm^2/g (hereafter referred to as SS5000) were also used to investigate the effect of SS fineness.

The $Ca(OH)_2$ and $CaCO_3$ contents of the SS were determined by thermogravimetric-differential thermal analysis (TG-DTA). As shown in Figure 1, the $Ca(OH)_2$ and $CaCO_3$ contents of the SS were 8.65% and 1.48%, respectively. The $CaCO_3$ was considered to have formed through carbonation of free lime during storage of the SS.

X-ray diffraction (XRD) analysis of the SS was also conducted using Cu Kα radiation under the following conditions: an operating voltage and current of 40 kV and 15 mA, respectively; a 1°–1°–0.3 mm slit system; a scanning rate of 4°/min; and a step size of 0.02°. The results are shown in Figure 2. The presence of

Table 1 Chemical composition of steelmaking slag (SS) and granulated blast-furnace slag (BFS) (wt.%)

Ground iron and steel slag	SiO_2	Fe_2O_3	Al_2O_3	CaO	MgO	MnO	TiO_2	K_2O	P_2O_5	SO_3	Others
SS	13.6	25.7	2.5	49.2	2.6	2.5	0.5	-	2.5	0.2	0.3
BFS4000	29.4	0.3	12.8	45.5	4.6	0.1	0.6	0.4	0.01	1.7	0.1
BFS6000	30.6	0.4	13.1	43.9	4.7	0.2	0.6	0.3	0.01	1.3	0.4
BFS8000	30.9	0.3	13.2	43.2	4.7	0.2	0.6	0.3	0.01	1.3	0.4

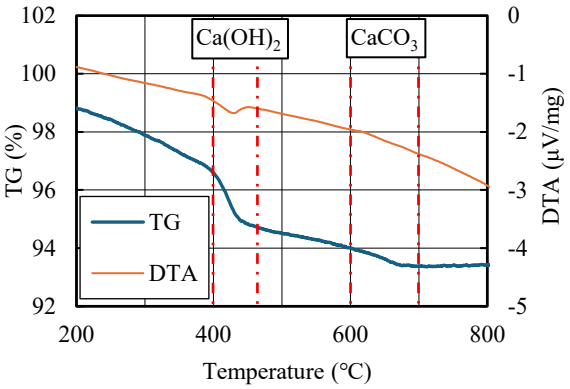

Figure 1 TG-DTA analysis result of SS

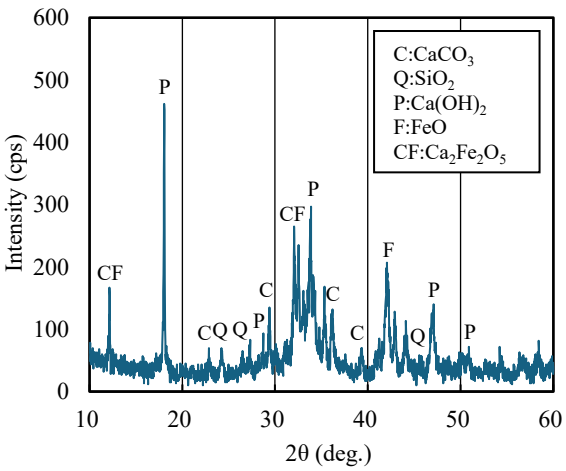

Figure 2 XRD analysis result of SS

$Ca(OH)_2$ in the SS was reconfirmed, and crystalline phases such as quartz and calcite were also identified. The free lime contained in the SS promotes the latent hydraulic activity of BFS, whereas the inactive crystalline phases remain as SS particle residues and act as fillers in the GC hardened matrix.

2.3 Additives

Powdered sodium bicarbonate reagent ($NaHCO_3$, abbreviated as Sb; purity: 95–98%; density: 2.2 g/cm^3) was added based on the total mass of BFS and SS.

2.4 Fine aggregate

The strength of GC was evaluated using mortar specimens. Sea sand in a saturated surface-dry condition was used as the fine aggregate in the mortar. The particle size distribution of the sea sand is shown

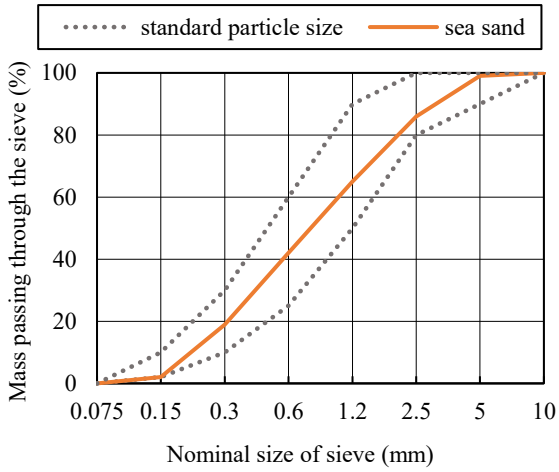

Figure 3 Particle size distribution of sea sand

in Figure 3. The other properties were as follows: saturated surface-dry density of 2.56 g/cm^3, bulk density of 1.63 kg/L, water absorption of 1.81%, solid volume percentage of 65.0%, fineness modulus of 2.87, particle size range of 0–5 mm, and chloride content of 0.002%.

3. Preparation and Characterization of Specimens

3.1 Preparation of specimens

A pan paste mixer or mortar mixer was used for mixing. The mixing proportions of SS, BFS, and Sb varied depending on the experimental series and are given in each figure showing the experimental results in Section 4. However, the water-to-GC mass ratio and fine aggregate-to-GC mass ratio were fixed at 0.50 and 2.0, respectively. The SS mixing ratio was defined as the mass percentage of SS relative to the total mass of BFS and SS. As the SS mixing ratio increased, the amount of BFS decreased. However, the amount of Sb added did not change with the SS mixing ratio, because it was determined based on the total mass of BFS and SS.

The GC mortar was mixed according to the following procedure. First, each material was weighed according to the specified mixing proportions. BFS, SS, and Sb were then mixed for 1 min. Fine aggregate in a saturated surface-dry condition was added and mixed for another 1 min. Finally, water was added, and the mixture was mixed for 2 min. After mixing, the mortar was placed into three-gang molds with dimensions of

40 × 40 × 160 mm, and strength test specimens were prepared using a vibrating table. The specimens were sealed and cured in air at 20 °C, and demolding was carried out after 24 hours.

As described above, ordinary SS powder was prepared by removing hard coarse particles that were difficult to grind. In some experiments, however, SS containing these coarse particles was used to examine the effect of SS fineness on GC strength.

3.2 Performance evaluation

After the GC mortar specimens reached a curing age of 28 days, flexural and compressive strength tests were conducted using a universal testing machine. The compressive strength was measured using the six broken portions obtained after the flexural strength test. For some mortar specimens, strength tests were conducted at ages of 28 and 91 days to examine the effect of prolonged curing.

4. Experimental Results and Discussion

4.1 Effect of the steelmaking slag mixing ratio on GC strength

The effect of the SS mixing ratio on the compressive strength of GC mortar prepared using BFS4000 and SS4000 is shown in Figure 4. Regardless of the Sb addition ratio, the compressive strength increased with increasing SS mixing ratio. However, once the SS mixing ratio exceeded a certain level, the compressive strength tended to decrease. The maximum compressive strength was obtained at an SS mixing ratio of 30%.

This tendency can be explained by the balance between free lime supply and BFS replacement. When the SS mixing ratio is low, free lime in SS is insufficient to activate BFS, resulting in a reduced strength. In contrast, when the SS mixing ratio is high, excessive replacement of reactive BFS by SS reduces both polycondensation and carbonate reactions, leading to a decrease in strength.

Based on these results, among the addition levels examined in this study, an SS mixing ratio of approximately 30% was considered to be optimal.

4.2 Effect of the sodium bicarbonate addition ratio on GC strength

The effect of the Sb addition ratio on the compressive strength of GC mortar prepared using BFS4000 and SS4000 is shown in Figure 5. As the Sb addition ratio increased, the compressive strength increased. However, when the addition ratio became excessively high, the strength tended to decrease.

This reduction in strength is assumed to be attributable to three factors. First, an excessive amount of Sb promotes the carbonate reaction between Sb and SS, thereby consuming free lime in SS and weakening the activation effect of SS on BFS. Second, the carbonate reaction between Sb and Ca^{2+} supplied from BFS consumes Ca^{2+}, which reduces the amount of reaction products of the hydration or polycondensation reaction of BFS. Third, the discontinuous $CaCO_3$ crystals formed by these reactions contribute less to

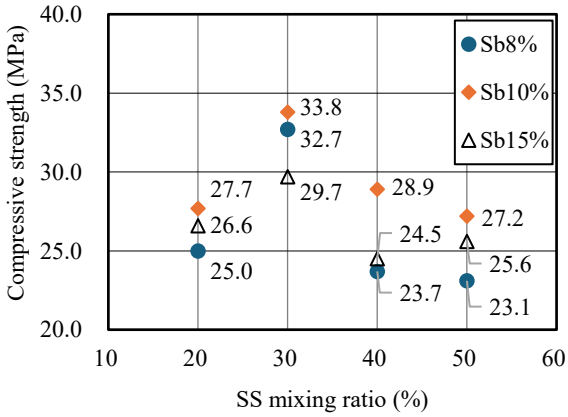

Figure 4 Effect of SS mixing ratio on compressive strength

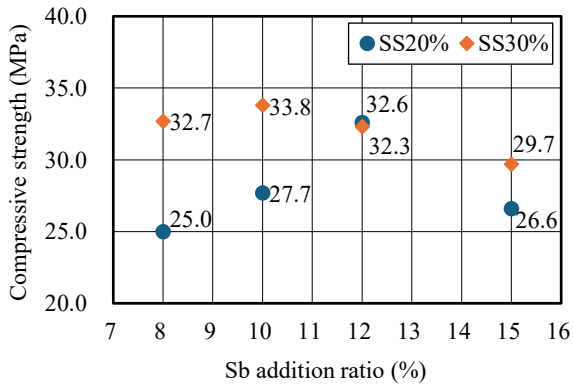

Figure 5 Effect of Sb addition ratio on compressive strength

the strength of the hardened matrix than GP gel and may disrupt the continuity of the GP gel network.

The strength of GC is influenced by both SS and sodium bicarbonate. Among the addition levels examined in this study, the optimum Sb addition ratio was considered to be 12% when the SS mixing ratio was 20%, and 10% when the SS mixing ratio was 30%.

4.3 Effects of slag powder fineness and curing age on GC strength

Figure 6 shows the compressive strengths at 28 and 91 days for GC mortars prepared by varying the fineness of BFS and SS, as well as the presence or absence of the hard coarse particles of SS that were difficult to grind. The compressive strength tended to increase when the curing age was extended from 28 to 91 days. In particular, for the mixtures prepared using SS without the hard coarse particles, the 91-day compressive strengths were approximately 20% higher than the corresponding 28-day strengths. At 91 days, the compressive strengths of all these mixtures exceeded 42.5 MPa, the JIS-specified value for the 28-day compressive strength of ordinary Portland cement.

This increase in strength may be attributed to the time required for the hardening reaction associated with the latent hydraulicity of BFS and for the gradual dissolution of free lime from within the SS particles. In addition, the compressive strength increased as the fineness of BFS increased, indicating that finer BFS promoted the reaction of GC. However, there was little difference between the GC mortars prepared using BFS6000 and BFS8000, and almost no improvement was observed from increasing the fineness of SS powder. These results suggest that there is a limit to the improvement in GC strength that can be achieved by increasing powder fineness.

On the other hand, in the series using SS powder containing the hard coarse particles, the compressive strength at 28 days was markedly lower than that of GC mortar prepared using SS powder without the hard coarse particles, and was nearly zero. However, the compressive strength increased substantially to 45.1 MPa at 91 days. This may be because the hard coarse particles had a lower free lime content than the fine SS particles, and their presence reduced the amount of fine SS particles in the GC. As a result, the amount of free lime leached from SS was insufficient at the early stage, leading to inadequate activation of BFS and delayed strength development.

During prolonged curing, however, free lime may have gradually dissolved from the hard coarse particles, contributing to the substantial increase in compressive strength observed at 91 days. These results indicate that both the particle size of SS and the

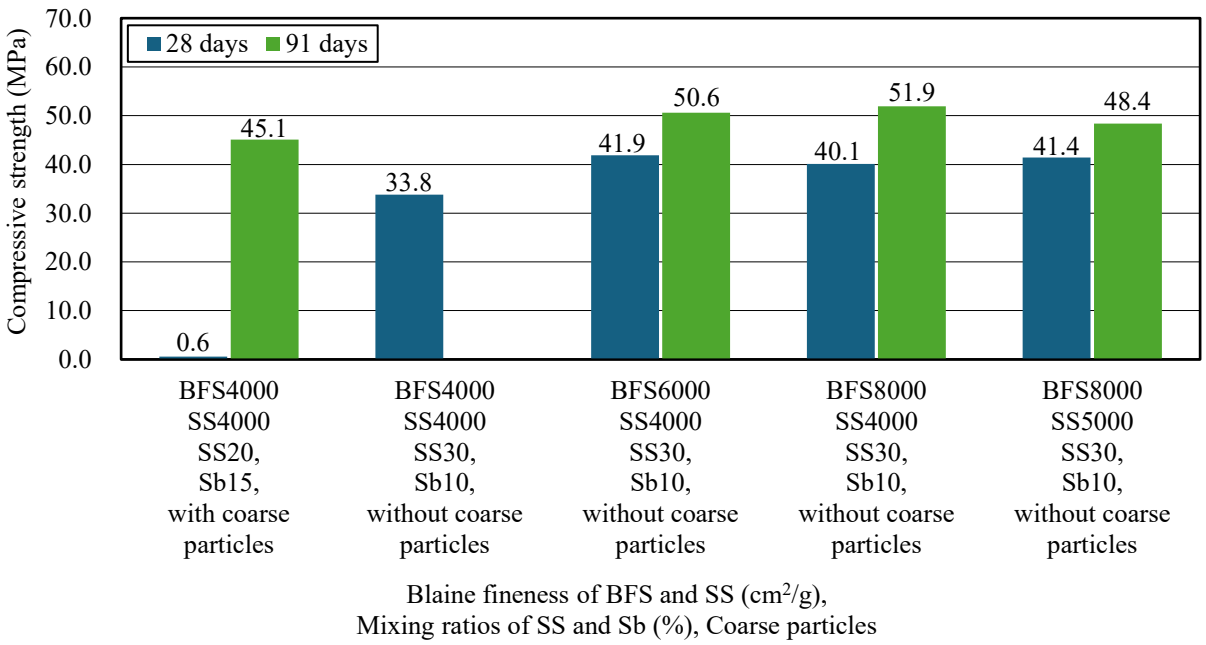

Figure 6 Effects of slag fineness and curing age on compressive strength

fineness of BFS influence the strength growth of GC. They also show that extending the curing age is effective in enhancing the strength of GC, particularly when the hard coarse particles are present in SS.

5. Conclusions

This study aimed to establish a production method for a non-sintered, limestone-free green cement (GC) using iron and steel slags and sodium bicarbonate. The proposed GC can be handled in a manner similar to ordinary Portland cement and has carbon-sequestering capability. To achieve this objective, the optimum mixing ratios of steelmaking slag powder and sodium bicarbonate were investigated. In addition, the effects of steelmaking slag fineness and curing age on the strength development of GC were examined to clarify the main factors affecting its mechanical performance.

1) GC can be produced by mixing ground granulated blast-furnace slag (BFS), steelmaking slag powder containing free lime (SS), and sodium bicarbonate powder (Sb). The results showed that the mixing ratios of SS and Sb strongly affected the strength of GC. The optimum mixing ratios of SS and Sb were 20–30% and 10–12%, respectively.
2) The strength of GC increased with increasing fineness of BFS and SS powders, indicating that finer powders promoted the hardening reaction. However, once the fineness exceeded a certain level, further increases in fineness resulted in only a slight improvement in strength. Considering both strength development and the energy required for grinding, the appropriate Blaine fineness values for BFS and SS used in GC were judged to be about 6000 cm^2/g and 4000 cm^2/g, respectively.
3) The strength of GC increased with curing age, demonstrating that GC continues to develop strength over time. This strength gain is considered to be related to the latent hydraulic reaction of BFS and the gradual dissolution of free lime from within the SS particles. The 91-day compressive strength of GC mortar exceeded 50.0 MPa, representing an increase of approximately 20% over the 28-day strength.

Reference

[1] Construction Research Institute, *Current Status and Future Outlook of the Cement Industry*, available at: https://www.kensetu-bukka.or.jp/article/15464/ accessed January 12, 2026. (in Japanese)

[2] Japan Cement Association, available at: https://www.jcassoc.or.jp/cement/3pdf/jh2_1100.pdf accessed January 12, 2026. (in Japanese)

[3] Nippon Slag Association, *Overview of Iron and Steel Slag Supply and Demand in FY2024*, available at: https://www.slg.jp/cms/wp-content/themes/original/pdf/slag-overview_2024.pdf accessed January 12, 2026. (in Japanese)

[4] Li, Z.: Quantitative consideration of the environmental impact of geopolymer concrete, *Symposium on the Current Status and Issues of Geopolymer Technology in the Construction Field*, pp. 43–50, June 2016. (in Japanese)

[5] Li, Z. and Fukaya, S.: Study on a hybrid binder of geopolymer and calcium carbonate, Part 1: CO_2 absorption, alkaline properties, and reaction products, *Summaries of Technical Papers of Annual Meeting, Architectural Institute of Japan*, Hokkaido, pp. 1235–1236, September 2022. (in Japanese)

[6] Huang, H. P., et al.: Dual alkali approaches for the capture and separation of CO_2, *Energy and Fuels*, Vol. 15, pp. 263–268, February 2001.

[7] New Scientist: UK's largest carbon capture project will turn CO_2 into baking soda, available at: https://www.newscientist.com/article/2325858-uks-largest-carbon-capture-project-will-turn-co2-into-baking-soda/ accessed January 17, 2026.

新規セメント添加材としてのリチウムスラグ粉末の基本特性および反応性の評価

Evaluation of Fundamental Properties and Reactivity of Lithium Slag Powder for Application as a New Cement Additives

安泰尹※1、金建佑※1、姜南圭※2、申相澈※3、金振晩※4

Tae-Yun, An, Geon-Woo Kim, Nam-Gyu Kang, Sang-Chul, Shin, Jin-Man Kim

ABSTRACT

Supplementary cementitious materials (SCMs) are key to decarbonizing the cement industry, but traditional SCM supply is declining. This study evaluates lithium slag powder (LSP) from secondary battery industry byproducts as a novel SCM. The properties of lithium slag powder were characterized using PSD, BET, Density, SEM-EDS, XRF, XRD, TG/DTG, and FT-IR, while pozzolanic reactivity was assessed via SAI, Frattini, and R_3 tests. The physicochemical properties of lithium slag powder exhibited a D_{50} of 13.50 μm, higher surface area than fly ash (FA), and met ASTM pozzolanic standards with SiO_2 + Al_2O_3 + Fe_2O_3 >70%. LSP showed high pozzolanic activity through selective fixation of CaO. Due to clinker dilution, 7-day strength was lower than the control, but pozzolanic reaction driven by higher $Ca(OH)_2$ consumption than FA enabled strength recovery to 110.8% at 91 days.

1. Introduction

As the global demand for electric vehicles and secondary batteries surges, spodumene-based lithium extraction has emerged as a critical supply source. However, the hydrometallurgical refining process generates a substantial amount of industrial by-products; approximately 9 tons of lithium slag powder (LSP) are produced for every ton of lithium hydroxide [1].

Despite this massive volume, efficient disposal and recycling strategies for LSP remain insufficient. Therefore, this study evaluates the basic physical properties and reactivity of LSP to explore its potential as a new cement additive, aiming to enhance both industrial sustainability and resource recovery.

2. Materials and methods

2.1 Properties of Lithium Slag Powder

To evaluate the feasibility of LSP as a new cementitious additive, its physicochemical properties were characterized at the raw material stage. The physical properties were analyzed using particle size distribution (PSD), BET specific surface area, and density. The chemical and mineralogical properties were analyzed using X-ray Fluorescence (XRF), X-ray Diffraction (XRD), and Thermogravimetric analysis (TGA).

2.2 Reactivity of Lithium Slag Powder

To evaluate the pozzolanic reactivity of the LSP, an experimental plan consisting of pozzolanic activity tests was established. The pozzolanic reactivity of

※1 大韓民国 国立公州大学校 建築工学科 博士課程
※2 大韓民国 国立公州大学校 建築工学科 修士課程
※3 大韓民国 国立公州大学校 建築工学科 研究教授 博士(工学)
※4 大韓民国 国立公州大学校 建築工学科 教授 博士(工学)

LSP was examined through three distinct methodologies. First, the Frattini test was conducted following DIN EN 196-5 to assess chemical reactivity. Second, the R^3(Rapid, Relevant, and Reliable) test was conducted according to ASTM C1897-20, involving isothermal calorimetry and bound water analysis, to characterize the reactivity of the LSP. Finally, the strength activity index was evaluated in accordance with KS L 5405.

3. Results and Discussion

3.1 Physicochemical Properties

The PSD, Density, and BET results are presented in Table 1. The LSP particles are comparable in size to cement and finer than fly ash. BET analysis confirmed that LSP has a high surface area due to their porous structure, resulting from rotary kiln calcination, sulfuric acid leaching, and extraction processes [2, 3].

The chemical composition was determined to XRF, are presented in Table 2. The chemical composition of LSP is similar with FA, with SiO_2+Al_2O_3+Fe_2O_3 making up over 70% of total oxides. In addition, the SO_3 was measured to be 10%, which is attributed to the gypsum formed during the neutralization process using sulfuric acid in the lithium extraction stage.

XRD (Fig. 1) analysis showed that most of the SiO_2 and Al_2O_3 are present in the form of a leached β-spodumene phases. Crystalline phase such as bassanite, quartz, and other feldspar minerals was also identified. The amorphous hump observed in XRD patterns is presumed to be mainly from aluminosilicate phases. Amorphous phases and aluminosilicate phases are to enhance pozzolanic reactions during cement hydration matrix.

TGA (Fig. 2) showed a mass loss of 1% from ~200°C, which is attributed to the evaporation of free water and the loss of bound water associated with gypsum [4]. A further mass loss of 2% observed in the range of 300~850°C is considered to dehydration of the aluminosilicate phase [5].

Table 1 PSD, Density, and BET

Category		OPC	FA	LSP
PSD (μm)	D10	2.10	5.37	2.03
	D50	13.33	27.74	13.50
	D90	41.45	105.36	53.64
Density (g/cm^3)		3.14	2.21	2.45
BET (m²/g)		1.73	1.04	4.05

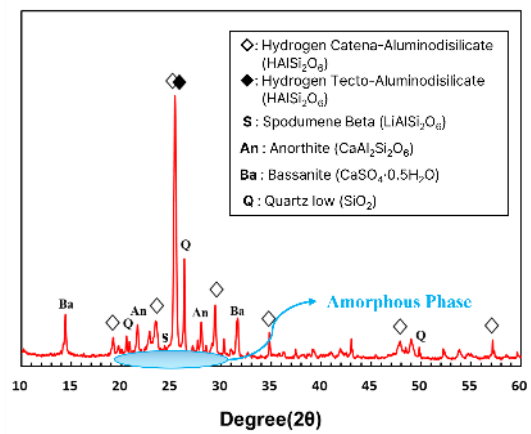

Figure 1 XRD

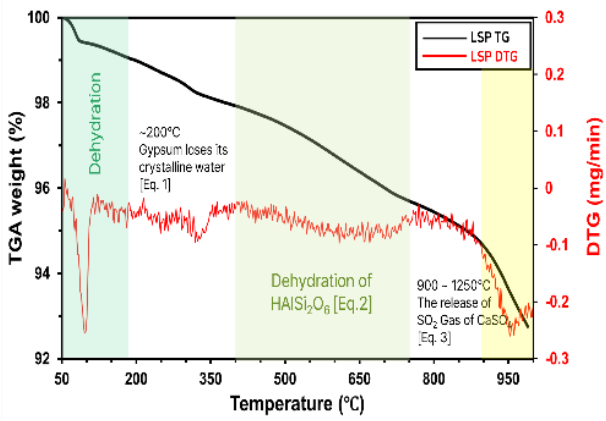

Figure 2 TGA

Table 1 Chemical composition of raw material

(%)	SiO_2	Al_2O_3	Fe_2O_3	CaO	MgO	SO_3	K_2O	Na_2O	Li_2O	LOI
OPC	18.1	4.2	2.1	65.3	3.5	2.3	0.9	0.4	-	2.6
LSP	50.4	21.0	1.9	6.0	1.3	10.0	0.9	0.5	1.5	6.4
FA	50.3	28.4	8.9	4.7	1.6	0.4	0.5	0.2	-	2.2

3.2 Reactivity

The results of the Frattini test are presented in Figure 3. Most of the materials were distributed near the lime saturation curve. In contrast, LSP was located clearly below the saturation curve, indicating pronounced pozzolanic activity. A significant reduction in Ca^{2+} ion was observed for LSP, whereas the decrease OH^- was relatively limited. This behavior is associated with the presence of gypsum, which contributes to the selective fixation of CaO through the formation of AFt and AFm phases.

The results of the R^3 Test are presented in Figure 4. The result showed that calcined clay (CC) exhibited the highest bound water content. LSP also showed a relatively high bound water content compared to other pozzolanic materials. TGA results showed that the Portlandite (CH) content of LSP paste exhibited a linear correlation with the bound water content, indicating that LSP possesses a high CH consumption and bound water content compared with other pozzolanic additives.

The isothermal calorimetry results are presented in Figure 5. The initial peak is associated with dissolution, precipitation, ion release, and the onset of reactions. It represents the C-S-H formation. CC showed high reactivity due to its dehydrated metakaolin structure. LSP also showed relatively good reactivity. The middle peak marks the activation of pozzolanic reactions and the formation of secondary hydration products. Case of LSP, its high gypsum content delayed the secondary peak.

The results of the SAI are presented in Figure 6. At 7 days, mortar specimens 10% LSP exhibited compressive strength comparable to OPC. However, at replacement levels of 20% or higher, the strength showed a linear decrease with increasing replacement ratio. At 28 and 91 days, LSP showed superior strength to OPC up to 30% replacement, due to pozzolanic reactions. The strength at later ages is attributed to the pozzolanic reactions of aluminosilicates, resulting in the formation of secondary hydration products, such as C-S-H and C-(A)-S-H [6].

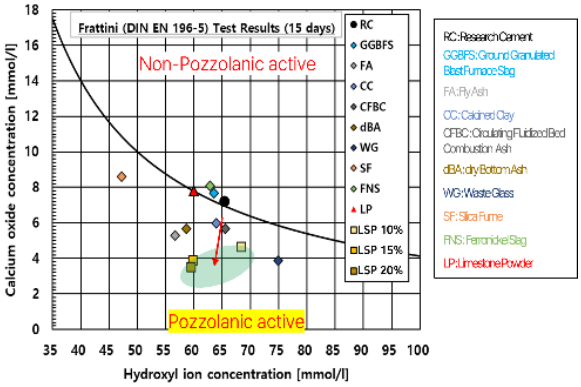

Figure 3 Frattini test (15days)

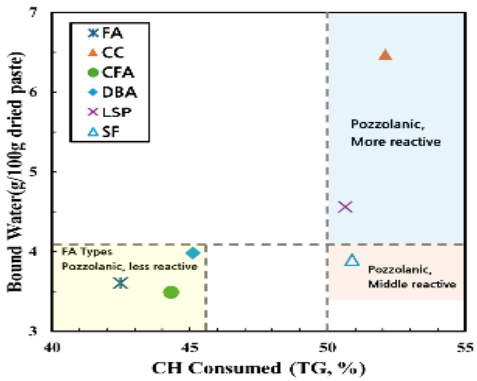

Figure 4 Bound water and CH contents

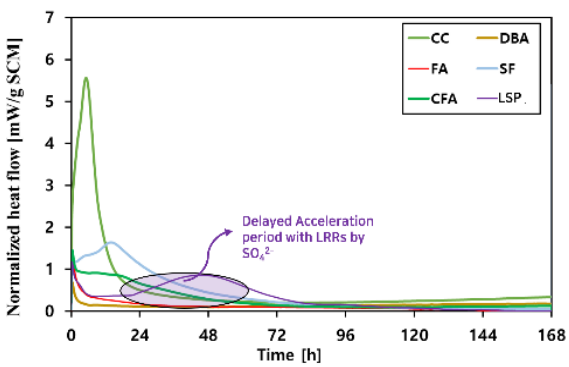

Figure 5 Isothermal calorimetry

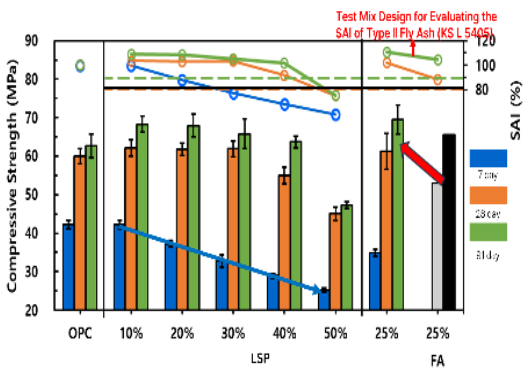

Figure 6 SAI (7, 28, 91 days)

4. Conclusions

The evaluation of the fundamental properties and reactivity of LSP led to the following conclusions.

（1）LSP consist of reactive aluminosilicates, quartz, and gypsum. Owing to their high SiO_2 and Al_2O_3 contents, appropriate particle size, and high specific surface area, LSP are considered to promising pozzolanic materials

（2）The Frattini test results confirmed that blended cements incorporating LSP at all three replacement levels exhibited clear pozzolanic activity.

（3）LSP satisfied KS L 5405 Type II FA strength criteria, showing OPC-level strength at 30% replacement after 28 days.

Acknowledgment

This work was supported by the Technology Innovation Program (RS-2023-00266009, Development of admixture and blended cement using unused inorganic resource) funded by the Ministry of Trade, Industry and Resources (MOTIR, Korea) and the Korea Institute for Advancement of Technology (KIAT) grant funded by the Korea Government (MOTIR) (RS-2024-00410787, HRD Program for Industrial Innovation)

Reference

[1] Sagzhanov, D., Shakenov, S., Sarsenov, A., The Role of Sustainable Lithium Processing in Renewable Energy Value Chains, Sustainability, 17(13), 5903, 2025

[2] Tan, H., Li, M., He, X., Su, Y., Yang, J., Zhao, H., Effect of Wet Grinded Lithium Slag on Compressive Strength and Hydration of Sulphoaluminate Cement System. Constr. Build. Mater. 2021, 267, 120465.

[3] He, Y., Zhang, Q., Chen, Q., Bian, J., Qi, C., Kang, Q., Feng, Y. Mechanical and Environmental Characteristics of Cemented Paste Backfill Containing Lithium Slag-Blended Binder. Constr. Build. Mater. 2021, 271.

[4] El Hazzat, M., Sifou, A., Arsalane, S., El Hamidi, A. Novel Approach to Thermal Degradation Kinetics of Gypsum: Application of Peak Deconvolution and Model-Free Isoconversional Method. J. Therm. Anal. Calorim. 2020, 140, 657–671.

[5] Bernal, S.A., Juenger, M.C.G., Ke, X., Matthes, W., Lothenbach, B., De Belie, N., Provis, J.L. Characterization of Supplementary Cementitious Materials by Thermal Analysis. Materials and Structures/Materiaux et Constructions 2017, 50.

[6] He, Y., Liu, S., Hooton, R.D., Zhang, X., He, S. Effects of TEA on Rheological Property and Hydration Performance of Lithium Slag-Cement Composite Binder. Constr. Build. Mater. 2022, 318, 125757.

ベトナムにおけるコンクリート塊のリサイクル
Concrete Waste Recycling in Vietnam

チャンティフク※1、道正泰弘※2、ディンバンリン※3、グエンアンドゥク※4
Phuc Tran Thi, Yasuhiro Dosho, Linh Dinh Van, Duc Nguyen Anh

ABSTRACT

現在，ベトナムでは急速な都市化と経済成長に伴い，建設活動が大幅に増加している．その結果，建設廃棄物(CDW)の発生量は 2010 年の 190 万 t から，2025 年には 960 万 t に達すると予測されている. 本報は, ベトナムにおける CDW 対策を構築することを目的に，CDW の再利用状況について整理するとともに，再生骨材および再生路盤材の品質について調査し，現状と課題を検討した．その結果，ベトナムの再生骨材は，レンガくずが混入していなければ，JIS A 5023 附属書 A に規定される RLG，RSL の吸水率を満足することから, 一定の容積混合率以下で普通骨材と混合することで所要のコンクリート性能を得る可能性があることが明らかとなった.

1. Introduction

The Socialist Republic of Vietnam is experiencing a rapid increase in construction activities driven by urbanization and economic growth. Consequently, the amount of Construction and Demolition Waste (CDW) is projected to increase from 1.9 million tons in 2010 to 9.6 million tons by 2025 [1]. In large cities such as Hanoi, CDW accounts for 20%–25% of total municipal solid waste. Its primary components are concrete waste and fired clay brick fragments (brick fragments). However, because comprehensive regulations and technical standards have not yet been established, much of this waste is disposed of in landfills or illegally dumped. This practice not only wastes valuable resources but also imposes a significant environmental burden. In contrast, since 2000, the recycling rate of concrete waste in Japan has exceeded 96%, enabling its effective use in infrastructure development [2]. This study aims to identify measures for improving CDW management in Vietnam by reviewing the current status of CDW recycling and evaluating the quality of recycled aggregates and recycled road base materials to clarify the associated challenges.

2. Current Status of CDW in Vietnam

2.1 Investigation of Recyclable CDW

Recyclable waste is generated from construction and demolition sites in the Hanoi area. This study focuses on concrete waste and mixed CDW generated by construction and demolition activities in the Hanoi region. Concrete waste can be processed through crushing and grading to produce recycled coarse aggregate (RGA) and recycled fine aggregate (RSA), thereby conserving natural resources and reducing the burden on landfills. In contrast, mixed CDW contains brick fragments mixed with concrete waste, and a high brick fragment content significantly increases the water absorption of the recycled aggregates, thereby degrading their quality. At present, effective recycling technologies and quality standards for such mixed CDW have not yet been adequately established in Vietnam. Therefore, technologies for its effective use as recycled road base material and in environmentally

※1 日本 名城大学学院理工学研究科環境創造工学専攻
※2 日本 名城大学理工学部環境創造工学科 教授 博士（工学）
※3 日本 鹿島道路(株) 修士（工学）
※4 ベトナム ベトナム海事大学土木工学部 博士（工学）

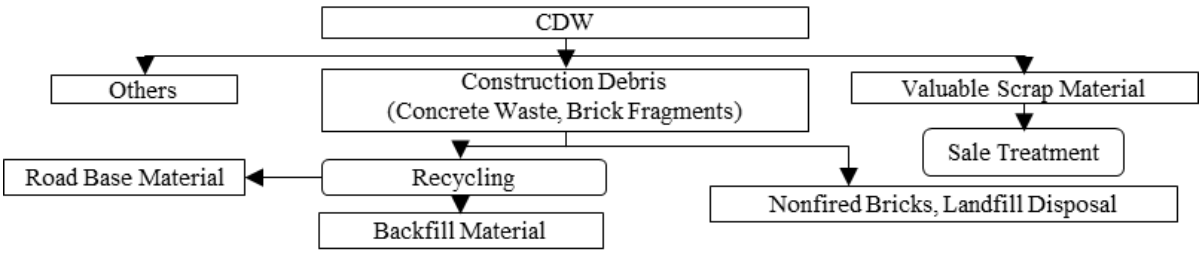

Figure 1 CDW Recycling Flow in Vietnam

friendly concrete need to be developed.

2.2 Current Status of CDW Generation, Collection, and Treatment in Vietnam

2.2.1 Current Status of Construction Waste in Vietnam

Photo 1 shows construction and demolition sites in Hanoi. Currently, many aging structures, primarily reinforced concrete buildings, are being demolished as urban redevelopment and replacement with new buildings progress throughout the city. The resulting CDW mainly consists of brick fragments and concrete waste. Brick masonry is used for wall construction, with the exterior surfaces finished with mortar, whereas foundations and columns are constructed of concrete. These two materials constitute the majority of the construction waste. Reinforcing steel bars are recovered either mechanically or manually, purchased by recycling companies, and transported by truck. In addition, plastics (PE, PP, PVC, etc.), metals, insulation materials, and other recyclable materials are separately collected by material type. Sanitary ware and other fixtures that can be removed without damage are directly reused at other construction sites. Concrete waste, brick fragments, stones, tiles, and similar materials are first broken into manageable sizes at the demolition site before being loaded onto trucks for transport.

2.2.2 Current Status of CDW Collection and Treatment in Vietnam

In recent years, the amount of CDW generated in Hanoi has increased rapidly due to urbanization and infrastructure development. As of 2026, approximately 10,000 tons of CDW are estimated to be generated daily [3]. The major components are

Photo 1 Construction and Demolition Site in Hanoi (Photographed in 2026)

concrete waste and brick fragments, along with iron scrap, aluminum, PVC pipes, and other materials. Although valuable materials such as iron scrap and aluminum are recovered and recycled, much of the concrete waste and brick fragments is collected and treated without adequate separation. Consequently, most CDW is still disposed of in landfills or used as backfill material, with recycling largely limited to applications such as recycled road base material.

Figure 1 illustrates the current CDW treatment and recycling flow in Vietnam. In recent years, the Vietnamese government has promoted CDW recycling by developing relevant legislation and technical standards and encouraging the expanded use of recycled materials. However, significant challenges remain, including the establishment of efficient collection and sorting systems, the development of recycling facilities, and quality assurance of recycled aggregates.

2.3 CDW Treatment and Recycling Methods

As of 2026, the amount of CDW generated in major cities such as Hanoi has increased rapidly due to urbanization and growing construction demand. Although CDW is recognized as a reusable resource, much of it is still disposed of in landfills or illegally dumped. Recycling remains limited, with crushed

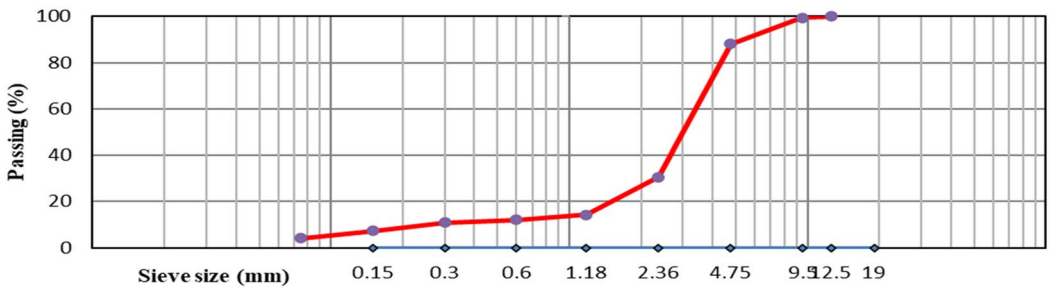

Figure 2 Particle Size Distribution of Recycled Crushed Stone

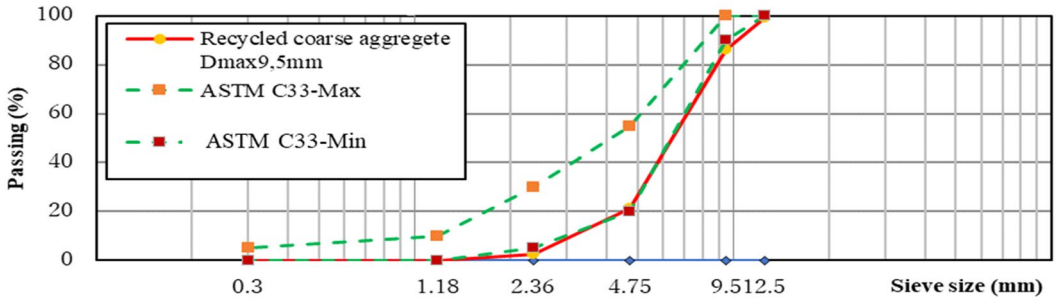

Figure 3 Particle Size Distribution of RGA_1 (9.5–0 mm)

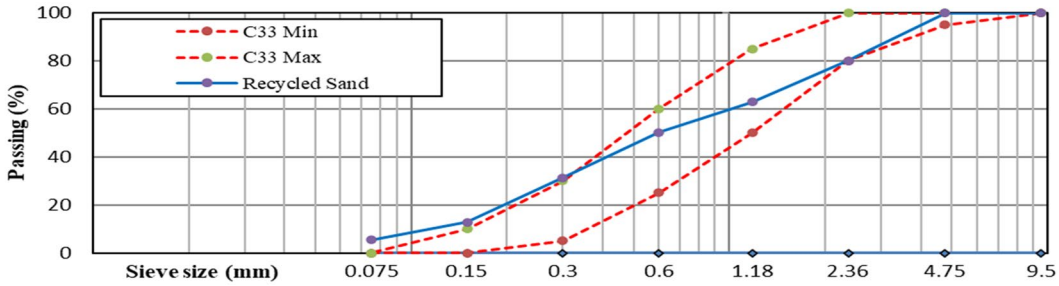

Figure 4 Particle Size Distribution of RSA_1 (5–0 mm)

materials used mainly as backfill and recycled road base materials.

Recovered concrete waste is processed through crushing, screening, and sorting before being used as recycled aggregates, nonfired bricks, and road base materials. However, because CDW is not adequately sorted at the source in Vietnam, the recycled aggregates contain significant amounts of brick fragments and adhered mortar or cement paste. As a result, their water absorption increases and density decreases, making it difficult for them to satisfy the quality requirements for concrete aggregates. In recent years, the Vietnamese government has established standards such as TCVN 11969:2018 [4] for RGA for concrete and TCVN 13694:2023 [5] for recycled materials used in road base applications to promote CDW recycling. However, widespread implementation still faces many challenges, including inadequate collection and processing infrastructure, high processing costs, and concerns regarding the quality of recycled materials. Therefore, promoting the recycling of concrete waste is important not only for conserving natural resources but also for advancing a circular economy and reducing greenhouse gas emissions in Vietnam.

2.3.1 Utilization as Road Base Materials

Recovered concrete waste is processed at recycling facilities through crushing, screening, and impurity removal to produce recycled road base materials. These materials are used as road base, backfill, and subgrade materials in road construction. Although their use has gradually increased in recent years, ensuring a stable supply of recycled road base materials continues to pose a challenge, as the CDW collection and sorting system has not yet been sufficiently put in place.

2.3.2 Landfill Disposal

Most CDW that is not recycled is disposed of in landfills. At treatment facilities, valuable materials are first recovered, after which excavated soil, brick fragments, and concrete waste are typically sent to landfill. Although landfill disposal is an effective method for handling large volumes of CDW, it presents challenges in securing landfill capacity and promoting efficient resource utilization. Therefore, reducing the amount of CDW sent to landfill and expanding recycling are important priorities for future CDW management.

2.4 Regulations Related to CDW Recycling

Table 1 summarizes the major laws, regulations, and technical standards related to CDW recycling in Vietnam [5-6].

2.4.1 Legal Framework and Management System for CDW

The legal framework for waste management and recycling in Vietnam is based on the Law on Environmental Protection No. 72/2020/QH14, promulgated on November 17, 2020, and effective from January 1, 2022. The law establishes waste reduction, reuse, recycling, and proper treatment as the fundamental principles of waste management while promoting a circular economy as a key national environmental policy. It also provides for the separate collection of municipal solid waste and the promotion of resource circulation, thereby supporting the development of a sustainable waste management system. Following its enactment, Decree No. 08/2022/NĐ-CP and Circular No. 02/2022/TT-BTNMT were issued to provide detailed regulations on waste collection, transportation, reuse, recycling, and proper treatment. Together, these legal instruments have strengthened Vietnam's framework for waste management and resource circulation.

2.4.2 Legal Framework and Management System for CDW

Previously, the National Strategy for Integrated Solid Waste Management (Prime Minister's Decision No. 2149/QĐ-TTg) established the gradual reduction of waste generation, reduced reliance on incineration and landfill disposal, and the promotion of reuse and recycling as its core policies. Subsequently, the National Environmental Protection Strategy to 2030 with a Vision to 2050 (Prime Minister's Decision No. 450/QĐ-TTg, 2022) was formulated to guide environmental protection and resource circulation. Its main objectives are as follows.

(1) Reduction of waste generation and promotion of source separation.

(2) Efficient resource use and promotion of a circular economy.

(3) Promotion of waste reuse and recycling.

(4) Gradual reduction of dependence on landfill disposal.

(5) Prevention of environmental pollution and strengthening of environmental protection.

CDW management in Vietnam is implemented through cooperation among the central government,

Table 1 Major Laws, Regulations, and Technical Standards Related to CDW Recycling in Vietnam

Law/Standard	Description
Law on Environmental Protection (2020)	Fundamental law governing environmental protection, waste management, and recycling in Vietnam.
Decree No. 08/2022/NĐ-CP	Specifies detailed provisions for implementing the Law on Environmental Protection, including the management, collection, reuse, recycling, and treatment of various types of waste, including construction waste.
Circular No. 02/2022/TT-BTNMT	Provides technical requirements and implementation procedures for waste management.
TCVN 11969:2018	National standard for recycled coarse aggregate for concrete.
TCVN 13694:2023	National standard for recycled materials for road base applications.
Decision No.450 / QĐ-TTg2022/	National strategy approving the National Environmental Protection Strategy to 2030 with a Vision to 2050.

local authorities, and relevant organizations under the Law on Environmental Protection (2020) and related regulations. The Ministry of Construction is responsible for CDW management and the promotion of recycled construction materials and has developed national (TCVN) and technical standards for recycled aggregates. Meanwhile, the Ministry of Agriculture and Environment is responsible for formulating waste management policies, implementing relevant regulations, environmental protection, and overall waste management. In addition, local authorities (People's Committees) oversee the collection, transportation, treatment, and supervision of CDW while developing management systems suited to local conditions. Furthermore, the Urban Environment Company and private recycling companies are responsible for operational activities, including the collection, crushing, sorting, and production of recycled materials from CDW.

As described above, government agencies and private companies in Vietnam work together to promote the proper management and recycling of CDW. However, challenges remain in the collection and sorting systems and in quality control. Therefore, understanding the quality characteristics of recycled aggregates is essential for expanding their utilization.

3. Utilization of CDW as Recycled Aggregate

3.1 Production of Recycled Aggregate

The recycled aggregates used for the quality evaluation were produced at three recycling plants, designated as Plants A, B, and C. At each plant, the collected CDW was crushed to produce recycled crushed stone, which was then screened to obtain RGA and RSA.

The recycled aggregates produced at Plant A were RGA_1 and RSA_1. These aggregates were produced from CDW containing brick fragments [2].

The recycled aggregates produced at Plant B were RGA_2 and RSA_2, which were produced from CDW without brick fragments. Plant C produced RSA_3 from CDW containing brick fragments [7].

3.2 Quality Characteristics of Recycled Aggregates

Table 2 summarizes the test methods for aggregates used in Vietnam. The tests were conducted in accordance with TCVN 7570:2006 [5]. Figures 2–4 show the particle size distributions of the recycled crushed stone, RGA_1, and RSA_1 produced at Plant A.

Table 3 summarizes the quality characteristics of the recycled aggregates produced at each recycling plant.

3.2.1 Particle Size Distribution

The recycled crushed stone passed the 19-mm nominal sieve completely, with more than 50% of the particles passing the 4.75-mm sieve. Figure 3 shows the particle size distribution of RGA_1 after grading adjustment. The adjustment was performed by removing a portion of the RSA smaller than 4.75 and 1.18 mm. Compared with the grading limits specified in ASTM C33/C33M-18 [8], the particle size distribution was slightly outside the specified range for coarse aggregates used in concrete.

As shown in Figure 4, the particle size distribution of RSA_1 indicates that the CDW contained a large proportion of brick fragments. In addition, because both the interior and exterior wall surfaces were finished with mortar, a considerable amount of mortar fragments was also present. These fragments increased

Table 2 Test Methods for Aggregates in Vietnam

Test Item	Standard
Test Methods for Aggregates for Concrete and Mortar	TCVN 7570：2006
Standard Specification for Concrete Aggregates	ASTM C33/C33M-18
Test Method for Water Absorption and Oven-dry Density of Aggregates	TCVN 7572-4：2006

Table 3 Quality Characteristics of Recycled Aggregates

Recycling Plant	A		B		C
Type	RGA_1	RSA_1	RGA_2	RSA_2	RSA_3
Maximum Size of Coarse Aggregate (mm)	9.5	-	20	-	-
Fineness Modulus	6.32	3.57	6.59	3.36	3.09
Oven-dry Density (g/cm^3)	2.23	2.46	2.41	1.95	2.11
Water Absorption (%)	11.34	12.15	5.68	8.84	10.05

the proportion of particles smaller than 0.3 mm.

The maximum particle size of RGA_1 was 9.5 mm, and its fineness modulus (FM) was 6.32. The FM of RSA_1 was 3.57. The maximum particle size of RGA_2 produced at Plant B was 20 mm, with an FM of 6.59, whereas the FM of RSA_2 was 3.36. The FM of RSA_3 produced at Plant C was 3.09.

3.2.2 Oven-dry Density and Water Absorption

The oven-dry density of RGA_1 was 2.23 g/cm³, and its water absorption was 11.34%. In contrast, the oven-dry density of RSA_1 was 2.46 g/cm³, and its water absorption was 12.15%. The oven-dry density of RGA_2 was 2.41 g/cm³, with a water absorption of 5.68%, whereas the oven-dry density of RSA_2 was 1.95 g/cm³, with a water absorption of 8.84%.

The recycled aggregates produced at Plant B exhibited lower water absorption than those produced at Plant A. The oven-dry density of RSA_3 was 2.11 g/cm³, and its water absorption was 10.05%. The water absorption of RGA_2 was 5.68%, slightly exceeding the Type I limit of 5.0% specified in TCVN 11969:2018. However, it satisfied the recycled aggregate class L (RLG) requirement in Annex A of JIS A 5023, which specifies a maximum water absorption of 7.0%. In addition, the water absorption of all RSA satisfied the recycled fine aggregate class L (RLS) requirement in Annex A of JIS A 5023, which specifies a maximum water absorption of 13.0%. RSA_1 and RSA_3 exhibited higher water absorption than RSA_2, because they were produced from CDW containing brick fragments.

4. Conclusions

This study investigated the current status of CDW generation, collection, and recycling in Vietnam and evaluated the quality of recycled crushed stone and recycled aggregates. The following conclusions were drawn.

(1) Because concrete waste is not adequately sorted at the source, the recycled aggregates contain significant amounts of brick fragments and adhered mortar or cement paste. Consequently, their water absorption, oven-dry density, and other quality characteristics are adversely affected, limiting their use as concrete aggregates.

(2) Although national standards (TCVN) for recycled aggregates have been established in Vietnam, the collection and sorting system, recycling facilities, and quality control remain inadequate. Consequently, substantial challenges remain in expanding the use of recycled aggregates.

(3) These results indicate that recycled aggregates produced in Vietnam can satisfy the water absorption requirements for RLG and RLS specified in Annex A of JIS A 5023, provided that they are produced from CDW without brick fragments. Therefore, the required concrete performance is expected to be achievable by blending them with natural aggregates at an appropriate replacement ratio.

Acknowledgement

The authors gratefully acknowledge the invaluable support of Assoc. Prof. Nguyen Thanh Sang of the University of Transport and Communications, Vietnam, in conducting the field survey on waste management and recycling.

References

[1] VnEconomy, https://vneconomy.vn/rac-thai-xay-dung-dang-tang-manh-gan-cham-moc-10-trieu-tannam.htmK.L.

[2] Dinh V. L., Nguyen A. D., Tao Y., Nishikigi, K. and Dosho Y., Application of recycled aggregate concrete technology for construction work in Vietnam, Meijo Asian Research Journal, 10(1) (2020) 5-20.

[3] Vtvonline, https://vtv.vn/khoang-10000-tan-phe-thai-xay-dung-moi-ngay-ha-noi-xu-ly-the-nao-10026061811575062.htm

[4] NATIONAL STANDARD, TCVN 11969:2018, 1st Publish.

[5] https://thuvienphapluat.vn/TCVN/Xay-dung/TCVN-13694-2023-Cap-phoi-tai-che-tu-chat-thai-ran-xay-dung-920299.asp.

[6] https://english.luatvietnam.vn/decision-no-450-qd-ttg-approving-the-national-environmental-protection-strategy-to-2030-with-a-vision-tow-219565-doc1.html

[7] Nguyen P. A. and Nguyen A. D., - Low Carbon Emission Geopolymer Mortar Using Recycled Fine Aggregate and Industrial By-Products, Civil Engineering and Architecture, 13(4) (2025) 3196-3206. DOI: 10.13189/cea.2025.130425

[8] ASTM C33/C33M-18 Standard Specification for Concrete Aggregates

Case study on engineering properties of mortar with waste plastic pyrolysis by-product

Hye-Young Youn※1, Gyu-Yong Kim※2, Byung-Cheol Choi※3, Sung-Jun Ji※1, Yeon-Woo Go※4, Seung-Hoon Song※4, Jeong-Soo Nam※2

ABSTRACT

This study investigates waste plastic pyrolysis by product WPPB, a residue from waste plastic oil r ecovery, as a partial fine aggregate replacement in mortar. Specimens with 0, 10, 20, and 30% repl acement were evaluated for fresh and hardened properties. Increasing WPPB content reduced wor kability and setting time while increasing air content. WPPB replaced specimens expanded rather t han shrank due to hydrogen gas generation between residual aluminum and the alkaline pore soluti on, which also lowered compressive strength. These results indicate WPPB requires further mix de sign optimization for practical use.

1. Introduction

The depletion of natural resources has become a critical issue in the construction industry, necessitating the development of sustainable alternatives to traditional fine aggregates. As the availability of natural sand diminishes, research on alternative materials incorporating recycled resources has gained significant attention, and a sustainable approach that prioritizes environmental considerations is essential [1]. At the same time, the accumulation of plastic waste represents a growing global environmental concern; due to their resistance to degradation, plastics pose long-term ecological risks, and effective treatment and recycling strategies are necessary to mitigate these effects. Addressing both challenges simultaneously, the use of recycled plastic-derived materials as fine aggregate substitutes offers a promising pathway toward more sustainable construction practices. Recent studies have highlighted pyrolysis as a promising technique for converting waste plastics into reusable fuels, with waste plastic pyrolysis by-product generated as a residue during the process [2].

The utilization of this by-product in construction materials represents an emerging research focus. Waste plastic pyrolysis by-product shares certain similarities with biochar, which has been shown, when incorporated in small amounts, to enhance mechanical properties through its porous and lightweight nature, contributing to reduced mortar density and mitigation of drying shrinkage. However, biochar is deliberately produced from organic biomass through a dedicated process, whereas waste plastic pyrolysis by-product is an unintended residue generated during oil recovery from waste plastics, requiring no additional dedicated production process and thus offering potential advantages in terms of energy consumption and resource efficiency. Despite this potential, its effects on the mechanical properties of mortar remain underexplored [3].

This study investigates the feasibility of using wast waste plastic pyrolysis by-product as a fine aggregate replacement in mortar, examining its engineering properties to assess its viability as a sustainable construction material.

2. Materials and methods

Ordinary Portland cement (OPC, H Company, Korea) was used, and natural sand served as the fine aggregate.

※1 Ph.D. Course, Dept. of Architectural Engineering, Chungnam National University, Korea
※2 Prof., Dept. of Architectural Engineering, Chungnam National University, Korea
※3 Ph.D., Dept. of Architectural Engineering, Chungnam National University, Korea
※4 Master's Course, Dept. of Architectural Engineering, Chungnam National University, Korea

A portion of the sand was substituted with waste

Table 1 Mix proportion of specimen plan

Specimen ID	W/C	Unit weight [kg/m^3]		
		Cement	Fine aggregate	Waste plastic pyrolysis by-product
WPPB - 0	0.5	1000	1000	-
WPPB - 10			900	100
WPPB - 20			800	200
WPPB - 30			700	300

plastic pyrolysis by-product, secondarily generated during oil recovery from waste plastics. The waste plastic pyrolysis by-product exhibited higher water absorption than natural sand. To minimize particle size effects, the particle size distribution of the waste plastic pyrolysis by-product was adjusted to be similar to that of natural sand Fig. 1 and Fig. 2 show the particle size distribution curves of natural sand and waste plastic pyrolysis by-product, respectively, measured using a particle size analyzer (PSA; Mastersizer 3000, Malvern).

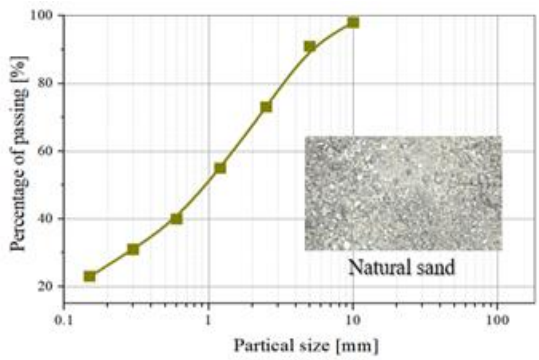

Figure 1 Natural sand particle size distribution.

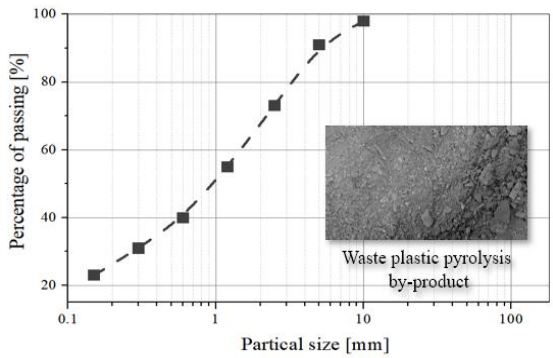

Figure 2 Waste plastic pyrolysis by-product particle size distribution.

Fig. 3 presents the physical appearance of the waste plastic pyrolysis by-product in its black powder form, while Fig. 4 shows an SEM image revealing its irregular and angular surface morphology, which is markedly different from the relatively smooth and rounded surface of natural sand. This irregular surface texture, combined with the porous microstructure inherited from the pyrolysis process, is considered to be closely related to the higher water absorption of the waste plastic pyrolysis by-product compared to natural sand.

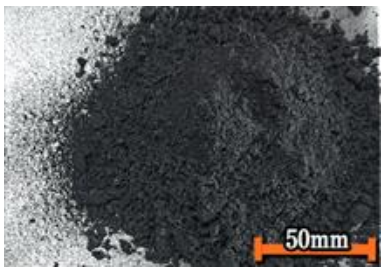

Figure 3 Waste plastic pyrolysis by-product.

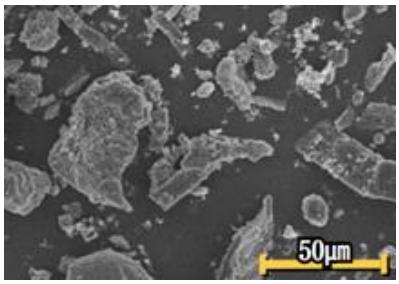

Figure 4 SEM image of WPPB.

The mix proportions and experimental plan are presented in Table 1. The water-to-cement ratio (W/C)

was fixed at 50%, and the waste plastic pyrolysis by-product replacement ratios were 0%, 10%, 20%, and 30%. Fresh properties such as air content, slump flow, setting time, and relative height change were measured, and compressive strength was tested at 28 and 56 days.

3. Results and Discussion

3.1 Fresh properties

Fig. 5 presents the results of the table flow test, showing that the workability of mortar decreased with increasing replacement ratios of pyrolysis by-products of waste plastics. The flow value of the plain specimen was highest before tapping and progressively decreased as the waste plastic pyrolysis by-product content increased. Likewise, the number of tapping blows required to reach the target flow increased, indicating that the waste plastic pyrolysis by-product reduced the flowability of the mixture. This reduction is attributed to the rough surface texture and high-water absorption capacity of the waste plastic pyrolysis by-product, which limit free water availability and increase internal friction.

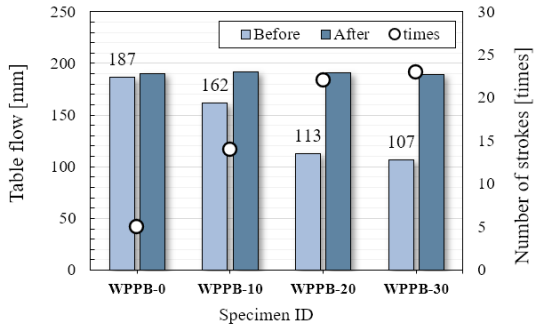

Figure 5 Flow table.

Fig. 6 shows the setting time test results using the Vicat apparatus, demonstrating that both initial and final setting times were shortened as the waste plastic pyrolysis by-product replacement ratio increased. This acceleration in setting is likely due to the waste plastic pyrolysis by-product absorbing free water in the mixture, thereby limiting the water available for hydration rather than promoting the reaction itself.

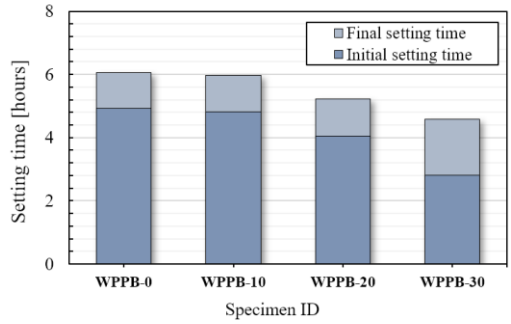

Figure 6 Setting time.

Fig. 7 presents the air content measurements, which increased with higher waste plastic pyrolysis by-product content. The irregular and rough surfaces of waste plastic pyrolysis by-product particles are believed to trap more air during mixing, leading to a higher entrained air volume compared to the plain specimen [4].

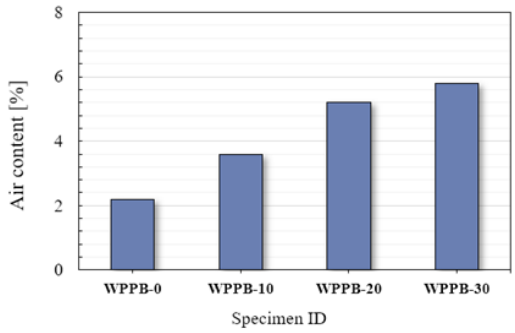

Figure 7 Air content.

3.2 hardened properties

Fig. 8 illustrates the relative height change of mortar specimens. The plain specimen exhibited a slight reduction in height, indicating typical drying shrinkage, whereas waste plastic pyrolysis by-product-replaced specimens showed a tendency toward expansion. This expansive behavior is attributed to hydrogen gas generation from the reaction between residual aluminum components in the waste plastic pyrolysis by-product and the alkaline pore solution of the cement matrix ($2Al + 2OH^- + 2H_2O \rightarrow 2AlO_2^- + 3H_2 \uparrow$), which appears to offset the shrinkage tendency and contribute to the observed expansion [5]. This suggests that the incorporation of waste plastic pyrolysis by-product affects the dimensional stability of mortar through a mechanism distinct from conventional shrinkage/expansion behavior.

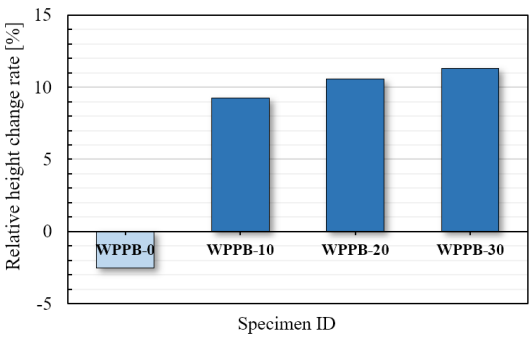

Figure 8 . Relative height change rate.

Fig. 9 shows the compressive strength development at 28 and 56 days. While the plain specimen demonstrated a steady increase in strength over time, specimens with waste plastic pyrolysis by-product replacement exhibited lower overall strength levels. This reduction is attributed to the waste plastic pyrolysis by-product's limited load-bearing capacity as a fine aggregate replacement, as well as the pores formed by the expansion associated with hydrogen gas generation, both of which hinder effective stress transfer within the mortar matrix and consequently reduce compressive strength development [6].

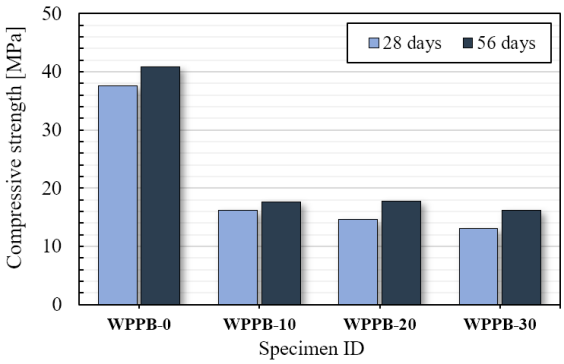

Figure 9 Comperssive strength.

The results show that the incorporation of waste plastic pyrolysis by-product reduces the workability and compressive strength of mortar, while increasing air content and inducing expansion, primarily due to hydrogen gas generation from the reaction between residual aluminum components and the alkaline pore solution. These changes in fresh and hardened properties indicate that the waste plastic pyrolysis by-product substantially alters the internal pore structure and dimensional stability of mortar compared to natural sand. Therefore, careful mix design optimization, considering replacement ratio and its associated effects on gas generation and pore formation, is essential to secure adequate workability and mechanical performance when utilizing waste plastic pyrolysis by-product as a fine aggregate replacement.

4. Conclusions

This study evaluates the properties of mortar incorporating waste plastic pyrolysis by-product as a partial fine aggregate replacement.

- The high water absorption and rough surface morphology of WPPB reduced flowability, shortened setting time, and increased air content.
- WPPB-replaced specimens exhibited expansion rather than shrinkage, attributed to hydrogen gas generation from the reaction between residual aluminum components and the alkaline pore solution.
- Compressive strength decreased with increasing replacement ratio, due to WPPB's limited load-bearing capacity and pore formation from expansion, which hindered effective stress transfer.

Overall, WPPB substitution significantly affects both the fresh and hardened properties of mortar, indicating that its practical application requires further investigation. Future studies should focus on optimizing mix design parameters, developing appropriate pretreatment methods to mitigate hydrogen gas generation, and conducting long-term durability assessments to establish WPPB as a viable sustainable construction material.

Reference

[1] M.C. Collivignarelli, G. Cillari, P. Ricciardi, M.C. Miino, V. Torretta, E.C. Rada, A. Abbà, The production of sustainable concrete with the use of alternative aggregates: A review, Sustainability, 12 (2020) 7903.

[2] B. Kunwar, H. Cheng, S.R. Chandrashekaran, B.K. Sharma, Plastics to fuel: A review, Renewable and Sustainable Energy Reviews, 54 (2016) 421-428.

[3] K. Burra, A. Gupta, Characteristics of char from co-pyrolysis of biomass and plastic waste, in: ASME 2018 Power Conference, American Society of Mechanical Engineers, 2018.

[4] X. Tian, F. Rao, C.A. León-Patiño, S. Song, Effects of aluminum on the expansion and microstructure

of alkali-activated MSWI fly ash-based pastes, Chemosphere, 240 (2020) 124986.
[5] Liu, S., Chen, Z., Shao, J., Luo, S., & Yu, D. (2025). Novel soybean dregs biochar concrete: Characterization and evaluation of the mechanical properties and microstructure. Construction and Building Materials, 458, 139512.
[6] H. Youn, G. Kim, B. Choi, S. Ji, Y. Pyo, J. Nam, Material characterization of waste plastic pyrolysis char (WPPC) and its applicability evaluation in mortar, Journal of Materials Research and Technology, 39 (2025) 1234–1245.

AAMs および低品質再生骨材を使用した環境配慮型コンクリートの開発

Development of Environmentally Friendly Concrete Fabricated Using Alkali-activated Materials and Low-quality Recycled Aggregates

岩野倭子※1、道正泰弘※2、田口翔太※3、近藤直斗※4
Wako Iwano, Yasuhiro Dosho, Shota Taguchi, Naoto Kondo

ABSTRACT

本研究は，GGBFS 系 AAM と低品質再生骨材を使用した環境配慮型コンクリートの開発を目的とし, 舗装用コンクリートへの適用性を評価するために基礎的性能について検討を行った．その結果，早強ポルトランドセメントを用いた場合，初期および長期強度においても継続的に強度の増加がみられた．しかし，中性化は副産アルカリ刺激剤を用いると速くなり，耐凍害性は，再生骨材の影響で劣るため改善が必要である．環境配慮型コンクリートは, 中性化や耐凍害性の影響を受けにくいコンポジット舗装の連続鉄筋コンクリートへの利用が期待でき, 持続的な構造形成が可能なセメント系刺激剤の使用が有効である.

1. Introduction

The construction sector faces increasing pressure to reduce CO_2 emissions, with the goal of achieving carbon neutrality by 2050. In previous research, the authors investigated the potential application of an environmentally friendly concrete to pavement construction [1]. This concrete is based on a ground granulated blast-furnace slag (GGBFS)-based alkali-activated material (AAM), which incorporates GGBFS as a binder combined with a byproduct alkali activator, alongside low-quality recycled aggregates equivalent to Class L aggregate. Road pavements are broadly categorized into asphalt pavements and concrete pavements. While asphalt pavements offer ease of maintenance and low initial cost, they exhibit low durability. Concrete pavements, on the other hand, have high initial costs but offer high durability. For this reason, composite pavements that combine these characteristics are recommended [2]. It has been demonstrated that environmentally friendly concrete can be used as a lower roadbed layer for asphalt pavements [3]. However, its relatively low resistance to carbonation and freeze–thawing its use in more exposed applications. Accordingly, its application has been proposed for continuously reinforced concrete slabs in underground composite pavement, where exposure to these environmental effects is expected to be reduced [4]. Enhancing the material's resistance to carbonation and freeze–thawing damage requires the careful selection and systematic evaluation of suitable alkali activators. This study aims to develop an environmentally friendly concrete using GGBFS-based AAM and low-quality recycled aggregates, and to investigate its fundamental properties to evaluate its applicability to pavement concrete.

2. Evaluation of activators

2.1 Materials

Table 1 lists the materials. Standard sand served as the aggregate. GGBFS was used as the binder. Four types of alkali activators were used: byproduct slaked lime (A1) and non-JIS standard slaked lime (A2) as byproduct-derived alkali activators, alongside ordinary Portland cement (NC) and high-early-

※1 日本 名城大学理工学研究科環境創造工学専攻
※2 日本 名城大学理工学部環境創造工学科 教授 博士(工学)
※3 日本 名城大学理工学研究科社会環境デザイン工学専攻
※4 日本 鹿島道路(株)技術研究所 修士(工学)

Table 1 Materials

Item	Material	Symbol	Remarks
Aggregate	Standard sand	S	-
	Recycled coarse aggregate	RLG	25−5 mm
	Recycled fine aggregate	RCS	≤ 5 mm
Binder	Ground granulated blast-furnace slag	GGBFS	JIS A 6206 (GGBFS4000)
Alkali activator (Reference)	Slaked lime	CH	JIS R 9001
Alkali activator	By-product lime	A1	-
	Non-JIS hydrated lime	A2	
	Ordinary Portland cement	NC	
	High-early-strength Portland cement	HC	
Mixing water	Tap water	W	-
Chemical admixture	Air-entraining and high-range water-reducing admixture	SP1	Poly carboxylic acid compounds
		SP2	
	Air entraining admixture	Ad1	Modified oxidized rosin compound system anionic surfactant
		Ad2	Higher fatty acid surfactant

Table 2 Mix proportions Fresh mortar and Hardened mortar

Type		P/B(%)	Mix proportion Unit weight (kg/m³) W	P GGGBFS	B A1	B A2	B NC	B HC	S	Fresh mortar Slump flow (mm)	Hardened mortar Flexural Strength (N/mm²) 7 days	28 days	91 days	Compressive Strength (N/mm²) 7 days	28 days	91 days
A1-10	A1	10	225	405	45	-	-	-	1350	179	5.0	6.3	6.7	15.1	21.8	23.9
A1-13.9		13.9		387	63	-	-	-		176	4.6	6.4	6.7	14.7	22.4	25.9
A1-20		20		360	90	-	-	-		178	4.8	6.0	6.9	13.8	21.2	24.8
A2-10	A2	10		450	-	45	-	-		165	6.1	7.1	8.0	21.0	30.2	34.0
A2-20		20		360	-	90	-	-		148	6.1	7.0	8.5	22.2	30.7	35.7
NC-10	NC	10		405	-	-	45	-		181	6.5	7.6	7.3	26.0	33.8	40.0
NC-30		30		315	-	-	135	-		180	7.0	9.1	9.4	34.1	53.3	63.9
NC-50		50		225	-	-	225	-		183	7.1	9.4	10.1	37.7	61.2	70.8
HC-10	HC	10		405	-	-	-	45		174	6.0	7.8	8.4	27.0	36.0	43.2
HC-30		30		315	-	-	-	135		175	7.1	8.5	8.7	37.0	54.2	66.0
HC-45		45		248	-	-	-	203		172	6.0	8.2	9.2	33.8	57.2	72.3
HC-50		50		225	-	-	-	225		171	6.7	8.9	9.4	41.2	60.3	76.3

Table 3 Test items and methods

Item			Test Method	Remarks
Mortar evaluation	Fresh mortar	Slump flow	JIS R 5201	-
	Hardened mortar	Flexural strength	JIS R 5201	At 7 and 28 days
		Compressive strength	JIS R 5201	At 7, 28, and 91 days
Concrete evaluation	Fresh concrete	Slump flow	JIS A 1150	Target Values: 500 ± 75mm
		Air content	JIS A 1128	Target Value: 4.5% ± 1.5%
		Concrete temperature	JIS A 1156	-
		Chloride ion content	JIS A 5023	Target Values ≤ 0.30 kg/m³
	Hardened concrete	Compressive strength	JIS A 1108	Target Values: 36 N/mm²
		Static modulus of elasticity	JIS A 1149	Target Values: 28 kN/mm²
		Flexural strength	JIS A1106	Target Values: 4.5 N/mm²
		Drying shrinkage	JIS A 1129-3	Method with dial gauge
		Accelerated carbonation	JIS A 1153	-
		Freezing-and-thawing	JIS A 1148	Method A

strength Portland cement (HC) as cementitious activators [5]. For comparison, slaked lime (CH) was also analyzed. A1 contains approximately 62% $Ca(OH)_2$, whereas A2 contains approximately 90% $Ca(OH)_2$, making its composition closer to pure CH than A1. HC is composed of approximately 65% Ca_3SiO_5(C_3S). Tap water (W) was used as the mixing water.

2.2 Mix proportion

Table 2 shows mortar mix proportions with 12 activator-to-binder ratios(P/B): A1 (10%, 13.9%, 20%), A2 (10%, 20%), NC (10%, 30%, 50%), and HC (10%, 30%, 45%, 50%).

2.3 Test items and methods

Table 3 lists the test items and methods. The fresh mortar was evaluated by measuring flow. The hardened mortar was assessed through both flexural strength and compressive strength tests. Mortar specimens were fabricated according to JIS R 5201, demolded the following day, and then cured underwater until testing at 7, 28, and 91days.

2.4 Experimental results

2.4.1 Fresh mortar

Table 2 presents the fresh mortar test results. The effects of increasing P/B on flow varied by material. For A1 and NC, flow values remained largely consistent despite increased P/B, indicating a minimal effect of alkali activator content. By contrast, A2 showed a tendency toward decreasing flow as P/B increased, with a slight reduction also observed for HC.

2.4.2 Hardened mortar

Table 2 presents the flexural and compressive strength test results, respectively. Flexural strength was high for NC and HC, generally increasing with P/B. Notably, HC exhibited high flexural strength across all testing ages. This was likely due to the supply of $Ca(OH)_2$ from the hydration of C_3S and other cement phases, which accelerated the reaction of GGBFS and promoted C-(A)-S-H formation [6]. Similarly, for compressive strength, an increase in P/B led to higher strengths at 7, 28, and 91days for both NC and HC. In particular, due to its active initial hydration, HC exhibited high 7day strength, with continuous strength development thereafter. However, flexural strength and compressive strength were low for A1 and A2, and the improvement effect of P/B was also minor. This is probably because their primary component is $Ca(OH)_2$, thereby limiting structural formation through the continuous hydration typical of cement [7]. The compressive strength generally increased in the order of A1 < A2 < NC < HC.

These findings suggest that A1 and A2, which consist predominantly of $Ca(OH)_2$, have limited capacity to sustain the formation of hydration products over time.

In contrast, the incorporation of cementitious activators (as in NC and HC) promotes the continuous development of the cementitious matrix, resulting in higher flexural and compressive strengths.

Table 4 Main properties of the recycled aggregates

Item		Test Method	RLG	RCS
Density in oven-dry condition (g/cm^3)		JIS A 1109	2.27	2.00
Water absorption (%)		JIS A 1110	5.3	11.5
Fineness modulus (F.M.)		JIS A 1102	6.89	3.80
Solid content (%)		JIS A 1104	62.1	68.9
Solid content for particle shape determination (%)		JIS A 5005	62.2	60.2
Content of materials finer than 75 μm sieve (%)		JIS A 1103	0.9	6.2
Chloride content (%)		JIS A 1154	0.01	0.01
Aggregate Crushing Value (%)		BS 812-110	26.6	-
Ten per cent fines value (kN)		BS 812-111	124	-
Abrasion loss (%)		JIS A 1121	32.0	-
Mass loss fraction (%)		JIS A 1122	50.6	25.9
Amount of contained impurities (mass%)	A	JIS A 5023	0.6	0.3
	B		0	0
	C		0	0
	D		0	0
	E		0	0
	F		0	0.02
	G		0	0
	Total		0.60	0.32
Alkali-Silica Reactivity		Appendix D of JIS A 5021	A	-

3. Performance evaluation of concrete

In Section 2, replacement ratios for concrete tests were selected for each activator. For A1, 13.9% (intermediate of 10%, 13.9%, and 20% of B) was chosen to evaluate aggregate effects, as hardening properties showed no clear differences. For A2 (10% and 20%), which also showed no distinct difference, 20% was selected to test higher replacement. For HC (10%, 30%, 45%, and 50%), 45% was adopted considering MLIT low-carbon trial guidelines [8], since no significant difference was observed between 45% and 50%.

3.1 Materials

Table 1 presents the materials used. Recycled aggregate was produced from concrete debris of unknown origin. Recycled aggregate was produced from unknown concrete debris. Using 7 and 27 mm screens, RC-40 was classified into coarse (RLG, 5–

Table 5 Mix proportions and Fresh concrete

No.	W/B (%)	P/B (%)	s/a (%)	Unit weight (kg/m³) W	B GGBFS	P A1	P A2	P HC	RLG	RCS	Chemical admixture (B×%) SP1	SP2	Ad1	Ad2	Performances of fresh concrete Slump flow (mm)	Air content* (%)	Concrete temperature (°C)	Chloride ion content (kg/m³)
1	35	13.9	41.9	160	393	64	-	-	865	588	1.3	-	0.010	-	575	5.1(0.8)	16	0.14
2	35	20.0	40.0	165	377	-	94	-	875	550	-	2.5	-	0.275	460	4.7(0.8)	13	0.14
3	35	45.0	40.0	165	259	-	-	212	895	564	-	1.2	-	0.280	520	4.2(0.8)	18	0.14

* (): Aggregate correction factor

25mm) and fine aggregates (RCS, ≤5mm).

Table 4 lists the main properties of the recycled aggregates. The quality of RLG meets the requirements of JIS A 5023, Annex A, whereas the grading of RCS does not meet the specifications. In terms of water absorption, RLG and RCS had values of 11.5% and 5.3%, respectively. These values were compared to the standards for Class L recycled aggregate (7.0% or less and 13.0% or less for RLG and RCS, respectively). The amount of contained impurities was 0.6% for RLG (Category A), 0.3% for RCS (Category A), and 0.02% for Category F. For RLG, the 400kN crushing value was 26.6%, the 10% fines value was 124kN, and the resistance to fragmentation (Los Angeles abrasion loss) was 32.0%. The mass-loss fraction was 50.6% for RLG and 25.9% for RCS. Both of these values exceed the soundness criteria for aggregates (12% for coarse aggregate and 10% for fine aggregate) specified in the Standard Specifications for Pavements [9]. In terms of alkali-silica reactivity, RLG is designated as Category A, which is considered as innocuous. Three types of alkali activators were used: A1 and A2, which are byproduct-derived alkali activators (referred to as activators), and HC, which was included to improve strength. Tap water (W) served as the mixing water. Chemical admixtures included high-range water-reducing AE agents (SP1, SP2) and air-entraining-and-reducing admixtures (Ad1, Ad2). The high-range water-reducing AE agents were specifically used to counteract increased viscosity and material segregation caused by attached mortar or paste on the recycled aggregates.

3.2 Mix proportion

The mix proportions of the concrete are shown in Table 5. For all specimens in the concrete investigation, the water-to-binder ratio (W/B) was kept constant at 35%. The unit water content was 160 kg/m³ for No. 1 and 165 kg/m³ for No. 2 and No. 3. The AAM binders comprised GGBFS and an activator (A1 for No. 1, A2 for No. 2, and HC for No. 3), with RLG and RCS used as aggregates.

3.3 Test items and methods

Table 3 lists the test items and methods. In terms of fresh concrete, slump, slump flow, air content, concrete temperature, and chloride ion content were measured. Tests included compressive strength, static modulus of elasticity, flexural strength, drying shrinkage, accelerated carbonation, and freezing and thawing. For compressive strength and static modulus of elasticity, cylindrical specimens with a diameter of 125mm and a height of 250mm were prepared and cured under standard conditions. Three specimens were fabricated for each curing age, with average values reported. The static modulus of elasticity was measured using a compressometer. For flexural strength, drying shrinkage, accelerated carbonation, and freeze-thawing, three prismatic specimens (100mm × 100mm × 400mm) were prepared for each testing age, and average values were reported. Specimens were cured underwater after demolding until the specified testing age. For drying shrinkage, specimens were maintained under moist conditions at 20°C ± 2°C after casting, demolded approximately 24h later, and then cured underwater for 7days. They were then conditioned in an environmental chamber at 20°C ± 2°C and a relative humidity of 60% ± 5% until the measurement ages. For accelerated carbonation, specimens were cured underwater at 20°C ± 2°C after demolding until four weeks of age, then conditioned in an environmental chamber at 20°C ± 2°C and a relative humidity of 60% ± 5% until 8weeks of age. Accelerated carbonation conditions were maintained

Table 6 Hardened concrete

No.	Compressive strength* (N/mm^2)			Static modulus elasticity (kN/m^2)			Flexural strength* (N/mm^2)	Drying shrinkage ($\times 10^{-6}$)	Carbonation rate coefficient ($mm\sqrt{week}$)	Durability factor
	7 days	28 days	91 days	7 days	28 days	91 days	28 days	8 weeks	4 weeks	
1	16.1 (0.9)	20.4 (0.8)	21.7 (1.2)	16.2	18.4	18.8	4.06 (0.2)	427	10.80	8
2	21.4 (0.6)	26.7 (0.9)	28.5 (0.3)	18.1	19.9	21.1	4.29 (0.4)	301	8.73	0
3	33.7 (2.3)	40.0 (2.6)	40.9 (2.2)	19.4	23.3	24.3	5.19 (0.5)	405	2.18	21

*(): Standard deviation

at 20℃ ± 2℃, a relative humidity of 60% ± 5%, and a carbon dioxide (CO_2) concentration of 5% ± 0.2%. For freeze-thawing, specimens were cured underwater for 4 weeks before testing.

3.4 Experimental results

3.4.1 Fresh concrete

As Table 5 shows, adjusting the types and dosages of chemical admixtures allowed the slump flow and air content to satisfy target values. Binder and aggregate types had no significant effect on these properties. Concrete temperatures ranged from 13℃ to 18℃. In addition, the chloride ion content met the target of 0.30kg/m³, with comparable values across all mixes.

3.4.2 Hardened concrete

The experiment results of hardened concrete are shown in Table 6. Compressive strength met the target value of 36N/mm² only for No.3. The compressive strength tended to increase in the order of alkali activators A1 < A2 < HC. The standard deviations shown in parentheses in Table 6 ranged from 0.3 to 1.2 for No. 1 and No. 2 at all curing ages, whereas No. 3 exhibited values approximately twice as large, ranging from 2.2 to 2.6. The compressive strength of No.1 was lower than a previously reported mix (W/B of 40% using A1) [4]. Although a lower W/B typically increases compressive strength, this study's results contradict that trend. This discrepancy is likely due to the lower strength of the RLG used in this study compared to aggregates in previous research. Specifically, the RLG's 10% fines value was 124kN in this study, a significant 33% reduction from the previous study's 187kN. Furthermore, the RLG's abrasion loss was 32.0%, significantly higher than the previous aggregate's 22.5%. Consequently, despite a reduced W/B of 35%, the RLG's low stiffness led to premature aggregate crushing, preventing any

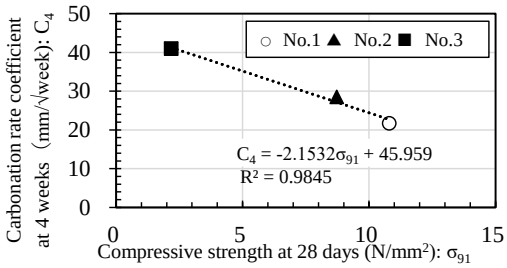

Figure 1 Relationship between compressive strength and carbonation rate coefficient

improvement in compressive strength. Although the compressive strength of No.2 (using A2) increased with curing age, it remained lower than that of the mix using HC. This was because A2, primarily consisting of $Ca(OH)_2$, lacks hydratable minerals such as C_3S and C_2S, thus offering no strength development through its own hydration reaction [10]. The compressive strength of No.3 (using HC) was high from an early age of 7days, with continuous increases in strength at 28 and 91days. This could be attributed to the fact that $Ca(OH)_2$, generated by the early hydration of C_3S, stimulated the latent-hydraulic reactivity of the GGBFS and promoted C-(A)-S-H formation [11].

Regarding flexural strength, only No. 3 satisfied the target value (4.5N/mm^2). No.3 exhibited the highest value at 5.19 N/mm^2, followed by No. 2 at 4.29 N/mm^2 and No.1 at 4.06N/mm^2.

Drying shrinkage measurements revealed comparable values for No.1 and No.3, whereas No.2 showed a reduction of approximately 30% compared to the other two.

Figure 1 presents the relationship between compressive strength and the rate coefficient of carbonation at an accelerated period of 4weeks. For No.1 and No.2, the carbonation rate coefficient at 4weeks were very large, measuring 10.80mm/√week and 8.73mm/√week, respectively. This behavior may be attributed to the high GGBFS content, which can reduce the alkalinity of the concrete because GGBFS consumes alkalis during its latent-hydraulic reaction

[12]. By contrast, that of No.3 was 2.18mm/√week, approximately 20% of the values for No.1 and No.2. This was likely due to the hydration reaction of C_3S (the main component of HC) and the high powder content (P/B=45%), which led to a densified pore structure and improved carbonation resistance [11].

Relative dynamic modulus of elasticity for No. 1 decreased to 12% at 60cycles, leading to test termination as it fell below the 60% criterion. For No.2, specimen collapse occurred at 30cycles, preventing further measurements. No.3 was measured up to 180cycles before the value dropped below 60%, leading to test termination. Because the durability factors of all concrete mixtures were significantly below the 60% test termination criterion, they all exhibited poor frost resistance. This behavior may also be associated with the high mass-loss ratio of the recycled aggregates used in this study [9]. HC used in No.3 is considered to have exhibited relatively higher resistance to freeze–thawing action due to the formation of a denser microstructure from cementitious hydration products. By contrast, A1 and A2, primarily $Ca(OH)_2$-based activators, resulted in limited microstructure densification by hydration products, leading to a highly porous structure and presumably early-stage degradation [3].

4. Conclusions

The performance of concrete produced using different activators in a GGBFS-based AAM system was evaluated. The conclusions are as follows.

Byproduct-derived slaked lime and non-JIS-compliant slaked lime, both composed primarily of $Ca(OH)_2$, showed limited ability to sustain the formation of hydration products. In contrast, cementitious activators promoted the continuous development of the matrix and resulted in higher flexural and compressive strengths. The fresh properties of environmentally friendly concrete met target values through optimized chemical admixture types and dosages. When high-early-strength Portland cement was used, the compressive strength of the environmentally friendly concrete exhibited continuous growth in both early and long-term ages. The static modulus of elasticity showed a trend similar to that of compressive strength. Flexural strength followed a comparable pattern. Although drying shrinkage of the environmentally friendly concrete was reduced depending on the activator type, carbonation accelerated with the use of byproduct-derived alkali activators. In addition, the durability factor was below 60 for all mixtures, indicating poor frost resistance, primarily due to the effects of the recycled aggregates.

These findings suggest that cementitious activators capable of promoting continuous matrix development may improve the applicability of this concrete to continuously reinforced concrete slabs in underground composite pavement systems, where the effects of carbonation and freeze-thawing are minimal.

References

[1] Kamishita R. et al., Research on by-product alkaline stimulants that make up AAM for environmentally friendly concrete, JSCE 2025 Annual Meeting, (2025) 12AM2-Ne-02.
[2] Ministry of Land, Infrastructure, Transport and Tourism (MLIT): Pavement Management for the Future, Document 3-2, 6th Subcommittee on Road Technology, Sep. 2016.
[3] Kamishita R. et al., Evaluation of materials with 100% by-products by a full-scale wheel load test. Transactions of the Japan Society of Civil Engineers, 79(21) (2023) 1-11.
[4] Iwano W. et al., Performance of environmentally friendly concrete fabricated using alkali-activated materials and low-quality recycled aggregates, Proceedings of the Japan Concrete Institute, 48(21) (2026) 1-11.
[5] Kondo N. et al., Study on Alkali Activator and Strength Characteristics of Mortars Using AAM, JSCE 2025 Annual Meeting, (2026) V-866.
[6] Tokumitsu N. et al., Hydration reaction of blast furnace slag fine powder, Research Reports of Akita National College of Technology, 35 (2017) 71-75
[7] Itoh T. et al., Effect of combined use of gypsum and calcium nitrite on the hydration reactivity of blast furnace slag added a small amount of calcium hydroxide, Cement Science and Concrete Technology, 76 (2022) 92-100.
[8] Ministry of Land. Regarding Trial Construction Using Low-Carbon Concrete, July 2025.
[9] Japan Society of Civil Engineers. Standard specifications for pavements, 2023
[10] Ishida S. et al., Characteristics of microstructural changes caused by carbonation in slaked lime and cement mortars, Proceedings of the Japan Concrete Institute, 33(1) (2011) 623-628.
[11] Adachi J. et al., Influence of anhydrite fineness on the hydration and initial strength development property of blast furnace slag cement, Cement and Concrete Proceedings, 75 (2021) 90-96.
[12] Borges, P. H. R. et al.: Carbonation of CH and C–S–H in composite cement pastes containing high amounts of BFS, Cement and Concrete Research, 40 (2010) 284-292.

高カルシウムフライアッシュ混合モルタルの産業的適用を考慮した早期炭酸化養生：CO_2吸収量、強度発現および寸法安定性

Industrially Relevant Early-Age Carbonation Curing of High-Calcium Fly Ash Blended Mortars: CO_2 Uptake, Strength Development, and Dimensional Stability

Md Mahmudullah[1*], Suk-Pyo Kang[2], Kyu-Eun Park[3], Byoung-Ky Lee[4]

ABSTRACT

Early-age carbonation curing can combine CO_2 utilization with performance enhancement in cementitious materials containing high-calcium fly ash (HFA). Mortars containing 10, 20, and 30% HFA were pre-cured for 12 h and then exposed to 20% CO_2 for 8 or 24 h. Carbonation depth and TG-derived CO_2 uptake were measured immediately after carbonation, while compressive strength, length change, and pore structure were evaluated at later ages. Carbonation depth and CO_2 uptake increased with curing duration and generally increased with HFA content. At 24 h, net CO_2 uptake was 7.91, 7.86, and 9.66% for HFA10, HFA20, and HFA30, respectively. The 28-day strengths of HFA10-24h and HFA20-24h reached 33.6 and 33.3 MPa, comparable to Plain (32.6 MPa), whereas HFA30-24h remained lower at 30.7 MPa. MIP showed that carbonation reduced the cumulative pore volume of HFA20 from 0.081 to approximately 0.068 mL/g, together with reduced long-term length change. HFA20 with 24 h carbonation curing therefore provided the most favorable balance among CO_2 utilization, strength recovery, and dimensional stability.

1 Introduction

Lower-carbon cement and concrete require reduced clinker consumption and greater use of industrial by-products. Supplementary cementitious materials (SCMs) are therefore central to low-carbon binder strategies [1,2]. High-calcium fly ash (HFA) is attractive because it contains reactive calcium-bearing phases, but excessive replacement can also reduce strength and impair dimensional stability when hydration-derived matrix formation becomes insufficient [2,3].

Early-age carbonation curing provides a complementary route for HFA utilization. Controlled CO_2 exposure can form carbonate-containing products, increasing CO_2 storage while modifying pore structure, strength, and dimensional stability [4-7]. However, a higher HFA content may supply more carbonatable calcium while simultaneously reducing clinker-derived hydration products. The optimum condition must therefore balance carbon utilization with engineering performance rather than maximize CO_2 uptake alone.

This study examined mortars containing 10-30% HFA and subjected to 20% CO_2 for 8 or 24 h after 12 h of pre-curing. Carbonation depth and TG-DTG quantified carbonation behavior, while compressive strength, 180-day length change, and MIP evaluated engineering performance and pore structure. The objective was to identify a short-duration curing condition that balances CO_2 uptake, strength recovery, and dimensional stability [5,8].

*1 Department of Construction Engineering, Woosuk University, Jincheon-eup, Chungcheongbuk-do 27841, Republic of Korea
*2 Department of Architecture, Woosuk University, Jincheon-eup, Chungcheongbuk-do 27841, Republic of Korea
*3 Department of Construction Convergence System, Woosuk University, Jincheon-eup, Chungcheongbuk-do 27841, Republic of Korea
*4 COCHEMS Co. Ltd., Daejeon 34368, Republic of Korea

2 Materials and methods

2.1 Materials and mixtures

Commercial ordinary Portland cement (OPC) and HFA obtained from a circulating fluidized bed boiler were used as binders. The HFA had a Blaine fineness of 4,717 cm^2/g, a density of 2.72 g/cm^3, and a CaO content of 37.6 wt.%. The HFA was supplied by Korea C&I Co. Ltd. XRD characterization of the original HFA identified calcium-rich phases including anhydrite, lime, calcite, and gehlenite, together with quartz and hematite. The presence of lime and other calcium-bearing phases provided potentially reactive constituents for subsequent carbonation. Key physical and chemical properties are summarized in Table 1.

Table 1. Key physical properties and chemical composition of OPC and HFA

Material	Blaine (cm^2/g)	Density (g/cm^3)	SiO_2	Al_2O_3	Fe_2O_3	CaO	SO_3	LOI
OPC	3300	3.15	21.2	5.2	3.2	63.1	2.2	2.5
HFA	4717	2.72	18.6	8.35	10.2	37.6	8.76	8.82

Mortars were prepared at a constant water-to-binder ratio of 0.40 and binder-to-sand ratio of 1:3 using standard silica sand. HFA replaced OPC by 10, 20, or 30% by binder mass. For each HFA level, non-carbonated, 8 h carbonation, and 24 h carbonation conditions were investigated. The mixture nomenclature and curing groups are summarized in Table 2.

Table 2. Mixture designation and carbonation-curing conditions

Base mix	OPC (wt.%)	HFA (wt.%)	Curing groups
Plain	100	0	Non-carbonated reference
HFA10	90	10	0 h, 8 h, 24 h
HFA20	80	20	0 h, 8 h, 24 h
HFA30	70	30	0 h, 8 h, 24 h

Note: W/B = 0.40 and B/S = 1:3 for all mixtures. Carbonation curing: 20% CO_2, 20 ± 2 °C, RH 90%, atmospheric pressure.

2.2 Specimen preparation and test methods

Fresh mortar was cast into 40 × 40 × 160 mm prismatic molds and compacted using a vibration table. All specimens were pre-cured in the molds for 12 h at 20 ± 2 °C and 60% relative humidity and were then demolded. Carbonation groups were exposed to 20% CO_2 at 20 ± 2 °C and 90% relative humidity for 8 or 24 h under atmospheric pressure. The non-carbonated control was exposed to the same temperature and humidity without CO_2 supply. After the designated early curing, all specimens were stored at 20 ± 2 °C and 60% relative humidity until testing.

Carbonation depth was determined immediately after carbonation by spraying phenolphthalein solution on freshly split surfaces. Eight measurements were averaged for each specimen. For TG-DTG analysis, paste samples with the same binder composition and W/B as the mortars were prepared without sand. Powder from the outer 0-5 mm region was collected immediately after carbonation and heated from 20 to 1000 °C at 10 °C/min under nitrogen. Because both OPC and HFA contained pre-existing carbonates, net CO_2 uptake was calculated by subtracting the value of the corresponding non-carbonated mixture from the total TG-derived CO_2 content. The original HFA contained approximately 16.3 wt.% $CaCO_3$-equivalent and 7.2 wt.% CO_2-equivalent, confirming the need for baseline correction. Based on the TG-DTG results, CH

and $CaCO_3$ contents were calculated from the mass losses within the corresponding decomposition regions, and CO_2 uptake was determined as follows:

$$CH(\%) = M_{CH}/M_{H_2O} * (M_{t1} - M_{t2}) \quad (1)$$

$$CaCO_3(\%) = \frac{M_{CaCO_3}}{M_{CO_2}} * (M_{t2} - M_{t3}) \quad (2)$$

$$CO_2 \text{ uptake } (\%) = M_{t2} - M_{t3} \quad (3)$$

where $M_{t1}-M_{t2}$ and $M_{t2}-M_{t3}$ represent the mass losses in the CH and carbonate decomposition regions, respectively; MCH, MH_2O, $MCaCO_3$, and MCO_2 are the corresponding molecular weights.

Figure 1 presents the TG-DTG curves of OPC and HFA. The CH and carbonate decomposition regions were identified at approximately 350–430 °C and 430–900 °C, respectively. HFA exhibited higher carbonate-related mass loss than OPC, corresponding to approximately 16.3 wt.% $CaCO_3$ and 7.2 wt.% CO_2, whereas OPC contained about 5.0 wt.% $CaCO_3$ and 2.2 wt.% CO_2. In addition, HFA contained approximately 2.6 wt.% CH, indicating the presence of potentially reactive calcium-bearing phases. These results confirm that HFA contains both pre-existing carbonate phases and reactive calcium species. Therefore, the initial carbonate content was considered as a baseline when calculating the net CO_2 uptake after carbonation curing.

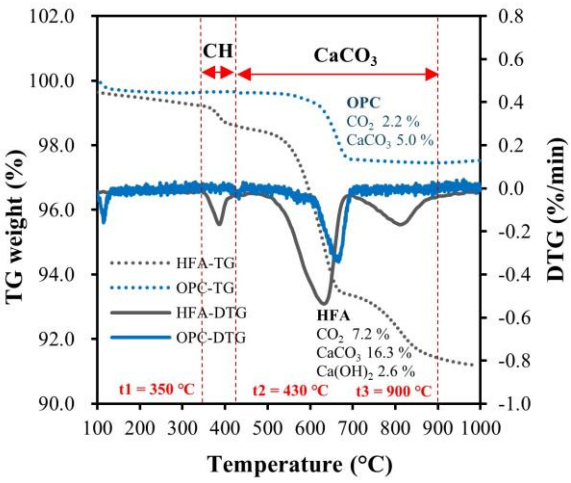

Figure 1. TG-DTG curves showing temperature ranges of OPC and HFA

Compressive strength was measured at 3, 7, and 28 days using three specimens for each condition; the coefficient of variation was below 5%. Length change was monitored by the comparator method up to 180 days using three replicate specimens, with the reference length established at a total age of 7 days after completion of the initial curing regime. MIP was conducted at 28 days on selected paste specimens (Plain, HFA20, and HFA20-24h) to relate the performance results to pore-structure changes.

3 Results and discussion

3.1 Carbonation behavior and CO_2 uptake

Figure 2 compares carbonation depth and TG-derived CO2 uptake after early carbonation curing. No measurable carbonation depth was observed in the non-carbonated controls; therefore, carbonation depth is presented only for CO2-cured specimens.

Carbonation depth increased with both curing duration and HFA replacement. For HFA10, the depth increased from 3.07 mm at 8 h to 3.71 mm at 24 h. HFA20 increased from 3.58 to 4.04 mm, while HFA30 showed the largest change, from 3.96 to 5.51 mm. At the same curing duration, a larger HFA replacement generally produced greater penetration. This trend can be associated with changes in calcium availability and pore characteristics caused by HFA incorporation, both of which influence CO_2 transport and reaction [9,10].

A similar trend was observed for TG-derived CO_2 uptake. The non-carbonated baseline values were 2.89% for Plain and 3.16, 4.05, and 4.77% for HFA10, HFA20, and HFA30, respectively. These values were not interpreted as CO_2 fixed during the controlled curing stage because the raw materials already contained carbonate phases. After 8 h of carbonation, the total CO_2 contents increased to 9.95, 9.15, and 13.23% for HFA10, HFA20, and HFA30; after 24 h, they further increased to 11.07, 11.91, and 14.43%, respectively. The corresponding net uptakes were 6.79-9.66% after subtraction of the non-carbonated baseline. The highest net uptake was obtained for

HFA30-24h (9.66%), showing that a high replacement level can increase the amount of CO_2 chemically retained by the binder phase. TG quantification also indicated progressive $CaCO_3$ formation with increasing HFA content and carbonation duration; the $CaCO_3$-equivalent content reached 32.82% for HFA30-24h, whereas the CH content remained within a comparatively narrow range. Thus, carbonate formation cannot be explained only by CH consumption and likely also involves additional reactive calcium-bearing phases in the HFA-blended system. Because TG-DTG alone cannot identify the individual reaction pathway, this observation is interpreted as evidence of an overall increase in carbonation extent rather than proof of a specific mechanism [7,11].

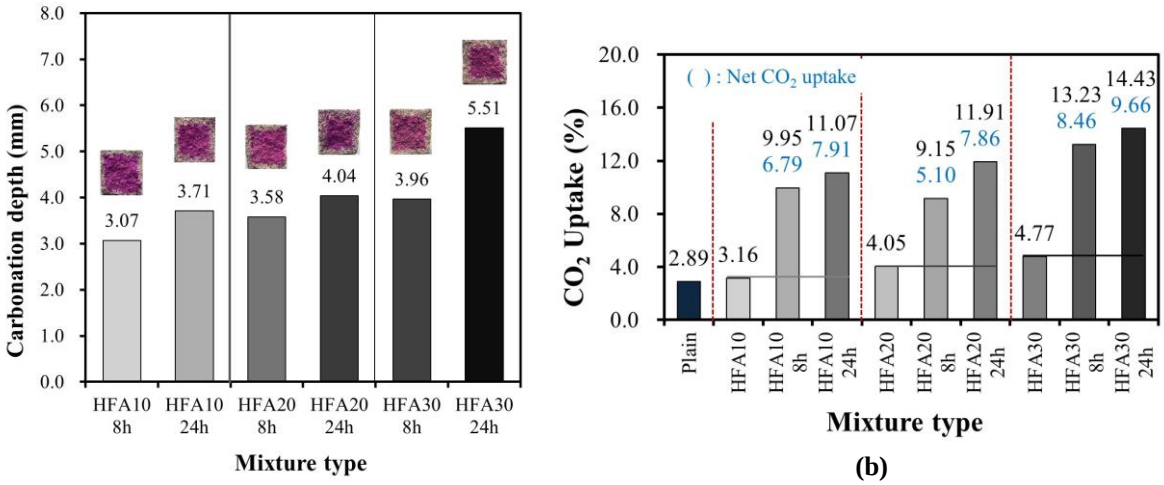

(a) (b)

Figure 2. Carbonation behavior of HFA-blended mortars and pastes: (a) carbonation depth and (b) TG-derived CO_2 uptake

These results are important for carbon-neutral cement and concrete because they demonstrate that increasing HFA replacement can enhance CO_2 uptake under short curing durations. However, the most carbon-reactive mixture is not necessarily the most suitable engineering mixture. The next sections therefore compare CO_2 uptake with strength and dimensional stability to identify the best overall balance.

3.2 Compressive strength development

Figure 3 summarizes the compressive strength at 3, 7, and 28 days. The dashed line in each panel represents the strength of Plain mortar at the corresponding age.

Early carbonation curing improved strength at all replacement levels, with the 24 h treatment consistently producing the strongest recovery. At 3 days, HFA10-24h, HFA20-24h, and HFA30-24h reached 31.8, 30.3, and 29.3 MPa, respectively, compared with 29.3 MPa for Plain. At 7 days, the corresponding values were 32.6, 34.2, and 30.5 MPa, while Plain reached 31.7 MPa. The improvement indicates that carbonate formation during early CO_2 exposure can compensate for part of the strength loss associated with cement replacement.

The 28-day results clearly show the effect of replacement level. HFA10-24h and HFA20-24h reached 33.6 and 33.3 MPa, respectively, which were comparable to or slightly higher than Plain (32.6 MPa). In contrast, HFA30-24h improved from 22.2 to 30.7 MPa but did not fully recover to the Plain level. Carbonation products can fill pores and modify the microstructure, but at 30% replacement the reduced clinker fraction limits hydration-driven matrix development. Therefore, the benefit of higher CO_2 uptake at HFA30 was accompanied by a persistent mechanical penalty.

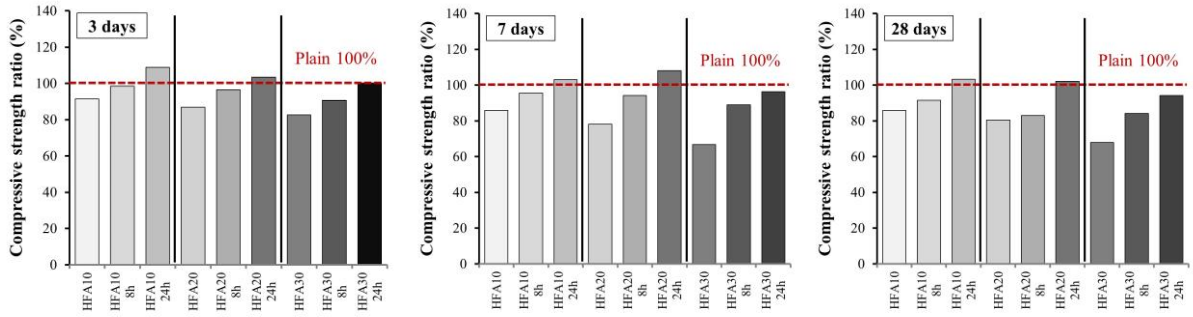

(a) **(b)** **(c)**

Figure 3. Compressive strength development of HFA-blended mortars under non-carbonated and early carbonation-curing conditions (a) 3 days, (b) 7 days and (c) 28 days

The difference between 8 h and 24 h also shows that curing duration is important. The 8 h treatment improved early strength but produced less consistent recovery at 28 days, especially for HFA20. Extending the CO_2 exposure to 24 h allowed a larger degree of carbonation and, within the present conditions, provided a more favorable balance between carbonation-induced densification and subsequent hydration. This agrees with previous observations that carbonation duration strongly controls the extent of microstructural modification and strength evolution [4,5,12].

Overall, the strength results identify a practical upper range near 20% HFA for the present curing regime. Although 30% HFA maximized CO_2 uptake, 10-20% HFA combined with 24 h carbonation curing was more effective in maintaining structural performance. This trade-off is central when carbonation curing is evaluated as a carbon-utilization process rather than solely as a sequestration test.

3.3 Microstructural Interpretation

Figure 4 presents the XRD patterns of the cement pastes at 28 days. The main crystalline phases identified were CH, $CaCO_3$, and residual C_3S. The persistence of residual C_3S indicates that unreacted clinker phases remained after curing, whereas detectable $CaCO_3$ peaks in the carbonation-cured specimens confirm that carbonation products formed during early CO_2 exposure remained present after subsequent curing.

Compared with the non-carbonated mixtures, the carbonation-cured specimens showed a more pronounced $CaCO_3$-related response, which is consistent with the increased carbonate content identified by TG-DTG analysis. These results suggest that early carbonation curing promoted the formation of relatively stable carbonate-containing products while hydration continued during post-curing. Therefore, hydration and carbonation reactions likely coexisted under the investigated conditions.

However, because the XRD analysis was qualitative, the relative peak intensities were not used to directly quantify the degree of hydration or carbonation. Instead, the XRD results were interpreted together with the TG-DTG results to support phase identification and to confirm the persistence of carbonation products within the cementitious matrix.

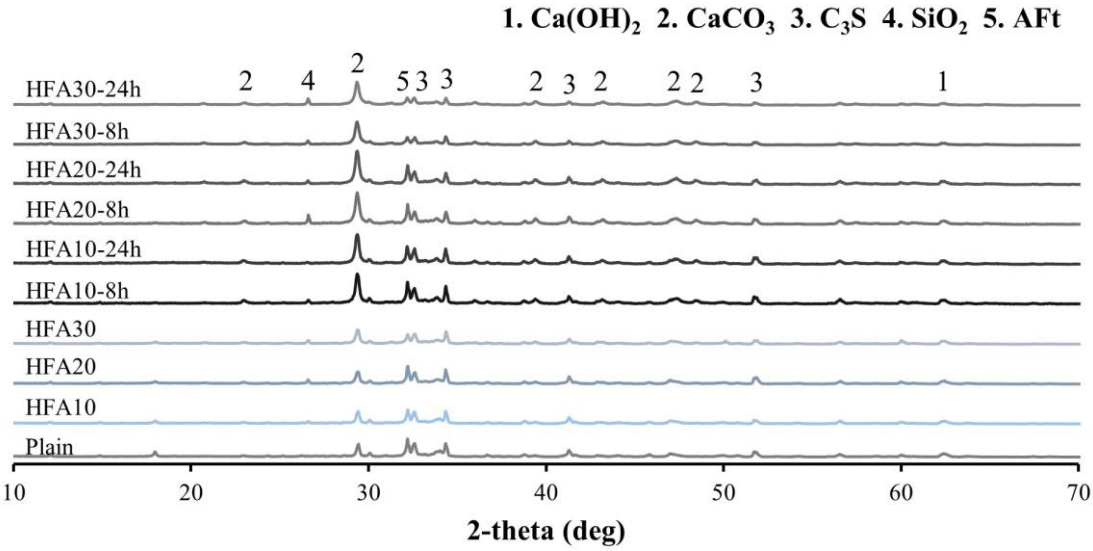

Figure 4. XRD patterns of cement pastes from different curing methods at 28 days

3.4 Pore structure and dimensional stability

MIP was used to examine whether the strength recovery of HFA20-24h was accompanied by pore refinement. Figure 5 compares Plain, HFA20, and HFA20-24h at 28 days. HFA20 showed a cumulative pore volume of approximately 0.081 mL/g, while carbonation curing reduced the value to approximately 0.068 mL/g. The differential distribution also showed lower pore intensity over part of the capillary-pore range after 24 h carbonation.

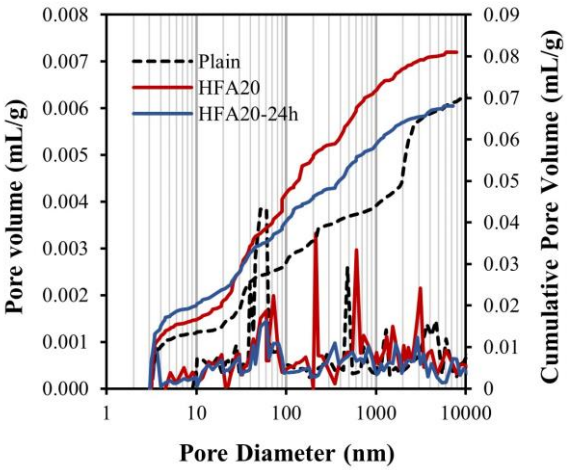

Figure 5. Pore size distributions of Plain, HFA20, and HFA20-24h at 28 days

The reduction in cumulative pore volume supports a pore-filling and microstructural-modification effect associated with carbonate formation. This result provides a plausible microstructural explanation for the recovery of compressive strength in HFA20-24h. Because MIP characterizes accessible pore structure rather than reaction chemistry, the result is interpreted together with TG evidence of increased carbonate formation rather than as direct identification of a specific carbonation product [7,11].

Long-term dimensional stability showed a similarly clear influence of carbonation curing. As shown in Figure 6, all mixtures exhibited a small early expansion followed by progressive length reduction. At 180 days, Plain reached approximately -720 με. Under non-carbonated conditions, HFA10, HFA20, and HFA30 reached approximately -650, -700, and -820 με, respectively. The larger magnitude observed for HFA30 indicates that high HFA replacement did not improve long-term dimensional stability under the investigated air-curing condition.

Both 8 h and 24 h carbonation curing reduced the magnitude of long-term length change at all HFA levels, and the mitigation was most pronounced for the 24 h treatment. HFA20-24h showed the greatest reduction among the investigated mixtures. The combined MIP and length-change results suggest that carbonation-induced pore refinement can reduce

moisture-transport pathways and capillary stress development, contributing to improved dimensional stability [6,12]. The 30% replacement level again exhibited a trade-off. Although HFA30 produced the highest CO_2 uptake, the improvements in strength and length change were less complete than at lower replacement levels. Thus, increasing carbonatable material beyond the level required for effective matrix formation does not necessarily improve overall performance. The HFA20-24h condition is therefore distinguished by simultaneous strength recovery, reduced pore volume, and improved dimensional stability rather than by maximum CO_2 uptake alone.

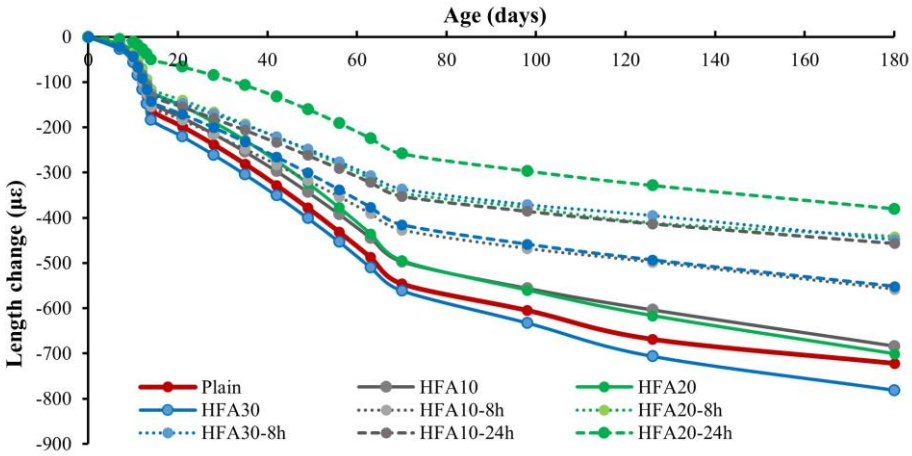

Figure 6. Length change of HFA-blended mortars up to 180 days

3.5 Implications for carbon-neutral concrete products

The present results indicate that short-duration carbonation curing can be used as a processing strategy for HFA-blended cementitious materials when CO_2 utilization and engineering performance are considered together. The 8 and 24 h curing periods were selected to represent time-constrained production scenarios rather than prolonged laboratory carbonation. Under these conditions, 24 h carbonation allowed HFA replacement up to 20% while maintaining 28-day compressive strength comparable to Plain and reducing long-term length change.

From a carbon-utilization perspective, HFA30-24h achieved the highest net CO_2 uptake, but its lower mechanical recovery and less favorable dimensional response illustrate an important design principle: maximum CO_2 uptake should not be used as the sole optimization criterion. For precast-type products, a mixture must satisfy both carbon and performance requirements. Within the present experimental range, HFA20-24h provided the most balanced response and therefore represents the most promising condition for further pilot-scale validation.

4 Conclusions

This study evaluated 10-30% HFA replacement combined with 8 or 24 h early carbonation curing in 20% CO_2. The following conclusions were obtained:

1. Carbonation depth increased with both HFA replacement and carbonation duration, while TG-derived CO_2 uptake increased with curing duration and generally increased with HFA replacement. The highest net uptake was 9.66% for HFA30-24h.

2. Without carbonation, compressive strength decreased as HFA replacement increased. After 24 h carbonation, HFA10 and HFA20 reached 28-day strengths of 33.6 and 33.3 MPa, comparable to Plain (32.6 MPa), whereas HFA30 remained lower at 30.7 MPa.

3. MIP showed that the cumulative pore volume of HFA20 decreased from approximately 0.081 to 0.068 mL/g after 24 h carbonation, supporting carbonation-induced pore refinement.

4. Early carbonation curing reduced long-term length change at all HFA levels, with the most favorable dimensional response observed for HFA20-24h.

5. Maximum CO_2 uptake did not coincide with the best engineering performance. Considering CO_2 utilization, strength, pore structure, and dimensional stability together, 20% HFA with 24 h carbonation curing provided the most favorable overall balance within the investigated conditions.

References

[1] K.L. Scrivener, V.M. John, E.M. Gartner, Eco-efficient cements: Potential economically viable solutions for a low-CO_2 cement-based materials industry, Cem. Concr. Res. 114 (2018) 2-26.

[2] T. Hemalatha, A. Ramaswamy, A review on fly ash characteristics - Towards promoting high volume utilization in developing sustainable concrete, J. Clean. Prod. 147 (2017) 546-559.

[3] G. Deng et al., Pozzolanic reactivity of carbonated high-calcium fly ash: A mechanism study, Constr. Build. Mater. 446 (2024) 138015.

[4] D. Zhang, X. Cai, Y. Shao, Carbonation curing of precast fly ash concrete, J. Mater. Civ. Eng. 28 (2016) 1-9.

[5] C. Liang et al., Effects of early-age carbonation curing on the properties of cement-based materials: A review, J. Build. Eng. 84 (2024) 108495.

[6] X. Xian, C. Logan, Y. Shao, Dimensional stability of cement paste and concrete subject to early-age carbonation curing, Mater. Struct. 55 (2022).

[7] V. Rostami, Y. Shao, A.J. Boyd, Z. He, Microstructure of cement paste subject to early carbonation curing, Cem. Concr. Res. 42 (2012) 186-193.

[8] J. Chen, L. Tang, J. Yi, K. Wu, J. Zhang, Progress analysis and prospect on the influence of early-age carbonation curing on properties of cement-based materials, Processes 14 (2025) 97.

[9] G.B. Belayneh et al., Effect of fly ash on hydration and carbonation of carbonation-cured Portland cements, J. CO_2 Util. 88 (2024) 102943.

[10] H. Justnes, J. Skocek, T.A. Chen, C.J. Engelsen, O. Skjølsvold, Microstructural changes of hydrated cement blended with fly ash upon carbonation, Cem. Concr. Res. 137 (2020) 106192.

[11] W. Ashraf, Carbonation of cement-based materials: Challenges and opportunities, Constr. Build. Mater. 120 (2016) 558-570.

[12] H. Sun, Y. Hou, X. Sun, S. He, J. Qian, CO_2 curing for improved strength and volume stability of cementitious materials containing high SO_3 CFBC fly ash, J. Build. Eng. 113 (2025) 114154.

Effect of adding blast furnace slag to alkali activated cement made from Hokkaido volcanic glass powder on the properties
北海道産火山ガラス微粉末を用いたアルカリ活性セメントの高炉スラグ添加による基礎性状への影響

Kaishi Kojima※1, Jihoon Kim※2, Madoka Taniguchi※3 and Yukio Hama※3
小島　海志, 金　志訓, 谷口　円, 濱　幸雄

概要

地域天然資源の有効活用および環境負荷低減効果に期待し、火山ガラス微粉末はコンクリート用混和材として 2020 年に JIS A 6209 に制定された。しかし、セメント混和材としての利用が主であり、アルカリ活性セメントとしての利用検討はほとんど行われていない。そこで、本研究では、北海道産火山灰を原料とした火山ガラス微粉末を主結合材とした AAC に CaO 供給による反応性や強度増進を期待して BFS を置換した場合の基礎性状への影響を物理的性質および化学分析より評価した。その結果、フレッシュ性状では、BFS 置換率増加に伴い流動性の向上が確認された。さらに、初期の反応性が向上したため、反応生成物量の増加による細孔の緻密化、圧縮強度向上といった影響を確認した。また、VGP 単味では、高温養生による反応促進を行ったにも関わらず、反応硬化しなかったことから VGP の反応速度は極めて遅く、単味使用するためにはアルカリ濃度や養生温度といった様々な項目での対検討が必要であると考えられる。

1. Introduction

In recent years, concrete structures have become the predominant choice for building construction because of their excellent constructability and durability. However, the production of ordinary Portland cement (OPC), the primary binder used in concrete, generates a large amount of CO_2[1] during the manufacturing process. Cement production is estimated to account for approximately 8 %[1] of global CO_2 emissions. Therefore, reducing cement consumption has become an important issue from the perspective of global carbon neutrality. To address this issue, the utilization and research of AAC, which uses industrial by-products such as blast furnace slag (BFS) and fly ash (FA) and hardens through reaction with alkaline activators without the use of OPC, have been actively promoted.

AAC is a cementitious material produced by the geopolymerization of aluminosilicate binders such as BFS, FA, and MK activated by alkaline activators. AAC has been reported to reduce CO_2 emissions by approximately 80%[2] while exhibiting superior strength development, fire resistance, and acid resistance compared with OPC concrete[3),4)].

AAC differs from OPC in its chemical composition because it incorporates BFS and FA. Furthermore, the external supply of Na and Si by alkaline activators leads to the formation of reaction products different from those of OPC[5)–7)]. Since the reaction products formed in AAC are determined by the materials used, its strength characteristics and physical properties also differ. Therefore, comprehensive investigations are required.

On the other hand, although Japan is one of the world's leading volcanic countries, the utilization of volcanic resources remains limited, and their effective utilization as underutilized resources is required. In recent years, studies on their application as supplementary cementitious materials have accelerated, and high-purity volcanic glass can be stably concentrated by dry gravity classification. The concentrated volcanic glass can be ground and used as a supplementary cementitious material, exhibiting compressive strength and durability[8),9)] comparable to those of OPC concrete depending on its fineness and replacement ratio. As a result, volcanic glass powder (VGP), which is manufactured from volcanic ejecta through concentration, classification, and pulverization, was

※1　Graduate Student, Division of Sustainable and Environmental Engineering, Muroran Institute of Technology, Japan
※2　Associate Professor, College of Design and Manufacturing Technology, Muroran Institute of Technology, Japan
※3　Professor, College of Design and Manufacturing Technology, Muroran Institute of Technology, Japan

standardized as JIS A 6209 in 2020. However, previous studies have mainly focused on VGP manufactured from the Ito-Shirasu pyroclastic deposits in southern Kyushu. Volcanic deposits are widely distributed throughout Japan, and abundant deposits are also known to exist in Hokkaido. Tomoyose et al.[10] and Daikokuya et al.[11] demonstrated the applicability of VGP manufactured from Hokkaido volcanic ash as a supplementary cementitious material for concrete. However, despite exhibiting performance comparable to that of VGP manufactured from Ito-Shirasu, VGP manufactured from Hokkaido volcanic ash has been investigated in only a limited number of studies, and further studies are needed.

Previous studies have demonstrated the applicability of VGP as a supplementary cementitious material for concrete. Although VGP is estimated to reduce CO_2 emissions by approximately 20% compared with OPC[12], its application to AAC, which is expected to achieve greater environmental impact, is required. However, although studies[13] on AAC incorporating volcanic deposits such as volcanic ash have been conducted both in Japan and overseas, only a limited number of studies[14),15] have investigated the use of VGP manufactured from volcanic deposits in accordance with JIS. Therefore, further studies on the application of VGP to AAC are needed to accumulate data for the effective utilization of Hokkaido-produced VGP and to contribute to a decarbonized society.

Therefore, this study investigates the fundamental properties of AAC using VGP manufactured from Hokkaido volcanic ash as the primary binder and BFS as a CaO source, with BFS expected to contribute to the reactivity and strength development. In addition, microstructural analyses were conducted to investigate the microstructure of the reaction products in VGP-based AAC and to evaluate its effects on the fundamental properties.

2. Experimental Overview

2.1 Experimental design

In this study, VGP was manufactured by classifying and grinding volcanic deposits collected from Mt. Tokachi (Kamui, Asahikawa) and Rubeshibe (Kitami). The glass content of the Mt. Tokachi volcanic ash was 63.4 % for the raw material, 85.0 % for the particle size fraction smaller than 0.15 mm, and 70.4 % for the 0.15 to 0.3 mm fraction. The corresponding values for the Rubeshibe volcanic ash were 94.8 % for raw material, 91.0 % for the particle size fraction smaller than 0.15 mm, and 97.5 % for the 0.15 to 0.3 mm fraction. The raw material, with a moisture content of less than 1 % and passing a 4.75 mm test sieve, was separated into five fractions using an air table based mainly on density and particle size. The fine fraction recovered by a cyclone was then ground using a roller mill, and the resulting powder (VGR: Volcanic Glass Roller mill) was used in this study. Table 1 shows the physical properties and chemical compositions of the VGR and BFS used in this study.

Table 2 shows the experimental plan. In this study, six samples were prepared: two samples using 100% VGR from each source as the binder, and four samples in which 20 % or 40 % of the VGR was replaced with BFS to provide CaO and thereby improve the reactivity and compressive strength. Mortar and paste specimens were prepared using an alkali activator obtained by mixing a 10 mol/L sodium hydroxide solution with a two-fold diluted sodium silicate solution at a mass ratio of 2:1 to achieve a Na_2O/B ratio of 0.1. The water-binder ratio (W/B), including the water contained in the alkaline activator, was fixed at 0.5, and the binder-sand ratio (B:S) was fixed at 1:2. Because the setting time is generally shortened when BFS is used in AAC, a high-range air-entraining water-reducing admixture (polycarboxylate ether-based, SP-8SV (SP)) was added to improve the setting time[16]. The paste specimens were hand-mixed for 3 min, placed in molds, cured at 80°C and 98 % RH for 24 h, and then demolded. After demolding, the specimens were subjected to sealed curing at 20°C until each measurement. The specimens were then prepared in the required shape and measured. In addition, preliminary tests confirmed no significant differences in the measured properties of the paste specimens between the two sources. Therefore, only the Mt. Tokachi VGP, which exhibited higher compressive strength, was used for the paste measurements. For the mortar specimens, the binder and fine aggregate were mixed in a mortar mixer at low speed for 30 s. The

Table 1 Physical properties and Chemical composition of BFS and VGR

Type	Density (g/cm^3)	Surface area (cm^3/g)	Chemical composition (%)							Moisture (%)	Ig. Loss
			SiO_2	Al_2O_3	MgO	CaO	Na_2O	Fe_2O_3	K_2O		
VGR_T	2.39	82300	73.0	13.7	0.30	0.76	3.30	1.28	4.11	0.9	3.29
VGR_R	2.33	93900	72.9	12.7	0.26	0.76	3.05	1.40	4.28	1.4	4.49
BFS	2.91	3930	34.03	14.36	6.51	43.36	0.18	0.83	0.31	-	0.2

Table 2 Experimental plan

Sample	Binder (wt %)		W/B	Pre curing	Measurement	
	VGR※	BFS			Mortar	Past
VGR_T_60	60	40	0.5	Heat curing at 80°C 98 % RH for 24 h →Sealed curing at 20°C (for each measurement age)	Mortar flow test Compressive strength test	Mercury Intrusion Porosimetry (MIP) TG-DTA ^{29}Si MAS NMR
VGR_T_80	80	20				
VGR_T_100	100	0				
VGR_R_60	60	40				
VGR_R_80	80	20				
VGR_R_100	100	0				

※VGP from Mt. Tokachi, Asahikawa (VGR_T), and Rubeshibe, Kitami (VGR_R).

alkaline activator was then added, followed by mixing for 60 s, scraping for 30 s, and further mixing at high speed for 120 s. After mixing, the mortar specimens were subjected to the same curing procedure as the paste specimens. The mortar specimens were measured at ages of 3, 7, 28, and 91 days, whereas the paste specimens were measured at ages of 3, 28, and 91 days.

2.2 Measurement

(1) Mortar flow test

The mortar flow test was performed in accordance with JIS R 5201 "Physical testing method for cement".

(2) Compressive strength test

The compressive strength test was performed in accordance with JIS A 1108, "Method of Test for Compressive Strength of Concrete" using cylindrical test specimens of φ50mm×100mm. Measurements were taken three times at each sample, and the average of those measurements was used as the result.

(3) Mercury Intrusion Porosimetry (MIP)

In the MIP, the specimens formed into 5mm cubes were used for the measurements. Hydration was stopped by 24 h acetone displacement, followed by 24 h vacuum freeze-drying, after which the specimens were used for measurement.

(4) TG-DTA

The HITACHI STA7200 was used for TG-DTA. The samples were heated from 20°C to 1000°C at a heating rate of 20°C/min, held at 1000°C for 5 min, and then allowed to cool naturally to room temperature. The samples used for TG–DTA were prepared by crushing the specimens used for MIP. The weight of the sample was 20 ± 2 mg, and all measurements were performed under a nitrogen atmosphere.

(5) ^{29}Si MAS NMR

A JEOL ECA-500 (11.75T) was used with a 3.2 mm φ probe was used for ^{29}Si MAS NMR. The measurement conditions for ^{29}Si MAS NMR were a spinning speed of 10 kHz, relaxation delay of 15 s, scans of 2048. The specimens used for the measurements were prepared by crushing the samples used for MIP, followed by acetone replacement for 24 h to stop hydration and then drying.

3. Results

3.1 Mortar flow test

Fig. 1 shows the mortar flow test results after 15 drops. Regardless of the VGR source, the flow value tended to increase with increasing BFS replacement ratio. The relative decrease in the specific surface area of the binder with increasing BFS replacement ratio likely resulted in improved fluidity. Furthermore, the flow values were comparable to those reported for BFS-based AAC[16], suggesting that the VGP used in this study had little influence on fluidity.

3.2 Compressive strength test

Fig. 2 shows the changes in compressive strength with age. VGR_T and R_100, without BFS, did not harden sufficiently even after 91 days despite heat curing,

preventing demolding and compressive strength measurement. A previous study[17] also reported that when volcanic glass powder was used alone, air curing after heat curing did not result in sufficient hardening, and no strength development was observed.

Compressive strength showed little change with age for all samples. This is likely because pre-curing by heat curing accelerated the binder reaction, resulting in relatively high early-age strength. In addition, sealed curing without additional moisture limited further hydration.

Furthermore, regardless of the VGR source, compressive strength increased with increasing BFS replacement ratio. As C-A-S-H is the primary reaction product in BFS-based AAC, this increase is attributed to the greater formation of C-A-S-H with a dense microstructure. Wang et al.[15] also reported that compressive strength decreased with increasing VGP content because of the formation of low-Ca gels.

3.3 Mercury Intrusion Porosimetry (MIP)

Fig. 3 and 4 show the MIP measurements for VGR_T_60 and VGR_T_80. As in the compressive strength test, the VGR100% specimens could not be measured because of insufficient hardening.

For the 60% BFS replacement specimens, pores were mainly distributed around 20 nm and became slightly finer with age. In contrast, the 80 % BFS replacement specimens showed pore size distribution peaks at 37 and 124.4 nm at 3 days, followed by pore coarsening with age. However, pore volume decreased, resulting in a lower cumulative pore volume. A reduction in pore volume with age was observed at both BFS replacement samples.

In addition, increasing the BFS replacement ratio produced finer pores and lower pore volume. The coarser pore structure of VGR_T_80 likely caused its lower compressive strength. Previous studies[18] have reported that pore structure densifies with increasing BFS replacement ratio because of differences in the reaction products.

3.4 TG-DTA

In this study, based on a previous study[6], C-A-S-H and N-A-S-H, the main reaction products of AAC, were assumed to decompose within the temperature range of 100–200°C. The weight loss within this temperature range was measured as the amount of AAC reaction products. Fig. 5 shows the amount of AAC reaction products determined by TG-DTA.

First, no significant difference in the amount of reaction products was observed between VGR_T_60 and VGR_T_80. However, VGR_T_100 produced only about half the amount of reaction products of the other samples, indicating that VGR alone reacted slowly even under heat curing. Consequently, the specimens did not harden sufficiently. The amount of reaction products increased with increasing BFS replacement ratio, consistent with Rashad et al.[13], whereas Wang et al.[15] reported the opposite trend. Furthermore, no increase in the amount of reaction products was observed with age. This is likely because the initial heat curing rapidly promoted the reaction, consuming most of the reactive binder, particularly BFS.

3.5 ^{29}Si MAS NMR

Fig. 6-8 shows the changes in the ^{29}Si MAS NMR spectra of each specimen with age. In AAC, the ^{29}Si MAS NMR peaks overlap, making it difficult to completely separate each peak by deconvolution. Therefore, in this study, based on previous studies[7], the spectra were analyzed within fixed chemical shift

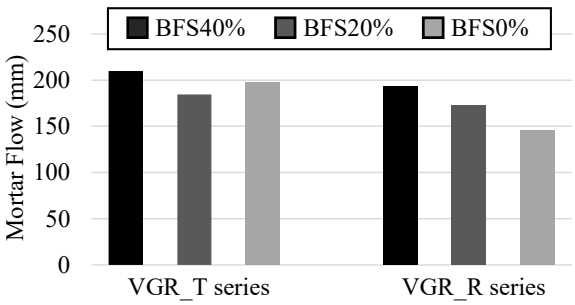

Fig. 1 Mortar flow test results

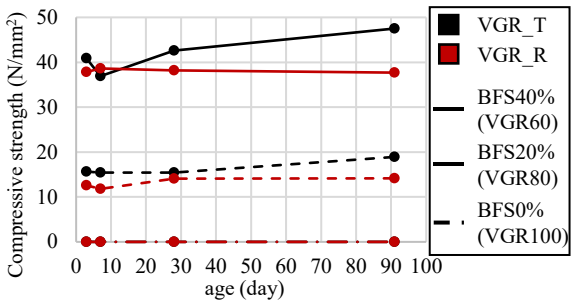

Fig. 2 Compressive strength development with age

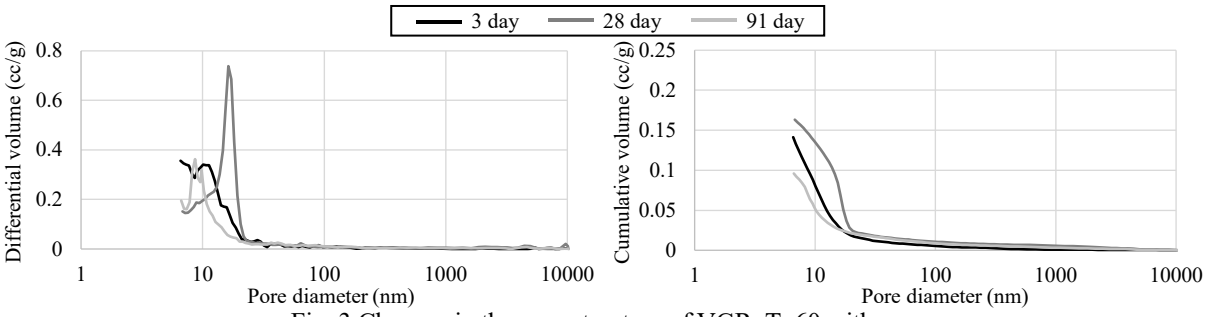

Fig. 3 Changes in the pore structure of VGR_T_60 with age

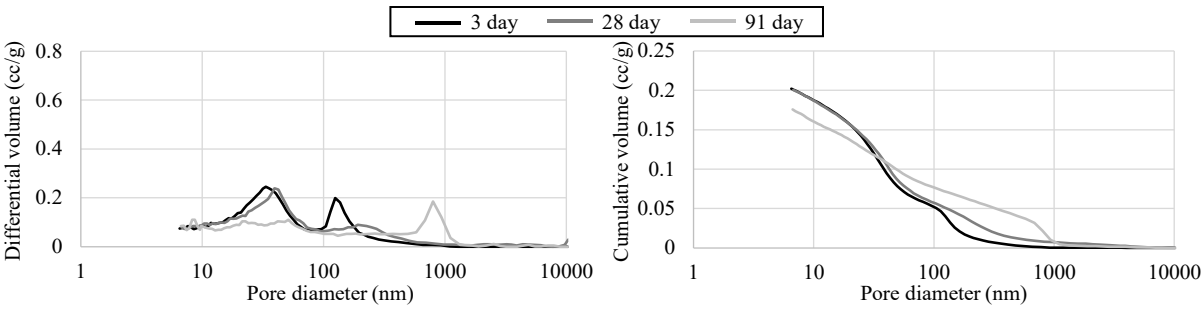

Fig. 4 Changes in the pore structure of VGR_T_80 with age

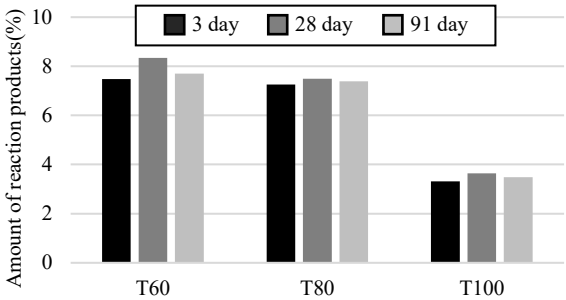

Fig. 5 Amount of reaction products by TG-DTA

ranges of Q^0, -66 to -78 ppm; Q^1, -78 ppm; Q^2, -80 to -89 ppm; Q^3, -89 to -100 ppm; and Q^4, -100 to -116 ppm.

Different peak distributions were observed depending on the BFS replacement ratio. At the 100% VGR sample, a broad Q^3 and Q^4 peak centered at -106 ppm was observed, whereas at the 60% VGR sample, a broad Q^2 peak centered at -84 ppm was observed. As the BFS replacement ratio increased, the lower-polymerized Q^2 and Q^3 peaks increased. In addition, the peak detected at -106 ppm for VGR_T_100 was located at the same chemical shift as that of unreacted VGR_T. The predominance of the Q^3 and Q^4 peaks suggests that N-A-S-H was mainly formed in specimens with a higher VGR contents. Since VGR has a chemical composition similar to that of FA, the formation of C-A-S-H, which has a CaO-based layered structure, is considered to have been limited. Furthermore, with age, the Q^3 and Q^4 peaks decreased slightly, while the Q^2 peak increased.

4. Conclusion

1) However, it remained comparable to that of conventional AAC, suggesting that VGP has little influence on fluidity.
2) As expected, replacing VGP with BFS improved the reactivity and compressive strength. Furthermore, increasing the BFS replacement ratio accelerated the initial reaction, increased the reaction product amount, densified the pore structure, and improved the compressive strength.
3) At later ages, little change was observed in compressive strength and the reaction product amount compared with the early-age values. This suggests that BFS reacted rapidly at an early age, contributing to compressive strength through the formation of reaction products. However, as measurements were conducted only up to 91 days, the slow reaction of VGP may not yet have progressed sufficiently, requiring further investigation.
4) The results suggest that the slow reaction of VGP limits its contribution to reaction product formation when used as the primary binder in AAC. In particular, specimens prepared with only VGP remained unhardened after 91 days. Therefore, further studies on materials and curing

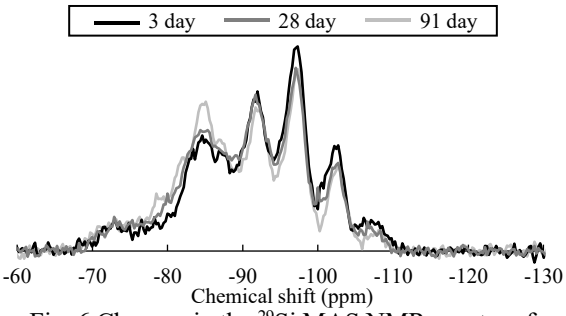

Fig. 6 Changes in the ^{29}Si MAS NMR spectra of VGR_T_60 with age

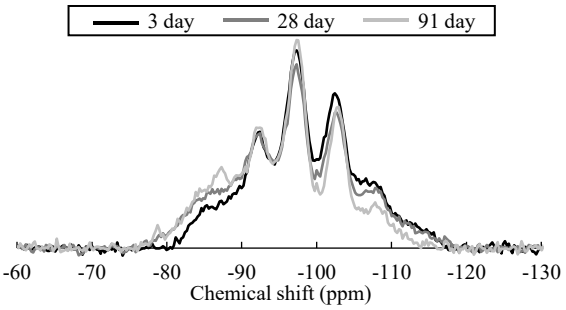

Fig. 7 Changes in the ^{29}Si MAS NMR spectra of VGR_T_80 with age

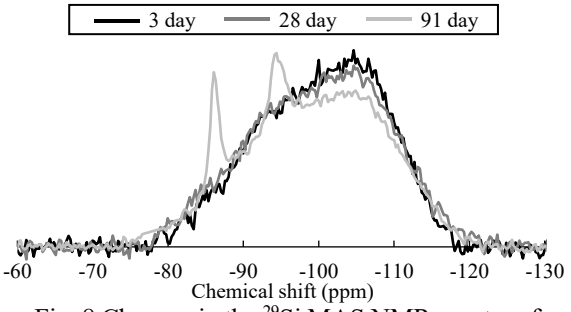

Fig. 8 Changes in the ^{29}Si MAS NMR spectra of VGR_T_100 with age

methods are required for its application in AAC.

Acknowledgments

The authors gratefully acknowledge the support of JST SPRING, Grant Number JPMJSP2153.

References

1) R. M. Andrew: Global CO_2 emissions from cement production, 1928-2018, Earth Syst. Sci. Data, 11, pp.1675-1710 (2019)
2) J. Davidovits: False values on CO_2 emission for geopolymer cement/concrete published in scientific papers, Geopolymer Institute Library, Technical paper #24 (2015)
3) Z. Li et al.: A comparative study on the mechanical properties, autogenous shrinkage and cracking proneness of alkali-activated concrete and ordinary Portland cement concrete, Construction and Building Materials, 292 (2021)
4) A. Wang et al.: The durability of alkali-activated materials in comparison with ordinary Portland cements and concretes: A review, Engineering, 6, pp.695-706 (2020)
5) A. Palomo et al.: A review on alkaline activation: new analytical perspectives, Materiales de Construccion, Vol.64, No.315 (2014)
6) N. K. Lee et al.: Reactivity and reaction products of alkali-activated, fly ash/slag paste, Construction and Building Materials, 81, pp.303-312 (2015)
7) X. Gao et al.: Apply ^{29}Si, ^{27}Al MAS NMR and selective dissolution in identifying the reaction degree of alkali activated slag-fly ash composites, Ceramics International, 43 (2017)
8) A. Tomoyose et al.: Fundamental study about volcanic glass classified from Ito-shirasu by gravity classification, Proceedings of the Japan Concrete Institute, Vol.39, No.1, pp.151-156 (2017) (in Japanese)
9) A. Tomoyose et al.: Concrete with high-purity volcanic glass fine powder manufactured from pyroclastic deposit, SN Applied Sciences, 2, 851 (2020)
10) A. Tomoyose et al.: Fundamental study on volcanic glass powder produced from Hokkaido volcanic ash, Proceedings of the Japan Concrete Institute, Vol.43, No.1, pp.143-148 (2021) (in Japanese)
11) Y. Daikokuya et al.: Effects of Hokkaido volcanic glass powder on concrete durability, hydtarion, and pozzolanic reaction of concrete, Proceedings of the Japan Concrete Institute, Vol.44, No.1, pp.160-165 (2022) (in Japanese)
12) A. Tomoyose et al.: Study on environmental impact reduction through the use volcanic glass powder, Proceedings of the Japan Concrete Institute, Vol.42, No.1, pp.137-142 (2020) (in Japanese)
13) A. M. Rashad et al.: Egyptian volcanic glass powder as a modifier agent for alkali-activated slag cement, Construction and Building Materials, 408 (2023)
14) Y. Osako et al.: Influence of curing methods on the performance of alkali-activated materials incorporating volcanic glass powder as the primary precursor, Journal of Advanced Concrete Technology, Vol.23, pp385-394 (2025)
15) W. Wang et al.: Influence of volcanic glass powder on alkali-silica reaction expansion in alkali-activated slag mortars, Cement and Concrete Composites, 152, (2024)
16) J. G. Jang et al.: Fresh and hardened properties of alkali-activated fly ash/slag pastes with superplasticizers, Construction and Building Materials, 50, pp.169-176 (2014)
17) Y. Osako et al.: Basic study on alkali-activated materials using volcanic glass powder, Proceedings of the Japan Concrete Institute, Vol.45, No.1, pp.970-975 (2023) (in Japanese)
18) S. Chen et al.: Pore structure of geopolymer materials and its correlations to engineering properties: A review, Construction and Building Materials, 328 (2022)

廃ヒトデを混入したセメントペーストの物理的特性

Physical Properties of Cement Paste Mixed with Waste Starfish

蔡炅俊※1、金智訓※1、鄭渶錫※1、兪在勻※2、李相洙※3

Kyoung-Jun Chae, Ji-Hun Kim, Yeong-Seok Jung, Jae-Gyun Yoo, Sang-Soo Lee

ABSTRACT

To mitigate the structural damage to concrete structures and environmental damage caused by deicing agents, it is necessary to utilize an eco-friendly material capable of adsorbing chloride ions. In this study, the physical properties of a cement paste mixed with waste starfish that has chloride ion adsorption capacity were evaluated by conducting the effect of steel corrosion test and the freeze–thaw test, with the aim of securing preliminary basic data for the development of permeable blocks with deicing damage mitigation performance. The tests were conducted in accordance with the deicing agent performance evaluation method proposed by the Ministry of Environment. The experimental results showed that, regardless of particle size, the relative corrosion rate and the relative mass loss rate tended to decrease as the mixing ratio increased, and both tests satisfied the preliminary research and development targets (a relative corrosion rate of 40% or less and a relative mass loss rate of 60% or less).

1. Introduction

Deicing agents are used to ensure road safety during winter, and approximately 80%–90% of the deicing agents used domestically consist of calcium chloride ($CaCl^2$) and sodium chloride (NaCl) [1]. However, chloride ions (Cl^-) contained in these deicing agents accelerate the deterioration of concrete through freeze–thaw action, leading to damage to buildings and roads. They also promote corrosion of steel, adversely affecting reinforcing bars within structures as well as vehicles. In addition, they increase osmotic pressure, disrupt nutrient balance, and infiltrate groundwater, thereby causing pollution of vegetation, soil, and water quality [2].

To address these issues, studies and patents have been developed on eco–friendly deicing agents containing corrosion inhibitors or porous spicules extracted from waste starfish. However, such alternatives are approximately two to three times more expensive than conventional deicing agents, and due to the large quantities required for deicing operations, their widespread application is limited under constrained budgets and resources. Therefore, additional research is required to reduce structural and environmental damage through alternative approaches that do not rely on modifying the composition of deicing agents.

Accordingly, this study aims to evaluate the physical properties of a cement paste mixed with waste starfish spicules capable of adsorbing chloride ions. By conducting this preliminary study for the development of permeable blocks mixed with waste starfish spicules with deicing damage mitigation performance, this study seeks to reduction of structural and environmental damage caused by chloride ions from deicing agents.

※1 大韓民国 国立 Hanbat 大学校 建設環境デザイン大学 建築工学科，修士課程
※2 大韓民国 国立 Hanbat 大学校 建設環境デザイン大学 建築工学科，博士課程
※3 大韓民国 国立 Hanbat 大学校 建設環境デザイン大学 建築工学科，教授 博士(工学)

2. Experimental overview

2.1 Experimental plan

In this study, the physical properties of cement paste mixed with waste starfish were evaluated. Ordinary portland cement was used as the binder, and the water–to–cement ratio was set at 37% to secure castable flowability. Waste starfish with chloride ion adsorption capacity were used as an admixture, and the particle size was classified into less than 0.6 mm and greater than or equal to 0.6 mm through a sieve analysis. The mixing ratios were set at 0, 5, 10, 15, and 20 (%), and water curing was conducted at a temperature of 20 ± 2℃. A freeze–thaw test and effect of steel corrosion test were set as experimental items to evaluate the physical properties. The freeze–thaw test was examined by relative loss rate in accordance with EM502-2 (Performance Evaluation of Deicing Agents–Concrete Freeze–Thaw Test Method) [3]. Effect of steel corrosion test was conducted by stirring the specimens in accordance with EM502-1 (Performance Evaluation of Deicing Agents – Steel Corrosion Effect Test Method) and then examined by relative corrosivity [4]. In addition, to satisfy the environmental labeling certification criteria established by the Ministry of Environment (Republic of Korea), which require a relative corrosion rate of 30% or less and a relative mass loss rate of 50% or less, the preliminary research and development targets were also set at a relative corrosion rate of 40% or less and a relative mass loss rate of 60% or less, and compliance with these targets was evaluated. The experimental factors and levels are summarized in Table 1. The mix proportions are summarized in Table 2.

Table 1 Experimental factors and levels

Experimental factor	Experimental level	Remarks
Binder conditions	OPC[1)]	1
Water/Cement (%)	37	1
Admixture	Waste starfish	1
Particle size of admixture (mm)	<0.6, 0.6≤	2
Mixing ratio of admixture (wt%[2)])	0, 5, 10, 15, 20	5
Curing condition	Water curing (Temperature: 20±2℃)	1
Experiment items	Effect of steel corrosion, Freeze–thaw	2

1) OPC : Ordinary portland cement
2) wt% : Weight percent

2.2 Waste starfish

In this study, the spicules of waste starfish were obtained through a pretreatment process to remove proteins from waste starfish, and the procedure was carried out in accordance with the pretreatment method described in Korean Registered Patent No. 10–1903171 (Eco–Friendly Snow Removal Agent Composition Comprising Porous Structure From Starfish) [5]. First, the starfish were washed to remove surface salts and foreign substances, and then immersed in a water bath with distilled water added. The temperature of the bath was maintained at 50℃, and a pretreatment solution was introduced and stirred for 5 minutes. The mixture was then left undisturbed for 3 days to allow the enzymatic reaction to proceed. After 3 days, the floating materials on the surface were removed, and repeated washing with distilled water was performed until only pale yellow solids remained. Finally, the recovered pale yellow solids were dried in an oven at 50℃ for more than 24 hours to obtain a starfish–derived porous structure in the form of a pale yellow powder.

In addition, based on preliminary sieve analysis results, the highest yield was obtained at a particle size of 0.6 mm, and the quantities of particles greater than or less than 0.6 mm were distributed at generally similar levels. Accordingly, to secure balanced sample quantities between comparison groups and to clearly evaluate changes in material properties according to particle size, 0.6 mm was selected as the cutoff particle size, and the waste starfish spicules were classified into two groups, namely particles of 0.6mm or larger and particles smaller than 0.6mm.

3. Experimental results and discussion

3.1 Effect of steel corrosion

Figures 1 and 2 present the results of the effect of steel corrosion test for the cement paste mixed with waste starfish. The results show that, regardless of particle size, the relative mass loss rate tended to decrease as both the agitation time and the mixing ratio increased. In addition, for both particle size ranges (less than 0.6 mm and greater than or equal to 0.6 mm), the preliminary research and development target of a relative corrosion ratee of 40% or less was achieved at agitation times of 96 h with mixing ratios of 20% or higher, at 120 h with mixing ratios of 10% or higher, and at 144 h and 168 h with mixing ratios of 5% or higher.

These results are considered to be due to the adsorption of chloride ions by the cement paste through physical adsorption driven by electrostatic attraction arising from the porous calcium carbonate structure of the waste starfish. In addition, according to the results of the previously conducted chloride ion adsorption performance test, the adsorption capacity for chloride ions increased as the mixing ratio of waste starfish increased. Therefore, the relative corrosion rate of steel is considered to have decreased with increasing mixing ratio of waste starfish.

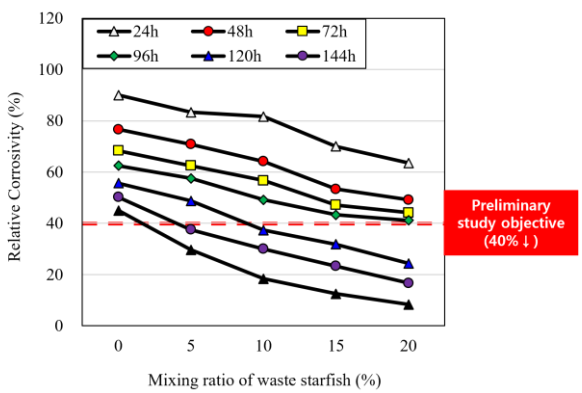

Figure 1 Effect of steel corrosion(<0.6mm)

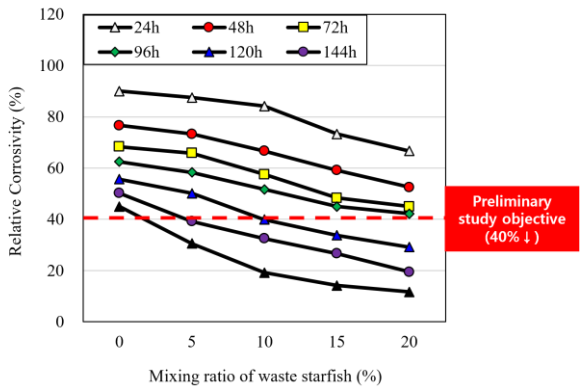

Figure 2 Effect of steel corrosion(0.6mm≤)

3.2 Freeze–thaw

Figures 3 and 4 present the results of the freeze–thaw test for the cement paste mixed with waste starfish. The results show that, regardless of particle size, the relative mass loss rate decreased as the mixing ratio increased. The cement paste mixed with waste starfish reduced the relative mass loss rate by 40.40%–95.70% compared to the reference specimen. In addition, for mixing ratios of 5% or higher, the cement paste mixed with waste starfish met the preliminary performance target of a relative mass loss rate of 60% or less, regardless of particle size.

These results are considered to be due to the same reason observed in the effect of steel corrosion test, as the waste starfish mixed into the cement paste enabled the adsorption of chloride ions through physical adsorption driven by electrostatic attraction arising from their porous calcium carbonate structure. In addition, freeze–thaw damage occurs as water within the pores of the hardened cement paste freezes, causing volumetric expansion and the accumulation of hydraulic pressure, which promotes the propagation of microcracks. It is therefore considered that the porous structure of the waste starfish alleviated the pressure generated by volumetric expansion, thereby reducing the relative mass loss rate [6].

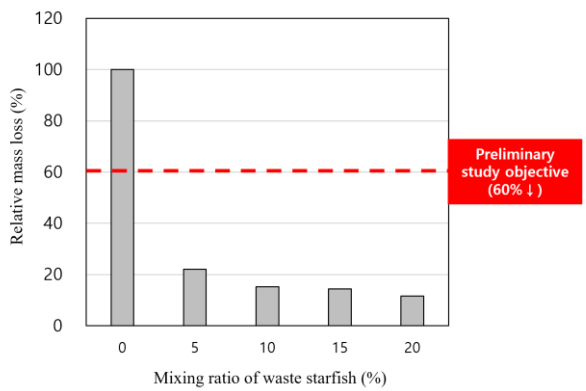

Figure 3 Freeze–thaw (<0.6mm)

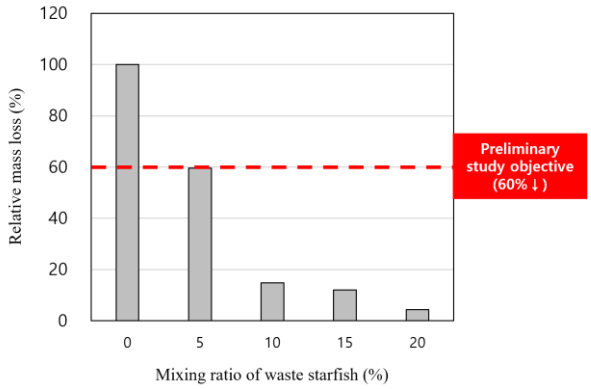

Figure 4 Freeze–thaw (0.6mm≤)

4. Conclusions

In this study, the physical properties of a cement paste mixed with waste starfish that has chloride ion adsorption capacity were evaluated as a means of mitigating the structural and environmental damage caused by chloride ions contained in deicing agents. The results of the effect of steel corrosion test showed that, regardless of particle size, the relative corrosion rate tended to decrease as both the agitation time and the mixing ratio increased. The preliminary research and development target of a relative corrosion rate of 40% or less was achieved at agitation times of 96 h with mixing ratios of 20% or higher, at 120 h with mixing ratios of 10% or higher, and at 144 h and 168 h with mixing ratios of 5% or higher. The results of the freeze–thaw test showed that, regardless of particle size, the relative mass loss rate decreased as the mixing ratio increased and was reduced by 40.40%–95.70% compared to the reference specimen. The preliminary research and development target of a relative mass loss rate of 60% or less was met at mixing ratios of 5% or higher, regardless of particle size. If future research examines flowability and strength properties and is ultimately extended to the application of permeable blocks, it is expected that a permeable block with deicing damage mitigation performance can be developed.

Reference

[1] B.D. Lee, Y.S. Kong, H.T. Kim, Performance evaluation of eco-friendly deicers and revision of deicer quality standards, in: Korea Expressway Corporation, Highway and Transportation Research Institute, 2015.

[2] S.S. Shin, S.D. Park, H.S. Kim, G.S. Lee, Effects of calcium chloride and eco-friendly deicers on plant growth, J. Korean Soc. Environ. Eng. 32(5) (2010) 487–498.

[3] EM502-2; Performance Assessment on De-icing Chemicals–Test Method for Freezing and Thawing Effect on Concrete. Ministry of Environment: Republic of Korea, 2014. Available from: https://www.mcee.go.kr/home/web/main.do

[4] EM502-1; Performance Assessment on De-icing Chemicals–Test Method of Corrosion Effect on Steel. Ministry of Environment: Republic of Korea, 2014. Available from: https://www.mcee.go.kr/home/web/main.do

[5] S.C. Yang, S.H. Kang, Eco-Friendly Snow Removal Agent Composition Comprising Porous Structure from Starfish, Korean Patent KR101903171B1 (application KR1021080008069A), Korean Intellectual Property Office (KIPO): Daejeon, Republic of Korea, 2018, p. 12. Available from: https://patents.google.com/patent/KR101903171B1/en

[6] M.T. Ley, R. Felice, J. Freeman, Assessment of Air Void System Requirements for Durable Concrete, in: National Concrete Pavement Technology Center, Iowa State University, Ames, IA, 2012. Available from: https://rosap.ntl.bts.gov/view/dot/26336

非焼成黄土を混入した環境配慮型コンクリートの超音波伝播速度と強度特性の相関分析

Correlation Analysis of Ultrasonic Pulse Velocity and Strength Characteristics of Eco-friendly Concrete Incorporating Non-sintered Hwangto

林廈峻※1、金泰亨※1、崔智恩※1、李泰圭※2
Ha-Jun Im, Tae-Hyeong Kim, Ji-Eun Choi, Tae-Gyu Lee

ABSTRACT

This study investigated the compressive strength and ultrasonic pulse velocity (UPV) of concrete incorporating nonsintered Hwangto (NSH) as a partial cement replacement and analyzed the correlation between these properties. Concrete mixtures were prepared with water-to-binder ratios of 0.41, 0.33, and 0.28, and NSH replacement ratios of 0%, 15%, 30%, and 45% to evaluate concrete over different strength ranges. Compressive strength and UPV were measured at different curing ages to examine the effects of NSH replacement and water-to-binder ratio. The results showed that compressive strength decreased as the NSH replacement ratio increased, while the 15% replacement mixtures exhibited the smallest difference from the corresponding plain concrete. UPV also decreased with increasing NSH content, although its reduction was relatively smaller than that of compressive strength. In addition, both compressive strength and UPV increased with curing age and decreasing water-to-binder ratio. Regression analysis of the experimental data showed a clear relationship between compressive strength and UPV, with an exponential function providing the most suitable representation. These results indicate that UPV can be used to evaluate the strength characteristics of concrete incorporating NSH.

1. Introduction

The construction industry has increasingly focused on reducing cement consumption because cement production is associated with substantial energy use and carbon dioxide emissions. Accordingly, various industrial by-products and natural materials have been investigated as partial cement replacements. Nonsintered Hwangto (NSH), a clay-based natural material widely available in Asia, can be used without an energy-intensive sintering process and therefore has potential as an environmentally friendly cement substitute [1-6].

However, NSH has relatively low reactivity and porous characteristics, which may adversely affect the strength development of concrete as its replacement ratio increases [7-9]. Therefore, an appropriate replacement level should be determined by evaluating the mechanical performance of NSH concrete. In addition to conventional compressive strength testing, ultrasonic pulse velocity (UPV) is widely used as a nondestructive method for assessing concrete quality because wave propagation is closely related to the internal condition and mechanical properties of concrete. Nevertheless, studies on the relationship between UPV and compressive strength in concrete incorporating NSH are still limited.

In this study, concrete mixtures with different water-to-binder ratios and NSH replacement ratios

※1 大韓民国 世明大学校 消防防災工学科 博士課程
※2 大韓民国 世明大学校 消防防災学科 教授

Table 1. Experimental plan.

Category	Details
Binder	Cement and nonsintered Hwangto
Replacement ratio	0%, 15%, 30%, and 45%
Water/binder	0.41, 0.33, and 0.28
Design of compressive strength	30, 45, and 60 MPa
Mechanical properties	Compressive strength Ultrasonic pulse velocity
Statistical analysis	Regression analysis

were evaluated in terms of compressive strength and UPV. The effects of NSH replacement on these two properties were examined, and regression analysis was performed to investigate the correlation between compressive strength and UPV. The results were used to assess the applicability of UPV for evaluating the strength characteristics of concrete incorporating NSH.

2. Experimental Procedure

2.1 Experimental plan

The experimental plan of this study is outlined in Table 1. The experimental program was designed to evaluate the compressive strength and ultrasonic pulse velocity (UPV) of concrete incorporating nonsintered Hwangto (NSH). The W/B ratios were set at 0.41, 0.33, and 0.28, corresponding to target compressive strengths of 30, 45, and 60 MPa, respectively, while NSH replaced 0%, 15%, 30%, and 45% of the cement by mass. Cylindrical specimens (Φ100 × 200 mm) were tested at 1, 3, 7, and 28 days. Compressive strength and UPV were measured in accordance with ASTM C39/C39M and ASTM C597, respectively, and their relationship was evaluated through regression analysis [10-11].

2.2 Materials

Type I ordinary Portland cement (OPC) and NSH were used as binder materials. The densities of OPC and NSH were 3,150 and 2,500 kg/m^3, respectively, with corresponding fineness values of 320 and 330 m^2/kg. NSH contained higher amounts of SiO_2 and Al_2O_3 and substantially less CaO than OPC. Crushed granite with a maximum size of 20 mm and river sand were used as coarse and fine aggregates, respectively, with densities of 2,680 and 2,540 kg/m^3.

3. Results and Discussion

3.1 Compressive strength

Figure 1 shows the compressive strength development of Plain and NSHC with different W/B ratios and NSH replacement levels. Compressive strength increased with curing age and decreasing W/B ratio, whereas higher NSH replacement generally resulted in lower strength. At 28 days, the

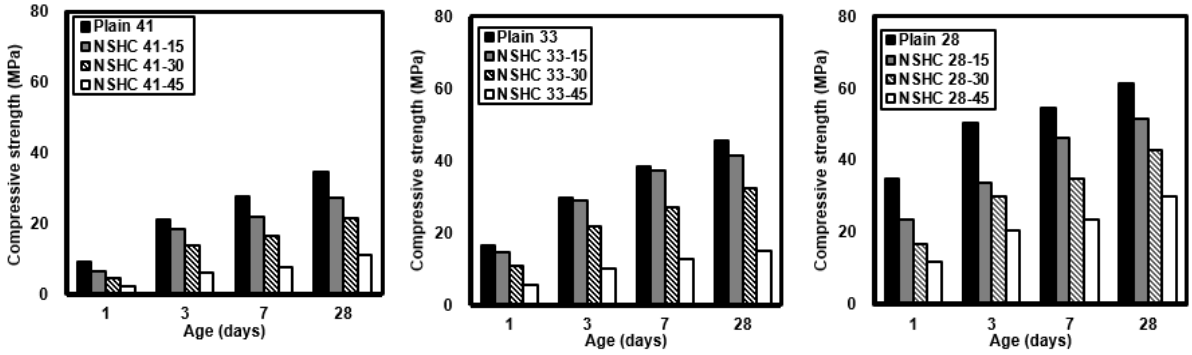

Figure 1 Compressive strength of concrete by age at various W/B

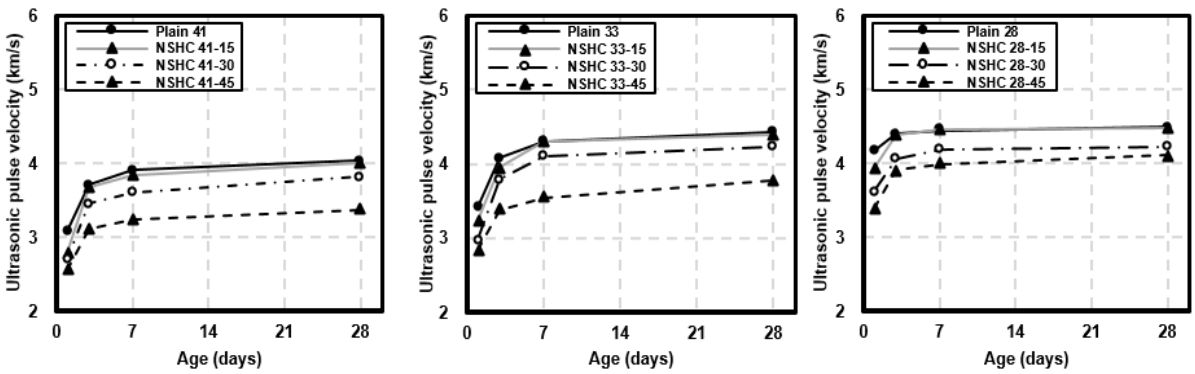

Figure 2 Comparison of UPV of concrete by age at various W/B

Plain mixtures with W/B ratios of 0.41, 0.33, and 0.28 reached 34.65, 45.60, and 61.30 MPa, respectively. At a 15% NSH replacement, the corresponding strengths were 27.44, 41.29, and 51.37 MPa, showing the smallest differences from the Plain mixtures among the NSHC series. Further increases in the NSH replacement ratio to 30% and 45% caused more pronounced reductions in compressive strength. These results indicate that excessive NSH replacement limits strength development due to the reduced cement content, while a replacement level of approximately 15% provides comparatively stable strength characteristics.

3.2 Ultrasonic pulse velocity

Figure 2 shows the ultrasonic pulse velocity (UPV) of Plain and NSHC according to curing age, W/B ratio, and NSH replacement level. UPV generally increased with curing age and decreased as the W/B ratio increased, showing a trend similar to that of compressive strength. In contrast, increasing the NSH replacement ratio resulted in lower UPV values. At 28 days, the Plain and 15% NSH mixtures exhibited UPV values above 4.0 km/s for all W/B ratios, whereas some mixtures with 30% and 45% replacement remained below this level. Although both compressive strength and UPV decreased with increasing NSH content, the reduction in UPV was relatively smaller than that observed for compressive strength. These results indicate that changes in NSH replacement and W/B ratio affect UPV in a manner generally consistent with compressive strength development, supporting the use of UPV for evaluating the strength characteristics of NSHC [12].

3.3 Regression analysis

Figure 3 shows the relationship between compressive strength and ultrasonic pulse velocity (UPV) for Plain and NSHC specimens. Compressive strength generally increased with increasing UPV regardless of the W/B ratio and NSH replacement level, indicating a clear correlation between the two properties. Regression analysis showed that an exponential function provided the most suitable

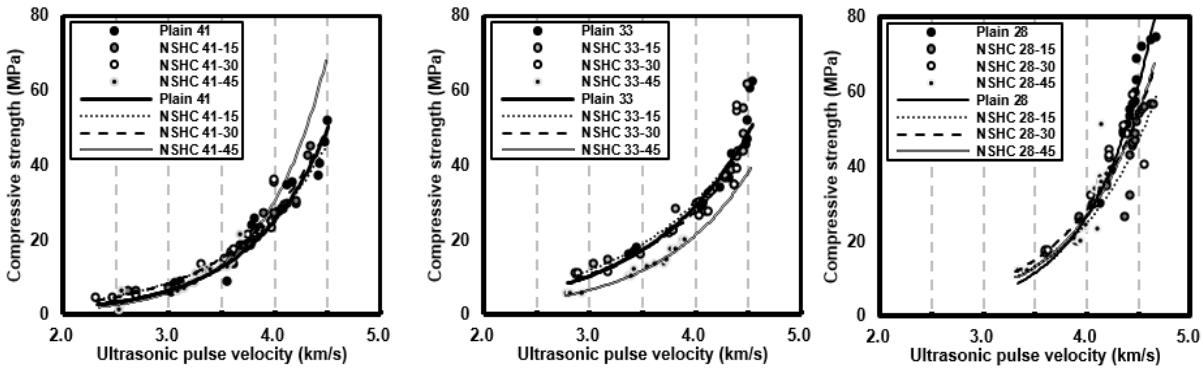

Figure 3 Predictive model through regression analysis of concrete by various W/B

representation of the experimental data. In the lower UPV range, compressive strength increased gradually with UPV, whereas a more pronounced increase in compressive strength was observed at higher UPV values. These results indicate that the relationship between UPV and compressive strength can be applied to evaluate the strength characteristics of concrete incorporating NSH, although the relationship may vary depending on the strength range and NSH replacement level.

4. Conclusions

The conclusions obtained from this study are summarized as follows:

1) Compressive strength increased with curing age and decreasing W/B ratio, whereas it decreased as the NSH replacement ratio increased. Among the NSHC mixtures, the 15% replacement level showed the smallest reduction compared with Plain concrete, while higher replacement ratios resulted in more pronounced strength reductions.

2) UPV generally increased with curing age and decreasing W/B ratio and decreased with increasing NSH replacement. This trend was similar to that observed for compressive strength, although the reduction in UPV caused by NSH replacement was relatively smaller than the reduction in compressive strength.

3) A positive relationship was observed between compressive strength and UPV regardless of the W/B ratio and NSH replacement level. Regression analysis indicated that an exponential function appropriately represented this relationship, suggesting that UPV has potential for evaluating the strength characteristics of concrete incorporating NSH.

Reference

[1] C. Y. Lee, J. H. Kim, W. G. Hyung, Properties of Non-Sintered Cement Mortar using Non-Activated Hwangto, Journal of Korea Society Waste Management, 2019, Vol. 36, No. 1, 82-87.

[2] R. Feiz, J. Ammenberg, L. Baas, M. Eklund, A. Helgstrand, R. Marshall, Improving the CO2 performance of cement, part I: utilizing life-cycle assessment and key performance indicators to assess development within the cement industry, Journal of Cleaner Production, 2015, Vol. 98, 272-281.

[3] J. G. J. Olivier, K. M. Schure, J. A. H. W. Peters, Trend in global CO2 and total greenhouse gas emission : 2017 Report, PBL Netherlands Environmental Assessment AgePlainy, 2017, No. 2674, 8-15.

[4] R. Choi, K. S. Kim, Solving Direction of the Facing Problems in Korean Cement Industry, Journal of the Korea CoPlainrete Institute, 2003, Vol. 15, No. 1, 6-9.

[5] Y. H. Kim, J. S. Im, D. H. Yoo, S. J. Lee, J. S. Bae, Y. M. Son, H. S. Jeon, D. H. Lee, Intended national determined contribution (INDC) and longterm strategy for low GHG emission of major countries under the Paris agreement, National Institute of Forest SciePlaine, 2017, No. 727, 5-19.

[6] P. K. Metha, P. M. Monteiro, CoPlainrete-Structure, Properties, and Materials, 2nd Edition, Prentice Hall, New-Jersey, 113-178.

[7] K. H. Yang, H. Z. Hwang, S. Y. Kim, J. K. Song, Development of a Cementless Mortar Using Hwangtoh Binder, Building and Environmentat, 2007, Vo. 42, No. 10, 3717-3725.

[8] S. J. Park, J. H. Kim, W. G. Hyung, Study on strength and durability of alkali activated slag mortar by replacement ratio on metakaolin, Journal of Korea Society of Waste Management, 2015, Vol. 32, No. 1, 70-77.

[9] S. S. Lee, A Study on the Fluidity Properties and Strength Properties of Non-sintered Hwangtoh mixed with PVA Fiber, Journal of the Korea Institute of Building Construction, 2010, Vol. 10, No. 3, 49-56.

[10] ASTM C39/C39M, Standard Test Method for Compressive Strength of Cylindrical CoPlainrete Specimens, American Society of Testing and Materials, 2018, pp. 1–8.

[11] ASTM C597 - 16, Standard Test Method for Pulse Velocity Through CoPlainrete, American Society of Testing and Materials, 2016, pp. 1–4.

[12 Y. Cho, H. Jung, S. Lee and H. Song, Engineering properties of Mortar according to the replacement ratio of Lime and the ratio between Non-sintered Hwangto and Sand, The Regional Association of Architectural Institute of Korea (2008) 919-924.

ACM センサによるコンクリート表面への水分作用評価に関する基礎的検討

Fundamental Research on Evaluating Wet Conditions of Concrete Surfaces Using ACM-Type Corrosion Sensor

左近柊彌※1、兼松学※1、金準鎬※1
Shuya Sakon, Manabu Kanematsu, Junho Kim

ABSTRACT

With the aim of conducting a fundamental investigation into the evaluation of moisture action on concrete surfaces, measurements were performed using an ACM (Atmospheric Corrosion Monitor) sensor, which is commonly employed for the assessment of atmospheric corrosion. First, water was sprayed onto the ACM sensor, and it was confirmed that the moisture adhesion ratio is proportional to the output current. Subsequently, various sensors were installed on a column-shaped mock-up specimen exposed outdoors, and their outputs during rainfall and snowfall events were measured. The results demonstrated that the time of wetness can be evaluated with consideration of wind direction.

1. はじめに

鉄筋コンクリート造建築物におけるコンクリートの中性化や鉄筋腐食は水分を媒介として進行することから，その進行速度はコンクリート中の水分状態に大きな影響を受ける。このことから，中性化や鉄筋腐食の進行予測を目的として，コンクリート中の水分状態を考慮に入れた研究が広く行われている。たとえば，日本建築学会の「鉄筋コンクリート造建築物の耐久設計施工指針・同解説」[1)]では中性化に関する予測式で雨がかりや外気湿度を考慮する手法が提案されている。さらに，近年では水分の有無に基づいて腐食環境を評価する設計法 [2)]が提案されており，水分環境の定量的評価手法の確立が求められている。一般環境においては，コンクリート中の水分は，外部環境から供給されコンクリート表面から内部に液水または水蒸気として浸透する。特に雨掛かりや水掛かりと呼ばれる液水の作用環境においては、コンクリート表面を濡らした液水が毛管張力を駆動力として浸透し，コンクリート内部の水分状態に大きく影響することが知られている。したがって，コンクリート表面への液水の作用，すなわち濡れの状態を精密に評価できれば，対象とする部材の耐久性や部材中の鉄筋の腐食環境の評価につながる可能性がある。

これまで，コンクリート表面に対する雨掛かりについては，石川ら [3)]，石崎ら [4)]が風向・風速を考慮したモデルを検討し，壁面の受ける雨量について，評価式を提案している。しかしながら，雨掛かりを含む液水の作用による濡れや作用後の濡れが継続する時間に基づいてコンクリートの水分状態を検討した研究は少ない。

そこで本研究では，コンクリート表面への水分の作用を評価する手法に関する基礎的検討を行うことを目的として，柱模擬試験体を用いて大気腐食評価に使用する ACM 型腐食センサ（以下，ACM センサ）を用いた測定を行った。

※1 日本国 東京理科大学大学院 建築学専攻 修士課程
※2 日本国 東京理科大学大学院 建築学科 教授 博士(工学)
※3 日本国 東京理科大学大学院 建築学科 講師 博士(工学)

2. 水分作用の評価手法

2.1 ACM センサによる評価手法

Fig. 1 に ACM センサの表面を示す。センサ部は，導体（Ag 層），絶縁体，基盤（Fe 層）で構成されており，水滴が絶縁層をまたいで Ag 層と Fe 層の間に付着すると腐食電流が発生する。Ag 層はセンサ部表面に縞状に配置されており，本研究では，この電流量を測定することでセンサ表面の濡れや濡れ時間を評価する。

2.2 ACM センサを用いた室内試験

ACM センサで測定される電流値については多くの研究がなされ，濡れ評価への有用性の出力電流について明らかにされている。しかしながら，センサ形状や測定装置の違いにより，電流値と濡れ量の関係性は異なると考えられる。本項では本研究の条件における関係性を把握することを目的として予備的実験を行った。

まず，ACM センサを恒温恒湿槽内に水平に設置し，設置後の出力電流値が 0.0006 μA 未満であることを確認したうえで蒸留水を 1 回～4 回スプレーを用いて噴霧した。あわせて，センサ表面の水滴の量を確認するため，水滴噴霧後にセンサ表面をカメラで撮影した。電流値の温度依存性を確認するため，設定温度 5, 10, 20, 40 ℃（湿度はいずれも 60 %RH）でそれぞれ実験を行った。

ここで，センサ部を覆う水滴の面積を簡易に評価するため，水滴が Ag 層の境界線上にある長さを積分し，境界線の全長（14.5 mm×30 本）に対する割合を式(1)から算出した。本稿ではこれを水分作用率 A と定義して電流の出力値との関係を検討した。

$$（水分作用率）\ A = \sum_i l_i / L \qquad (1)$$

ここで，l_i：水滴が Ag 層の境界線上をまたぐ長さ，L：Ag 層の境界線の全長。

2.3 実験結果に基づく水分の作用評価

水分作用率と ACM センサの出力電流値を初期のセンサ（Fig. 1）および 5 ヵ月間実環境にて使用し，センサ部に腐食がみられるセンサ (Fig. 2) を示す。また，初期センサにおける水分作用率と測定した電流値の関係を Fig. 3 に示す。Fig. 3 より出力電流と水分の付着量には比例関係がみられた。また，温度ごとに比較すると，5, 10, 20 ℃においてはおおむね同様の直線上に分布していると考えられるのに対し，40 ℃はほかの温度に比べ電流値が大きい結果となった。

3. 屋外暴露試験体を用いた検討

3.1 屋外曝露試験体概要

本研究で用いた試験体は 600 mm×600 mm 断面で高さ 900 mm の鉄筋コンクリート造部材である。コンクリートの調合は Table.1 に示すとおりである。打設は 2014 年 8 月に行い，千葉県野田市内

Fig.1 ACM surface at the start of the test

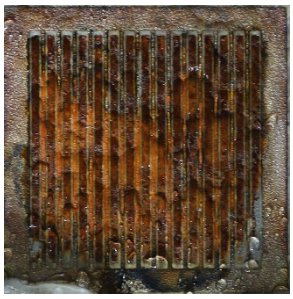

Fig.2 ACM surface after corrosion

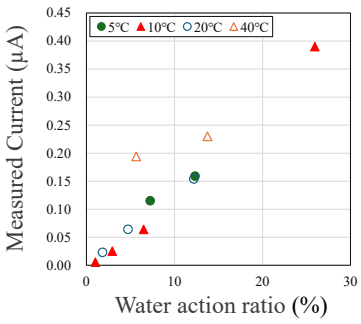

Fig.3 Relationship between Water action ratio and current

の暴露場に屋外暴露している。試験体の 4 側面は東西南北面に向くように設置しており，全面打放しである。

上記の試験体について，コンクリート表面（側面 4 面）への水分の作用およびコンクリート内部の水分状態に関する測定を行った。各種センサは，2025 年 11 月 14 日に設置・測定開始し 2026 年 4 月 20 日まで測定を行った。また，上記測定期間中の気象条件（気温，湿度，降水量，風況）も，暴露場近くに設置した通風型温湿度計等を用いて測定する。また，暴露場の相対湿度を雰囲気相対湿度と示す。

3.2　測定概要

柱模擬試験体への水分の作用を評価することを目的として，前章で用いた ACM センサおよび電流計を用いた測定を行った。ここで，降水量，降水時間が同じであっても，風速・風向が異なれば，試験体各面への水分の作用の度合い（雨のかかり方）が異なると考えられる。そこで，柱模擬試験体の側面 4 面（東西南北面）にそれぞれ ACM センサを設置し電流値を比較することとした。ACM センサは地上面から約 600 mm の高さに設置した。また，電流値の測定は 10 分間隔で行い，降水のない日中 2 日間における測定電流値が 0.0006μA 未満であったことから測定時間ごとの出力電流値が 0.0006μA を閾値として濡れを判断した。

4.　結果と考察

Fig. 4 に測定期間全体における降雨量と方位別の ACM センサの電流量について，Fig. 5 に測定期間中の 2/24 から 2/26 における降雨量と雰囲

Table.1 Concrete mix proportion

W/C	s/a	Air	Slump
55 %	45.9 %	4.7 %	18.5 cm

W	C	S1	S2	G	Ad
184 kg/m^3	335 kg/m^3	476 kg/m^3	325 kg/m^3	972 kg/m^3	2.39 kg/m^3

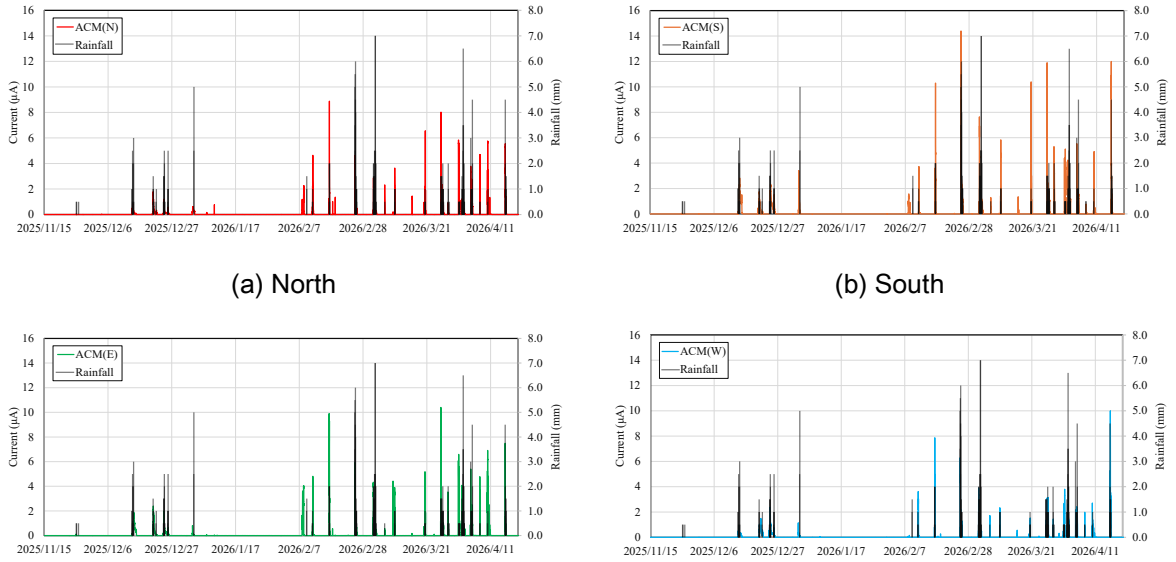

(a) North　(b) South

(c) East　(d) West

Fig.4 Relationship between ACM sensor currents on four orientations and rainfall

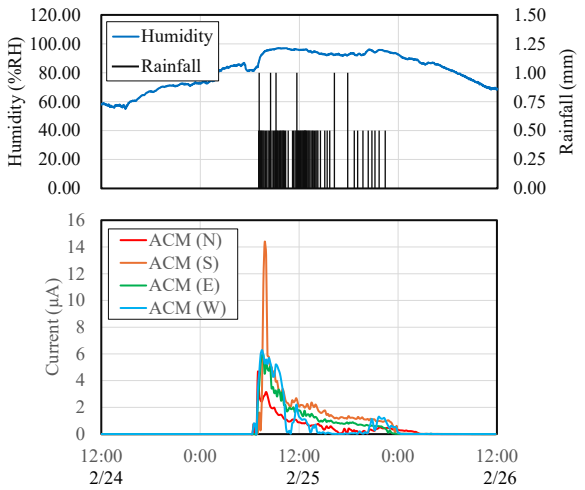

(a) Rainfall, relative humidity at the exposure site, measured current of the ACM sensor

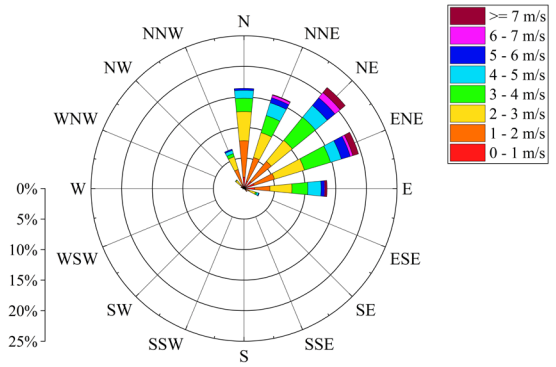

(a) WindRose

Fig.5 Measurement results during the rainfall event of Feb. 24–26

気相対湿度およびACMセンサの測定電流量と風況を示す。Fig.4より同じ降雨において測定される電流は方位で異なる。また，電流量は降雨量に相関しない。Fig.5より設置方角による出力が閾値を超えた時間について，大きな差は確認されなかった。また，閾値を超えた時間は降雨が確認されてから，大気中の相対湿度が 80 %を超えている時間で確認された。一方で電流量に着目すると風向が確認されなかった南面にてACMセンサの出力が大きくみられた。これは雨滴が降下する時，試験体側面へ吹く風の方向が影響することは石川ら[3)]の研究から明らかであるがACMセンサの出力に影響する雨滴はセンサ表面上に滞留する。そのためある一方向の試験体側面への風向頻度が小さいときその面に対する雨滴の付着量は小さくなるが雨滴の乾燥は抑制されると考えられる。

5. まとめ

コンクリート表面への水分の作用を評価する手法に関する基礎的検討を行った。本研究において得られた知見を以下にまとめる。

1. ACMセンサの出力電流値の温度依存性について検討を行い，表面の濡れと電流値の関係を把握するとともに温度の影響を確認した。
2. ACMセンサを用いて濡れ時間の評価を行い，降水時の出力について測定し，風向を考慮した濡れ時間の評価が可能であることが示唆された。

参考文献

1) 鉄筋コンクリート造建築物の耐久設計施工指針・同解説，日本建築学会，2016.
2) 日本建築学会：建築工事標準仕様書・同解説 JASS5. 鉄筋コンクリート工事, 2022.
3) 石川，橋本佳大：壁面に衝突する雨滴の傾斜角の推定 ：外壁面におよぼす雨がかり負荷の評価に関する基礎的研究，日本建築学会構造系論文集, vol.611, pp.13-20, 2007
4) 石崎潑雄，光田寧，佐野雄二：暴風雨時に壁面に衝突する雨について，京都大学防災研究所年報.A, vol.13, pp.433-439, 1970.

初期凍害を受けたコンクリートの UPV 強度評価に及ぼすデータ集約と材齢の影響

Effects of Data Aggregation and Test Age on UPV Strength Assessment of Early-Age Frozen Concrete

李磊※1、崔亨吉※2
Lei Li, Hyeonggil Choi

ABSTRACT

This study examined how data aggregation and test age affect ultrasonic pulse velocity (UPV)-based assessment of compressive-strength reduction in concrete subjected to early-age subzero exposure. Individual results from 36 concrete cylinders were obtained at 3, 7, and 28 days using direct-transmission UPV at nominal frequencies of 54 and 250 kHz. Absolute specimen-level regressions yielded R^2 values of 0.663 and 0.698, respectively, whereas aggregation into 12 condition-by-age means increased these values to 0.820 and 0.900. After the 27 exposed specimens were normalized to the same-age Plain means, R^2 decreased to 0.256 and 0.207. Age-specific slopes varied substantially and became negative at 28 days. Leave-one-age-out validation yielded ${R^2}_{pred}$ values of −1.320 and −1.203 and RMSEs of 22.3 and 21.7 percentage points at 54 and 250 kHz, respectively. Averaging strengthened the apparent relationship between absolute UPV and strength, while the pooled fits also reflected their common age-dependent development.

1. Introduction

Concrete exposed to subfreezing temperatures before adequate early strength develops may experience delayed hydration and freezing-related disruption of the cementitious microstructure [1,2,14-16]. Because internal changes can occur before visible surface damage, ultrasonic pulse velocity (UPV) is attractive for early nondestructive assessment [3,4,8,13]. UPV generally increases as hydration creates a more continuous solid skeleton, whereas pores, cracks, weak interfaces, moisture state, and coupling conditions can alter wave propagation [4,7,9,12]. A high correlation between absolute UPV and compressive strength does not necessarily mean that an exposure-induced percentage reduction in UPV corresponds to an equivalent reduction in compressive strength. Both properties increase with age but reflect different material characteristics: UPV is a path-averaged elastic-wave response, whereas compressive failure is governed by localized weak zones and nonlinear fracture [4-6,10,11]. Pooling multiple ages introduces a common hydration trend, while averaging replicate results suppresses within-group scatter; both effects can increase the apparent R^2. This study therefore compares absolute-value regressions using 36 individual specimens and 12 condition-by-age group means, followed by same-age-normalized reduction regressions, age-specific fits, and leave-one-age-out validation at 54 and 250 kHz. The objective is to distinguish associations caused by age and data aggregation from a relationship capable of estimating strength reduction across ages.

2. Experimental Program and Analysis

2.1 Materials

The mixture proportions are given in Table 1. One normal-weight concrete mixture with a water-to-cement ratio of 0.50 and a fine aggregate ratio of 47%

※1 大韓民国 慶北國立大學 建築工学科 博士課程
※2 大韓民国 慶北國立大學 建築工学科 教授 博士(工学)

was used for all groups to isolate the effects of data aggregation and test age.

After 24 h in molds, Plain specimens were water-cured at 20 ± 1 °C. The CFD specimens were covered with 10 mm-thick aluminum-foil-faced insulation as listed in Table 2, exposed at −10 °C for 24 h, and then water-cured at 20 ± 1 °C. The nominal exposed height ranged from 0 to 200 mm as the insulated portion decreased. Because internal temperatures were not measured, the CFD labels indicate external exposure conditions rather than confirmed freezing or damage depths.

2.2 UPV and compressive-strength tests

Cylindrical specimens measuring 100 mm in diameter and 200 mm in height were used. At 3, 7, and 28 days, direct-transmission UPV was measured along the cylinder axis using nominal 54 and 250 kHz transducers in accordance with ASTM C597/C597M [3]. Velocity was calculated from the measured specimen height divided by transit time. The transmitter and receiver were placed on the two circular end faces so that the pulse traveled through the full longitudinal axis of the cylinder.

Immediately after UPV measurement, the same cylinder was tested in compression. Strength was obtained from the maximum load divided by the measured cross-sectional area. This sequence paired the ultrasonic and mechanical observations for each specimen and avoided between-specimen matching. Each condition at each age contained three independent cylinders. Group means were used for condition-level comparisons, whereas individual results were retained for specimen-level regressions and leave-one-age-out validation.

2.3 Reduction indices

For specimen j at age a under exposure condition e, the compressive-strength and frequency-specific UPV reduction indices were defined relative to the mean Plain value at the same age:

$$D_{f,a,e,j} = 1 - \frac{f_{c,a,e,j}}{\bar{f}_{c,Plain,a}} \quad (1)$$

$$D_{V,q,a,e,j} = 1 - \frac{V_{q,a,e,j}}{\bar{V}_{q,Plain,a}} \quad (2)$$

Here, f_c and V denote the measured compressive strength and UPV, respectively; q denotes the frequency of 54 or 250 kHz; a denotes the test age of 3, 7, or 28 days; e denotes CFD-00, CFD-10, or CFD-20; and j denotes replicate 1-3. A positive index indicates a value below the same-age Plain mean. The indices were multiplied by 100 when reported as percentages. For visualization purposes, results are also expressed as an achievement (retention) rate, defined as A=(1−D)×100, giving the measured value as a percentage of the same-age Plain mean. Fig. 2

Table 1. Concrete mixture proportions

W/C (%)	s/a (%)	Water (kg/m³)	Cement (kg/m³)	Fine aggregate (kg/m³)	Coarse aggregate (kg/m³)	Admixture
50	47	170	340	827	969	AE agent

Table 2. Low-temperature exposure conditions and test program

Condition	Chamber exposure	Nominal exposed height(mm)	Insulated portion	Test age(days)
Plain	Not exposed	-	-	3, 7, 28
CFD-00	-10 °C, 24 h	0	Entire height	3, 7, 28
CFD-10		100	Lower 100 mm	3, 7, 28
CFD-20		200	None	3, 7, 28

reports strength and UPV results in this form, whereas D_f and D_V are used in all subsequent regression and validation analyses. The term reduction index is used instead of damage index because internal freezing and microstructural damage were not directly measured.

Same-age normalization expresses each CFD result relative to normally cured concrete at the corresponding age, but it does not make observations from different ages statistically equivalent. Mean reductions may therefore still vary with age. In addition, all nine CFD observations at a given age share the Plain reference estimated from three cylinders.

2.4 Regression and validation strategy

Ordinary least-squares regressions were fitted separately at 54 and 250 kHz. To isolate the effect of data aggregation, absolute compressive strength was regressed on absolute UPV using both the 36 individual specimens and the 12 condition-by-age group means. The normalized analysis regressed D_f on D_V using the 27 CFD specimens, followed by descriptive age-specific fits containing nine specimens at each age. The absolute regressions describe the overall co-development of UPV and strength, whereas the normalized regressions examine whether relative UPV reduction tracks relative strength reduction after using a same-age reference.

Leave-one-age-out validation was performed by training the normalized model on two ages and applying it to the excluded age. The three folds used the 7 and 28 days data to predict 3 days, the 3 and 28 days data to predict 7 days, and the 3 and 7 days data to predict 28 days. Prediction performance was evaluated using ${R^2}_{pred}$ and RMSE:

$$ {R^2}_{pred} = 1 - \frac{\sum_i (D_{f,i} - \widehat{D_{f,i}})^2}{\sum_i (D_{f,i} - \overline{D_f})^2} \quad (3) $$

Here, $\overline{D_f}$ is the mean of all 27 observed strength-reduction indices included in the pooled validation result. A negative ${R^2}_{pred}$ indicates that the cross-age model performs worse than prediction using the overall observed mean. RMSE is reported in percentage points.

3. Results and Discussion

3.1 Absolute age development

The Plain concrete showed concurrent increases in compressive strength and UPV with test age (Fig. 1). Mean compressive strength increased from 17.89 MPa at 3 days to 24.28 MPa at 7 days and 30.33 MPa at 28 days. Over the same period, UPV increased from 3735 to 4086 m/s at 54 kHz and from 3790 to 4119 m/s at 250 kHz. This concurrent development is consistent with continued hydration and densification of the concrete matrix. It also demonstrates that test age creates a strong common trend between absolute UPV and compressive strength, which may increase the apparent correlation when data from different ages are pooled.

All CFD group means remained below the corresponding Plain values, although the differences generally narrowed after subsequent water curing. The later-age rankings were not fully monotonic with nominal exposed height. Therefore, the absolute results indicate both a dominant age-related development trend and comparatively smaller exposure-related differences at later ages.

3.2 Age-dependent reduction response

Compressive-strength achievement rates fell sharply by 3 days. CFD-00, CFD-10, and CFD-20 reached only 66.7%, 61.2%, and 54.4%, respectively (Fig.2(a)). In contrast, the corresponding UPV achievement rates remained much closer to 100%, ranging from 88.1% to 91.5% at 54 kHz and from 91.6% to 94.1% at 250 kHz. Although the UPV achievement

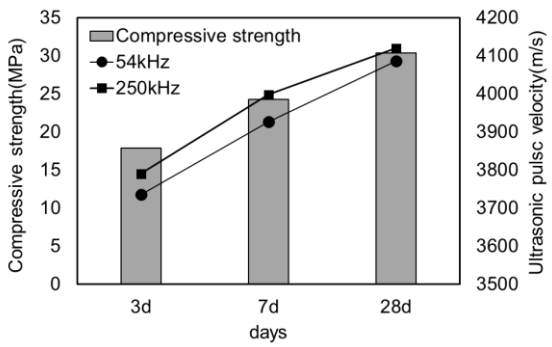

Fig. 1. Strength and UPV development in Plain concrete.

Table 3. Comparison of regression and validation results at different analysis levels.

Analysis level	n	Statistic	54 kHz	250 kHz
Individual specimens, absolute values	36	R^2	0.663	0.698
Condition-by-age means, absolute values	12	R^2	0.820	0.900
Individual CFD specimens, same-age normalized	27	R^2	0.256	0.207
Leave-one-age-out validation	27	${R^2}_{pred}$	-1.320	-1.203

rates at both frequencies followed the nominal exposure-height order, their departure from the Plain reference remained substantially smaller than that of compressive strength.

By 7 days, the strength achievement rate had recovered to 84.0–91.4%, compared with UPV achievement rates of 93.6–96.1% at 54 kHz and 95.4–96.9% at 250 kHz (Fig. 2(b)). By 28 days, the strength achievement rate further increased to 90.2–94.2%, whereas the corresponding UPV achievement rates were 91.4–93.1% and 93.6–95.8%, respectively (Fig. 2(c)). This indicates that the relative sensitivity between compressive-strength and UPV recovery shifts with curing age.

3.3 Effect of data aggregation and normalization

At the individual-specimen level, absolute UPV-strength regressions based on 36 measurements yielded R^2 values of 0.663 at 54 kHz and 0.698 at 250 kHz (Table 3, Fig. 3). Figure 3 shows that the 36 individual measurements follow a broadly positive trend but with substantial within-age scatter. Aggregation into 12 condition-by-age means increased these values to 0.820 and 0.900, respectively. Figure 4 shows that the group means also formed distinct age-related clusters, with the 3-d data occupying the lower-strength range and the 28-d data occupying the upper-strength range. The increase in R^2 is consistent with reduced within-group scatter after averaging, but the fitted relationships also include the common age-dependent development of UPV and strength. Therefore, the high group-mean R^2 values do not by themselves demonstrate accurate assessment of exposure-related strength reduction.

After the 27 CFD specimens were normalized to the same-age Plain means, R^2 decreased to 0.256 at 54 kHz and 0.207 at 250 kHz (Table 3, **Fig. 5**). The corresponding RMSEs were 12.6 and 13.0 percentage points. As shown in Fig. 5, removing the common age

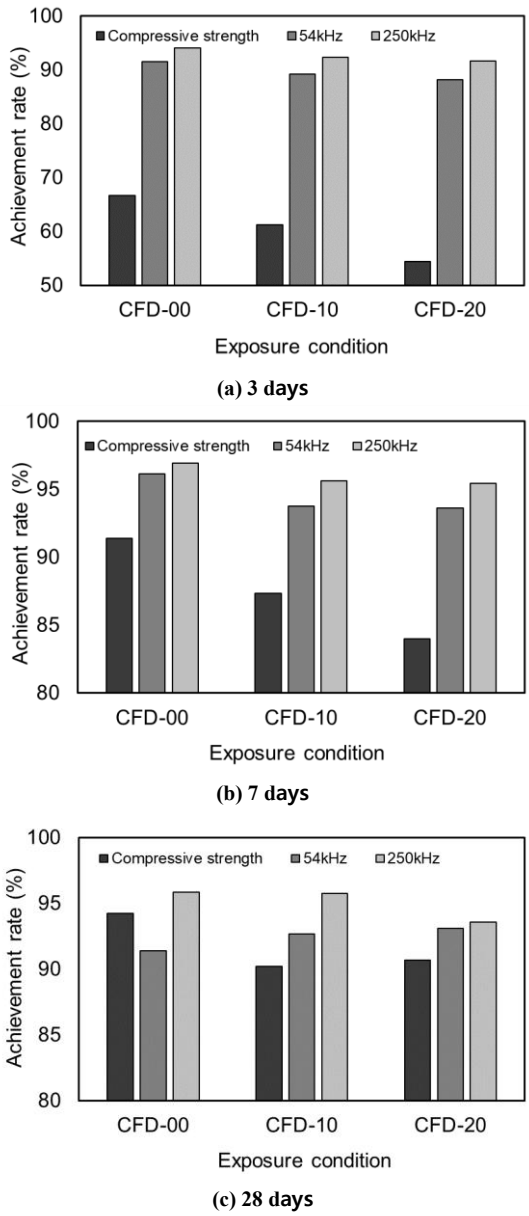

Fig. 2. Strength and UPV retention rates relative to same-age Plain concrete

trend leaves a much looser, more scattered relationship with no clear age-based clustering. Moreover, the mean strength-reduction index decreased from 39.2% at 3 days to 12.4% at 7 days and 8.3% at 28 days. Same-age normalization therefore reduced the common absolute age trend but did not produce a stable, age-independent conversion between UPV reduction and strength reduction.

3.4 Stability of age-specific relationships

The age-specific relationships were unstable. At 54 kHz, R^2 values were 0.518, 0.362, and 0.066 at 3, 7, and 28 days, respectively, with corresponding slopes of 2.059, 1.496, and -0.232. At 250 kHz, R^2 values were 0.275, less than 0.001, and 0.130, with slopes of 1.512, 0.025, and -0.719. Because each age-specific fit contained only nine CFD specimens and the later-age reductions covered narrow ranges, the negative 28 days slopes indicate model instability rather than an inverse physical relationship. A single cross-age conversion coefficient is therefore not supported. In addition, 250 kHz showed the higher absolute group-mean R^2, whereas 54 kHz showed the higher normalized specimen-level R^2; neither frequency was universally superior under the investigated conditions.

3.5 Cross-age transferability

Leave-one-age-out validation confirmed poor cross-age transferability (Fig. 6). Held-out predictions yielded negative R^2_{pred} (-1.320 at 54 kHz and -1.203 at 250 kHz) and RMSEs of 22.3 and 21.7 percentage points, respectively. Models trained on 7 and 28 days data underestimated 3-d strength reduction (observed 39.2% vs. predicted 10.4% and 9.5%). Conversely,

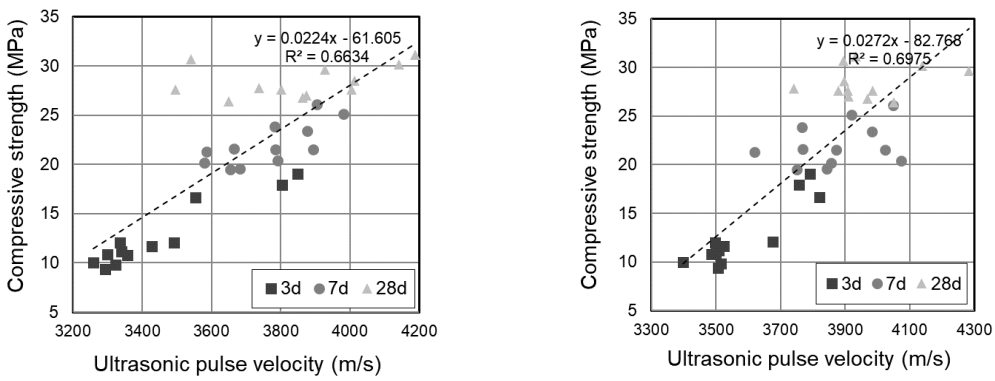

(a) 54 kHz **(b) 250 kHz**

Fig 3. Individual-specimen absolute UPV-strength relationships (n=36)

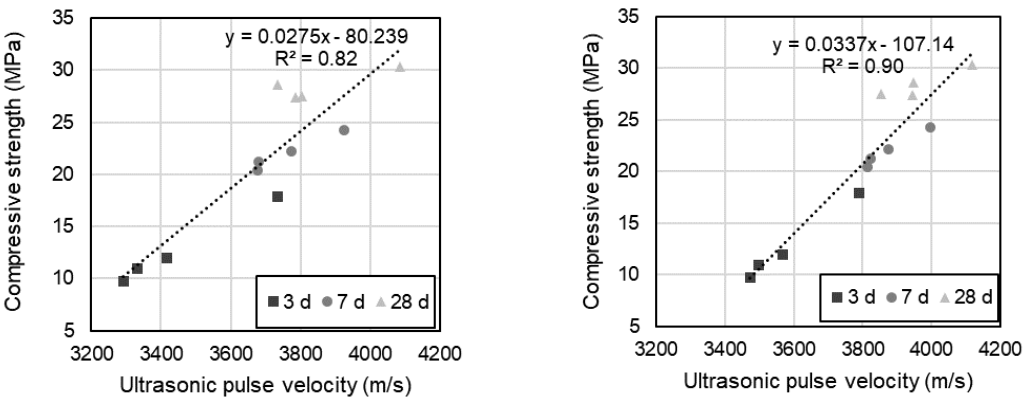

(a) 54 kHz **(b) 250 kHz**

Fig 4. Pooled absolute UPV-strength relationships based on 12 condition-by-age group means.

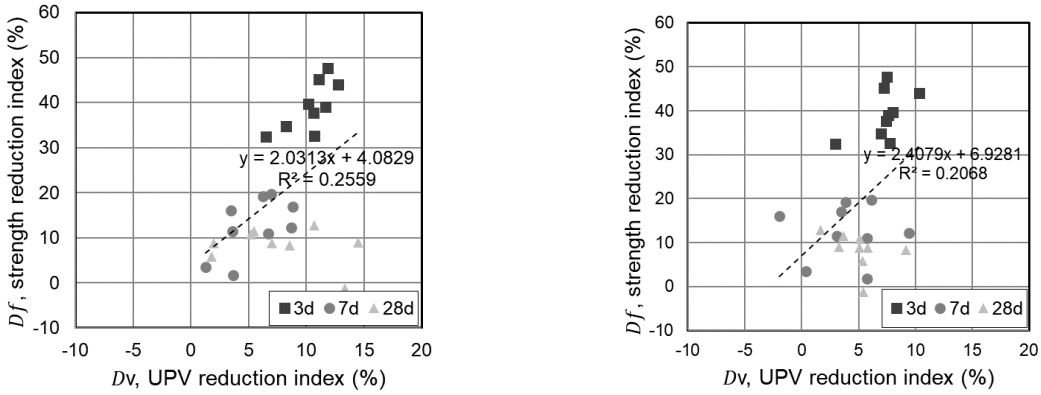

(a) 54 kHz **(b) 250 kHz**

Fig 5. Same-age normalized Df–DV relationships for 27 CFD specimens.

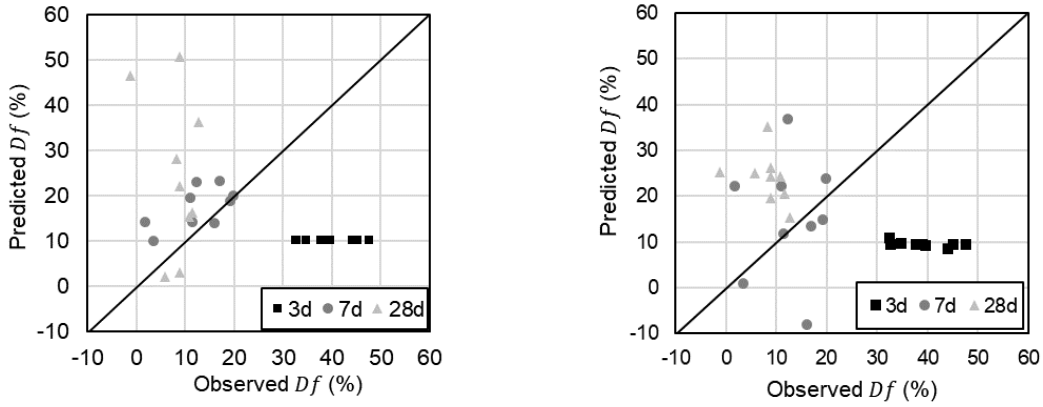

(a) 54 kHz **(b) 250 kHz**

Fig 6 Leave-one-age-out predictions

models trained on 3 and 7 days data overestimated 28-d response (observed 8.3% vs. predicted 24.6% and 24.0%). Thus, normalized UPV-reduction relationships are unsuitable for quantitative cross-age prediction without age or maturity-specific calibration.

4. Conclusions

During the initial 3-day curing, compressive strength reductions (33.3–45.6%) markedly exceeded UPV reductions (5.9–11.9%). Data aggregation improved absolute UPV–strength R^2 values from 0.663 to 0.820 (54 kHz) and 0.698 to 0.900 (250 kHz). The same-age-normalized relationships remained weak (R^2 = 0.256 and 0.207), and age-specific fits were unstable, exhibiting negative slopes at 28 days. Leave-one-age-out validation further confirmed poor cross-age transferability (R^2_{pred} of -1.320 and -1.203; RMSEs≈ 22%). Overall, while UPV suits qualitative screening, quantitative strength-loss assessment requires age- or maturity-specific calibration with independent validation. These findings are bounded by the study's scope: a single mix design, one subzero exposure regime, three specimens per condition, and no internal temperature tracking.

References

[1] ACI Committee 306. Guide to Cold Weather Concreting, ACI 306R-16. American Concrete Institute, Farmington Hills, MI (2016).

[2] Karagöl, F., Demirboğa, R., Khushefati, W.H. Behavior of fresh and hardened concretes with antifreeze admixtures in deep-freeze low

temperatures and exterior winter conditions. Constr. Build. Mater. 76, 388-395 (2015).

[3] ASTM International. ASTM C597/C597M-22: Standard Test Method for Ultrasonic Pulse Velocity Through Concrete. West Conshohocken, PA (2022).

[4] Malhotra, V.M., Carino, N.J. Handbook on Nondestructive Testing of Concrete, 2nd ed. CRC Press, Boca Raton (2004).

[5] Bogas, J.A., Gomes, M.G., Gomes, A. Compressive strength evaluation of structural lightweight concrete by non-destructive ultrasonic pulse velocity method. Ultrasonics 53(5), 962-972 (2013).

[6] Pereira, N., Romão, X. Assessing concrete strength variability in existing structures based on the results of NDTs. Constr. Build. Mater. 173, 786-800 (2018).

[7] Lencis, U., Udris, A., Korjakins, A. Frost influence on the ultrasonic pulse velocity in concrete at early phases of hydration process. Case Stud. Constr. Mater. 15, e00614 (2021).

[8] Moon, S., Lee, T.G., Choi, H.S., Choi, H.G. Assessment of Ultrasonic Pulse Velocity Method for Early Detection of Frost Damage in Concrete. J. Korea Inst. Build. Constr. 24(2), 193-202 (2024). doi:10.5345/JKIBC.2024.24.2.193.

[9] Yim, H.J., Bae, Y.H., Jun, Y. Hydration and microstructural characterization of early-age cement paste with ultrasonic wave velocity and electrical resistivity measurements. Constr. Build. Mater. 303, 124508 (2021).

[10] Trtnik, G., Kavcic, F., Turk, G. Prediction of concrete strength using ultrasonic pulse velocity and artificial neural networks. Ultrasonics 49(1), 53-60 (2009).

[11] Kouddane, B., Sbartaï, Z.M., Alwash, M., Ali-Benyahia, K., Elachachi, S.M., Lamdouar, N., Kenai, S. Assessment of concrete strength using the combination of NDT - review and performance analysis. Appl. Sci. 12(23), 12190 (2022).

[12] Ohdaira, E., Masuzawa, N. Water content and its effect on ultrasound propagation in concrete - the possibility of NDE. Ultrasonics 38(1-8), 546-552 (2000).

[13] McCann, D.M., Forde, M.C. Review of NDT methods in the assessment of concrete and masonry structures. NDT E Int. 34(2), 71-84 (2001).

[14] Choi, H., Zhang, W., Hama, Y. Method for determining early-age frost damage of concrete by using air-permeability index and influence of early-age frost damage on concrete durability. Constr. Build. Mater. 153, 630-639 (2017).

[15] Hu, X., Peng, G., Niu, D., Zhao, N. Damage study on service performance of early-age frozen concrete. Constr. Build. Mater. 210, 22-31 (2019).

[16] Wang, C., Hao, B., Liu, S., Yuan, L. Influence of early freezing on the pore structure characteristics of concrete and its correlation with mechanical properties. Buildings 14(1), 47 (2024).

高炉スラグを使用したコンクリート中の溶融亜鉛めっき鉄筋における腐食挙動

Corrosion Behavior of Hot-Dip Galvanized Reinforcing Bars Embedded in Concrete Containing Ground Granulated Blast-Furnace Slag

ジョン　ジュンテク※1、チェ　ホンボク※2、兼松学※3
Jun-Taek, Jeong, Hong-bok, Choe, Manabu, Kanematsu

ABSTRACT

This study evaluated the corrosion behavior and bond performance of hot-dip galvanized reinforcing bars embedded in blast-furnace slag concrete. Accelerated corrosion tests, pull-out tests were conducted. The results showed that the electrochemical behavior varied depending on the cement and reinforcing bar types, while the bond performance of galvanized reinforcing bars was comparable to that of ordinary reinforcing bars. Therefore, this study aims to clarify the corrosion behavior and bond performance of galvanized reinforcing bars embedded in concrete containing ground granulated blast-furnace slag.

1. Introduction

Hot-dip galvanized reinforcing bars (hereafter referred to as galvanized rebars) are widely recognized as corrosion-resistant reinforcing bars. In addition to the barrier protection provided by the zinc coating, which prevents the ingress of corrosion agents such as water and oxygen, galvanized rebars exhibit sacrificial protection because the zinc coating preferentially corrodes before the steel substrate. Owing to these characteristics, their effectiveness in preventing reinforcement corrosion has been widely reported.[1,2]

Since galvanized rebars are coated with a zinc layer approximately 100 μm thick, which has lower stiffness than the steel substrate, many studies have investigated their influence on bond performance.[3,4] Most studies have reported that the zinc coating has little effect on the bond performance between concrete and reinforcing bars. For example, in a previous study, ordinary and galvanized rebars were immersed in a 3.0 wt% NaCl solution and subjected to impressed-current accelerated corrosion. Changes in the corrosion potential and bond stress obtained from pull-out tests were evaluated. The results showed no significant difference in bond performance between galvanized and ordinary rebars. Furthermore, the increase in the initial bond stiffness, defined as the bond stress at a free-end slip of 0.002 times the bar diameter, was greater for galvanized rebars than for ordinary rebars.[3,5]

Recently, the application of galvanized rebars to environmentally friendly concrete has attracted increasing attention. Although the corrosion characteristics of ordinary reinforcing bars in such concrete have been extensively investigated,[6,7,8,9] limited information is available regarding galvanized rebars. Moreover, it has been reported that the reaction between zinc and the highly alkaline fresh concrete may generate hydrogen gas, resulting in a porous zone around the reinforcing bar and a possible reduction in bond performance.[10] However, it remains unclear whether similar phenomena occur in environmentally friendly concrete. Therefore, this study aims to clarify the bond performance of galvanized reinforcing bars during corrosion when embedded in concrete containing ground granulated blast-furnace slag.

※1 日本　東京理科大学　創域理工学研究科　建築専攻　博士課程
※2 日本　日本大学 生産工学部　建築工学科　助教・博士（工学）
※3 東京理科大学　創域理工学部　建築学科　教授・博士（工学）

2. Materials and methods

2.1 Materials

Table 1 lists the experimental variables and levels. In this study, the cement type, reinforcing bar type, and degree of corrosion were selected as the experimental parameters. Two types of cement were used: ordinary Portland cement (hereafter referred to as N) and blast-furnace slag cement equivalent to Type C (hereafter referred to as BC), in which 70% of the ordinary Portland cement was replaced with ground granulated blast-furnace slag 4000 (JIS A 6206). Two types of reinforcing bars were investigated: hot-dip galvanized reinforcing bars and ordinary reinforcing bars with mill scale. Based on a previous study,[5] the degree of corrosion was controlled by varying the accumulated electric charge during accelerated corrosion and was classified into three levels: sound, low corrosion, and moderate corrosion.

Table 1 Experimental Variables and Levels

Variable	Level	Number of Levels
Cement type	Ordinary Portland cement (N) Blast-furnace slag cement, Type C (BC)	2
Reinforcing bar type	Hot-dip galvanized reinforcing bar Ordinary reinforcing bar	2
Degree of corrosion (Accumulated current, mA·h/cm²))	Uncorroded (0) Low corrosion (76.71) Moderate corrosion (153.42)	3

2.2 Specimen Details

Figure 1 illustrates the geometry of the test specimens. The specimen dimensions and bonded length were designed in accordance with JSTM C 2101T, Standard Test Method for Bond Strength between Reinforcing Bars and Concrete by Pull-out Test, established by the Japan Testing Center for Construction Materials.

The reinforcing bars were D16 SD295 deformed bars. To prevent splitting failure of the concrete during the pull-out test, ordinary steel spiral reinforcement was provided around the embedded reinforcing bar. The bonded length and unbonded length were 64 mm and 36 mm, respectively. In the unbonded region, a Teflon sheet and vinyl tape were wrapped around the reinforcing bar to eliminate bond.

The target corrosion levels were determined based on the previous study.[5] The low corrosion level corresponded to an accumulated electric charge of 76.71 mA·h/cm², at which the corrosion potential of the galvanized reinforcing bar ceased to increase and became stable. The moderate corrosion level was defined as twice this accumulated electric charge.

Table 2 presents the concrete mix proportions and the fresh properties of the concrete used in this study.

2.3 Accelerated Corrosion Procedure and Measurement Methods

(1) Accelerated Corrosion Test

Figure 2 illustrates the accelerated corrosion test setup. Accelerated corrosion of the reinforcing bars was induced using an impressed-current corrosion method.

To prevent direct corrosion of the reinforcing bars caused by moisture entering through the top and bottom surfaces of the specimen, approximately 100 mm of the reinforcing bar at the top surface was coated with epoxy resin, while the reinforcing bar at the bottom surface was coated with epoxy resin over its entire length. This treatment was intended to minimize the influence of the external environment at the specimen ends and to enable an appropriate evaluation of the corrosion behavior of the reinforcing bars embedded in concrete.

After the epoxy coating had cured, the specimens were immersed in a 3.0 wt% NaCl aqueous solution, and a 10 mA direct current was applied with the reinforcing bar serving as the anode and a stainless steel plate as the cathode.

(2) Measurement of Corrosion Current Density by Potentiodynamic Polarization

Figure 3 shows the experimental setup for measuring the corrosion current density of reinforcing bars embedded in concrete. Potentiodynamic polarization measurements were conducted to electrochemically evaluate the corrosion condition of the reinforcing bars. An Ag/AgCl electrode was used as the reference electrode, the galvanized or ordinary reinforcing bar as the working electrode, and a stainless-steel plate as the counter electrode.

The potential scan rate was set at 1 mV/s. Anodic polarization was conducted from the corrosion potential to +200 mV, while cathodic polarization was conducted from the corrosion potential to −200 mV. The electrochemical measurements were performed at predetermined accumulated current levels, during which the impressed-current corrosion test was temporarily suspended.

The corrosion current density, i_{corr}, which represents the degree of corrosion, was calculated using the Stern–Geary equation shown in Eq. (1), based on the polarization resistance obtained from the slope of the Tafel curve at each measurement stage. Furthermore, the corrosion rate can be evaluated from i_{corr} in accordance with RILEM TC 154-EMC, and the corresponding ranges are presented in Table 3.

$$i_{corr} = \mathrm{B} \times R_p^{-1} = \left[\frac{\beta_a \times \beta_c}{2.3 \times (\beta_a + \beta_c)}\right] \times R_p^{-1} \quad (1)$$

where i_{corr} is the corrosion current density (μA/cm²), B is the Tafel constant (mV), β_a and β_c are the anodic and cathodic Tafel slopes (mV/decade), respectively, and R_p is the polarization resistance (Ω·cm²).

Table 2 Concrete Mix Proportions and Fresh Properties

Cement type		N	BC
Unit content (kg/m3)	W/B (%)	55	
	s/a (%)	50	
	W	180	
	C	327	98
	BC	0	229
	S	874	866
	G	888	880
Slump (cm)		18.5	19.5
Air content (%)		4.3	4.4

Table 3 Criteria for Assessing Corrosion Level Based on i_{corr}

i_{corr} (μA/cm 2)	Corrosion level
≤ 0.1	Passive
0.1 ~ 0.5	Low
0.5 ~ 1.0	Moderate
> 1.0	High

Note: Values up to 0.2 μA/cm² may be considered to indicate a passive state.

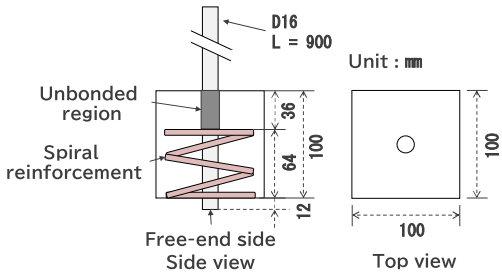

Figure 1 Specimen Details

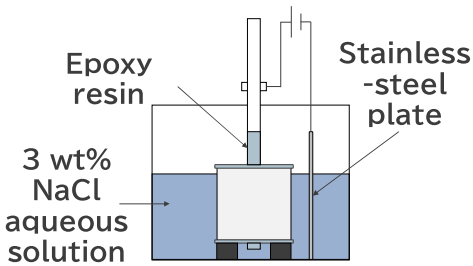

Figure 2 Accelerated Corrosion Test Setup

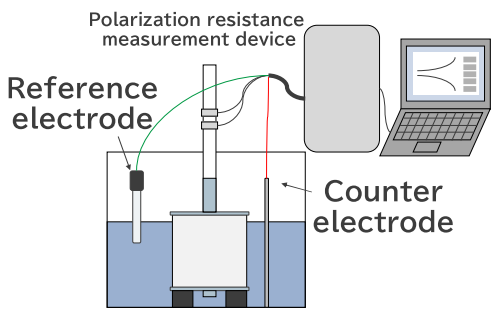

Figure 3 Setup for Measuring the Corrosion Current Density

2.4 Pull-Out Test

Figure 4 illustrates the setup of the pull-out test. The pull-out test was conducted after completion of the accelerated corrosion test in accordance with JSTM C 2101T. The specimen was placed on a testing frame equipped with a displacement gauge to measure the free-end slip, and the test was carried out using a hydraulic jack for bond testing.

The load was applied continuously without impact, and the loading rate was controlled so that the increase in bond stress did not exceed 49 N/mm² per minute. The bond stress was calculated using Eq. (2).

$$\tau = \frac{P}{4\pi D^2} \times \alpha \qquad (2)$$

where τ is the bond stress (N/mm²), P is the tensile load (N), D is the diameter of the reinforcing bar (mm), α is the correction factor for the compressive strength of concrete, defined as $\alpha = 30/\sigma_c$, and σ_c is the 28-day compressive strength of the cylindrical specimens cast at the same time (N/mm²).

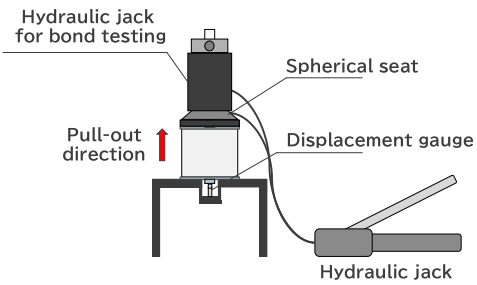

Figure 4 Pull-Out Test Setup

3. Results and Discussion

3.1 Corrosion Current Density (i_{corr})

Figure 6 shows the relationship between i_{corr}, measured using a potentiostat, and the accumulated current, while Figure 7 shows the relationship between the accumulated current and the accumulated corrosion current density, hereafter referred to as accumulated i_{corr}. The accumulated i_{corr} was calculated by cumulatively summing the measured i_{corr} values over time at each measurement point.

As shown in Figure 6, N exhibited lower corrosion current density values than BC, although this electrochemical trend does not necessarily indicate a lower degree of actual corrosion. A previous study comparing the corrosion behavior of reinforcing bars embedded in N and BC under chloride exposure reported that, although the i_{corr} of N was lower than that of BC, BC exhibited greater resistance to chloride penetration and suppressed rust formation on the reinforcing bar surface.[11] The study also suggested that the relatively high i_{corr} observed in BC may be attributable to the reduction reaction of sulfide ions. Therefore, the higher i_{corr} values observed in BC in the present study may have been influenced by electrochemical reactions specific to blast-furnace slag cement. Accordingly, caution is required when evaluating corrosion behavior solely on the basis of i_{corr}

With regard to the reinforcing bar type, the i_{corr} of the galvanized reinforcing bars tended to be lower than that of the ordinary reinforcing bars at the low corrosion level. At the moderate corrosion level, however, the galvanized and ordinary reinforcing bars exhibited similar i_{corr} trends in BC, whereas the

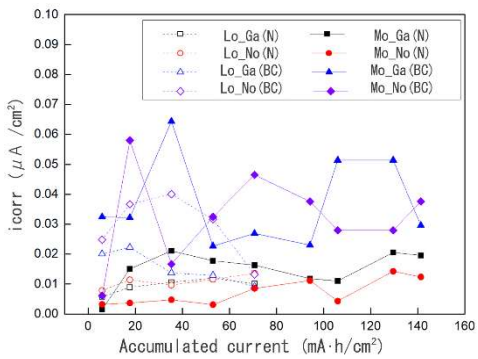

Figure 6 Relationship Between Accumulated Current and i_{corr}

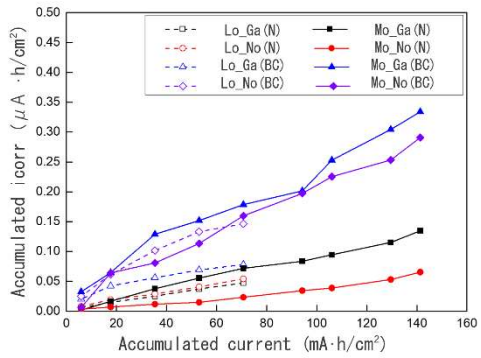

Figure 7 Relationship Between Accumulated Current and Accumulated i_{corr}

galvanized reinforcing bars showed slightly higher values than the ordinary reinforcing bars in N. These results are considered to reflect the initial corrosion protection provided by the galvanized coating and changes in electrochemical behavior according to the stage of corrosion progression.

The accumulated i_{corr} results shown in Figure 7 indicate that, in BC, the accumulated i_{corr} of the ordinary reinforcing bars was higher than that of the galvanized reinforcing bars at the low corrosion level, while the values were approximately the same at the moderate corrosion level. In N, the ordinary reinforcing bars likewise exhibited higher accumulated i_{corr} than the galvanized reinforcing bars at the low corrosion level. At the moderate corrosion level, however, the galvanized reinforcing bars exhibited higher values than the ordinary reinforcing bars.

These results confirm that the trend in accumulated i_{corr} varied depending on the stage of corrosion progression and the cement type. According to RILEM TC 154-EMC, corrosion current density estimates may be affected by various electrochemical reactions. Therefore, caution is required when evaluating corrosion behavior solely on the basis of i_{corr}.

3.2 Bond Performance

Figure 8 shows the relationship between the accumulated current and the maximum bond stress, Figure 9 shows the slip at the maximum bond stress for each corrosion level, and Figure 10 shows the

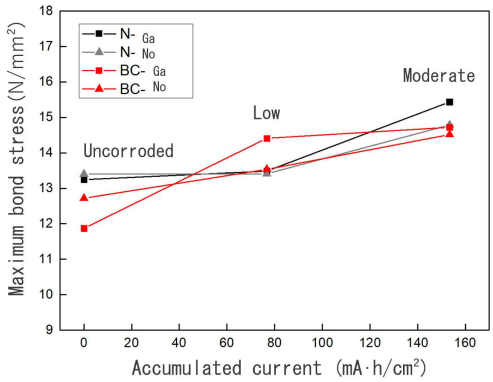

Figure 8 Relationship Between Accumulated Current and Maximum Bond Stress

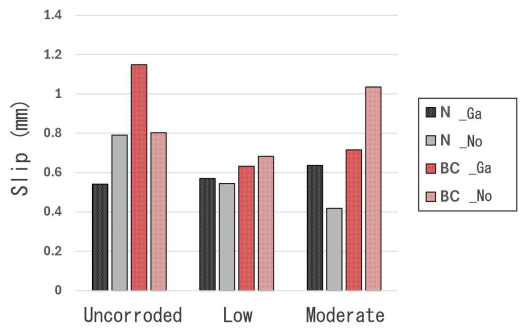

Figure 9 Slip at Maximum Bond Stress for Each Corrosion Level

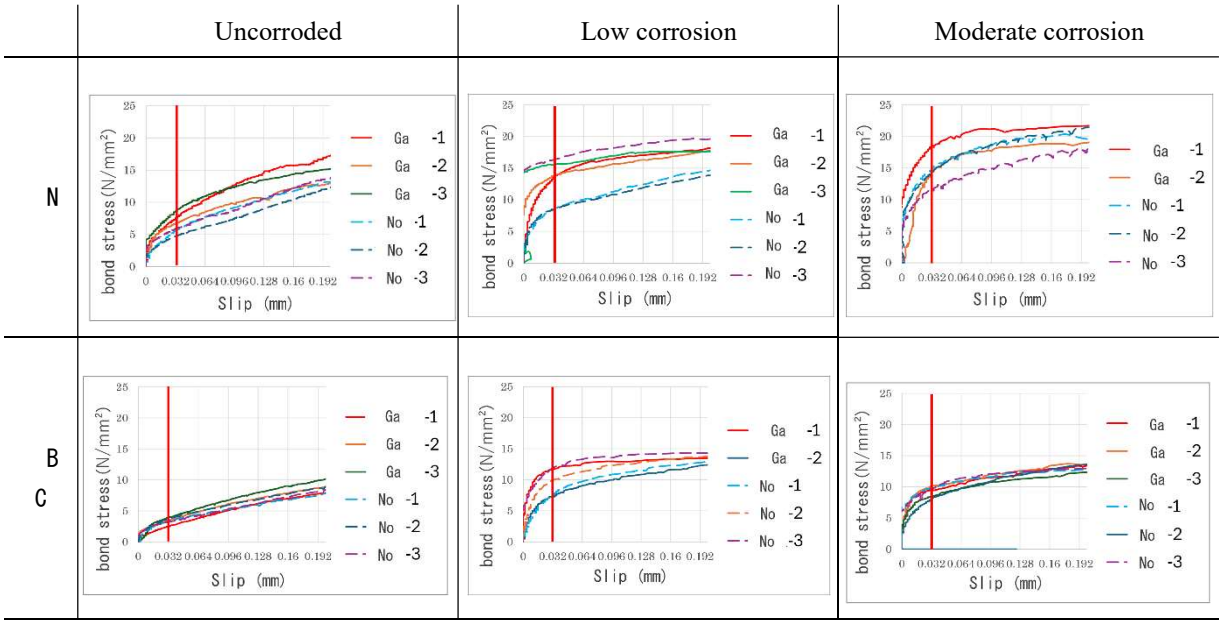

Figure 10 Relationship Between Bond Stress and Free-End Slip

relationship between the bond stress and free-end slip.

As shown in Figure 8, the maximum bond stress tended to increase with increasing accumulated current under all conditions. Previous studies on the bond strength of galvanized and ordinary reinforcing bars embedded in ordinary concrete reported that the increase in bond strength at the initial stage of corrosion was caused by the expansion of the reinforcing bar associated with the formation of corrosion products on its surface, whereas prolonged corrosion resulted in a reduction in bond performance.[5,12] Therefore, the increases in maximum bond stress observed at the low and moderate corrosion levels in the present study were also attributed to increased mechanical interlocking between the reinforcing bar and concrete caused by corrosion products.

As shown in Figure 9, when N was used, the slip of the galvanized reinforcing bars increased slightly with corrosion progression, whereas that of the ordinary reinforcing bars tended to decrease. When BC was used, the slip decreased slightly at the low corrosion level regardless of the reinforcing bar type, but increased again at the moderate corrosion level.

As shown in Figure 10, the initial stiffness increased with corrosion progression in N. In BC, however, the initial stiffness was maintained or slightly decreased at the moderate corrosion level. Although differences in bond behavior were observed depending on the cement type, no clear differences were observed depending on the reinforcing bar type. Based on the initial stiffness results, the changes in slip shown in Figure 9 can be interpreted as follows: when N was used, the increase in initial stiffness resulted in the slip being maintained or reduced, whereas when BC was used, the decrease in initial stiffness resulted in an increase in slip.

4. Conclusions

(1) The corrosion current density and accumulated corrosion current density varied depending on the cement type, reinforcing bar type, and stage of corrosion. Electrochemically, BC tended to exhibit higher values than N, and ordinary reinforcing bars in BC tended to exhibit higher values than galvanized reinforcing bars, particularly at the low corrosion level.

(2) Regarding bond performance, within the scope of this study, in which an accumulated current of 153.42 mA·h/cm² was applied, hot-dip galvanized reinforcing bars and ordinary reinforcing bars exhibited comparable performance. Although the initial stiffness of BC decreased with increasing accumulated current, the maximum bond stress of both N and BC did not decrease, but rather tended to increase.

Reference

[1] Murakami, K., Maekawa, A., and Yuasa, Y., “Bond Characteristics between Hot-Dip Galvanizing and Concrete,” Lead and Zinc, Vol. 40, No. 1, pp. 38–43, 2003.

[2] Kayali, O., and Yeomans, S. R., “Bond of Galvanized Steel in Concrete,” Cement and Concrete Composites, Vol. 22, No. 6, pp. 459–467, 2000.

[3] Pokorny, P., Dobias, D., and Vokac, M., “Bond Strength of Hot-Dip Galvanized Reinforcement with Concrete,” Metalurgija, Vol. 55, No. 3, pp. 337–340, 2016.

[4] Nishikata, A., “Initial Corrosion Behavior of Hot-Dip Galvanized Reinforcing Bars in Concrete,” Lead and Zinc, No. 285, pp. 24–31, 2017.

[5] Niwa, A., Choe, H., and Kanematsu, M., “Effect of Corrosion of Hot-Dip Galvanized Reinforcing Bars on Bond Performance with Concrete,” Proceedings of the Japan Concrete Institute, Vol. 40, No. 1, pp. 969–974, 2018.

[6] Belda Revert, A., Danner, T., and Geiker, M. R., “Carbonation and Corrosion of Steel in Fly Ash Concrete: Concluding Investigation of Five-Year-Old Laboratory Specimens and Preliminary Field Data,” Cement, Vol. 16, 2024.

[7] Choi, Y.-S., Kim, J.-G., and Lee, K.-M., “Corrosion Behavior of Steel Bar Embedded in Fly Ash Concrete,” Corrosion Science, Vol. 48, No. 7, pp. 1733–1745, 2006.

[8] Al-Saadoun, S. S., Rasheeduzzafar, and Al-Gahtani, A. S., “Corrosion of Reinforcing Steel in Fly Ash Blended Cement Concrete,” Journal of Materials in Civil Engineering, Vol. 5, No. 3, pp. 356–371, 1993.

[9] O’Reilly, M., Farshadfar, O., and Darwin, D., “Effect of Supplementary Cementitious Materials on Chloride Threshold and Corrosion Rate of Reinforcement,” ACI Materials Journal, Vol. 116, 2019.

[10] Takeshita, R., et al., “Corrosion Resistance of Galvanized Reinforcing Bars under Highly Alkaline Conditions,” Proceedings of the Japan Concrete Institute, Vol. 39, No. 1, pp. 967–972, 2017.

[11] Bouteiller, V., et al., “Corrosion Initiation of Reinforced Concretes Based on Portland or GGBS Cements: Chloride Contents and Electrochemical Characterizations versus Time,” Cement and Concrete Research, Vol. 42, pp. 1456–1467, 2012.

[12] Sasaki, J., Maruyama, K., Shimizu, K., and Yoneda, N., “Effect of Reinforcement Corrosion on Bond Behavior,” Proceedings of the Japan Concrete Institute, Vol. 13, No. 2, pp. 139–144, 1991.

Assessment of Residual Mechanical Characteristic Factors of Concrete Exposed to High-Temperature History Using Weighted Analysis Techniques

張 永雅※1、 金 時坤※1、金 源昌※1、李泰圭※2

Young-A Jang, Si-Gon Kim, Won-Chang Kim, Tae-Gyu Lee

ABSTRACT

Post-fire assessment of reinforced concrete structures hinges on the residual compressive strength of the material, yet the literature offers no consensus on which mix-design variables govern it: rankings produced by SHAP, permutation importance, and related single-model tools disagree across studies analysing overlapping data. This study applies a multi-method variable-importance framework—standardised regression coefficients as suppression diagnostics, dominance analysis (DA) as a relative-importance decomposition designed for correlated predictors, and Random Forest with Boruta shadow-feature testing as the non-linear counterpart—to a database of 492 mix–temperature observations of plain concrete compiled from 44 published heating experiments (N = 476 after predefined screening). Twelve predictors are analysed, covering exposure conditions and mix design including the oxide composition of the cement. Exposure temperature dominates the raw data (r = −0.82; 94 % of the dominance weight) and masks the mix-design signal: after temperature residualisation, all eleven remaining predictors are confirmed by Boruta, and DA attributes the largest weights to water (29.8 %), fine aggregate (21.3 %) and SiO2 (10.7 %). Temperature-stratified analysis reveals a systematic regime shift in the dominant descriptor, and grouped cross-validation shows that the model transfers across specimen series (R^2 = 0.863) but attenuates across source studies (0.559).

1. Introduction

The post-fire assessment of reinforced concrete structures turns on residual compressive strength: it decides whether a fire-damaged building is repaired and returned to service or demolished. Reliable prediction is difficult because thermal degradation is governed by coupled, non-linear physicochemical processes—release of bound water, portlandite decomposition and C-S-H breakdown, aggregate–paste expansion mismatch, and decarbonation beyond 600 °C—which interact with heating rate, moisture state and mixture proportions. The field has responded with machine learning: predictive models routinely report R^2 > 0.90, paired with post-hoc interpretation tools such as SHAP and permutation importance. Yet these tools have produced no consensus on which input variables physically matter; rankings shift with the algorithm, the interpretation technique and the data subset. The essential obstacle is that concrete composition data carry a multi-layered predictor-dependency structure—stoichiometric constraints among the cement oxides, the customary coupling of mix proportions, and experimental confounding whereby one mixture is tested at several peak temperatures—which destabilises single-model importance measures. This study therefore applies a multi-method variable-importance framework with cluster-robust inference to identify which mix-design variables govern residual strength after high-temperature exposure.

2. Materials and methods

A database of 492 mix–temperature observations of plain concrete was compiled from 44 published heating experiments comprising 95 mixture series. Predefined screening and per-temperature-level interquartile-range outlier removal reduced the sample to N = 476. Twelve predictors are analysed in three groups: exposure conditions (peak temperature T and

heating rate), mix proportions (cement, water, fine and coarse aggregate, density and Blaine fineness), and the oxide composition of the cement (SiO_2, CaO, Al_2O_3, Fe_2O_3). Because published heating programmes test one mixture at several temperatures, the database has a repeated-measures structure; all uncertainty statements therefore use a series-cluster bootstrap (2,000 resamples), and generalisation is assessed by random, series-grouped and study-grouped 10-fold cross-validation. The linear stage computes zero-order and partial correlations, variance inflation factors and standardised coefficients β* as suppression diagnostics, and dominance analysis (DA) decomposes R^2 into general dominance weights—the average incremental R^2 each predictor contributes across all subsets of the remaining predictors. Because temperature absorbs nearly all explainable variance, the eleven non-temperature predictors and the target were residualised on T, and the data were additionally stratified into four a-priori thermal bins (100–200, 300–450, 500–650 and 700–800 °C). The non-linear counterpart is Random Forest regression (400 trees) with permutation importance and a Boruta shadow-feature procedure (Bonferroni-corrected, $\alpha = 0.05$).

3. Results and discussion

Exposure temperature dominates the raw data ($r(T, R) = -0.82$) and absorbs 94.2 % of the explained variance of the full linear model. More importantly, it masks the mix-design signal: with T among the candidates, Boruta rejects every mix predictor except fine aggregate, whereas after temperature residualisation all eleven remaining predictors are confirmed and partial correlations grow two- to seven-fold. On the T-residualised data ($R^2 = 0.167$), DA attributes the largest weights to water (29.8 % of R^2), fine aggregate (21.3 %) and SiO_2 (10.7 %); however, the series-cluster bootstrap rank distributions of the leading predictors overlap, and no pairwise separation among the top five is decisive. Comparison of |β*| and DA rankings reveals suppression effects—coarse aggregate rises six positions under DA—so standardised coefficients alone are unreliable under this correlation structure. Temperature-stratified DA reveals a systematic regime shift consistent with cement chemistry: water leads below 450 °C (dehydration), fine aggregate at 500–650 °C (portlandite and C-S-H breakdown), and the heating rate (28.5 %) together with SiO2 at 700–800 °C (decarbonation). The non-linear analysis converges on fine aggregate as the strongest signal—permutation-importance rank 1 with 28.9 % of the total—consistent with threshold-type interfacial damage mechanisms that linear models understate. Grouped cross-validation bounds generalisation: the full model transfers across specimen series ($R^2 = 0.863$) but attenuates across source studies (0.559), and the mix-only signal transfers across series (0.553) but not across studies. A four-predictor core (water, fine aggregate, SiO2, coarse aggregate) retains 77 % of the full eleven-predictor R^2.

4. Conclusion

This study demonstrates that exposure temperature does not merely outweigh the mix-design signal in fire-exposed concrete—it conceals it: importance analyses that leave temperature in the predictor set spuriously reject nearly all mix variables. After residualisation, water, fine aggregate and SiO_2 carry the largest dominance weights, but their cluster-robust rank distributions overlap, indicating that single-method importance rankings in this field are unstable, helping to explain the disagreement in the literature. The dominant mix descriptor shifts systematically with the exposure regime, so mix effects are temperature-interactive and should be modelled as such, and random-split accuracies overstate transferability to unseen studies. Dominance analysis, Boruta testing and cluster-robust inference together offer a template for such analyses.

コンクリート床用表面強化剤の耐摩耗性の経時変化と向上過程

Time-Dependent Changes and Improvement Process in Wear Resistance of Surface Reinforcing Materials for Concrete Floors

濵田蒼太※1，福田眞太郎※2，古賀純子※3
Sohta HAMADA, Shintaro FUKUDA and Junko KOGA

ABSTRACT

In recent years, the expansion of the e-commerce market has increased AGV traffic in logistics facilities, making concrete floor wear a critical issue. This study aimed to elucidate the process of improving the abrasion resistance of surface reinforcing materials (SRMs), which densify the concrete surface layer. To this end, a Caster Running Abrasion Test was conducted on specimens approximately three years after SRMs application, alongside scratch tests evaluated up to 72 weeks post-application. The Caster Running Abrasion Test showed a significant improvement in abrasion resistance from the early post-application period to 1.5 years; however, no further enhancement occurred between 1.5 and 3 years. Similarly, the scratch test revealed that surface strength increased only up to 20–30 weeks post-application, after which it converged to a constant value.

1. Introduction

In recent years, the rapid growth of e-commerce and mail-order services has led to a significant increase in automated guided vehicle (AGV) traffic on concrete floors in warehouses and distribution facilities, making surface wear a critical concern. As a simple and effective countermeasure to improve abrasion resistance, the application of surface reinforcing materials (SRMs) to concrete surfaces has drawn growing attention. his method functions by allowing the SRM to penetrate the concrete matrix and generate reaction products such as sodium silicate hydrates, thereby densifying the surface layer.

Previous research[1)] reported that the abrasion resistance of concrete improves over time following the application of SRMs. However, the precise process of this improvement remains unclarified. Therefore, clarifying the relationship between abrasion resistance and elapsed time is essential for quality control after application. This report presents the evaluation results of abrasion resistance approximately three years after application, using test specimens identical to those in the full-scale Caster Running Abrasion Test reported in a previous study[1)], along with the subsequent time-dependent changes in surface strength determined by the scratch tests reported in another previous study[2)].

2. Materials and Methods

2.1 Caster Running Abrasion Test

A subset of the test specimens used in a previous study[1)] was employed (Table 1). SRMs 1 and 2 are sodium silicate-based compounds with solid contents of 10–20% and 3.0–7.0%, respectively.

Using a twist load tester (Photo 1), capable of reproducing the torsional loads generated by caster deflection during the transport of heavy loads, was used to apply a repeated load of 600 kgf to the specimens. The resulting wear depth was measured using steel angle and taper gauge. The testing

※1 日本 東京科学大学 環境・社会理工学院 建築学系 修士課程
※2 日本 東京科学大学 環境・社会理工学院 建築学系 准教授 博士(工学)
※3 日本 東京科学大学 環境・社会理工学院 建築学系 教授 博士(工学)

machine was stopped at appropriate intervals to measure the wear depth, and the test was continued up to 8,000 cycles. Measurements were taken at two locations within the ruts generated by the machine's movement, and the average of these two values was defined as the wear depth. At the time of testing, approximately three years had elapsed since the application of the SRMs.

Photo 1 Twist load tester

2.2 Scratch Test

Test specimens (Table 2) were prepared by applying three types of SRMs under various application and curing conditions to concrete substrates fabricated in a previous study[2]. For the scratch test, a scratch tester certified by the Japan Floor Coating Contractors Association was used to apply a vertical force of 1.0 kgf to the specimen surface. The width of the scratch generated by dragging the tester over a length of approximately 10 cm was measured using a crack scale and a magnifying loupe with a light. Since a certain correlation between scratch width and wear resistance has been reported[1], this test was conducted to estimate time-dependent changes in wear resistance. SRMs 1 and 2 were identical to those described in Section 2.1, whereas surface hardener 3 was a lithium silicate-based agent (content undisclosed).

3. Results and Discussion

3.1 Results of Caster Running Abrasion Test

Figure 1 shows the results of the abrasion tests on the six test specimens, along with the results reported in a previous study[1] for abrasion tests conducted 4 to 12 weeks after application of the SRMs (hereinafter referred to as "early post-application") and 83 to 92 weeks after application (hereinafter referred to as "1.5 years post-application"). Compared to the early post-application period, the wear depth decreased after 1.5 years, confirming an improvement in abrasion resistance. On the other hand, from 1.5 years to the 3-year mark evaluated in this study, the wear depths for five test specimens (excluding Bc1) remained at comparable levels or showed slight reductions. This indicates that further improvement in abrasion resistance by the SRMs cannot be expected between 1.5 and 3 years after application, suggesting that the chemical reactions contributing to the enhancement of abrasion resistance are completed within the first 1.5 years following application.

3.2 Results of Scratch Test

Figure 2 shows an example of the scratch test results. A decrease in scratch width was observed up to 20 to 30 weeks after application; however, no noticeable change was observed beyond 30 weeks, with the

Table 1 Overview of test specimens (Caster Running Abrasion Test)

Surface Finish	Curing Condition	SRMs1	SRMs 2
B Wooden trowel (1time) ・Steel trowel (2times)	a None	Ba1	Ba2
	b Water sprinkling (1time) ・sheet curing (5days)	Bb1	Bb2
	c Water ponding(5days)	Bc1	Bc2

Table 2 Overview of test specimens (Scratch Test)

Surface Finish	Curing Condition	Application and Curing Conditions	SRMs 1	SRMs 2	SRMs 3
Steel trowel	Water curing(5days)	A Application exceeding specified dosage	1-1A	2-1A	3-1A
		B Application immediately after placement	1-1B	2-1B	3-1B
		C Double application	1-1C	2-1C	3-1C
		D Water sprinkling curing	1-1D	2-1D	3-1D
		E Low-temperature curing (3°C)	1-1E	2-1E	3-1E

scratch width converging to approximately 0.35 mm, and no further improvement in surface strength was confirmed.

These trends were consistent across all types of SRMs as well as all application and curing conditions.

3.3 Discussion

Figure 3 shows a comparison of the wear depth after 8,000 cycles in the Caster Running Abrasion Test at each elapsed time following application. Although a reduction in wear depth was observed from the early post-application period through 1.5 years, no further reduction was observed between 1.5 and 3 years. Furthermore, as described in Section 3.2, the scratch test results indicate that no additional improvement in surface strength occurs after approximately 30 weeks following application. Therefore, within the scope of this study, it is estimated that the elapsed time required to ensure the enhanced abrasion resistance of concrete floors treated with a SRMs is approximately 30 weeks after application.

4. Conclusion

This study was conducted to elucidate the process of improving the abrasion resistance of concrete floors treated with surface SRMs. In the Caster Running Abrasion Test, no significant improvement in abrasion resistance was observed between 1.5 and 3 years after application. In contrast, the scratch test confirmed that abrasion resistance reached a stable level within approximately 30 weeks post-application. Although a certain correlation exists between the results of these two tests, they do not show exact consistency. Future work will investigate whether the hypothesis—that abrasion resistance levels off 30 weeks after SRMs application—can be similarly verified through the Caster Running Abrasion Test.

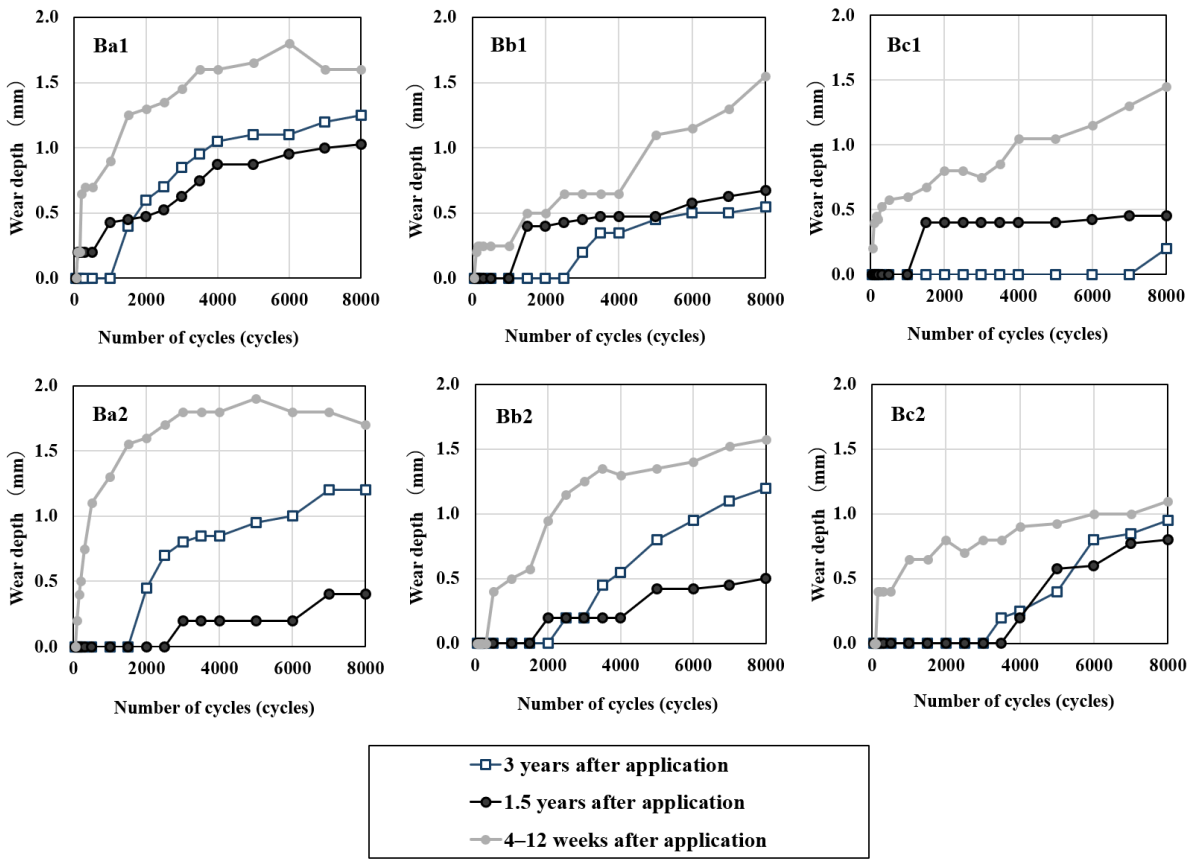

Fig. 1 Changes in wear depth over number of cycles in Caster Running Abrasion Test

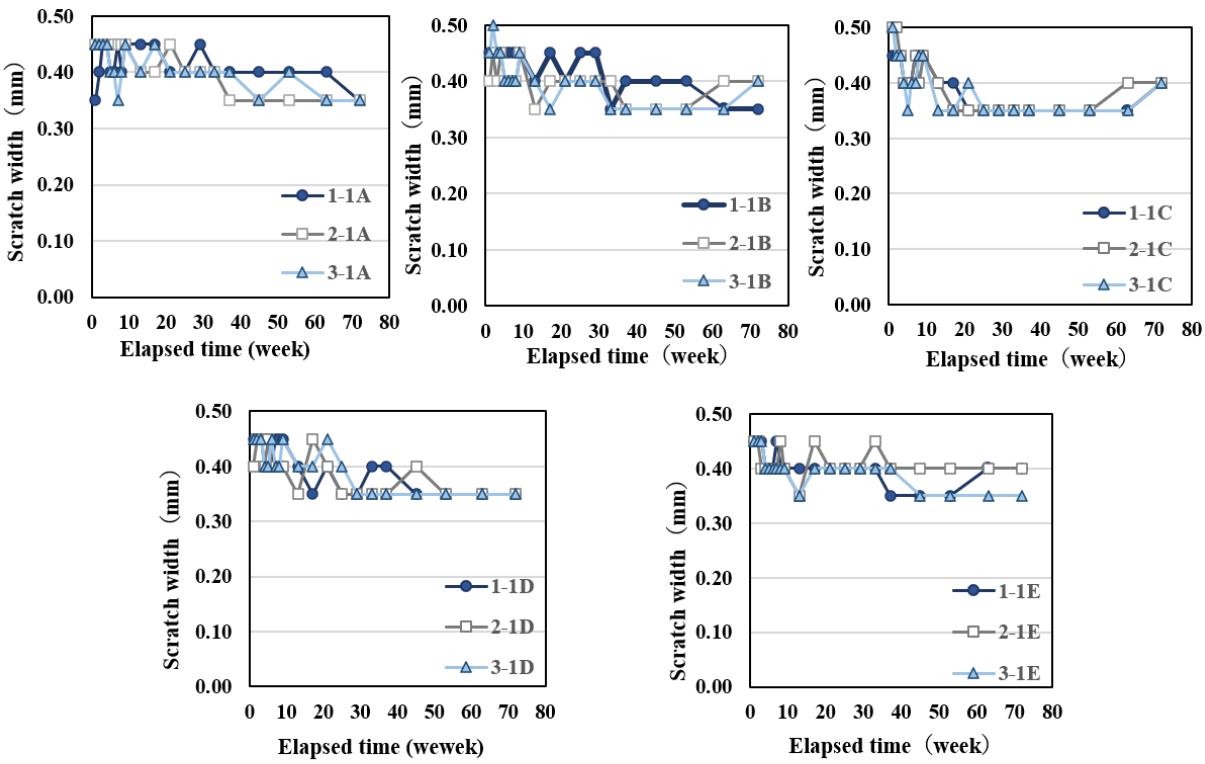

Fig. 2 Example of time-dependent changes in scratch width

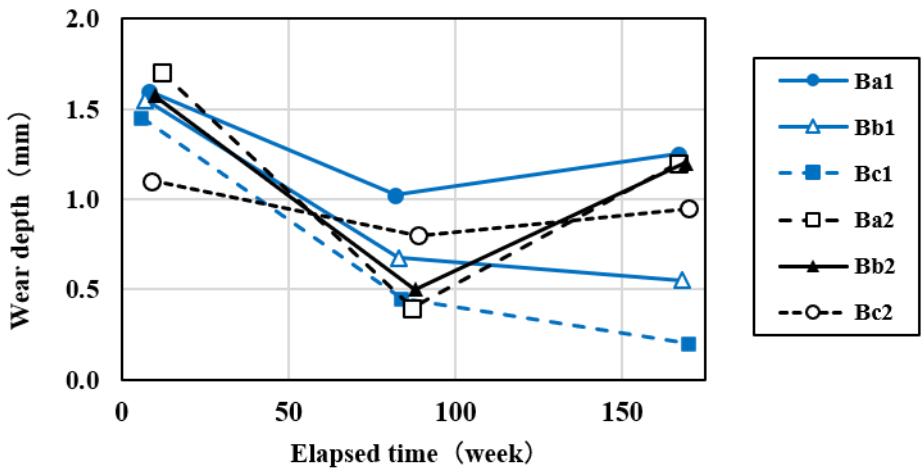

Fig.3 Comparison of wear depth after 8,000 cycles for different elapsed times after application

Reference

[1] Koga, J. et al., "Study on the Wear Resistance of Concrete Floors Treated with Surface Hardening Agents Under Caster Traffic," Journal of Structural and Construction Engineering (Transactions of AIJ), Vol. 90, No. 828, pp. 186–191, Feb. 2025.

[2] Seno, K. et al., "Verification of the Wear Resistance of Surface Hardening Agents for Concrete Floors Over Time," Proceedings of Annual Meeting, Architectural Institute of Japan (Materials and Construction), pp. 835–836, Jul. 2025.

建物区画火災における入口部での外部熱流束を用いた内部火災状況の検出可能性に関する検討

Review of the Possibility of Detecting Internal Fire Conditions Using External Heat Flux at Entrances in Building Compartment Fires

南榮鎭※1、張永雅※1、金時坤※2、李泰圭※3

Young-Jin, Nam, Young-A Jang, Si-Gon Kim, Tae-Gyu Lee

ABSTRACT

This study compared the explicitness and decision-making competence of domestic and international laws and standards regarding internal entry into structured fires. Data from domestic SOPs, Japan's FDMA, the U.S. OSHA, NIOSH, and NIST, Canada's WorkSafeBC, Australia's NSW, and the United Kingdom were classified into 10 domains and coded as S=3, A=2, B=1, and 0=0 to calculate the Quality of Inclusion Rating (QRI). EV1 and EV2 were also distinguished by examining source, legal status, scope of application, behavioral linkage, and measurement completeness. Although the QRIs of Korea and the U.S. were 83.3, the functions of their standards differed; conversely, while the WorkSafeBC had a score of 63.3, the feasibility of personnel and rescue team standards was high. The candidate worksheet scored 93.3 but lacked qualified quantitative criteria. QRI is a document explicitness index rather than a safety level, and a benchmark combining international standards by domain was deemed more valid than national rankings. The entry decision requires a non-compensatory structure that sequentially reviews mission benefits, personnel, SCBA, communications, exit routes, and rescue capabilities, risks and uncertainties, and withdrawal and re-entry conditions. As this result is a preliminary analysis evaluating the reference value of international standards, subsequent double-coding and verification of scenarios and incident data are required.

1. Introduction

Internal entry into a structural fire is a dynamic decision that requires simultaneous consideration of rescuer survivability, fire behavior, thermal and toxic environments, structural stability, and the resources and escape routes of the entry team. However, due to time pressure and information uncertainty, the judgments of the commander and the field safety officer may differ even in the same situation. Domestic standard operating procedures for disaster sites include criteria regarding entry team organization, communication, air breathing apparatus, emergency escape, and collapse risk; however, some quantitative values require further verification regarding their connection to the measurement target, location, equipment, exposure time, and actions to be taken upon exceeding [1].

International standards also do not provide universal allowable entry temperatures or gas concentrations. OSHA's two-person entry and two-person standby and SCBA are prerequisites for entry, not standards that guarantee the safety of the fire compartment [2].

※1 大韓民国 セミョン大学 消防防災工学科 博士課程

※2 大韓民国 セミョン大学 消防防災工学科 修士課程

※3 大韓民国 セミョン大学 消防防災学科 教授

WorkSafeBC specifically defines the personnel and preparation timelines for the entry and rescue teams [3], whereas Japan presents an air management procedure that links the scheduled escape time, remaining air volume, escape time, and low-pressure alarm [4]. Accordingly, this study evaluated the comparative reference value that each document group provides for internal entry judgments, rather than the superiority or inferiority of countries.

2. Research methods

The subjects of analysis were domestic SOPs, Japanese FDMA, US OSHA, NIOSH, NIST, WorkSafeBC, NSW RFS, and UK public verification data. The unit of analysis was set to individual clauses, and 10 domains were applied: D1 (Claims/Survival), D2 (Fire Behavior), D3 (Thermal Environment), D4 (Atmospheric Environment), D5 (Structural Stability), D6 (Readiness for Entry), D7 (PPE/SCBA), D8 (Command/Crew Management/Re-evaluation), D9 (RIT/Mayday), and D10 (Withdrawal/Re-entry).

Each domain was coded as S=3, A=2, B=1, and 0=0, and the QRI was calculated according to Equation.

3. Results and Discussion

Although the QRIs of Korea and the United States were identical at 83.3 points, the functions of the standards differed. The domestic SOPs had high domain comprehensiveness, while the U.S. document group combined OSHA's legal prerequisites with research indicators from NIOSH and NIST. BC had a QRI of 63.3 points but included criteria directly linked to action, such as an entry team of at least two firefighters and a rescue team of at least two firefighters, with the rescue team established before deployment of a second entry team and within 10 minutes of the initial attack and within 10 minutes of the initial attack. On the other hand, Japan lacked S but demonstrated procedural strengths by linking remaining air volume with escape time.

The candidate worksheet had the highest QRI at 93.3 points, but it was not converted to EV1 or EV2 because none of the eight S domains met the conditions for source, scope of application, measurement protocol, or action linkage. Additionally, CO 1,200 ppm, O_2 19.5%, SCBA 30 minutes, and heat flux 20 kW/m² could not be used as standalone entry acceptance lines because they were IDLH classification, respiratory protection/equipment qualification, or experimental fire phenomenon indicators, respectively [2, 5, 6].

4. Conclusions

QRI merely indicated the explicitness of the standards and did not signify national safety levels or actual judgment outcomes. The foreign documentation pool demonstrated varying strengths across domains, such as personnel and respiratory protection, air management, dynamic reassessment, and collapse risk, making it difficult to explain the entire entry process based on a single standard. Therefore, it is appropriate to utilize domain-specific standards, which ensure evidence and actionability, as a comparative benchmark rather than total national scores. Further verification through double coding, scenarios, and field data is required.

Reference

[1] National Fire Agency of Korea, *Standard Operating Procedures for Disaster Scene Operations*, 2025. [In Korean]

[2] Occupational Safety and Health Administration, *29 CFR 1910.134—Respiratory Protection*, U.S. Department of Labor.

[3] WorkSafeBC, *Occupational Health and Safety Regulation, Part 31: Firefighting*, Workers' Compensation Board of British Columbia.

[4] Fire and Disaster Management Agency, *Safety Management Manual for Firefighting and Training Operations*, Ministry of Internal Affairs and Communications, Japan, 2026. [In Japanese]

[5] Peacock, R.D., Reneke, P.A., Bukowski, R.W., and Babrauskas, V., "Defining flashover for fire hazard calculations," *Fire Safety Journal*, Vol. 32, No. 4, pp. 331–345, 1999. https://doi.org/10.1016/S0379-7112(98)00048-4

[6] National Institute for Occupational Safety and Health, *Preventing Deaths and Injuries to Fire Fighters by Establishing Collapse Zones at Structure Fires*, DHHS (NIOSH) Publication No. 2014-120, 2014.

築 40 年を経過した地下遊水池コンクリートの物理的・化学的特性

Physical and Chemical Properties of Concrete in a 40-Year-Old Underground Retention Basin

井浦耀太※1、濱崎仁※2、福田杉夫※3
Yota Iura, Hitoshi Hamasaki, Sugio Fukuda

ABSTRACT

An approximately 40-year-old unwaterproofed reinforced concrete retention basin was investigated to clarify long-term moisture effects on underground concrete. Through-wall cores from four locations were examined for moisture, carbonation, pH, total porosity, compressive strength, and SEM-EDS characteristics. Moisture generally increased toward the soil side, while carbonation was suppressed under highly moist conditions and progressed further at the relatively dry N1 location. Interior porosity was generally comparable, with localized increases near reinforcement and both surfaces of S1. S1 showed the highest compressive strength despite comparable central porosity, indicating that strength was not governed by total porosity alone. SEM-EDS showed slightly lower mean Ca/Si and Ca/(Si+Al) ratios on the soil side, but no clear systematic compositional change. Overall, long-term moisture effects varied with location and property, indicating the need for evaluation using multiple indicators.

1. Introduction

Underground reinforced concrete (RC) structures are exposed to moisture from backfill soil and groundwater. The authors previously reported that a sound waterproofing layer reduces the influence of the surrounding moisture environment [1]. In unwaterproofed retention basins without a superstructure, however, the outer wall is in direct contact with soil, while the inner surface is exposed to rainfall-induced water-level fluctuations, solar radiation, and airflow.

This study investigates an approximately 40-year-old unwaterproofed RC retention basin to clarify how long-term moisture supply from backfill soil affects moisture distribution, carbonation behavior, pore structure, compressive strength, and elemental composition through the wall thickness.

2. Outline of Investigation

2.1 Target Structure and Environment

Table 1 Overview of the investigated structure

Item	Description
Location	Tsurugashima City, Saitama Prefecture
Year of completion	1986
Structure	Reinforced concrete retention basin
Waterproofing	None
Wall thickness	320–370 mm
Core locations	N1, W1, W2, S1
Core diameter	100 mm
Investigation date	January 22 and 23, 2026

※1 芝浦工業大学大学院 理工学研究科 建築学専攻 修士課程
※2 芝浦工業大学 建築学部 建築学科 教授 博士(工学)
※3 芝浦工業大学 建築学部 建築学科 客員研究員 博士(工学)

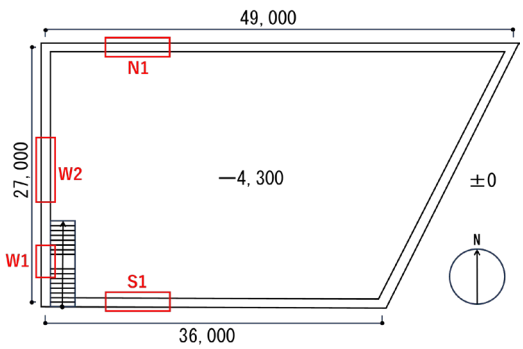

Fig. 1 Plan of the retention basin

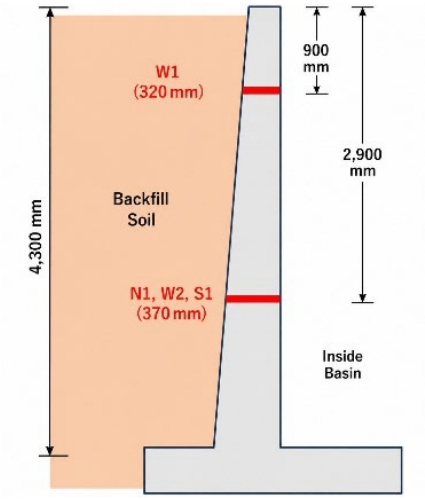

Fig. 2 Cross-sectional view

Photo 1 Retention basin during rainfall

The investigated structure was an approximately 40-year-old unwaterproofed RC retention basin in Tsurugashima City, Saitama Prefecture. Its outer walls were in direct contact with backfill soil, while the inner surfaces were exposed to rainfall-induced water-level fluctuations. Operational records showed that the water level reached about 20% of the basin depth for roughly 30 days annually and about 50% four or five times a year when daily precipitation exceeded 50 mm, leaving the lower walls frequently wet. On January 22–23, 2026, 100-mm-diameter through-wall cores were collected from N1, W1, W2, and S1 (Figs. 1 and 2).

2.2 Investigation Items and Measurement Methods

(1) Environment and Moisture Conditions

The CO_2 concentration near the backfill soil was measured through the core holes, and the water content of the collected soil was determined. Concrete moisture content was measured by oven-drying at 105°C using depth-specific powder samples collected from two 16-mm-diameter boreholes, based on the method proposed by Kino et al. [2]. Surface-layer moisture was also measured using an electrical-resistance concrete moisture meter.

(2) Carbonation Depth

Carbonation depth was measured on the split surfaces after compressive strength testing in accordance with JIS A 1152 [3].

(3) pH Distribution

Cores were sliced at 10-mm intervals and pulverized. The pH of hot-water extracts prepared at a solid-to-liquid ratio of 1:5 was measured in accordance with JIS Z 8802 [4].

(4) Compressive Strength

Compressive strength was measured in the atmospheric-side and central regions of the cores in accordance with JIS A 1107 [5].

(5) Total Porosity

Quarter-disk specimens approximately 45 mm in radius, 90° in central angle, and 20 mm in thickness were prepared from the cores. The specimens were evacuated in a vacuum desiccator for 1 h and water-saturated for 24 h. After the saturated surface-dry and submerged masses were measured, the specimens were oven-dried at 105°C to a constant mass. Total porosity was calculated from these masses using the Archimedes method. The water-accessible porosity determined by this method is hereafter referred to as total porosity.

(6) SEM-EDS Analysis

SEM-EDS analysis was conducted on selected fields containing cement paste in the central and soil-side regions of S1. Area analyses were performed to obtain Ca, Si, and Al atomic concentrations and the Ca/Si and Ca/(Si+Al) ratios. Supplementary point analyses were also conducted in the central region to examine local compositional variation.

Table 2 Summary of investigation results

Category	Item	Side/region	N1 (North wall)	W1 (West, upper)	W2 (West, lower)	S1 (South wall)
Soil	Water content (% by dry mass)	–	90.7	68.7	106.0	101.5
	CO_2 concentration (ppm)	–	641	574	560	572
Concrete	Gravimetric moisture content at deepest point (%)	–	5.06	6.20	8.93	13.29
	Concrete cover (mm)	–	34.0	41.0	61.3	104.0
	Carbonation depth (mm)	Atmospheric side	47.4	36.9	40.7	32.2
		Soil side	0.8	1.1	1.2	3.6
	Carbonation coefficient (mm/√year)	Atmospheric side	7.50	5.84	6.43	5.10
		Soil side	0.12	0.17	0.18	0.56
	Compressive strength (N/mm²)	Atmospheric-side region	24.4	25.3	25.9	28.9
		Central region	25.9	26.3	26.7	30.1

3. Results and Discussion

3.1 Moisture Conditions in Soil and Concrete

The soil water content (Table 2) was 90.7% at N1 and 101.5% at S1. On the west wall, W2 in the lower section showed a higher value (106.0%) than W1 in the upper section (68.7%), indicating differences in water retention with location and height. The gravimetric moisture content profiles (Fig. 3) were approximately 1% near the atmospherically exposed surface at all locations and generally increased toward the soil side. The deepest-point moisture contents were 5.06%, 6.20%, 8.93%, and 13.29% at N1, W1, W2, and S1, respectively. Thus, the measured moisture conditions within the concrete generally reflected those of the surrounding soil, particularly at W2 and S1. The exceptionally high S1 value may have been influenced by water retained near the soil–concrete interface. During specimen preparation, the soil-side portion of S1 was observed to be locally friable and prone to disintegration, although the cause could not be identified from visual observation alone. In addition, surface moisture measured using the electrical-resistance moisture meter (Fig. 4) was higher at S1 (3.5%) than at N1 (2.2%) at a depth of 50 mm, indicating differences in surface drying conditions among wall orientations.

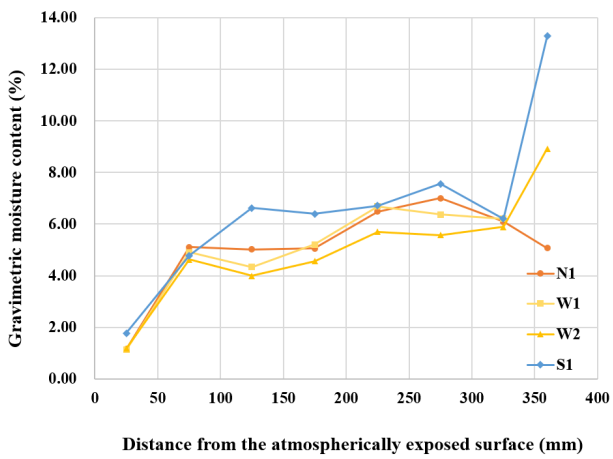

Fig. 3 Gravimetric moisture content profile

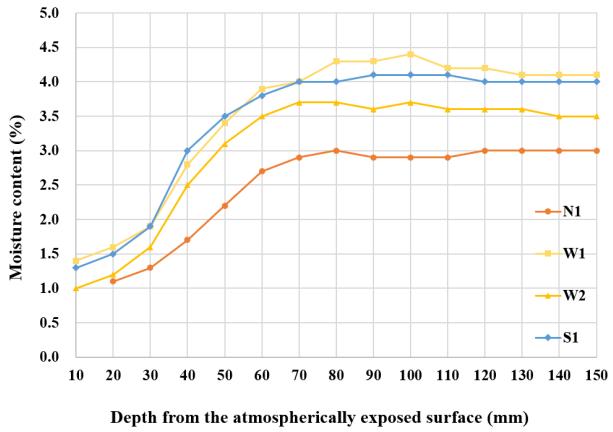

Fig. 4 Moisture content profile (HI-800)

3.2 Carbonation Behavior and pH Discrepancies

Figure 5 shows the pH profiles obtained from sliced and pulverized core samples, and Table 2 summarizes the carbonation depths. On the soil side, all cores generally maintained high pH values, and the carbonation depths were limited to 0.8–3.6 mm. Although the CO_2 concentration near the backfill soil ranged from 560 to 641 ppm, CO_2 diffusion was considered to have been restricted by the high degree of pore saturation. In contrast, the depth of pH reduction on the atmospherically exposed side varied among the sampling locations. At N1, the pH decreased to a depth of approximately 40 mm, and the carbonation depth of 47.4 mm exceeded the concrete cover thickness of 34.0 mm. The corresponding carbonation coefficient was 7.50 mm/√year, the highest among the investigated locations. At S1, which exhibited a relatively high moisture content, the carbonation depth was the smallest at 32.2 mm, with a carbonation coefficient of 5.10 mm/√year. However, the powder sample collected at a depth of 10–20 mm showed a pH of 10.9 within the region judged to be carbonated by the phenolphthalein method. The differences in carbonation behavior among the orientations were attributed to the balance between moisture supply from the backfill soil and drying from the atmospherically exposed surface. At N1, the atmospherically exposed inner surface faced south and had a relatively low moisture content, allowing both CO_2 diffusion and carbonation reactions to proceed. In contrast, the atmospherically exposed inner surface of S1 faced north and was subjected to less solar radiation and slower drying, resulting in a relatively high surface moisture content and restricted CO_2 diffusion. At W2, the pH locally decreased to approximately 7. This behavior may have been influenced by long-term local moisture conditions, including possible movement of alkaline components, although the mechanism could not be identified in the present investigation. The discrepancy at S1 between the powder-extraction pH and the carbonation depth determined by the phenolphthalein method may reflect differences in the spatial scale and chemical conditions represented by the two measurement methods.

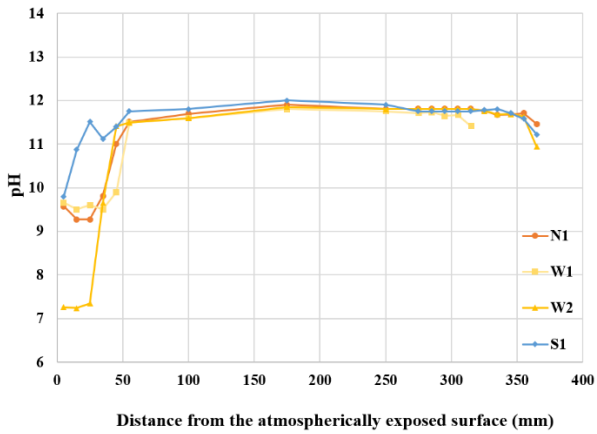

Fig. 5 pH profile through the wall

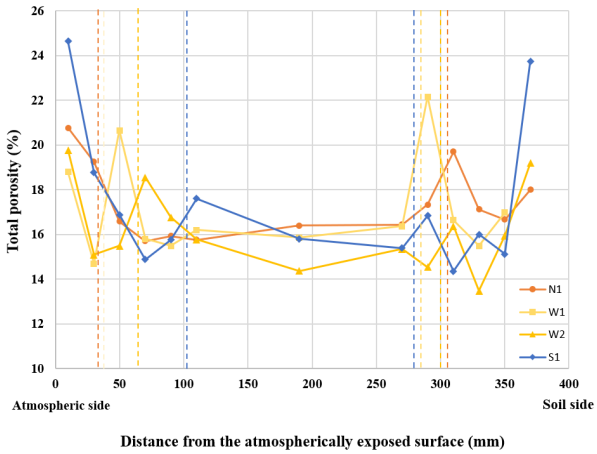

Fig. 6 Total porosity profile through the wall

Note: Colored dashed lines indicate reinforcement positions.

3.3 Total Porosity and Compressive Strength

Figure 6 shows the total porosity profiles through the wall. Excluding surface regions and reinforcement positions, total porosity was generally 14–18% at all locations, with no systematic difference among N1, W1, W2, and S1. Local increases at several depths in N1, W1, and W2 approximately corresponded to reinforcement positions and may reflect local heterogeneity around the reinforcement.

At S1, total porosity reached approximately 24% near both the atmospherically exposed and soil-side surfaces. The soil-side value was about 5–7 percentage points higher than the corresponding values at the other locations. However, the central region of S1 was comparable to the other cores, indicating that the higher porosity was localized near the surfaces rather than distributed through the wall thickness. Long-term

moisture supply from the backfill soil may have contributed to the high soil-side value. However, because a similarly high value occurred near the atmospherically exposed surface, backfill moisture alone cannot explain it. Surface exposure conditions, original material characteristics, and local heterogeneity may also have contributed.

Compressive strength was highest at S1, reaching 28.9 N/mm² in the atmospheric-side region and 30.1 N/mm² in the central region. Because the central porosity of S1 was comparable to those of the other cores, its higher strength cannot be explained by total porosity alone. Pore-size distribution, pore connectivity, microcracking, and local material variability may also have influenced the strength. Further evaluation of pore structure is therefore needed to clarify this relationship.

3.4 SEM-EDS Analysis

Figure 7 compares representative SEM images and EDS elemental maps of Ca, Si, and Al in the central and soil-side regions of S1. Heterogeneous elemental distributions were observed in both regions. Because the analyzed fields contained multiple phases at the millimeter scale, the area analyses represent average compositions of the selected fields rather than those of individual hydration phases.

As shown in Table 3, the mean Ca/Si ratios were 0.60 in the central region and 0.56 on the soil side, while the corresponding Ca/(Si+Al) ratios were 0.50 and 0.48, respectively. Decalcification associated with calcium leaching or carbonation can decrease the Ca/Si ratio; therefore, the slightly lower ratios on the soil side are qualitatively consistent with possible local decalcification. The similar tendency observed for Ca/(Si+Al) also supports this interpretation. However, the differences were small and the ranges of the individual measurements overlapped.

The area-averaged Ca/Si ratios were relatively low. Supplementary point analyses in the central region identified Ca-Si-rich locations with Ca/Si ratios of 1.59 and 1.99, showing that local compositions differed substantially within the analyzed cement paste. These results indicate compositional heterogeneity and suggest that the area-averaged ratios should not be interpreted directly as the Ca/Si ratio of a single C-S-H phase.

The high porosity and local friability observed near the soil-side surface of S1, together with the slightly lower area-averaged Ca-based ratios, may indicate localized microstructural alteration under long-term moisture exposure. However, high porosity was also observed near the atmospheric surface, and no clear systematic compositional shift was identified by SEM-EDS. Thus, the observed physical characteristics cannot be attributed specifically to calcium leaching from the present results.

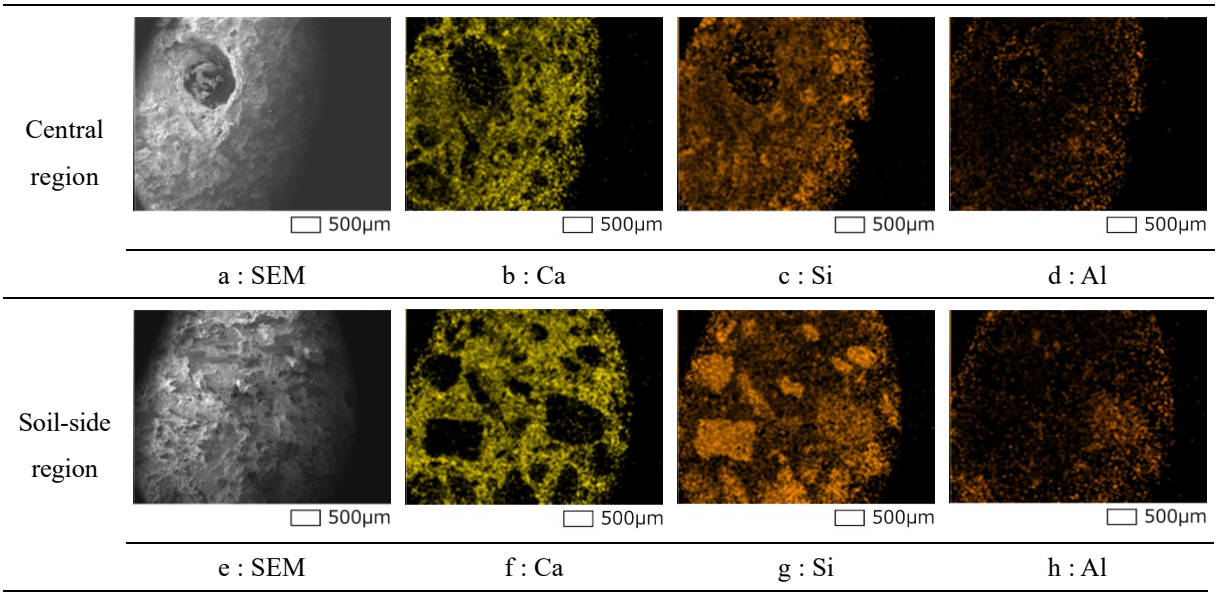

Fig. 7 SEM images and EDS elemental maps of S1: (a–d) central region and (e–h) soil-side region

Table 3 Quantitative SEM-EDS area-analysis results for the central and soil-side regions of S1

Region	Ca (at.%)	Si (at.%)	Al (at.%)	Ca/Si	Ca/(Si+Al)
Central region	7.39	13.48	2.62	0.55	0.46
	7.72	11.85	2.57	0.65	0.54
Central region mean (n=2)	7.56	12.67	2.60	0.60	0.50
Soil-side region	7.24	11.80	1.97	0.61	0.53
	6.10	12.12	1.73	0.50	0.44
	6.49	12.19	2.34	0.53	0.45
	7.55	12.85	2.64	0.59	0.49
Soil-side region mean (n=4)	6.85	12.24	2.17	0.56	0.48

Note: Ca/Si and Ca/(Si+Al) are area-averaged atomic ratios and do not represent a single hydration phase.

4. Conclusions

The investigation of an approximately 40-year-old unwaterproofed reinforced concrete underground retention basin led to the following conclusions.

(1) Concrete moisture generally increased toward the soil side and reflected the water-retention conditions of the backfill soil, while surface moisture varied with wall orientation and drying conditions.

(2) Carbonation was suppressed under highly moist conditions, particularly on the soil side and on the atmospheric side at S1, but progressed further at the relatively dry N1 location.

(3) Total porosity in the wall interior was generally comparable among the four locations. Local increases near reinforcement and both surfaces of S1 indicated localized pore-structure heterogeneity.

(4) S1 showed the highest compressive strength despite central porosity comparable to the other locations, indicating that pore-size distribution and other microstructural characteristics should also be considered.

(5) SEM-EDS showed slightly lower mean Ca/Si and Ca/(Si+Al) ratios on the soil side. Although this tendency is consistent with possible local decalcification, the overlapping values and lack of a clear compositional shift do not provide sufficient evidence of calcium leaching.

Overall, long-term moisture effects varied among locations and properties, indicating the need for assessment using multiple indicators.

Acknowledgments

We would like to express our deepest gratitude to everyone at the Saitama Plant, Waterproofing Production Department, Tajima Roofing Inc., for their cooperation in this investigation.

References

[1] Y. Iura et al., Physical property evaluation and discussion of underground concrete structures and waterproofing layers in a 94-year-old reinforced concrete building, Proceedings of the 2025 Annual Meeting of the Japan Society for Finishings Technology, pp. 185–188, 2025. (in Japanese)

[2] Kino et al., Measurement of moisture content and electrical resistivity using drilling powder: Various nondestructive tests on a full-scale reinforced concrete wall specimen exposed outdoors for 22 years, Part 5, Summaries of Technical Papers of the Annual Meeting, Architectural Institute of Japan, pp. 55–56, 2025. (in Japanese)

[3] JIS A 1152:2018; Method for Measuring Carbonation Depth of Concrete. Japanese Standards Association: Tokyo, Japan, 2018.

[4] JIS Z 8802:2011; Methods for Determination of pH of Aqueous Solutions. Japanese Standards Association: Tokyo, Japan, 2011.

[5] JIS A 1107:2022; Method of Sampling and Testing for Compressive Strength of Drilled Cores of Concrete. Japanese Standards Association: Tokyo, Japan, 2022.

論文

中性子回折法を用いた鉄筋の腐食がコンクリートとの付着性能に及ぼす影響に関する研究

林　颯太朗*1，　周　佳遠*1，　小林　謙祐*2，　KIM　JUNHO*3，　兼松　学*4

Experimental Research on the Influence of Steel Corrosion on Bond Performance with Concrete Using Neutron Diffraction Method

Hayashi SOUTARO *1, Jiayuan ZHOU*1, Kensuke Kobayashi*2, Junho KIM*3 and Manabu KANEMATSU*4

ABSTRACT：To clarify the influence of steel bar corrosion on bond performance with concrete, this study measured the stress distribution of PC steel bars with three different rib shapes embedded in concrete using the neutron diffraction method (RESA) at JRR-3. Sound and corroded specimens with three rib geometries, comprising combinations of rib angle (45°, 90°) and rib spacing (3.0, 12.0 mm), were tested; the corroded specimens were subjected to accelerated corrosion up to an integrated current density of 153.42 mA·h/cm². For sound bars, the steepest stress-decay gradient was obtained for the smallest rib angle and rib spacing, and increasing either the rib angle or the rib spacing made the gradient gentler. After corrosion, the stress-decay gradients converged to a similar trend regardless of rib shape. The anchorage length and bond stress, backcalculated from the stress distribution curves, showed that corrosion increased bond stress and decreased anchorage length, with values converging across rib shapes.

Keywords：Reinforced concrete, Corrosion, Bond, Rib, Neutron diffraction method

1. はじめに

鉄筋コンクリート構造物において，鉄筋とコンクリートの付着性状は，外力を適切に伝達する上で重要な役割を果たしており，その把握は構造物の性能評価や合理的な設計に不可欠である。これまで，健全な黒皮鉄筋を対象として，節間隔や節角度などの表面形状の違いが付着性状に及ぼす影響について，多くの研究が行われてきた。[1)]

一方，実構造物では，塩害や中性化などの使用環境や経年劣化により鉄筋腐食が生じることがある。腐食が進行すると，鉄筋断面の減少に加え，鉄筋表面に生成した腐食生成物が節形状を覆い，さらに腐食膨張圧がコンクリートに作用するため，付着性状は健全時とは異なる挙動を示すと考えられる。[2)]しかし，腐食のような鉄筋の表面状態の変化を考慮し，表面形状との関係を含めて付着性状を評価した研究は限られている。

また，付着性状を測定する手段として，鉄筋にひずみゲージを貼付する方法が挙げられる。しかし，この方法ではゲージの貼付自体が鉄筋とコンクリートの界面の付着性状に影響を及ぼすため，鉄筋内部に生じる応力分布を直接把握することは困難である。一方，中性子回折法では中性子の高い透過性を利用し，コンクリート内部に埋め込まれた鉄筋の内部応力分布を非破壊的に測定することが可能である。[3)]本研究では，節角度および節間隔を変化させた表面形状の異なる鉄筋を対象に，健全時および腐食時の鉄筋の応力分布を中性子回折法により非破壊的に取得した。得られた応力分布から鉄筋応力勾配および実効定着長を算出し，鉄筋の表面形状と腐食の有無が付着挙動に及ぼす影響について検討した。

2. 実験概要

2.1 実験水準

実験水準を Table 1 に示す。実験水準は節角度及び節間隔，腐食の有無とし，いずれの水準も節高さ 0.7mm，節頂点幅 1.0mm とした。いずれも PC 鋼棒を切削加工することにより作製した。なお節角度、節高さ、節間隔の定義は fig.1 の通り。

*1 東京理科大学大学院創域理工学研究科建築学専攻　修士課程
*2 東京理科大学大学院創域理工学研究科建築学専攻　博士後期課程
*3 東京理科大学創域理工学部建築学科　助教
*4 東京理科大学創域理工学部建築学科　教授

Table 1 Experimental parameters

Parameter	
Rib angle (°)	45, 90
Rib spacing (mm)	3.0, 12.0
Corrosion	Sound, Corroded

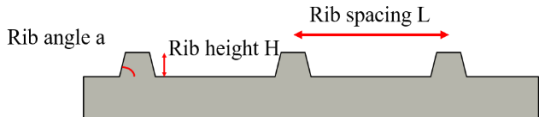

Fig. 1 Rib geometry

中性子回折法による測定は，節角度 45°・節間隔 3.0mm，節角度 45°・節間隔 12.0mm，節角度 90°・節間隔 3.0mm の 3 水準について実施した。

2.2 試験体概要

試験体の概要を Fig. 2 に示す。コンクリート母材は幅 40mm×高さ 80mm×長さ 170mm とし，中心部に長さ 190mm の PC 鋼棒（径 10mm）を配置した。付着区間は 140mm，非付着区間は 30mm とし，非付着区間は打設時に設置した油塗布ゴムホースを硬化後に抜き取ることで作製した。

中性子透過性を高めるため薄肉断面とし，割裂破壊防止のためφ25mm の穴を設けたアルミ角パイプにコンクリートを充填して作製した。型枠はコンパネ製とし，アルミ角パイプの外側に設置して打設した。

コンクリートの材料および調合を Table 2，Table 3 に示す。打設 24 時間後に脱型し，材齢 14 日まで 20℃水中養生を行った後，気中乾燥および 60℃機械乾燥（材齢 27 日，55 日まで）を行った。乾燥後の試験体表面にはアルミテープを貼付し，材齢 55 日から 5 日間で中性子回折法による応力測定を実施した。測定は 1 水準につき 1 体とした。

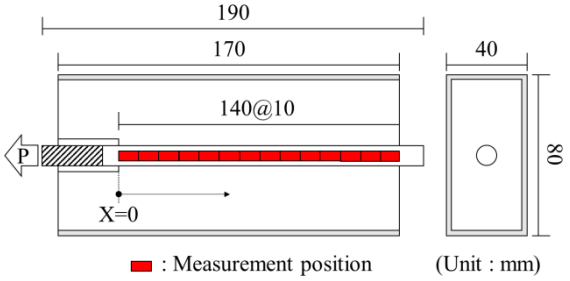

Fig. 2 Specimen overview and measurement points

Table 2 Materials of concrete

Material	Type / properties
Water	Deionized water
Cement	Ordinary Portland cement Density 3.16 g/cm³
Fine aggregate	Land sand, Kakegawa Oven-dry density 2.58 g/cm³
Coarse aggregate	Crushed stone, Ome
AE water reducer	Type N

Table 3 Mix proportions of concrete

W/C (%)	S/a (%)	Unit weight (kg/m³)				Ad (g)	SL (cm)	Air (%)
		W	C	S	G			
60	46	175	294	808	993	C*1.2%	18.5	4.1

2.3 鉄筋の腐食促進方法

鉄筋の腐食促進は電食試験により行った。試験体上下面をエポキシ樹脂で保護後，3%NaCl 水溶液に浸漬し，鉄筋をアノード，銅板をカソードとして電流密度 0.455mA/cm² の直流電流を印加した。

丹羽ら[4)]の研究を参考に，最大付着応力度が得られる積算電流密度 153.42mA・h/cm²（通電時間 337.39h）まで腐食させた。なお，健全時の質量が不明であったため，質量減少率による腐食量の定量化は行っていない。

2.4 中性子回折法の測定概要

(1) 中性子回折法の原理

鉄筋応力の測定には，日本原子力研究開発機構の研究用原子炉 JRR-3 に設置された中性子応力測定装置 RESA を用いた。中性子回折法（角度分散法）により，式(1)のブラッグの回折条件式を満たす回折角の変化Δθから弾性ひずみを算出する。

$$2d\sin = n\lambda \qquad (1)$$

ここで，d：格子面間隔，θ：回折角，n：回折次数，λ：入射中性子線の波長である。

弾性ひずみに回折弾性係数（20.0kN/mm²）を乗じて鉄筋応力を算出した。乾燥収縮等の影響を除くため，低応力載荷状態の格子面間隔を初期状態とした。

RESA の概要を Fig. 3 に示す。研究用原子炉か

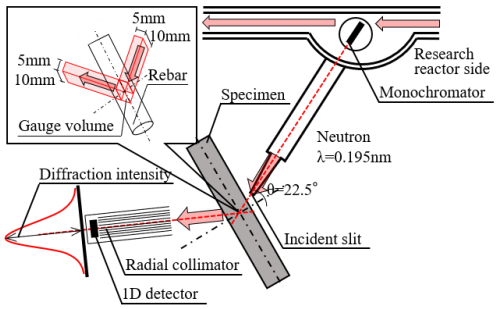

Fig. 3 Overview of RESA

ら 0.159nm の単一波長の熱中性子を取り出し，5mm×10mm の入射スリットによって整形された中性子が試料に照射され，試料により回折された中性子のみがラジアルコリメータを通過し 1 次元検出器によって検出される。この際，検出器では到達した中性子の回折角ごとの個数を一定時間計測しており回折角度を取得する。

(2) 測定および載荷条件

応力測定位置は計 14 点とし，1 点あたり 40 分測定した。X=0mm および X=150mm は，それぞれ理論値 181N/mm²および 0N/mm²としてプロットした。

目標載荷応力は鉄筋(SD295)の長期許容応力度 195MPa とし，低応力(14MPa)載荷時との差分から鉄筋応力分布を得た。測定中のクリープによる応力緩和は皿バネで抑制した。

3. 実験結果および考察

Fig. 4(a)に腐食なしの PC 鋼棒の応力分布を示す。a45_L3.0 の応力分布の傾きが最も大きく，節角度の増大，節間隔の増大のいずれによっても傾きが小さくなっていることが分かる。Fig. 4(b)に腐食ありの PC 鋼棒の応力分布を示す。腐食後は全試験体で応力減少勾配が概ね同様の傾向となり，腐食した補強材の応力分布は，節形状の影響をほとんど受けないことが分かる。また，a45_L3.0 を除く 2 水準では，腐食した試験体の傾きが大きくなっている。

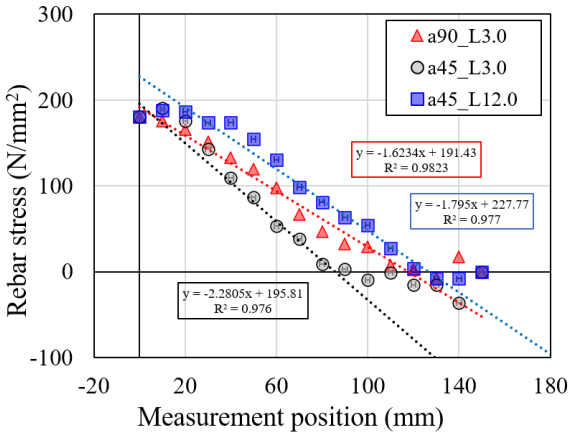

(a) Sound

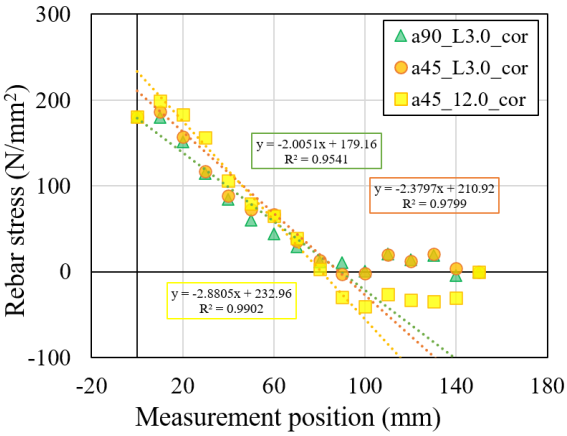

(b) Corroded

Fig. 4 Stress distribution of steel bar

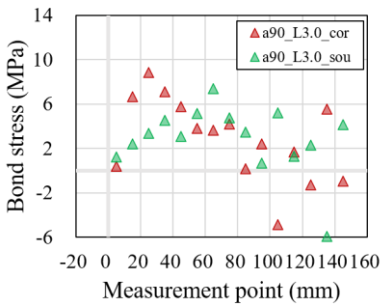

(a) a90_L3.0

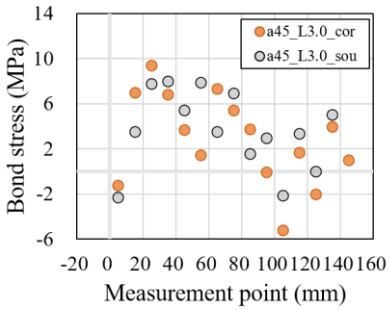

(b) a45_L3.0

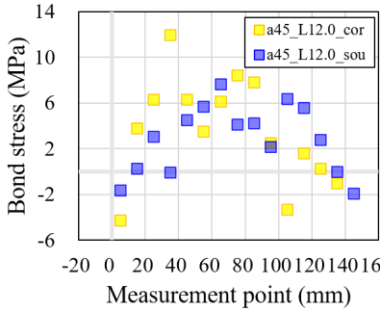

(c) a45_L12.0

Fig. 5 Bond stress distribution

Table 4 Stress gradient of steel bar and effective anchorage length

Parameter		Stress gradient	Effective anchorage length
Sound	a90_L3.0	1.62	111.7
	a45_L3.0	2.28	79.4
	a45_L12.0	1.80	100.6
Corroded	a90_L3.0	2.01	90.1
	a45_L3.0	2.38	76.1
	a45_L12.0	2.88	62.9

Fig. 5 に示した付着応力分布を見ると，a45_L3.0 を除く 2 水準については, 載荷側 40mm までの付着応力が腐食時のものが大きくなっており, それ以降の腐食鉄筋の付着応力分布はいずれも同じような分布になっている。

Fig. 4 に示す近似線は，小林らの研究[5] を参考に，3 点移動平均した腐食 PC 鋼棒の応力分布について, 計測時の導入応力の変化が激しい載荷端付近 20mm を除いた上で自由端側から除いていって, 最初に一番近似が良くなった区間で近似することにより作製した。この近似式より算出した鉄筋応力勾配および実効定着長を Table 4 に示す。

Table 4 より, 腐食に伴い応力勾配が増大し，定着長が減少することが分かる。健全時に大きく異なっていた定着長は, 腐食後にはその差が縮まっており, 節形状によらず同程度の付着性能になったといえる。

4. まとめ

本研究で得られた知見を以下に示す。

1） 節間隔，節角度の増大に伴い応力減少勾配が緩やかになる傾向が確認された。また，節角度より節間隔のほうが鉄筋の応力分布に及ぼす影響は大きいことが明らかとなった。

2） 健全時に最も鉄筋応力勾配の大きかった a45_L3.0 に関しては, 腐食の前後で付着特性における変化はほとんど見られなかった。

3） 節間隔が大きい鉄筋で見られた腐食後の実効定着長の短縮は，特に載荷側 40mm までの区間での付着応力の増大が主な要因であり，一方でそれ以降の区間での付着応力分布は健全時のものとほとんど変わらないことが確認された。

4） 中性子回折法により得られた応力分布曲線の分析により，腐食鉄筋については節形状の違いが応力分布に与える影響は小さいことが明らかとなった。積算電流密度 153.42 mA・h/cm^2 までの腐食では，腐食によるコンクリートとの噛み合いが顕著となり，鉄筋とコンクリートとの付着が増大すると同時に，節角度の影響を小さくしたものと考える。

謝辞

本研究は JSPS 科研費 JP20H02302 の助成を受けたものである。また，中性子回折実験は 2024・2025 年度日本原子力研究開発機構・量子科学技術研究開発機構施設利用共同研究（課題番号：2024105207，2025105204）として実施した。実施にあたり関係各位のご協力をいただいた。ここに記して謝意を表す。

参考文献

1) A.P.Clark：Bond of Concrete Reinforcing Bars, ACI Journal，Proceedings Vol.46，No.3，pp.161-184，Nov.1949
2) 山本恭史，島弘，堤知明：鉄筋の腐食量とひび割れおよび付着強度の関係について，土木学会年次論文報告集，V-251，pp.528-529，1990.9
3) 兼松 学，野口貴文，安田正雪，鈴木裕士：残留応力解析用中性子回折装置(RESA)による鉄筋応力の非破壊測定，コンクリート工学年次論文集，Vol.30，No.2，pp.775-780，2008.7
4) 丹羽章暢，崔烘福，兼松学：溶融亜鉛めっき鉄筋の腐食がコンクリートの構造耐力に及ぼす影響，コンクリート工学，Vol.40，No.1，pp.969-974，2018
5) 小林謙祐ほか：RC 造建築物等の長寿命化に資する溶融亜鉛めっき鉄筋の付着性能および部材の構造性能に関する実験的研究 その 2 コンクリート調合の違いにおける付着性能評価，日本建築学会大会学術講演梗概集，構造IV，pp.27-28，2024.7

Analysis of Vibration Behavior of an Oscillating Water Column Under Marine Environmental Conditions

Pebrian Candra Dwi※1,Gyu-Yong Kim※2,Ha-Min Eu※3,Jeong-Taek Lee※4Min-Jeong Ko※1、
Minh Triet Van※1,Jeong-Soo Nam※2

Oscillating Water Column (OWC) systems are exposed to marine environmental loading that affects structural vibration behavior. This study investigated the vibration characteristics of an offshore OWC near Jeju Island, Republic Korea, using acceleration measurements and ERA5 data. RMS analysis showed increased vibration responses under high-wave conditions. A time delay between wave loading and RMS response was observed due to cumulative wave effects and structural inertia. RMS analysis is effective for evaluating OWC vibration.

1. Introduction

Oscillating Water Column (OWC) is one of the most widely studied wave energy conversion technologies due to its simple configuration, durability, and suitability for both coastal and offshore applications. By utilizing oscillations of the internal water column to generate airflow and drive a turbine, OWC systems can effectively convert wave energy into electricity. As offshore renewable energy infrastructure continues to expand, ensuring the long-term structural safety and reliability of OWC systems has become increasingly important [1].

OWC structures operate in harsh marine environments and are continuously subjected to waves, wind, and fluctuating sea conditions. These environmental loads can induce structural vibrations that may affect structural performance and durability over time. While vibration-based indicators such as acceleration response, natural frequency, and vibration energy have been widely applied for structural health monitoring of offshore structures, studies on the vibration behavior of OWC systems remain relatively limited.

Among these indicators, the Root Mean Square (RMS) acceleration is a practical measure of vibration energy and can be used to assess changes in structural response under varying environmental conditions. Therefore, this study investigates the vibration characteristics of an offshore OWC using acceleration measurements and ERA5 marine environmental data, with a focus on RMS [2].

2. Experimental Method

2.1 Target Structure and Measurement System

This study investigated an offshore Oscillating Water Column (OWC) wave energy converter near Jeju Island, Republic of Korea. A tri-axial accelerometer installed inside the reinforced concrete caisson measured X, Y, and Z- directional responses enabling the evaluation of vibration behavior under actual marine environmental conditions. The measured acceleration data were analyzed to characterize the dynamic response of the OWC.

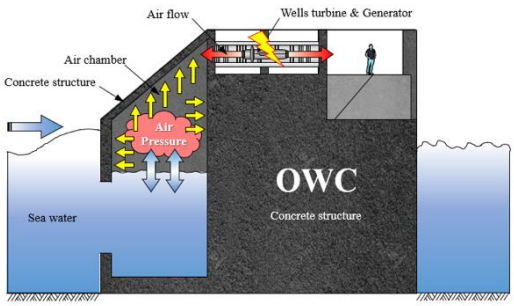

Figure 1 Basic Principle of OWC

※1 Master's Course, Dept. of Architectural Engineering, Chungnam National University, Korea
※2 Prof., Dept. of Architectural Engineering, Chungnam National University, Korea
※3 Ph.D., Dept. of Architectural Engineering, Chungnam National University, Korea
※4 Ph.D. Course, Dept. of Architectural Engineering, Chungnam National University, Korea

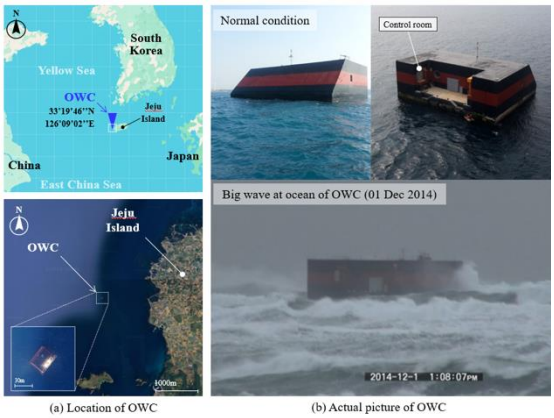

Figure 2 Actual OWC Testbed showing the installation site

The vibration data were collected from the operational OWC testbed under actual marine conditions. Figure 2 shows the actual OWC testbed and the installation environment where the vibration measurements were performed.

2.2 Marine Environmental Data

Marine environmental conditions were obtained from the ERA5 reanalysis data set provided by the European Centre for Medium-Range Weather Forecasts (ECMWF). ERA5 data were adopted because wave measurements from the on-site SCADA system contained frequent missing records due to offshore operational conditions. Therefore, ERA5 was used as stable and continuous source of environmental information.

The environmental variables considered in this study included: wind speed (m/s), significant wave height (m), Maximum wave height (m), Air temperature (°C). These parameters were collected at an hourly interval and used to represent the surrounding marine environment affecting the OWC vibration response.

2.3 Vibration RMS Analysis

The measured acceleration signals were processed to quantify structural vibration energy using the Root Mean Square (RMS) method. RMS is widely used as an indicator of vibration intensity because it reflects the overall vibration energy during a specified time interval. The RMS value was calculated using:

$$RMS = \sqrt{\frac{1}{N}\sum_{i=1}^{N} a_i^2} \quad (1)$$

a_i^2 : Measured acceleration

N : total number of samples within the analysis interval

Hourly RMS values were calculated for each acceleration axis and used to evaluate temporal variations in vibration behavior throughout the measurement period.

2.4 Relationship between Marine Environment and Vibration Response

The vibration characteristics of the OWC were analyzed by comparing RMS values with the corresponding marine environmental conditions. Attention was given to periods with elevated vibration levels associated with high-wave events. Furthermore, the temporal relationship between wave conditions and vibration responses was investigated to identify possible response delays caused by the large inertia of the caisson-type OWC structure. Through this approach, the influence of environmental loading on OWC vibration behavior was examined under actual operating conditions [3].

3. Results and Discussion

The Vibration behavior of the OWC structure was evaluated using measured acceleration data under actual marine conditions. The results showed that wave-induced loading significantly affected vibration responses of the structure, with higher RMS accelerations observed under severe sea states due to increased wave excitation and dynamic loading effects. In contrast, the structure exhibited relatively stable vibration behavior under calm marine environmental conditions, indicating limited structural response and reduced dynamic fluctuations. These findings highlight the importance of considering varying marine conditions when assessing the operational stability and long-term performance of OWC structures.

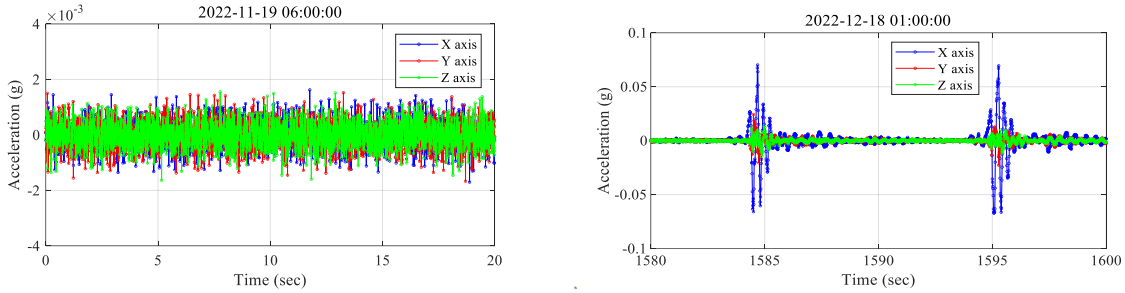

(a) Normal vibration **(b) Big Vibration**

Figure 3 Comparation of acceleration data normal and big vibration

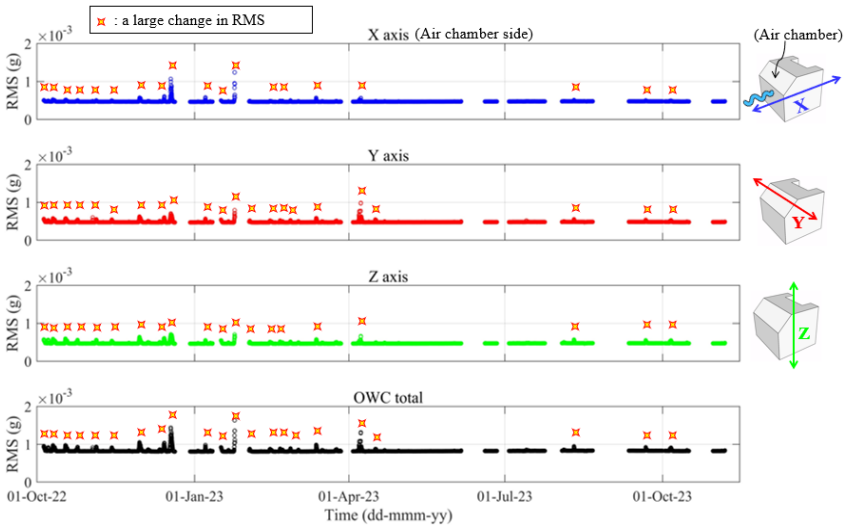

Figure 4 RMS Value of acceleration data on each axis over the entire measurement period

Figure 3 compares representative acceleration signals under normal and large-vibration conditions. During normal conditions, the acceleration amplitudes remained small and relatively constant. In contrast, during high-wave events, noticeable acceleration peaks were observed, indicating increased dynamic excitation of the OWC structure by marine loading. These results suggest that wave conditions strongly influence the vibration response of the OWC.

To quantitatively evaluate vibration intensity, the acceleration data were converted into root mean square (RMS) values. Figure 4 shows the RMS variation of the three acceleration axes during selected monitoring periods. Elevated RMS values were observed during periods of high wave activity, indicating an increase in vibration energy acting on the structure. The RMS values remained close to a stable baseline during non-extreme marine conditions, whereas large fluctuations appeared during severe environmental events.

In addition, a comparison between the ERA5 marine environmental data and the OWC RMS values revealed a distinct response delay between external loading conditions and the structural vibration response. As shown in Figure 5, increases in significant wave height were generally followed by increases in RMS values several hours later rather than occurring simultaneously. This delay is attributed to cumulative wave loading and structural inertia. The OWC vibration response is influenced by both environmental conditions and accumulated wave effects over time.

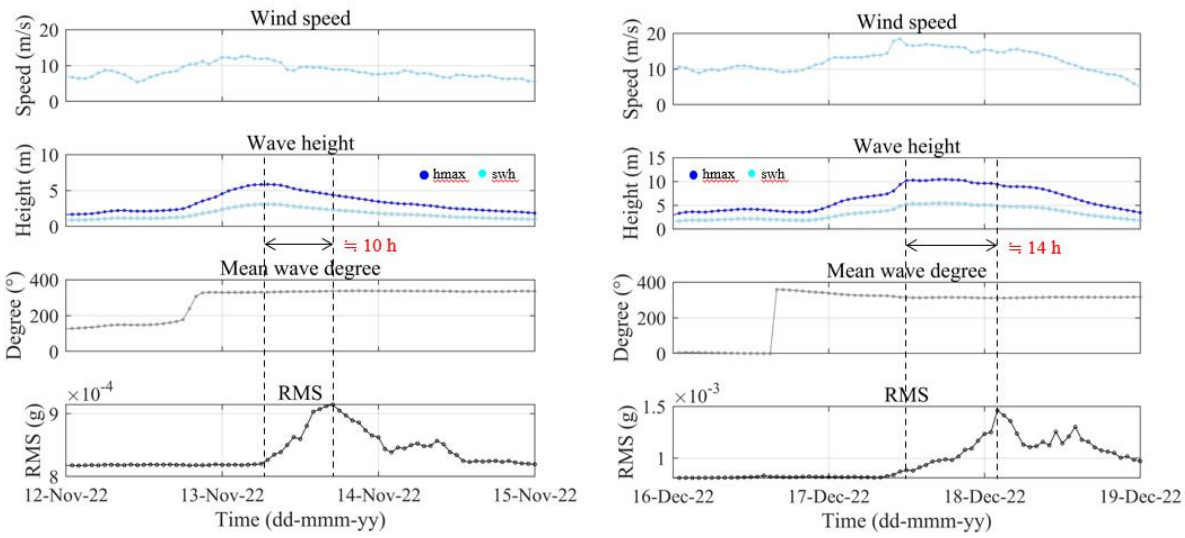

(a) 2022/11/12-2022/11/15 **(b) 2022/11/12-2022/11/15**

Figure 5 Time differences between ERA 5 data and OWC RMS values (Time Delay Observation)

Overall, the results demonstrate that wave-induced forces are the dominant factor governing OWC vibration behavior. The RMS value effectively represents vibration energy and can be used as a practical indicator for monitoring structural response and evaluating the vibration condition of OWC structures under marine environmental loading.

4. Conclusion

This study investigated the vibration behavior of an offshore Oscillating Water Column (OWC) wave energy converter under actual marine environmental conditions using long-term acceleration measurements and ERA5 marine environmental data. Vibration characteristics were evaluated using acceleration signals and Root Mean Square (RMS) values. The results showed that the OWC remained relatively stable under normal sea conditions, while vibration amplitude and RMS increased significantly during high-wave events, confirming that wave-induced loading is the primary factor governing structural vibration. A noticeable time delay between wave height and RMS response was also observed, indicating the effects of cumulative wave loading and the inertia of the reinforced-concrete caisson structure. These findings highlight the importance of considering both environmental loading conditions and structural response characteristics in evaluating offshore wave energy systems. Furthermore, the results demonstrate that RMS can serve as an effective indicator for assessing OWC vibration behavior and has strong potential as a practical tool for long-term structural condition monitoring, performance evaluation, and maintenance planning of offshore.

Acknowledgment

This research was supported by the Korea Institute of Marine Science & Technology Promotion (KIMST) funded by the Ministry of Oceans and Fisheries (RS-2023-00254688).

Reference

[1] H. Eu, G. Kim, S. Hwang, C. Lim, K. Kim, J. Park, Y. Lee, J. Nam, Vibration RMS and impact monitoring for marine oscillating water column structure using ERA5 and deep learning, Ocean Engineering 354 (2026) 124983.

[2] J. Falens, A review of wave-energy extraction, Marine Structures 20 (2007) 185–201.

[3] A. Clément, P. McCullen, A. Falcão, A. Fiorentino, F. Gardner, K. Hammarlund, T. Lewis, K. Nielsen, M.T. Pontes, T. Thorpe, Wave energy in Europe: Status and perspectives (2002) 405–431.

中国の RC スラブを対象とした居住性からみた歩行振動の評価方法の適用性に関する検討

A method to evaluate the habitability of walking-induced vibration on reinforced concrete residential buildings in China

潘瑞琪※1、福田眞太郎※2
Ruiqi Pan, FUKUDA Shintaro

ABSTRACT

近年、中国の RC 住宅床では歩行に伴う振動が居住快適性の問題として顕在化している。しかし中国の現行快適性評価基準は振動性能値が限界値を超えるか否かのみを指標とし、居住者感覚を十分に考慮していない。一方、日本では振動性能値と官能評価を統合した手法が確立されている。本研究は日本の評価方法を中国住宅に適用し、振動性能値と居住者感覚の関係を検討し、今後の中国に適した評価方法の構築に向けた基礎的知見を提供する。

1. Introduction

As housing quality has improved in recent years, Residents in China have paid greater attention to residential habitability. Residential buildings in urban China are predominantly high-rise reinforced concrete (RC) apartment buildings, where relatively thin floor slabs are commonly used. Walking vibration in these buildings may therefore be noticeable and may cause discomfort or complaints. These conditions have increased the need to evaluate walking vibration from the viewpoint of habitability in China.

The current Chinese habitability standard for walking vibration mainly uses a threshold-based approach, in which physical floor vibration performance values are compared with prescribed limits. However, this approach does not directly indicate how residents perceive the vibration. Consequently, the relationship between vibration performance values and human subjective responses remains unclear.

In contrast, the Japanese evaluation method uses sensory experiments to quantity participants' responses to floor vibration. Psychological scales constructed from participants' responses are related to vibration performance values, allowing perceived vibration and annoyance to be evaluated quantitatively in relation to physical vibration performance. This approach places greater emphasis on how floor vibration affects residential comfort.

Based on this background, the purpose of this study is to apply the Japanese evaluation method[1)] to walking vibration in the Chinese residential environment and to examine the relationship between vibration performance values and the perceptions of Chinese participants.

2. Setting Floor Vibration Samples

To conduct the sensory experiment, floor vibration samples were prepared to reflect the characteristics of walking vibration in RC residential buildings in China. The samples set included 5 measured samples, 25 FEA-simulated samples, and 9 supplementary samples, for a total of 39 samples.

2.1 Measured vibration

Measured vibration samples were obtained from the living rooms of three RC residential buildings in China with different slab thicknesses: Building A had no floor finish, whereas Buildings B and C had floor finishes. The floor dimensions of Building A are shown in Fig.1 (a) as an example.

Heel-drop excitation tests were conducted on each floor, and the identified natural frequencies were 13.67 Hz, 35.15 Hz, and 42.97 Hz for Buildings A, B, and C,

※1 日本 東京科学大学 建築工学科 修士課程
※2 日本 東京科学大学 建築工学科 准教授・博士

respectively.

Walking vibration responses were measured using the layout shown in Fig.1 (a). The walking step frequency was set to 2.0 Hz to represent a typical daily walking pace. One person stood at the receiving position, 400 mm from the walking path. This was the same position as that used by the evaluator in the sensory experiment.

The acceleration responses measured at the center of the floor slab were used as the vibration samples, and example of the measured walking acceleration response are shown in Fig.1 (b).

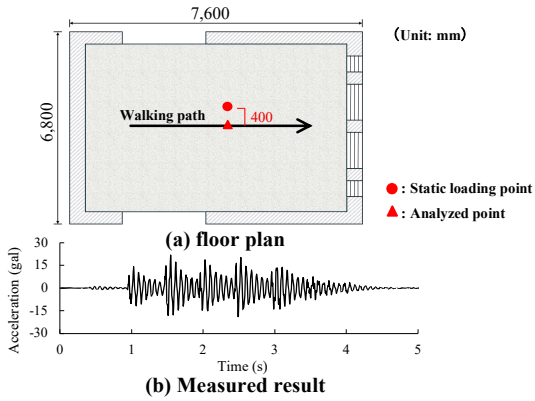

(b) Measured result

Fig.1 Example of the floor plan and measured result (Building A)

2.2 FEA-simulated vibration

FEA-simulated vibration samples were prepared to reproduce a wider variety of floor conditions in Chinese residential buildings.

2.2.1 Reference model

The reference model was based on the measured floor of Building A, for which detailed structural drawings were available. It was used as the basis for preparing the simulated vibration samples.

Fig.2 shows the first and second mode shapes obtained from the analysis of the reference model, for which the corresponding natural frequencies are compared with the measured values in Table 1.

These results indicate that the dynamic characteristics identified from the measurement were generally reproduced by the reference model.

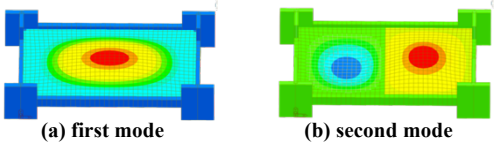

(a) first mode **(b) second mode**

Fig.2 Model shapes of reference model

Table 1 Comparison of nature frequencies between measurement and reference model

Mode	Measurement (Hz)	Reference Model (Hz)
First mode	13.67	13.57
Second mode	29.69	28.88

2.2.2 Model modification

Based on the reference model, several modified models were created by changing floor conditions that can influence the dynamic response of floor slabs. The specific conditions of the modified models are summarized in Table 2.

2.2.3 Walking load and response extraction

A measured walking load was used as the input in the time-history analysis of each model. The vertical acceleration response at the slab center was selected as the vibration sample. Examples of the simulated responses are shown in Fig.3.

Table 2 Model modification conditions

Modified item	Variable	Range / options
Slab	thickness	8 – 48 cm
Wall	thickness	10 – 30 cm
Beam	width	10 – 30 cm
	height	40 – 80 cm
Span	longer span	400 – 890 cm
	shorter span	400 – 760 cm
Floor finish	—	with / without
Boundary condition	—	pinned / rigid
Damping ratio	—	0.02 / 0.03

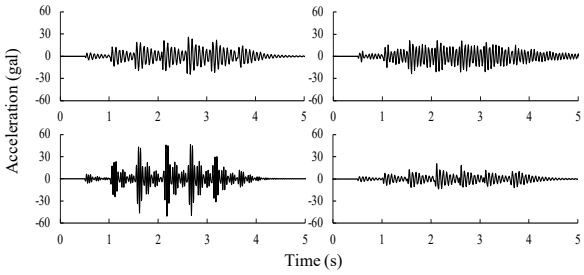

Fig.3 Examples of analyze result of walking vibration

2.3 Supplementary vibrations

Supplementary samples were added to extend the range of vibration characteristics and consisted of measured type and generated type. The measured type included walking vibration in timber buildings and traffic vibration in buildings near railway tracks. The generated type included 4 Hz steady vibrations with different amplitudes, each lasting approximately 10 s.

All vibration samples used in the sensory experiment, covering a wide range of *VLT* [1] values calculated in Section 4, are summarized in Table 3.

Table 3 Summary of the vibration samples

Type	Sample group	*VLT* range (dB)
Type A	Field measurement	60.52 – 86.34
Type B	FEA simulation	67.01 – 94.92
Type C	Steady vibration	73.96 – 93.80
Type D	Timber floor	66.71 – 91.23
Type E	Traffic vibration	72.24 – 89.60

Table 4 Summary of sensory test

Psychological scale	Amplitude scale , Annoyance scale	
Method to create scale	Method of successive categories	
Floor application	Residential room	
Question	How do you feel about this vibration when you relax in the residential room?	
Judgement category	Amplitude scale	Annoyance scale
	1.Extremely large	1.Extremely annoyed
	2.Slightly large	2.Very annoyed
	3.Clearly feel	3.Fairly annoyed
	4.Slightly feel	4.Moderately annoyed
	5.Neither perceptible nor imperceptible	5.Slightly annoyed
	6.Hardly feel	6.Hardly annoyed
	7.Insentient	7.Not annoyed
Number of vibrations	Vibration samples from Section 2: 39 pieces	
Panel members	20 Chinese and 20 Japanese,（age：21 - 35，weight：40 - 90kg）	
Posture	Sitting on the chair(wearing socks and without using backrest	

Fig.4 Situation of sensory test

Table 5 Result of analysis of variance

		Chinese participants		Japanese participants	
		Amplitude scale	Annoyance scale	Amplitude scale	Annoyance scale
Variance ratio	Main effect	52.9804*	41.7247*	82.3795*	74.5221*
	Individual differences	30.5451*	34.6976*	29.8276*	36.7745*
Contribution ratio	Main effect	59.6%	52.2%	72.2%	68.1%
	Individual differences	16.9%	21.6%	11.4%	14.8%

*: The level of significance is less than 1%.

3. Conducting Sensory Experiment and Constructing Psychological Scales

3.1 Outline of the sensory test

Table 4 shows the outline of the sensory test. The main items are described below.

3.1.1 Psychological scales

Two types of scales were constructed: the "amplitude scale," which represents whether participants noticed the vibration or how strongly they perceived it; the "annoyance scale," which represents the degree to which the vibration was annoying.

3.1.2 Participants

The participants comprised 20 Chinese participants and 20 Japanese participants. Chinese participants were included as the main target group of this study, while Japanese participants were included for comparison. The age range and other basic attributes of the participants are summarized in Table 4.

3.1.3 Test method

The test was conducted using a 2m × 2m electromagnetic shaking table installed in an experimental room at a temperature of 20°C.

The order of the presented samples was randomized, and the order was changed for each participant to avoid order effects. In addition, each sample was presented three times.

3.1.4 Posture

The participants were seated on a chair. Specifically, as shown in Fig.4, a wooden chair without a cushion was firmly fixed to the shaking table. The participants were instructed to sit on the chair in a relaxed posture, with both soles placed on the floor and without using the backrest.

3.1.5 Scales and method of scale construction

The time required for one participant was approximately 1 hour for the assumed residential relaxation condition. In addition, based on the measurement results obtained from the accelerometer installed on the shaking table, it was confirmed that the vibrations used as test samples were almost constant regardless of the participant.

Table 5 shows the results of the analysis of variance for the sensory test. The results confirmed that the differences among the vibration samples were sufficiently reflected in the participants' judgments. After confirming the significance of the participants' responses, psychological scales were constructed from the response data using the method of successive categories.

4. Calculating *VLT* as Performance Value of Floor Vibration

VLT , which is used as a performance value in the Japanese method for evaluating walking vibration, was adopted in this study. It was calculated using the reference values for walking vibration adopted in Japan, as defined by the following equation:

$$VLT = VL\max + 20 \cdot \log10\ (T^{1/4})$$

VL_{max} : maximum value of VL(dB)

VL : level values of a'rms calculated by the following equation(dB)

$VL = 20 \cdot \log10(a'rms / a0rms)$

a'_{rms} : acceleration after frequency weighting based on the. perception of vertical vibration specified in JIS C 1510, processed with a specified time constant of 25 ms. (m/s^2)

a_{0rms} : reference RMS acceleration ($1\times10^{-5} m/s^2$(rms))

T : total duration for which VL is 60 dB or greater (s)

5. Relationships between Psychological Scales and *VLT*

5.1 Applicability of *VLT* to Chinese

Fig 5 (a) shows the relationships between *VLT* and the psychological scales obtained from Chinese participants. In both the perceived amplitude and annoyance scales, the scale values tended to increase as *VLT* increased, and the plotted data generally corresponded well to the fitted regression lines. These results indicate that *VLT* can serve as a performance value for evaluating both perceived amplitude and annoyance in Chinese participants.

5.2 Sensitivity Difference between Chinese and Japanese

Fig.5 (b) shows the results for Japanese participants. In both scales, the Japanese regression lines had larger slopes than the Chinese regression lines.

Table 6 summarizes the *VLT* values corresponding to each judgement category for Chinese and Japanese participants in both the perceived amplitude and annoyance scales.For lower judgement categorie（5）, the difference was small, about 1.5 dB. However, as the judgement categories became higher（1-4）, the difference increased to about 5 dB.In addition, the difference between Chinese and Japanese participants became larger as the vibration became stronger.

These results suggest that the difference between Chinese and Japanese participants was small for lower vibration levels but became clearer for higher vibration levels. Japanese participants showed lower tolerance to larger walking vibration.

6. Conclusion

In this paper the applicability of *VLT* to the evaluation of walking vibration in reinforced concrete residential buildings in China was examined. The results showed that *VLT* corresponded well with the psychological scales obtained from Chinese participants, indicating that it can be used as a performance value for walking vibration. However, some samples affected by accompanying sound during the shaking-table reproduction deviated from the regression lines. Therefore, further work is needed to clarify the influence of sound on the subjective evaluation of walking vibration and on the applicability of *VLT*.

7. Reference

1） 横山裕， 黒田瑛一， 福田眞太郎． 剛性の高い床に適用する性能値に関する基礎的検討 木造大スパン床の歩行振動の居住性からみた評価方法 （その 2）[J]． 日本建築学会環境系論文集，2015，80(712)： 509-518.

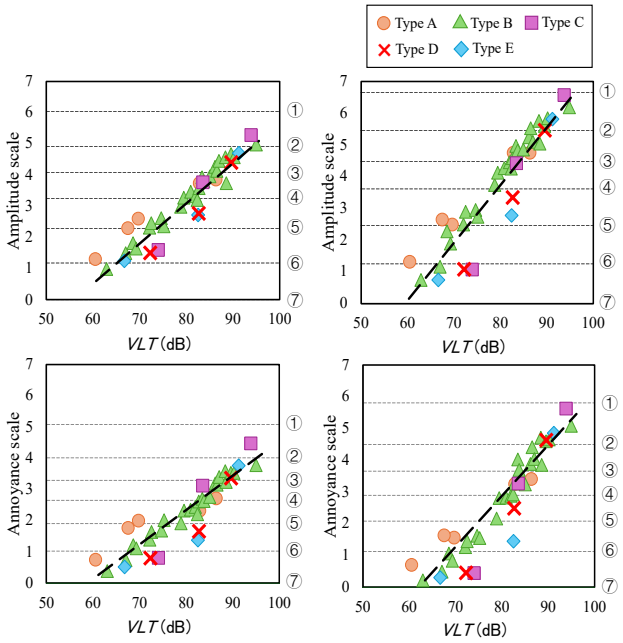

(a) Chinese participants (b) Japanese participants

Fig. 5 Relationship between psychological scale and *VLT*

Table 6 Comparison of *VLT* between Chinese and Japanese

(a) Amplitude scale

Judgement category	Chinese(dB)	Japanese(dB)	Δ (J-C)
1.Slightly large	93.78	89.22	-4.56
2.Clearly feel	87.05	83.72	-3.33
3.Slightly feel	80.41	78.75	-1.66
4.Neither perceptible nor imperceptible	72.73	72.23	-0.5
5.Hardly feel	63.87	65.46	1.59

(b) Annoyance scale

Judgement category	Chinese(dB)	Japanese(dB)	Δ (J-C)
1.Very annoyed	95.97	90.78	-5.18
2.Fairly annoyed	89.37	85.64	-3.73
3.Moderately annoyed	83.44	81.04	-2.4
4.Slightly annoyed	76.45	76.09	-0.36
5.Hardly annoyed	68.34	70.18	1.85

Complex Network Analysis of the Building Fire Ecosystem and Evaluation of Risk Control Utility by Policy Intervention

金源昌※1、林廈峻※1、金泰亨※1、李泰圭※2

Won-Chang Kim, Ha-Jun Im, Tae-Hyung Kim, Tae-Gyu Lee

ABSTRACT

Modern urban fires are complex socio-technical disasters, yet existing frequency-based safety policies often fail to prevent mass casualty events. This study proposes a hybrid analytical framework utilizing 2015-2024 fire and meteorological data from Busan, South Korea, to uncover mass casualty mechanisms and simulate evidence-based control scenarios. By applying a target-oriented K-Means clustering algorithm, incidents were stratified into isolated and mass casualty groups, achieving high statistical validity with effect sizes of 0.80 for deaths and 0.54 for injuries. Network topology analysis identified critical brokers, revealing that mass casualties are driven by active triggers interacting with extreme passive environmental constraints. Simulations of six intervention scenarios demonstrated that executing targeted shutdowns of all active factors (Scenario 6) significantly collapsed 24.828% and 19.527% of the isolated fatality and mass casualty network edges, respectively. Paradoxically, the residual passive core density increased, indicating a deactivated but highly condensed environmental skeleton. The findings provide a robust framework for proactive, data-driven disaster safety governance by proving that dismantling active triggers during extreme conditions effectively neutralizes mass casualty networks.

1. Introduction

Fires in high-density urban environments can no longer be adequately explained merely by physicochemical combustion reactions. Today's large-scale fires must be understood as typical failures of socio-technical systems, which explosively manifest when active triggers, such as human cognitive errors or mechanical defects, interlock with overarching passive environmental constraints like extreme weather or vulnerable time slots. However, existing disaster safety governance relies heavily on the mere frequency of fire occurrences, exhausting limited resources on routine accidents. A high occurrence frequency does not translate directly into massive human casualties; true catastrophes occur when a remarkably small number of low-frequency, high-risk factors generate fatal synergies. Therefore, this study aims to perform risk stratification based on unsupervised machine learning targeting the number of casualties. Furthermore, it seeks to simulate evidence-based disaster control scenarios through the topological dissection of the derived mass casualty catastrophe network to identify critical broker factors and scientifically validate network collapse effects.

2. Research design and methodological framework

To elucidate the complex mechanisms of the metropolitan fire ecosystem, this study utilized building fire incident data from 2015 to 2024 provided by the Busan Fire and Disaster Headquarters, integrated with meteorological observation data from the Korea Meteorological Administration (KMA). Continuous meteorological variables were categorized into four equal intervals (Q1-Q4), and temporal variables were reclassified into four hourly categories to capture macroscopic circadian rhythms. A K-Means clustering algorithm

was then applied with a strong scalar weight (weight factor = 10.0) assigned to the casualty count to bias the algorithm toward consequential impacts. The optimal number of clusters (k = 2) was determined via the elbow method and silhouette scores, which peaked at approximately 0.62 for deaths and 0.77 for injuries. Following this, a one-way ANOVA was conducted to evaluate the practical explanatory power of the clustering by calculating the eta-squared effect size (η^2). Finally, each derived risk cluster was modeled as an independent network to calculate degree and betweenness centrality. Based on these metrics, a six-step evidence-based policy intervention scenario was designed to strictly distinguish uncontrollable passive environmental constraints from controllable active triggers, allowing for the simulation of edge collapse rates and network density changes when active factors are forcefully shut down.

3. Results and discussion

The target-centric clustering bifurcated the dataset into the Isolated Fatality Group (IFG; 113 incidents) and Mass Casualty Group (MCG; 11 incidents, average 2.27 deaths), along with the Isolated Injury Group (IIG; 633 incidents) and Mass Injury Group (MIG; 10 incidents, maximum 23 injuries). A one-way ANOVA confirmed exceptional statistical validity, yielding an effect size of $\eta^2 = 0.80$ for the death model and $\eta^2 = 0.54$ for the injury model. Network centrality analysis revealed that the MCG network formed an overwhelming degree centrality hub in the night time slot (10.472) combined with extreme strong winds (8.616), where arson acted as a robust mediating broker (betweenness centrality 0.037) atop adverse weather. Similarly, the MIG network was driven by localized wind speed variations (betweenness centrality 0.072) intersecting with explosive human-induced factors like gas leaks. The intervention simulation demonstrated a balloon effect under fragmented administrative controls; for example, blocking only electronic overloads in the MCG caused the betweenness centrality of arson to surge to 0.042. However, when an integrated masterplan controlling all human-induced active factors (Scenario 6) was executed, the MCG edges significantly collapsed by 19.527%. Concurrently, the network density of the MCG paradoxically surged by 10.700%, from 0.450 to 0.498, and the MIG density increased by 12.472%. This "paradox of density increase" mathematically proves that removing active triggers leaves a highly condensed but deactivated skeletal structure of environmental factors, entirely stripping the network of its momentum to induce mass casualties.

4. Conclusion

This research quantitatively verified that massive fire catastrophes are heterogeneous complex network phenomena that detonate only when passive constraints fuse with active triggers. By stratifying fires based on consequential lethality, the unsupervised machine learning model secured robust validity, controlling 80% and 54% of the variance in death and injury counts, respectively. The network collapse simulations strongly warn that myopic administrative interventions can precipitate a balloon effect, generating new fatal mediating factors within the disaster network. Ultimately, executing an integrated masterplan to shut down human-induced factors during severe weather warnings triggers a massive collapse of network edges and a paradoxical increase in passive core density. This visual and quantitative evidence confirms that neutralizing human-induced mediating variables is sufficient to perfectly sever the systemic collapse loop leading to massive fatality catastrophes, thereby providing a highly reliable scientific foundation for modern disaster governance.

竹細工を応用した積層ラメラグリッドシェルの構築手法に関する検証
—3 層複合グリッド模型による実験—

Verification of a Structural Framework for Layered Lamellar Grid Shells Utilizing Bamboo Craftsmanship—Experiments Using a Three-Layer Composite Grid Model—

堤明日香※1, 江尻憲泰※2
Asuka Tsutsumi, Norihiro Ejiri

ABSTRACT

伝統工芸に用いられる竹を実用的な建築材料として活用する着想から、本研究は竹工芸の技法を建築用ラメラ構造へ応用することを検討した。竹は軽量で柔軟だが、大規模建築に必要な剛性を欠く。そこで、下部２層を積層して高い剛性を確保し、最上層を編み込んで部材を拘束する「３層複合グリッドモデル」による新たな工法を提案した。圧縮試験の結果、本工法はアーチ(単層)と比較して耐荷重能力が大幅に向上し、脆性破壊を起こさず粘性的な挙動を示した。積層と編み込みの組み合わせにより、柔軟な竹を堅牢な建築用シェルシステムへと変容させ得ることが裏付けられた。

1. Introduction

1.1 Research Background

Japanese traditional woodworking techniques, such as *yosegi-zaiku* (A traditional craft that combines pieces of wood in various colors and grain patterns to create intricate geometric designs.) and *Kumiki* (It is a technique that involves cutting notches into wood and fitting them together three-dimensionally like a puzzle, without using nails or adhesive.), achieve both the strength and the beauty through the precise assembly of wooden materials without steel materials like nails or metal plates. These represent an extremely sophisticated system where micro-patterns are integrated into a single cohesive structure. In contemporary architecture, TLDC Tsumiki Pavilion (2018) by architect Kengo Kuma embodies this accumulation of small members. By designing a very simple one-unit triangular block and fitting and stacking them together, a huge pavilion is constructed.

In this study, we attempt to apply this old yet new concept of “aggregations of small patterns (lamella)” to the material “bamboo”, which will be discussed below. Bamboo has been a material deeply rooted in the lives of people in Japan and East Asia since ancient times.

Bamboo is considered to have ideal characteristics as “small members” constituting a lamella structure due to its extremely fast growth rate compared to other natural materials. However, its current use in Japan is limited to interior materials or small-scale crafts, and the establishment of methods for its use as a structural material remains an important hurdle. Traditional bamboo crafts, such as baskets and colanders, are formed by intricately weaving thin bamboo strips (bamboo strips), creating a strong curved surface through the repulsive and frictional forces of the members without the use of adhesives or nails. This traditional weaving can be seen as a type of grid shell structure utilizing the elastic deformation energy of the members and the frictional force of the joints.

※1 東京科学大学 環境・社会理工学院 建築学系 建築学コース 修士課程
※2 日本女子大学 建築デザイン学部 建築デザイン学科 教授

1.2 Purpose of the Research

Applying the bamboo weaving technique to an architectural scale faces the physical limitation of insufficient rigidity. The purpose of this study is to clarify the mechanical characteristics of the lamella structure through model experiments using bamboo strips and to verify its practicality as an architectural structure.

Figure 1 TLDC Tsumiki Pavilion [1]

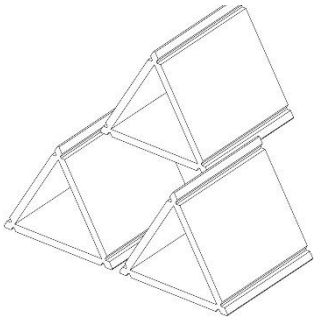

Figure 2 Unit Diagram [1]

2. Lamellar Structures and Existing Architecture

2.1 Interpretation of Lamella Structure

Architect Kengo Kuma describes the lamella structure as a form of "leaning structure [2]" in his book "Small Architecture". The lamella structure uses triangles generated by members leaning against each other diagonally as its basic unit. In this study, the lamella structure is interpreted not merely as geometric pattern, but as "self-organizing support system established by linear members crossing diagonally and mutually entrusting loads to each other".

2.2 Comparison with Existing Bamboo Architecture

In Southeast Asia, architects like VTN Architects and IBUKU actively use bamboo as a structural material. VTN Architects approach focuses on bundling a large number of individual bamboo poles with low strength and rigidity to create a pseudo-large-section member, ensuring rigidity similar to wooden frameworks or steel structures. In contrast, this study aims to establish a lamella structure by taking advantage of bamboo's flexibility, restraining the intersections by "weaving" rather than bunding.

Figure 3 Casamia Community House [3]

Figure 4 Grand World Phu Quoc Welcome Center [4]

2.3 Application of Traditional Weaving Methods

Traditional bamboo crafts rely solely on the frictional force between members and mutual restraint through weaving. Among various weaving patterns, "hexagonal pattern (*mutsume-ami*)" forms a geometrically stable triangular grid by intersecting members from three directions (0, 60, and 120 degrees), making it highly capable of retaining its shape while being lightweight. Therefore, the principle of hexagonal pattern is considered most suitable for

constructing a lamella dome.

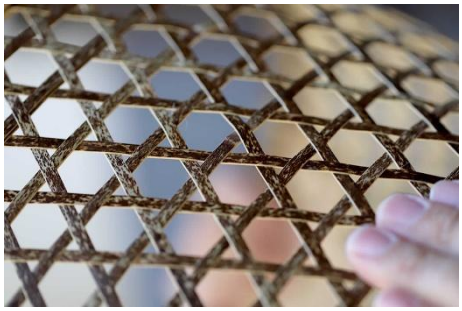

Figure 5 Hexagonal Pattern(*mutume-ami*) [5]

3. Fundamental Experiments

Fundamental experiments were conducted to confirm the mechanical behavior and the reinforcement effect of stacking.

The experiments included loading tests on single-strip arches, two-strip arches, and a single-layer hexagonal patterns dome using bamboo strips.

3.1 Experimental Method

A ring-shaped base with a span of 265 mm was created using a single bamboo strip bent after being heated with a gas burner. Bamboo strips were crossed at the center of the base to form arches with three different rises: 100 mm, 200 mm, and 300 mm. Both single-strip and two-strip arch models were tested. A universal testing machine was used to apply a vertical load to the top of the test specimens to find the maximum proof load until initial buckling.

3.2 Results of Arch Experiments

The maximum proof loads for the single-strip arches were 24.7 N (Rise 100 mm), 16.0 N (Rise 200 mm), and 9.7 N (Rise 300 mm). The maximum proof loads for the two-strip arches were 56.6 N (Rise 100 mm), 26.5 N (Rise 200 mm), and 17.0 N (Rise 300 mm). Stacking two bamboo strips significantly improved both the initial rigidity and the maximum proof load, achieving approximately 1.5 to 2.3 times the maximum load of the single-strip arches. In the two-strip arches, behavior resisting the load while slipping occurred between the two bamboo strips.

3.3 Results of Single-Layer Hexagonal Pattern Dome

A single-layer hexagonal pattern dome was created using a 400 mm span base and a rise of 100 mm. The maximum proof load of the single-strip dome was 61.9 N. This represents about 2.5 times the strength of the simple single-strip arch (24.7 N), confirming a stable shell effect compared to single arches.

3.4 Comparison with Theoretical Values

The theoretical Euler buckling load for a straight bamboo strip used in the experiment is calculated as: $P_k = \frac{\pi EI}{L^2} \approx 2.0\ N$

The theoretical buckling load for a circular arch subject to a concentrated load at the center is given by: $P_{cr} \approx (\frac{\pi}{a})^2 \frac{EI}{R^2}$

Substituting the geometric parameter values (R ≈ 138 mm, a ≈ 1,29 rad) yields a theoretical buckling load of approximately 15.5 N. The experimental value (24.7 N) was approximately 1.6 times higher than the theoretical value, likely because the actual support condition included fixation by adhesive rather than being a perfect pin support.

Table 1 Results of Basic Compression Tests

		Maximum Load Capacity, N
Single-strip arches	Rise100mm	24.7
Single-strip arches	Rise200mm	16.0
Single-strip arches	Rise300mm	9.7
Two-strip arches	Rise100mm	56.6
Two-strip arches	Rise200mm	26.5
Two-strip arches	Rise300mm	17.0

4. Plan and Fabrication of Dome Model Applying Bamboo Basketry

4.1 Proposed Construction Method

Based on the fundamental experiments, a construction method combining the lifting of the center of a flat bamboo grid and traditional hexagonal weaving was proposed. The method involves a two-step process:

Step 1: Stacking (1st and 2nd layers): The bottom and middle layers are stacked rather than woven, maximizing the rigidity of the members and stabilizing the structure.

Step 2: Restraining by Weaving (3rd layer): Only the top layer is woven into the lower layers, preventing the stacked members from becoming unstable and acting as a restraining material that integrates the whole structure into a dome.

4.2 Fabrication and Experimental Methods

A base ring with a span of 400 mm was made using three bamboo strips stacked vertically to ensure sufficient rigidity. To increase the rigidity at the top, bundles of three bamboo strips were arranged radially, shifting the phase by 60 degrees. The 1st and 2nd layers were spaced 20 mm apart without weaving, temporarily fixed, and then bonded with epoxy resin adhesive. The 3rd layer was woven using a modified hexagonal weaving method to prevent the bamboo strips from breaking. Two models were tested: Experimental Model-1 and an improved Experimental Model-2 (where bamboo arches were fixed to the base avoiding contact with the bottom surface).

4.3 Experimental Results

The maximum proof load was 307.5 N for Experimental Model-1 and 366.3 N for Experimental Model-2. In Model-2, the load increased linearly in proportion to the deformation up to about 10-15 mm. It reached a maximum load of 366.3 N (approx. 37 kgf) at a deformation of about 35 mm, demonstrating the strength to support the weight of a 10-year-old child. Even after reaching the maximum load, the specimen did not exhibit brittle failure and maintained a load of approximately 280 N even at a deformation of 60 mm.

5. Discussion on the Compression Test

5.1 Mechanism of Yield Strength Improvement

The final model demonstrated sufficient initial rigidity, likely because the triangular grids of the hexagonal weave restrained each other, suppressing the deformation of individual members. The structure showed tenacious behavior; the slip and friction of the contact points due to “weaving” acted as a cushion, preventing total collapse even when some members reached their limits. By not weaving the 1st and 2nd layers, the bamboo strips were assembled linearly, maintaining their axial force as arches, which contributed to high rigidity. The 3rd layer of weaving functioned as a physical fastener suppressing the displacement of the 1st and 2nd layers under load.

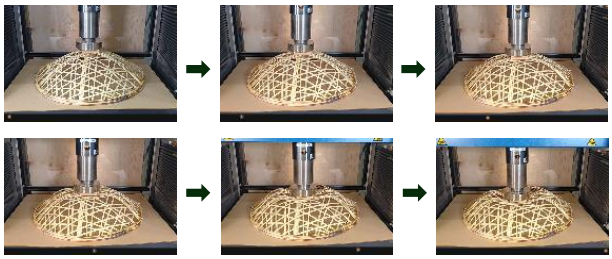

Figure 6 Experimental Model 1: Observations

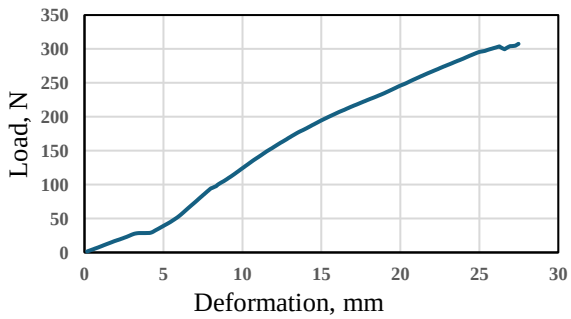

Figure 7 Test Model-1: Load-Displacement Curve

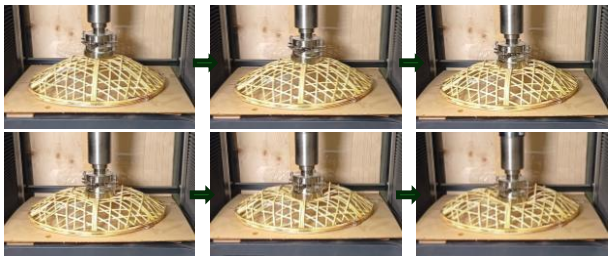

Figure 8 Experimental Model 2: Observations

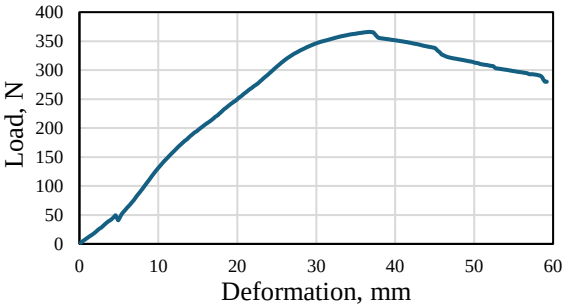

Figure 9 Test Model-2: Load-Displacement Curve

5.2 Conversion for Full-Scale Structures Based on the Law of Similarity

While there are various similarity rules, there is no single, definitive one. Therefore, we performed the calculation using the similarity rules that are commonly used. Using the similarity rule (square law), $L^2 : R^2 = l^2 : r^2$, the necessary member thickness R for a full-scale structure with a span L = 3,000 mm based on the model scale (l = 100 mm, r=2 mm) is calculated as follows: $R = r \times \frac{L}{l}$

The calculation yields R = 60 mm, which matches the standard dimensions of general laminated bamboo and the average diameter of natural Japanese timber bamboo. Therefore, the scale and member dimensions of this experimental model hold extremely realistic validity for bamboo architecture design.

6. Conclusion and Future Prospects

The experiment demonstrated that even flexible bamboo strips can function as a structural material and secure sufficient rigidity by stacking and weaving them. To realize this as an actual architectural space, it is necessary to verify the safety against self-weight, wind loads, and snow loads through larger-scale mockups. Developing new connection methods that maintain high rigidity (e.g., replacing plastic ties with natural materials like hemp rope or biodegradable plastics, or using bolts for rigid fixation) is a future challenge. Considering bamboo's high hygroscopicity, combining it with preservative / anti-termite treatments or highly waterproof membrane materials is essential for permanent use. The proposed structure is highly suitable for temporary pavilions due to its lightweight and rapid construction capabilities.

Figure 10 Conceptual Diagram of the Dome

Reference

[1] Kengo Kuma & Associates: Taichung Flower Expo Taikai Building Blocks Concept Pavilion, https://kkaa.co.jp/project/tldc-tsumiki-pavilion/, Accessed January 11, 2026.

[2] Kengo Kuma: Small Architecture. Iwanami Shinsho, 2013.

[3] VTN architects: Grand World Phu Quoc Welcome Center, https://vtnarchitects.net/casamia-community-house-pe268.html, Accessed January 12, 2026.

[4]IBUKU: The Arc, https://ibuku.com/project/the-arc, Accessed January 12, 2026.

[5] Taketora, a Specialty Store for Tiger-Striped Bamboo: Hexagonal weaving (*mutume-ami*), https://www.taketora.co.jp/c/special/takeam, Accessed January 16, 2026.

都市における産業用建築物の空間的特性に基づく火災被害拡大要因およびリスク評価

Assessment of Fire Damage Spread Factors and Risks According to Spatial Characteristics of Industrial Buildings in Cities

崔智恩※1、 南榮鎭※1、 張永雅※1、李泰圭※2

Ji-Eun Choi, Young-Jin Nam, Young-A Jang, Tae-Gyu Lee

ABSTRACT

Incident-only fire records cannot identify the probability that a building catches fire, because buildings that did not burn are absent from the data. We therefore restrict the estimand to the probability that an observed fire spreads beyond 50 m² of burned area. We analysed 20,365 industrial-building fires recorded in the Republic of Korea between 2019 and 2023. The 50 m² threshold was set at the 90th percentile of the 2019–2021 development set only (2,129 events, 10.5%). A six-step benchmark ladder, running from the rule practitioners can already apply — inspect the largest 10% of buildings by gross floor area — to the full model, was evaluated with a single algorithm on a single hold-out. All preprocessing was fitted inside training folds, district-level GroupKFold was compared with random splitting, 2022 was used for model selection, and the locked 2023 year was evaluated once; confidence intervals were confirmed with district-cluster bootstrapping. On the 2023 hold-out (n = 3,722; 352 high-spread events; prevalence 0.095) the full model reached a PR-AUC of 0.197 (95% CI 0.169–0.233), 2.08 times the prevalence baseline. The floor-area rule achieved a lift of only 1.11, indistinguishable from random screening, whereas the model achieved 2.62 at the same selected volume — size alone does not screen for spread risk. The gains came from combining building and spatial variables (+0.044, 95% CI +0.020 to +0.070) and from ignition context (+0.029, +0.005 to +0.052); adding dispatch and travel times (+0.005, −0.002 to +0.013) and switching from one-hot logistic regression to CatBoost (+0.019, −0.001 to +0.040) did not reach significance. Removing all categorical variables, by contrast, lowered PR-AUC by 23.9% (+0.048, +0.021 to +0.076). What mattered was not the algorithm but whether high-cardinality categorical information was used without leakage.

1. Introduction

Industrial facilities combine large open volumes, dense fuel loads, varied heat sources and heterogeneous structural systems. Fires with similar ignition causes therefore diverge sharply in outcome: some are contained at the point of origin, others consume large floor areas. The operative question for prevention and response is not only where fires start but under what conditions they spread once started.

Risk is conventionally defined as the joint consideration of scenario likelihood and consequence magnitude [1], [2]. The source data used here, however, contain only events in which a fire occurred; industrial buildings that did not burn during the same period are absent. The quantity that can be estimated is thus not the ignition probability of a building but the conditional probability that an observed fire escalates. Unless the title, the analysis and the conclusions are aligned on this point, a study of spread risk is easily read as a study of ignition risk.

Machine learning has been applied to spatio-temporal fire prediction, inspection prioritisation, response times and outcomes, and city- or building-level risk classification [3]–[7]. Event-level studies of spread in industrial facilities remain comparatively rare, and the

representation of high-cardinality categorical variables — district, facility subtype, ignition cause, first ignited material — remains an open methodological question. Target statistics computed on the full data set, or suppression durations that are determined after the outcome, introduce leakage [13]; splitting spatially adjacent events at random inflates apparent performance [10].

A further omission is common in applied work: the justification for adopting a model at all. That larger buildings tend to lose more floor area is expected a priori, so unless a multivariable model is shown to outperform a simple size criterion, its methodological contribution cannot be judged. This study therefore (i) defines the conditional spread estimand explicitly, (ii) isolates the incremental value of each variable block against a simple size benchmark, (iii) compares categorical representations under controlled conditions, (iv) validates across both space and time, and (v) reports top-k selection lift so that decision usefulness can be assessed directly.

2. Research Scope and Methods

2.1 Study population and Otcome dfinition

This study used nationwide building and structural fire records maintained by the National Fire Agency of Korea from 2019 to 2023. The 17 metropolitan-level and 249 municipal-level jurisdictions served as the principal spatial units. Of 25,907 fires initially classified as industrial-facility incidents, those involving livestock buildings, greenhouses, mushroom-cultivation facilities, waste-treatment facilities, and underground facilities were excluded because they differed structurally and locationally from factory-type premises. The remaining 20,462 incidents involved factories, warehouses, workshops, and power-generation facilities. After removing 97 incidents without identifiable municipal jurisdictions, the final sample comprised 20,365 fires: 4,287 in 2019, 4,134 in 2020, 4,100 in 2021, 4,122 in 2022, and 3,722 in 2023.

The primary outcome was a high-spread fire, defined as a burned area of at least 50 m². The threshold was derived exclusively from the 90th percentile of the 2019–2021 development data, preventing test-year information from influencing its definition. Overall, 2,129 incidents (10.5%) met this criterion, with annual rates of 9.5%–11.2%. Because absolute burned area is associated with building size, two supplementary outcomes were examined: burned area divided by gross floor area ≥0.10 and the 90th percentile of burned area calculated within each gross-floor-area quartile of the development data. The absolute criterion remained primary because fire-service mobilisation depends on the absolute affected area. Although 14,202 incidents (69.7%) recorded no burned area, 97.5% had positive property damage, suggesting no structural loss rather than no damage.

Conditional fire-spread risk for incident (i) was defined as:

$$R_spread(i) = P(\, A(i) \geq 50\ m^2 \mid F(i) = 1, X(i)\,) \quad \textbf{(1)}$$

where (A_i) is burned area, (F_i=1) denotes an observed fire, and (X_i) represents the available predictors. This is not ignition probability, but the probability that an observed fire reaches at least 50 m². It may support inspection prioritisation, data collection, and regional planning, but should not independently determine legal liability, insurance ratings, or facility certification

2.2 Predictors, Model Roles, and Validation

Predictors were grouped into four blocks. Building variables included above- and below-ground storeys, log-transformed gross floor and footprint areas, structural type, roof form, and condition. Spatial variables included distances to the fire station and 119 Safety Centre, municipal and metropolitan jurisdictions, and urban status. Emergency-response

※1 大韓民国 世明大学校 消防防災学科 博士課程
※2 大韓民国 世明大学校 消防防災学科 教授

variables comprised dispatch delay and travel time. Ignition-context variables included heat source, ignition cause, first material ignited, facility type and subtype, and weekday. Travel times over 60 minutes were treated as missing. Suppression duration was excluded because its dependence on fire size creates reverse causality and outcome leakage. Reporting delay was unavailable because ignition time was not recorded.

Model A0 used building and spatial variables and was the only pre-incident model. Model A added ignition context, while Model B further added emergency-response times. Therefore, pre-fire inspection performance must be assessed using A0 because ignition cause and first material ignited are unknown ex ante.

Categorical representations were compared using fixed predictors and identical partitions. E1 grouped categories occurring fewer than 30 times in training and applied one-hot-encoded penalised logistic regression. E2 supplied the original categories to CatBoost, which used ordered target statistics [8], while E3 removed all categorical variables. Imputation, rare-category grouping, scaling, and encoding were fitted only within training folds [13].

Using 2019–2021 data, five-fold GroupKFold validation by municipal jurisdiction was compared with random five-fold validation to quantify optimism from spatial dependence [10]. The 2022 data were reserved for selecting boosting iterations and the operating threshold. The selected model was refitted on 2019–2022 data and evaluated once on the locked 2023 holdout. The operating threshold used the top-(k) proportion of predicted risks rather than a fixed probability, preserving operational meaning after refitting; a cutoff of 0.1925 produced a 10.5% alert rate before and after refitting.

PR-AUC was the primary metric because the outcome was imbalanced [11]. Secondary metrics included ROC-AUC, Brier score, calibration intercept and slope [12], precision, and lift. Percentile confidence intervals used 2,000 bootstrap replicates at the incident and municipal-cluster levels. SHAP values described predictive contributions rather than causal effects [9].

The benchmark ladder comprised prevalence (B0), a top-10%-by-floor-area rule (B1), a univariate log-floor-area model (B2), A0 (B3), A (B4), and B (B5). CatBoost was used for B2–B5 to isolate predictor-block gains from algorithm effects. Analyses used Python 3.10.12, CatBoost 1.2.10, and scikit-learn 1.7.2. CatBoost used a learning rate of 0.05, depth 6, L2 regularisation of 3, 200-round early stopping based on 2022 log loss, and seed 20240808. Reporting followed TRIPOD [14].

3 Results

3.1 Descriptive Statistics

Median gross floor area was 490 m², median travel time 6.0 minutes, and median fire-station distance 9 km. High-spread rates varied by structure: steel-reinforced concrete, 16.1% (n = 230); reinforced concrete, 14.9% (n = 4,610); steel frame, 12.0% (n = 8,906); sandwich panel, 6.3% (n = 2,252); and container, 0.7% (n = 1,220). Rates increased from 7.6% in single-storey buildings (n = 12,764) to 16.9% in buildings with four or more storeys (n = 1,589), while median floor area rose from 205 to 4,830 m², indicating confounding between storeys and size. Factories had a 13.0% rate and warehouses 6.2%. High-spread incidents had shorter travel times (5.7 vs. 6.0 minutes) and station distances (7 vs. 9 km), but distributions overlapped. This likely reflected the urban concentration of large facilities and was not causal evidence.

3.2 Risk-Contributing Factors

In the block-wise ablation analysis, removing ignition-context variables reduced the PR-AUC by 0.038. Removing municipal- and metropolitan-level jurisdiction variables reduced it by 0.015, while removing structural categories and emergency-response times reduced it by 0.006 and 0.005, respectively. In contrast, removing spatial-distance variables increased the PR-AUC by 0.009, and removing building-size variables increased it by 0.003, indicating that neither block provided an independent improvement in predictive

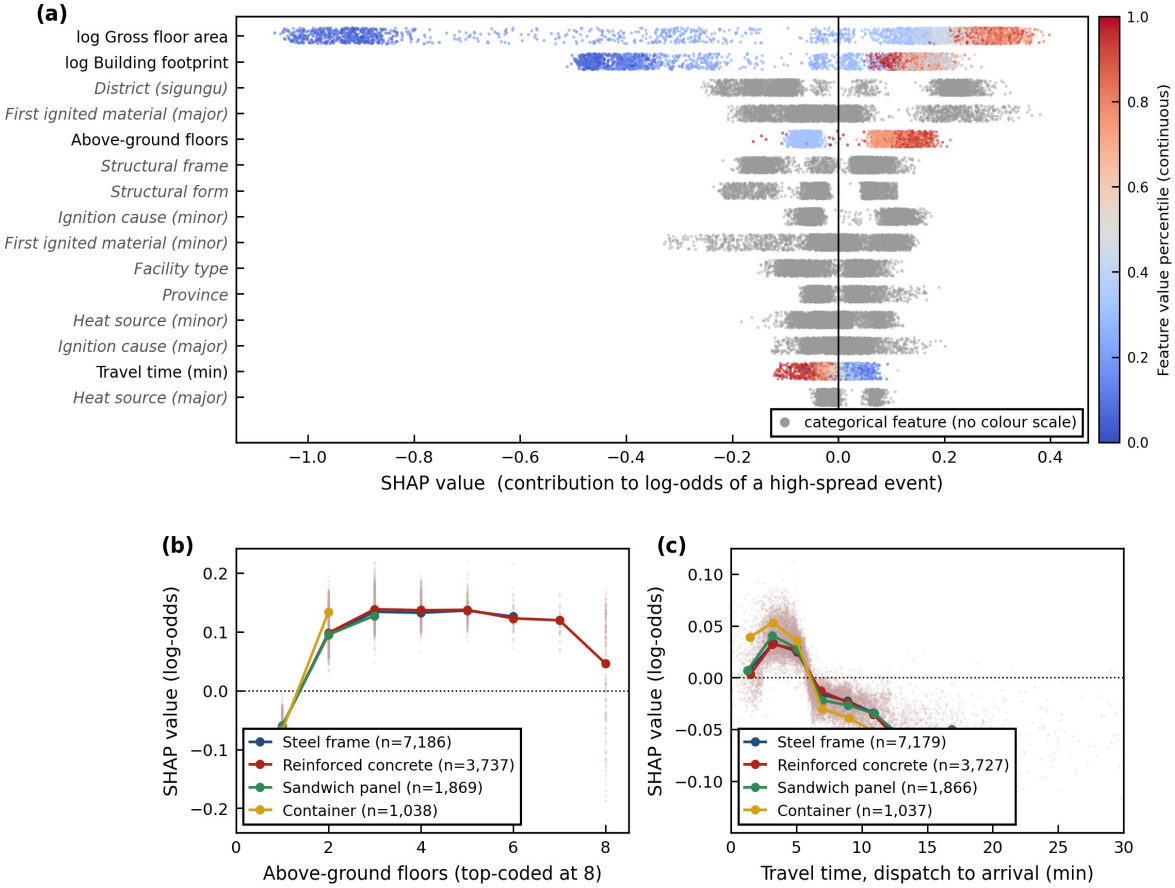

(a) Global SHAP Summary of the Leading Predictors

(b) SHAP Contribution of Above-Ground Storeys by Structural Frame

(c) SHAP Contribution of Dispatch-to-Arrival Travel Time by Structural Frame

Figure 1 SHAP-Based Interpretation of the Conditional High-Spread Fire Risk Model

performance.

The building-size block had virtually no ablation effect despite having the highest SHAP importance. This apparent discrepancy reflects strong correlations among gross floor area, building footprint area, number of storeys, facility type, and structural type. Consequently, when one variable or predictor block is removed, the remaining correlated variables can substitute for the information it contained.

The leading global mean absolute SHAP values were 0.354 for log-transformed gross floor area, 0.197 for log-transformed building footprint area, 0.155 for municipal jurisdiction, 0.092 for first material ignited, 0.080 for the number of above-ground storeys, and 0.078 for structural type. Travel time ranked 14th, with a mean absolute SHAP value of 0.031.

The SHAP contribution of the number of storeys reached a shallow peak between two and five storeys and subsequently declined. The decline above six storeys was confined to reinforced concrete buildings. The contribution of travel time changed sign at approximately five minutes but remained small, with an absolute magnitude below 0.05. These values represent contributions to model predictions and should not be interpreted as causal effects.

3.3 Robustness Analyses

Lowering the high-spread threshold to the 75th percentile (5 m²; prevalence = 0.235) produced a PR-AUC of 0.358 and a ROC-AUC of 0.653. Raising it to the 95th percentile (150 m²; prevalence = 0.045) produced values of 0.122 and 0.736, respectively.

Under the relative criterion for addressing size

confounding—burned area divided by gross floor area ≥ 0.10—the prevalence was 0.098 and the PR-AUC was 0.169, equivalent to 1.73 times the prevalence baseline. Although lower than under the absolute-area criterion, the model retained discriminatory ability. Log-transformed gross floor area remained the leading SHAP contributor (mean absolute value = 0.427), indicating that its importance was not solely an artefact of the absolute-area outcome.

When the 90th-percentile threshold was calculated separately within each gross-floor-area quartile, PR-AUC ranged from 0.130 to 0.178, approximately 1.5–1.9 times the respective prevalence baselines.

PR-AUC was 0.202 in urban cities and districts (n = 2,904; 95% CI: 0.173–0.240) and 0.190 in rural counties (n = 818; 43 high-spread incidents; 95% CI: 0.100–0.305). The wide rural confidence interval precluded a substantive urban–rural comparison. Treating the 97 incidents without identifiable municipal jurisdictions as a separate category yielded a PR-AUC of 0.203 and did not alter the conclusions.

4. Conclusions

This study distinguished fire-occurrence probability from post-fire damage-spread risk, defining the latter as the conditional probability that an observed fire reaches a burned area of at least 50 m². In the locked 2023 holdout, the primary model achieved a PR-AUC of 0.197 (95% CI: 0.169–0.233), 2.08 times the prevalence baseline. At a 10% selection rate, its lift was 2.62, compared with 1.11 for the gross-floor-area rule. The improvement over the univariate size model was +0.078 (95% CI: +0.050 to +0.108), supporting the added value of multivariable modelling.

Performance gains were driven mainly by building, spatial, and ignition-context variables, whereas response times added no significant value. Removing categorical variables reduced PR-AUC by 23.9%, but CatBoost did not significantly outperform one-hot-encoded logistic regression, indicating that categorical-information handling mattered more than algorithm choice. Spatial optimism was limited to 0.6%–2.2%, and sensitivity analyses using relative or size-stratified outcomes retained discrimination at 1.5–1.9 times their prevalence baselines.

The pre-incident model captured 19.9% of high-spread fires when selecting the top 10% of predicted risks. This score should be used as an intermediate prioritisation signal for inspections and regional planning, not for ignition prediction, facility safety certification, or causal inference. Future research should integrate denominator data for buildings with and without fires with fire-protection systems, fuel loads, and damage costs to assess both fire occurrence and consequences.

Reference

[1] S. Kaplan, B.J. Garrick, On the quantitative definition of risk, Risk Anal. 1 (1981) 11–27.

[2] International Organization for Standardization (ISO), ISO 16732-1:2012, Fire safety engineering—Fire risk assessment—Part 1: General, Geneva, 2012.

[3] B.S. Walia et al., A dynamic pipeline for spatio-temporal fire risk prediction, in: Proceedings of the 24th ACM SIGKDD International Conference on Knowledge Discovery & Data Mining, 2018, pp. 764–773.

[4] Y. Hao, M. Li, J. Wang, X. Li, J. Chen, A high-resolution spatial distribution-based integration machine learning algorithm for urban fire risk assessment : A Case Study in Chengdu, China, ISPRS Int. J. Geo-Inf. 12 (2023) 404.

[5] S. Ahn, J. Won, J. Lee, C. Choi, Comprehensive building fire risk prediction using machine learning and stacking ensemble methods, Fire 7(10) (2024) 336.

[6] J. Lee, J. Shin, J. Lee, C. Park, D. Sohn, Development of a data-based machine learning model for classifying and predicting property damage caused by fire, Appl. Sci. 13(21) (2023) 11866.

[7] T. Buffington, O.A. Ezekoye, Statistical analysis of fire department response times and effects on fire outcomes in the United States, Fire Technol. 55 (2019) 2369–2393.

[8] L. Prokhorenkova, G. Gusev, A. Vorobev, A.V. Dorogush, A. Gulin, CatBoost: unbiased boosting with categorical features, in: Advances in Neural Information Processing Systems, vol. 31, 2018, pp. 6638–6648.

[9] S.M. Lundberg, S.-I. Lee, A unified approach to interpreting model predictions, in: Advances in Neural Information Processing Systems, vol. 30,

2017, pp. 4765–4774.
[10] D.R. Roberts et al., Cross-validation strategies for data with temporal, spatial, hierarchical, or phylogenetic structure, Ecography 40(8) (2017) 913–929.
[11] T. Saito, M. Rehmsmeier, The precision–recall plot is more informative than the ROC plot when evaluating binary classifiers on imbalanced datasets, PLoS ONE 10(3), e0118432 (2015) e0118432.
[12] B. Van Calster, D.J. McLernon, M. van Smeden, L. Wynants, E.W. Steyerberg, Calibration: the Achilles heel of predictive analytics, BMC Med. 17 (2019) 230.
[13] S. Kaufman, S. Rosset, C. Perlich, O. Stitelman, Leakage in data mining: formulation, detection, and avoidance, ACM Trans. Knowl. Discov. Data 6(4), Article (2012) 15:1–15:21.
[14] G.S. Collins, J.B. Reitsma, D.G. Altman, K.G.M. Moons, Transparent reporting of a multivariable prediction model for individual prognosis or diagnosis (TRIPOD): the TRIPOD statement, Ann. Intern. Med. 162(1) (2015) 55–63.

床の摩耗を生じさせる歩行時のこすり現象の荷重性状の把握

Load Characteristics of Rubbing during Walking that Causes Floor Wear

森田 歩花※1, 福田 眞太郎※2
Ayuka Morita, Shintaro Fukuda

ABSTRACT

Floors in public facilities are designed to prevent excessive slipperiness for safe pedestrian use. However, heavy pedestrian traffic, such as in railway stations, can wear floor surfaces and increase slipperiness to unsafe levels. This study aims to establish a method for predicting changes in slipperiness caused by floor wear. In this paper, differences among pedestrians and walking movements were investigated using the load characteristics and frequency of rubbing during heel strike, which is considered the primary cause of floor wear. The horizontal and vertical forces, rubbing duration, and the number of steps per unit walking distance were identified as the relevant parameters. Compared with normal walking, fast walking tended to produce slightly greater rubbing loads but a lower rubbing frequency. Although considerable inter-subject variability was observed, conservative ranges for predicting floor wear were also identified.

1. Introduction

Floor slipperiness is an important performance characteristic for everyday safety. In Japan, the Coefficient of Slip Resistance (*C.S.R*) [1], which is specified in Japanese Industrial Standards [2], is widely used as an index of floor slipperiness. A lower *C.S.R* value indicates greater floor slipperiness, and a floor with a *C.S.R* value below 0.4 is considered too slippery for normal walking. Therefore, flooring materials used in Japanese railway stations are selected to ensure *C.S.R* values well above 0.4.

However, in facilities with extremely large numbers of pedestrians, such as railway stations, repeated pedestrian traffic progressively wears the floor surface and increases floor slipperiness. As a result, slip-and-fall accidents have been reported. Fig.1 shows an example of *C.S.R* measurements for the same flooring material installed at multiple railway stations [3]. The horizontal axis represents the cummulative number of passengers using each station, while the vertical axis represents the *C.S.R* measured under wet conditions simulating rainfall. As shown in the figure, stations

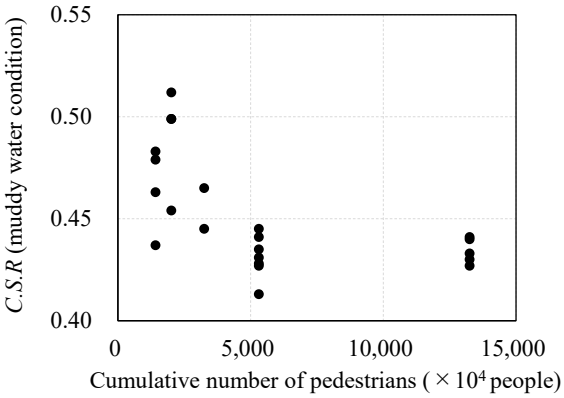

Fig.1 *C.S.R* for the same floor material at multiple stations [3]

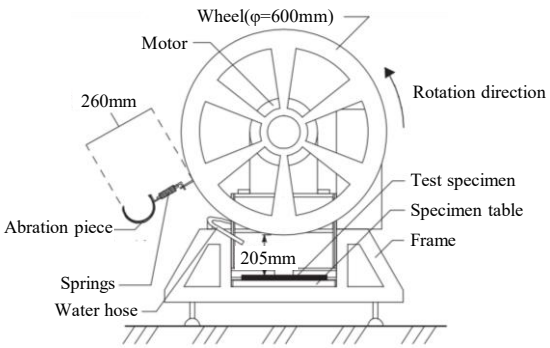

Fig.2 Wear acceleration machine [5]

※1 日本 東京科学大学 環境・社会理工学院 修士課程
※2 日本 東京科学大学 環境・社会理工学院 准教授 博士(工学)

with larger passenger volumes tend to have lower *C.S.R* values under wet conditions, indicating that floors become more slippery as the cumulative number of pedestrians increases. Therefore, to maintain a safe level of floor slipperiness over the long term, a method is needed to predict changes in floor slipperiness caused by pedestrian-induced wear.

Kudo et al. [4] investigated floor wear caused by normal walking and demonstrated that the primary cause of floor wear is rubbing that occurs during heel strike. They also developed the Wear acceleration machine shown in Fig.2, which reproduces the rubbing load to estimate changes in floor slipperiness [5]. Using this machine, Fukuda et al. [3] investigated its applicability to the floors of several existing buildings and found that rubbing loads differ among location to another even within the same facility. This difference is considered to result from variations in pedestrian movements at each location, which cause differences in both the magnitude and the frequency of rubbing. To accurately predict changes in floor slipperiness, it is desirable to identify the load generated during rubbing and its frequency of occurrence for different types of pedestrian movement and incorporate these factors into the prediction method.

Accordingly, this study focuses on Japanese railway stations, where pedestrian traffic is particularly heavy and floor wear is likely to occur. This study aims to clarify differences in wear loads among different pedestrian movements. This paper presents the results of an investigation into these differences in wear loads, focusing on the load characteristics during rubbing.

2. Target Movements

Table 1 lists pedestrian movements that are assumed to cause rubbing on the floor during heel strike. The movements are classified according to walking speed and the change of direction angle, both of which are considered to affect the magnitude of the rubbing load. Observations of pedestrian behavior in an actual railway station confirmed the occurrence of the movements indicated by the cells highlighted in blue in the table. Although would be desirable examing all of these movements, doing so is impractical. Therefore, this study focuses on the representative movements indicated by ● and ○ in the table. Running, starting to run, and sudden stopping were also observed in the station. However, these movements occur only sporadically and are unlikely to be repeated at the same location. Therefore, even if they generate relatively large abrasion loads per occurrence, their cumulative abrasion load is unlikely to be significant, and these movements were excluded from the scope of this study. This paper presents the results for normal walking and fast walking, indicated by ● in the table.

3. Measurement Overview and Procedure

3.1 Measurement Overview

Fig.3 shows an overview of the walkway used to measure the load characteristics during walking. As shown in the figure, a force plate was installed in part of the walkway to measure the vertical and horizontal (anteroposterior) loads after the subject had reached a steady gait. The same single-layer vinyl floor tile was installed on both the walkway and the force plate.

Table 1 Classification of pedestrian movements considered to cause rubbing

		Change in direction angle				
		0° (Straight)	…	90° (Right-angle turn)	…	180° (U-turn)
Constant-speed movement	Slow walking	○		○		
	⋮					
	Normal walking	●		○		
	⋮					
	Fast Walking	●		○		
	⋮					
	Running					
Movement with speed changes	Starting to run					
	Decelerating	○				
	Sudden stop					

Legend : ●, ○ = Movement considered in this sturdy.

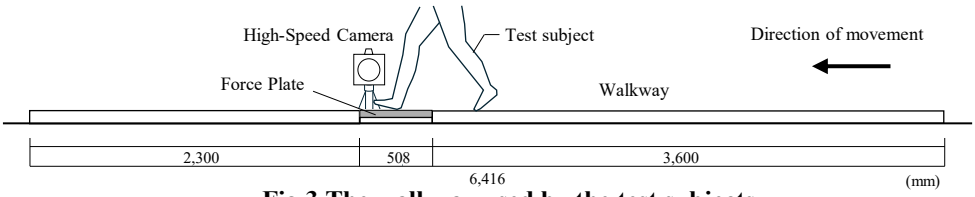

Fig.3 The walkway used by the test subjects

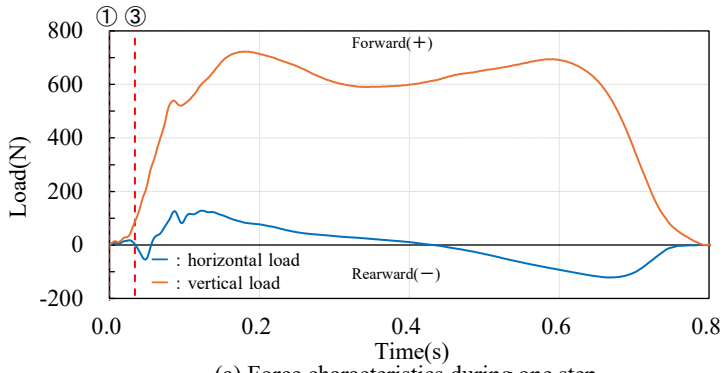

(a) Force characteristics during one step

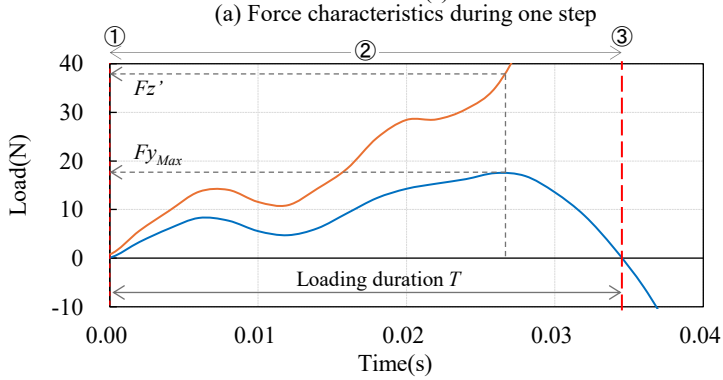

(b) Force characteristics during the rubbing phenomenon (enlarged view of (a))

Fig. 4 Example of measured load characteristics

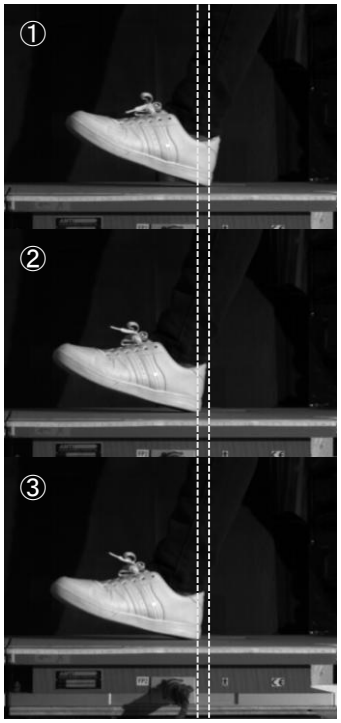

Photo 1 Situation immediately after heel contact

3.2 Identification of the Load Characteristics Corresponding to Rubbing

To identify the segment of the walking force history corresponding to rubbing, a preliminary measurement was conducted with one participant walking at a normal speed. The subject wore ordinary athletic shoes during the measurement. In addition, foot-floor contact was recorded using a high-speed camera.

Fig.4 shows the measured load characteristics, and Photo 1 shows the heel motion immediately after heel contact. As shown in the photo, the following sequence of motion was observed:

①The heel contacts the floor.

②The heel slides forward while remaining in contact with the floor.

③The forward sliding motion ends, and the forefoot begins to contact the floor.

Comparison of this motion sequence with the measured force histories showed that the rubbing phase corresponds to the period indicated by the dashed lines in Fig.4(b). These results indicate that rubbing is characterized by a slight forward horizontal load acting immediately after heel strike. Based on these findings, the portion of the walking load characteristics exhibiting a slight forward horizontal load was regarded as corresponding to rubbing in the subsequent analysis.

4. Measurement Results

4.1 Normal Walking

The load characteristics associated with rubbing were measured during normal walking for 13 subjects (age: 22-35 years; body weight: 50-88 kg), and each subject performed 50 trials. No specific instructions were given regarding stride length or walking cadence. All subjects wore the same type of athletic shoes as those used in Section 3.

From the measured load characteristics, the parameters representing the magnitude and frequency

of rubbing were extracted and compared. Specifically, the magnitude of the load during rubbing was evaluated using the maximum horizontal load (denoted by Fy_{max}) and the vertical load at the instant when Fy_{max} occurred (denoted by Fz'). The cumulative rubbing distance per unit walking distance was evaluated using L, expressed as

$$L = V_W \cdot T \cdot N_W$$

where V_w is the foot velocity at heel contact (m/s), T is the duration of rubbing (s), and N_w is the number of steps per unit walking distance (steps/m). Among these parameters, T was obtained from the measured load characteristics, while N_w was determined from videos recorded during the measurements. Fig.4(b) shows the portions of the load characteristics from which Fy_{max}, Fz', and T were extracted.

Fig.5 presents the extracted values of Fy_{max}, Fz', and T, while Fig.6 shows the results for N_w. In both figures, the results for normal walking are shown in black. For each parameter, the distributions of the 50 measurements are presented as box-and-whisker plots. Focusing on differences among subjects, Subjects B, C, and M exhibited relatively high values of Fy_{max} and Fz', whereas Subjects J, K, and L exhibited relatively smaller values. These results indicate that the magnitude of the load during rubbing varies among individuals, suggesting that some people are more likely to generate larger rubbing loads than others.

The floor wear considered in this study becomes apparent as abrasion loads produced by an unspecified number of pedestrians accumulate over a long period. Therefore, for the parameters extracted in Fig.5 and Fig.6, it is appropriate to characterize each parameter using values that exclude relatively large values occurring only occasionally. These values may result from differences among individuals and step-to-step variability within the same individual. However, because the prediction of changes in floor slipperiness should be performed conservatively, the third quartile value was adopted as the representative value.

As shown in the figures, the third quartile values for all subjects during normal walking were as follows:

- Fy_{max} : 1.0 - 14.3 N
- Fz' : 10.0 - 42.3 N
- T : 0.002 - 0.025 s

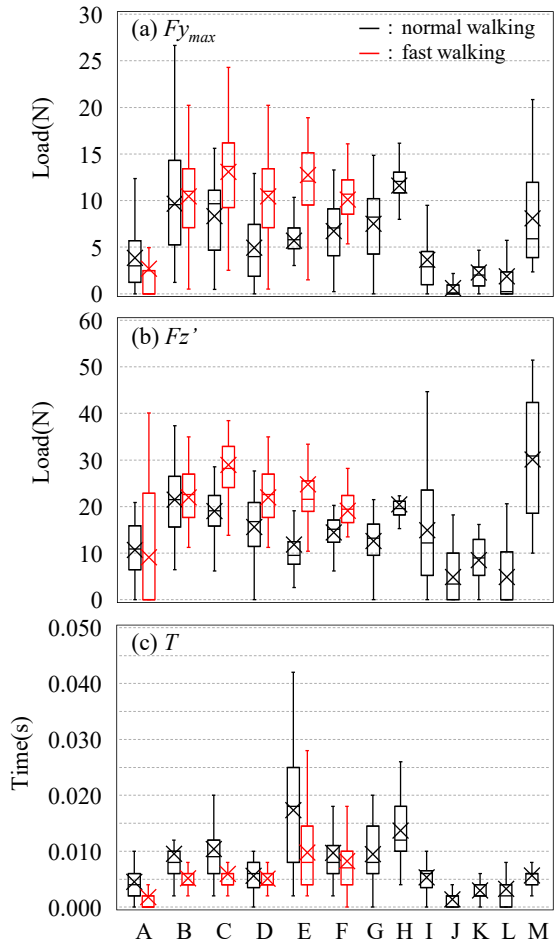

Fig.5 Results of Fy_{max}, Fz', and T for each test subject

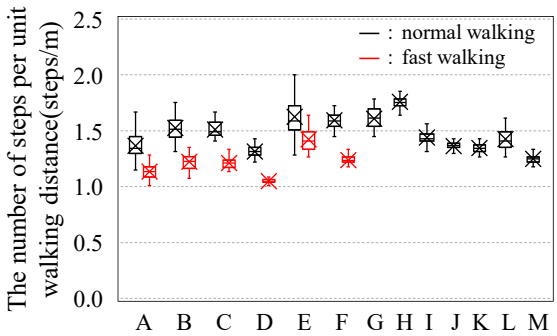

Fig.6 Results of N_w for each test subject

- N_w : 1.27 - 1.79 steps/m

4.2 Fast Walking

Next, to examine differences in load characteristics due to walking speed, the load characteristics during fast walking were measured for a subset of the subjects using the same procedure as that used for normal walking.

The results for fast walking are shown in red in Fig.5 and Fig.6. As shown in the figures, the third quartile values during fast walking were as follows:

- Fy_{max} : 2.7 - 16.2 N
- Fz' : 22.4 - 32.9 N
- T : 0.002 - 0.015 s
- N_w : 1.05 - 1.49 steps/m

Both Fy_{max} and Fz' tended to be larger during fast walking than during normal walking for most subjects. In contrast, T showed lower values than those during normal walking for all subjects. In addition, N_w was lower in fast walking than in normal walking for all subjects.

These results indicate that, as walking speed increases, the load generated during rubbing tends to become slightly larger, whereas the number of rubbing events tends to decrease compared with normal walking.

5. Comparison with the Load Characteristics of the Wear Acceleration Machine

The load characteristics obtained for normal walking in Section 4.1 were compared with those of the existing Wear acceleration machine. To ensure consistency with the measurement conditions described in Section 4, a rubber sheet was used as the abrasion piece, and a single-layer vinyl floor tile was attached to the force plate during measurements using the Wear acceleration machine.

The measurements showed that the maximum horizontal load was approximately 7.0 N, and the vertical load at the maximum horizontal load was approximately 11.4 N. These values fell within the ranges of Fy_{max} and Fz' obtained in Section 4.1, indicating that the Wear acceleration machine can generally reproduce the load characteristics observed during normal walking.

On the other hand, as shown in Section 4.2, both Fy_{max} and Fz' tended to be larger during fast walking than during normal walking. Therefore, for facilities where fast walking frequently occurs, such as railway stations, the load conditions of the Wear acceleration machine should be adjusted.

6. Conclusions

The load characteristics corresponding to rubbing were identified, and differences in abrasion loads were investigated by examining multiple subjects. Using the method presented in this paper, further detailed investigations will be conducted on different types of pedestrian movements.

Acknowledgement

The authors would like to thank all participants for their cooperation during the measurements.

Reference

[1] Hidenori Ono et al.: Study on the Slipperiness of Building Floors and It's Evaluating Method, Transactions of the Architectural Institute of Japan, No. 356, pp. 1-8, 1985. 10

[2] Japanese Industrial Standards Committee: JIS A 1454: 2016 Test Methods-Resilient Floor coverings, 2016

[3] Shintaro Fukuda et al.: Investigation on Applicability of Abrasion Acceleration Machine for Actual Building Floors, Development of Abrasion Accelerating Machine of the Floor for Reproducing Change of the Slip Resistance from Abrasion in Walking, The Speedy Estimation Method for Change of the Slip Resistance of Floors Caused from Abrasion Part 3, Journal of Structural and Construction Engineering, Vol.86, No.779, pp.11-20, 2021.1

[4] Rumi Kudou et al.: Preparatory Examination for Change of the Slip Resistance of Floors Caused from Abrasion in Walking, The Speedy Estimation Method for Change of the Slip Resistance of Floors Caused from Abrasion Part 1, Journal of Structural and Construction Engineering, No.618, pp.7-13, 2007.8.

[5] Rumi Kudou et al.: Development of Abrasion Accelerating Machine of the Floor for Reproducing Change of the Slip Resistance from Abrasion in Walking, The Speedy Estimation Method for Change of the Slip Resistance of Floors Caused from Abrasion Part 2, Journal of Structural and Construction Engineering, Vol. 73, No. 631, pp. 1473-1487, 2008. 9

日本の住専危機と韓国の非銀行金融機関不動産 PF 不良の構造的比較研究

A Structural Comparative Study on Japan's Jusen Crisis and Korea's Non-Bank Financial Institution Real Estate PF Distress

황수현 ※1、정경태※2、 박재현※2、 양승진※1、이동훈※3

Suhyeon Hwang, Kyeongtae Jeong, Jaehyun Park, Seungjin Yang, Donghoon Lee

ABSTRACT

"This study examines Korea's non-bank financial institution (NBFI) real estate project financing (PF) distress by comparing it with Japan's 1990s jusen crisis, using Milhaupt's (1997) regulatory cartel model as an analytical framework. Using a case study approach based on Yin (2003) and pattern matching, the two cases are compared across four dimensions: supervisory structure, risk concentration, liability transfer, and government backstop. While both share a "no exit"-type mechanism delaying insolvency, liability transfer differs fundamentally: Japan's occurred vertically within the financial sector, while Korea's is externalized horizontally to construction companies through completion guarantees. A regression analysis (N=17) confirms that the savings bank NPL ratio is strongly associated with the base rate and construction industry conditions (Adj.R^2 = .674, $p < .001$). These findings suggest that Korea's risk-transfer pattern may concentrate systemic risk within the construction industry despite easing short-term financial pressure. The study proposes a typology based on the direction of liability transfer and offers policy implications for integrated supervision and deposit insurance capacity.

1. Introduction

Real estate project financing (PF) is generally defined as a financing technique that raises capital based on a project's future cash flows rather than the developer's creditworthiness [1]. In Korea, however, PF has operated under a distinctive structure that relies heavily on completion guarantees and credit enhancement provided by construction companies. Under this structure, PF distress arising during real estate market downturns carries an inherent risk of transmission beyond the financial sector into a chain of insolvency across the construction industry as a whole. During the recent downturn in Korea's real estate PF market, liquidity crises at multiple construction firms became visible, illustrating a pattern of risk transmission between the financial and construction sectors. This situation in Korea invites structural comparison with Japan's jusen (住専, housing loan companies) crisis of the 1990s. The jusen crisis represents a prominent case in which the insolvency of non-bank financial institutions, following the collapse of the real estate bubble, remained unresolved and accumulated over an extended period. Underlying this outcome was a distinctive mode of Japanese financial supervision, characterized as a "regulatory cartel" and comprising four normative principles: survival of the weakest, no exit, responsibility and equitable subordination, and implicit government insurance.

This framework contributed to systemic stability during Japan's period of high economic growth [2]. However, as the system transitioned into a phase of slower growth, it evolved into regulatory forbearance—concealing insolvency and delaying its resolution [3].

This study uses the institutional mechanisms embedded in the resolution process of Japan's jusen

※1 大韓民国 国立한밭大学校 建築工学科 修士課程

※2 大韓民国 国立한밭大学校 建築工学科 博士課程

※3 大韓民国 国立한밭大学校 建築工学科 教授 博士(工学)

crisis as an analytical framework to examine the structure of NBFI real estate PF distress in Korea.

Employing a case study approach based on Yin's (2003) methodology and pattern matching, the two cases are examined across four analytical dimensions: supervisory structure, risk concentration mechanisms, liability transfer structure, and the pathway of government backstop.

Whereas Japan's liability transfer occurred vertically within the financial sector—from the distressed subsidiary to the parent bank—Korea's liability transfer takes the form of horizontal externalization toward a non-financial industry actor, the construction company. This contrast carries implications for PF risk management and supervisory design from the perspective of the construction industry.

Meanwhile, domestic research has also examined the mechanism of inter-industry risk transmission Prior domestic research has also embedded in the Korean-style PF structure. Empirically demonstrated, using twelve years (2008–2019) of construction firm financial data, the mechanism by which credit enhancement measures such as construction companies' completion guarantees strip Korean-style PF of its non-recourse character, thereby amplifying the distress risk of both construction firms and financial institutions during macroeconomic downturns and escalating it into systemic risk [4]. This typology constitutes an analytical framework that goes beyond a simple comparison of phenomena, explaining how the direction of liability transfer shapes the mode of government intervention during the resolution process—specifically, whether fiscal funds are directly injected, and which sector ultimately absorbs the risk.

2. Research Methods

This study adopts a qualitative comparative analysis based on a case study approach following Yin's (2003) methodology. Case selection follows three criteria: (1) non-bank financial institutions serve as the primary supplier of real estate credit, (2) changes in the interest rate environment act as a triggering factor for distress, and (3) institutional government response is involved.

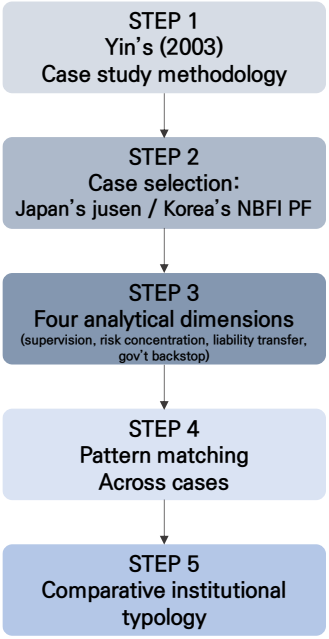

Figure 1 Research flowchart

Japan's jusen crisis (1990s) and Korea's non-bank PF sector (2022–present) were selected as cases satisfying all three conditions. The overall research process is summarized in Figure 1.

The unit of analysis comprises four dimensions: (1) supervisory structure, (2) risk concentration mechanism, (3) liability transfer structure, and (4) the pathway of government backstop.

The tertium comparationis is set as "a non-bank financial institution-centered real estate financing crisis." Although the two cases experienced this common phenomenon within different institutional contexts, this framework allows for identifying both the structural commonalities of the crisis and the differences in institutional response.

Data are drawn from academic literature, official policy reports (FSA, Financial Services Commission, Bank of Korea, AMRO), and statistical data, with analysis conducted using pattern matching and explanation building techniques.

3.Theoretical Background: Japan's Regulatory Cartel Model and the Jusen Crisis

3.1 The Four Substantive Norms of the Regulatory Carte

The operation of Japanese financial supervision has been characterized as a 'regulatory cartel,' in which the regulator and regulated institutions cooperate to jointly control market entry and output [2].

Under this model, Japanese financial regulation operates according to four substantive norms. First, a policy ensuring the survival of the weakest member ('survival of the weakest'). Second, a principle preventing any member from exiting the market through bankruptcy ('no exit'). Third, when a subsidiary or affiliated firm faces the risk of insolvency, the parent company or principal financier assumes responsibility and voluntarily subordinates its own claims to those of other creditors ('responsibility and equitable subordination'). Fourth, the combination of these principles gives rise to an implicit government insurance, whereby the government ultimately guarantees the system as a whole [2].

3.2 Regulatory Forbearance and the Development of the Crisis

This normative framework functioned effectively during periods of high growth and stability; however, in phases of slower growth or unavoidable restructuring, it delayed the resolution of insolvency and deepened the crisis. Japan's financial crisis of the 1990s did not emerge suddenly, but was the product of a gradual structural transformation unfolding over roughly two decades, including a policy error consisting of years of regulatory forbearance in the face of serious non-performing loan problems [5].

3.3 The Unfolding of the Jusen Crisis

On March 27, 1990, the Ministry of Finance (MOF) issued administrative guidance aimed at curbing the rapid expansion of real estate lending, restricting the growth rate of real-estate-related bank lending to within the overall loan growth rate. However, this guidance excluded housing loan companies (jusen) and agricultural cooperative financial institutions from its scope, which substantially weakened its effectiveness. As a result, real estate lending by these excluded institutions continued to expand even as bank lending growth slowed, and the subsequent insolvency of the jusen sector following the bubble's collapse gave rise to the jusen problem [6].

The cartel norms were also clearly manifested in the loss-allocation process once the insolvency materialized. Under the resolution plan finalized in 1996, the founder banks of the jusen companies wrote off ¥3.5 trillion in loans, and other creditor banks wrote off an additional ¥1.7 trillion, consistent with the norm of responsibility and equitable subordination. By contrast, the agricultural cooperative sector—despite being the largest lender group—contributed only ¥530 billion, reflecting the survival of the weakest norm that protected the group classified as most vulnerable. The residual ¥680 billion was ultimately covered by fiscal funds from the Japanese government, illustrating how the implicit government insurance norm operated in practice at the final stage of the cartel's resolution process [7].

4. The Structure of NBFI Real Estate PF Distress in Korea

4.1 Fragmented Supervisory Structure and the Path of Deregulation

Unlike Japan's regulatory cartel model, which was based on a high degree of regulatory concentration and patterning centered on a single supervisory authority (MOF), Korea's supervisory framework for non-bank financial institutions is fragmented across sectors. Policy research has noted that such a fragmented structure, characterized by multiple supervisors and protection agencies, increases the likelihood of inter-sectoral competition rather than industry-wide policy coordination, whereas consolidation into a single supervisory authority could enhance the capacity to prevent and respond to crises among distressed financial institutions [8].

Against this backdrop of fragmented supervision, a

series of deregulatory measures in the mid-2000s—including the approval of savings bank group affiliation and the easing of single-borrower lending limits—encouraged savings banks, in particular, to expand investment in high-risk assets such as real estate PF loans. As the real estate market subsequently contracted following the 2008 global financial crisis, insolvency became increasingly visible among large savings banks, leading to a structural restructuring of the sector [9].

4.2 Recurrence of Recent PF Distress and Inter-Sectoral Transmission

Despite this historical experience, a similar pattern of risk concentration reemerged during the recent downturn in Korea's real estate PF market: the NPL ratio for real estate PF loans across the financial sector rose sharply from 5.1% at the end of 2023 to 11.2% by mid-2024 [10].

A regression analysis using the savings bank NPL ratio as the dependent variable, with the BOK base rate and construction GDP YoY growth as independent variables (N=17, 2021Q1–2025Q1), showed strong explanatory power (Adj.R^2 = .674, $F(2,14) = 17.565$, $p < .001$), as summarized in Table 1. The base rate had a significant positive effect ($\beta = .628$, $p = .001$), while construction GDP growth had a significant negative effect ($\beta = -.543$, $p = .002$), with no evidence of multicollinearity (VIF = 1.001 for both variables). These results suggest that savings bank PF distress is strongly linked to both rising interest rates and the contraction of the real construction economy.

Table 1 Regression Results for Savings Bank NPL Ratio (N=17, 2021Q1–2025Q1)

Independent Variable	β	t	p
BOK Base Rate	.628	4.400	.001***
Construction GDP YoY	-.543	-3.806	.002**

This structure of risk transfer, arising from deregulation and fragmented supervision, is functionally similar to the mechanism in Japan's regulatory cartel model, in which the survival of the weakest and no exit norms limited competition among sector participants and enabled the externalization of distress. However, a key difference lies in the origin of the mechanism: in Japan, it was the product of deliberate coordination through administrative guidance from a single supervisory authority, whereas in Korea, it emerged as an unintended, structural consequence of deregulation and fragmented supervision.

4.3 Completion Guarantee Structure of Construction Companies: Horizontal Externalization of Risk Across Industries

Unlike Japan's responsibility and equitable subordination norm, which constituted a vertical transfer structure in which a financial institution—the parent bank—shared responsibility for the insolvency of its subsidiary (jusen) within the financial sector, Korea's real estate PF adopts a structure in which construction companies provide credit enhancement in the form of completion guarantees or conditional debt assumption. That is, while the nominal borrower of the PF loan is the developer (SPC), if completion is not achieved within the loan maturity period, the construction company assumes the debt or bears repayment responsibility on its own credit, such that the substantive credit risk ultimately accrues to the construction company. This structure differs fundamentally from the Japanese pattern of liability transfer, which occurred vertically within the financial sector, in that Korea's risk is externalized horizontally from the financial sector to a

non-financial industry actor—the construction industry. Whereas financial institutions such as parent banks tend to have relatively greater capital buffers and access to policy support, construction companies have comparatively weak capital structures, and the accumulation of PF distress carries a substantial risk of cascading into insolvency across the construction sector. Indeed, the recent visibility of liquidity crises among multiple construction firms during the downturn in Korea's real estate PF market illustrates that, while this inter-industry externalization of risk may contribute to short-term financial system stability, it can also give rise to a new form of systemic risk by shifting risk onto the real economy.

4.4 Differences in the Pathway of Government Backstop

With respect to the government's role as ultimate guarantor, whereas Japan's implicit government insurance norm led to the direct injection of public funds in the resolution of the jusen crisis, Korea, despite substantial capital impairment at the Korea Deposit Insurance Corporation's deposit insurance fund during the 2011 savings bank crisis, has handled related distress using the fund's own resources without a separate injection of public funds. This difference illustrates that the two countries diverge in the fiscal pathway through which the implicit government insurance norm is realized—direct injection of public funds versus internal absorption through a deposit insurance fund—suggesting that, should Korea's NBFI PF distress deepen further, policy consideration is needed as to whether the deposit insurance fund alone would be sufficient to absorb the impact. Table 2 summarizes these structural differences between the two cases.

Table 2 Structural Comparison of Japan's Jusen Crisis and Korea's NBFI PF Distress

Dimension	Japan (Jusen)	Korea (NBFI/PF)
Supervisory structure	Centralized (MOF)	Fragmented (FSC, FSS, etc.)
Risk concentration	Convoy; coops excluded	Arbitrage to non-banks
Liability transfer	Bank absorbs subsidiary	Contractor guarantees
Distress resolution	No exit; 6-yr delay	Rate/GDP-linked; ongoing
Loss allocation	Banks ¥5.2T; coops ¥530B	Deposit insurance fund
Gov't backstop	Direct injection (¥680B)	Indirect (fund-based)
Transfer direction	Vertical	Horizontal

5. Conclusions

This study uses the regulatory cartel model as an analytical framework, comparing Japan's jusen crisis and Korea's non-bank financial institution (NBFI) real estate PF distress through pattern matching [2]. Both cases shared a "no exit"-type mechanism that delayed the immediate surfacing of insolvency, as well as a structure of liability transfer; however, the way these mechanisms operated and the ultimate locus of risk differed fundamentally between the two countries.

In Japan, within a deliberately coordinated cartel structure centered on a single supervisory authority (MOF), the parent bank—an actor internal to the financial sector—shared responsibility for the jusen's insolvency, with risk ultimately resolved through the direct injection of government fiscal funds. In Korea, by contrast, unintended risk concentration arose from a fragmented supervisory structure and deregulation, and the resulting credit risk was horizontally externalized from the financial sector to the construction industry—a real economic sector—through construction companies' completion

guarantees. This difference suggests that while Korea's pattern of risk transfer may cushion the financial system from short-term shocks, it may also embed a new form of systemic risk by concentrating risk in the construction industry, whose capital buffers are comparatively weak.

The policy implications can be summarized as follows.

First, strengthened integrated monitoring of the supervisory system is needed. Under the current fragmented supervisory structure, it is difficult to comprehensively track risk transmission across the non-bank sector.

Second, a separate monitoring framework is required for the inter-industry risk transmission embedded in the structure of contractors' completion guarantees. Because financial soundness indicators alone cannot capture the pathway through which PF distress transmits to the construction industry, information sharing and a joint response framework between financial supervisory authorities and industry ministries such as the Ministry of Land, Infrastructure and Transport are needed.

Third, a preemptive assessment of the deposit insurance fund's capacity is needed. The substantial capital impairment experienced by the deposit insurance fund during the 2011 savings bank crisis suggests that the same resolution approach may reach its limits should PF distress deepen further. Japan's experience of directly injecting fiscal funds in resolving the jusen crisis suggests that, should the limits of a fund-based resolution approach become apparent, social consensus on an expanded government role should be discussed in advance.

Finally, this study has limitations in generalizability, as it is a qualitative comparative analysis based on two cases. The regression analysis (N=17) confirmed a strong association between the base rate, construction industry conditions, and the savings bank NPL ratio (Adj.R^2 = .674, $p < .001$); however, caution is warranted in generalizing these results given the small sample size. Future research should extend the time-series data, broaden the scope of analysis to the non-bank sector as a whole—including mutual finance institutions—and further strengthen the quantitative comparison with the Japanese jusen case.

Reference

[1] S.S. Koh, E. Choi, A study on the measurement of contingent liability of construction companies and their corporate values, Korea Spat. Plan. Rev. 59 (2008) 189–202.

[2] C.J. Milhaupt, G.P. Miller, A regulatory cartel model of decisionmaking in Japanese finance, Z. Jpn. Recht 4 (1997) 18–29.

[3] C.J. Milhaupt, G.P. Miller, Regulatory failure and the collapse of Japan's home mortgage lending industry: a legal and economic analysis, Law Policy 22 (2000) 245–290.

[4] K.J. Kim, System risk transition analysis and policy alternatives for PF risk in construction and real estate industry, Korean J. Financ. Eng. 24 (2025) 173–203.

[5] T. Hoshi, H. Patrick, The Japanese financial system: an introductory overview, in: T. Hoshi, H. Patrick (Eds.), Crisis and Change in the Japanese Financial System, Kluwer Academic Publishers, Boston, 2000, pp. 1–30.

[6] S. Hyun, Lessons and implications of Japan's real estate loan quota regulation, Capital Mark. Focus 2017-18 (2017) 1–6.

[7] H. Nakaso, The financial crisis in Japan during the 1990s: how the Bank of Japan responded and the lessons learnt, Bank for International Settlements, 2011.

[8] I.C. Hwang, H.S. Kim, S.J. Lee, D.K. Kim, S.Y. An, Improvement measures for the deposit insurance and resolution system, Korea Insurance Research Institute, 2020.

[9] Financial Services Commission (Korea), Evaluation of savings bank restructuring outcomes and future policy directions, press release, 2014.7.3. Available from: https://fsc.go.kr/po010101/71188

[10] Financial Services Commission (Korea), Fourth review meeting on the soft landing measures for real estate PF, press release, 2024.8.29. Available from: https://fsc.go.kr/no010101/82983

04

POSTER SESSION

The 17th Korea-Japan Joint Symposium
on Building Materials & Construction

Building a Sustainable Future-
Carbon Neutrality in Cement & Concrete

セメント系材料における MICP 候補菌株としての廃コンクリート由来 *Lysinibacillus fusiformis* A15 のアルカリ安定性および高胞子形成能

Waste Concrete-Derived *Lysinibacillus fusiformis* A15 as an Alkaline-Stable and Highly Sporulating Candidate for MICP in Cementitious Materials

宋河然 [1] ・ 崔世珍 [2*]・金貞美 [3*]

Ha-Yeon Song[1], Se-Jin Choi[2*], and Jung-Mi Kim[3*]

ABSTRACT

Microbially induced calcite precipitation (MICP) holds promise for enhancing the durability of cementitious materials, but its practical application is hindered by the extreme alkalinity of cement pore solutions, which typically exceed pH 12. We isolated a ureolytic bacterium, *Lysinibacillus fusiformis* strain A15, from waste concrete and evaluated its performance under construction-relevant alkaline conditions. Strain A15 retained 95.5% of its ureolytic activity at pH 13 and demonstrated consistent $CaCO_3$ precipitation across pH 9–12, outperforming other *L. fusiformis* strains under identical conditions. A15 exhibited 96% sporulation efficiency, supporting long-term persistence and functional stability within cement matrices. Whole-genome sequencing identified an intact urease operon alongside conserved genetic networks governing sporulation, metal ion transport, and stress response. The convergence of cement-derived ecological origin, sustained ureolytic functionality, and high sporulation capacity positions A15 as a strong candidate for MICP-based concrete durability enhancement.

1. Introduction

MICP is a bio-mediated process in which microbial ureolytic activity promotes $CaCO_3$ formation, contributing to crack closure, pore refinement, and reduced permeability in cementitious materials [1,2]. However, practical implementation is constrained by cement pore solution alkalinity, which typically exceeds pH 11–13 during early hydration, imposing severe stress on vegetative cells [3]. Encapsulation strategies improve bacterial viability but increase material complexity and raise scalability concerns [4,5]. Endospore-forming bacteria offer a more construction-compatible alternative, though sporulation efficiency and post-germination uricolytic function vary considerably among strains [6,7].

Waste concrete represents a selective ecological niche defined by elevated pH and calcium-rich mineral phases, closely mirroring cement matrix conditions. Habitat-matched strain selection may offer a practical advantage, as ecological origin has been shown to influence precipitation kinetics and mineral–surface interactions [5,8]. Furthermore, identifying strains that combine high sporulation capacity with alkaline-tolerant ureolytic activity

※1 Research Professor, Ph.D, Institute of Life Science and Natural Resources, Wonkwang University, Iksan, Jeonbuk, 54538 Republic of Korea

※2 Professor, Ph.D, Department of Architectural Engineering, Wonkwang University, Iksan, Jeonbuk, 54538 Republic of Korea, Corresponding author (csj2378@wku.ac.kr)

※3 Professor, Ph.D, Department of Biomedical Materials Science, Wonkwang University, Iksan, Jeonbuk, 54538 Republic of Korea, Corresponding author (micro@wku.ac.kr)

could reduce the need for costly encapsulation, offering a more scalable route to durable, self-healing concrete [4,5]. Given the accelerating global generation of waste concrete, sustainable strain sourcing from such waste streams also aligns MICP development with circular-economy approaches to construction material management. In this study, we isolated *L. fusiformis* strain A15 from waste concrete and evaluated its ureolytic functionality, calcite precipitation capacity, sporulation efficiency, and genomic architecture as traits critical to MICP application in highly alkaline cementitious systems.

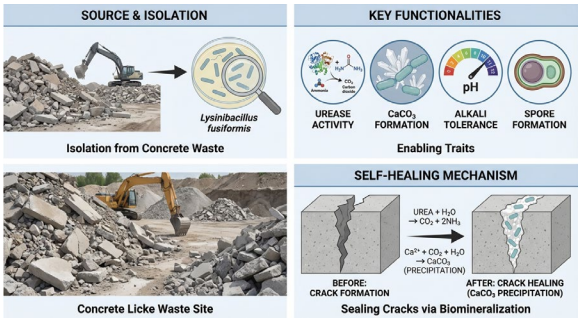

Figure 1. Schematic overview of the study design, illustrating the isolation of *L. fusiformis* A15 from waste concrete and its evaluation as a candidate for MICP-based durability enhancement in cementitious materials.

2. Materials and methods

2.1 Bacterial isolation and identification

Waste concrete debris from Jeonbuk, Republic of Korea (35.51°N, 127.22°E) was heat-treated at 65°C for 25 min, suspended in sterile PBS, and spread onto BPU agar (pH 7.0 or 9.0). Urease-active colonies were purified on YA agar and identified via 16S rRNA gene sequencing and BLASTn analysis. *E. coli* ATCC 25922 was included as a non-ureolytic reference.

2.2 Urease activity and $CaCO_3$ precipitation

Urease activity was assessed qualitatively on Christensen's urea agar and quantitatively in Stuart's urea broth (OD_{570}) following pre-culture in BPU at pH 7.0–13.0. For precipitation assays, strains were cultured in BPU broth at pH 9.0–12.0 for 72 h; filtered supernatants were treated with $CaCl_2$ (0.35 M), and dried precipitates were weighed. Precipitate morphology and elemental composition were examined by FE-SEM coupled with EDS.

2.3 Sporulation assay

Sporulation was induced in Difco Sporulation Medium at 30°C for 72 h and quantified by hemocytometer enumeration.

2.4 Whole-genome sequencing and statistical analysis

Sequencing was performed on the PacBio Sequel II platform with Flye assembly. BUSCO completeness and ANI (>95–96% threshold) confirmed assembly quality and species assignment. Functional annotation used Prokka and EggNOG-mapper. The genome was deposited in NCBI GenBank (CP182815.1; BioProject PRJNA1222761). All experiments were conducted in biological triplicate (n = 3); significance was assessed by one- or two-way ANOVA with Tukey's HSD test using GraphPad Prism v11.0.0.

3. Results and Discussion

3.1 Isolate recovery and identification

Eleven isolates were recovered from heat-enriched waste concrete suspensions, all belonging to order Bacillales (genera *Bacillus*, *Lysinibacillus*, *Peribacillus*, *Sporosarcina*, *Alkalihalophilus*, and *Paenibacillus*). The predominance of endospore-forming taxa reflects the dual selective pressure of in situ alkalinity and heat enrichment, confirming waste concrete as a reservoir of stress-tolerant, functionally relevant strains for MICP applications.

3.2 Ureolytic activity under alkaline conditions

At pH 13, A15 reached OD_{570} of 0.503 ± 0.002 at 12 h, significantly exceeding 1193 (0.250 ± 0.002) and 15323 (0.094 ± 0.001) ($P < 0.05$). Normalized to neutral controls, A15 retained 95.5% of ureolytic activity after pH 13 exposure, versus 85.5% for 1193 and 54.5% for 15323. This sustained enzymatic function under extreme alkalinity is critical for MICP in cement matrices where pore solution pH frequently exceeds 12 during early hydration [3].

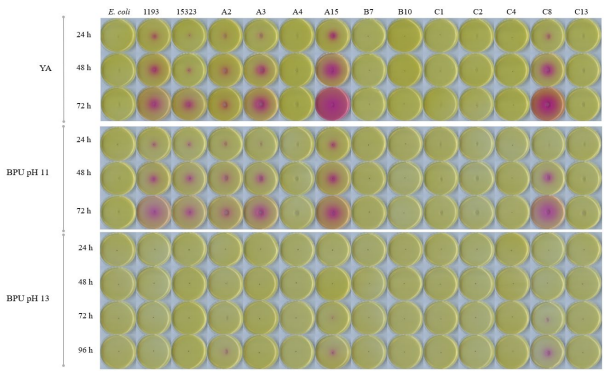

Figure 2. Qualitative urease activity of strain A15 and reference strains (1193, 15323) on solid agar media (YA, BPU pH 11, BPU pH 13) over 24–96 h, visualized by phenol red color change (yellow to pink/magenta indicates urease activity).

3.3 $CaCO_3$ precipitation across cement-relevant pH

A15 yielded the highest $CaCO_3$ output at pH 9 (13.7 ± 0.17 mg) and pH 10 (13.17 ± 0.46 mg), significantly exceeding reference strains ($P < 0.05$). Although yield declined to 9.33 ± 0.59 mg at pH 12 (~32% reduction), A15 consistently dominated across the entire pH 9–12 gradient. SEM confirmed cell-associated spherical mineral deposits, and EDS revealed the highest Ca enrichment in A15, consistent with bacterially mediated $CaCO_3$ formation relevant to pore refinement and crack infilling in cementitious systems.

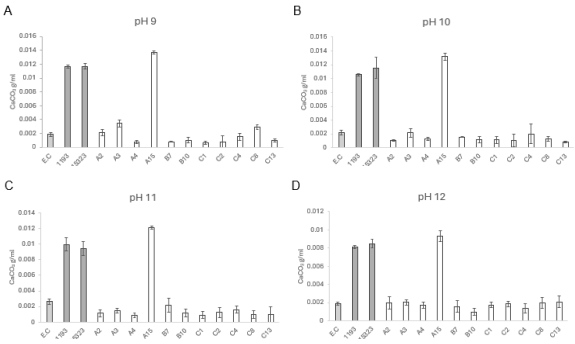

Figure 3. $CaCO_3$ precipitation by strain A15 and reference strains at pH 9–12. (a-d) $CaCO_3$ yield (mg).

3.4 Sporulation efficiency

A15 achieved a sporulation efficiency of 96.07 ± 1.14%, markedly exceeding 1193 (11.32 ± 3.86%) and 15323 (7.26 ± 0.86%) ($P < 0.05$). This high endospore-forming capacity supports long-term persistence and functional stability within cement matrices.

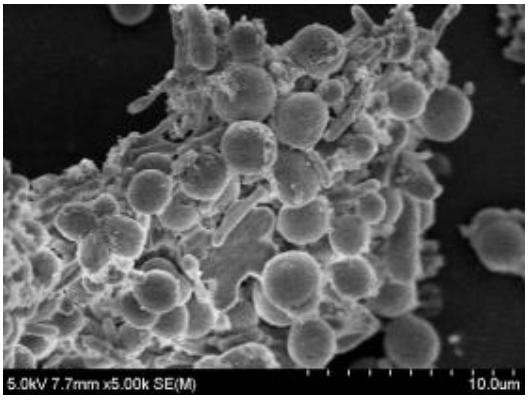

Figure 4. Biomineralized $CaCO_3$ precipitates formed by strain A15, observed by FE-SEM.

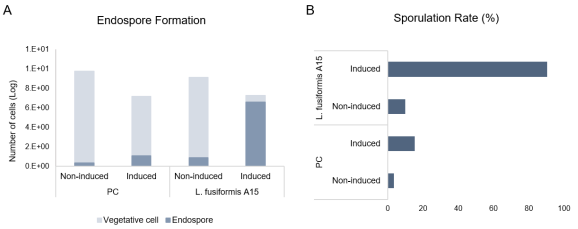

Figure 5. Endospore formation by strain A15. (a) Number of vegetative cells and endospores (log CFU) under non-induced and induced sporulation conditions. (b) Sporulation rate (%), calculated as endospore counts relative to total cell counts. Mean ± SD (n = 3).

3.5 Genomic basis of functional phenotypes

The complete circular chromosome (4,738,618 bp; GC: 37.5%; BUSCO: 99.19%) harbors a contiguous *ureABCDEFG* operon with associated ABC-type Ni transport systems, providing genetic support for sustained ureolysis. Comprehensive sporulation gene networks and stress adaptation modules—including catalases, peroxidases, and Na^+/H^+ antiporters—are consistent with the experimentally observed phenotypes. No plasmids were detected, indicating chromosomal encoding of adaptive traits. ANI of 98.22% with *L. fusiformis* MGMM7 confirmed species-level classification while demonstrating strain-level genomic differentiation.

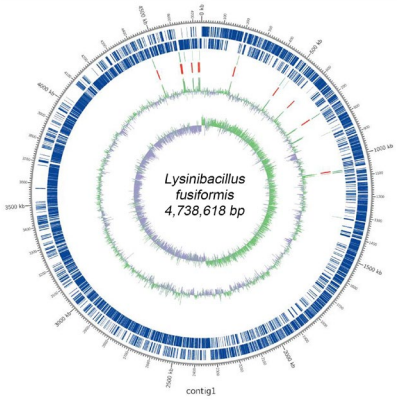

Figure 6. Circular genome map of *L. fusiformis* A15 (4,738,618 bp; GC content 37.5%).

4. Conclusions

L. fusiformis strain A15, isolated from waste concrete, demonstrated sustained ureolytic activity (95.5% retention at pH 13), consistent $CaCO_3$ precipitation across pH 9–12, and 96% sporulation efficiency relative to phylogenetically related reference strains. Whole-genome analysis confirmed an intact ureolytic and stress-adaptive genetic framework, providing a mechanistic basis for the observed phenotypes. The intrinsic adaptation of A15 to cement-derived conditions reduces reliance on external encapsulation strategies, offering a practical and scalable foundation for MICP-based concrete crack remediation, pore refinement, and durability enhancement in highly alkaline cementitious construction materials.

Reference

[1] W. De Muynck, N. De Belie, W. Verstraete, Microbial carbonate precipitation in construction materials: A review, Ecol. Eng. 36 (2010) 118–136.

[2] A.J. Phillips, E. Lauchnor, J. Eldring, R. Esposito, A.C. Mitchell, R. Gerlach, A.B. Cunningham, L.H. Spangler, Potential CO_2 leakage reduction through biofilm-induced calcium carbonate precipitation, Environ. Sci. Technol. 47 (2013) 142–149.

[3] R. Jakubovskis, A. Ivaškė, J. Malaiškienė, J. Urbonavičius, Impact of Portland cement type on bacterial viability in biological concrete, Cem. Concr. Compos. 127 (2022) 104413.

[4] J. Wang, N. De Belie, W. Verstraete, Diatomaceous earth as a protective vehicle for bacteria applied for self-healing concrete, Cem. Concr. Res. 92 (2017) 38–46.

[5] B.J. Reeksting, T.D. Hoffmann, L. Tan, K. Paine, S. Gebhard, In-depth profiling of calcite precipitation by environmental bacteria reveals fundamental mechanistic differences with relevance to application, Appl. Environ. Microbiol. 86 (2020) e02739-19.

[6] W.L. Nicholson, N. Munakata, G. Horneck, H.J. Melosh, P. Setlow, Resistance of Bacillus endospores to extreme terrestrial and extraterrestrial environments, Microbiol. Mol. Biol. Rev. 64 (2000) 548–572.

[7] P. Setlow, Spores of Bacillus subtilis: their resistance to and killing by radiation, heat and chemicals, J. Appl. Microbiol. 101 (2006) 514–525.

[8] F.G. Ferris, V. Phoenix, Y. Fujita, R.W. Smith, Kinetics of calcite precipitation induced by ureolytic bacteria at 10 to 20°C in artificial groundwater, Geochim. Cosmochim. Acta 68 (2004) 1701–1710.

点群データを用いた建築仕上げ面品質測定アルゴリズムの開発

Development of a Quality Measurement An Algorithm for Building Finish

張允豪※1、鄭琥整※2、徐勝河※1、池秀敏※1、金成眞※4

Yoonho Jang, Hojeong Jeong, Seung Ha, Sumin Ji, Seongjin Kim

ABSTRACT

The construction industry faces a growing shortage of skilled labor, while finish-surface inspection still relies on manual work. This study proposes a five-step algorithm for horizontal floor surfaces — outlier removal, floor separation, RANSAC plane estimation, crack detection, and an illustrative ±3 mm classification derived from KCS 41 46 01 — implemented as a Streamlit-based web system. On a synthetic ground-truth dataset, plane estimation was accurate and floor/wall separation reliable except at the wall–floor junction, reproducing a known failure mode. Protrusion/depression classification traded precision for recall. The original point-wise crack detector failed entirely (0% recall); a 2D grid-based Hessian ridge-detection approach raised crack F1 from 0 to 0.523, a gain that held (F1 0.540) on an independently generated crack of different shape. Full-pipeline held-out testing and real-world validation remain future work.

1. Introduction

The construction industry plays a critical role in national infrastructure and housing supply, yet it faces a severe workforce transition: as of February 2025, workers aged 60 and above in Korea's registered construction workforce (277,432) exceeded those in their 40s for the first time, with over half of all technicians aged 50+ and average age up 4.5 years since 2018 [1]. This aging, combined with youth labor shortages, is expected to affect construction more severely than other industries [2].

In addition to this workforce problem, the construction industry has been slower than other industries in adopting digital transformation, limiting productivity and efficiency and making labor-intensive practices an obstacle to continuous improvement. To address these issues, growing attention has been paid to smart construction technologies that incorporate IoT, artificial intelligence, and big data [3]. manual inspection; and Li et al. [8] developed a 3D LiDAR system for prefabricated concrete elements, noting a remaining dependence on skilled personnel.

These prior studies have demonstrated the feasibility of surface quality evaluation using point cloud data; however, most rely on expensive specialized equipment and software and lack the ability to immediately review analysis results on-site (Table 1). This study proposes an algorithm pipeline that integrates outlier removal, reference plane estimation, and normal-vector-based crack detection, together with a web-based visualization system that allows analysis results to be reviewed immediately in 2D and 3D.

Accordingly, this study aims to develop an algorithm that quantitatively measures the quality of building finish surfaces using point cloud data and to propose a method for visualizing the results, contributing to reduced dependence on skilled labor and improved quality-control efficiency at construction sites.

※1 大韓民国 国立 Hanbat 大学校 建設環境デザイン大学 建築工学科，修士課程
※2 大韓民国 国立 Hanbat 大学校 建設環境デザイン大学 建築工学科，博士課程
※3 大韓民国 国立 Hanbat 大学校 建設環境デザイン大学 建築工学科，教授 博士(工学)

Figure 1 illustrates the overall research procedure: point cloud acquisition, algorithm development, web system implementation, and quality analysis and validation.

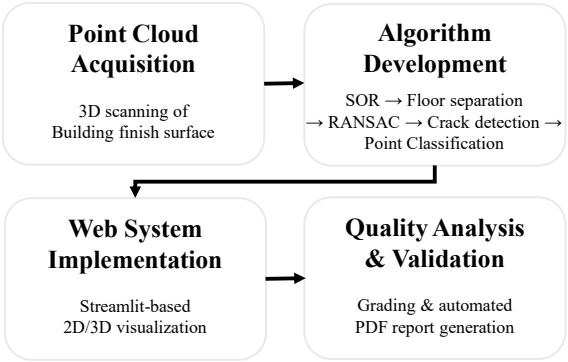

Figure 1. Overall research flowchart

Table 1. Comparison of prior studies and the proposed method

Study	Quality items evaluated	Browser-based visualization	Reported equipment / software cost
Cai et al. [4]	Flatness, verticality, squareness	Color-coded map (offline)	High (3D scanner + specialized SW)
Wang et al. [6]	Flatness, verticality, opening dimension	Not reported	High
Liu et al. [5]	Dimensional/surface quality, flatness, verticality	BIM-linked (offline)	High (BIM + laser scanning)
Li et al. [7]	Flatness, verticality	Not reported	Medium–High
Li et al. [8]	Dimensional quality	Not reported	High (LiDAR system)
This study	Flatness, protrusion/depression, crack	2D/3D, in web browser	Low (open-source analysis software only)

"Not reported" indicates that the cited publication does not describe the corresponding capability, not that the capability is confirmed absent. The cost basis is not uniform across rows: for prior studies it reflects the equipment and software described in the cited work, whereas for this study it reflects analysis software only, since acquisition hardware was not evaluated here; the "Low" rating should not be read as a total-system cost claim.

2. Algorithm Development

Figure 2 shows the logical flow of the five-step algorithm developed in this study, including the two branch points discussed in detail in Section 2.2: the OR/AND combination rule used in floor separation (Step 2) and the class-priority rule used in point classification (Step 5).

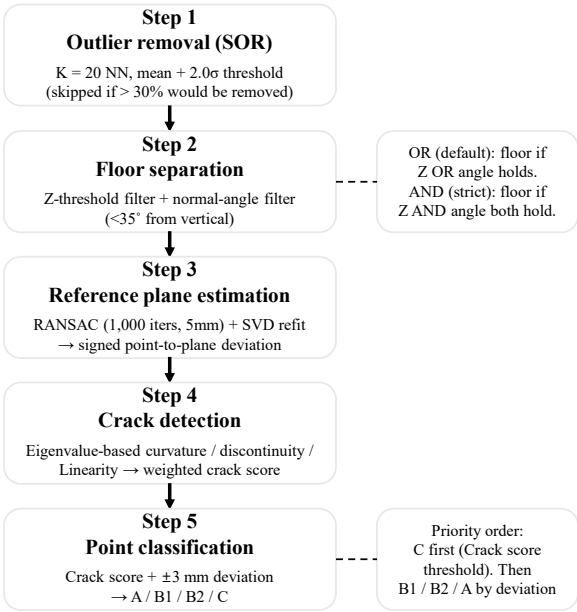

Figure 2. Logical flow of the five-step quality-measurement algorithm

2.1 Reference Algorithms

The finish-surface quality measurement algorithm developed in this study is based on three algorithms that have been widely used in point cloud processing.

Statistical Outlier Removal (SOR) [9] computes the mean distance of each point to its k-nearest neighbors and removes points deviating from the overall mean by more than a defined number of standard deviations. RANSAC [10] robustly estimates an optimal plane model by repeatedly sampling random subsets of noisy data and maximizing inlier count. Normal-vector-based geometric feature analysis, following the eigenvalue-based local features of Weinmann et al. [11], derives curvature, normal

discontinuity, and linearity through eigenvalue decomposition (PCA) of a point's local-neighborhood covariance matrix.

2.2 Proposed Algorithm

As shown in Figure 1, the proposed algorithm consists of five steps: outlier removal, floor separation, reference plane estimation, crack detection, and point classification. This study targets horizontal floor surfaces; extending it to walls, ceilings, or other non-horizontal surfaces is left to future work.

Step 1: Outlier removal. For each point, the mean distance to its k = 20 nearest neighbors is computed; points exceeding the dataset mean by more than 2.0 standard deviations are removed as noise. Removal is skipped if it would remove over 30% of points — a heuristic safeguard whose effect near sparse regions such as crack edges has not been analyzed.

Step 2: Floor separation. A Z-value threshold filter and a normal-vector angle filter combine to separate floor from wall points. A point is Z-eligible if its height is within a margin (default 0.05 m) above the cloud's lowest point — a relative threshold sensitive to residual outliers. The normal direction comes from the smallest-eigenvalue eigenvector of the k = 10 neighbors' covariance matrix, using its absolute Z-component (sign is arbitrary); points within 35° of vertical are classified as horizontal. By default the two criteria combine by OR, favoring recall but risking misclassification of other horizontal surfaces or wall bottoms within the Z margin; a stricter AND mode is available.

Step 3: Reference plane estimation. RANSAC draws random 3-point samples over 1,000 iterations and selects the plane with the most inliers within a 5 mm threshold (minimum inlier ratio 30%); inliers are re-fit by SVD, and each point's perpendicular deviation is calculated (normal fixed upward: positive = protrusion, negative = depression). Since this 5 mm threshold is looser than the ±3 mm classification tolerance in Step 5, points later classified as protrusion/depression can still count as inliers, biasing the estimate if defective regions are extensive — quantifying this is future work.

Step 4: Crack detection. Eigenvalue decomposition of each point's k = 15 neighbors' covariance matrix ($\lambda_0 \leq \lambda_1 \leq \lambda_2$) yields curvature $\lambda_0/(\lambda_0+\lambda_1+\lambda_2)$, normal discontinuity (mean angle to neighboring normals), and linearity $(\lambda_2-\lambda_1)/\lambda_2$. Each is min–max normalized; the crack score is their weighted sum (discontinuity 40%, curvature 40%, linearity 20%), flagged crack-like above a threshold (default 0.65). Section 3.2 shows these defaults detect none of the synthetic cracks (0% recall), traced to linearity's low discriminative power and a search radius too large relative to the crack's half-width; a revised 2D grid-based Hessian scheme reaches F1 0.523 on the tuning dataset and 0.540 on an independent held-out crack. Here “crack” means a linear geometric discontinuity identified by this score, not a structurally verified crack.

Step 5: Point classification. Each point is classified using the crack score and the ±3 mm deviation tolerance adopted from KCS 41 46 01 [12], in priority order: C (crack-like) if the crack score exceeds the threshold, regardless of deviation; otherwise B1 (protrusion) if deviation exceeds +3 mm, B2 (depression) if below −3 mm, else A (normal). Because C takes priority, a point with both a large deviation and a high crack score is reported only as C, so B1/B2 proportions can understate severe height deviation. KCS 41 46 01 defines floor flatness tolerance via a straightedge over a gauge length — a local measurement; this study instead applies the same ±3 mm figure to each point's deviation from a single whole-area plane fit — a global measurement with a different meaning, and thus a practical working criterion, not an official conformity determination.

3. System Implementation and Results

3.1 Web-Based Visualization System

To make the developed algorithm intuitively usable on-site, a Streamlit-based web visualization system was implemented. The system automatically executes the algorithm pipeline on the input point cloud data and provides analysis results in several forms.

Visualization is provided in four forms: a 2D

deviation heat map (SciPy griddata interpolation, RdYlGn color scale), a 3D surface view with Z-axis exaggeration (×1–×500) to make millimeter-scale deviations visible, a 3D classification scatter plot color-coded by point class (A, B1, B2, C), and a deviation histogram with ±3 mm reference lines for overall quality assessment.

Based on the defect ratio, the analysis result is classified into four overall grades defined for this study: Excellent (≤5%), Good (≤15%), Fair (≤30%), and Poor (>30%).

3.2 Synthetic Dataset Generation and Ground-Truth Validation

We generated a synthetic point cloud dataset with known defect locations and sizes and compared its ground truth directly against the pipeline's output (fixed seeds, reproducible). The dataset places 67,536 points (53,868 floor + 13,668 wall) on a 3 m × 4 m horizontal floor and an adjoining wall down to the floor–wall junction, both on a 15 mm grid (±3 mm jitter, 1.0 mm Gaussian noise). Defects were two protrusions (+5 to +6 mm), two depressions (−5.5 to −6.5 mm), one diagonal crack, and 539 injected outliers (1%). The crack is a 2.97 m diagonal band of half-width 30 mm with a smooth raised-cosine cross-section reaching −3 mm depth at its centerline — a wide, tapered groove rather than a hairline fissure, whose representativeness of real cracks has not been established. Ground-truth classes were assigned from the pre-noise design amplitude using the same ±3 mm tolerance as Step 5 (A 52,445 / B1 201 / B2 222 / C 1,000).

We ran the Section 2.2 pipeline on this dataset with default parameters and compared each stage's output against ground truth (Table 2), matched by construction via shared point indices. The Table 2/3 classification metrics cover only points that survived outlier removal and were correctly retained as floor — the 611 wall→floor misclassifications and SOR-removed points are excluded. Scoring all 67,536 points end-to-end instead gives 96.95% (65,476/67,536), close to but distinct from the 97.48% conditional figure above.

Table 2. Ground-truth comparison results

Stage	Metric	Result
Outlier removal (SOR)	Recall / false removals	99.4% (536/539) / 106 pts
Floor/wall separation	Floor precision / recall (floor = positive)	98.87% / 99.99%
	Wall recall (wall = positive)	95.52%
Reference plane estimation	Normal angle error / offset error	0.0006° / 0.057 mm
Point-to-plane deviation	MAE / RMSE	0.80 / 1.00 mm
Point classification (A/B1/B2/C)	Overall accuracy (conditional)	97.48%
End-to-end pipeline	Overall accuracy, all 67,536 pts	96.95% (65,476/67,536)

Reference-plane estimation closely matched ground truth (normal angle error 0.0006°; deviation RMSE 1.00 mm, essentially equal to the 1.0 mm injected noise). Floor/wall separation reached floor precision 98.87%/recall 99.99%, but wall recall was only 95.52%: 611 wall–floor junction points were misclassified as floor, reproducing the OR-mode Z-condition failure from Section 2.2 (both results assume uniform point density; non-uniform real-scanner density was not tested). Per-class results were uneven (Table 3, “Original”): class A reached F1 0.989; B1/B2 showed high recall (83.4%/87.3%) but modest precision (59.5%/41.1%); class C scored 0% — none of the designed cracks were detected.

This was traced to the k = 15 search radius (≈33 mm) approaching the crack's 30 mm half-width, mixing in flat-plane points and diluting the curvature/discontinuity signal, with linearity showing

no discriminative power. We therefore replaced the point-wise neighborhood with a 2D grid-based ridge-detection approach adapted from Frangi et al.'s Hessian vesselness filter [13]: the deviation field is interpolated onto a regular grid, and at each cell we compute the local Hessian's eigenvalues (36 mm smoothing scale) to score directional curvature, distinguishing linear cracks from circular defects. The top 6% of this score is thresholded, split into connected components, and kept only if length > 0.3 m and aspect ratio > 3.5. On a defect-free surface, this scheme still flags 1.73% of floor points as false positives; parameters were tuned on this same dataset. Exact formulas are in validation/crack_hessian.py (seed = 2024).

Held-out check on an independently generated crack. To test whether F1 0.523 reflects genuine signal or overfitting, we applied both detectors, parameters unchanged, to a second, independently generated dataset (13,635 points, 30 mm grid, no outliers or wall points) with a curved, sinusoidal crack of varying half-width (12–22 mm) and depth (7–12 mm) — geometrically unlike the fixed straight crack used for tuning. The original point-wise detector remained weak (F1 0.210; precision 97.4%, recall 11.8%). The Hessian scheme reached F1 0.540 (precision 37.7%, recall 94.9%), matching its in-sample F1 despite the different shape, width, depth, and generator — one supporting data point, not proof of general validity. Code: validation/validate_external_crack.py.

Table 3. Per-class precision/recall/F1, ground truth vs. pipeline output (Original vs. revised; full confusion matrix omitted for space)

Class	Orig. prec.	Orig. recall	Orig. F1	Rev. prec.	Rev. recall	Rev. F1
A (normal)	98.30%	99.44%	0.989	99.52%	97.09%	0.983
B1 (protrusion)	59.50%	83.42%	0.695	60.22%	82.91%	0.698
B2 (depression)	41.06%	87.33%	0.559	61.66%	87.33%	0.723
C (crack)	0.00%	0.00%	-	38.58%	81.38%	0.523
Overall accuracy	97.48%			96.71%		

The revised scheme raised crack recall from 0% to 81.4% (F1 0 → 0.523) and improved B2 F1 from 0.559 to 0.723 as a side effect, at the cost of a 0.77-point drop in overall accuracy (97.48% → 96.71%) from normal points now flagged as cracks — on this class-imbalanced dataset (A is 97% of points), per-class metrics are needed to see this trade-off. Notably, the ground-truth defect ratio (B1+B2+C) is 2.64%, whereas the original pipeline under-reports it as 1.51% and the revised scheme over-reports it as 5.05%; under this study's grading scale (Excellent ≤5%), the original stays “Excellent” while the revised crosses into “Good,” reflecting an illustrative rather than calibrated threshold.

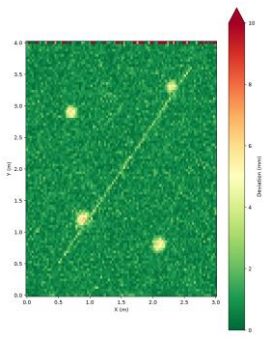

Figure 3. 2D deviation heat map

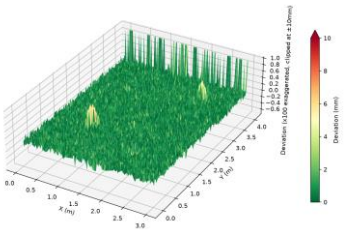

Figure 4. 3D surface visualization

4. Conclusions

This study developed a point-cloud-based algorithm for measuring horizontal floor finish-surface quality and implemented it as a web-based visualization system with 2D/3D output and overall grading, using only open-source software. Ground-truth validation on a synthetic 67,536-point dataset showed reference-plane estimation and floor/wall separation are quantitatively accurate away from the wall–floor junction, where a known OR-mode failure mode (Section 2.2) was reproduced; protrusion/depression classification trades recall for precision; and the original point-wise crack detector does not function at all, though a revised Hessian-based approach raised crack F1 from 0 to 0.523 and, when re-tested unmodified on an independently generated crack of different shape and width, held at F1 0.540 — an early sign this improvement generalizes beyond the tuning dataset. This moves the study's validation beyond a qualitative impression to per-class, quantified evidence of which stages are reliable, conditionally reliable, or not yet functional. Testing the full pipeline on held-out data, improving B1/B2 precision, and validating on real measured data remain for future work.

Future work will validate the algorithm on real point cloud data from diverse finish materials and construction sites, extending it toward real-time quality monitoring.

Reference

[1] Seo, T.-W. (2025, May 26). Average age of construction technicians reaches 52.2 — those in their 60s and above surpass those in their 40s for the first time as the younger workforce shrinks [in Korean]. TopicTree. Data originally from Korea Construction Human Resources Policy Research Institute analysis of Korea Construction Engineers Association registration statistics. https://topictree.co.kr/economy/aging-of-construction-industry-workforce/

[2] Seong, Y.-K. et al. (2025). Trends in construction workforce change and strategies to secure technical personnel [in Korean]. Korea Institute of Construction Industry. https://www.cerik.re.kr/uploads/report/2990/

[3] KDB Future Strategy Research Institute. (2025). Status and implications of smart construction [in Korean]. KDI Economic Information and Education Center.

[4] Cai, D. et al. (2023). Point cloud-based smart building acceptance system for surface quality evaluation. Buildings, 13(11), 2893.

[5] Liu, Z., Liu, Z., Sun, Z., Zhang, Q., & Zhao, L. (2025). Intelligent detection method for construction quality of building structures based on point cloud data and BIM models. Journal of Building Engineering, 112, 113492.

[6] Tan, Y., Liu, X., Jin, S., Wang, Q., Wang, D., & Xie, X. (2024). A terrestrial laser scanning-based method for indoor geometric quality measurement. Remote Sensing, 16(1), 59.

[7] Li, D. et al. (2022). A deep learning-based indoor acceptance system for assessment on flatness and verticality quality of concrete surfaces. Journal of Building Engineering, 51, 104284.

[8] Li, S. et al. (2024). Development of automated 3D LiDAR system for dimensional quality inspection of prefabricated concrete elements. Sensors, 24(23), 7486.

[9] Rusu, R. B., & Cousins, S. (2011). 3D is here: Point Cloud Library (PCL). Proceedings of the IEEE International Conference on Robotics and Automation (ICRA).

[10] Fischler, M. A., & Bolles, R. C. (1981). Random sample consensus: A paradigm for model fitting with applications to image analysis and automated cartography. Communications of the ACM, 24(6), 381–395.

[11] Weinmann, M., Jutzi, B., Hinz, S., & Mallet, C. (2015). Semantic point cloud interpretation based on optimal neighborhoods, relevant features and efficient classifiers. ISPRS Journal of Photogrammetry and Remote Sensing, 105, 286–304.

[12] Ministry of Land, Infrastructure and Transport / National Construction Standard Center (2021). KCS 41 46 01 Plastering work — general provisions [in Korean]. Korea Construction Standards.

[13] Frangi, A. F., Niessen, W. J., Vincken, K. L., & Viergever, M. A. (1998). Multiscale vessel enhancement filtering. In Medical Image Computing and Computer-Assisted Intervention — MICCAI'98 (pp. 130–137). Springer.

廃プラスチックを混入したセメントペーストの物理的・熱的特性

Physical and Thermal Properties of Cement Paste with Waste Plastics

柳昶宇※1、蔡炅俊※2、金智訓※2、鄭漢錫※2、 鄭泫洙※1、李相洙※3
Chang-Woo Ryoo, Kyoung-Jun Chae, Ji-Hun Kim, Yeong-Seok Jung, Hyun-Soo Jung, Sang-Soo Lee

ABSTRACT

This study is fundamental research aimed at utilizing recyclable waste plastics as construction materials. Polypropylene (PP), low-density polyethylene (LDPE), and high-density polyethylene (HDPE), the three types generated in the largest quantities domestically, were incorporated into cement paste at 0 (plain), 5, 10, 15, and 20 (wt%) of cement mass at a water–to–cement ratio of 37% to secure castable flowability, and their effects on the physical and thermal properties of the hardened paste were investigated. Regardless of plastic type, unit weight, density, flexural and compressive strength, and thermal conductivity decreased, while air content and water absorption increased, with increasing mixing ratio, mainly due to the lower density and hydrophobic surface of the plastics relative to cement. Flow decreased continuously with mixing ratio, and PP and LDPE showed a marked reduction exceeding 10% relative to the previous ratio at 15 wt% and above. Considering both castability and the flexural performance required for cement boards, an optimal mixing ratio of 10 wt% was determined for all three plastic types, providing a basis for the subsequent development of waste-plastic cement boards.

1. Introduction

Plastics are synthetic polymers produced through petrochemical processes, valued for their light weight, durability, and processability, and are now used extensively across packaging, electronics, medical devices, and construction. However, large-scale plastic use has led to a serious waste problem: global waste-plastic generation reached approximately 460 million tons in 2019 and continues to grow every year [1]. Only about 9% of plastics produced worldwide are recycled, and in the Republic of Korea, per-capita waste-plastic generation is the highest among OECD countries while the recycling rate remains only 16.4% [2].

Un-recycled plastic waste causes environmental problems: incineration emits greenhouse gases, and landfilling generates microplastics that pollute soil and water. Accordingly, recycling waste plastics as construction materials, including composite building materials, pavement blocks, and artificial flooring, has been actively studied [3, 4]. Cement-based materials are particularly promising for high-value recycling owing to their large usage volume and tunable physical performance. However, an excessive mixing ratio can increase porosity and interfacial defects, degrading strength and dimensional stability, so the optimal mixing range must be quantitatively identified [5].

This study selected the three waste plastics generated in the largest quantities domestically, polypropylene (PP), low-density polyethylene (LDPE), and high-density polyethylene (HDPE), and investigated the effect of their type and mixing ratio on the physical and thermal properties of cement paste, with the aim of determining an optimal mixing ratio as a basis for the subsequent development of waste-plastic cement boards.

2. Experimental overview

2.1 Experimental plan

Ordinary portland cement (OPC) was used as the binder, and the water–to–cement ratio was set at 37% to secure castable flowability. PP, LDPE, and HDPE were used as an admixture at 0 (plain), 5, 10, 15, and 20 (wt%) of cement mass, with water curing at 20 ± 5°C. Unit weight, flow, and air content of the fresh

※1 大韓民国 国立 Hanbat 大学校 建設環境デザイン大学 建築工学科, 博士課程
※2 大韓民国 国立 Hanbat 大学校 建設環境デザイン大学 建築工学科, 修士課程
※3 大韓民国 国立 Hanbat 大学校 建設環境デザイン大学 建築工学科, 教授 博士(工学)

paste were measured per KS F 2409, KS F 5111, and KS F 2421 [6-8]; density and water absorption per KS F 2459 using 50×50×50 mm specimens cured for 28 days [9]; flexural and compressive strength per KS L ISO 679 using 40×40×160 mm specimens at 3, 7, and 28 days [10]; and thermal conductivity per ISO 22007 using the transient plane source method on 50×50×50 mm specimens [11]. The experimental factors and levels are summarized in Table 1

Table 1 Experimental factors and levels

Experimental factor	Experimental level	Remarks
Binder conditions	OPC[1)]	1
Water/Cement (%)	37	1
Admixture	PP, LDPE, HDPE	3
Mixing ratio of admixture (wt%[2)])	0, 5, 10, 15, 20	5
Curing condition	Water curing (Temperature: 20±5°C)	1
Experiment items	Unit weight, Flowability, Air content, Density, Water absorption, Flexural strength, Compressive strength, Thermal conductivity	8

1) OPC : Ordinary portland cement
2) wt% : Weight percent

2.2 Materials

Recycled PP, LDPE, and HDPE were used as received; their physical properties are summarized in Table 2. PP showed the highest tensile yield strength (36 MPa) and melting point (165°C) [12], whereas LDPE showed the lowest density and melting point owing to its branched molecular structure from free-radical polymerization [13].

Table 2 Physical properties of materials

Material	Density (g/cm^3)	Melting point (°C)	Tensile yield strength (MPa)
OPC[1)]	3.15	-	-
PP	0.90	165	36
LDPE	0.93	105-115	10-15
HDPE	0.95	130-136	25-30

1) OPC : Ordinary portland cement

3. Experimental results and discussion

3.1 Unit weight and flow

Figure 1 shows the unit weight of the fresh cement paste. Regardless of plastic type, unit weight decreased continuously with mixing ratio, since plastic density (0.90-0.95 g/cm^3) is lower than cement (3.15 g/cm^3). At 20 wt%, unit weight decreased by 15.7% relative to the plain specimen for all three plastics, with negligible difference among types.

Figure 2 shows the flow of the fresh cement paste. Flow decreased with mixing ratio for all plastic types, attributed to interference with workability and reduced bond caused by the hydrophobic plastic surface [5]. PP and LDPE showed a reduction exceeding 10% relative to the previous ratio at 15 wt% and above, whereas HDPE decreased more gradually.

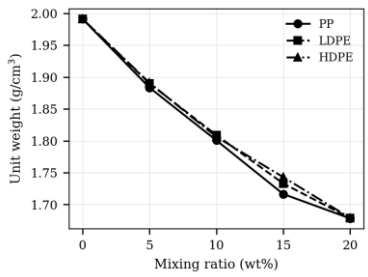

Figure 1 Unit weight

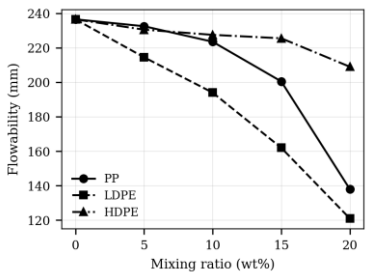

Figure 2 Flowability

3.2 Air content and density

Figure 3 shows that air content increased with mixing ratio for all plastic types, since the hydrophobic surface and irregular shape of the plastics hinder air-bubble release during mixing [5]. Figure 4 shows that density decreased with mixing ratio, following the same trend as unit weight; at 20 wt%, density decreased by 18.1, 14.8, and 14.3% for PP, LDPE, and HDPE, respectively.

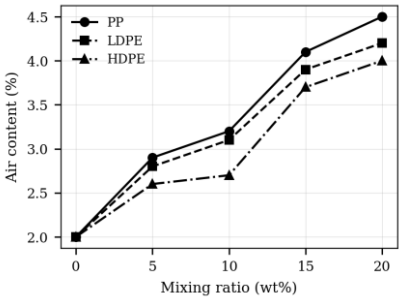

Figure 3 Air content

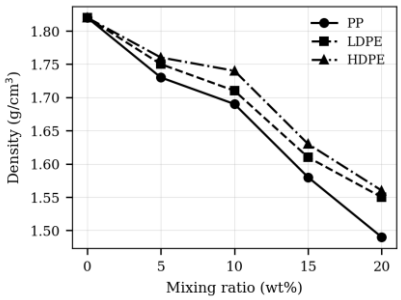

Figure 4 Density

3.3 Water absorption

Figure 5 shows that water absorption increased with mixing ratio, following the order PP > LDPE > HDPE, consistent with the air-content trend, since greater entrained air raises internal porosity and thus absorption.

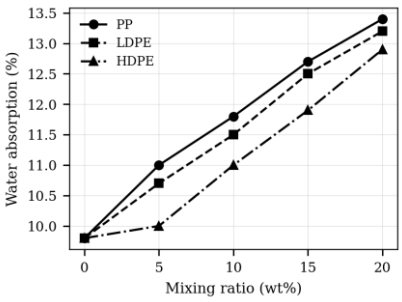

Figure 5 Water absorption

3.4 Flexural and compressive strength

Figure 6 and Figure 7 show the 28-day flexural and compressive strength. Both decreased with mixing ratio for all plastic types, owing to reduced interfacial bond between the hydrophobic plastic surface and paste, crack initiation, and restricted water supply for hydration [5]. At 20 wt%, flexural strength decreased by 37.3, 52.0, and 47.9%, and compressive strength by 47.8, 67.6, and 50.5%, for PP, LDPE, and HDPE, respectively. PP retained the highest strength, consistent with its higher tensile yield strength (Table 3).

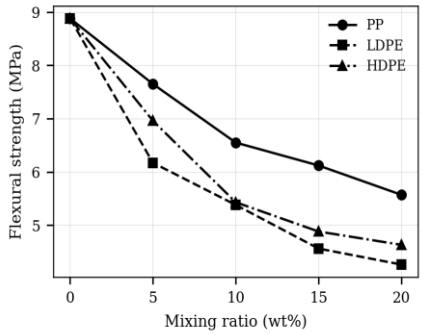

Figure 6 Flexural strength(28 d)

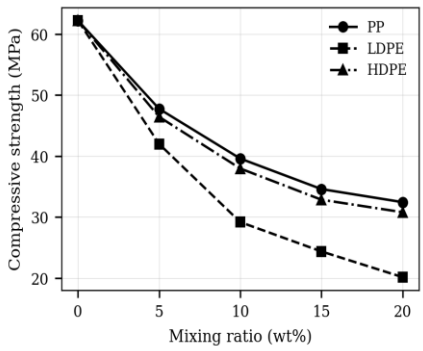

Figure 7 Compressive strength(28 d)

3.5 Thermal conductivity

Figure 8 shows that thermal conductivity decreased with mixing ratio for all plastic types, since entrained air, with much lower conductivity (≈ 0.0264 W/(m·K)) than the solid matrix, lowers the effective conductivity. At 20 wt%, conductivity decreased by 41.0, 30.4, and 19.6% for PP, LDPE, and HDPE, respectively.

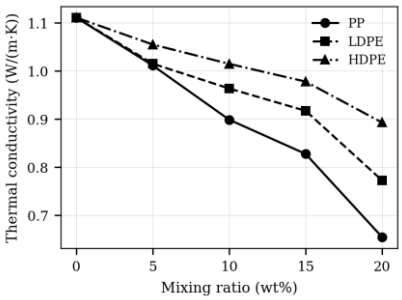

Figure 8 Thermal conductivity

4. Conclusions

In this study, the waste plastics generated in the largest quantities domestically, PP, LDPE, and HDPE, were incorporated into cement paste at mixing ratios of 0, 5, 10, 15, and 20 wt% to evaluate their effects on physical and thermal properties, and to determine the optimal mixing ratio. The following conclusions were drawn.

(1) Regardless of plastic type, increasing the mixing ratio decreased the unit weight, density, flexural strength, compressive strength, and thermal conductivity of the hardened cement paste, while increasing the air content and water absorption, mainly due to the lower density and hydrophobic surface of the plastics relative to cement.

(2) Flow decreased continuously with increasing mixing ratio, with PP and LDPE showing a reduction exceeding 10% relative to the previous mixing ratio at 15 wt% and above, while HDPE decreased more gradually.

(3) At 20 wt%, flexural strength decreased by 37.3-52.0% and compressive strength by 47.8-67.6% relative to the plain specimen; PP retained the highest strength among the three plastics, consistent with its higher tensile yield strength.

(4) Considering castability and the flexural performance required for cement boards, an optimal mixing ratio of 10 wt% was determined for all three waste plastics.

(5) Based on these results, cement boards incorporating 10 wt% PP, LDPE, and HDPE will be fabricated and their performance evaluated in follow-up research, to identify the optimal waste plastic type for practical application as a building material.

Reference

[1] OECD, Global Plastics Outlook:Economic Drivers, Environmental Impacts and Policy Options, OECD Publishing, Paris, 2022.

[2] T.J. Kang, Y.J. Lee, H.S. Kim, N.G. Park, S.C. Lee, B.C. Choi, D.M. Jeon, S.H. Kang, Analysis of domestic and international policies and market trends for activating a circular economy based on waste plastics, J. Clim. Change Res. 18(2) (2023) 205-235.

[3] Y.M. Park, Policy and corporate responses to the plastic pollution crisis, KIET Ind. Econ. Rev. 274 (2021) 62-79.

[4] J.C. Gal, D.J. Kim, J.H. Kang, N.J. Choi, A study on the mechanical properties of composite artificial flooring using recycled waste plastics and waste stone powder, J. Korea Acad.-Ind. Coop. Soc. 25(8) (2024).

[5] A.J. Babafemi, B. Šavija, S.C. Paul, V. Anggraini, Engineering properties of concrete with waste recycled plastic: a review, Sustainability 10(11) (2018) 3875.

[6] KS F 2409, Unit weight and air content (gravimetric) of fresh concrete, Korea Standard Committee.

[7] KS F 5111, Flow table for use in tests of hydraulic cement, Korea Standard Committee.

[8] KS F 2421, Air content of fresh concrete by the pressure method, Korea Standard Committee.

[9] KS F 2459, Apparent density, water content, water absorption, and compressive strength of cellular concrete, Korea Standard Committee.

[10] KS L ISO 679, Cement-test methods-determination of strength, Korea Standard Committee, 2022.

[11] ISO 22007, Plastics-determination of thermal conductivity and thermal diffusivity, ISO.

[12] H.A. Maddah, Polypropylene as a promising plastic: a review, Am. J. Polym. Sci. 6(1) (2016) 1-11.

[13] N.T.H. Pham, Characterization of low-density polyethylene and LDPE-based/ethylene-vinyl acetate with medium content of vinyl acetate, Polymers 13(14) (2021) 2352.

ベーマイト／ポリ（アクリル酸）／酸化グラフェンハイブリッド多層ナノコンポジットによる難燃性の相乗的向上

Synergistic flame retardancy enabled by boehmite/poly(acrylic acid)/ graphene oxide hybrid multilayered nanocomposites

李仁英※1 ・ 趙忠演 2

Inyoung Lee and Chungyeon Cho

ABSTRACT

This study presents boehmite/poly(acrylic acid)/graphene oxide (BMT/PAA/GO) hybrid multilayer nanocoatings for improving the flame retardancy of cotton fabric and polyurethane foam (PUF). The BMT/PAA/GO trilayer (TL) coating was fabricated by layer-by-layer (LbL) assembly, in which PAA was introduced as an interlayer between BMT and GO to enhance hydrogen bonding and electrostatic interactions. Compared with the BMT/GO bilayer (BL) coating, the BMT/PAA/GO TL coating exhibited enhanced multilayer growth and formed a denser surface morphology, as confirmed by AFM and SEM analyses. In vertical flame tests, the coated cotton fabrics retained char residue and preserved their textile structure after flame exposure, whereas the uncoated cotton fabric was almost completely consumed. Cone calorimetry showed that the BMT/PAA/GO TL coating effectively suppressed the second heat release rate (HRR) peak of PUF and reduced TSR, TSP, MARHE, and EHC by 58.7%, 60.0%, 42.9%, and 11.3%, respectively, compared with the uncoated PUF. These results indicate that the BMT/PAA/GO hybrid multilayer coating improves flame retardancy by forming a protective clay-carbonaceous char barrier that suppresses heat transfer, flame propagation, oxygen diffusion, and volatile release during combustion.

1. Introduction

Cotton fabrics and polyurethane foams (PUFs) are widely used in interior materials, furniture, bedding, packaging, insulation, and sound-absorbing applications because of their lightweight, flexible, and porous structures. However, these polymer-based substrates are highly flammable and can rapidly release heat, smoke, and volatile decomposition products during combustion. Therefore, improving their fire safety using an effective halogen-free flame-retardant coating is important for practical building and interior applications. Layer-by-layer (LbL) assembly is a useful surface-coating method for introducing functional nanoparticles onto complex substrates such as cotton fabrics and open-cell PUF. Inorganic clay and graphene-based materials can suppress heat transfer and volatile release by forming protective barrier layers during combustion. However, simple bilayer coatings can have limited nanoparticle loading and relatively loose coating structures. In this study, a BMT/PAA/GO trilayer coating was fabricated by introducing PAA as an interlayer between BMT and GO. The PAA interlayer enhances interfacial interactions through hydrogen bonding and electrostatic attraction, leading to denser multilayer growth. The surface morphology and flame-retardant performance of the BMT/PAA/GO coating were evaluated on cotton fabric and PUF.

※1 Ph.D. student, Department of Biomedical Materials Science, Jeonbuk Advanced Bio-convergence Academy, Wonkwang University, Iksan, Jeonbuk 54538, Republic of Korea

※2 Professor, Ph.D., Department of Biomedical Materials Science, Jeonbuk Advanced Bio-convergence Academy, Wonkwang University, Iksan, Jeonbuk 54538, Republic of Korea

2. Materials and methods

BMT nanopowder and GO aqueous dispersion were used as inorganic and carbonaceous components, respectively, while PAA was used as a polymer interlayer to enhance the interaction between BMT and GO during LbL assembly. BPEI and PAA were used as primer layers to form a charged surface before multilayer deposition. The pH of the BMT, PAA, and GO coating solutions was adjusted to 2.5 to promote electrostatic interactions and hydrogen bonding.

Before multilayer deposition, the substrates were sequentially immersed in BPEI and PAA solutions to form a primer layer. BMT/GO bilayer (BL) coatings were fabricated by alternately depositing BMT and GO, whereas BMT/PAA/GO trilayer (TL) coatings were prepared by sequential deposition of BMT, PAA, and GO. The first deposition cycle was conducted for 5 min per step, and subsequent cycles were performed for 1 min per step with intermediate water rinsing. Silicon wafers were used for film growth and surface morphology analysis, while cotton fabric and PUF were used as flame-test substrates.

The thickness of the multilayer coatings was measured using a profilometer, and surface morphology was observed using AFM and FE-SEM. Vertical flame tests (VFTs) were conducted according to ASTM D6413 to evaluate the flame-retardant performance of coated cotton fabrics. Cone calorimetry was performed on uncoated and coated PUF specimens according to ISO 5660-1 under an external heat flux of 35 kW m^{-2}. HRR, TSR, TSP, MARHE, and EHC were analyzed to evaluate the combustion behavior of the coated PUF samples.

3. Results and Discussion

3.1 Surface morphology of the BMT-MMT coating

BMT/GO BL and BMT/PAA/GO TL nanocoatings were fabricated using the LbL assembly process. In the BL system, multilayer growth was mainly driven by electrostatic attraction between positively charged BMT and negatively charged GO. In the TL system, PAA was introduced as an interlayer between BMT and GO, where partially protonated PAA at pH 2.5 could bridge the inorganic and carbonaceous components through hydrogen bonding and electrostatic interactions.

The coating thickness increased linearly with deposition cycles, but the TL coating showed a much higher growth rate than the BL coating. The average thickness increment increased from approximately 2.4 nm per BL to 27.5 nm per TL, indicating enhanced BMT and GO deposition by the PAA interlayer. As shown in Fig. 1, AFM and SEM images confirmed that the BMT/PAA/GO TL coating formed a denser and more compact surface morphology than the BMT/GO BL coating. This compact hybrid multilayer structure is expected to contribute to protective barrier formation during combustion.

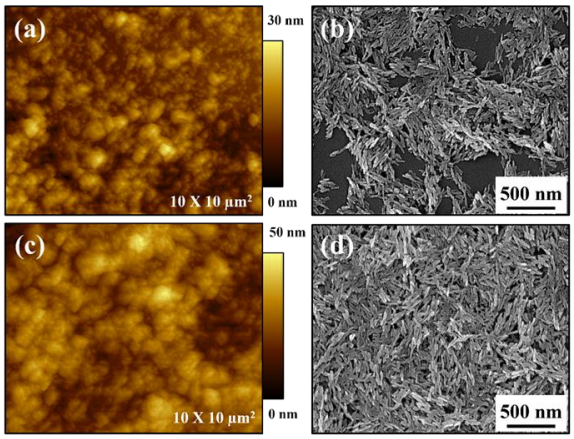

Fig. 1. AFM height images of (a) 4 BL BMT/GO and (c) 4 TL BMT/PAA/GO thin films. SEM surface images of (b) 3 BL BMT/GO and (d) 3 TL BMT/PAA/GO nanocomposites.

3.2 Flame-retardant behavior of coated cotton fabric

The flame-retardant performance of the LbL-coated cotton fabrics was evaluated using VFT, as shown in Fig. 2. The uncoated cotton fabric rapidly ignited and was almost completely consumed after flame exposure, leaving negligible char residue. In contrast, the BMT/GO- and BMT/PAA/GO-coated cotton

fabrics formed char residue and retained their macroscopic textile structure after VFT. In particular, the PAA-containing TL coating produced more stable char residue than the BL coating, indicating that the introduction of PAA improved the fire resistance of the multilayer coating.

SEM analysis further confirmed the protective effect of the multilayer nanocoatings. Before flame exposure, the uncoated cotton fabric showed a relatively smooth fiber surface, whereas the coated cotton fabrics exhibited clear surface coverage on individual fibers. The BMT/PAA/GO TL coating showed a rougher and more aggregated surface morphology, which is attributed to the higher loading of BMT and GO within the PAA-mediated multilayer structure. After VFT, the uncoated fabric was almost completely burned, while the coated fabrics retained their woven structure and fiber architecture. High-magnification SEM images showed that clay and carbonaceous components remained on the fiber surface after flame exposure, forming a protective char layer. These results demonstrate that the BMT/PAA/GO TL coating enhanced the flame retardancy of cotton fabric by promoting char formation and preserving the textile structure during combustion.

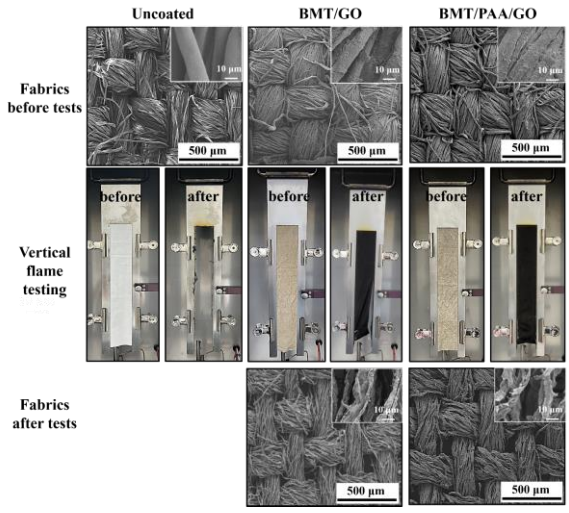

Fig. 2. SEM images of fabrics before (top) and after (bottom) vertical flame tests and photographs (middle) taken before and after vertical flame tests of uncoated and 10 BL BMT/GO and 10 TL BMT/PAA/GO-coated fabrics.

3.3 Cone calorimetry of BMT-MMT-treated PUF

Cone calorimetry was conducted to quantitatively evaluate the flame-retardant performance of BMT/GO- and BMT/PAA/GO-coated PUF, as shown in Fig. 3. The uncoated PUF exhibited two distinct HRR peaks during combustion, corresponding to early-stage ignition/foam collapse and subsequent rapid combustion of volatile decomposition products. The BMT/GO BL coating reduced the second HRR peak, whereas the BMT/PAA/GO TL coating effectively eliminated this peak, indicating a stronger barrier effect against heat transfer and volatile release.

The BMT/PAA/GO TL coating also significantly reduced TSR, TSP, MARHE, and EHC by 58.7%, 60.0%, 42.9%, and 11.3%, respectively, compared with the uncoated PUF. These reductions indicate that the TL coating effectively suppressed smoke generation, heat emission, and combustion intensity. The improved flame retardancy is attributed to the dense BMT/PAA/GO multilayer structure, in which BMT promotes thermally stable inorganic residue formation and GO reinforces the carbonaceous char layer. As a result, the TL coating forms a continuous protective barrier that suppresses heat transfer, flame propagation, oxygen diffusion, and volatile release during combustion.

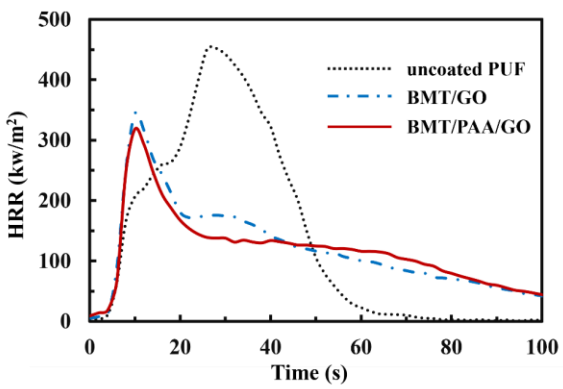

Fig. 3. Heat-release rate (HRR), as a function of time, during cone calorimeter testing, for uncoated control

and 10 BL BMT/GO and 10 TL BMT/PAA/GO assemblies that are coated on PUF.

4. Conclusions

This study demonstrated that BMT/PAA/GO hybrid multilayer nanocoatings can effectively improve the flame retardancy of cotton fabric and PUF. The PAA interlayer enhanced multilayer growth, resulting in a thicker and denser TL coating than the BMT/GO BL coating. AFM and SEM analyses confirmed that the TL coating formed a compact surface morphology with closely packed clay and carbonaceous components. In VFT, the coated cotton fabrics retained char residue and preserved their textile structure, whereas the uncoated fabric was almost completely consumed. Cone calorimetry showed that the BMT/PAA/GO TL coating suppressed the second HRR peak of PUF and reduced TSR, TSP, MARHE, and EHC. These improvements are attributed to the formation of a protective clay-carbonaceous char barrier that suppresses heat transfer, flame propagation, and volatile release during combustion. Therefore, the BMT/PAA/GO hybrid multilayer coating provides an effective halogen-free strategy for improving the fire safety of textile and foam substrates.

Reference

[1] A. Dasari, Z.-Z. Yu, G.-P. Cai, Y.-W. Mai, Recent developments in the fire retardancy of polymeric materials, Prog. Polym. Sci. 38 (2013) 1357–1387.

[2] X. Qiu, Z. Li, X. Li, Z. Zhang, Flame retardant coatings prepared using layer by layer assembly: A review, Chem. Eng. J. 334 (2018) 108–122.

[3] K.M. Holder, R.J. Smith, J.C. Grunlan, A review of flame retardant nanocoatings prepared using layer-by-layer assembly of polyelectrolytes, J. Mater. Sci. 52 (2017) 12923–12959.

[4] F. Carosio, L. Maddalena, J. Gomez, G. Saracco, A. Fina, Graphene oxide exoskeleton to produce self-extinguishing, nonignitable, and flame resistant flexible foams: A mechanically tough alternative to inorganic aerogels, Adv. Mater. Interfaces 5 (2018) 1801288.

Effect of Core Diameter and Coarse Aggregate Content on the Material Properties of Small-Diameter Concrete Cores

Jeong-Taek, Lee※1, Gyu-Yong, Kim※4, Ha-Min, Eu※3, Yae-Chan, Lee※1, Min-Jeong, Ko※2, Van Minh Triet※2, Jeong-Soo, Nam※4

ABSTRACT

As a fundamental study for correcting the compressive strength deviation of small-diameter concrete cores (SDC, diameter ≤ 50 mm), this study investigated the material properties of core specimens according to the core diameter (Ø100, Ø68, Ø44, Ø31.5 mm) and coarse aggregate content (30, 37, 44 vol%), and examined the influence of the coarse aggregate characteristics within SDC on the material properties. The experimental results showed that the bulk density and UPV tended to increase as the coarse aggregate content increased, and the standard deviations of both properties increased as the core diameter decreased. The compressive strength tended to decrease as the core diameter decreased, regardless of the coarse aggregate content, and its standard deviation also tended to increase. Furthermore, as the coarse aggregate content within SDC increased, the bulk density and UPV tended to increase. In contrast, no clear correlation was identified between the compressive strength and the coarse aggregate content within SDC.

1. Introduction

Research is being conducted to estimate compressive strength using Small Diameter Cores (SDC) (50 mm or less) in order to reduce damage to concrete structures and secure the reliability of strength evaluation[1]. However, because of their small diameter, SDC specimens exhibit non-uniform amounts and distributions of coarse aggregate, resulting in variations in compressive strength[1-4]. Accordingly, correction of the compressive strength deviation of SDC is required, along with a means of quantitatively evaluating the amount and distribution of coarse aggregate in SDC.

As a means of quantitatively evaluating the coarse aggregate characteristics of SDC, Ultrasonic Pulse Velocity (UPV) is available. UPV is a non-destructive test capable of assessing the uniformity of concrete, enabling quantitative evaluation of its material properties. Moreover, it has been reported that UPV responds more sensitively to the coarse aggregate content than to the water/cement ratio of concrete[2]. However, few studies have quantitatively evaluated the coarse aggregate content of SDC using UPV, and the influence of the coarse aggregate characteristics of SDC on UPV needs to be further investigated.

Therefore, in this study, to improve the compressive strength deviation of SDC, the material properties according to the amount and diameter of coarse aggregate in the core specimens, as well as the influence of the coarse aggregate content within SDC on the material properties, were investigated. For this purpose, concrete core specimens were fabricated in the laboratory according to the coarse aggregate content (30, 37, 44 vol%) and core diameter (Ø100, Ø68, Ø44, Ø31.5 (mm)), and their bulk density, UPV, and compressive strength were evaluated. In addition, the influence of the coarse aggregate content within SDC (Ø44) on the material properties was investigated.

※1 Ph.D. Course, Dept. of Architectural Engineering, Chungnam National University, Korea
※2 Master's Course, Dept. of Architectural Engineering, Chungnam National University, Korea
※3 Ph.D., Dept. of Architectural Engineering, Chungnam National University, Korea
※4 Prof., Dept. of Architectural Engineering, Chungnam National University, Korea

Table 1 Mixing ratio of concrete

Mix ID	W/C (%)	C/S (%)	S/a (%)	W (kg/m^3)	C (kg/m^3)	S (kg/m^3)	G (kg/m^3)	AD_1 (kg/m^3)	AD_2 (kg/m^3)
G30	51	44	52	192	377	865	828	0.8	1.7
G37	51	44	44	171	335	770	1021	0.7	1.7
G44	51	44	37	150	294	675	1213	0.6	1.5

W/C = water-to-cement ratio; C/S = cement-to-sand ratio; S/a = sand-to-total aggregate ratio;
W = water; C = cement; S = sand; G = gravel; AD_1 = air-entraining agent; AD_2 = water-reducing agent.

2. Materials and methods

2.1 Materials

The cement used in this experiment was ordinary Portland cement with a density of 3.15 g/cm³ and a fineness of 3,740 cm²/g. Crushed fine aggregate with a density of 2.66 g/cm³ and a fineness modulus of 2.55 was used as the fine aggregate. The coarse aggregate was crushed aggregate with a maximum size of 25 mm, a density of 2.75 g/cm³, and a fineness modulus of 7.02, and it was washed before use. As chemical admixtures, a polycarboxylate-based air-entraining (AE) agent and a water-reducing agent were used to secure the slump and air content.

In this experiment, to analyze the characteristics of the cores according to the amount and diameter of coarse aggregate, three concrete mixtures were designed based on the coarse aggregate content. Table 1 presents the concrete mixtures. The water-cement ratio (W/C) was fixed at 51%, and the fine aggregate ratio (S/a) was adjusted to 52, 44, and 37 (vol%) to control the coarse aggregate content (30, 37, 44 vol%). Depending on the coarse aggregate content of each mixture, the mixtures were designated as G30, G37, and G44.

2.2 Methods

The bulk density and compressive strength tests were conducted in accordance with KS F 2405 (Standard Test Method for Compressive Strength of Concrete), and the UPV test was measured in accordance with KS F 2731 (Standard Test Method for Ultrasonic Pulse Velocity for Estimating Compressive Strength of Concrete).

The measurement of the coarse aggregate weight and fineness modulus of the core specimens was performed on Ø44 (G30, G44) specimens that had completed the bulk density, UPV, and compressive strength tests. The separation of coarse aggregate from the core specimens was carried out by removing the mortar attached to the coarse aggregate surface using hydrochloric acid, which was diluted with distilled water to a concentration of 10%. The weight and fineness modulus of the separated coarse aggregate were determined in accordance with KS F 2503 (Standard Test Method for Density and Absorption of Coarse Aggregate) and KS F 2502 (Standard Test Method for Sieve Analysis of Fine and Coarse Aggregates).

3. Results and Discussion

3.1 Bulk density, UPV, Compressive strength

Table 2 summarizes the mean values and standard deviations of the bulk density, UPV, and compressive strength of the core specimens according to the coarse aggregate content (G30, G37, G44) and core diameter (Ø100, Ø68, Ø44, Ø31.5).

The bulk density ranged from 2,231 to 2,285 kg/m³ for G30, from 2,210 to 2,247 kg/m³ for G37, and from 2,329 to 2,366 kg/m³ for G44. G44, which had the highest coarse aggregate content, generally exhibited the highest values, while G37 and G30 showed similar results. Meanwhile, the bulk density according to specimen diameter showed no clear trend regardless of the mixture, whereas the standard deviation increased as the diameter decreased.

The UPV showed a trend similar to that of the bulk

Table 2 Experimental results and standard deviations of bulk density, UPV, and compressive strength

Type	Diameter of core specimen (mm)	Bulk density (kg/m^3)/ Standard deviation (kg/m^3)	Ultrasonic pulse velocity (m/s) /Standard deviation (m/s)	Compressive strength (MPa)/ Standard deviation (MPa)
G30	100	2285/8.9	4397.7/19.4	33.0/1.2
	68	2260/2.9	4508.8/40.2	32.7/1.4
	44	2231/28.7	4352.5/80.9	26.0/4.2
	31.5	2245/29.3	4361.2/108.6	21.6/6.5
G37	100	2245/6.1	4337.1/24.5	29.4/0.4
	68	2247/7.1	4471.1/84.7	31.3/1.1
	44	2235/22.0	4484.0/116.8	25.0/3.6
	31.5	2210/26.3	4310.5/160.6	22.1/3.2
G44	100	2338/3.9	4526.6/26.7	32.4/0.8
	68	2329/6.1	4570.9/18.5	26.5/3.7
	44	2366/21.0	4582.7/105.4	25.1/3.7
	31.5	2336/30.3	4549.7/117.3	23.0/5.5

For Ø100 and Ø68, the average of 3 specimens was used, while for Ø44 and Ø31.5, the average of 15 specimens was used.

density. G44 exhibited high measurement results, ranging from 4,526 to 4,583 m/s, because the UPV increases as the coarse aggregate content within the specimen increases. In addition, the UPV according to specimen diameter showed no clear trend regardless of the mixture, and the standard deviation increased as the diameter decreased.

In contrast, the compressive strength ranged from 21.6 to 33.0 MPa for G30, from 22.1 to 31.3 MPa for G37, and from 23.0 to 32.4 MPa for G44, with G30, which had the lowest coarse aggregate content, generally showing the highest measurement results. This is considered to be because the standard specimen of G30 exhibited the highest compressive strength (35.6 MPa) among the three mixtures, resulting in higher compressive strength for the G30 core specimens. On the other hand, for Ø31.5, the compressive strength of G44 was the highest at 23.0 MPa, which was 6.5% higher than that of G30 and 4.1% higher than that of G37.

The compressive strength of the core specimens according to diameter showed a decreasing tendency as the diameter decreased regardless of the mixture, consistent with previous studies[1-4]. This is because, as the core diameter decreases, the ratio of the cut area (ITZ-damaged area) to the total cross-sectional area of the core specimen increases. Furthermore, as the core diameter decreases, the deviation in coarse aggregate content between specimens increases, and thus the standard deviation of the compressive strength tended to increase.

3.2 Effect of coarse aggregate weight within SDC

This study analyzed the influence of the coarse aggregate weight within SDC on the bulk density, UPV, and compressive strength. The analysis was conducted on the Ø44 specimens of G30 and G44, based on 14 data points each (28 in total), excluding damaged specimens.

Figure 1(A) shows the influence of the coarse aggregate weight of SDC on the bulk density. The

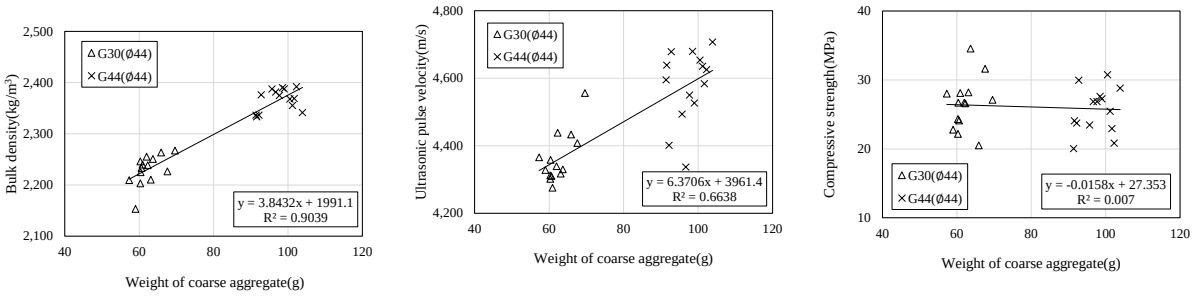

(A) Bulk density **(B) UPV** **(C) Compressive strength**

Figure 1 Effect of coarse aggregate weight on material properties of SDC

coarse aggregate weight and bulk density exhibited a high coefficient of determination ($R^2 = 0.90$), and the bulk density tended to increase as the coarse aggregate weight increased.

Figure 1(B) shows the influence of the coarse aggregate weight of SDC on the UPV. The UPV exhibited a linear relationship in which it increased as the coarse aggregate weight increased, but it showed a weaker correlation ($R^2 = 0.66$) than in previous studies. This is because, although the mixtures were prepared according to the coarse aggregate content, the fineness modulus of the coarse aggregate in the SDC varied.

Figure 1(C) shows the correlation between the coarse aggregate weight and compressive strength of SDC. Within the data range of this study, no clear trend was identified between the compressive strength and the coarse aggregate weight. Previous studies have also reported that the compressive strength of SDC shows no correlation with the coarse aggregate weight, and that changes in the stress transfer path and eccentricity can occur depending on the distribution of the coarse aggregate[3].

4. Conclusions

This study investigated the material properties of core specimens according to the amount and diameter of coarse aggregate, as well as the influence of the coarse aggregate content within SDC on the material properties. The experimental results are as follows:

The bulk density and UPV tended to increase as the coarse aggregate content of the core specimens increased, and the standard deviation increased as the core diameter decreased.

The compressive strength decreased as the core diameter decreased, regardless of the coarse aggregate content, and the standard deviation tended to increase. The higher the coarse aggregate content within SDC, the more the bulk density and UPV tended to increase. In contrast, the compressive strength showed no correlation with the coarse aggregate content within SDC.

Reference

[1] M. Tuncan, O. Arioz, K. Ramyar, B. Karasu, Assessing concrete strength by means of small diameter cores, Constr. Build. Mater. 22 (2008) 981-988.

[2] G. Trtnik, F. Kavčič, G. Turk, Prediction of concrete strength using ultrasonic pulse velocity and artificial neural networks, Ultrasonics 49 (2009) 53-60.

[3] M. Kunimoto, N. Yuasa, Y. Kasai, I. Matsui, Study on compressive strength testing method of concrete using small-diameter cores, Proc. Jpn. Concr. Inst. 22 (2000) 427-432.

[3] H. Katahira, K. Morihama, H. Ikenaga, Experimental study on the effect of core specimen size reduction on compressive strength, Proc. Jpn. Concr. Inst. 26 (2004) 399-404.

Role of Kenaf Fibers in Improving the Spalling Resistance of Polymer-Modified Cement Mortar

Sung-Jun Ji※1, Gyu-Yong Kim※2, Byung-Cheol Choi※3, Hye-Young Youn※1,
Yeon-Woo Go※4, Seung-Hoon Song※4, Jeong-Soo Nam※2

ABSTRACT

This study investigated the effect of the presence and content of kenaf fiber on the suppression of high-temperature spalling in repair polymer cement mortar. The evaluation items were flow, compressive strength, modulus of elasticity, and the temperature, water vapor pressure, Restrained stress, and tensile strain measured by the ring-restraint heating test. The results showed that adding 0.2 vol.% or more of kenaf fiber can suppress the spalling of polymer cement mortar. In addition, the incorporation of kenaf fiber suppressed the rise in water vapor pressure near the heated surface of the ring-restraint specimens. Furthermore, the Restrained stress tended to decrease as the kenaf fiber content increased.

1. Introduction

The social demand for extending the service life of building structures has increased, and the application of polymer cement mortar(Polymer Cement Mortar, PCM) as a repair and strengthening material for maintenance is expanding. PCM exhibits superior adhesion, tensile strength, and durability compared with ordinary cement mortar, and is widely used for section repair and strengthening methods. However, PCM has a dense matrix, so when it is exposed to a high-temperature environment such as fire, internal moisture is not easily released to the outside, and the resulting rise in water vapor pressure can cause spalling[1, 2].

PCM spalling has been reported as a phenomenon in which the moisture migration accompanying heating, the pressure rise within pores, and the thermal stress arising from temperature gradients are complexly involved[3]. During high-temperature exposure, free water and capillary water vaporize and form internal pressure; meanwhile, the denser the material structure, the lower its air and water permeability, so vapor discharge is delayed and pressure tends to accumulate.

In addition, strain mismatch arises from the temperature difference between the surface and the interior, and under restrained conditions the tensile stress increases; therefore, when these factors overlap, local damage and delamination progress and spalling may ultimately occur.

In general, to secure the fire resistance of high-strength concrete and mortar, methods that incorporate organic fibers such as polypropylene or nylon fibers are adopted. These fibers melt at high temperature and form vapor-discharge paths, thereby providing a mechanism that relieves internal pressure.

Meanwhile, against the backdrop of growing interest in sustainability and environmentally friendly materials, the potential use of natural fibers has been examined in recent years. However, natural fibers readily absorb mixing water during proportioning, which reduces flowability and workability. Therefore, to apply natural fibers to PCM, in addition to a mix design that accounts for the water-absorption characteristics of the fibers, it is necessary to organize the spalling-suppression mechanism at high temperature. In particular, it is important to grasp the influence of the moisture state inside the fibers on

※1 Ph.D. Course, Dept. of Architectural Engineering, Chungnam National University, Korea
※2 Prof., Dept. of Architectural Engineering, Chungnam National University, Korea
※3 Ph.D., Dept. of Architectural Engineering, Chungnam National University, Korea
※4 Master's Course, Dept. of Architectural Engineering, Chungnam National University, Korea

moisture migration and water vapor pressure behavior during high-temperature exposure.

However, in reports that applied natural fibers to PCM, the evaluation items and test conditions differ from study to study, so room remains to organize the moisture migration and water vapor pressure behavior at high temperature. Moreover, studies that address the moisture state of the fibers are limited, and few cases have systematically compared its influence.

Therefore, in this study, the effects of the kenaf fiber content and the presence or absence of pre-wetting(pre-wetting) treatment on the flow and hardened mechanical properties of PCM were evaluated. Furthermore, a ring-restraint heating test was conducted, and by measuring the temperature, water vapor pressure, Restrained stress, and tensile strain under restrained conditions, the spalling-suppression characteristics and mechanism of kenaf-fiber-reinforced PCM were examined. In addition, the temporal changes in temperature and water vapor pressure during heating were captured together, with the aim of comparing and discussing the behavioral differences due to fiber incorporation and the presence or absence of pre-wetting.

Table 1 Mix proportions

ID	W/C	Cement	Water	Sand
Unit	w.%	kg/m^3	kg/m^3	kg/m^3
Plain	31	905	282	1138
K0.2				
K0.2P				
K0.4				

ID	P/C	Polymer	Kenaf
Unit	w.%	kg/m^3	kg/m^3
Plain	5	45.25	-
K0.2			3.35
K0.2P			3.35
K0.4			6.70

Table 2 Mechanical properties of kenaf fiber

Properties	Length	Diameter	Density	Absorption rate
Unit	mm	μm	g/cm^3	%
Kenaf	10-12	50-100	1.4	10-13

2. Materials and methods

2.1 Mix Proportions

The mix proportions of the PCM used in this study are shown in Table 1. Ordinary Portland cement was used, and the water-to-cement ratio was set to 31%. An ethylene–vinyl acetate (Ethylene-Vinyl Acetate, EVA) powder admixture was used, and the polymer-to-cement ratio was kept constant at 5%. An omni-mixer was used for mixing the mortar.

Kenaf fibers were used in two conditions: a dry state stored at room temperature, and a pre-wetted state saturated by immersion in the mixing water for 72 hours before mixing. The main physical properties of kenaf fiber are given in Table 2, and the appearance and cross-sectional photographs of the kenaf fiber used in the mix are shown in Fig. 1.

The specimen ID without kenaf fiber was designated Plain. Depending on the fiber content and the presence or absence of pre-wetting, a content of 0.2vol.% was designated K0.2; a content of 0.2vol.% with pre-wetting applied, K0.2P; and a content of 0.4vol.%, K0.4.

2.2 Overview of the Ring-Restraint Specimen

In this study, ring-restraint specimens were fabricated with reference to the concrete spalling test method of the Japan Concrete Institute. The dimensions of the steel ring used as the restraining body were an outer diameter of 300mm, a height of 50mm, and a thickness of 8mm, as shown in Fig. 2.

To capture changes in the internal state of the mortar, thermocouples for temperature measurement and a stainless-steel pipe for water vapor pressure measurement were embedded. In addition, to measure the Restrained stress, thermocouples and strain gauges were attached at 2 opposing points on the outer circumference of the ring. Because the heat-resistant

Fig. 1 Kenaf fiber and cross-sectional shape

temperature of the strain gauges used was 80°C, the data up to the point at which the ring surface temperature reached 80°C were used as valid values.

The installation position of each sensor was set based on the distance from the heated surface. The thermocouples and pipe inside the mortar and the thermocouples and strain gauges outside the ring were placed at 5, 10, 25, and 40 mm from the heated surface, respectively.

2.2 Heating Test

The heating test was performed as shown in Fig. 3 at an age of 42 days using a small electric furnace. Before the test, the electric furnace was preheated to 1,050°C and the internal temperature was kept constant. The test procedure was as follows. First, the pipe inside the ring-restraint specimen was filled with silicone oil, and a pressure gauge was connected to prepare for water vapor pressure measurement. Next, the top lid of the electric furnace was opened, and at the same time the specimen was set so that its bottom face was located at the center of the furnace. If spalling occurred during heating, the time of occurrence was recorded, and after the test the spalling depth was measured on the cooled specimen. The heating start time was taken as the moment the specimen was placed in the furnace, and the temperature, water vapor pressure, and strain were organized on the same time axis. The occurrence of spalling was judged from visual observation and the confirmation of sounds during heating, together with the damage state of the heated surface after the test.

In addition, for the quantitative evaluation of the spalling behavior, the Restrained stress and the tensile strain arising from thermal stress were calculated from the strain and temperature measured during heating using Eqs. (1) and (2) [4].

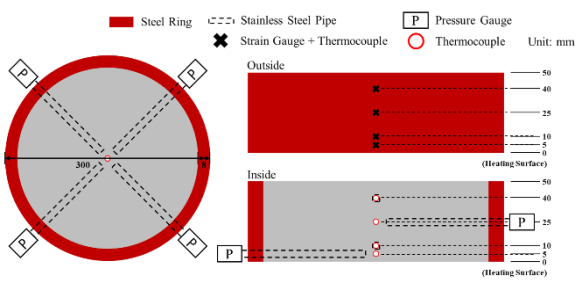

Fig. 2 Overview of the ring-restraint specimen

$$\sigma_{re} = \varepsilon_\theta \cdot E_s \cdot \frac{t}{R} \quad (1)$$

$$\varepsilon_z = \frac{v_s(\sigma_{x-s} + \sigma_{y-s})}{E_m(T_s)} \quad (2)$$

σ_{re}: Restrained stress (= σ_{x-s}= σ_{y-s})
ε_θ: circumferential strain of the steel ring
E_s: modulus of elasticity of the steel ring
t : thickness of the steel ring
R : inner radius of the steel ring
ε_z: tensile strain
T_s: internal temperature
$E_m(T_s)$: residual modulus of elasticity at internal temperature T_s
v_s: apparent Poisson's ratio

3. Results and Discussion

3.1 Flow

The flow test results for each mix are shown in Table 3. The average flow of Plain was 167.5mm. For the fiber-reinforced mixes, K0.2 was 150.5mm and K0.4 was 133.4mm, showing that the flow tended to decrease as the fiber content increased. Meanwhile, at the same fiber content (0.2vol.%) with pre-wetting applied, K0.2P showed an average of 169.9mm, a level comparable to that of Plain.

This decrease in flow is considered to result from the dry kenaf fibers absorbing mixing water during mixing, which reduced the free water that contributes to the flowability of the mortar. In contrast, for K0.2P, pre-wetting suppressed additional water absorption by the fibers, so the mixing water is considered to have contributed to maintaining the flowability of the mortar[5].

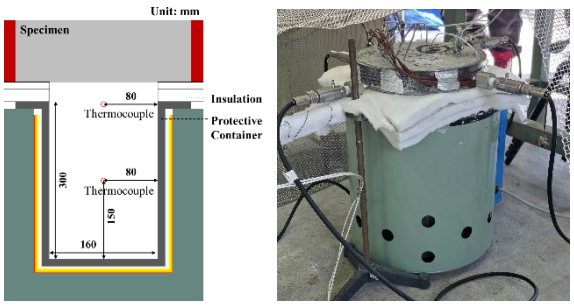

Fig. 3 Overview of the heating test and full view of the test setup

3.2 Compressive Strength and Modulus of Elasticity

The measured compressive strength and modulus of elasticity for each mix are shown in Fig. 4. The compressive strength was measured as follows: for Plain, 63.9MPa; for K0.2, 71.5MPa; for K0.4, 68.4MPa; and for K0.2P, 66.6MPa. For Plain, K0.2, K0.4, and K0.2P, the modulus of elasticity was 30.8, 29.2, 28.7, and 27.4 GPa, respectively.

The increase in compressive strength is explained by the effect whereby the kenaf fibers absorbed mixing water and reduced the amount of free water, thereby lowering the effective water-to-cement ratio and promoting densification of the matrix. However, for K0.4, compared with the benefit of the reduced free-water content, the influence of air entrainment accompanying the reduced flowability and of the increased interfacial transition zone (ITZ) became relatively larger, which is interpreted as the reason its compressive strength was lower than that of K0.2. For K0.2P, because pre-wetting suppressed additional water absorption by the fibers, the densification effect from reduced free water was smaller than for K0.2; meanwhile, the influence of the ITZ characteristics around the fibers became relatively larger, which can be understood as the reason its compressive strength was lower than that of K0.2.

Meanwhile, the modulus of elasticity is considered to have decreased relative to Plain because, in addition to the low stiffness of the fibers themselves, the ITZ increased by fiber incorporation and the micro-pores increased the initial deformation.

Table 3 Flow of PCM

ID	Plain[2]	K0.2	K0.2P	K0.4
Min	167.0	147.0	165.9	133.1
Max	168.0	154.0	166.0	133.8
Aver.	167.5	150.5	165.9	133.4

3.3 Appearance of the Specimens after Heating

The condition of the heated surface of each specimen after the heating test is shown in Fig. 5. For Plain, spalling with a maximum depth of 4.6 mm occurred at the center of the heated surface, and local delamination and loss were confirmed on part of the heated surface. In contrast, no clear spalling or cross-sectional loss was observed in any specimen containing kenaf fiber. When the fiber-reinforced specimens were compared with one another, no large difference in cracking was found, and in every specimens cracking was limited to surface cracks.

For Plain, the dense structure of the PCM made it difficult for water vapor to be discharged to the outside, and as a result of the local concentration of

water vapor pressure and thermal stress, spalling is considered to have occurred. In contrast, for the fiber-reinforced mixes, it is inferred that the hollow structure of the kenaf fibers and their thermal

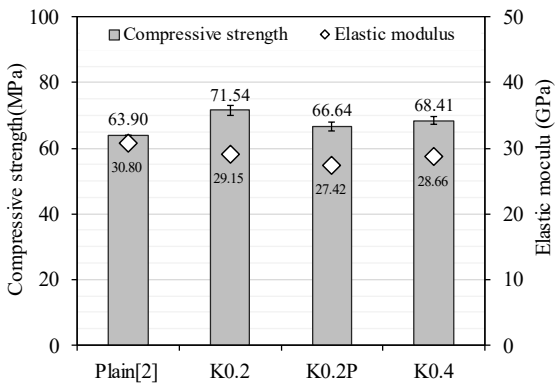

Fig. 4 Compressive strength and elastic modulus of PCM

(a) Plain[2] (b) K0.2 (c) K0.2P (d) K0.4

Fig. 5 Heated surface of the specimens after the heating test

decomposition and shrinkage during heating formed voids that serve as vapor-migration paths, relieving the rapid accumulation of pressure and thereby suppressing spalling[3].

3.4 Change in the Internal Temperature

The temperature changes at each depth from the heated surface of the ring-restraint heating test specimens with elapsed heating time are shown in Fig. 6. At the same elapsed time, the fiber-reinforced specimens, especially near the heated surface, recorded an overall lower internal temperature than Plain. This confirms a tendency for fiber incorporation to make heat transfer somewhat slower and to delay the rise in internal temperature. This is because fiber incorporation increases the micro-pores, making moisture migration and vaporization relatively more active in the early stage of heating. As a result, the internal-temperature rise at a given time point is considered to have been suppressed.

3.5 Change in Water Vapor Pressure

Fig. 7 shows the water vapor pressure measurement results. For Plain, spalling occurred at around 150s,

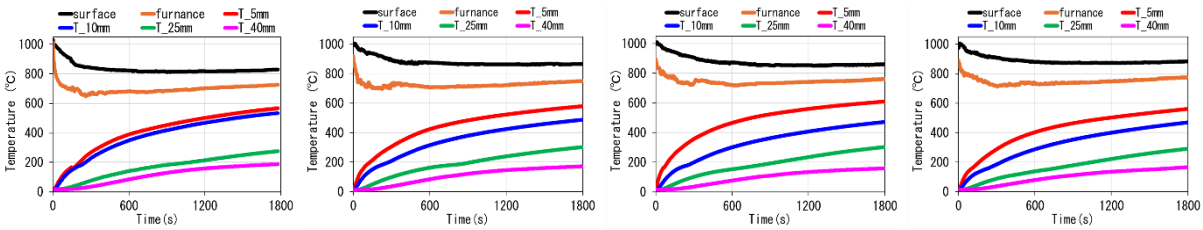

(a) Plain[2] (b) K0.2 (c) K0.2P (d) K0.4

Fig. 6 Internal temperature with heating time

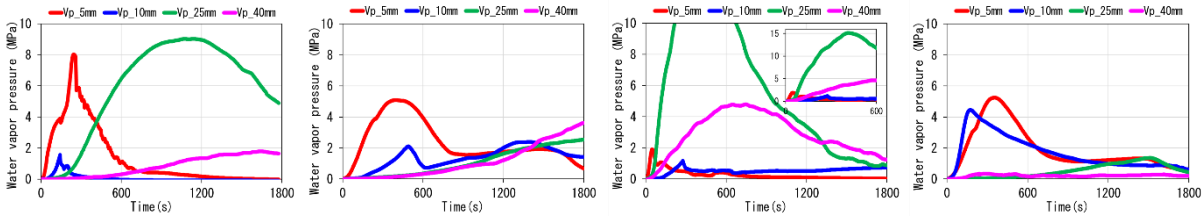

(a) Plain[2] (b) K0.2 (c) K0.2P (d) K0.4

Fig. 7 Water vapor pressure with heating time

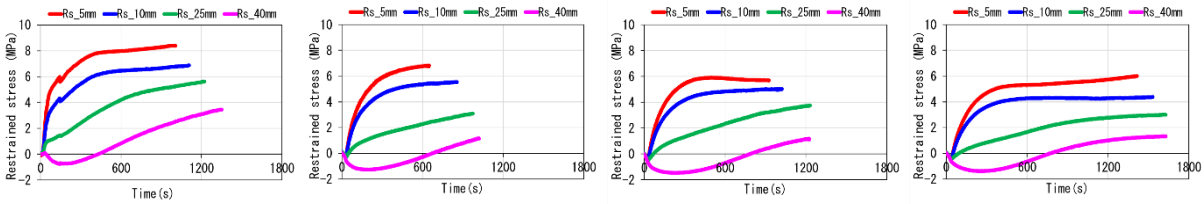

(a) Plain[2] (b) K0.2 (c) K0.2P (d) K0.4

Fig. 8 Restrained stress with heating time

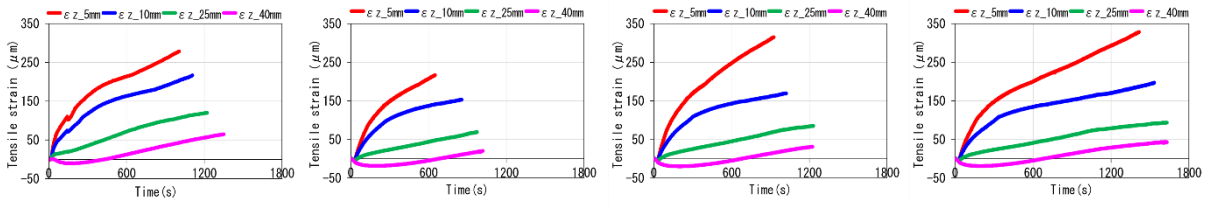

(a) Plain[2] (b) K0.2 (c) K0.2P (d) K0.4

Fig. 9 Tensile strain with heating time

and the maximum water vapor pressure rose to about 8MPa. After the start of heating, the water vapor pressure at a depth of 5mm increased sharply, and it is highly likely to have acted as a direct cause of spalling. In contrast, for K0.2, the maximum water vapor pressure decreased to about 5MPa, while K0.4 showed a level comparable to K0.2. K0.2P exhibited in which the rise in water vapor pressure was suppressed overall.

The temporal change in water vapor pressure is considered to depend not only on the amount of moisture but also on the moisture-migration path and the ease of discharge. The tendency for the maximum water vapor pressure to decrease in the fiber-reinforced mixes is consistent with the possibility that, at high temperature, the hollow structure of the natural fibers formed micro-pores that can contribute to vapor migration[6]. Meanwhile, the behavior in which the rise in water vapor pressure was suppressed for K0.2P suggests that the moisture state of the fibers affected the ITZ characteristics around the fibers, so that migration and release became relatively dominant over pressure accumulation[3]. However, these are inferences based on the measurement results, and verification by direct observation of the pore structure and ITZ remains a future task.

3.6 Change in Restrained Stress and Tensile Strain

The changes in Restrained stress and tensile strain

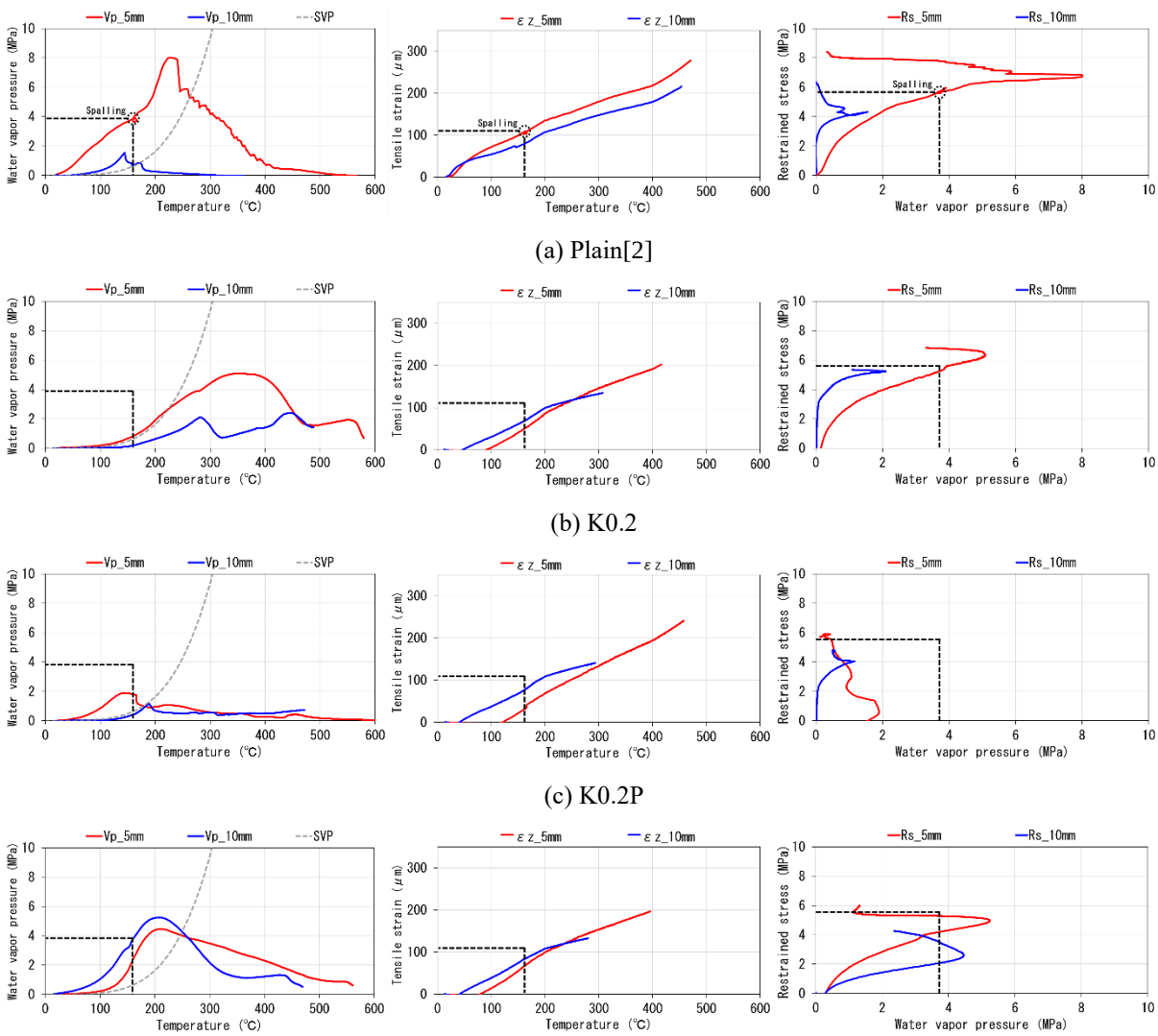

(a) Plain[2]

(b) K0.2

(c) K0.2P

(d) K0.4

Fig. 10 Comparison of heating characteristics by mix (left: water vapor pressure–temperature, center: tensile strain–temperature, right: Restrained stress–water vapor pressure)--

are shown in Fig. 8 and Fig. 9. Plain showed a sharp increase in stress and strain in the early stage of heating, with an abrupt change at the moment of spalling. In contrast, in the fiber-reinforced specimens the increase in stress and strain was relatively gradual, and the maximum levels also tended to be lower. In particular, when compared over the same time span up to the moment of spalling in Plain, the maximum Restrained stress near the heated surface in the fiber-reinforced specimens was lower than that of Plain.

Moreover, the maximum tensile strain in the same time span was also lower than that of Plain, which is interpreted as suppression of the sharp stress and strain concentration that induces spalling. This is considered to be because, at high temperature, the presence of the fibers contributed to the formation of micro-pores and discharge paths, thereby relieving the accumulation of water vapor pressure and the concentration of stress and strain.

3.7 Discussion of the Spalling-Suppression Mechanism of Kenaf Fiber

To examine the spalling-suppression mechanism of kenaf fiber, comparisons were made using the moment of spalling in Plain as the reference. That is, assuming that spalling occurs under conditions equal to or exceeding the stress and water vapor pressure at the moment of spalling in Plain, this is shown in Fig. 10. In Fig. 10, Vp denotes water vapor pressure (vapor pressure), SVP denotes saturated vapour pressure, and Rs denotes the Restrained stress calculated from the strain of the steel ring.

As a result, although K0.2 showed a tendency similar to Plain in the Restrained stress–water vapor pressure relationship, it maintained values lower than the spalling level of Plain in the other indices. K0.4 showed overall low stress levels, but the rate of water vapor pressure rise at a depth of 5 mm tended to be greater than that of K0.2. For K0.2P, the rise in water vapor pressure was suppressed overall, and the other indices also remained in a range lower than the spalling level of Plain.

For Plain, the water vapor pressure increased sharply near a depth of 5 mm and reached a high-pressure state in a short time. In contrast, in the fiber-reinforced specimens the maximum water vapor pressure decreased, and the rapid increase in Restrained stress and tensile strain was also suppressed. In the post-heating appearance observation as well, spalling was confirmed for Plain, whereas no spalling occurred in any of the fiber-reinforced specimens. When the fiber-reinforced specimens were compared with one another, no large difference in cracking was observed. From these results, the incorporation of kenaf fiber may have suppressed spalling by relieving the accumulation of internal pressure and the concentration of stress and strain.

Such behavior is considered to be related to the shape change and thermal-decomposition behavior of kenaf fiber at high temperature. Kenaf fiber is a cellulose-based natural fiber, and through dehydration, shrinkage, thermal decomposition, and carbonization accompanying heating, it can form micro-pores inside and around the fibers. As a result, the hollow structure of the kenaf fiber and the pores after thermal decomposition may have functioned as vapor-migration paths and relieved the rise in water vapor pressure.

The rapid rise and fall of water vapor pressure observed for K0.4 is considered to be because, as the fiber content increased, both the amount of vaporized moisture and the vapor-discharge paths increased. In addition, the behavior in which the water vapor pressure rise was suppressed overall for K0.2P may have been influenced by the change in the ITZ characteristics around the fibers associated with pre-wetting[7].

From the above, the spalling-suppression effect of kenaf fiber is considered to result from the void formation during heating and the securing of vapor-migration paths, which relieved the rapid increases in internal water vapor pressure, Restrained stress, and tensile strain.

Because PCM, which is used as a repair and strengthening material, has a dense structure, moisture discharge can be delayed at high temperature. When water vapor pressure and Restrained stress rise simultaneously at this time, the risk of directly leading to spalling is high. A distinctive feature of this study is

that it experimentally showed not merely whether spalling occurs, but that fiber incorporation can significantly control the main indices of heating behavior—for example, by changing the rise and accumulation behavior of internal water vapor pressure and relieving the rapid changes in Restrained stress and tensile strain.

In particular, from the viewpoint of field application, fiber incorporation reduces the spalling risk that causes cross-sectional spall-off and a rapid drop in performance during fire exposure, and can be an effective measure that enhances the fire resistance and reliability of repair and strengthening PCM.

Meanwhile, because this study was conducted with ring-restraint specimens under a single heating condition, the spalling and water vapor pressure behavior may change when the heating curve, specimen dimensions, or external restraint conditions differ. In the future, using X-ray CT and scanning electron microscopy, in addition to quantitative evaluation of the pore structure and ITZ microstructure, it will be necessary to verify reproducibility and extend the applicable range through repeated tests under different heating protocols.

4. Conclusions

In this study, using the ring-restraint heating test method, it was confirmed that the incorporation of kenaf fiber changes the heating behavior of PCM and can suppress spalling, and the following conclusions were obtained.

(1) Plain showed a sharp rise in internal water vapor pressure, and spalling occurred at around 150 s. In contrast, no spalling was observed in the fiber-reinforced specimens.

(2) In the fiber-reinforced specimens, a tendency was observed for the maximum water vapor pressure to decrease or for the pressure rise to be suppressed overall. In particular, for K0.2P, suppression of water vapor pressure accumulation was confirmed.

(3) The Restrained stress and tensile strain increased sharply in the early stage of heating for Plain, whereas in the fiber-reinforced specimens they increased relatively steadily.

Reference

[1] Sugino, Y., Ozawa, M., & Sukekawa, M. (2023). Fire spalling behavior of various polymer modified mortars under ring restraint. Journal of Advanced Concrete Technology, 21(5), 367-379.

[2] 古賀 丈太郎，小山 拓，福井 拓也，小澤 満津雄：リング拘束加熱試験法を用いた若材齢期におけるポリマーセメントモルタルの爆裂リスクの評価,コンクリート工学年次論文集,Vol.47, No.1,pp.1968－1973,2025

[3] Ozawa, M., & Morimoto, H. (2014). Effects of various fibres on high-temperature spalling in high-performance concrete. Construction and building materials, 71, 83-92.

[4] 谷辺徹， 小澤満津雄， 鎌田亮太， 内田裕市，六郷恵哲：高温環境下での高強度コンクリートの耐爆裂性評価における爆裂発生指標の提案，土木学会論文集 E2，Vol.70, No.1, pp.104-117，2014.3

[5] Nguyen, T. B. T., Saengsoy, W., & Tangtermsirikul, S. (2018). Effect of initial moisture of wet fly ash on the workability and compressive strength of mortar and concrete. Construction and Building Materials, 183, 408-416.

[6] Choe, G., Kim, G., Nam, J., Kim, H., Hwang, E., & Lee, S. (2020). Effect of mass loss of organic fiber on the water vapor pressure and moisture migration of 150 and 200 MPa ultra-high strength concrete exposed to high temperature. Journal of Advanced Concrete Technology, 18(6), 339-351.

[7] Sabziparvar, A., Taleponga, D., & Foruzanmehr, M. R. (2024). Enhancing hydration and internal curing in cementitious mixes: The impact of pre-treated milkweed fibres. Case Studies in Construction Materials, 20, e03079.

各種塩害対策手法による補修モルタルのマクロセル腐食抑制効果

Macrocell Corrosion Inhibition Effects of Repair Mortars
with Application of Various Countermeasures for Chloride Attack

隈本創士[*1]、山田陸生[*2]、南真樹[*3]、高井修[*4]、濱幸雄[*5]
Kumamoto Soshi, Yamada Rikuo, Minami Maki, Takai Osamu, Hama Yukio

ABSTRACT

本研究では、塩害環境下における断面修復後の鉄筋腐食に対する高炉スラグ微粉末（GGBFS）およびセメント系防錆剤の効果を検討した。断面修復では既存鉄筋の腐食や塩化物イオンが残存する可能性があり、既存腐食部の進展や既設部と補修部の界面で生じるマクロセル腐食が課題となる。そこで、既設部と補修部を有する打継供試体を作製し、あらかじめ腐食させた鉄筋を埋設したうえで、3.5%NaCl 水溶液を用いた乾湿繰り返し試験を 10 サイクル実施した。試験後は鉄筋の発錆面積を測定するとともに、分割鉄筋を用いて腐食電流を測定し、腐食挙動を評価した。その結果、セメント系防錆剤は界面腐食の抑制に有効であり、GGBFS を 20%混合した FRPCM は界面腐食と既存腐食部進展の双方を抑制する優れた効果を示した。

1. Introduction

In coastal areas and cold regions with heavy snowfall, measures to protect repair materials from salt damage are necessary due to the presence of airborne salt and salt in de-icing agents. These chloride sources can penetrate concrete over long periods of exposure, accelerating the corrosion of reinforcing steel and reducing the durability and service life of reinforced concrete structures. Therefore, improving the long-term corrosion resistance of repair materials has become an important issue in the maintenance of aging infrastructure. In cross-sectional repair, the deteriorated concrete is chiseled away, the rebars are cleaned, a rust inhibitor is applied, and the void is then filled with a repair material such as PCM; however, it is anticipated that manual cleaning will not completely remove chloride ions or corroded areas. In a previous report[1)], we investigated the phenomenon of such residual corrosion expanding within the mortar and reported that corrosion progression is suppressed in mortars and FRPCM containing granulated blast furnace slag (GGBFS) or cement-based rust inhibitors.

On the other hand, when repairing actual structures, in addition to the progression of existing corrosion areas mentioned earlier, there is concern about the occurrence of macrocell corrosion due to the concentration of chloride ions at the interface between the existing and repaired sections. Furthermore, in actual repair work, it is expected that FRPCM—a mixture of cement-based rust inhibitors and GGBFS—will be used simultaneously. Therefore, the objective of this study was to investigate the inhibitory effects of GGBFS and cement-based rust inhibitors on the combined corrosion behavior of these two materials. To examine changes over time, two types of jointed test specimens with the same mix design but different structures were prepared, and the corrosion area and corrosion current of the rebars were evaluated.

2. Materials and Experimental plan

2.1 Corrosion Area

Table 1 shows the experimental design. Assuming an actual structure, jointed test specimens with existing

*1 北海道大学大学院　工学院修士課程
*2 北電総合設計株式会社　修士（工学）／室蘭工業大学大学院　工学研究科　博士課程
*3 株式会社南組
*4 株式会社エフモル工業
*5 室蘭工業大学大学院　工学研究科　教授／北海道大学大学院　工学研究院　教授　博士（工学）

Table 1 Experimental Design

name	Mortar				Rebar
	Existing Section	Repair Section			Rust inhibitor
	Blending	Blending	GGBFS [B×wt%]	Fine aggregate	
M0	W/B=50% B:S=1:2.5	W/B=50% B:S=1:2.5	0	land sand	×
M0c			0		○
M20			20		×
F0		FRPCM W/B=30% Polymer 2% Fiber 0.5%	0	silica sand	×
F0c			0		○
F10			10	blast furnace slag fine aggregate	×
F20			20		×

and repaired sections were fabricated. The existing section consisted of standard mortar with a water-to-binder ratio (W/B) of 50% and a binder-to-sand ratio (B:S) of 1:2.5. For the repair section, the base mortar mix was as follows: M consisted of ordinary mortar with W/B = 50% and B:S = 1:2.5, while F consisted of a pre-mixed fiber-reinforced polymer-cement mortar (FRPCM) with W/B = 30%, containing 2% acrylic polymer and 0.5% short organic fibers. The GGBFS content was set at 0–20% of the binder. For fine aggregate, land sand was used in M; for F, silica sand was used in the two levels where GGBFS was not used in the binder, and blast furnace slag fine aggregate was used in the two levels where GGBFS was used. Furthermore, to simulate actual PCM repair methods, M0c and F0c were established, in which a cement-based rust inhibitor was applied to the embedded rebars. A commercially available polymer-cement-based product, whose main component is an adsorbent that adsorbs chloride ions and releases nitrite ions, was used as the cement-based rust inhibitor and applied to the rebarss within the repair area, as shown in Photo 1.

2.2 Corrosion Current

Table 1 shows the experimental design. Jointed test specimens with existing and repaired sections were prepared. The only difference from the corrosion area experiments was the specimen structure; the mix proportions of mortar and fine aggregate were kept identical in all cases. To limit the surface through which chloride ions could penetrate during corrosion acceleration, all sides of the specimen except for one longitudinal side were coated with an epoxy hardener.

Photo1 Areas Where Cement-Based Rust Inhibitors Are Applied

3. Experimental Method

3.1 Corrosion Area

Figure 1 shows an overview of the test specimens. The test specimens were rectangular prisms measuring 40 × 40 × 160 mm, fabricated by joining an existing section with a repaired section. Of the embedded rebars' total length of 150 mm, the central 30 mm were pre-corroded using salt water[1]. After the repair section was cast, the specimens were sealed and cured for 7 days.

The accelerated corrosion test was conducted using the wet-dry cycling method (refer to JCI-SC3). One cycle consisted of a 3-day wetting period—during which the specimens were immersed in a 3.5% NaCl aqueous solution at 60°C—followed by a 4-day drying period in air at 10°C and 60% relative humidity. This wet-dry cycle was repeated 10 times. After the test, the test specimens were split open to remove the rebars; the corroded areas were traced to measure the rusted surface area, and the evaluation was performed by dividing the area into the regions shown in Figure 2. The interior of the existing rebar section was designated as section a, the sound portion within the repaired

section as section b, and the existing corroded section as section c. The rusted area was defined as follows: the central progression (b_c) was the 10 mm on either side of the existing corroded section; the

interface on the existing section side (a_b) and the interface on the repaired section side (b_a) were each 10 mm from the interface. Furthermore, the rusted area values were calculated as the average of the three test specimens.

3.2 Corrosion Current

Figure 3 shows an overview of the test specimens. The specimens were rectangular prisms measuring 40 × 40 × 160 mm, fabricated by joining an existing section with a repaired section. To measure only the microcell corrosion current—as opposed to the microcell corrosion current—segmented rebrs, which were electrically integrated via wire connections, were embedded[3]). Rebar c, which simulated a corroded area, was uniformly corroded on its surface in advance using saltwater. A commercially available polymer-cement paste-type cement-based rust inhibitor, which adsorbs chloride ions and releases nitrite ions, was applied to rebars b and c within the repair section, as shown in Figure 4. The test specimens were sealed and cured for 14 days to age the repair area; after measuring the initial current value, they were subjected to repeated wetting and drying cycles using saltwater. The wet-dry cycling was conducted in the same manner as in the corrosion area test: one cycle consisted of a 3-day wetting period (immersion in a 3.5% NaCl aqueous solution at 60°C) followed by a 4-day drying period (air drying at 10°C and 60% relative humidity). This cycle was repeated 10 times. Starting with the wetting cycle, the current flowing between the rebars was measured at the end of each cycle. As shown in Figure 5, bar b was used as the anode, and the direction of current flow from bars a and c was defined as positive; the current was measured using a resistance-free ammeter.

The measured values were recorded 30 seconds after connecting the leads to the resistance-free ammeter. Photo 2 shows the measurement setup.

4. Result and Discussion

4.1 Corrosion Area

The evaluation areas shown in Figure 2 are indicated by color in the post-test trace images of the corroded rebar sections in Figure 6. The measured corrosion areas are shown in Figure 7.

Compared to M0, the corrosion area in F0 increased slightly across the entire interface (a_b+b_a) but decreased in the central progression zone (b_c). It is considered that macrocell corrosion at the interface cannot be suppressed when there is a significant difference in chloride ion penetration resistance between the existing and repaired sections.

In M0c, the corrosion area decreased in both the entire interface (a_b + b_a) and the central progression zone (b_c) compared to M0. On the other hand, in F0c, while the corrosion area in the entire interface (a_b + b_a)

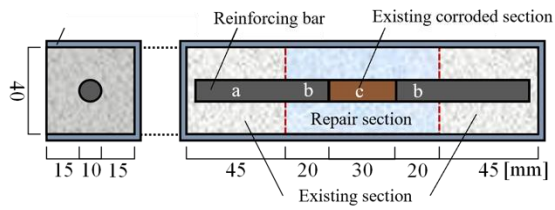

Figure 1 Test specimen(Corrosion Area)

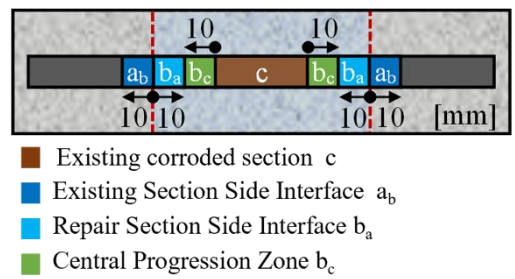

Figure 2 Range for Evaluating the Area of Rust Formation

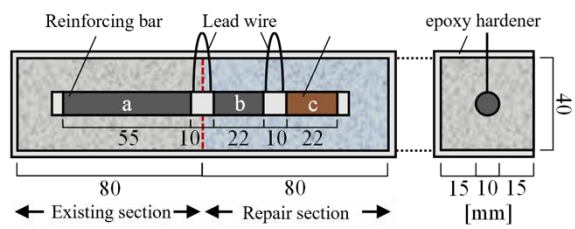

Figure 3 Test specimen(Corrosion Current)

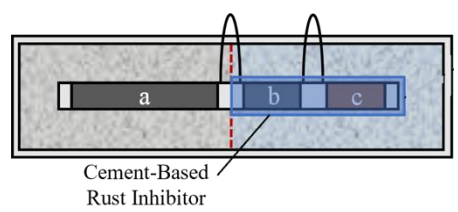

Figure 4 Areas Where Cement-Based Rust Inhibitors Are Applied

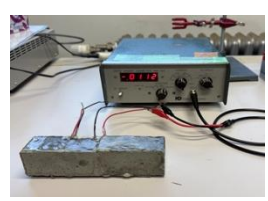

Photo 2 Corrosion current measurement device

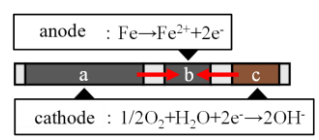

Figure 5 Sign of the Current Value

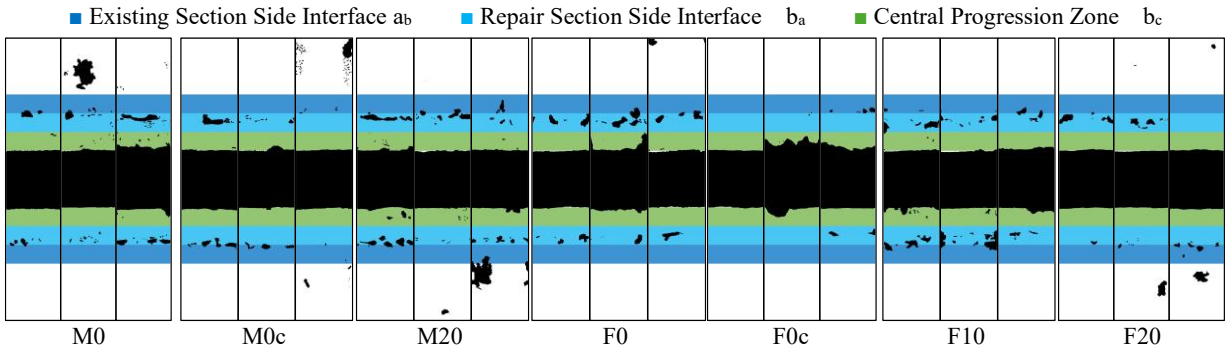

Figure 6 Corroded Areas of Rebars After an Accelerated Corrosion Test

decreased significantly compared to F0, the corrosion area in the central progression zone (b_c) increased significantly. F0c is based on FRPCM, which results in a difference in chloride ion penetration resistance between the existing and repaired sections. Consequently, chloride ions became unevenly distributed, and nitrite ions derived from the cement-based rust inhibitor were supplied only near the interface; thus, while the rusted area on the repaired side (b_a) of the interface decreased, the rusted area in the central progression region (b_c) did not decrease.

In M20, compared to M0, the rusted area increased across the entire interface (a_b + b_a), while the rusted area in the central progression (b_c) decreased. In F10, compared to F0, the rusted area increased in both the entire interface (a_b + b_a) and the central progression (b_c). In contrast, in F20, the rusted area decreased in both regions. I is believed that the corrosion behavior was influenced by the salt-barrier effect resulting from the densification of the hardened matrix and the reduction in reaction activity due to lower dissolved oxygen levels near the rebars[2),3)]. Consequently, corrosion was suppressed within the repair sections of M20 and F20—which contained higher amounts of GGBFS—and the rusted area in the central progression region (b_c) is thought to have decreased.

The effects of cement-based rust inhibitors and GGBFS on the rusted area in each section varied depending on the type of base mortar and the mixing ratio. Within the scope of this experiment, it was determined that F0c had the greatest inhibitory effect on interfacial corrosion, while F20 had the greatest inhibitory effect on the progression of existing corrosion.

4.2 Corrosion Current

Figure 8 shows the current values between each rebar element. Overall, the fluctuations in these values began to increase after two wet-dry cycles, and thereafter, the signs of the current values remained nearly identical until the end of the 10th cycle. Table 2

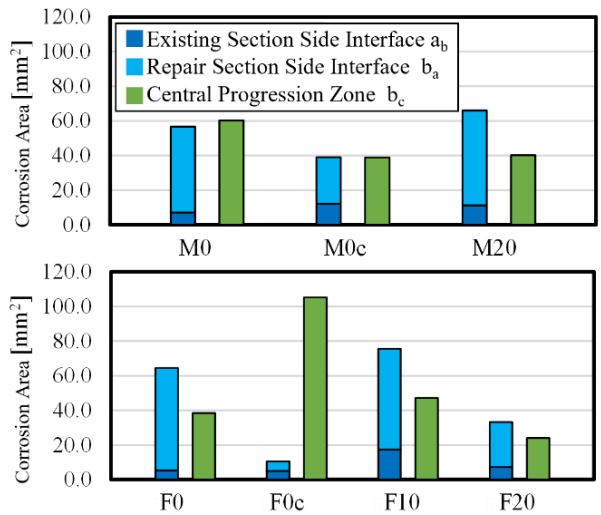

Figure 7 Rust Area by Evaluation Range

indicates whether each rebar was determined to be an anode or a cathode based on the sign of the current value, and also lists the macrocell corrosion current density for Rebar b. The macrocell corrosion current density was calculated by summing the current values between a and b and between b and c, and dividing the result by the surface area of rebar b, based on previous research[3)].

Compared to M0, in the repaired section using F0, the current value between b and c was smaller because chloride ions were less likely to penetrate due to the low W/B ratio and the addition of polymer admixtures; consequently, the concentration difference with the existing section increased, leading to a larger current value between a and b.

In both M0c and F0c, which used cement-based rust inhibitors, the current value between a and b decreased. This is thought to be because the cement-based rust inhibitors absorbed chloride ions that had penetrated near the interface and supplied nitrite ions. On the other hand, the sign of the current between b and c differed between M0c and F0c; in F0c, a current with b as the

Table 2 Condition of the Reinforcing Steel Element after 10 Wet-Dry Cycles

name	Rebar Between elements	Determining the Anode or Cathode			Current Density [μA/cm^2]
		a Rebar	b Rebar	c Rebar	
M0	a-b	cathode	anode	—	0.11
	b-c	—	cathode	anode	
M0c	a-b	cathode	anode	—	-0.11
	b-c	—	cathode	anode	
M20	a-b	anode	cathode	—	0.03
	b-c	—	anode	cathode	
F0	a-b	anode	cathode	—	-0.49
	b-c	—	anode	cathode	
F0c	a-b	cathode	anode	—	0.77
	b-c	—	anode	cathode	
F10	a-b	anode	cathode	—	-0.16
	b-c	—	anode	cathode	
F20	a-b	cathode	anode	—	0.01
	b-c	—	cathode	anode	

anode was generated, and the current density was also high. This behavior is consistent with the results for corrosion area, which showed that the existing corrosion area in F0c expanded; it is thought that, in the rebars within the repaired area where corrosion remained, corrosion was promoted by the uneven distribution of nitrite ions, with the sound portions of the rebars acting as anodes[2)].

In M20 and F10/F20, which contained GGBFS, the current values between b and c tended to be lower than those in the reference samples M0 and F0, respectively. Regarding the current values between a and b, M20 showed the opposite sign to M0; while the a-rebar within the existing structure—where chloride ion penetration is presumed to be easier—acted as the anode, no decrease in current values was observed. In F10 and F20, the current values between a and b were lower than those in F0. Although a concentration gradient of chloride ions is presumed to exist between the a and b rebars, the current values have decreased. Since it is estimated that the densification of the hardened matrix caused by GGBFS inhibited the formation of macrocells, further investigation—such as measurements of electrical resistance—is considered necessary.

5. Conclusions

5.1 Corrosion Area

(1) Applying a cement-based rust inhibitor to the rebar in the repaired area suppresses interfacial corrosion of the rebars.

(2) Mortar containing at least 20% GGBFS and FRPCM suppress the progression of existing corrosion in the rebars.

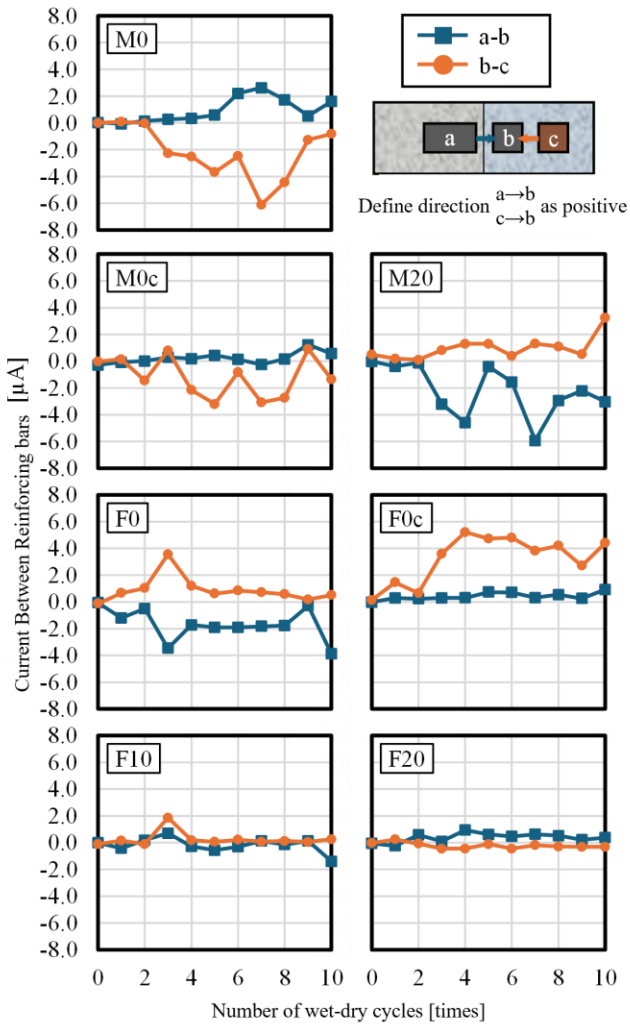

Figure 8 Macrocell Corrosion Current Measurement Results

(3) Depending on the material properties and performance of the repair section, corrosion may not be suppressed by cement-based rust inhibitors or GGBFS. FRPCM mixed with 20% GGBFS demonstrated a suppressive effect on both interfacial corrosion and the progression of existing corrosion and is expected to provide more stable corrosion suppression performance.

5.2 Corrosion Current

(4) The use of a cement-based rust inhibitor suppressed the macrocell corrosion current occurring at the interface between the existing and repaired sections. The macrocell corrosion current between the corroded and sound sections increased when FRPCM was used in combination with a cement-based rust inhibitor.

(5) The use of GGBFS suppressed the macrocell corrosion current between the corroded and sound sections of the rebars within the repaired area. Regarding the macrocell corrosion current occurring at the interface between the existing and repaired sections, it was suppressed when FRPCM and GGBFS were used in combination.

References

(1) Rikuo Yamada et al.: Study on the Effectiveness of Repair Mortars Using Various Salt Damage Mitigation Methods in Inhibiting the Progression of Reinforcement Corrosion, Abstracts of Academic Presentations at the Annual Conference of the Architectural Institute of Japan, pp. 237–238, 2025

(2) Keiyu Kawai et al.: Development of Oxygen-Reducing Admixtures to Inhibit Corrosion of Steel in Concrete, Concrete Engineering, Vol. 59, No. 5, p. 441, 2021

(3) Li Jingwen et al.: Corrosion Inhibition Effect of Mortar Containing Fine-Grained Blast Furnace Slag and Amine-Based Rust Inhibitors on Rebars, Proceedings of the Upgrade Conference, Vol. 24, pp. 269–274, 2024

(4) Shinichi Miyazato et al.: Experimental and Theoretical Study of a Macrocell Current Measurement Method Using Segmented Rebars, Annual Proceedings of the Concrete Engineering Society, Vol. 23, No. 2, pp. 547–552, 2001

(5) Amir Zomorodian, Ali Behnood: Review of Rust Inhibitors in Reinforced Concrete: Conventional and Green Materials, Buildings 2023, 13, 1170

積層パラメータを変化させた 3DP コンクリート内部空隙構造と耐凍害性の関係

Relationship between Intra-filament Void Structure and Freeze-Thaw Resistance of 3D printed Concrete with Different Printing Parameters

牧野貴哉※1、山田海矢※1、中瀬皓太※2、橋本勝文※3、濱幸雄※4
Makino Takaya, Yamada Kaiya, Nakase Kota, Hashimoto Katsufumi, Hama Yukio

要旨

3D コンクリートプリンティング（3DCP）では、押出しおよび積層過程で形成される intra-filament void の構造が耐久性に影響を及ぼすと考えられる。本研究では、異なる printing parameter で造形した 3D プリントモルタルを対象に、X 線 CT 法による intra-filament void 構造の評価と、液体窒素を用いた凍結融解試験による耐凍害性の評価を行う。その結果、intra-filament void はノズル移動方向に大きく伸長する異方的な形状を示す。また、検討した範囲では v/E の影響は限定的である。一方、Mix B は Mix A より空隙率および気泡間隔係数が大きく、凍結融解試験における相対動弾性係数の低下も大きい。さらに、3D プリント供試体では相対動弾性係数のばらつきが大きい。以上より、3D プリントモルタルの耐凍害性は、printing parameter だけでなく、配合条件により変化する intra-filament void 構造とも関連する。

1. Introduction

In recent years, extensive research and development have been conducted on three-dimensional concrete printing (3DCP) technology that eliminates the need for formwork and improves construction efficiency. Concrete and mortar fabricated using 3DCP are produced by extruding cementitious materials and depositing them layer by layer in the form of filaments. It is well known that voids are formed both between and within filaments during the printing process [1]. These voids are broadly classified into two categories: Inter-filament voids, which are formed between adjacent filaments, and Intra-filament voids, which exist within individual filaments.

It is known that inter-filament voids act as crack propagation paths during the facture process of 3D printed concrete [2]. However, their adverse effects can be mitigated by improving the material properties and printing conditions. In contrast, intra-filament void corresponds to the air voids and pores present in conventionally cast concrete, and their formation is unavoidable. Therefore, controlling the morphology and distribution of Intra-filament voids is important for improving the performance of 3D-printed concrete.

Previous studies have suggested that the morphology of intra-filament void changes during the extrusion and layer-by-layer printing process [3]. Because the material extrusion direction is perpendicular to the nozzle traveling direction, intra-filament void is expected to undergo anisotropic deformation during printing. Nakase et al, also reported that printing parameters influence the geometric characteristic of intra-filament void [4]. However, the relationship between printing parameters and the three-dimensional intra-filament void structure has not yet been systematically clarified.

As 3D concrete printing becomes more widely

※1 日本国 北海道大学大学 工学院 修士課程
※2 日本国 北海道大学大学 工学研究院 JSPS 特別研究員(PD) 博士(工学)
※3 日本国 北海道大学大学院 工学研究院 准教授 博士(工学)
※4 日本国 室蘭工業大学大学院 もの創造系領域 教授 博士(工学)

adopted in construction sites, the importance of its durability has gained greater recognition. Among the various durability properties, freeze-thaw resistance is particularly important for structures exposed to cold environments. Freeze-thaw resistance depends not only on the total air content but also on the internal air-void system [5]. In particular, intentionally entrained fine air voids alleviate the hydraulic pressure generated by the movement of unfrozen water during freezing [6]. In 3D-printed concrete, printing parameters are expected to influence not only the spacing factor but also the air content, voids morphology, and spatial distribution of intra-filament void. Furthermore, as improvements in interlayer bonding reduce the influence of layer interfaces and Inter-filament voids, it becomes increasingly important to clarify how the intra-filament void structure affects freeze-thaw resistance.

Therefore, this study aimed to clarify the influence of printing parameters on the three-dimensional intra-filament void structure and freeze-thaw resistance of3D-printed mortar. The intra-filament void structure was quantitatively evaluated using X-ray computed tomography (X-ray CT), and freeze-thaw resistance was evaluated by a liquid-nitrogen freeze-thaw test. Finally, the relationship between the intra-filament void structure and freeze-thaw resistance was discussed.

2. Materials and methods

2.1 Materials

Mortar with a water-to-cement ratio (W/C) of 23% and a sand-to-cement ratio (S/C) of 0.55 was prepared using ordinary Portland cement (density: 3.16g/cm^3), silica sand (density: 2.68g/cm^3), and ahigh-range air entraining water-reducing admixture (HRAE). This mixture was designed as Mix A. The air content of the fresh mortar was 3.8%, and the 15-drop flow value was 140mm. Mortar with a water-to-cement ratio (W/C) of 35% and a sand-to-cement ratio (S/C) of 0.55 was prepared using ordinary Portland cement (density: 3.16g/cm^3), silica sand (density: 2.68g/cm^3), and Elcon, a viscosity-modifying admixture (VMA, TAIHEIYO MATERIALS CORPORATION). This mixture was designated as MIX B. The air content of fresh mortar was 4.65%, and the 15-drop flow values was 140 mm. The mixture proportion and fresh properties of the printable concrete mixture are summarized in Table 1.

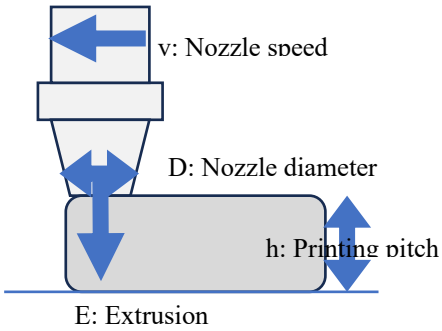

Fig.1 3D printer setting

Table 2 Specification of the filament specimens

Name	Mixture	*v/E*	*h/D*
A1.0		1.0	
A2.0	A	2.0	
A3.0		3.0	1.0
B1.0		1.0	
B2.0	B	2.0	
B3.0		3.0	

A cartridge-type material extrusion 3D printer was used in this study. As shown in Fig1, the extrusion rate (*E*), nozzle printing speed (*v*), nozzle diameter (*D*), and layer height (*h*) were selected as the printing parameters. Printing was carried out under different printing conditions by varying the nozzle travel speed-to-extrusion rate ratio (*v/E*) while controlling the layer height-to-nozzle diameter ratio (*h/D*), as summarized in Table 2.

For each printing condition, filaments were first printed continuously and then cut into 50-mm-long specimens. Five filament specimens were prepared for each printing condition. For comparison, five cast

Table 1 Mix proportions and fresh properties of the filament mixture

Mixture	W/C (%)	S/C (%)	SP/C (%)	VMA/C (%)	Air (%)	15-drop Flow (mm)
A	23	55	2.6	-	3.8	147
B	35	55	-	0.57	4.6	140

specimens with a diameter of 20 mm and a length of 50 mm were prepared using the same mortar mixture in cylindrical molds. After fabrication, all specimens were air-cured under controlled condition at 20 °C and 60 % relative humidity (R.H.) until the age of 28 days.

2.2 Methods

The intra-filament void structure of filament specimens was three-dimensionally evaluated using X-ray computed tomography (X-ray CT). The X-ray tube voltage and tube current were set to 100 kV and 200 μA, respectively. During scanning, a 0.2-mm-thick copper (Cu) filter was used to reduce imaging artifacts. After X-ray scanning, the acquired projection data were reconstructed to generate cross-section images with an image size of 2864 × 2864 pixels and a voxel size of 17.6 μm/pixel.

Because the filament specimens (approximately 10-20 mm in diameter and 50 mm in length) did not satisfy the specimen dimensions specified in the JIS A 1148 freeze-thaw test standard, a freeze-thaw test using liquid nitrogen, which has previously been applied to conventionally cast concrete [7], was conducted at the age of 28 days. Prior to the freeze-thaw test, the specimens were vacuum-saturated with water for 24 h. The freeze-thaw test consisted of 10 cycles. Each cycle comprised 5 min of exposure to liquid nitrogen (approximately -196℃), followed by 5 min of immersion in water at 40℃, causing the specimen temperature to repeatedly change between approximately 40℃ and -196℃. After each freeze-thaw cycle, the specimen length and ultrasonic pulse velocity were measured, and the relative dynamic modulus of elasticity was calculated using Eq. (1) [8].

$$RDM_n = VL_n^2 / VL_0^2 \times 100 \qquad (1)$$

Where RDM_n is the relative dynamic modulus of elasticity, VL_n is the ultrasonic pulse velocity after n freeze-thaw cycles, and VL_0 is the initial ultrasonic pulse velocity before the freeze-thaw test.

3. Results and Discussion

3.1 Evaluation of the internal void structure

The porosity and spacing factor obtained from the consecutive X-ray CT images are summarized in Table 3. Since the diameter of the filament specimens varied depending on the printing condition, three randomly selected cubic regions of interest (ROIs), each measuring 5×5×5 mm, were extracted from the X-ray CT images of each specimen. The porosity was calculated as the ratio of the total void volume within each ROI to the total ROI volume. The mean values and standard deviations obtained from the three ROIs are presented in Table 3. The procedure for calculating the spacing factor is described below [9].

For the voids extracted from the X-ray CT images, an equivalent uniform void distribution was assumed by dividing the total void volume within each ROI by the number of extracted voids. The Equivalent Spherical Diameter (ESD) was calculated from the volume of an individual void. The specific surface area (α) was calculated using Eq. (2), where R is the Equivalent Spherical Diameter.

$$\alpha = \frac{3}{R} \qquad (2)$$

Based on the above assumptions, the spacing factor was calculated using Eq. (3)

$$S.P. = \frac{3}{\alpha}\left(1.4\sqrt[3]{\frac{P+A}{A}} - 1\right) \qquad (3)$$

Here, SP is the spacing factor, P is the volume fraction of cement paste in the mortar, and A is the volume fraction of air in the mortar.

As shown in Table 3, the 3D-printed specimens exhibited higher porosity and smaller spacing factors than the corresponding cast specimens. This indicates that the extrusion and deposition processes increased

Table 3 Porosity and spacing factor measured from X-ray CT images

sample	Porosity (%)	Spacing factor (μm)
A1.0	3.97±1.15	269±34
A2.0	2.11±1.04	350±41
A3.0	2.21±1.08	299±38
Cast A	1.20±1.02	560±48
B1.0	5.08±1.07	398±38
B2.0	5.10±1.14	373±33
B3.0	4.99±1.04	412±42
Cast B	3.78±1.03	437±46

the amount of void and decreased the spacing between neighboring voids within the filament specimens. In addition, Mix B exhibited higher porosity and a larger spacing factor than Mix A. This result indicates that Mix B contained a greater amount of void with a lager characteristic size than Mix A, rather than simply having a greater total amount of fine entrained air voids.

3.2 Evaluation of void deformation

The X-ray CT images were binarized to extract the internal voids. As shown in Fig. 1, the x- and y-axes were defined as the cross-sectional directions of the filament specimen, while the z-axis was defined as the longitudinal direction corresponding to the nozzle travel direction. The deformation of the internal voids along each axis was quantified by comparing the projected diameter of each void along each axis with its Equivalent Spherical Diameter (ESD), which was calculated as the diameter of a sphere having the same number of voxels as the extracted void.

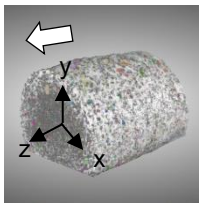

Fig. 1 Definition of axes

Figures 3 and 4 show representative relationships between the ESD and the projected diameter of the internal voids along each axis. A larger difference between the projected diameter and the ESD indicates a greater deviation of the void shape from a spherical shape. Therefore, a steeper slope of the regression line

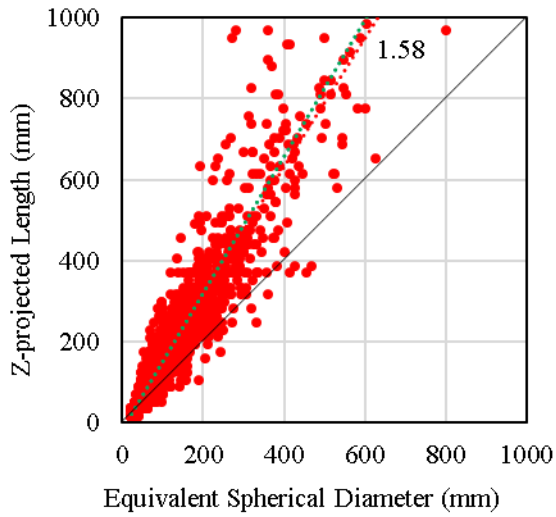

Fig.3 The relationship between the equivalent void diameter and the printed diameter in z axial (A1.0)

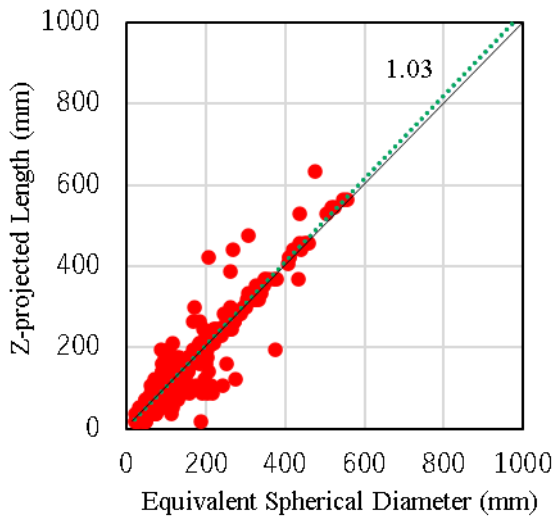

Fig.4 The relationship between the equivalent void diameter and the printed diameter in z axial (Cast A)

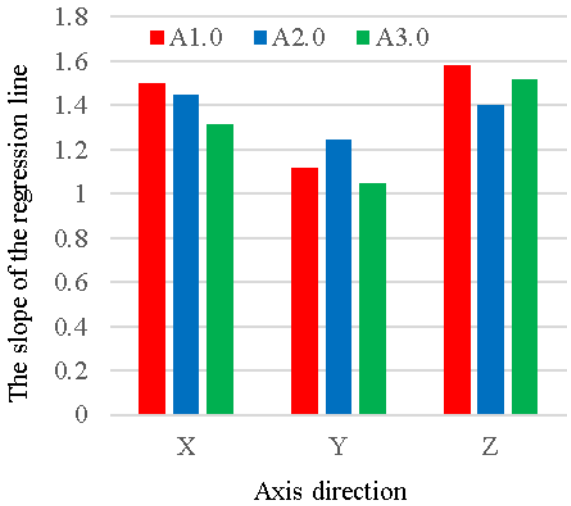

Fig.5 Slopes of the regression lines for the interval voids in each axial direction (Mix A)

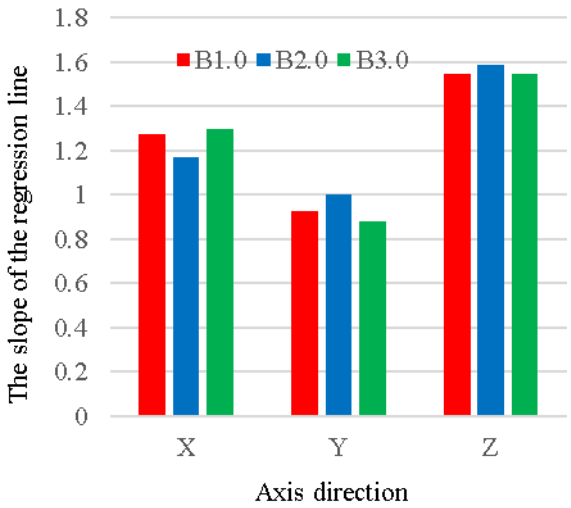

Fig.6 Slopes of the regression lines for the interval voids in each axial direction (Mix B)

indicates greater elongation of the internal voids along the corresponding axis.

Figures. 5 and 6 summarize the slope of the regression lines for each axial direction. For both Mix A and Mix B, the slopes were the largest in the z-direction and the smallest in the y-direction. This indicates that the internal voids were preferentially elongated in the z-direction, corresponding to the nozzle travel direction, while their deformation was smaller in the y-direction, which is perpendicular to the nozzle travel direction and corresponds to the material extrusion direction. These results indicate that the extrusion and deposition processes deformed the internal voids anisotropically, with greater elongation occurring along the nozzle travel direction.

In Mix A, the slopes in the x- and z- directions decreased slightly with increasing v/E, whereas no clear change was observed in Mix B. As v/E increased, the amount of material deposited per unit length decreased, which reduced the deformation imposed on the filament during deposition. Consequently, the elongation of the internal voids decreased in Mix A. However, the change in slope with v/E was relatively small compared with the difference among the axial directions, indicating that the influence of v/E on void deformation was limited within the range of printing conditions investigated in this study.

The differences in the regression slopes between Mix A and Mix B were relatively small, indicating that the influence of mixture composition on the deformation of internal voids was less pronounced than that of the printing direction.

3.3 The freeze-thaw test using liquid nitrogen

Figures 7 and 8 show the changes in the relative dynamic modulus of elasticity during the freeze-thaw test for Mix A and Mix B, respectively. Each data point represents the mean value obtained from the specimens, and the error bars represent the standard deviation. In both mixtures, the cast specimens maintained higher relative dynamic moduli than the corresponding 3D-printed specimens throughout the test. In contrast, the relative dynamic modulus of the 3D-printed specimens decreased continuously with increasing numbers of freeze-thaw cycles. These results indicate that the 3D-printed specimens exhibited lower freeze-thaw resistance than the corresponding cast specimens. No clear influence of the printing parameter v/E on the freeze-thaw resistance was observed for either mixture.

A comparison between the two mixtures revealed that Mix B exhibited a more pronounced reduction in the relative dynamic modulus than Mix A. After ten freeze-thaw cycles, the relative dynamic modulus of the 3D-printed specimens in Mix A remained approximately 40-50%, whereas that of Mix B decreased to approximately 10-20%, indicating substantially lower freeze-thaw resistance for Mix B. In addition, the scatter of the measured values increased with increasing numbers of freeze-thaw cycles, particularly for the 3D-printed specimens. The error bars of the cast specimens remained relatively small throughout the test, whereas those of the 3D-printed specimens became larger after several cycles, especially for Mix B.

The lower freeze-thaw resistance of the 3D-printed specimens is related to their internal void structure. The X-ray CT analysis showed that the 3D-printed

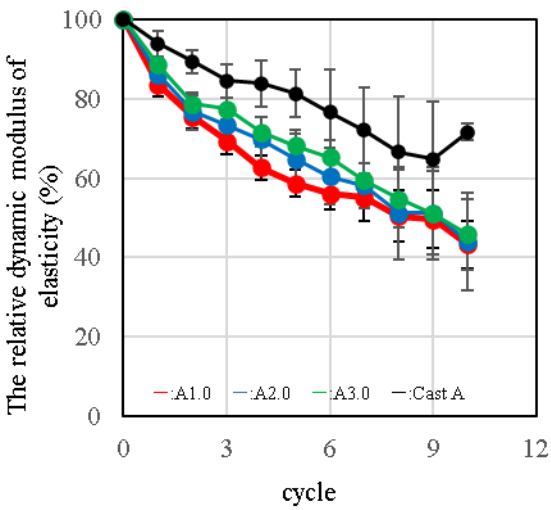

Fig.7 Changes in the relative dynamic modulus of elasticity during freeze-thaw cycles (Mix A)

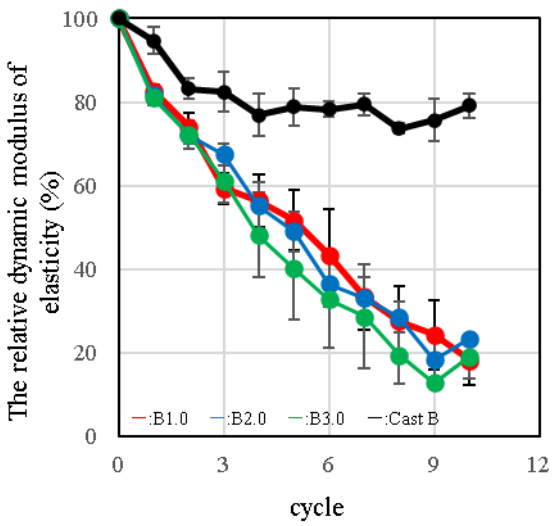

Fig.8 Changes in the relative dynamic modulus of elasticity during freeze-thaw cycles (Mix B)

specimens had higher porosity and more anisotropic void deformation than the cast specimens. In addition, Mix B exhibited higher porosity and a larger spacing factor than Mix A. These differences in the internal void structure are consistent with the greater reduction in the relative dynamic modulus observed for Mix B. The larger scatter observed for the 3D-printed specimens, particularly for Mix B, indicates that the progression of frost damage varied among the specimens. This variation may be associated with differences in the internal void structure among the specimens.

4.Conclusions

The study evaluates the effects of printing parameters on the internal void structure and freeze-thaw resistance of 3D-printed mortar. The main conclusions are as follows.

1. The 3D-printed specimens exhibit higher porosity and smaller spacing factors than the corresponding cast specimens. In addition, the internal voids are anisotropically deformed, with greater elongation in the nozzle travel direction. These results indicate that the extrusion and deposition processes affect not only the amount of voids but also their shape and spatial characteristics.
2. Increasing v/E slightly reduces the deformation of internal voids in Mix A, whereas no clear influence is observed in Mix B. The influence of v/E on freeze–thaw resistance is also not clearly observed within the investigated range. Therefore, the printing direction has a more pronounced influence on void deformation than v/E under the conditions investigated in this study.
3. The 3D-printed specimens exhibit a greater reduction in the relative dynamic modulus of elasticity during the freeze–thaw test than the corresponding cast specimens, indicating lower freeze–thaw resistance. In addition, Mix B shows a greater reduction in the relative dynamic modulus than Mix A. The larger scatter observed for the 3D-printed specimens, particularly for Mix B, also indicates greater variation in freeze–thaw damage among the specimens.
4. The X-ray CT results show differences in porosity, spacing factor, and void deformation between the specimen types and mixtures, and these differences correspond to the differences in freeze–thaw resistance. These results indicate that the internal void structure is an important factor in the freeze–thaw resistance of 3D-printed mortar.

Acknowledgements
This work is supported by the Japan Cement Association (JCA) under the 39th Research Grant.

Reference

[1] Sun, X., Mazur, M., Cheng, C. T.: A review of void reduction strategies in material extrusion-based additive manufacturing, Additive Manufacturing, Vol. 67, 103463, Apr.2023.
[2] Nakase, K., et al.: Influence of print paths on mechanical properties and fracture propagation of 3D printed concrete, Construction and Building Materials, Vol.438, 137019, Jun.2024.
[3] Jacques, K., Anton, P., Gideon, Z.: An investigation into the porosity of extrusion-based 3D printed concrete, Additive Manufacturing, Vol. 37, 101740, Jan.2021.
[4] Nakase, K., Yamada K., Hashimoto, K. Sugiyama, T., Hama, Y.: Influence of printing parameters on geometric and topological evolution of intra-filament voids in 3D printed concrete, Additive Manufacturing, Vol. 127, 105274, Jul.2026.
[5] Sakata, N., Sugamata, T., Hayashi, D., and Hashimoto, M.: Investigation for Relationship between Frost Damage Resistance and Air-Void System in Concrete, *Journal of Advanced Concrete Technology* (or *Concrete Research and Technology*, depending on your journal's prescribed English journal name), Vol. 23, No. 1, pp. 35–47, 2012.
[6] Hama, Y., Aba, M., and Atarashi, D.: Mechanism of Frost Damage of Concrete and Techniques for Controlling of Air Voids System, *Concrete Journal*, Vol. 56, No. 5, pp. 431–435, 2018
[7] Hashimoto, S., Hashimoto, C., Watanabe, K., and Ueda, T.: Proposal of a Simplified Freeze–Thaw Test for Concrete Using Liquid Nitrogen, Proceedings of the Japan Concrete Institute, Vol. 27, No. 1, pp. 757–762, 2005.
[8] Takada, R., Guo, S., Ogata, H., and Hattori, K.: Evaluation of the Freeze–Thaw Resistance of Concrete by the Ultrasonic Pulse Method, Proceedings of the Japan Concrete Institute, Vol. 26, No. 1, pp. 1911–1916, 2004.
[9] Sugiyama, T., Shimura, K., and Hatakeda, D.: Investigation of Pore Structures in AE Mortar Using High-Resolution-Type X-ray CT, Journal of JSCE, Ser. E2 (Materials and Concrete Structures), Vol. 67, No. 3, pp. 351–360, 2011.

Study on affect of fly ash and slag on bond strength of geopolymer concrete

Nguyen Thien Thanh ※1、 Tran Cao Thanh Ngoc ※3、 Le Anh Tuan ※2

ABSTRACT

The affecting of geopolymer concrete bond strength with steel bar are such as activated strength, aggregate type, bar size, and bar surface characteristics. In this research, bond characteristics of steel bars in geopolymer concrete are investigated by bond strength and slip. The diameter of bar in range from 10 to 32 mm are experiment, respectively. The strength of geopolymer concrete are investigated in range from 20 to 40 Mpa. The results are indicated that the relationship between bond stress and deformation is relatively similar for ordinary concrete and geopolymer concrete. It is seen that bond strength is tend to increase with an increase in strength grade. Hence, the bond stress of geopolymer concrete remains relatively uniform and stable as the steel bar diameter varies

1. Introduction

Fly ash-based GPC is an innovative and environmentally friendly alternative to traditional Portland cement concrete. Its popularity has grown due to its superior durability and sustainability [1, 2]. Geopolymer concrete is made using industrial by-products such as fly ash, Ground Granulated Blast Furnace Slag (GGBS), rice husk ash, red mud, and metakaolin [3], which are activated by alkaline solutions, like sodium hydroxide (NaOH) and sodium silicate (Na_2SiO_3). One key property of geopolymer concrete reinforced steel bar is its bond strength, the adhesion between reinforcing steel bars and the surrounding concrete matrix, which is crucial for the structural integrity of the reinforced concrete. In corrosive environments, such as marine areas or places exposed to deicing salts, steel reinforcement in conventional concrete can corrode, weakening the bond strength and compromising the structural performance

In this research, the relationship between geopolymer concrete strength and bond stress is investigated by various activated strength and steel bar.

2. Materials and Testing methodology

This study chose geopolymer binders, such as fly ash, Na_2SiO_3, and Na_2O. The fly ash "Class F" was used with a 2.5 g/cm3 density. The chemical compositions of fly ash are shown in Table 1. (SF; Taiwang International, KR). These materials are either inorganic natural minerals or IRR derived from other industries and produced through additional processing. The physical properties and chemical compositions, identified using X-ray fluorescence (XRF; ZSX PrimusII, Rigaku) and particle size analysis (PSA; Mastersizer 3000, Malvern), are represented in Table 1. The activating solution mixture used to induce bonding in the composite material consists of sodium silicate (Na_2SiO_3) and sodium hydroxide (NaOH) solutions. It also serves as the moistening agent for the

Table 1 Chemical composition of fly ash

Oxide	SiO_2	Al_2O_3	Fe_2O_3	CaO	Na_2O	MgO	SO_3	Log
%	53.9	34.5	4.0	1.0	0.3	0.81	0.25	9.63

※1 Ph.D., Faculty of Civil Engineering, Ho Chi Minh City University of Technology (HCMUT), Vietnam National University Ho Chi Minh City, Vietnam
※2 Assco. Prof., Faculty of Civil Engineering, Ho Chi Minh City University of Technology (HCMUT), Vietnam National University Ho Chi Minh City, Vietnam
※3 Assco. Prof., School of Civil Engineering and Management, International University, Vietnam National University Ho Chi Minh City, Vietnam

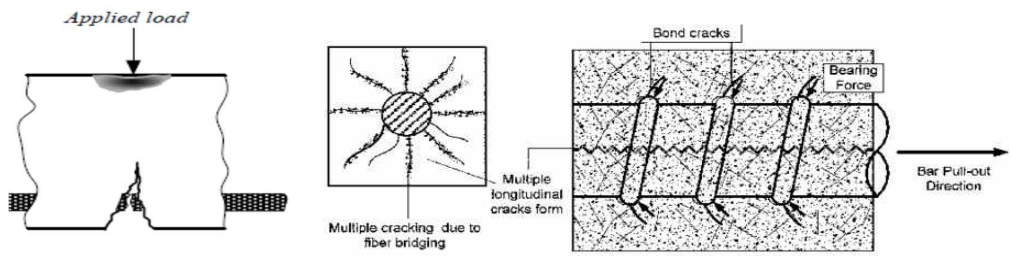

Figure 1 Load-bearing mechanism of reinforced concrete flexural members [4]

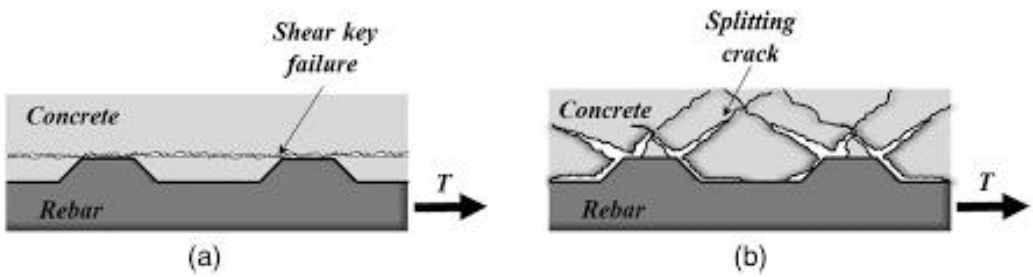

Figure 2 Model for determining bond stress and shear deformation values [5]

molding and compaction process. The sodium silicate used in this study had a composition of 30.1% SiO_2, 9.4% Na_2O, and 60.5% H_2O. It featured an SiO_2/Na_2O ratio of 3.2 and a density of 1.42 ± 0.01 g/mL; the solution was opaque white. The sodium hydroxide solution was prepared from solid sodium hydroxide (opaque white, >90% purity, density 2,130 kg/m³), with a molar concentration of 10 M used for the experiment.

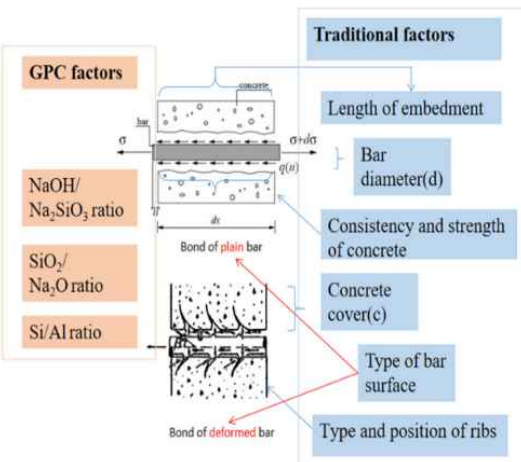

Figure 3 Factors affecting the bond between geopolymer concrete and reinforcing steel [6]

The steel bar used has a yield strength of 230 N/mm², an ultimate tensile strength of 440 N/mm², and an elongation of 32%. Pull-out tests were conducted on reinforcing bars with diameters of 10, 12, 14, 16, 18, 20, 22, 25, and 32 mm, respectively. On the other hand, geopolymer concrete (GC) based fly ash were investigated with design strength various from 20 Mpa, 30 Mpa, 35 Mpa, and 40 Mpa, respectively, in accordance with ASTM C39. Fresh GC was cast and compacted into two types of cylindrical molds: 100 mm × 200 mm for the compressive strength test and 150 mm × 300 mm for the pullout test.

This study conducted an experimental program to evaluate the bond behavior of reinforced GC under accelerated corrosion conditions, focusing on both the compressive strength and pullout performance. For the compressive strength test, three specimens 100 mm × 200 mm were prepared from each mixture group. The test was performed on 150 mm × 300 mm cylinders using axial loading at a rate between 0.15 MPa/s and 0.35 MPa/s until failure. The direct pullout test setup and specimen preparation followed the methodology as illustrated in Figure 5. The bond stress is calculated by assuming that it is uniformly distributed along the embed length of the bar:

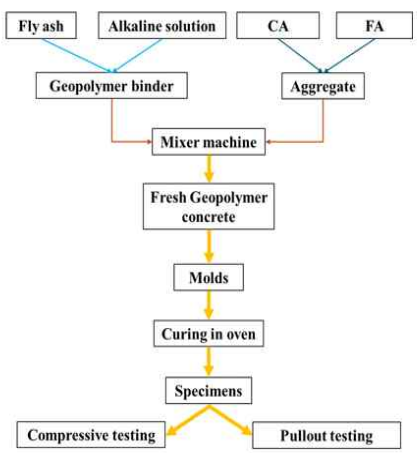

Figure 4 Experimental process on testing

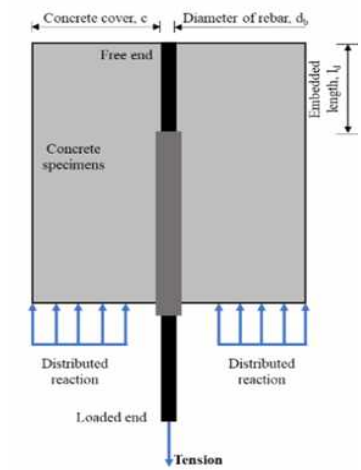

Figure 5 Experimental process on testing

$$\tau_{m\ ax} = \frac{P_{m\ ax}}{\pi d_b l_d}$$

where $\tau_{m\ ax}$ is the maximum bond stress, $P_{m\ ax}$ is the corresponding applied force at failure, d_b is the bar diameter, and l_d is the bar embedded length; in the current work l_d=5d_b

3. Results and Discussion

Geopolymer concrete exhibits excellent bonding performance with reinforcement due to its dense microstructure and strong adhesion. Tests were conducted on geopolymer concrete with compressive strengths ranging from 20 to 40 MPa to evaluate the bond strength between the concrete matrix and the reinforcement. The bond strength of geopolymer concrete is influenced by factors such as the condition of the steel bars, the alkaline solution, the GPC mixture composition, and the curing conditions and temperature.

The relationship between bond stress and deformation in geopolymer concrete is relatively similar to that of conventional concrete. The bond-slip curves for the different mix designs exhibit similar shapes. As seen in Figure 6, the ascending branch exhibits a steeper slope, while the descending branch is shallower compared to that of ordinary concrete. This observation highlights the strong bonding characteristics of the geopolymer binder and the dense interfacial transition zone (ITZ), resulting in higher initial bond stiffness that significantly enhances crack-restraining capacity in reinforced structures

As seen in Figure 7 and Figure 8, the experimental results indicate that the bond stress of both geopolymer concrete and conventional concrete is directly proportional to the concrete strength; higher strength grades yield higher bond stress values. However, it is evident that the results for conventional concrete samples exhibit greater stability than those for geopolymer concrete samples when the steel bar diameter is varied. Experimental results demonstrate the relationships between key variables affecting the bond strength of geopolymer concrete—such as concrete strength, aggregate type, bar size, and bar surface characteristics. Furthermore, it is shown that the strong bond between geopolymer concrete and steel bars prevents debonding to a greater extent than in conventional concrete

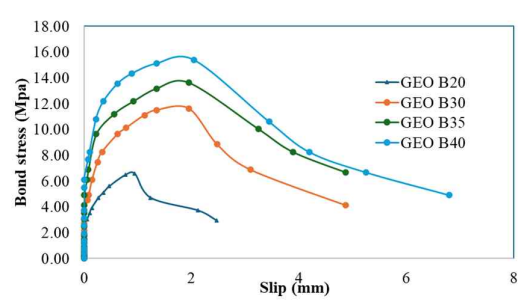

Figure 6 Bond stress-slip relationship of geopolymer concrete

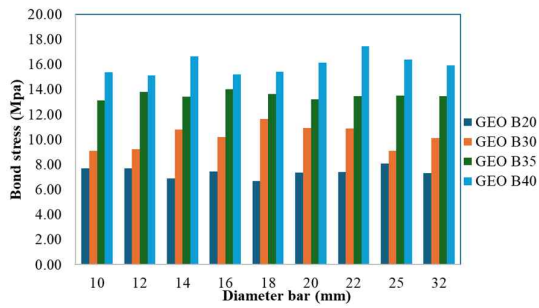

Figure 7 Bond stress relationship with geopolymer concrete

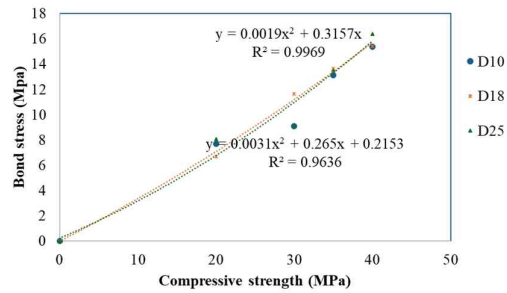

Figure 8 Concrete strength-bond stress relationship curve in geopolymer concrete

4. Conclusion

This study evaluates the interaction between reinforcement and the geopolymer matrix by demonstrating the correlation between bond stress and reinforcement bar diameter across various strength grades. The results indicate that:

(1) The relationship between bond stress and deformation is relatively similar for ordinary concrete and geopolymer concrete specimens.

(2) The bond stress of geopolymer concrete is 15–30% higher than that of conventional concrete of the same grade (compared at the same level of deformation).

(3) The bond stress of geopolymer concrete remains relatively uniform and stable as the steel bar diameter varies. On the other hand, the bond stress of geopolymer concrete is 10–50% higher than that of conventional concrete.

Reference

[1] P. S. Deb, P. Nath, and P. K. Sarker, "The effects of ground granulated blast-furnace slag blending with fly ash and activator content on the workability and strength properties of geopolymer concrete cured at ambient temperature," Materials & Design (1980-2015), vol. 62, pp. 32 39, Oct. (2014).

[2] A. A. Amiruddin, M. Tumpu, P. R. Rangan, R. Irmawaty, B. Bakri, and Mansyur, "A Potential Pozzolanic Material consisting of Rice Straw Ash and Fly Ash for Geopolymer Mortar Production-based Cementitious System," Engineering, Technology & Applied Science Research, vol. 14, no. 6, pp. 18189–18198, Dec. 2024.

[3] J. Davidovits, Chemistry and Applications 3rd edition. Institute Geopolymere, (2011).

[4] Shih-Ho Chao, Antoine E. Naaman, and Gustavo J. Parra-Montesinos. “Bond Behavior of Reinforcing Bars in Tensile Strain-Hardening Fiber-Reinforced Cement Composites”, ACI, Vol. 106, No. 6, pp. 897-906, (2009). DOI: 10.14359/51663191.

[5] Min-Jun Kim, Hyeong-Gook Kim, Jae-Man Lee, Yong-Jun Lee, and Kil-Hee Kim, A Prediction Model for Bond Deterioration in RC Members. I: Bond Stress-Slip Behavior for Splitting Failure; Journal of Structural Engineering, Vol. 144, Issue 3, (2018).

[6] Cui, Y., Ai, W., Tekle, B.H. et al. State of the art review on the production and bond behaviour of reinforced geopolymer concrete. Low-carbon Mater. Green Constr. 1, 25 (2023).

Mechanical Strengths of High-Strength Concrete with Fly Ash Aggregate under Various Moisture States

Phuong Trinh, Bui※1, Dinh Khoi, Doan※1, Anh Tuan, Le※1

ABSTRACT

The mechanical properties of high-strength concrete (HSC) containing artificial fly ash aggregate (FAA) under various moisture states, in comparison with those of concrete using crushed stone (CS), were investigated to evaluate the applicability of FAA as a partial CS replacement. Three moisture states of FAA were considered: saturated surface-dry (SSD), air-dried (AD), and oven-dried (OD). Experimental results showed that the FAA replacement reduced the slump of fresh concrete, regardless of the aggregate's moisture states. This replacement also decreased the mechanical strengths of the hardened concrete across all moisture states and curing ages, due to the inferior properties of FAA compared to CS. The moisture state of FAA remarkably affected the slump of fresh concrete, owing to the high water absorption of FAA under OD or AD conditions. In addition, the moisture state of FAA had significant effects on the mechanical strengths of hardened concrete, which is attributed to the complicated water absorption and desorption processes of FAA acting as an internal curing agent. Consequently, using FAA as a partial CS replacement by up to 20% by volume is feasible for producing HSC with 28-day compressive and flexural strengths exceeding 60 MPa and 6 MPa, respectively, irrespective of the FAA moisture state.

1. Introduction

High-strength concrete (HSC) is one of the materials widely used in various construction projects due to its superior performance compared to that of traditional normal-strength concrete (NSC), such as higher strength and better durability [1]. The gradually increasing demand for concrete in general, and HSC in particular, has led to the over-exploitation of natural resources for aggregates, which adversely impacts the environment and human life. Therefore, sustainable alternatives to natural aggregates for producing concrete have gained widespread popularity in recent decades to conserve natural resources, protect the environment, and ensure human well-being, moving towards the sustainable development goals of the construction industry.

Waste materials have been proposed as potential candidates for replacing primary raw materials, such as Portland cement (PC) and natural aggregates, in concrete production. Among these waste materials, fly ash (FA), a by-product generated from the operation of coal-fired power stations, is the most widely used as a PC replacement to improve the workability of fresh concrete, reduce the PC hydration heat, and enhance the long-term properties of hardened concrete, owing to its pozzolanic reaction [2]. However, FA is often used to replace PC by up to 30% to ensure the desired properties of concrete [3]. In recent years, FA has been employed as a main component to produce artificial aggregates as substitutions for natural aggregates in concrete production through several advanced technologies, such as sintering, cold-bonding, CO_2 curing, and the alkali-activation approach [4-11]. Cold-bonding techniques are commonly used to fabricate FA aggregate (FAA) because of their simplicity, economic benefits, and environmental friendliness [5]. Almost all previous studies regarding the engineering

※1Faculty of Civil Engineering, Ho Chi Minh City University of Technology (HCMUT), VNU-HCM

Table 1 Chemical compostions of PC (% by mass)

CaO	SiO_2	Al_2O_3	Fe_2O_3	K_2O	MgO	Na_2O	SO_3	Loss on ignition
64.50	22.46	4.16	1.98	0.85	1.38	2.30	2.51	2.30

properties of several FAAs, and the effects of FAAs on the performance of fresh and hardened concrete, have concluded that FAA is a potential alternative to natural aggregates for manufacturing concrete. Nevertheless, FAA still has inferior properties compared to natural aggregates, especially a high water absorption rate, which remarkably affects the concrete properties. To date, the effectiveness of using FAA under various moisture states on the performance of HSC has not yet been fully evaluated.

Therefore, this paper focuses on investigating the mechanical properties of HSC with FAA under various moisture states in comparison with those of concrete using CS, to evaluate the applicability of FAA under various moisture states as a partial CS replacement in producing such concrete.

2. Experiment

2.1 Materials

Portland cement (PC) supplied by the Vicem Ha Tien Company was used as the binder for producing the concrete. This cement had a density of 3.1 g/cm³, a Blaine surface area of 3590 cm²/g, and a 28-day compressive strength of 50.1 MPa, thereby meeting the specifications stipulated by TCVN 2682:2020 [12]. Table 1 shows the chemical compositions of PC used in this study.

Meanwhile, natural river sand (RS) used as the fine aggregate had particle sizes ranging from 0.14 mm to 5 mm, a density of 2.65 g/cm³, a bulk density of 1420 kg/m³, and a fineness modulus of 2.43, meeting the specifications stipulated by TCVN 7570:2006 [13]. Natural crushed stone (CS) and artificial cold-bonded FAA, as seen in Figures 1 (a) and (b), respectively, were used as the coarse aggregates. They had particle sizes ranging from 5 mm to 20 mm and their engineering properties under various moisture states–including saturated surface dry (SSD), air dried (AD), and oven-dried (OD) states–are listed in Table 2. When compared with CS, FAA had a lower density and bulk density, but a higher crushing value, regardless of the aggregate's moisture states, demonstrating that FAA had inferior properties to CS. Table 2 also shows that FAA-SSD had the highest density, bulk density, and crushing value, while FAA-OD had the lowest density, bulk density, and crushing value, thereby confirming that the moisture state had significant effects on the engineering properties of FAA.

(a) natural CS

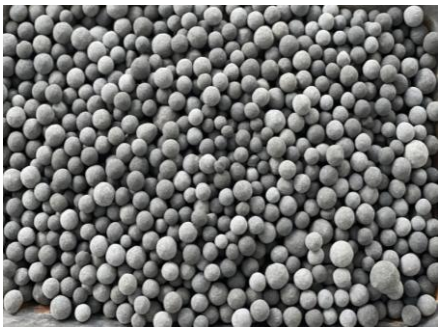

(b) artificial FAA

Figure 1 Coarse aggregates

Figure 2 shows the particle size distribution curves of RS, CS, FAA, and the blend of CS and FAA in comparison with the limits specified in TCVN 7570:2006 [13], indicating that FAA had coarser particles than CS. However, FAA, CS, and the blend all had particle sizes ranging from 5 mm to 20 mm, which fell within the allowable ranges stipulated by TCVN 7570:2006 [13]. Additionally, tap water (W)

Table 2 Engineering properties of coarse aggregates

Items	Particle size (mm)	Density (g/cm^3)	Bulk density (kg/m^3)	Crushing value (%)
CS-OD	5–20	2.71	1515	2.46
FAA-SSD	5–20	2.05	1130	23.18
FAA-AD	5–20	1.88	1060	22.15
FAA-OD	5–20	1.86	1020	21.44

and a water-reducing agent (WRA), meeting the specifications stipulated by TCVN 4506:2012 [14] and ASTM C494/C494M-24 [15], respectively, were employed to produce the fresh control concrete without FAA which had a targeted slump of 180–220 mm.

2.2 Mixture proportions

Based on TCVN 10306:2014 [16] and several trial mixes in the laboratory, the mixture proportion of the control concrete without FAA and containing 100% CS under the OD state (CC), as shown in Table 3, was determined to achieve a targeted 28-day compressive strength of at least 60 MPa and a slump of 180–220 mm. For the concrete mixture proportions containing FAA, the volumetric replacement ratio of CS with FAA was fixed at 20% of the total coarse aggregate volume. Three concrete mixture proportions incorporating FAA under various moisture states (C20F-SSD, C20F-AD, and C20F-OD) are also listed in Table 3 to evaluate their subsequent effects on mechanical strengths.

2.3 Specimen preparation

Concrete specimen preparation was conducted in the laboratory at a temperature of 27 ± 2 °C and a high humidity of 85±5% which were recorded by a digital thermometer. The mixing procedure of the fresh concrete for each mixture proportion was carried out in six steps as follows: (1) weighing all components as shown in Table 3; (2) pre-mixing W and WRA to produce a uniform liquid; (3) adding PC and RS to

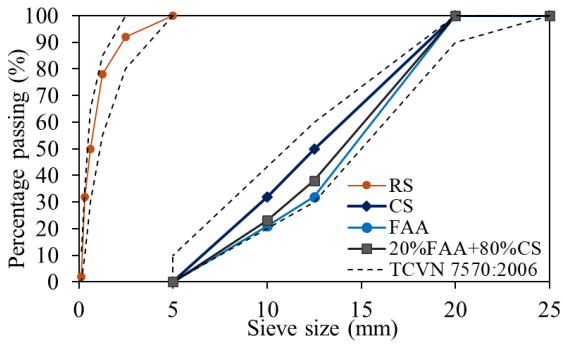

Figure 2 Particle size distribution curves of coarse aggregates

the pre-wetted mixer and mixing for approximately 30 s; (4) adding half of the premixed liquid to the mixer and mixing for approximately 30 s (Figure 3 (a)); (5) adding CS and FAA under the designated moisture state (if any) to the mixer and mixing for approximately 30 s (Figure 3 (b)); and (6) adding the remaining liquid and mixing for approximately 90 s until a homogenous, fresh concrete mix was obtained (Figure 3 (c)).

Subsequently, the slump of the fresh concrete corresponding to each mixture proportion was immediately tested in accordance with TCVN 3106:2022 [17] (Figure 3 (d)). Following the slump test, the concrete specimens were cast into steel molds and covered with polyethylene sheets for 24 ± 4 h to prevent water evaporation and carbonation. After this initial period, the concrete specimens were demolded and then submerged in a water bath at a temperature of 27 ± 2 °C for curing until being tested for mechanical properties at the designated ages.

Table 3 Mixture proportions of all concretes

Items	FAA replacement (%)	WRA (% by mass of cement)	Unit: kg/m³				
			W	PC	RS	CS	FAA
CC	0	0.8	160	420	943	943	0
C20F-SSD	20	0.8	160	420	943	756	143
C20F-AD	20	0.8	160	420	943	756	131
C20F-OD	20	0.8	160	420	943	756	130

2.4 Mechanical Property Test

Similar to the concrete specimen preparation, the mechanical property testing of all hardened concrete was carried out in the laboratory under the same environmental conditions (a temperature of 27 ± 2 °C and a high humidity of 85 ± 5%). The evaluated mechanical properties of the hardened concretes, both with and without FAA under the various moisture states, included the compressive strength at 3, 7, and 28 days using 150 × 150 × 150 mm cubic specimens, and the flexural strength at 7 and 28 days using 150 × 150 × 600 mm prismatic specimens. The compressive strength value for each mixture proportion at a specific curing age was the average obtained from three specimens tested using a compression machine with a loading rate of 0.6 ± 0.2 MPa/s, in accordance with TCVN 3118:2022 [18] (Figure 4 (a)). Meanwhile, the flexural strength was calculated as the average value of two specimens tested in accordance with TCVN 3119:2022 [19] using a bending machine with a loading rate of 0.05 ± 0.01 MPa/s (Figure 4 (b)).

(a) adding liquid (b) mixing

(c) fresh concrete (d) slump test

Figure 3 Mixing and testing procedures of fresh concrete

(a) compression test (b) bending test

Figure 4 Testing properties of hardened concretes

3. Results and Discussion

3.1 Slump of fresh concrete

Figure 5 shows the slump values of the fresh concrete containing FAA under various moisture states in comparison with that of the control concrete without FAA (CC). The slump of the control concrete was 190 mm, meeting the targeted slump range of 180–220 mm. For the concrete mixtures containing FAA, only C20F-SSD achieved a slump value (185

mm) that met the targeted range. In contrast, C20F-AD and C20F-OD exhibited slump values of 165 mm and 120 mm, respectively, neither of which satisfied the target slump. When compared with the control concrete (CC), the slumps of the fresh concrete with FAA under SSD, AD, and OD states were lower by 2.63%, 13.16%, and 36.84%, respectively. Although FAA consisted of round, smooth, and coarse particles (Figure 1 (b)) that could theoretically increase the workability of fresh concrete, the results presented in Figure 5 imply that the FAA replacement reduced the slump of fresh concrete, irrespective of the aggregate's moisture states. A minor reduction in slump was observed in the fresh concrete with FAA under the SSD state (C20F-SSD), indicating that the use of FAA under the SSD state still ensured the targeted slump. Meanwhile, using FAA under AD or OD states remarkably reduced the workability of C20F-AD and C20F-OD, owing to the partial absorption of the mixing water by the FAA under these unsaturated conditions. Additionally, the higher water absorption capacity of FAA under the OD state compared to the AD state resulted in a greater slump reduction in C20F-OD than in C20F-AD. García-González et al. [20] also discovered that with a constant mixing water content, the slump of fresh concrete containing recycled concrete aggregate (RCA) under the OD state was the lowest among all investigated moisture states. In summary, the moisture state of FAA remarkably affected the slump of fresh concrete, suggesting that FAA should be utilized in the SSD state to ensure targeted workability.

3.2 Compressive strength of hardened concrete

Figure 6 describes the compressive strengths at 3, 7, and 28 days of the hardened concrete mixtures containing FAA under various moisture states in comparison with that of the control concrete without FAA. Generally, the compressive strength of all hardened concretes increased with curing age, regardless of the FAA moisture state or replacement. This demonstrates that PC hydration continuously proceeded in all specimens. All hardened concretes had 28-day compressive strengths exceeding 60 MPa,

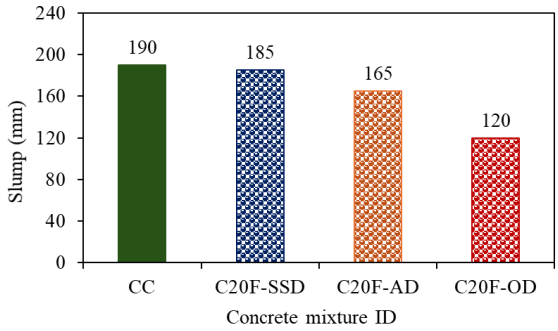

Figure 5 Slump of fresh concrete containing FAA under various moisture states in comparison with that of control concrete without FAA

thereby meeting the designed compressive strength requirements for HSC. When compared with the control concrete (CC), the concrete containing FAA exhibited lower compressive strengths by 8.13–14.02%, irrespective of the FAA moisture state and curing age. This lower compressive strength compared to the control concrete was attributed to the inferior properties of FAA relative to CS, such as a higher crushing value (Table 2) and poorer bonding between the FAA and the matrix caused by the smooth, round texture of the FAA particles (Figure 1 (b)). Among the hardened concretes containing FAA at early ages (i.e., 3 and 7 days), the C20F-OD specimen had the highest compressive strength, followed by C20F-AD, while the C20F-SSD specimen exhibited the lowest strength. This tendency could be explained by the fact that during the mixing process, the unsaturated FAA-OD and FAA-AD partially absorbed mixing water. This led to a reduction in slump for the C20F-OD and C20F-AD mixes (Figure 5), which decreased the amount of free water in the fresh concrete that would otherwise evaporate and form voids in the hardened cement matrix. Furthermore, during the hardening process, this absorbed water was gradually released from the FAA-OD or FAA-AD and participated in the secondary hydration of PC. This generated additional hydration products that refined the microstructure, thereby increasing the early-age compressive strength of the C20F-OD and C20F-AD specimens (Figure 6). Meanwhile, the water existing within the FAA-SSD had not yet participated significantly in additional

hydration at early ages. This would be confirmed by further microstructural analysis. Furthermore, FAA-SSD had a higher crushing value when compared with FAA-AD and FAA-OD (Table 2), partially contributing to the reduced compressive strength of this concrete.

However, at the later age (i.e., 28 days), the C20F-SSD specimen achieved the highest compressive strength, followed by C20F-AD, while the C20F-OD specimen had the lowest strength. The improvement in 28-day compressive strength for the C20F-SSD specimen could be attributed to the prolonged release of internal water from the FAA-SSD, which reacted with unhydrated PC to form further hydration products at 28 days. In other words, the effectiveness of internal curing provided by the FAA under the SSD state surpassed that of FAA under the OD or AD state on the long-term strength of hardened concrete. Through a review of previous studies related to the influence of aggregate's moisture states on performance, Zhang et al. [21] found that the water absorption and desorption processes of RCA under various moisture states are extremely complicated, which can lead to a divergence in compressive strength. These processes for FAA under various moisture states should be further explored in future work to confirm the precise internal curing kinetics of FAA in concrete.

Figure 7 shows the gain in compressive strength at t days (i.e., 3 and 7 days) compared with that at 28 days of all hardened concretes. Generally, the strength gains at 3 and 7 days were in the ranges of 73.45–79.85% and 83.59–88.87% of their 28-day strengths, respectively, regardless of the FAA moisture state or replacement. Among the concrete mixtures incorporating FAA, the C20F-OD specimen exhibited the highest early-age strength ratio (79.85% at 3 days and 88.87% at 7 days), followed by the C20F-AD specimen (75.35% at 3 days and 85.25% at 7 days), while the C20F-SSD specimen had the lowest (73.45% at 3 days and 83.59% at 7 days). These results demonstrate that using FAA under the OD or AD state enhanced the compressive strength at early ages (i.e., 3 and 7 days) more effectively than using FAA under the SSD state. Moreover, utilizing FAA under the OD state enhanced early-age compressive strength development significantly more than the control concrete (CC) (Figure 7), which is attributed to the rapid internal curing effect provided by the FAA-OD.

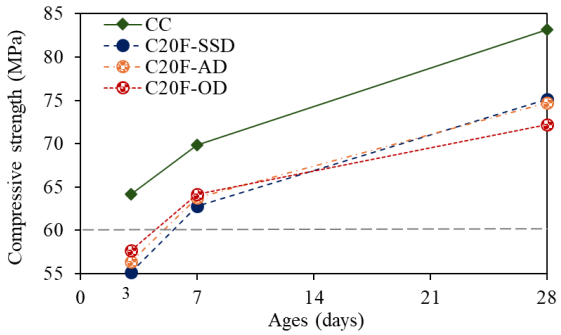

Figure 6 Compressive strength up to 28 days of hardened concrete containing FAA under various moisture states in comparison with that of control concrete without FAA

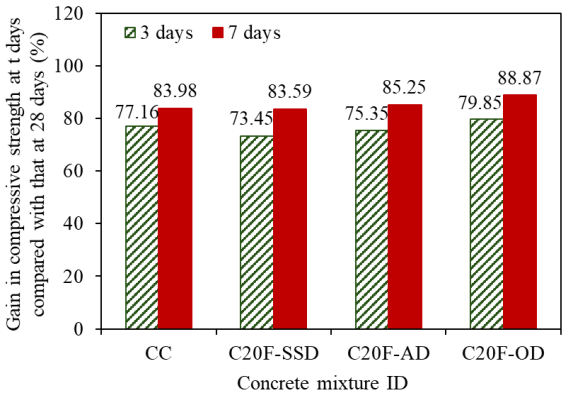

Figure 7 Gain in compressive strength at t days (i.e., 3 and 7 days) compared with that at 28 days of all hardened concretes

3.3 Flexural strength of hardened concrete

Figure 8 depicts the flexural strengths at 7 and 28 days of the hardened concrete containing FAA under various moisture states in comparison with that of the control concrete without FAA. Similar to the compressive strength results seen in Figure 6, the flexural strength of all hardened concrete increased with curing age, regardless of the FAA moisture state or replacement. This trend again confirms that PC hydration continuously proceeded in all specimens. When compared with the control concrete (CC), the concretes containing FAA exhibited lower flexural strengths by 8.91–23.26%, regardless of the FAA moisture state and curing age, owing to the inferior properties of FAA relative to CS. Among the concretes containing FAA, the C20F-SSD specimen exhibited the lowest flexural strength at both 7 and 28 days, which is attributed to the highest crushing value of FAA-SSD compared with those of FAA-AD and FAA-OD (Table 2). This finding aligns with a study by de Oliveira and Vazquez [22], who reported that the flexural strength of concrete containing RCA under the SSD state was remarkably lower than that of concrete containing RCA under other moisture states.

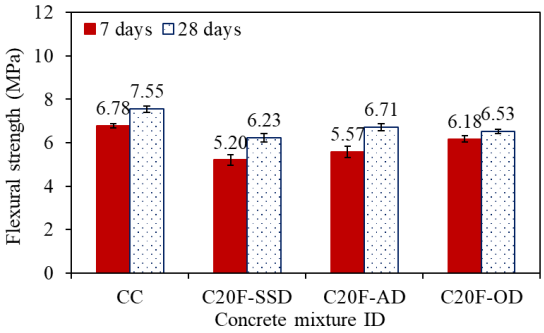

Figure 8 Flexural strength at 7 and 28 days of hardened concrete containing FAA under various moisture states in comparison with that of control concrete without FAA

4. Conclusions

The mechanical properties of HSC containing FAA under various moisture states, in comparison with those of concrete using CS under the OD state, were investigated in this study. Based on the experimental results, the key findings can be summarized as follows:

The FAA replacement reduced the slump of fresh concrete, regardless of the aggregate's moisture state. This replacement also decreased the mechanical strengths of the hardened concrete, irrespective of the FAA moisture state or curing age, resulting from the inferior properties of FAA compared to those of CS.

The moisture state of FAA remarkably affected the slump of fresh concrete, owing to the high water absorption rate of FAA under OD or AD states. Additionally, the moisture state of FAA had significant effects on the mechanical strengths of the hardened concrete, which is attributed to the complicated water absorption and desorption processes of FAA under various moisture states acting as an internal curing agent for the concrete. These mechanisms need to be further explored in future work.

Consequently, using FAA as a partial CS replacement by up to 20% by volume is feasible for producing HSC with 28-day compressive and flexural strengths exceeding 60 MPa and 6 MPa, respectively, irrespective of the FAA moisture state. Utilizing FAA under the SSD state should be prioritized to ensure the targeted workability of fresh concrete and improve the 28-day compressive strength of the hardened concrete.

Acknowledgement

We acknowledge Ho Chi Minh City University of Technology (HCMUT), VNU-HCM for supporting this study.

Reference

[1] S. Sidhu, R. Siddique, Review on effect of curing methods on high strength concrete, Constr. Build. Mater. 438 (2024) 136858.

[2] A.A. Jhatial, I. Nováková, E. Gjerløw, A review on emerging cementitious materials, reactivity evaluation and treatment methods, Build. 13(2) (2023) 526.

[3] M. Amran, R. Fediuk, G. Murali, S. Avudaiappan,

T. Ozbakkaloglu, N. Vatin, M. Karelina, S. Klyuev, A. Gholamour, Fly ash-based eco-efficient concretes: a comprehensive review of the short-term properties, Mater. 14(15) (2021) 4264.

[4] P. Gomathi, A. Sivakumar, Accelerated curing effects on the mechanical performance of cold bonded and sintered fly ash aggregate concrete, Constr. Build. Mater. 77 (2015) 276–287.

[5] F. Colangelo, F. Messina, R. Cioffi, Recycling of MSWI fly ash by means of cementitious double step cold bonding pelletization: technological assessment for the production of lightweight artificial aggregates, J. Hazard. Mater. 299 (2015) 181–191.

[6] M.S. Nadesan, D. Pasala, Materials and methods of sintered flyash lightweight aggregate, Indian J. Sci. Res. 17 (2018) 24–31.

[7] B. Dong, C. Chen, G. Wei, G. Fang, K. Wu, Y. Wang, Fly ash-based artificial aggregates synthesized through alkali-activated cold-bonded pelletization technology, Constr. Build. Mater. 344 (2022) 128268.

[8] A.R. Shrestha, J. Xia, L.D. Sarno, C.S. Chin, Feasibility study of utilizing Autoclaved Aerated Concrete (AAC) waste for the production of cold bonded lightweight artificial aggregate using high volume fly ash (HVFA) binders, Constr. Build. Mater. 449 (2024) 138414.

[9] P. Kumar, D. Pasla, J.S. Thiyagarajan, Synergetic effect of coarse sintered fly ash aggregates and supplementary cementitious materials in self-compacting concrete: From durability and corrosion perspective, J. Buil. Engi. 108 (2025) 112969.

[10] P.T. Bui, T.L. Tran, Q.T. Nguyen, A comprehensive performance assessment of cold-bonded aggregate with various Class-F fly ash and Portland cement amounts, Constr. Build. Mater. 473 (2025) 140936.

[11] Z. Li, Z. Wu, Q. Long, W. Feng, S. Liu, X. Yuan, Preparation of municipal waste incineration fly ash artificial aggregate using CO_2 curing and its properties, J. CO_2 Util. 93 (2025) 103042.

[12] TCVN 2682:2020; Portland Cements. Ministry of Science and Technology, Vietnam, 2020.

[13] TCVN 7570:2006; Aggregates for Concrete and Mortar – Specifications. Ministry of Science and Technology, Vietnam, 2006.

[14] TCVN 4506:2012; Water for Concrete and Mortar – Technical Specification. Ministry of Science and Technology, Vietnam, 2012.

[15] ASTM C494/C494M-24; Standard Specification for Chemical Admixtures for Concrete. American Society for Testing and Materials, West Conshohocken, PA, USA, 2024.

[16] TCVN 10306:2014; High Strength Concrete - Proportional Design with Cylinder Sample. Ministry of Science and Technology, Vietnam, 2014.

[17] TCVN 3106:2022; Fresh Concrete - Test Method for Slump. Ministry of Science and Technology, Vietnam, 2022.

[18] TCVN 3118:2022; Hardened Concrete - Test Method for Compressive Strength. Ministry of Science and Technology, Vietnam, 2022.

[19] TCVN 3119:2022; Hardened Concrete - Test Method for Flexural Tensile Strength. Ministry of Science and Technology, Vietnam, 2022.

[20] J. García-González, D. Rodríguez-Robles, A. Juan-Valdés, J.M. Morán-del Pozo, M.I. Guerra-Romero, Pre-saturation technique of the recycled aggregates: Solution to the water absorption drawback in the recycled concrete manufacture, Mater., 7(9) (2014) 6224–6236.

[21] H. Zhang, X. Xu, W. Liu, B. Zhao, Q. Wang, Influence of the moisture states of aggregate recycled from waste concrete on the performance of the prepared recycled aggregate concrete (RAC) – A review, Constr. Build. Mater. 326 (2022) 126891.

[22] M.B. de Oliveira, E. Vazquez, The influence of retained moisture in aggregates from recycling on the properties of new hardened concrete, Waste Manag. 16 (1-3) (1996) 113–117.

From Site Planning to Material Production: A Decentralized Carbon-Neutral Framework for Post Disaster Housing Reconstruction

Allis Nurdini※1, Lily Tambunan※2, Dewi Larasati※2

Post-disaster reconstruction often generates high carbon emissions due to intensive use of cement, concrete, transportation, and centralized supply chains. This study proposes a decentralized carbon-neutral reconstruction framework integrating site planning, disaster-debris recovery, volcanic ash utilization, and community-based material production. Comparative case studies from the Semeru relocation and Cianjur land-consolidation programs were combined with a material-inventory assessment using a baseline assumption of 15 ton (t) of debris per damaged housing unit. Results indicate that approximately 19,463 t of recoverable material could be generated from the Semeru reconstruction program. Additionally, companion laboratory studies showed that POFA-MSWIBA foam brick achieved 7.78 MPa compressive strength (Standard National of Indonesia Class IA) and reduced embodied carbon by up to 51.5% compared with conventional clay-brick walls. The proposed framework embeds material recovery and local production within early reconstruction planning, reducing dependence on centralized prefabrication systems. Scenario analysis suggests potential carbon-emission reductions of 35-50%, demonstrating that carbon neutrality should be integrated from planning to material production through circular resource use and community-based reconstruction.

1. Introduction

The building and construction sector contributes significantly to global greenhouse-gas emissions, with cement and concrete production representing one of the largest sources of embodied carbon within the built environment [1-3]. Growing attention to carbon neutrality has therefore stimulated research into supplementary cementitious materials (SCMs), recycled aggregates, and low-carbon construction technologies [2-6].

Post-disaster reconstruction presents additional challenges. Large quantities of damaged buildings must be demolished and rebuilt within short time frames. As a result, reconstruction programmed often depend on procurement systems, conventional construction materials, and long-distance transportation networks. Such approaches frequently overlook opportunities to recover and reuse construction debris generated disaster itself [7-10].

Indonesia provides a relevant context for examining this issue. The 2021 Semeru eruption buried some settlements beneath volcanic deposits and required relocation of approximately 1,951 households. Similarly, the 2022 Cianjur earthquake damaged extensive housing stock and initiated large-scale reconstruction programmed through land consolidation and rebuilding mechanism [25, 26].

Although reconstruction programs generally emphasize rapid delivery and safety, carbon-neutrality considerations are rarely integrated into site planning. Furthermore, many reconstruction systems remain dependent upon prefabricated components manufactured externally. While systems such as *Rumah Instan Sederhana Sehat* (RISHA) or Indonesia Health Instant Prefabricated House have demonstrated advantages in rapid and efficient housing provision, they may also reinforce dependence on centralized production systems and external supply chains. Such reliance can limit local resource utilization and reduce opportunities for community.

※1 Associate Professor, Housing and Human Settlement Research Group, School of Architecture Planning and Policy Development, Center for Rural Empowerment, Institut Teknologi Bandung, Indonesia
※2 Associate Professor, Building Technology Research Group, School of Architecture Planning and Policy Development, Center for Rural Empowerment, Institut Teknologi Bandung, Indonesia

Conversely, disasters generate substantial secondary resources in the form of damaged masonry, concrete rubble, steel components, timber, and volcanic materials. Research from Japan, Korea, China, and Southeast Asia suggests that recovered construction materials can be reintroduced into reconstruction processes through circular-construction approaches [11-18].

This study argues that carbon neutrality should begin during post-disaster site planning. Rather than treating debris as waste, reconstruction programs should integrate material inventory mapping, recovery facilities, and community-based production systems within reconstruction layouts. On this basis, the study proposes decentralized carbon-neutral reconstruction framework linking housing planning, resource recovery, and low-carbon housing material production.

The paper addresses three research questions: (i) How can site planning incorporate circular-construction principles in post-disaster reconstruction? (ii) What quantities of reusable materials may potentially be recovered from disaster debris? (iii) To what extent might decentralized material production systems contribute to carbon-emission reduction.

2. Framework Principles and Methods

2.1 Principles

a. Carbon Neutrality and Construction Materials

Recent studies identify clinker substitution, SCM utilization, recycled aggregate concrete, and circular-material management as major pathways for reducing carbon emissions from construction [2,3,5,6]. East Asian countries have demonstrated significant advances in the use of recycled concrete aggregates and alternative cementitious materials [11-16]. However, most carbon-neutrality studies remain focused on material performance rather than spatial planning and reconstruction systems.

Complementary to volcanic ash and recycled debris, Indonesia generates substantial industrial and urban waste streams, including palm oil fuel ash (POFA), municipal solid waste incineration bottom ash (MSWIBA), and underutilized coconut fiber biomass, that remain underexplored in post-disaster reconstruction contexts. Prior research has examined these materials individually as partial cement or aggregate substitutes at laboratory scale [5,13,19]. Companion laboratory research by the authors provides preliminary evidence that integrating such waste streams into community-producible wall systems can substantially lower embodied carbon while valorizing locally available resources beyond disaster debris alone.

b. Circular Construction after Disasters

Following the Great East Japan Earthquake, substantial quantities of construction debris were recycled into infrastructure and reconstruction projects [11,12]. Similar strategies have been explored following earthquake in China throughout recycled concrete aggregate programs [7,8]. Circular-construction approaches provide opportunities to reduce landfill requirements, decrease extraction of virgin materials, reduce transportation demand, and lower embodied carbon.

c. Community-Based Low-Carbon Wall Material Production

Beyond debris recycling, decentralized reconstruction requires wall materials that communities can produce using appropriate technology with minimal industrial infrastructure. Community participation in post-disaster housing has been widely discussed [20-22]; however, technical validation of locally manufacturable low-carbon wall systems remains limited in the literature.

Ongoing laboratory research by the authors addresses this gap through two parallel material tracks: POFA–MSWIBA foam brick and coconut fiber cellular lightweight concrete (CLC). Preliminary highlights indicate that the optimal POFA–MSWIBA mix (20% POFA, 30% MSWIBA, with vibrator compaction) achieved 7.78 MPa compressive strength, meeting SNI 8640:2018 Class IA for structural outdoor application. Without vibrator compaction, strength ranged 1.88–3.48 MPa (non-structural grades), suggesting tiered application whereby communities may produce partition blocks manually and structural blocks with simple vibrator-assisted processing. Coconut fiber CLC formulations met ideal lightweight criteria (dry density below 1680 kg/m³, water

absorption 16–20%) with ductile post-peak behavior, offering a complementary pathway for lightweight wall applications.

Environmental comparison using a Type-36 house wall model indicates that composite foam brick reduced wall embodied carbon by 51.5% compared with conventional clay brick (22.01 versus 45.36 $kgCO_2/m^2$), with approximately 292.5 kg urban waste and 102–151 kg palm solid waste valorized per m^2 of wall. Decentralized production using local waste collection within 5 km further reduces operational emissions beyond intrinsic material savings. A Participatory Action Research (PAR) framework comprising technology transfer, community-based manufacturing, and end-user feedback, has been designed to validate constructability under field conditions, aligning with the community-production hub concept developed in this study.

d. Site Planning and Reconstruction

Site planning remains a central activity in post-disaster recovery. Typical planning task includes hazard assessment, relocation decisions, infrastructure provision, housing allocation, and land management. Nevertheless, debris recovery and carbon-neutral material production are rarely incorporated into site planning processes [20, 21, 22, 24]. This gap suggests the need for an integrated framework linking planning decisions with material flows and carbon performance. Laboratory evidence from companion studies further suggests that site planning should also account for non-debris local waste streams, such as POFA, MSWIBA, and coconut biomass that may be mapped and allocated to community production hubs alongside debris-recovery facilities.

2.2 Methods

This study adopts a comparative case-study approach to examine post-disaster reconstruction processes and their potential for decentralized, carbon-neutral reconstruction. The first case is the Semeru Mount Eruption Recovery, where volcanic deposits buried settlements and required the relocation of approximately 1,951 households [24]. The second case is the Cianjur Reconstruction, where the earthquake recovery program employed land-consolidation mechanisms to maintain settlement continuity while reorganizing infrastructure, housing arrangements, and spatial layouts [26]. The authors were involved in both reconstruction processes, providing practical insights into site planning and implementation.

The study combines reconstruction-process analysis, site-planning review, material-inventory estimation, and scenario-based carbon analysis. The assessment examines how disaster debris and locally available waste materials can be incorporated into reconstruction planning and community-based material production. For material-inventory estimation, a baseline assumption of 15 t of debris per damaged housing unit was adopted, based on typical Indonesian masonry houses with a floor area of approximately 36–45 m^2. This baseline was then used to estimate the potential quantity of recoverable materials and evaluate their implications for decentralized reconstruction and carbon reduction.

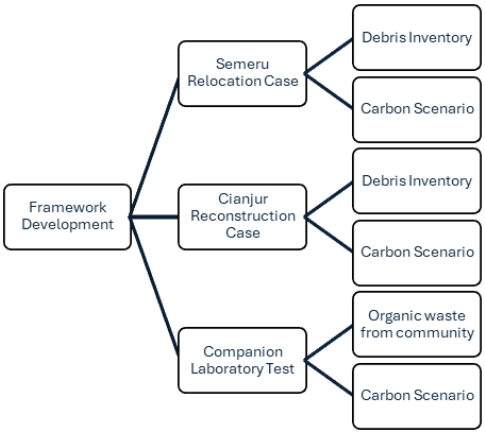

Figure 1 Research Design

3. Results and Discussion

3.1 Estimated Recoverable Construction Materials

A baseline scenario of 15t/unit was selected because typical Indonesian masonry houses generally generate 10-20t of demolition debris depending on wall systems, roof materials, and structural configuration. The results indicate that approximately 66-70% of debris may potentially be recovered and reprocessed into secondary construction materials. Similar recovery rates have been reported in China and post-earthquake reconstruction programmes in Japan [7,11].

Table 1 Post-Disaster Material Recovery Potential

Parameter	Semeru Relocation	Cianjur Pilot Project
Housing units	1,951	53
Debris generation (ton (t)/unit)	15	15
Total debris generated (t)	29,265	795
Recoverable masonry (70%) (t)	12,291	334
Recoverable concrete (80%) (t)	5,854	159
Recoverable steel (90%)	1,318	36
Total recoverable material (t)	19,463	529

3.2 Potential Resource Streams

Volcanic ash generated during the Semeru eruption offers additional opportunities as supplementary cementitious material, complementing conventional debris-recycling strategies [2,5.16,17]. As seen on Table 2 there are several resource possibilities, source and proposed use from concrete debris, masonry rubble, steel elements, volcanic ash, and timber debris.

Table 2 Resource Streams for Circular Reconstruction

Resource Stream	Source	Proposed Use
Concrete debris	Foundation and columns	Recycled aggregate concrete
Masonry rubble	Brick walls	Blocks and paving units
Steel elements	Reinforcement	Secondary reinforcement
Volcanic ash	Semeru deposits	SCM replacement
Timber debris	Roofing structures	Temporary construction

Table 2 demonstrates that post-disaster environments contain a diverse range of materials that can be reintegrated into reconstruction activities through circular-construction strategies. Rather than being treated as waste requiring disposal, concrete debris, masonry rubble, steel components, volcanic ash, and timber remnants may serve as valuable secondary resources for rebuilding efforts. The reuse of these materials can reduce dependence on virgin raw materials, minimize transportation requirements, decrease landfill pressure, and lower the overall environmental footprint of reconstruction projects.

3.3 Validated Low-Carbon Wall Material Options

While Tables 1 and 2 quantify debris-derived and volcanic resources, companion laboratory research confirms the technical feasibility of converting distinct local waste streams into community-producible wall materials. Table 3 summarizes selected performance highlights from ongoing experiments [5,6,14,15,16,17].

Table 3 Selected laboratory highlights for community-producible wall materials

Material System	Key Performance Highlight	Relevance to Framework
POFA-MSWIBA foam brick	7.78 MPa (20% POFA, 30% MSWIBA, vibrator); SNI Class IA	Structural wall at community hubs
POFA-MSWIBA foam brick	1.88-3.48 MPa (manual compaction)	Non-structural partition blocks
Coconut fibre CLC	Density <1680 kg/m3; absorption 16-20%	Lightweight ductile walls
Composite foam brick (BFk)	51.5% embodied carbon reduction vs clay brick (Type-36)	Carbon-sensitive material strategy
Waste valorisation	~292.5 kg MSWIBA + 102-151 kg POFA per m2 wall	Circular recovery settlement scale

These findings demonstrate that community production hubs proposed in the reconstruction framework may deploy technically validated wall systems beyond debris reprocessing alone. Tiered application is feasible: manual compaction for partition blocks, vibrator-assisted processing for structural grades, and coconut fibre CLC for lightweight applications—all requiring equipment within community capacity.

3.4 Decentralized Carbon-Neutral Reconstruction Framework

Current reconstruction systems generally separate planning and material production. The proposed framework embeds material recovery directly into planning processes.

Table 4 Conventional and Proposed Reconstruction Models

Variable	Conventional System	Proposed Framework
Material source	External suppliers	Local recovery + external support
Aggregate source	Virgin aggregate	Recycled aggregate
SCM Utilization	Limited	Volcanic ash and organic waste substitution
Production system	Centralized	Community-based
Transportation distance	Long	Short
Community role	Recipient	Producer and builder
Waste management	Disposal	Circular recovery

Table 5 Integration Between Site Planning and Material Production

Planning Stage	Conventional Outcome	Carbon-Neutral Outcome
Damage assessment	Building survey	Building + material inventory
Site planning	Housing layout	Housing + recovery
Infrastructure planning	Roads/utilities	Roads + logistic routes
Construction planning	External procurement	Local production network
Community engagement	Consultation	Co-production

The community-production hubs envisioned in this framework may deploy validated low-carbon wall systems identified through companion laboratory research. POFA–MSWIBA foam brick offers structural-grade performance (7.78 MPa, Standard National of Indonesia Class IA) where vibrator compaction is available, while coconut fibre CLC provides lightweight ductile alternatives; both align with the community-based production model in Table 4 and Table 5 and require only appropriate technology, manual moulds, portable foam generator, cement mixer, and optionally a vibrator, consistent with decentralized reconstruction principles.

3.5. Estimated Carbon Reduction Potential

Table 6 Carbon Reduction Scenario

Intervention	Assumption	Reduction (%)
SCM substitution	20% cement replacement	15-20
Recycled aggregate use	30% replacement	10-15
Localized production	Reduced transport distance	5-10
Landfill avoidance	70% debris recovery	5-8
Combined reduction	Integrated framework	35-50

The proposed framework combines four complementary intervention mechanisms that address different stages of the post-disaster reconstruction process, from site planning and material recovery to local production and resource utilization. By integrating these mechanisms, the framework aims to reduce carbon emissions not only through low-carbon material innovation but also through changes in planning, logistics, and reconstruction organization. The scenario analysis indicates that substantial carbon-emission reductions can be achieved when

material recovery, decentralized production, and shortened supply chains are systematically incorporated into reconstruction planning. The combined effect of supplementary cementitious material substitution recycled aggregate utilization, localized manufacturing, and landfill avoidance has the potential to reduce reconstruction-related emissions by approximately 35-50%. These findings suggest that carbon neutrality in post-disaster reconstruction should be approached as a system-wide planning objective rather than solely as a material-technology challenge. Consequently, planners, architects, engineers, and local communities need to work collaboratively to integrate resource recovery, low-carbon material strategies, and spatial planning decisions from the earliest stages of reconstruction, ensuring that environmental sustainability and community resilience are advanced simultaneously.

Table 7 Estimated Carbon Savings for Semeru Reconstruction

Indicator	Conventional	Proposed
Housing units	1,951	1,951
Carbon intensity (tCO_2e/unit)	6.0	3.0-3.9
Total emissions (tCO_2e)	11,706	5,853-7,609
Potential savings (tCO_2e)	-	4,097-5,853
Reduction (%)	-	35-50

The values shown in Table 7 represent scenario-based estimates and should not be interpreted as measured life-cycle assessment results [2,3,4]. Companion laboratory results further indicate that composite foam brick alone achieves 51.5% embodied carbon reduction at the wall-material scale, suggesting that settlement-scale carbon savings in Table 6 and Table 7 may be reinforced when community hubs produce validated low-carbon wall systems alongside debris-recovery operations.

The findings indicate that carbon neutrality should not be understood solely as a material-science challenge. Decisions made during site planning directly influence material flows, transportation requirements, resource recovery, and waste generation [2,3]. The proposed framework expands the scope of carbon-neutrality analysis from the material scale to the settlement scale. Rather than relying exclusively on externally produced construction systems, communities may participate in processing secondary resources generated by the disaster itself, thereby strengthening local adaptive capacity and community resilience through collective action and resource recovery processes [8,20,21,27].

Companion laboratory research reinforces this settlement-scale perspective by demonstrating that communities need not depend exclusively on debris reprocessing. Industrial palm ash, urban incineration residue, and agricultural biomass which the resources often available near reconstruction sites, can be converted into wall materials achieving up to 51.5% embodied carbon reduction compared with conventional clay brick walls, provided that processing techniques such as vibrator compaction are incorporated into community training programmes within production hubs [20,21.28].

For planners, architects, and engineers, the implies new responsibilities. Reconstruction planning should incorporate: i) Debris inventory mapping; ii) Recovery-facility allocation; iii) Local logistics systems; iv) Community-production hubs; and v) Carbon-sensitive material strategies. Such integration can simultaneously support environmental sustainability, local economic participation, and reconstruction resilience, particularly when local social networks are mobilized as part of community-based recovery mechanisms [22,28].

4. Conclusion

This study proposed a decentralized carbon-neutral framework integrating site planning and material production within post-disaster reconstruction. The results suggest that:

a. Post-disaster settlements contain substantial recoverable material resources.
b. Approximately 19,463 t of recoverable material may potentially be generated from the Semeru reconstruction program under the baseline scenario.

c. Volcanic ash can provide an additional source of supplementary cementitious materials.
d. Community-based production systems can reduce dependence on centralized reconstruction sully chains.
e. Laboratory-validated POFA–MSWIBA foam brick and coconut fibre CLC demonstrate that community-producible wall materials can achieve structural-grade performance (7.78 MPa, Standard National of Indonesia Class IA) and up to 51.5% embodied carbon reduction compared with conventional clay brick walls.
f. Integrated planning and material-recovery strategies may reduce reconstruction-related carbon emissions by approximately 35-50%.

The study demonstrates that carbon neutrality should be embedded from the earliest stages of post-disaster planning, linking site planning, resource recovery, and construction-material production within a single reconstruction framework.

Acknowledgment

This research was supported by School of Architecture, Planning, and Policy Development, Institut Teknologi Bandung, Indonesia.

References

[1] United Nations Environment Programme (UNEP), 2022 Global Status Report for Buildings and Construction: Towards a Zero-Emission, Efficient and Resilient Buildings and Construction Sector, Nairobi, 2022.

[2] K.L. Scrivener, V. John, E.M. Gartner, Eco-efficient cements: potential, economically viable solutions for a low-CO2 cement-based materials industry, Cement and Concrete Research 114 (2018) 2-26.

[3] G. Habert, M. Miller, S. John, V.M. Provis, A. Favier, A. Horvath, K.L. Scrivener, Environmental impacts and decarbonization strategies in the cement and concrete industries, Nature Reviews Earth & Environment 1 (2020) 559-573.

[4] S. Miller, Supplemental cementitious materials to mitigate greenhouse gas emissions from concrete: Can there be too much of a good thing ? Journal of Cleaner Production 178 (2018) 587-598.

[5] E.A. Aprianti, A huge number of artificial waste materials can be supplementary cementitious material (SCM) for concrete production: A review, Journal of Cleaner Production 142 (2017) 417-494.

[6] E.A. Aprianti, P. Shafigh, S. Bahri, J.N. Farahani, Supplementary cementitious materials originating from agricultural wastes: A review, Construction and Building Materials 74 (2015) 176-187.

[7] J. Xiao, L. Li, F. Pan, X. Huang, An overview of study on recycled aggregate concrete in China, Construction and Building Materials 31 (2012) 364-383.

[8] G. Ge, Y. Sarksis, Sustainability, wellbeing, and the circular economy in construction, Resources, Conservation and Recycling 168 (2021).

[9] T.M. Tam, V.W.Y. On, The effectiveness in implementing a waste-management-plan method in construction, Waste Management 28 (2008) 1072-1080.

[10] C.S. Poon, Z.H. Lam, M. Lam, E.T. L. Chan, Optimized recycled aggregate concrete prepared with two-stage mixing approach, Construction and Building Materials 15 (2004) 461-468.

[11] I.Maruyama, M. Sogo, T. Sogabe, et al., Recycling concrete debris after the Great East Japan Earthquake, Journal of Advanced Concrete Technology 15 (2017) 24-42.

[12] T. Noguchi, R. Kitagaki, M. Tsujino, Sustainable use of recycled aggregates in Japan, Journal of Asian Architecture and Building Engineering 13 (2014) 1-8.

[13] J.M. Kim, K.M. Lee, C.K. Park, Carbon reduction strategies for concrete infrastructure in Korea, KSCE Journal of Civil Engineering 25 (2021) 2451-2462.

[14] F.P. Avet, N.I. Snellings, R. Alujas-Diaz, Development of a new rapid, relevant and reliable test method to evaluate pozzolanic reactivity of calcined clays, Cement and Concrete Research 85 (2016) 1-11.

[15] R.Snellings, Assessing, understanding and unlocking supplementary cementitious materials, RILEM Technical Letters 1 (2016) 50-55.

[16] L. Li, Q. Qiao, H. Li, A. Li, Performance of waste glass powder as a pozzolanic material in blended cement mortar, Construction and Building Materials 324 (2022) 126531.

[17] C.R. Wu, B.J. Zhan, Z.Q. Hong, S.C. Cui, P. Cui, S.C. Kou, Hydration behavior of circulating fluidized bed fly ash (CFBFA) as a cementitious binder, Construction and Building Materials 314 (2021) 125625.

[18]. P.K. Mehta, Greening of the concrete industry for sustainable development, Concr. Int. 24(7) (2002) 23-28.

[19] R. Siddique, Utilization of industrial by-products in concrete, Resour. Conserv. Recycl. 55(11) (2011) 923-932.

[20] C.H. Davidson, C. Johnson, G. Lizarralde, N. Dikmen, A. Sliwinski, Truths and myths about community participation in post-disaster housing projects, Habitat Int. 31(1) (2007) 100-115.

[21] A. Opdyke, A. Javernick-Will, M. Koschmann, Household participation in shelter projects: A comparative analysis, Disasters 43(4) (2019) 926-953.

[22] R. Djalante, R. Shaw, A. DeWit, Building resilience to natural hazards in Indonesia, Sustainability 12(2) (2020) 646.

[23] S. Meerow, J.P. Newell, M. Stults, Defining urban resilience: A review, Landsc. Urban Plan. 147 (2016) 38-49.

[24] N. Yuliastuti, R. Haryanto, Land consolidation and community participation in settlement upgrading, IOP Conf. Ser.: Earth Environ. Sci. 447 (2020) 012040.

[25] Rumah Amal Salman, Final Report Recovery Program of Mount Semeru Eruption, 2022.

[26] A. Nurdini, N.F. Hadianto, S. Suryani, Emerging housing choices for community resilience capacity in flood-prone areas of Bandung Regency, Indonesia, J. Housing Built Environ. 36 (2021) 1563-1583.

[27] P. Ghisellini, C. Cialani, S. Ulgiati, A review on circular economy: The expected transition to a balanced interplay of environmental and economic systems, J. Clean. Prod. 114 (2016) 11-32.

[28] Shirleyana, S. Hawken, R.Y. Sunindijo, D. Sanderson, The critical role of community networks in building everyday resilience: Insights from the urban villages of Surabaya, Int. J. Disaster Risk Reduct. 98 (2023) 104090.

Participants

Cheongju National University

Prof. Han Cheongoo

Seoul National University Science and Tech.

Prof. Oh Sangkeun

Hoseo University

Prof. Kwon Youngjin

Kongju National University

Prof. Kim Jinman
Ph.D Shin Sangchul
Ph.D student Kim Geonwoo
Ph.D student An Taeyun
Master' student Park Boyoung
Master' student Kang Namgyu
Undergraduate student Kim Hyeonwoo
Undergraduate student Lee Dongseo
Undergraduate student Yun Junseok

Chungnam National University

Prof. Kim Gyuyong
Prof. Nam Jeongsoo
Ph.D student Lee Jeongtaek
Ph.D student Ji Sungjun
Ph.D student Youn Hyeyoung
Ph.D student Lee Yaechan
Master' student Go Yeonwoo
Master' student Ko Minjeong
Master' student Song Seunghoon
Master' student Kim Yongjun
Master' student Van Minh Triet
Master' student Pebrian Candra Dwi
Master' student Nguyen Thinh Phat

Ho Chi Minh City University of Tech.

Prof. Bui Phuong Trinh

Hanbat National University

Prof. Lee Sangsoo
Prof. Lee Donghoon
Prof. Kim Sungjin
Ph.D student Kim Dogyun
Ph.D student Ryoo Changwoo
Ph.D student Yoo Jaegyun
Ph.D student Jeong Hyunsu
Ph.D student Park Jaehyun
Ph.D student Jeong Kyeongtae
Ph.D student Jeong Hojeong
Master's student Jeong Yeongseok
Master's student Chae Kyoungjun
Master's student Hwang Suhyeon
Master's student Jang Yoonho
Master's student Kim Jihun
Master's student Cho Byoungjoon
Master's student Jung Kwanyong
Master's student Kim Giuk
Master's student Yang Seungjin
Master's student Seo Seungha
Undergraduate student Ji Sumin
Undergraduate student Kyung Hyeyun

Wonkwang University

Prof. Choi Sejin
Prof. Cho Chungyeon
Ph.D Song Hayeon
Ph.D Lee Jaein
Ph.D student Lee Inyoung
Master's student Shin Minji
Master's student Park Jeongyeon
Undergraduate student An Eunbee
Undergraduate student Park Doyeong

Woosuk University

Prof. Kang Sukpyo
Ph.D student Park kyueun
Master's student Mahmudullah Md

Mokwon University

Prof. Park Sungyu
Ph.D student Kim Jusung
Master's student Lee Duhyuk

Kyungpook University

Prof. Choi Hyeonggil
Ph.D student Li Lei

Semyong University

Prof. Lee Taegyu
Ph.D student Kim Wonchang
Ph.D student Im Hajun
Ph.D student Choi Jieun
Ph.D student Nam Youngjin
Ph.D student Jang Younga
Master's student Kim Sigon

Gyeongsang National University

Prof. Han Dongyeop

Korea National University of Transportation

Prof. Lee Guncheol

Seoul National University of Science and Tech.

Prof. Kim Byoungil

Dongeui University

Prof. Lee Jaeyoung

Korea Aggregates Research Institute

Senior Researcher Ra Jeongmin

Korea Cement Association

Managing Director Kim Euichoel

Global waterproofing Sciences Technology Research Center

Researcher Oh Kyuhwan

Hanil Cement

Laboratory Chief Cho Sunghyun
Researcher Kang Ingyu

Korea Institute of Ceramic Engineering and Technology

Chief Researcher Song Hun

Muroran Institute of Technology

Prof. Hama Yukio
Prof. Taniguchi Madoka
Prof. Kim Jihoon
Ph.D student Kojima Kaishi
Master's student Goda Rikuto

Hokkaido University

Prof. Kitagaki Ryoma
Master's student Kumamoto Soshi
Master's student Makino Takaya

Meijo University

Prof. Dosho Yasuhiro
Master's student Inden Ichito
Master's student Okada Yuta
Master's student Onoyama Kohta
Master's student Yamasaki Riko
Master's student Tran Thi Phuc
Master's student Iwano Wako

Tokyo University of Science

Prof. Li Yutong
Prof. Kim Junho
Prof. Kanematsu Manabu
Ph.D student Jeong Juntaek
Master's student Sakon Shuya
Master's student Toyoshima Akihiro
Master's student Hayashi Sotaro

Institute of Science Tokyo

Prof. Koga Junko
Master's student Tsutsumi Asuka
Master's student Morita Ayuka
Master's student Minegishi Yuma
Master's student Ruiqi Pan
Master's student Hamada Sohta

Tokyo City University

Prof. Sato Sachie
Master's student Saito Shintaro
Master's student Tamura Shota
Undergraduate student Tsuji Takumi

Yamaguchi University

Prof. LI Zhuguo
Master's student Ota Niman
Master's student Nishimura Jion

Shibaura Institute of Technology

Prof. Hamasaki Hitoshi
Master's student Iura Yota

Kyushu University

Prof. Koyama Tomoyuki

Nihon University

Prof. Yuasa Noboru

Chiba Institute of Technology

Prof. Ishihara Saori

University of the Ryukyus

Prof. Sakihara Kohei

Tokai University

Prof. Ito Korekiyo

Kyushu Sangyo University

Prof. Seo Wonwoo

SANDOH Construction Co., Ltd.

Researcher Matsumoto Takuya
Senior Managing Director Fukumoto Katsuya

The 17th KOREA - JAPAN JOINT SYMPOSIUM ON BUILDING MATERIALS & CONSTRUCTION

Building a Sustainable Future-Carbon Neutrality
In Cement & Concrete

Organized By

공주대학교 산학협력단 KONGJU INDUSTRY-UNIVERSITY COOPERATION FOUNDATION
ABM Lab. Advanced Building Materials in KNU
室蘭工業大学 MURORAN INSTITUTE OF TECHNOLOGY
충남대학교 사회기반시설기술연구소
WONKWANG UNIVERSITY Sustainable Construction Materials Lab
한국건설순환자원학회 Korean Recycled Construction Resources Institute

Sponsored By

국립공주대학교 KONGJU NATIONAL UNIVERSITY
한국시멘트협회 KOREA CEMENT ASSOCIATION

Participating Institution

국립공주대학교 KONGJU NATIONAL UNIVERSITY
충남대학교 Chungnam National University
호서대학교 HOSEO UNIVERSITY
원광대학교 WONKWANG UNIVERSITY
국립한밭대학교 HANBAT NATIONAL UNIVERSITY
목원대학교 MOKWON UNIVERSITY
우석대학교 WOOSUK UNIVERSITY
서울과학기술대학교 SEOULTECH SEOUL NATIONAL UNIVERSITY OF SCIENCE & TECHNOLOGY
경북대학교 KYUNGPOOK NATIONAL UNIVERSITY
경상국립대학교 GYEONGSANG NATIONAL UNIVERSITY
국립한국교통대학교 KOREA NATIONAL UNIVERSITY OF TRANSPORTATION
세명대학교 SEMYUNG UNIVERSITY
청주대학교 CHEONGJU UNIVERSITY
동의대학교 DONG-EUI UNIVERSITY
室蘭工業大学 MURORAN INSTITUTE OF TECHNOLOGY
北海道大学 HOKKAIDO UNIVERSITY
九州大学 KYUSHU UNIVERSITY
MEIJO UNIVERSITY
東京理科大学 TOKYO UNIVERSITY OF SCIENCE
Institute of SCIENCE TOKYO
日本大学 NIHON UNIVERSITY
千葉工業大学 CHIBA INSTITUTE OF TECHNOLOGY
芝浦工業大學 SHIBAURA INSTITUTE OF TECHNOLOGY
山口大学 YAMAGUCHI UNIVERSITY
琉球大学 UNIVERSITY OF THE RYUKYUS
KSU | 九州産業大学
東海大学
東京都市大学 TOKYO CITY UNIVERSITY
KCL 한국건설생활환경시험연구원 Korea Conformity Laboratories
한국골재산업연구원 Korea Aggregates Research Institute
(주)씨에스엠
DODAM ENGINEERING AND CONSTRUCTION
한일시멘트
KICET 한국세라믹기술원 KOREA INSTITUTE OF CERAMIC ENGINEERING & TECHNOLOGY
SANDOH